

27th EYGEC

27th European Young
Geotechnical Engineers

Conference

Double Events - MYGEC & EYGEC

26-27th September, 2019

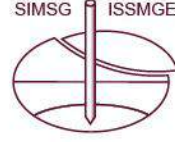
Kefaluka Resort Hotel Bodrum, Muğla-Turkey

PROCEEDINGS



www.eygec2019.org

27th EYGEC
27th European Young
Geotechnical Engineers
Conference
Double Events - MYGEC & EYGEC
26-27th September, 2019
Kefaluka Resort Hotel Bodrum, Muğla-Turkey



Turkish Society for ISSMGE (ZMGM)

Muğla Sıtkı Koçman University (MSKU)

International Society for Soil Mechanics and Geotechnical Engineering (ISSMGE)

Proceedings of the

27th European Young Geotechnical Engineers Conference

26-27 Eylül 2019, Bodrum, Turkey

EDITORS

Deniz ÜLGEN

Altuğ SAYGILI

Mehmet Rifat KAHYAOĞLU

Selda DURMAZ

Onur TOYGAR

Aysu GÖÇÜGENCİ

COMMITTEES

Organizing Committee

Deniz ÜLGEN (Muğla Sıtkı Koçman University)
Altuğ SAYGILI (Muğla Sıtkı Koçman University)
M. Rifat KAHYAOĞLU (Muğla Sıtkı Koçman University)
Onur TOYGAR (Muğla Sıtkı Koçman University)
Selda DURMAZ (Muğla Sıtkı Koçman University)
Aysu GÖÇÜGENCİ (Muğla Sıtkı Koçman University)
MUYAP-Construction Society (Muğla Sıtkı Koçman University)

International Advisory Committee

Prof.Dr. Charles W.W. Ng (President of ISSMGE)
Prof.Dr. Mario MANASSERO (Vice-President of the ISSMGE for Europe (2017-2021))
Prof.Dr. Roger FRANK (President of the ISSMGE (2013-2017))
Prof.Dr. Neil TAYLOR (ISSMGE Secretary General)
Prof.Dr. Antonio GENS (Immediate Past Vice-President of the ISSMGE for Europe (2013-2017))
Prof.Dr. George GAZETAS (Hellenic Society of SMGE - President)
Prof.Dr. Pierre DELAGE (Ecole Nationale des Ponts et Chaussées, Paris Laboratoire Navier/CERMES)
Assist.Prof.Dr. Andrea DOMINIJANNI (Politecnico di Torino-Italy/ISSMGE TC 215 Secretary)
Prof.Dr. Helmut SCHWEIGER (Austrian National Committee of ISSMGE)
Assoc.Prof.Dr. Ernest OLINIC (Romanian Society for Geotechnical and Foundation Engineering-Secretary)

Local Advisory Committee

Prof.Dr. Safiye Feyza ÇİNİCİOĞLU (ZMGM-Turkish Society for ISSMGE-President)
MSc. Müge İNANIR (ZMGM-Turkish Society for ISSMGE-Board Member)
Prof.Dr. Recep İYİSAN (ZMGM-Turkish Society for ISSMGE-Board Member)
Prof.Dr. Kutay ÖZAYDIN (ZMGM-Turkish Society for ISSMGE-Board Member)
Prof.Dr. Hilmi Turan DURGUNOĞLU (ZMGM-Turkish Society for ISSMGE-Board Member)
Prof.Dr. Fazlı Erol GÜLER (ZMGM-Turkish Society for ISSMGE-Board Member)
Prof.Dr. Kemal Önder ÇETİN (ZMGM-Turkish Society for ISSMGE-Board Member)
Prof.Dr. Mehmet Muhit BERİLGİN (ZMGM-Turkish Society for ISSMGE-Board Member)
Prof.Dr. İlknur BOZBEY (ZMGM-Turkish Society for ISSMGE-Board Member)

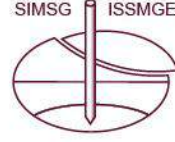
27th EYGEC
27th European Young
Geotechnical Engineers
Conference

Double Events - MYGEC & EYGEC

26-27th September, 2019

Kefaluka Resort Hotel Bodrum, Muğla-Turkey

SIMSG ISSMGE



MUĞLA



SPONSORS

Workshop Sponsor



Gold Sponsor



Silver Sponsor



Bronze Sponsor



SCIENTIFIC PROGRAMME

Thursday, 26th September, 2019

09:00 – 09:30 Registration

09:30 – 10:00 Welcome Ceremony

Chairperson: Prof. Mario Manassero

10:00 – 10:45 Keynote Speaker: Prof. Pierre Delage

Topic: The mechanical properties of Martian soils: insights from InSight

10:45 – 11:00 Coffee Break

11:00 – 12:15 Session I

Chairperson: Prof. Roger Frank

Optimization of monopile foundation for offshore wind turbines through advanced modelling
Soroosh Jalilvand

Scandinavian practices for calculation of second-order effects and buckling of precast concrete piles in soft soils
Jakob Rahbek Udengaard

Concrete stress-strain behavior and elastic modulus determination in foundation pile load test interpretation
Mateusz Wiszniewski, Adam Krasiniński

Laboratory experimental research of loading forces development acting on the side surface of the tapered piles in structurally unstable soils
Kupreichyk A.Yu

Deep borehole disposal (3000 - 5000 m) of spent nuclear fuel and radioactive waste - Considerations within a research project
Tino Rosenzweig, Wilhelm Bollingerfehr, Christin Dieterichs, Maxi Herold, Wolfram Kudla, Matthias Reich

12:15 – 13:30 Lunch Break

Chairperson: Assoc. Prof. Mehmet Barış Can Ülker

13:30 – 14:15 Keynote Speaker: Dr. Nejan Huvaj

Topic: Stability of natural and man-made slopes: from FS to RFEM and MPM

14:15 – 14:30 Coffee Break

14:30 – 15:45 Session II

Chairperson: Müge İnanır

Corrosion damage on cantilever walls

Rebhan Matthias J., Marte Roman, Tschuchnigg Franz, Vorwagner Alois

Reconstruction of the existing block of Atlantska Plovidba on Batala (Dubrovnik), in the business-residential complex

Andrea Milardović

Global stability analysis of reinforced earth retaining wall for Dubrovnik Airport expansion project

Ivan Mališa

A winkler type approach for the dynamic response of flexible walls retaining inhomogeneous soil

Koutsantonakis A. Christos, Kanellopoulos G. Konstantinos

Bearing capacity correction factors for soils and rocks

Ana Alencar, Svetlana Melentijevic, Rubén Galindo

15:45 – 16:00 Coffee Break

16:00 – 17:15 Session III

Chairperson: Prof. Mehmet Muhit Berilgen

Semi-analytical approach to ballast bed modelling during compaction

Olja Barbir, Dietmar Adam, Fritz Kopf, Johannes Pistor, Florian Auer, Bernhard Antony

Design challenges of a deep cofferdam quay wall in an arctic environment

Margarita Palaiologou, Hans Verbraeken, Michel Zeicher

Vulnerability of traffic embankments to liquefaction-induced deformations

Aleš Oblak, Janko Logar, Sebastjan Kuder, Antonio Viana Da Fonseca

Internal erosion and dam stability

Arthur Jedenius

Influence of crust thickness in relation to slip band development beneath embankments

Zülal Akbay Arama, S. Feyza Çinicioğlu

17:15 – 17:30 Coffee Break

17:30 – 19:00 Session IV

Chairperson: Dr. Harun Kürşat Engin

A numerical study upon the effect of cracks on the stability of dikes
Maria Luisa Taccari, Maria Konstantinou, Arno Rozing,

Influence of spatial variability of shear strength parameters on reliability-based assessment of dykes

Divya Varkey, Michael A. Hicks, Philip J. Vardon, Abraham P. Van Den Eijnden

Hoek - Brown failure criterion and importance of triaxial testing in a project of deep geological repository

Mgr. Radek Onysko

On evaluating slope stability in sensitive clay-a comparison of methods through a case study
Carolina Sellin

Influence of grain size and shape on evaluation of shear zone geometry
Candaş Öner, Çağdaş Arda, Özer Çinicioğlu

Residual shear strength of an overconsolidated clay: Back analysis and laboratory tests
Natalia S. Montero Cubillo, José Estaire Gepp

Friday, 27th September, 2019

Chairperson: Prof. Pierre Delage

09:00 – 09:45 Keynote Speaker: Dr. Andrea Dominijanni

Topic: Chemico-osmotic effects in bentonite-based barriers for containment applications

09:45 – 10:00 Coffee Break

10:00 – 11:15 Session V

Chairperson: Prof. Gürkan Özden

Cavity expansion analysis in elastic – brittle plastic rock mass
Haythem Gharsallaoui, Mustafa Jafari, Alain Holeyman

New 2D approach to estimate the displacements induced by tunnel boring machines
Nicolas Berthoz

Viséan limestone, karst and the N6 Galway City Ring Road, Western Ireland
Megan J. Dolan

Design and construction of a temporary launch pit for the Humber Feeder 9 pipeline and tunnel
Natalie Davey

Ground movement due to shaft construction
Joseph Newhouse

11:15 – 11:30 Coffee Break

11:30 – 12:30 Session VI

Chairperson: Dr. Andrea Dominijanni

Influence of stress state and stress history on the rate of secondary deformation for a high plasticity paleogene clay

Emil Mejlhede Kinslev, Ole Hededal, Irene Rocchi, Varvara Zania,

Correlations between soil conductivity and geotechnical parameters in Finnish clays

Markus Haikola

Laboratory testing and numerical modelling of the dynamic behaviour of Tagus River sand

Lúís Miranda, Laura Caldeira, João Serra, André Barbosa

Numerical modelling of consolidation processes of fine-grained dredged sediments: The containment facility of The Port of Gaeta

Armando De Lillis, Giada Maria Rotisciani, Salvatore Miliziano

12:30 – 13:30 Lunch Break

Chairperson: Bas Van Dijk

13:30 – 14:15 Keynote Speaker: Prof. İlknur Bozbey

Topic: Effects of soil pulverization level on lime stabilized clays: Implications on pavement design and performance

14:15 – 14:30 Coffee Break

14:30 – 15:30 Session VII

Chairperson: Dr. Nejan Huvaj

Soil permeability reduction of a dike by injecting organic matter and aluminum: Field data analysis

Saara Lassila

Liquefaction hazard assessment and zoning based on in-situ investigations – Case study

Jordanka Chaneva, Julijana Bojadjeva, Vlatko Sheshov, Kemal Edip, Toni Kitanovski

Investigation of the fluidised zone in deep vibrocompaction

Moritz Wotzlaw

Laboratory research on the physical and mechanical properties of soils improved with cement by deep mixing: Long-term behaviour

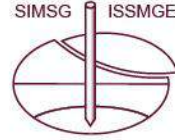
Oana Carasca

27th EYGEC
27th European Young
Geotechnical Engineers
Conference

Double Events - MYGEC & EYGEC

26-27th September, 2019

Kefaluka Resort Hotel Bodrum, Muğla-Turkey



15:30 – 15:45 Coffee Break

15:45 – 17:00 Session VIII

Chairperson: Assoc. Prof. Selman Sağlam

Construction of two storm water basins in the sand of pliocene
Lisa Miotti

Seismic behaviour of laterally disconnected shallow foundations
Viviana Mangraviti, Orazio Casablanca, Giovanni Biondi, Claudio Di Prisco, Ernesto Cascone

Calculation of the reinforced foundation of the sunflower seed oil warehouse in Mariupol
Commercial Seaport
A.V. Shokarev, E.A. Shokarev

Some aspects regarding the effect of foundations system on deformation behavior for buildings
on sloped terrain: Case study
O.C. Mureşan, V. F. Chiorean,

Levelling of skirted subsea structures and suction bucket jackets by application of suction or
overpressure in Plaxis 3D
Jesper Bjerre, Erik R. Sørli

17:00 – 17:15 Coffee Break

17:15 – 17:45 Closing Ceremony

TABLE OF CONTENTS

Corrosion damage on cantilever walls	1
Rebhan Matthias J., Marte Roman, Tschuchnigg Franz, Vorwagner Alois	
Semi-analytical approach to ballast bed modelling during compaction	7
Dipl.-Ing. Olja Barbir*, Univ.Prof. Dipl.-Ing. Dr.techn. Dietmar Adam,Priv.Do. Dipl.-Ing. Dr.techn. Fritz Kopf ,Dipl.-Ing. Dr.techn. Johannes Pistor	
Design challenges of a deep cofferdam quay wall in an arctic environment	13
Margarita Palaiologou*, Dr. Hans Verbraken, Michel Zeicher	
Cavity expansion analysis in elastic – brittle plastic rock mass	21
Haythem Gharsallaoui, Mustafa Jafari, Alain Holeyman	
Reconstruction of the existing block of Atlantska Plovidba on Batala (Dubrovnik), in the business-residential complex	29
Andrea Milardović	
Global stability analysis of reinforced earth retaining wall for Dubrovnik Airport expansion project	37
Ivan Mališa	
Influence of stress state and stress history on the rate of secondary deformation for a high plasticity paleogene clay	45
Emil Mejlhede Kinslev, Ole Hededal, Irene Rocchi, Varvara Zania,	
Scandinavian practices for calculation of second-order effects and buckling of precast concrete piles in soft soils	53
Jakob Rahbek Udengaard	
Correlations between soil conductivity and geotechnical parameters in Finnish clays	61
Markus Haikola	
Soil permeability reduction of a dike by injecting organic matter and aluminum: Field data analysis	69
Saara Lassila	

Construction of two storm water basins in the sand of pliocene	77
Lisa Miotti	
New 2D approach to estimate the displacements induced by tunnel boring machines	83
Nicolas Berthoz	
Investigation of the fluidised zone in deep vibrocompaction	91
Moritz Wotzlaw	
Deep borehole disposal (3000 - 5000 m) of spent nuclear fuel and radioactive waste - Considerations within a research project	99
Tino Rosenzweig, Wilhelm Bollingerfehr, Christin Dieterichs, Maxi Herold, Wolfram Kudla, Matthias Reich	
A winkler type approach for the dynamic response of flexible walls retaining inhomogeneous soil	107
Koutsantonakis A. Christos, Kanellopoulos G. Konstantinos	
Viséan limestone, karst and the N6 Galway City Ring Road, Western Ireland	115
Megan J. Dolan	
Optimization of monopile foundation for offshore wind turbines through advanced modelling	123
Soroosh Jalilvand	
Numerical modelling of consolidation processes of fine-grained dredged sediments: The containment facility of The Port of Gaeta	131
Armando De Lillis, Giada Maria Rotisciani, Salvatore Miliziano	
Seismic behaviour of laterally disconnected shallow foundations	137
Viviana Mangraviti, Orazio Casablanca, Giovanni Biondi, Claudio Di Prisco, Ernesto Cascone	
Liquefaction hazard assessment and zoning based on in-situ investigations – Case study	145
Jordanka Chaneva, Julijana Bojadjieva, Vlatko Sheshov, Kemal Edip, Toni Kitanovski	
Influence of spatial variability of shear strength parameters on reliability-based assessment of dykes	153
Divya Varkey, Michael A. Hicks, Philip J. Vardon, Abraham P. Van Den Eijnden	

A numerical study upon the effect of cracks on the stability of dikes	161
Maria Luisa Taccari, Maria Konstantinou, Arno Rozing,	
Levelling of skirted subsea structures and suction bucket jackets by application of suction or overpressure in Plaxis 3D	169
Jesper Bjerre, Erik R. Sørli	
Concrete stress-strain behavior and elastic modulus determination in foundation pile load test interpretation	177
Mateusz Wiszniewski, Adam Krasieński	
Laboratory testing and numerical modelling of the dynamic behaviour of Tagus River sand	185
Luís Miranda, Laura Caldeira, João Serra, André Barbosa	
Laboratory research on the physical and mechanical properties of soils improved with cement by deep mixing: Long-term behaviour	193
Oana Carasca	
Some aspects regarding the effect of foundations system on deformation behavior for buildings on sloped terrain: Case study	201
Olimpiu .C. Mureşan, V. F. Chiorean,	
Hoek - Brown failure criterion and importance of triaxial testing in a project of deep geological repository	209
Mgr. Radek Onysko	
Vulnerability of traffic embankments to liquefaction-induced deformations	217
Aleš Oblak, Janko Logar, Sebastjan Kuder, Antonio Viana Da Fonseca	
Bearing capacity correction factors for soils and rocks	225
Ana Alencar, Svetlana Melentijevic, Rubén Galindo	
Residual shear strength of an overconsolidated clay: Back analysis and laboratory tests	233
Natalia S. Montero Cubillo, José Estaire Gepp	
Internal erosion and dam stability	241
Arthur Jedenius	

27th EYGEC
27th European Young
Geotechnical Engineers
Conference

Double Events - MYGEC & EYGEC

26-27th September, 2019

Kefaluka Resort Hotel Bodrum, Muğla-Turkey



On evaluating slope stability in sensitive clay-a comparison of methods through a case study	249
Carolina Sellin	
Influence of grain size and shape on evaluation of shear zone geometry	255
Candaş Öner, Çağdaş Arda, Özer Çinicioğlu	
Influence of crust thickness in relation to slip band development beneath embankments	263
Zülal Akbay Arama, S. Feyza Çinicioğlu	
Ground movement due to shaft construction	271
Joseph Newhouse	
Design and construction of a temporary launch pit for the Humber Feeder 9 pipeline and tunnel	279
Natalie Davey	
Laboratory experimental research of loading forces development acting on the side surface of the tapered piles in structurally unstable soils	287
Kupreichyk A.Yu	
Calculation of the reinforced foundation of the sunflower seed oil warehouse in Mariupol Commercial Seaport	293
A.V. Shokarev, E.A. Shokarev	

CORROSION DAMAGE ON CANTILEVER WALLS

Rebhan Matthias J. *, *Graz University of Technology, Institute of Soil Mechanics, Foundation Engineering and Computational Geotechnics, rebhan@tugraz.at*

Marte Roman, *Graz University of Technology, Institute of Soil Mechanics, Foundation Engineering and Computational Geotechnics, roman.marte@tugraz.at*

Tschuchnigg Franz, *Graz University of Technology, Institute of Soil Mechanics, Foundation Engineering and Computational Geotechnics, franz.tschuchnigg@tugraz.at*

Vorwagner Alois, *AIT - Austrian Institute of Technology, alois.vorwagner@ait.ac.at*

ABSTRACT

Over the last years, an increase of damages and defects of geotechnical structures has been observed during detailed safety assessments. Most of the retaining structures along the Austrian road and railway network consists either of stone formations (stone pitchings and claddings) or concrete structures. For reinforced concrete (RC) structures, the damages are mainly resulting from reinforcement corrosion, which leads, next to a decrease in the service life of the structure, to a decrease of its bearing capacity. Due to the limitations of destructive and non-destructive methods for the determination of such damages, structural monitoring is often used for the safety assessment of retaining structures e.g. a cantilever wall. The first part of this paper concentrates on a developed monitoring system, which is based on an analytical approach. The second part describes a test set-up used for the validation of this monitoring system. In conclusion, the results from the test set-up are compared with the analytical approach of the problem and possible further developments of the monitoring system are addressed.

Keywords: Retaining Structures, Corrosion, Monitoring, Analytical Methods

1. CORROSION DAMAGES ON CANTILEVER WALLS

When it comes to the safety assessment of retaining structures [1] & [2] a main concern are corrosion damages on RC-structures. Associated with retaining structures, this type of damage can mostly be found on structures with a high degree of reinforcement such as cantilever walls or walls with an additional heal (Figure 1 Left).



Figure 1. Left: schematic cross-section of a cantilever wall with additional heal; Centre: Top view on the construction joint of a collapsed cantilever wall; Right: Detail of a corrosion damaged reinforcement bar along a construction joint

The concept shown in Figure 2 presents a new approach [8]. The graphic on the left side shows a concept to consider (and implement) a corrosion damage in an analytical model. The vertical part of a cantilever wall is modelled using a standard (and statically determined) cantilever [9], whereby the bending stiffness along its axis varies and considers uncracked ($EI_{t=\infty}^I$) and cracked ($EI_{t=\infty}^{II}$) regions of the cross-section. Additionally, the corrosion damage is taken into account by a decrease of the reinforcement diameter along a certain height (h_k). This decrease in bending stiffness ($EI_{t=\infty}^{II}$) leads to an increase in the deformation of the structure (deflection along the vertical axis [rad/1000], as shown in Figure 2 Centre). This diagram shows that an assumed increasing earth pressure (from increased active earth pressure E_{50-50} to earth pressure at rest E_0) results in an increase of the deformation of the structure. Additionally the deflection shows, that a decrease of the bearing capacity (due to corrosion) also leads to an increase in deformation. Besides deformation changes of the structural part (cantilever), the effect of corrosion on the cross-section resistance can also be identified. This is exemplary shown in the diagram on the right hand side of Figure 2. Within this diagram, different load levels (bending moments resulting from earth pressure) and different cross-section resistances (due to the reduction of the reinforcement diameter) are plotted. One can see, that both, changes in the earth pressure and changes of the cross-section resistance result in an increase of the strain distribution (concrete compression) of the cross-section.

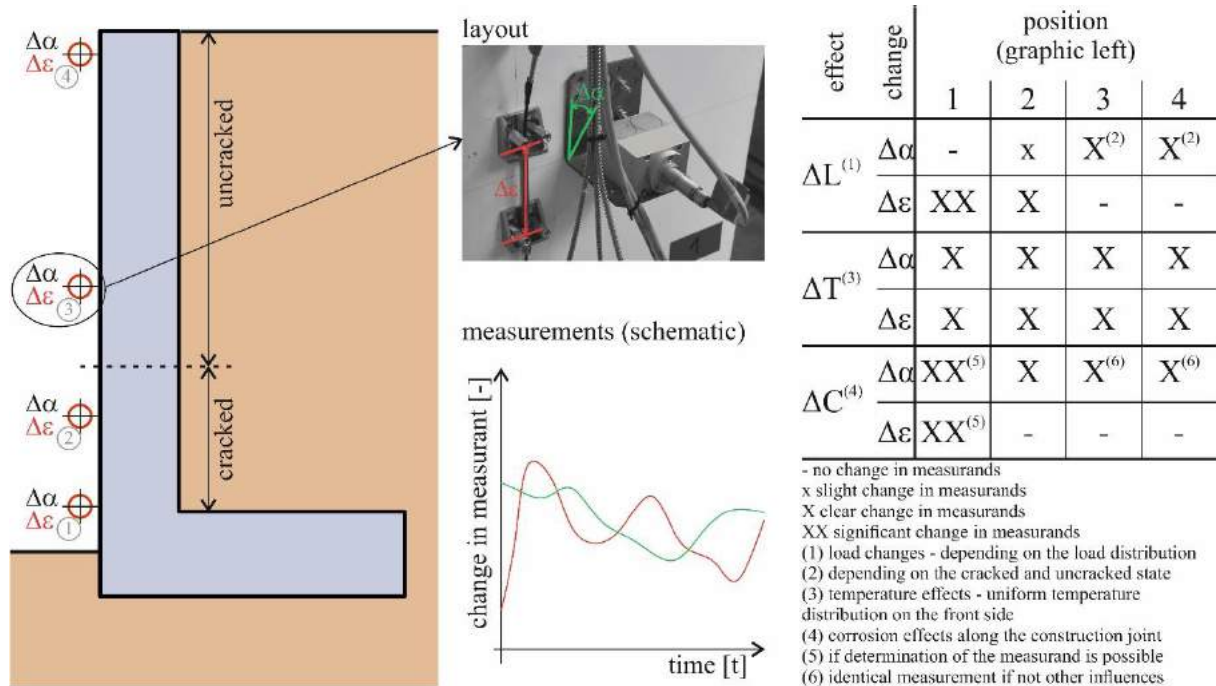


Figure 3. Schematic representation of the monitoring concept for corrosion damaged retaining structures; Left: Position of the sensors; Centre Top: Layout; Centre Bottom: Schematic measurement series; Right: Detection possibilities of the monitoring concept

Figure 3 shows the possibilities of the monitoring concept, when in addition to the inclination changes ($\Delta\alpha$) also the changes in concrete compression ($\Delta\varepsilon$) are determined. The graphic on the left side shows a schematic representation of sensors for the installation of the monitoring concept, which consists of a combination of tilt and strain sensors (sensor types - Figure 3 Centre Top) placed on the front side of a cantilever wall. The position of these sensors (① to ④ in Figure 3 Left) is divided into the uncracked (③ & ④) and cracked regions (① & ②) of the cantilever. Additionally, sensor ① is placed directly along the construction joint, to be able to measure influences due to reinforcement corrosion. The table on the right side of Figure 3 shows

the possibilities of this monitoring concept, where one can see, that for different positions and sensor types, different effects (load, temperature, corrosion) can be identified. For example, a corrosion damage (along the construction joint) will lead to changes in the concrete compression on sensor position ①, while the rest of the cross-section is unaffected. On the other hand, a (uniform) temperature load on the front side of the structure will lead to a constant increase in inclination and concrete compression (of the whole structure).

3. TEST SET-UP SIBS_V3

For the verification of the monitoring concept described in chapter 2, different test set-ups have been derived. Additionally, to mock-ups consisting of u-shaped cantilevers [10], a four-point bending test for corrosion damaged RC-structures has been studied.

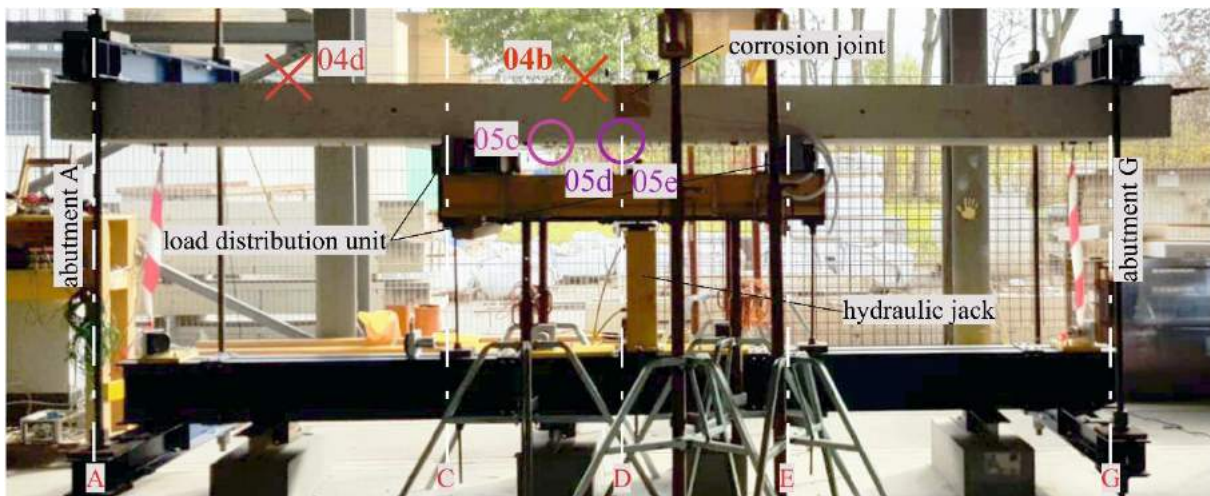


Figure 4. 4-point bending test - test set-up for the validation of the monitoring concept on corrosion damaged RC-structures (adapted acc. to [8])

The picture in Figure 4 shows the test set-up. A pre-cast concrete plate with a length of 5.00 m, a width of 1.37 m, a thickness of 0.25 m with a degree of reinforcement of $\rho = 0,63\%$ and a concrete quality C30/37 has been used. The main reinforcement (on the upper side of the plate) consisted of BSt 550, while for the rest of the reinforcement, stainless steel bars have been used and were electrically decoupled [10]. This was necessary because of the usage of Electro Chemical Machining (ECM) to simulate a corrosion damage along a joint (axis D). For the loading of the plate, a hydraulic jack (axis D) was installed, which transferred the load via two bearings (axes C and E) into the plate and was bypassed through the plate to the abutments (axes A & G). This loading procedure offered the possibility to simulate a constant bending moment between the axes C and E.

Next to a general overview of the test set-up (some parts of) the used measurement equipment and their position is schematically shown in Figure 4. The two sensors (X on the upper side) represent the position of two inclinometers at the midline of the plate. The sensor 04b was placed next to the corrosion joint, while the sensor 04d was placed outside the “influence zone” of the corroded area. On the bottom of the plate, three strain sensors were installed. The sensors 05c and 05d are placed at the midline of the plate, while the sensor 05e was placed on its edge. Same as the inclinometers, the sensors 05d and 05e were influenced by the corrosion joint. Additionally, to these sensors, other measurement equipment has been installed for the validation of the results and for reasons of redundancy.

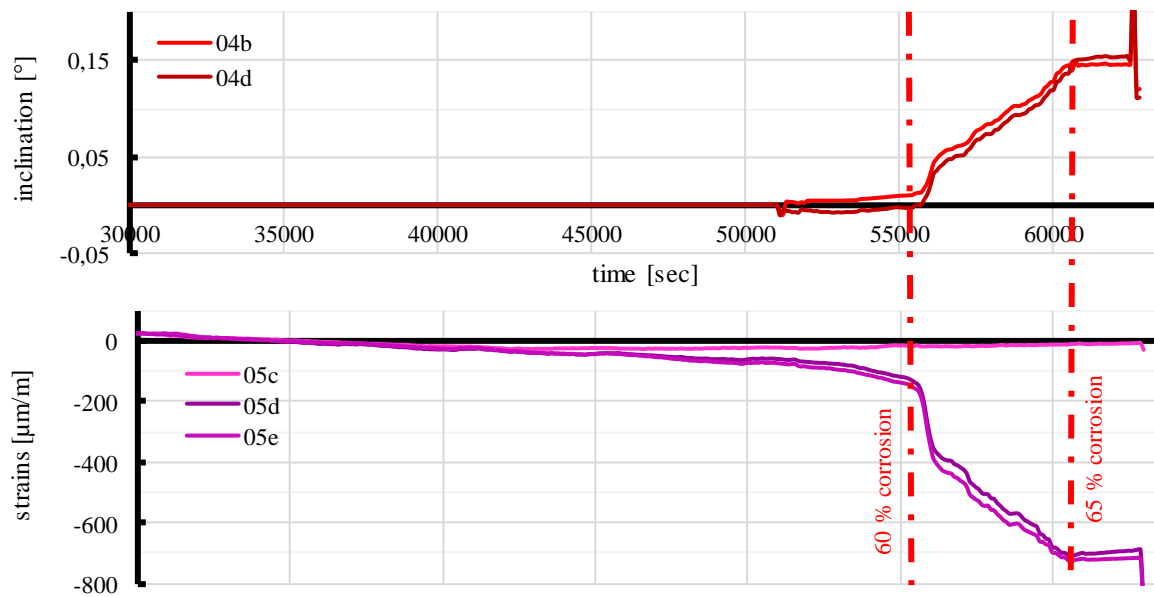


Figure 5. Results of the test set-up; Top: Changes in inclination; Bottom: Changes in concrete compression (adapted acc. to [8])

Some results for a corrosion damage simulated on the test set-up are shown in Figure 5. The diagram on top represents the results of the two inclinometers 04b and 04d, while the measurement values for the strain sensors (05c, 05d, and 05e) are shown in the diagram at the bottom. These two diagrams are related to a rate of corrosion of around 50 to 65 %. As one can see, the inclinometers show the same behaviour and only slight changes in the measured values have been obtained. On the other hand, the strain sensors (05d and 05e) show a slight increase during the conduction of the test and end with a strong increase at a rate of corrosion of 60 %. Furthermore, it can be seen, that the sensor outside the corrosion joint (05c) is not influenced by the corrosion.

These results show, that in general, an identification of a corrosion damage by changes in the inclination of a structure is possible. Nevertheless, this is only valid for a shear corrosion induced effect (as shown within this test set-up) on the structure. From a practical point of view, a combination of more than one effect will take place. Therefore, the determination of the concrete compressions (on certain points of the structure) offers additional and necessary information, which can assist in the identification of the effects leading to the change in the behaviour of the structure.

4. CONCLUSION

The analytical simulation and the results of the test set-up presented in this paper show, that the monitoring of corrosion damaged cantilever walls and other RC-structures is possible. Using the combination of inclination and strain sensors offers a wide range of possibilities. First, the determination of the behaviour of a RC-structure is possible, which enables the development of new methods when it comes to a safety assessment of such structures. Furthermore, a distinction between different influences on the behaviour of a cantilever wall is possible, which offers the possibility to distinguish between load, temperature and corrosion related effects on a structure. This could result in a much better (and applicable) safety assessment and will thereby increase the safety of geotechnical structures (and the adjacent infrastructure).

Additionally, to this analytical approach to take corrosion damage into account and the validation of the monitoring concept, a wide range of numerical simulations ([4], [11] & [12])

has been conducted. Furthermore to the topic of corroded retaining structures, other damages (e.g. corrosion of anchors) and new data acquisition methods for the safety assessment (e.g. the usage of Mobile Mapping Systems) have been addressed within the research project SIBS [13].

ACKNOWLEDGEMENT

This research was conducted within the scope of the national research project SIBS – “Safety assessment of existing retaining structures” - which is managed and supported by the Austrian Federation of Drilling-, Well Construction- and Special Foundation Constructors, the Autobahnen- und Schnellstraßen- Finanzierungs- Aktiengesellschaft and the Austrian Federal Railways and founded by the Austrian Research Promotion Agency FFG.

REFERENCES

- [1] RVS 13.03.61, 2014. „Qualitätssicherung bauliche Erhaltung – Überwachung, Kontrolle und Prüfung von Kunstbauten – Nicht geankerte Stützbauwerke“, Österreichische Forschungsgesellschaft Straße, Schiene, Verkehr, Austria.
- [2] ÖGG Empfehlungen, 2019. „Empfehlungen zur vertieften Prüfung und Beurteilung bestehender, unverankerter Stützbauwerke“, Austrian Society for Geomechanics, Austria.
- [3] Nürnberger, U., 1995. „Korrosion und Korrosionsschutz im Bauwesen: Band 1: Grundlagen Betonbau, Band 2: Metallbau, Korrosionsprüfung“, Bauverlag, Berlin, 1346 pages.
- [4] Rebhan, M.J., Vorwagner, A., Kwapisz, M., Marte, R., Tschuchnigg, F., Burtscher, S., 2017. „Safety assessment of existing retaining structures“, Geomechanics and Tunneling, 10(5): 524-532.
- [5] Kalenjuk, S., Lienhart, W., Rebhan, M.J., Marte, R., 2018. „Neue Ansätze zur Zustandsbewertung bestehender Stützbauwerke basierend auf 3D-Modellen aus dynamischem Laserscanning“, Messen in der Geotechnik, 22-23 February 2018, Braunschweig, Germany.
- [6] Kalenjuk, S., Leinhart, W., Rebhan, M., Marte, R., 2019. „Large-scale monitoring of retaining structures: new approaches on the safety assessment of retaining structures using mobile mapping“, Proceedings SPIE, Sensors and Smart Structures Technologies for Civil, Mechanical and Aerospace Systems, 27 March 2019, Denver, Colorado, USA.
- [7] GUMA, 2014. „Evaluation de l'état des murs de soutènement béton à semelles Etude pilote: Rapport de synthèse des phases 1 et 2“, Zurich, Switzerland.
- [8] Rebhan, M.J., 2019. „Korrosionsschäden bei Winkelstützmauern“, PhD Thesis, Graz University of Technology, Austria, 200 pages.
- [9] Suda, J., Hofmann, R., Strauss, R., Wendner, R., 2009. „Bemessung eines Stützbauwerkes nach Eurocode – Teil 1: Ständige Bemessungssituation“, Bautechnik, 86(12): 782-793.
- [10] Wöls, D., 2018. „Versuchstechnische Untersuchungen von korrosionsgeschädigten Winkelstützmauern“, M.Sc Thesis, Graz University of Technology, Austria, 175 pages.
- [11] Kwapisz, M., Vorwagner, A., Lechner, A., Rebhan, M.J., 2018. „Investigations on Existing Concrete Cantilever Walls Subjected to Reinforcement Corrosion“, Proceedings of the 2017 fib Symposium - High Tech Concrete - Where Technology and Engineering Meet, pp. 2083-2091, 12-14 June 2017, Maastricht, Netherlands.
- [12] Rebhan, M.J., Marte, R., Tschuchnigg, F., Vorwagner, A., Kwapisz, M., 2019, „Safety assessment of existing retaining structures“, Proceedings of the XVII European Conference on Soil Mechanics and Geotechnical Engineering, unpublished, Reykjavik, Island.
- [13] Forschungsgruppe SIBS, 2019, „Abschlussbericht Forschungsprojekt SIBS – Sicherheitsbewertung bestehender Stützbauwerke“, Eigenverlag VÖBU, Vienna, Austria.

SEMI-ANALYTICAL APPROACH TO BALLAST BED MODELLING DURING COMPACTION

Dipl.-Ing. Olja Barbir*, *TU Wien, Institute of Geotechnics, olja.barbir@tuwien.ac.at*

Univ.Prof. Dipl.-Ing. Dr.techn. Dietmar Adam, *TU Wien, Institute of Geotechnics; dietmar.adam@tuwien.ac.at*

Priv.Do. Dipl.-Ing. Dr.techn. Fritz Kopf, *FCP Fritsch, Chiari & Partner ZT GmbH, Vienna, kopf@fcp.at*

Dipl.-Ing. Dr.techn. Johannes Pistor, BSc, *TU Wien, Institute of Geotechnics; johannes.pistor@tuwien.ac.at*

Dipl.-Ing. Dr.techn. Florian Auer, *Plasser & Theurer, Vienna; florian.auer@plassertheurer.com*

Dipl.-Ing. Bernhard Antony, BSc, *Plasser & Theurer, Vienna; bernhard.antony@plassertheurer.com*

ABSTRACT

Throughout the world, the condition of the ballast bed is one of the most important parameters for a safe and economical operation of railway systems. Better knowledge of ballast condition provides an advantage in defining the optimum time for ballast bed cleaning or renewal. Tamping process is the core maintenance activity in ballasted track and it is crucial to the economical service life of the track and essential in restoring the track geometry for safe train operations. During the tamping process, the tamping tines interact with the ballast matrix, transferring the displacement caused by the dynamic excitation to the ballast, compacting it under the sleeper. This interaction is observed and measured in-situ within the framework of this research project. Serving as a mean of comparison and confirmation with the conducted in-situ measurements, a semi-analytical model of the tamping unit – ballast matrix interaction is developed. The tamping unit is presented by a simple system of rods with a dynamic excitation overlapped by a hydraulic cylinder movement modelled with a variable rod length. The ground model is based on a semi-infinite truncated cone for vertical translation, the half space being represented by the Kelvin-Voigt model [5], which consists of a purely elastic spring and a purely viscous damper connected in parallel. The soil model has been extended by an additional plastic spring, modelling the plastic deformation of the ballast matrix, i.e. its compaction under the sleeper. The ballast model described presents a reliable method of modeling non-cohesive soils, and can as such be implemented on other granular materials under dynamic loading.

Keywords: Track Tamping, Track Ballast Compaction, Semi-analytical Modelling

1. INTRODUCTION

During the tamping process, the tamping tines interact with the ballast matrix, transferring the displacement caused by the dynamic excitation overlapped with the extension in the hydraulic cylinder to the ballast, compacting it under the sleeper. This interaction is observed and measured in-situ in several locations in Austria. Conclusions regarding differences in response and resistance to compaction of both new and fouled ballast material are made and presented in this paper.

2. EXPERIMENTAL APPROACH

The operating principle of a tamping machine i.e. tamping unit (Figure 1) is lifting the track up to the level determined by previous measurements and simultaneously position it laterally. Once the track is in the intended position, the tamping tines penetrate the ballast and the tamping process begins. The squeezing movement begins subsequently and is defined as a closing movement of the tines around the sleeper with the objective of refilling the gap created beneath the sleeper and compacting the ballast. The non-synchronous tamping principle, in which the tamping is performed, described as movement of all tamping tines with the same force, independent of the path, together with directional vibrations, ensures a uniform ballast compaction. [1]

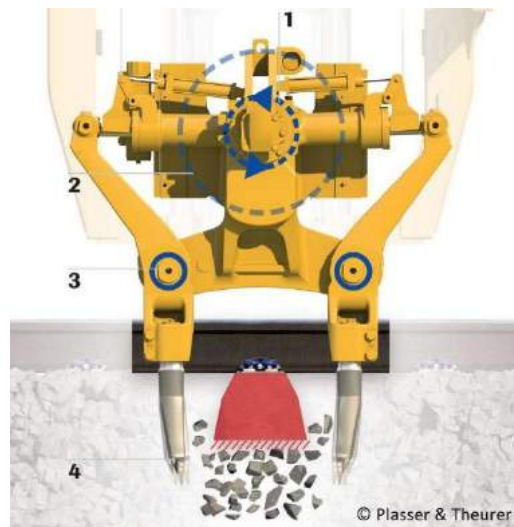


Figure 1. Tamping unit lowered into work position: (1)Vibration by eccentric shaft, (2)Power reserve from balance weight, (3)Fixed pivot, (4)Stable amplitude

Within the framework of a joint research project of Plasser & Theurer, Export von Baumaschinen, GmbH, and the Institute of Geotechnics, TU Wien, the „Dynamic Tamping Express 09-4X E^{3c}“ tamping machine was equipped with a number of strategically positioned sensors (Figure 2) in order to describe the interaction of the tamping tines with the ballast. Strain gauges (Figure 2; red) were applied and used to measure the lowering and lateral tine forces. Accelerometers (Figure 2; blue) placed on the upper point of the tamping arm allowed a precise calculation of the tine oscillation amplitude in a local coordinate system. In conjunction with the pressure (Figure 2; yellow) and elongation measurement at the hydraulic cylinders (Figure 2; green) the tamping process could be fully documented and subdivided [2].

2.1. Experimental Results

An initial approach towards successful data analysis implies a newly developed method of dynamic measurement analysis [6], the load-displacement curve i.e. lateral force-oscillation displacement diagram, presenting a single cycle during the tamping process (Figure 3). This presentation allows an insight into seven tamping parameters essential for a successful data evaluation:

- oscillation amplitude (1)
- maximal lateral force (2)
- ballast matrix stiffness/response during loading (3) and unloading (4)
- energy transferred into the ballast (area under the curve) (5)
- points of tamping tine - ballast contact - begin (6) and loss of contact (7)

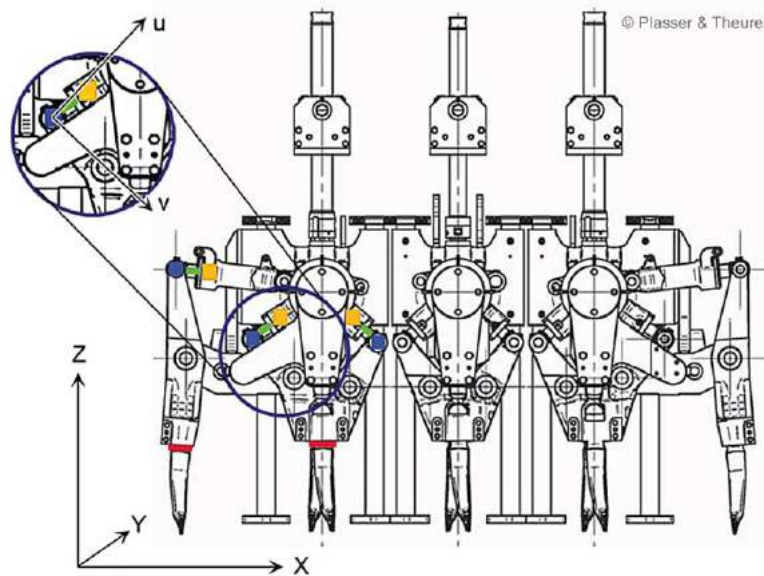


Figure 2. Position of the measuring units [2]

Depending on the observed part of the tamping process, the load-displacement curve can take several different shapes. During initial contact, while penetrating the ballast, the diagram displays a typical elliptical shape, caused by the unsymmetrical shape of the tine. During the course of a squeezing movement, the tamping tines compact the ballast beneath the sleeper, forming a typical curve, as can be seen in Figure 3. The eccentricity of the curve is attributed to the squeezing velocity, where the negative part of the curve would decrease with the increase of velocity. However, the velocity has to be kept under certain limits for the tamping tine to remain in contact with the ballast for the time required for the transfer of energy (minimal required impulse duration - 0.8 to 1.2 seconds) [7].

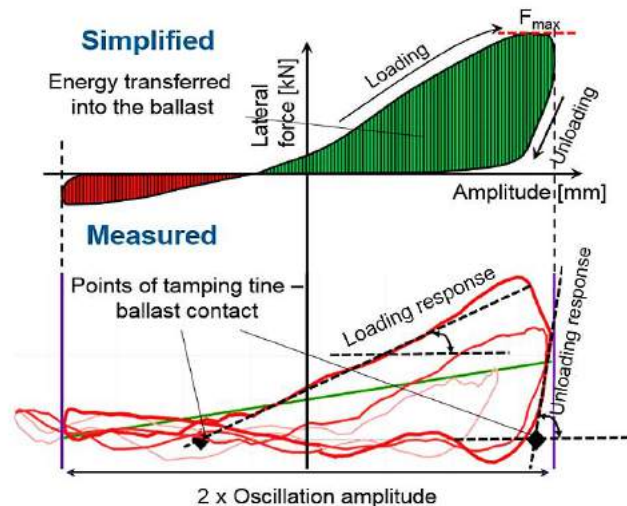


Figure 3. Simplified load – displacement curve (above), and the curve as a result of the conducted measurements (below)[1]

3. TAMPING UNIT - BALLAST MATRIX INTERACTION

A semi-analytical mechanical model of the tamping tine - ballast interaction during the squeezing movement is developed and is used as a tool for future development of a condition based tamping process. The mechanical model consists of two fundamental parts – the tamping unit and the soil or the ballast matrix model, focusing especially on the interaction between two parts, and on the tamping tine - soil contact conditions. The calculations are done using Matlab R2017b.

The calculation of all state variables is time dependent, based on the selected sampling rate and time step. Due to the semi-analytical calculation, a vector is calculated for each state variable, portraying their development throughout the squeezing process modeled. The simulation time of 1 second is selected based on the state-of-the-art tamping machine characteristics, working with a squeezing time ranging from 0.8 to 1.2 seconds.

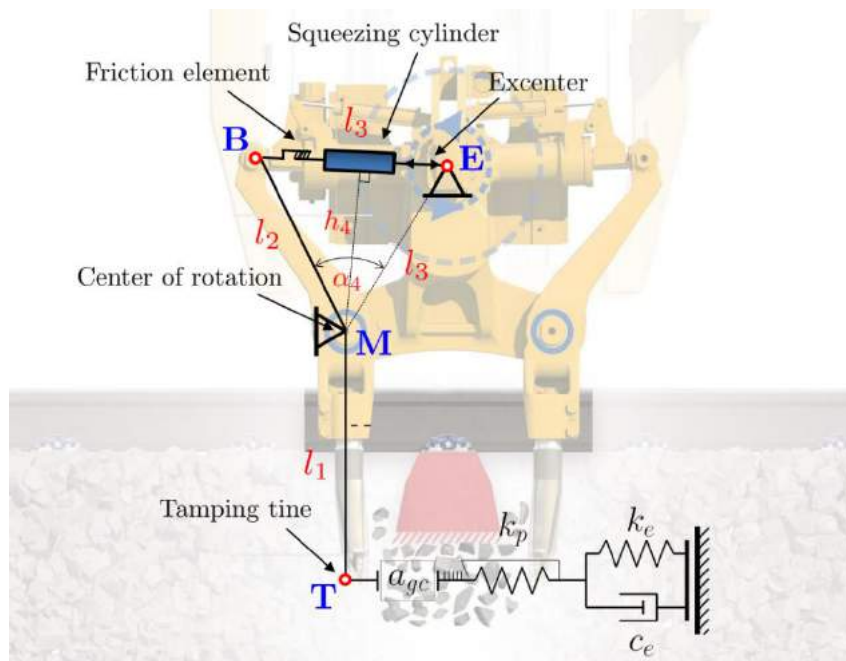


Figure 4. Mechanical model of the tamping unit – ballast matrix interaction [2]

3.1. Tamping Unit

The tamping unit is modelled as a simple system of rods with a dynamic excitation overlapped by a hydraulic cylinder movement modelled with a variable rod length. It is additionally extended with a friction element, incorporated into the upper part of the tamping arm (Figure 4). The model is based on the exact geometry of the „Dynamic Tamping Express 09-4X E³“ [2].

3.2. Ballast Matrix Model

The ballast matrix model used to show ballast compaction under the sleeper is made up of three components (Figure 4):

- Kelvin-Voigt model - elastic deformation of the ballast matrix, half space of an idealized homogeneous soil is represented by a purely elastic spring and a purely viscous damper connected in parallel
- Plastic spring - plastic deformation of the ballast matrix
- Gap-closing acceleration

During the tamping process, the motion of the tamping tine is imposed on the ballast, thereby inducing deformation of the matrix.

3.3. Mechanical Model Operating Phases

The semi-analytical approach is able to model both the displacement and force-controlled motion of the tamping unit, as well as all three operating phases of one cycle during the squeezing process:

- Loading – tamping tine in contact with the ballast matrix, both elastic and the plastic segments of the model are activate (compressed).
- Unloading – backward movement of the tamping tine, still in contact with the ballast matrix. The elastic spring stretches back, modelling the elasticity od the ballast matrix, while the plastic spring remains „locked“, modelling the remaining plastic deformation of the matrix, i.e. ballast compaction under the sleeper.
- Withdraw – tamping tine loses contact with the ballast matrix and reaches back before the next cycle begins. Following the loss of contact between the tamping tine during its backwards movement and the ballast matrix, a vertical ballast wall forms between the two model components. In order to enable the modelling of ballast grains motion during this phase of the cycle, an acceleration of the ballast stones during loss of contact i.e. during withdraw a_{gc} (Figure 4) is calculated. Implementation of the "gap closing acceleration" enables calculation of the exact ballast matrix position before the tamping tine reaches it again and the next cycle begins.

This approach grants a possibility to model all of the different ballast conditions and phenomena measured in-situ, ranging from new and clean to the fouled ballast bed conditions, as well as a verification of the in-situ measured load-displacement curves.

4. RESULT COMPARISON

Following data analysis of the selected in-situ measurements first reference values can be established for the two edge cases of the track condition:

- Track reconstruction / new ballast conditions
- Track maintenance / fouled ballast conditions

The highest level of divergence between the two edge cases can be noted for the following four tamping parameters: maximum force, energy per squeezing movement and loading and unloading response of the ballast matrix (Table 1), as well as in the shape of the load-displacement curves (Figure 5).

Correlation between the in-situ and the semi-analytical approach can be observed, confirming the reliability of the developed model (Figure 5). The same model is used to display both ballast conditions, and the ballast fouling process is presented as a decrease of the ballast elasticity. In the semi-analytical approach, this phenomenon is modelled as an increase of the elastic spring stiffness in the Kelvin-Voigt model that progresses with the fouling of the material, making it less elastic and more resistant to compaction.

Table 1. Parameter comparison of the two ballast conditions [1]

Tamping force	[kN]	New < Fouled
Energy per squeezing movement	[J/s]	New < Fouled
Loading response	[MN/m]	New < Fouled
Unloading response	[MN/m]	(-) New (+) Fouled

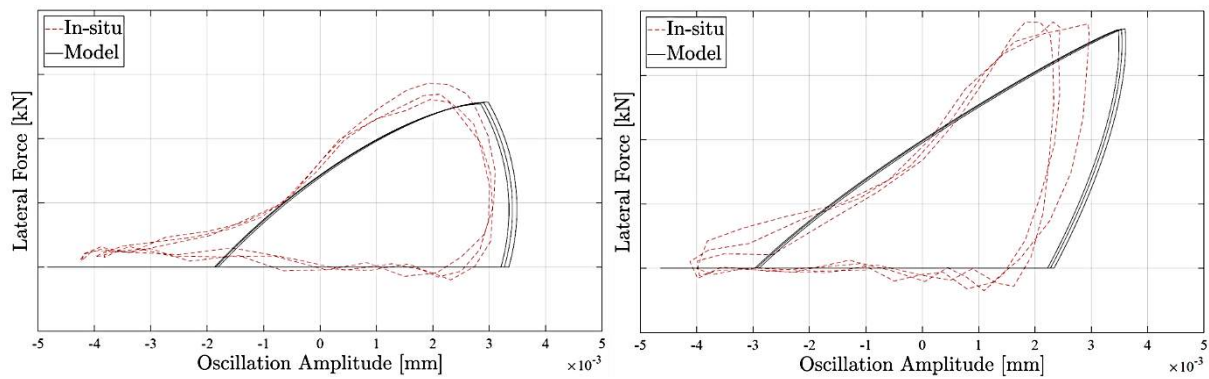


Figure 5. Load-displacement curves of the two selected in-situ measurements compared to the semi-analytical approach (new ballast (left), fouled ballast (right)) [1]

5. CONCLUSION

Mechanical model developed can depict both edge cases of the ballast condition, as well as the progression of ballast fouling. It is used as a reliable tool for a parameter study as well as a determination of the tamping parameters that should be adapted according to the condition of the ballast material at a given location (condition-based tamping). Tamping process adjusted to the in-situ ballast condition would increase the probability to achieve the optimum ballast compaction. Better knowledge of ballast condition provides the infrastructure manager the additional advantage of defining the optimum time for ballast bed cleaning or renewal, in addition to the increase of quality of the whole track system while reducing costs by extending maintenance cycles.

REFERENCES

- [1] Barbir et al., 2019. “*Compaction energy as an indicator for ballast quality*”, 12th World Congress on Railway Research, 28. Oktober – 01. November 2019, Tokyo, Japan (unpublished)
- [2] Barbir O., “*Development of condition-based tamping process in railway engineering*”, Doctoral thesis, TU Wien, Vienna, Austria (unpublished)
- [3] Kopf, F., 1999. „*Flächendeckende dynamische Verdichtungskontrolle (FDVK) bei der Verdichtung von Böden durch dynamische Walzen mit unterschiedlichen Anregungsarten*“ (in German). Doctoral thesis, TU Wien, Vienna, Austria, 408 pages
- [4] Pistorl, J., 2016. „*Verdichtung mit Oszillationswalzen*“ (in German), Doctoral thesis, TU Wien, Vienna, Austria, 335 pages.
- [5] Wolf, J. P., 1994. „*Foundation Vibration Analysis Using Simple Physical Models*”. Prentice Hall. Lausanne, Switzerland, 233 pages.
- [6] Plasser Theurer, Export von Bahnbaumaschinen GmbH, 2017. „*Stopfen mit Verdichtungskontrolle - Verfahren und Vorrichtung zum Verdichten eines Gleisschotterbetts*“ (in German), Patent submitted 29.05.2017 in Vienna, Austria
- [7] Fischer, J., 1983. „*Einfluss von Frequenz und Amplitude auf die Stabilisierung von Oberbauschotter*“ (in German), Doctoral thesis, Technical University Graz, Austria, 332 pages.

DESIGN CHALLENGES OF A DEEP COFFERDAM QUAY WALL IN AN ARCTIC ENVIRONMENT

Margarita Palaiologou*, *BESIX*, mpalaiologou@besix.com

Dr. Hans Verbraken, *BESIX*, hverbraken@besix.com

Michel Zeicher, *BESIX*, mzeicher@besix.com

ABSTRACT

In the region of Nunavut, Canada, a new quay is required in to enable the increase of the production rate of a mine. The dock will comprise a 180m long and 25.5m high quay wall supporting a conveyor and shiploader system. The arctic conditions impose very tight planning restrictions to the construction process. The quay is designed as a deep cofferdam structure, which appeared the preferred solution in order to limit the environmental impact during construction. It consists of a combined wall system, with tubular steel piles driven through weak surficial layers and medium dense sands. It will be filled with rockfill which will also provide support for a shiploader travelling along the quaywall on rails supported by a reinforced concrete slab foundation. The quay wall will be subjected to berthing and mooring loads from Panamax and Capesize vessels, ice floes and earthquake. However, the main complexity lies on the fulfilment of the serviceability criteria of the shiploader under its heavy loading during operation. This paper presents the main geotechnical design challenges of the deep cofferdam and the developed approach to ensure a safe construction and a durable long term operation of the quay.

Keywords: Cofferdam Quay Wall Design, Arctic Environment, Shiploader, Earthquake, Displacement Control

1. INTRODUCTION

BESIX VanPile JV has been awarded the design and construction of a quay in Nunavut, Canada. The quay needs to accommodate Panamax (65000 DWT) to Capesize (175000 DWT) vessels and consists of a circa 180m long, 25.5 deep cofferdam and dock area (Figure 1). A shiploader supported on a main pivot foundation point and on a shallow slab foundation will operate over the full length of the quay (Figure 1).

The extreme climatic conditions of the arctic environment impose significant constructability and time limitations (e.g. difficulty to cast in situ reinforced concrete elements, limited access to supply and construction time). Subsequently, the quay wall will follow a deep cofferdam combiwall construction. The cofferdam will be the first structure to be installed in the open sea and then the area behind it will be backfilled to form the dock area. The cofferdam will be constructed by advancement of a trolley system supported on the parts of the cofferdam being already driven, as shown in Figure 1. The trolley system will reach the quay wall area via an access trestle.

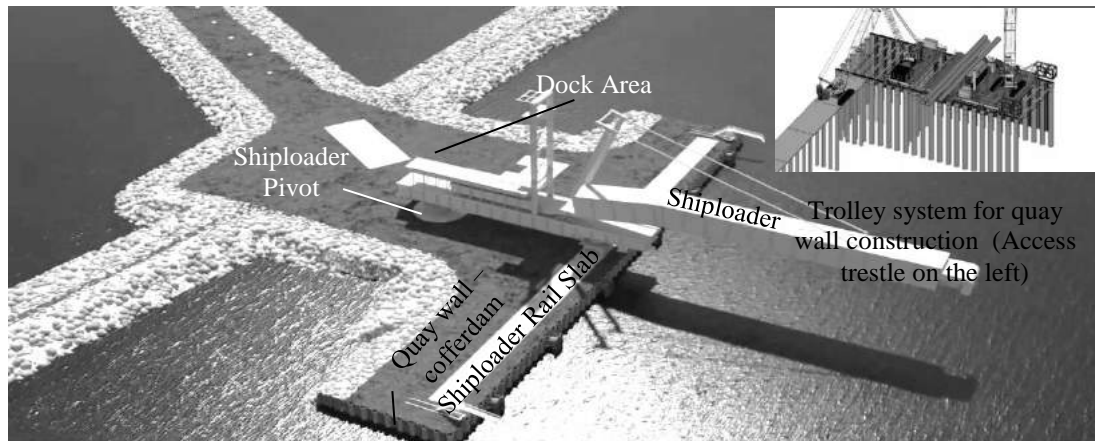


Figure 1. Quay layout. On the right: Access trestle and trolley system during construction.

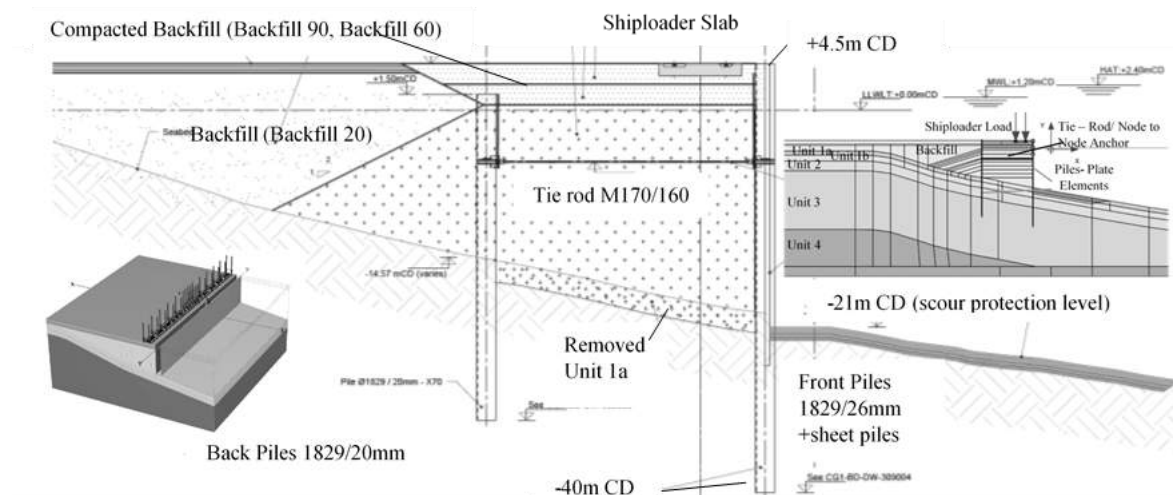


Figure 2. Quay wall typical cross section. Up right: Plaxis 2D cross section. Down left: Plaxis 3D model

The quay wall typical cross section is illustrated in Figure 2. The 25.5m high cofferdam comprises a combiwall at seas-side, with a front row of steel piles. The piles are at a centre to centre distance 3.37m and they are connected to each other with sheet piles. The front row is then anchored through a tie rod to a back row of anchor piles. The piles embedded depth extends to 20m below the seabed. The backfill will be heavily compacted at the upper 4m (above the sea water level) and it will be placed on a seabed covered by a layer of sensitive fines (Unit 1a-average 2m thickness), followed by silty sand soil layers deeper than 30m (Unit 1b, Unit 2-4) at a slope of approximately 9.5 - 12° degrees. The upper 2 meters of weak soil layers are removed inside the cofferdam. More details on the soil properties are provided in section 2. Apart from the shiploader and mooring/berthing loads, the quaywall is exposed to ice and earthquake loads (PGA=0.042g for firm soil conditions)

The design has to comply with the Canadian LFRD (Load and Resistance Factored Design) approach, as described in [1] and [2]. Additional international guidelines are also advised ([3], [4]). Last but not least, during operation the travelling part of the shiploader that rests on a

shallow foundation imposes very demanding displacement criteria in compliance to ISO 12488-1 [5].

Attention is paid in this paper to two of the key aspects of the design, namely the settlement of the foundation of the shiploader, which is related to the service limit state of the structure and the dynamic behaviour of the cofferdam during earthquake loading (extreme event).

2. METHODOLOGY

The following paragraphs describe the methodology adopted to provide a design that allows for a reliable displacement control during the service life of the structure and a reliable assessment of the dynamic soil –structure interaction during earthquake loading.

2.1. Selection of Geotechnical and Structural Models

Due to the complexity of the geometry, loads and soil conditions, finite element modelling deems appropriate. Plaxis 2D nonlinear FEM [6] is used as the baseline model to describe the overall quay wall behaviour under static loading conditions. However, since the rail slab design is mainly affected by 3D phenomena not captured in Plaxis 2D (load distribution along the slab), Plaxis 3D analyses are also required for specific aspects.

To capture the impact of the local site topography effects during earthquake (inclined soil profile in combination with very deep cofferdam), dynamic time history analyses in Plaxis 2D are preferred against more simplified methods (design response spectra provided by design codes).

The structural design and the deflection control of the shiploader shallow foundation is carried out using a structural slab on a subgrade in a finite element code [7].

2.2. Constitutive Model and Material Properties

Hardening Soil with Small Strain Stiffness-HS_{small} [8] is used in static analyses, as it is more reliable in working load conditions. The same model is also used for the dynamic case, as it allows the simulation of hysteretic damping (G- γ attenuation curve).

CPT and SCPT tests were carried out at the project area in 2017 and 2018 and the available results have been used to derive the parameters of the HS_{small} soil model. Indicative CPT q_c results are available in Figure 3. Hardening Soil model main input parameters are the soil stiffness, expressed through the triaxial loading stiffness, E_{50} , the triaxial unloading stiffness, E_{ur} , and the oedometer loading stiffness, E_{oed} . The derivation of the oedometer modulus for the Plaxis model is based on empirical correlations with q_c results (e.g. [9]). Then, the triaxial stiffness of the soil is defined following the average values $E_{ur}=3E_{50}$ and $E_{oed}=E_{50}$ [6]. Since the HS_{small} accounts for the stress-dependency of stiffness moduli, the input stiffness values are related to a reference stress (p_{ref}).

HS_{small} describes also the increased soil stiffness at small strains, G_0 , and its attenuation when strains (γ) increase. Thus, the small strain stiffness, G_0 , of the soil and the strain at which the soil stiffness has decreased to 70% its initial value ($\gamma_{0.7}$) is required. G_0 is related to the shear wave velocity through the simple law: $G_0 = \rho v_s^2$, where ρ is the soil unit density and v_s is the shear wave velocity. As shown in Figure 4 and Figure 5, the available SCPT data were comparatively assessed against the shear wave velocity –CPT correlations provided by [10], [11], [12]. Then, conservative estimates of the shear wave velocity profile are adopted for the design (Table 1). $\gamma_{0.7}$ values are selected assuming for all soils that they follow the Ishibashi – Zhang [13] G- γ attenuation curves. Regarding the backfill, the majority of which will be installed below water surface, low estimate values were assumed. G_0 values were derived using

the Alpan [14] curves. The soil material properties adopted for the design are illustrated in Table 1.

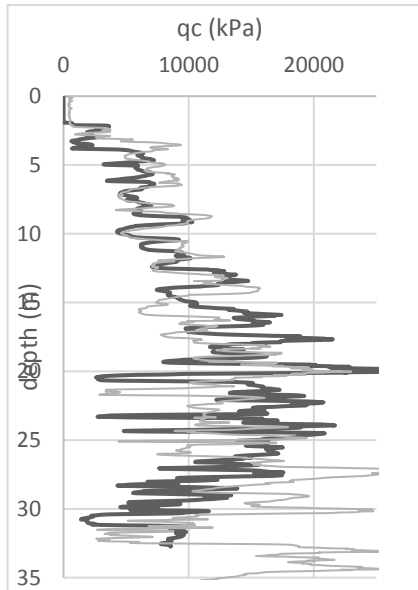


Figure 3. Indicative CPT results

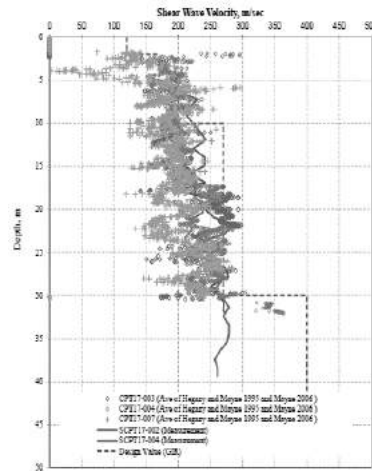


Figure 4. Shear wave velocity profile based on Hegazy and Mayne (1995) and Mayne (2006) equations.

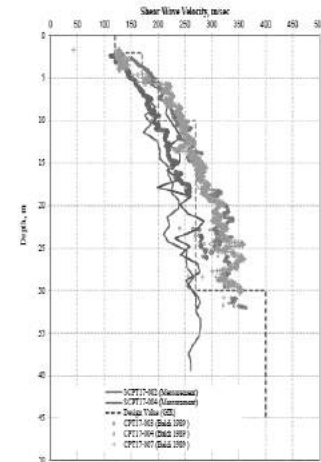


Figure 5. Shear wave velocity profile based on Baldi et al. (1989) equation.

Table 1. Soil material properties and HSsmall input parameters

Material	Elevation (varies mCD)	Description	E50 – ref (kN/m ²)	Eoed(kN/m ²)	Eur (kN/m ²)	pref (kN/m ²)	m	φ'	Go,ref (kPa)	γ0.7	qc (MPa)	Vs (m/s)
Backfill 90	4.5	Compacted Granural	90000	90000	270000	18	0.5	37.50	225000	0.2 x 10 ⁻³		
Backfill 60	2.5	Compacted Granural	60000	60000	180000	50	0.5	37.5	187500	0.12x10 ⁻³		
Backfill 20	0.5	Uncompacted Granular	20000	20000	60000	60	0.5	37.50	90000	0.15x10 ⁻³		
Unit 1a	-21	Sensitive Fines	3000	3000	9000	7	0.7	22	25920	0.19x10 ⁻³	0.4-0.7	120
Unit 1b	-23	Silty SAND, loose	9000	9000	27120	25	0.5	26	50000	0.14x10 ⁻³	1.5-2.5	170
Unit 2	-26	CLEAN SAND and SILTY SAND.	28000	28000	84000	60	0.5	32	81600	0.23x10 ⁻³	5-10	200
Unit 3	-31	Fine to coarse grained SAND and gravel.	35740	35740	107000	113	0.5	34	156000	0.55x10 ⁻³	7-20	270
Unit 4	-51	Dense unit).	60000	60000	180000	387	0.5	34	343000	0.55x10 ⁻³	>15	400
Secant triaxial stiffness at 50% yield stress, E50 –ref (kN/m ²)						Effective cohesion, c' (kN/m ²) =0kPa for all soil layers						
Tangent Oedometer modulus at pref, Eoed(kN/m ²)						Peak effective friction angle, φ						
Unloading stiffness modules at pref, Eur (kN/m ²)						Dilation angle ψ (7.5° only for the backfill layers, 0° for all other soils)						
Reference pressure, pref (kN/m ²)						Average Tip Resistance from CPT (MPa)						
Power for stress level dependency of stiffness, m						Shear Wave velocity profile (before backfill installation) measured						

2.3. Plaxis 3D-Plaxis 2D-SCIA Calibration

Since the rail slab design is mainly affected by 3D phenomena not captured in Plaxis 2D (load distribution along the slab), Plaxis 3D analyses are required to calibrate the equivalent load from the finite shiploader into an “infinite strip load” to input in the 2D analyses. In both Plaxis 2D and 3D models, the combined wall is modelled using plate elements.

The discrete wheel loads of the shiploader are therefore inserted in a Plaxis 3D model and the displacements on the quaywall are calculated. Then, equivalent ‘infinitely’ long surface loads over the width of the reinforced concrete slab are inserted in Plaxis 2D in an iterative process, with the aim of achieving a compatibility of displacements between the 2D and 3D model. The calibrated “equivalent” loads are finally adopted for the Plaxis 2D Finite Element Analysis.

For the structural design of the slab in SCIA software, the soil structure interaction is described by “soil springs” with a (elastic) subgrade modulus. The subgrade modulus is derived through calibration against Plaxis 3D displacement analyses results.

2.4. Earthquake Dynamic Modelling

As mentioned before, the earthquake loading is approached through a dynamic time history analysis to capture the local site effects. Five real time histories with the characteristics (magnitude, soil conditions and PGAs) of seismic sources that can occur at the project location have been selected and matched to the target response spectrum of the NBCC 2015[15] for a return period of 475 years; namely the Sierra Madre 1991, the Whittier Narrows 1987, the Chamfant Valley 1986[16], the Ano Liosia 1999 and the Gran Sasso 2009[17] time histories. The vertical component of the ground acceleration is not considered due to its low magnitude. To reduce uncertainty, the peak values and not the average are considered for the design.

Prior 1-D equivalent linear site response analyses with STRATA [18] software are run to enable a preliminary assessment of the soil behaviour (disregarding topography phenomena) and provide input for the finite element analysis. Then, a Plaxis 1D model is created to calibrate the soil parameters. After the validation of the Plaxis 1D response against the 1D equivalent linear results, the full Plaxis 2D time-history analysis can be run. A Rayleigh damping equal to 1% between 1Hz-5Hz is attributed to the soil layers, to account for hysteretic damping at very small strains. The hydrodynamic pressure developed in the saturated rockfill is also taken into account. The pressure is estimated following Westergaards [19] equation and is inserted as a linear load (increasing with depth) in the model.

3. RESULTS AND DISCUSSION

3.1 Static Analyses: Displacement Control of Shiploader Foundation

The calibration process between Plaxis 3D and Plaxis 2D led to the conclusion that a load reduction factor of 0.60 could achieve a compatibility of displacements between the Plaxis 3D and Plaxis 2D model. This reduction factor represents the fact that the load is spread through the soil before acting on the quay wall. This reduction factor can also be related to a ‘distribution angle’ of 36°, in order to take into account the distance from the shiploader foundation to the quay wall. Indicative results demonstrating the matching achieved between the Plaxis 2D model and the Plaxis 3D model under a load of 375kN/m per rail for a load spreading at an angle of 36° is available in Figure 6.

The efficient calibration between the SCIA soil springs and the Plaxis 3D model is illustrated in Figure 7. The satisfactory calibration of the models in combination with the use of Hardening Soil Small model enabled a reliable assessment of the anticipated displacements during operation. In this way, it enhanced the detailed design of the preloading phases of the slab before

the operation of the shiploader and the detailing of the shiploader rail adaptation systems in order to ensure a compliance with ISO 12488-1.

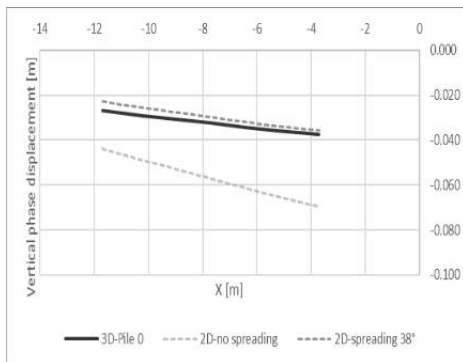


Figure 6. Phase displacements – transversal cross section – comparison 2D-3D

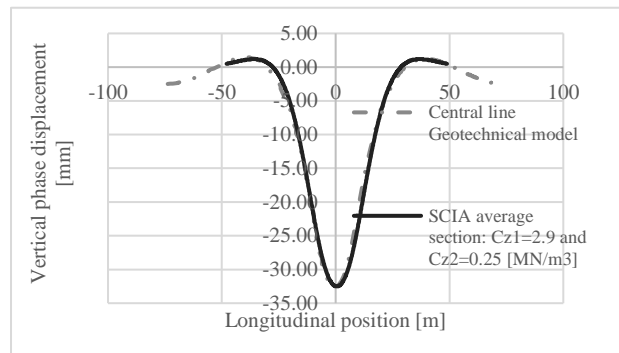


Figure 7. Geotechnical and SCIA FEM vertical displacements

3.2 Dynamic Analysis

Indicative results illustrating the quay wall behaviour under dynamic loading are provided below. Figure 8 shows the comparison between the design response spectrum provided by the NBCC for the same site class category and event probability, the response spectrum resulting from the 1D equivalent linear site response analysis in STRATA and the free field response at the middle of the shiploader slab for one indicative time history (Acc1x). It becomes apparent that the simplified response spectra provided by codes cannot describe sufficiently the soil response near the frontline when thick soil layers or local site effects (e.g. slope) are present.

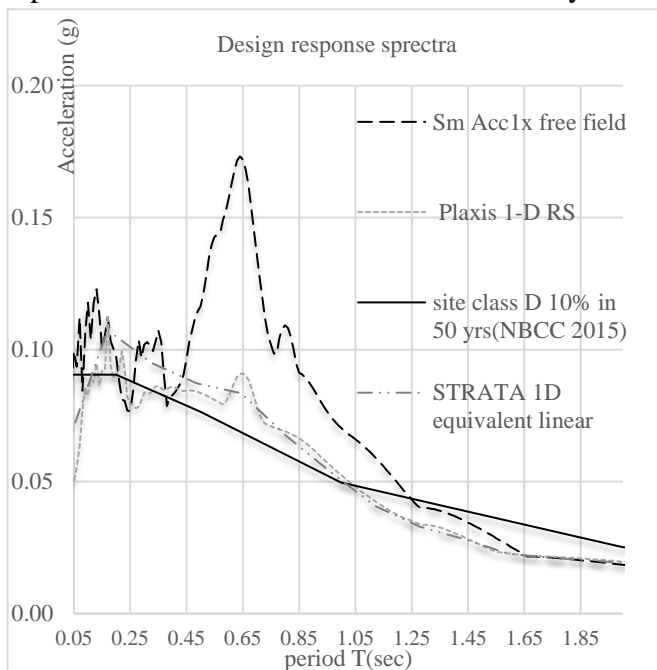


Figure 8. Comparison of response spectra at the quay wall area

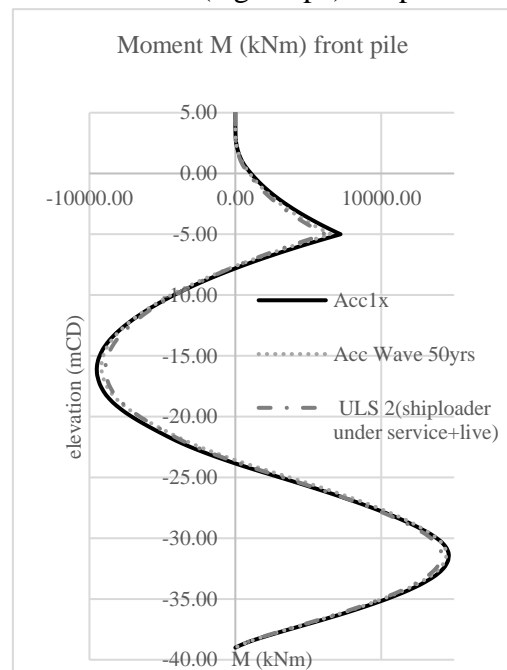


Figure 9. Moment distribution along the front pile of the cofferdam for representative static and dynamic load combinations

The ground motion is substantially amplified for the range of periods up to approximately 1.2 seconds while the resonant period is pushed to the right. This can be justified, if one takes into account the height of the cofferdam in combination with the inclination of the soil profile that makes the system more flexible. This behaviour does not have a significant impact on the design of the quay wall. The earthquake became the governing load combination, but only marginally.

Figure 9 illustrates the moment distribution along the front pile for two representative load combinations, ULS 2 service load and live load on the platform 15kN/m^2 and the 50 year wave load combination, and an earthquake load combination (Acc1x). The difference on the developed moments is at the order of 5%. This is anticipated, as major part of the load on this quay wall is related to the significant backfill height behind it and the current input motion is not that onerous. On the other hand, the design of the structures installed on the quay wall had to take into account for this interaction.

4. CONCLUSION

This paper describes the methodology used to address in geotechnical design the displacement control issues of quay walls during industrial operations, such as shiploader loads.

Advanced soil models, such as Hardening soil small need to be used, when displacements or dynamic modelling is part of the design. The basic steps to assign soil model properties for advanced soil models were presented, emphasising on the estimation of G_0 values. It was shown that a combination of 3D geotechnical software with 2D geotechnical and structural software can induce significant design efficiencies to a project and enhance the displacement control during design to ensure the long term operation of the shiploader.

Regarding the dynamic modelling, the benefits introduced to a design by detailed time history analysis are highlighted. As it was shown in this paper, even if the earthquake motion does not have an onerous impact on the design of the marine structure itself, it can have an impact on the design of the structures founded on top of the quay wall. The importance of a coordinated geotechnical - structural design is demonstrated.

Nevertheless, the lack of available (large scale) testing of the backfill during the design phase imposed several limitations. The assumption of conservative values prevents design enhancements. Large scale testing and monitoring of backfill behaviour could be an interesting and useful aspect of future research.

ACKNOWLEDGEMENT

Special acknowledgements have to be made to the design team of BESIX Engineering Department, Lionel Delhaye, Valerie Whenham, Toby Barnett, Wim De Wilde, Ariston de Souza, Bieke Peeters, Xavier Raucroix, Jean Francois Keyaerts, Carlos Esteves and Sam Christie and Yu Zhang, COWI North America, for their contribution and support.

REFERENCES

- [1] Canadian Geotechnical Society, 2006. "*Canadian Foundation Engineering Manual*", 4th edition, BiTech Publishers Ltd., Canada, 488 pages.
- [2] CSA (Canadian Standards Association), 2014. "*Canadian Highway Bridge design code. CAN/CSA-S6*". CSA Group, Canada, 894 pages

- [3] HTG, 2015. “*Recommendations of the committee for waterfront structures harbours and waterways EAU 2012*”. John Wiley & Sons, Germany, 676 pages.
- [4] de Gijt, J.G. and Broeken, M.L. eds., 2005. “*Handbook of Quay Walls*”. CRC Press, Netherlands, 656 pages.
- [5] International Organisation for Standardisation, 2012. “*ISO 12488-1:2012. Cranes -- Tolerances for wheels and travel and traversing tracks -- Part 1: General*”, ISO publications, Switzerland
- [6] Brinkgreve, R.B.J., Kumarswamy, S., Swolfs, W.M., 2015. “*Plaxis, Reference Manual*”. Plaxis BV, Delft.
- [7] Engineer, S.C.I.A., 2013. “*SCIA engineer manuals*”, Columbia, MD.
- [8] Benz, T., Vermeer, P.A. and Schwab, R., 2009. “*A small- strain overlay model*”, International journal for numerical and analytical methods in geomechanics, 33(1):25-44.
- [9] Lunne, T., Powell, J.J. and Robertson, P.K., 2002. “*Cone penetration testing in geotechnical practice*”. CRC Press, London, 352 pages.
- [10] Hegazy, Y.A. and Mayne, P.W., 1995. “*Statistical correlations between Vs and cone penetration data for different soil types*”, International Symposium on Cone Penetration Testing, CPT, Vol. 95, pp. 173-178, 4-5 October 1995, Sweden.
- [11] Mayne, P.W., 2006. “*In-situ test calibrations for evaluating soil parameters*”, Second International Workshop on Characterisation and Engineering Properties of Natural Soils, pp. 1601-1652, 29 November-1 December 2006, Singapore.
- [12] Baldi, G., Bellotti, R., Ghionna, V.N., Jamiolkowski, M. and Lo Presti, D.C., 1989. “*Modulus of sands from CPTs and DMTs*”, stress,2, p.5.
- [13] Ishibashi, I. and Zhang, X., 1993. “*Unified dynamic shear moduli and damping ratios of sand and clay*”, Soils and Foundations, 33(1):182-191.
- [14] Alpan, I. 1970. “*The geotechnical properties of soils*”. Earth Science Reviews, 6:5-49.
- [15] Canadian Commission on Building and Fire Codes National Research Council of Canada, 2015. “*National Building Code of Canada*”, NRC, Canada.
- [16] Chiou, B., Darragh, R., Gregor, N. and Silva, W., 2008. “*NGA project strong-motion database*”, Earthquake Spectra, 24(1):23-44.
- [17] Akkar, S., Sandikkaya, M.A., Şenyurt, M., Sisi, A.A., Ay, B.Ö., Traversa, P., Douglas, J., Cotton, F., Luzi, L., Hernandez, B. and Godey, S., 2014. “*Reference database for seismic ground-motion in Europe (RESORCE)*”, Bulletin of earthquake engineering, 12(1):311-339
- [18] Kottke, A.R. and Rathje, E.M., 2008. “*Technical manual for Strata*”; University of California, Berkeley.
- [19] Westergaards, HM, 1933. “*Water Pressures on Dams During Earthquake*”. Transactions, American Society of Civil Engineers (ASCE), Vol. 98, Paper No. 1835, New York City, NY, pp. 418-433.

CAVITY EXPANSION ANALYSIS IN ELASTIC – BRITTLE PLASTIC ROCK MASS

Haythem Gharsallaoui*, *Institute of Mechanics, Materials and Civil engineering (iMMC) – GCE – UCLouvain – Belgium, haythem.gharsallaoui@uclouvain.be*

Mustafa Jafari, *Institute of Mechanics, Materials and Civil engineering (iMMC) – GCE – UCLouvain – Belgium, mustafa.jafari@uclouvain.be*

Alain Holeyman, *Institute of Mechanics, Materials and Civil engineering (iMMC) – GCE – UCLouvain – Belgium, alain.holeyman@uclouvain.be*

ABSTRACT

A comprehensive approach is presented for the analyses of both cylindrical and spherical cavity expansion in an infinite elastic – brittle plastic rock mass. The rock mass obeys the nonlinear generalized “Hoek – Brown” (H-B) failure criterion which is expressed in a scaled form. A plastic flow rule characterized by a constant dilatancy angle ψ is adopted. Closed form solutions are presented for the extent of the plastic region and the distribution of radial and circumferential stresses. For displacement field, solutions in the plastic region are developed based on small strain theory. Finally, the solutions are validated using finite element method.

Keywords: Hoek – Brown Failure Criterion, Cylindrical and Spherical Cavity Expansion, Elastic – Brittle Plastic Post Failure, Small Strain Theory.

1. INTRODUCTION

The cavity expansion theory has been widely used to solve many problems in geotechnical engineering such as interpretation of in-situ tests, predicting the end bearing and shaft capacity of driven piles. Moreover, an important class of civil engineering problems deals with cavities in rock masses and most practical applications still consider rock as a soil and predict their behavior by using soil-related failure criteria such as the linear Mohr-Coulomb (M-C) criterion. Furthermore, extensive literature [1] is available on cavity analysis in a medium consisting of M-C material. However, the non-linear Hoek-Brown (H-B) [2] failure criterion more rigorously represents rock mass behavior. Since its introduction in 1980's, this criterion has been mostly used in cavity contraction analyses for tunneling applications. In this light, Brown et al. [3] presented a closed form solution for the cavity unloading problem in an elastic – brittle plastic material as well as an elastic strain softening plastic material obeying the 1980 H-B failure criterion version [4]. Carranza-Torres and Fairhurst [5] studied also the elasto-plastic response of underground excavation in rock masses obeying the 1997 H-B failure criterion version [6] in which the excavation process is treated as a uniform reduction of internal pressure in symmetrically loaded cylindrical and spherical cavities. In addition to the published closed form expressions, they provided a dimensional graphical representation of their solutions that allows direct estimates of the response of excavations.

However, to the authors' knowledge, not much has been published for cavity expansion problem in a material obeying the H-B failure criterion. In this paper, both cylindrical and spherical cavities in elastic – brittle plastic H-B material are considered. To simplify the governing equations of the problem, the generalized H-B failure criterion expression [2] is used

in a “scaled”/non-dimensional form. The use of this scaled form leads to considerable simplification in analyzing the elasto-brittle plastic response of the rock.

This paper starts with a brief recall of the generalized H-B failure criterion and the adopted normalization method. Then, analytical solutions are derived and validated by Finite Element Method (FEM).

2. H-B FAILURE CRITERION

The H-B failure criterion [2] is an empirical criterion developed through curve-fitting of triaxial test data. This criterion assumes isotropic rock and should only be applied to rock masses in which there is a sufficient number of closely spaced discontinuities. In other words, the H-B failure criterion is valid for intact rocks or heavily jointed rock masses (i.e. sufficient dense and randomly distributed joints). The latest version of the H-B criterion [2] is defined by:

$$\sigma'_1 = \sigma'_3 + \sigma_{ci}(m_b \sigma'_3 / \sigma_{ci} + s)^a \quad (1)$$

here σ'_1 and σ'_3 denote, respectively, the major and the minor principal stresses at failure. σ_{ci} is the uniaxial compressive strength of the intact rock. The parameters m_b , s and a describe the rock mass characteristics and depend on the Geotechnical Strength Index GSI , the disturbance factor D and the the intact frictional strength component m_i . They are calculated as:

$$m_b/m_i = e^{\left(\frac{GSI-100}{28-14D}\right)}; s = e^{\left(\frac{GSI-100}{9-3D}\right)}; a = 0.5 + \left(e^{\left(-\frac{GSI}{15}\right)} - e^{\left(-\frac{20}{3}\right)}\right)/6, \quad (2)$$

The H-B failure criterion expression (Eq. (1)) defines a relationship between minor and major principal stresses depending on four independent parameters, which can be reducing to a single one using a “scaled” form of the criterion. The suggested transformation involves dividing Eq. (1) by $(\sigma_{ci} m_b^\beta)$ and adding the term $(s/m_b^{\beta/a})$ to both sides. With these manipulations, the H-B failure criterion expression becomes:

$$\sigma'_1/(\sigma_{ci} m_b^\beta) + s/m_b^{\beta/a} = \sigma'_3/(\sigma_{ci} m_b^\beta) + s/m_b^{\beta/a} + (\sigma'_3/(\sigma_{ci} m_b^\beta) + s/m_b^{\beta/a})^a; \beta = \frac{a}{1-a} \quad (3)$$

Thus, the scaled (non-dimensional) minor and major principal stresses are defined naturally as,

$$\sigma_j^* = \sigma'_j/(\sigma_{ci} m_b^\beta) + s/m_b^{\beta/a}; \quad j = \{1,3\} \quad (4)$$

From now on, normalized stresses will have an asterisk as superscript. For sake of brevity, the term “scaled” will be mostly dropped when referring to a scaled variable unless stated otherwise. When expressed in terms of σ_1^* and σ_3^* , the H-B failure criterion permits a simplified and normalized treatment of the rock mass failure condition. Thanks to such a scaling, the H-B failure criterion is formally simplified as follows:

$$\sigma_1^* = \sigma_3^* + (\sigma_3^*)^a \quad (5)$$

3. PROBLEM STATEMENT

Both cylindrical and spherical cavities in elastic-brittle-plastic H-B material are considered. The geometry of the problem and the boundary conditions are as shown in Figure 1. Let r_i be the internal radius of the cavity and P_0 the far field radial pressure. Let P_i be the internal pressure applied on cavity wall that increases monotonically from its initial value P_0 . As the internal pressure P_i increases, the rock mass will initially behave in an elastic manner, until reaching a yield pressure P_y . When the internal pressure P_i exceeds P_y , a plastic region will start spreading

from r_i to the “plastic” radius r_p . The remainder of the domain ($r \geq r_p$) belongs to the elastic region.

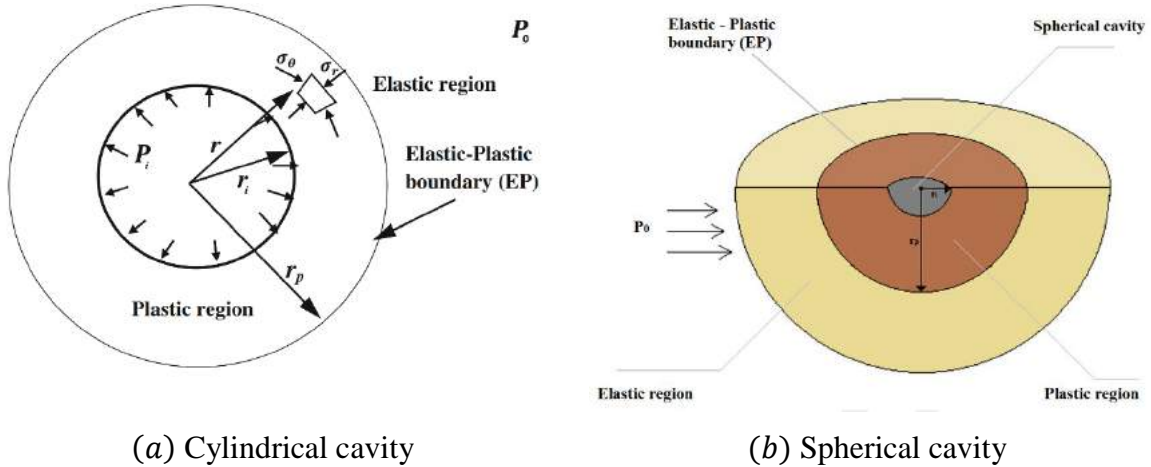


Figure 1: Geometry of the problem and boundary conditions

It should be emphasized that as soon as the materials yields, the peak strength parameters m_b^{peak} and s^{peak} and the peak deformation modulus E^{peak} drop to residual strength parameters m_b^{res} and s^{res} and residual deformation modulus E^{res} . Therefore, two cases can be distinguished:

- If residual strength parameters are equal to the peak parameters, then we are defining an "ideally" elastic-plastic material (cf. Figure 2).
- If not, Hoek [7] said that they, rock engineering community, do not have good models to describe this post failure behavior but he suggested two post failure: Elastic-brittle (cf. Figure 2) and strain softening as a starting point. The latter one is beyond the scope of this paper.

To ensure that closed form solution can be obtained, it is necessary to further assume that after yield, the strength of rock drops suddenly to its residual values. Note that the disturbance factor D can be used to achieve a strength and modulus reduction after failure. It is found that $D = 0.7$ is appropriate in most cases [7]. In what follows, only brittle plastic post failure is considered. The perfectly plastic model is simply a limiting case of the brittle one.

The analytical study described hereinafter is conducted based on the scaled form of the H-B failure criterion and pressures and stresses are scaled using residual strength parameters reflected by ‘res’ as a superscript. On the other hand, the equation of equilibrium for the cavity problem is expressed in terms of radial and circumferential stresses (scaled) as:

$$d\sigma_r^{*res}/dr + k(\sigma_r^{*res} - \sigma_\theta^{*res})/r = 0 \quad (6)$$

here k is a coefficient equal to 1 in case of a cylindrical cavity and it is equal to 2 in case of a spherical one. Note that major and minor principal stresses are assumed to be equal to radial and circumferential stresses, respectively, i.e. $\sigma_1 = \sigma_r$ and $\sigma_3 = \sigma_\theta$.

4. STRESS AND DIPLACEMENT FIELD – ANALYTICAL SOLUTION

When the internal pressure P_i exceeds P_y , a plastic region starts spreading from r_i to the plastic radius r_p . The remainder of the domain ($r \geq r_p$) belongs to the elastic region. The latter is first studied before investigating the plastic region but firstly, the yield pressure expression is provided hereinafter.

4.1. Yield Pressure

When the internal pressure P_i applied on the cavity wall reaches the yield pressure P_y , the stress of the rock mass at cavity face will satisfy the failure criterion expressed as a function of the peak strength parameters. Thus, the net yield pressure $\Delta P_y^{*peak} = (P_y^{*peak} - P_0^{*peak})$ should satisfy the following equation:

$$\Delta P_y^{*peak} = -\Delta P_y^{*peak} / k + [P_0^{*peak} - \Delta P_y^{*peak} / k]^a \quad (7)$$

The superscript ‘*peak*’ in the above equation means that pressures are scaled using peak strength parameters m_b^{peak} and s^{peak} . The yield pressure depends only on the far field pressure P_0^{*peak} and the exponent a . The above equation provides an explicit solution when $a = 0.5$:

$$\Delta P_y^{*peak}|_{a=0.5} = k \left(\sqrt{4P_0^{*peak} (k+1)^2 + 1} - 1 \right) / (2(k+1)^2) \quad (8)$$

When $a \neq 0.5$, there is no explicit solution and Eq. (7) should be solved numerically. The evolution of P_y^{*peak} as a function of P_0^{*peak} is plotted in Figure 3. As can be seen, when $P_0^{*peak} \rightarrow 0$, P_y^{*peak} approaches $2P_0^{*peak}$ for cylindrical cavity and approaches $3P_0^{*peak}$ for the spherical one. Secondly, the yield pressure is relatively constant when $GSI > 30$ since the exponent $a \cong 0.5$. Since the governing equations of the problem are scaled using residual strength parameters, the following relationship relating P_y^{*res} to P_y^{*peak} should be used once P_y^{*peak} is found per Eq.(7)

$$P_y^{*res} = (m_b^{peak} / m_b^{res})^\beta P_y^{*peak} + (m_b^{res})^{-\beta} (s^{res} / m_b^{res} - s^{peak} / m_b^{peak}) \quad (9)$$

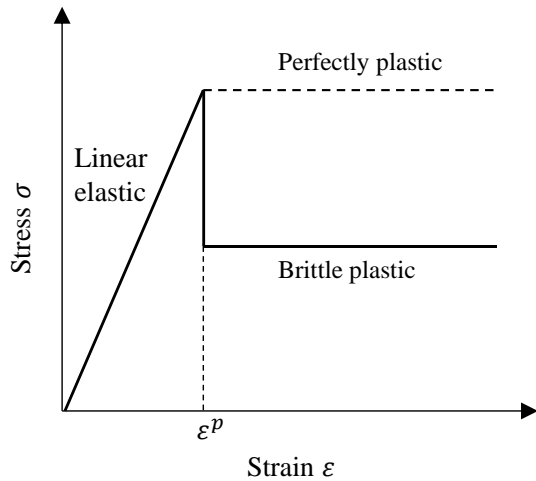


Figure 2: Perfectly plastic and brittle plastic post failure.

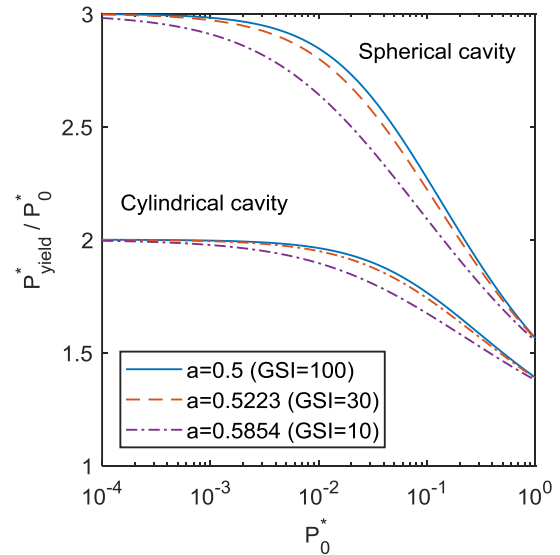


Figure 3 Scaled yield pressure.

4.2. Elastic Region ($r \geq r_p$)

Since the solution for this region is well known, only, main results are presented hereinafter. By considering the boundary conditions $\sigma_r^{*res}(r = r_p) = P_y^{*res}$ and $\sigma_r^{*res}(r = \infty) = P_0^{*res}$, radial and circumferential stresses are expressed as:

$$\sigma_r^{*res} - P_0^{*res} = -k(\sigma_\theta^{*res} - P_0^{*res}) = (P_y^{*res} - P_0^{*res})(r_p/r)^{k+1} \quad (10)$$

On the other hand, total strains are written as functions of elastic and plastic strains as follows:

$$\varepsilon_r = \varepsilon_r^e + \varepsilon_r^p \quad ; \quad \varepsilon_\theta = \varepsilon_\theta^e + \varepsilon_\theta^p \quad (11)$$

where ε_r^p and ε_θ^p denote, respectively, the radial and the circumferential plastic strains. They will be evaluated in the next subsection whereas ε_r^e and ε_θ^e are, respectively, the radial and the circumferential elastic strains given as:

$$\varepsilon_r^e = \left((1 + \nu(k - 2))(\sigma_r^{*res} - P_0^{*res}) - k\nu(\sigma_\theta^{*res} - P_0^{*res}) \right) / (2I_r(1 + \nu)^{k-1}) \quad (12)$$

$$\varepsilon_\theta^e = \left((1 - \nu)(\sigma_\theta^{*res} - P_0^{*res}) - \nu(\sigma_r^{*res} - P_0^{*res}) \right) / (2I_r(1 + \nu)^{k-1}) \quad (13)$$

in which, ν is the Poisson's ratio. I_r is the rigidity index of the rock mass and it is expressed according to the region state. When the elastic region prevails which is the case here, I_r is expressed as a function of the peak shear modulus as $I_r = G^{peak} / (\sigma_{ci}(m_b^{res})^\beta)$

by substituting Eqs. (10) into Eqs. (12) and (13) and by taking into account that infinitesimal strain can be written in terms of radial displacement u as $\varepsilon_r = -\frac{du}{dr}$ and $\varepsilon_\theta = -\frac{u}{r}$, the radial displacement can be evaluated as:

$$u = u_{EPB}(r_p/r)^k \quad ; \quad u_{EPB} = r_p(P_y^{*res} - P_0^{*res}) / (2kI_r) \quad (14)$$

here u_{EPB} is the radial displacement at the Elastic – Plastic Boundary (EPB).

4.3. Plastic Region ($r_i \leq r \leq r_p$)

In this section, analytical solution for the extent of the plastic region and the related stresses and displacement fields are investigated.

4.3.1. Stress field

Substituting the scaled H-B failure criterion expression (Eq. (5)) in the equilibrium equations (Eq. (6)) results in the following differential equation of the circumferential stress:

$$d\sigma_\theta^{*res} / dr + d(\sigma_\theta^{*res})^a / dr + k(\sigma_\theta^{*res})^a / r = 0 \quad (15)$$

The general solution of the above first-order nonlinear differential equation can be written as:

$$\sigma_\theta^{*res}(r) = \left[aW_0 \left(C_1 r^{-\frac{k}{\beta}} \right) \right]^{\beta/a} \quad (16)$$

where C_1 is a constant. W_0 is the 0th branch of the Lambert W -function (Omega function). Lambert W -function is the solution of the equation $x = W(x)e^{W(x)}$. To simplify the expressions, the change of variable $R = C_1 r^{-\frac{k}{\beta}}$ will be used which allow the circumferential stress and radial stress (Eq. (5)) to be reduced to

$$\sigma_r^{*res}(R) = [aW_0(R)]^{\beta/a} + [aW_0(R)]^\beta \quad ; \quad \sigma_\theta^{*res}(R) = [aW_0(R)]^{\beta/a} \quad (17)$$

Based on the hypothesis of the continuous radial stress at the (EPB) and knowing that an internal pressure P_i^{*res} is exerted at the cavity wall, i.e.,

$$P_y^{*res} = [aW_0(R_p)]^{\beta/a} + [aW_0(R_p)]^\beta \quad ; \quad P_i^{*res} = [aW_0(R_i)]^{\beta/a} + [aW_0(R_i)]^\beta \quad (18)$$

the plastic radius r_p can be calculated once Eqs. (18) is solved for $R_p = C_1 r_p^{\frac{k}{\beta}}$ and $R_i = C_1 r_i^{\frac{k}{\beta}}$. Thus, the normalized plastic radius is simply evaluated as $r_p/r_i = (R_i/R_p)^{\frac{\beta}{k}}$.

When $a = 0.5$, a closed form solution of the plastic radius can be provided as:

$$(r_p/r_i)_{a=0.5} = \left(\left(\sqrt{4P_i^{*res} + 1} - 1 \right) e^{\sqrt{4P_i^{*res} + 1} - 1} \right)^{\frac{1}{k}} \left(\left(\sqrt{4P_y^{*res}|_{a=0.5} + 1} - 1 \right) e^{\sqrt{4P_y^{*res}|_{a=0.5} + 1} - 1} \right)^{\frac{1}{k}} \quad (19)$$

When $a \neq 0.5$, there is no closed form solution for the plastic radius and Eqs. (18) should be solved numerically.

The distribution of radial and circumferential stresses are shown in Figure 4 for both cylindrical and spherical cavities. As can be seen, a discontinuity due to the brittle character is evidenced for the circumferential stress.

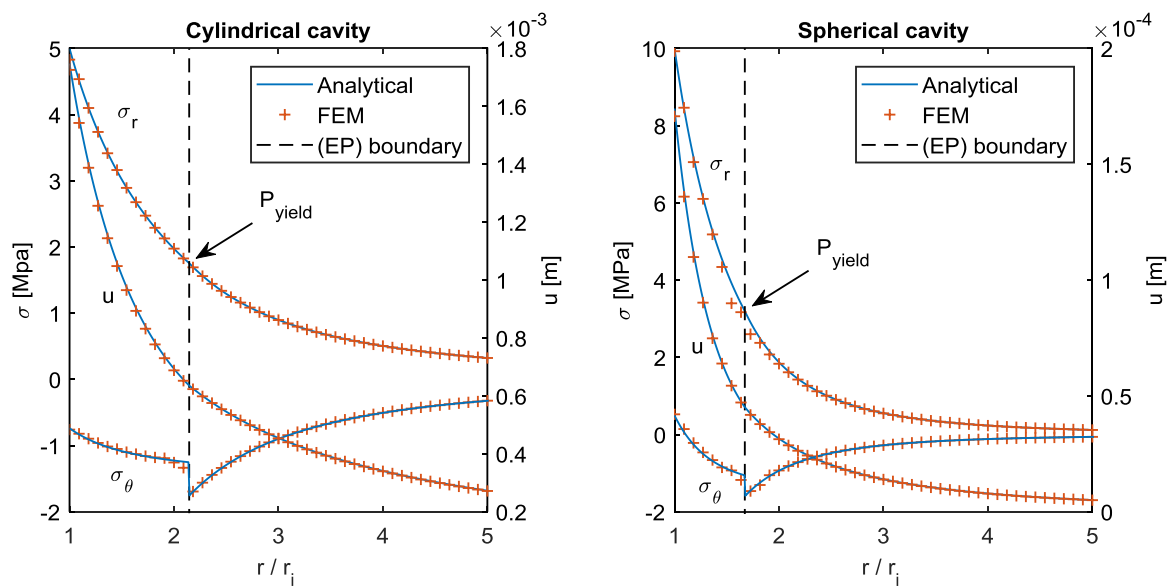


Figure 4: Distribution of radial and circumferential stresses and displacement for both cylindrical and spherical cavities in a H-B material with $\sigma_{ci} = 35$ [MPa], $GSI = 80$, $m_i = 4$, $P_0 = 0$, $MR = \frac{E_i}{\sigma_{ci}} = 250$, $\nu = 0.3$ and $\psi = 0^\circ$

4.3.2. Displacement field

To determine the displacement field in the plastic zone, a plastic flow rule is needed. Thus, a non-associated flow rule with a constant dilatancy angle ψ is adopted as

$$\varepsilon_r^p + k\omega\varepsilon_\theta^p = 0 \quad ; \quad \omega = \frac{1 - \sin(\psi)}{1 + \sin(\psi)} \quad (20)$$

which can be further expressed per Eqs. (11) as:

$$\varepsilon_r + k\omega\varepsilon_\theta = \varepsilon_r^e + k\omega\varepsilon_\theta^e \quad (21)$$

On the other hand, infinitesimal strains are expressed in terms of radial displacement u as follows:

$$\varepsilon_r = -du/dr \quad ; \quad \varepsilon_\theta = -u/r \quad (22)$$

Substituting the above equations into Eq. (21) combined with Eqs. (12) and (13) results in the following differential equation of the radial displacement:

$$\frac{du}{dr} + k\omega \frac{u}{r} + D_1(\sigma_{\theta}^{*res} - P_0^{*res}) + D_2(\sigma_{\theta}^{*res})^a = 0 \quad (23)$$

where D_1 and D_2 are two dimensionless coefficients defined respectively as $\frac{(1+k\omega)(1-2\nu)}{2I_r(1+\nu)^{k-1}}$ and $\frac{(1+\nu(k-2)-\nu k\omega)}{2I_r(1+\nu)^{k-1}}$. It is important to mention that the rigidity index is expressed this time as a function of the residual shear modulus as $I_r = G^{res}/(\sigma_{ci}(m_b^{res})^\beta)$. Knowing the displacement at the (EPB), the solution of the above differential equation is expressed as:

$$u(r) = r^{-k\omega} \left[u_{EPB} r_p^{k\omega} + \int_r^{r_p} \rho^{k\omega} (D_1(\sigma_{\theta}^* - P_0^*) + D_2(\sigma_{\theta}^*)^a) d\rho \right] \quad (24)$$

Figure 4 shows the evolution of $u(r)$ for both cylindrical and spherical cavities.

5. VALIDATION

Using the finite element software RS² 9 Modeler [8], a finite element analysis is conducted to validate the analytical results. The geometry of the models as well as the selected boundary conditions for both cylindrical and spherical cavities are as shown in Figure 5. A plane strain conditions are assumed for the cylindrical cavity with an internal radius of 1m and default external boundary set as infinite. On the other hand, a spherical cavity with an internal radius $r_i = 0.1 \text{ m}$ is modeled with a rock domain broad enough ($120r_i \times 240r_i$) to prevent boundary effect. The spherical cavity is located at a depth of 12m.

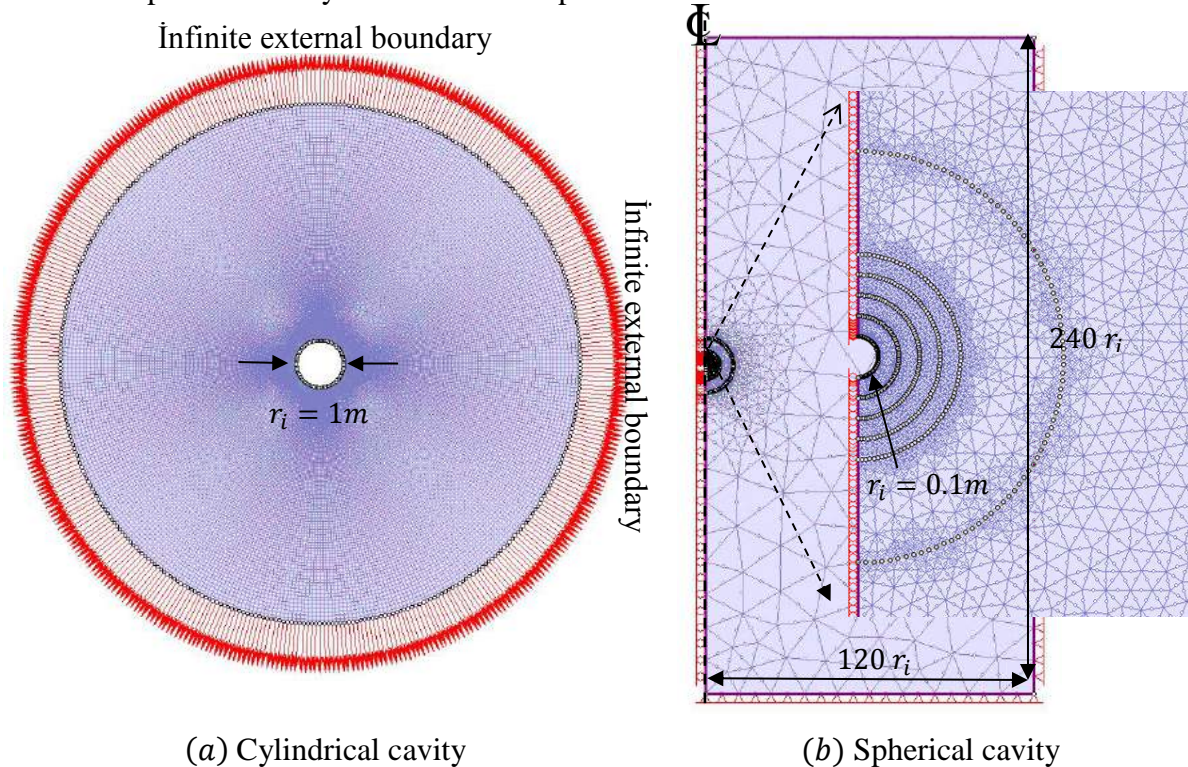


Figure 5: Geometry and boundary conditions of the problem

A distributed load normal to the cylindrical and the spherical cavity cluster of 5 [MPa] and 10 [MPa], respectively is prescribed. It should be emphasized that the spherical cavity

expansion is a relatively hard boundary value problem which consumes a significant amount of computational power when solved using the finite element method.

The rock mass in the FEM model has properties similar to that of an undisturbed claystone ($D = 0$) with: $\sigma_{ci} = 35$ [MPa], $m_i = 4$ and $MR = E_i/\sigma_{ci} = 250$ and $GSI = 80$. The peak and residual deformation modulus are evaluated based on H-B core parameters as 7703 [MPa] and 4715 [MPa], respectively. These values can be simply estimated from the software library [8]. Since the Poisson's ratio ν does not usually affect rock behavior in a significant manner, a standard value equals to 0.3 is used. Note that the dilatancy angle ψ as well as the far field pressure P_0 are set equal to zero. As shown in Figure 4, analytical solutions are in excellent agreement with the FEM predictions emphasizing the accuracy of the developed solutions.

6. CONCLUSION

The expansion of cylindrical and spherical cavities in an infinite medium consisting of an elastic – brittle plastic Hoek-Brown material is investigated. The use of a scaled form of the H-B failure criterion leads to considerable simplifications in defining the elastoplastic response of the rock mass. Analytical expressions are obtained for the stress and displacement field. Although the solutions require some numerical integrations over the plastic region, they have the advantage of being highly robust considerably in comparison with other numerical techniques such as the finite element method. The analytical expressions were validated employing the finite element method.

ACKNOWLEDGEMENTS

The financial support offered by the Belgian Member Society of the ISSMGE (BGGG-GBMS) to the first author is gracefully acknowledged.

REFERENCES

- [1]H.-S. Yu., 2000. "Elastic-perfectly plastic solutions," in *Cavity Expansion Methods in Geomechanics*, Dordrecht: Springer Netherlands, pp. 32–94.
- [2]Hoek, E., Carranza, C., Corkum B., 2002. "Hoek-brown failure criterion – 2002 edition," *Narms-Tac*, vol. 1, pp. 267–273.
- [3]Brown E.T., Bray J.W., Ladanyi, B., Hoek E., 1983. "Ground Response Curves for Rock Tunnels" *J. Geotech. Eng.*, 109(1): 15–39.
- [4]Hoek, E., Brown, E., 1980. "Empirical strength criterion for rock masses," *J. Geotech. Engng Div.*, ASCE, 106(GT9):1013–1035.
- [5]Carranza-Torres, C., Fairhurst, C., 1999. "The elasto-plastic response of underground excavations in rock masses that satisfy the Hoek-Brown failure criterion" *Int. J. Rock Mech. Min. Sci.*, 36(6):777–809.
- [6]Hoek, E., Brown, E.T.T., 1997. "Practical estimates of rock mass strength", *Int. J. Rock Mech. Min. Sci.*, 34(8): 1165–1186.
- [7]Hoek, E., 2006. "How do I estimate the residual value of the parameter m_i ?" Available online: <https://support.rocsience.com/hc/en-us/articles/206734737-For-plastic-analysis-how-do-I-estimate-the-residual-value-of-the-parameter-mi->.
- [8]Rocscience, 2019. "RS2 (Phase2 9.0) 2D Geotechnical Finite Element Analysis" .

RECONSTRUCTION OF THE EXISTING BLOCK OF ATLANTSKA PLOVIDBA ON BATALA (DUBROVNIK), IN THE BUSINESS-RESIDENTIAL COMPLEX

Andrea Milardović, *KREŠO GEO Ltd. Zagreb, andrea@kresogeo.hr*

ABSTRACT

The subject of this paper is construction of excavation pit protection for reconstruction of the existing block of Atlantska plovidba in a business-residential complex in Dubrovnik, Croatia, around 35 m from the coast. It is planned to reconstruct part of the existing buildings in a business-residential building with 7 above ground floors (G+6) and 3 underground garage floors (G-3), [1]. For the construction pit protection, three basic problems need to be solved: ensuring stability and waterproofing of the construction pit/minimizing horizontal displacements, and ensuring the water tightness of excavation bottom with the aim of reducing the groundwater flow into the construction pit and uplift control on the object during construction work. The design of the construction pit protection consists of vertical secant pile wall supported with geotechnical anchors. Large diameter piles have been selected (diameter is Ø90 cm, placed in 65 cm spacing) to ensure overlap/water tightness. Every second pile is reinforced. Three and four rows of self-drilling geotechnical anchors are designed, to ensure horizontal support of the secant pile wall. Secant pile wall is coated with 5-10 cm thick shotcrete and a reinforced mesh that serves as a base for laying waterproofing. Jet grouting and consolidation grouting of the bottom are designed to reduce the groundwater inflow and secure excavation and structure of water uplift in construction phase. Six wells and drainage system are designed for water drainage i.e. maintaining a water level below the elevation of the bottom ground slab during construction phase. The designed structure ensures the stability and water tightness of the construction pit's sides as well as securing the object from the buoyancy until the state of equilibrium is achieved under the weight of building.

Keywords: Secant Pile Wall, Geotechnical Anchors, Jet Grouting, Consolidation Grouting

1. INTRODUCTION

The city of Dubrovnik, with the high utilization of construction plots, has an increasing need for parking lots, so many investors decide to build underground garage.

It is planned to reconstruct part of the existing buildings in a business-residential building with 7 above ground floors (G+6) and 3 underground garage floors (G-3), [1].

The residential-business complex, block A and block B, has 3 underground garage floors and the the lowest excavation is at terrain elevation -9.90 m a.s.l., that is 11 - 16 m below the level of the existing terrain. ($\pm 0.00 = 1.80$ a.s.l.). The groundwater level is about 0.5 - 0.7 m a.s.l., which corresponds to sea level, [2], [3].

Size of the building, [1]

- max. floor plan 50.67 x 26.80 m (ground floor), 51.65 x 40.15 m (basement floor - common area for Block A and Block B)
- Floors G-3, G-2, G-1, G, G + 1, G + 2, G + 3, G + 4, G + 5, G + 6
- Building is 10795.14 m² (6824.24 m² without garage)
- The plot area is 1649 m²

2. GEOTECHNICAL CHARACTERISTICS OF SOIL AND ROCK ON LOCATION

2.1. Geotechnical Characteristics

The wider area of the research site is located in the depression of the narrow northwestern - southeast valley, passing through the territory of Gruž, and divides to the continental part of Dubrovnik, with the peninsula towards Lapad. According to the basic geological map, the wider area of Dubrovnik [4], is consisted of the upper cretaceous - K₂³ (mastiht). The earliest deposits of the lower division of the upper cretaceous are located in the western and central part of the city, and are built by bank dolomites and dolomite breccia. Northern part of Lapad, is composed primarily of the limestone. Northeastern parts are composed of bank limestones in alteration of dolomites, and localized plain limestone in alteration with dolomite. The layers are generally inclined towards the northeast with slopes of about 30 to 40 degrees. There is a fault in northwest-southeast direction, passes through the valley. Diagonally, there are faults in northeast-southwest direction.

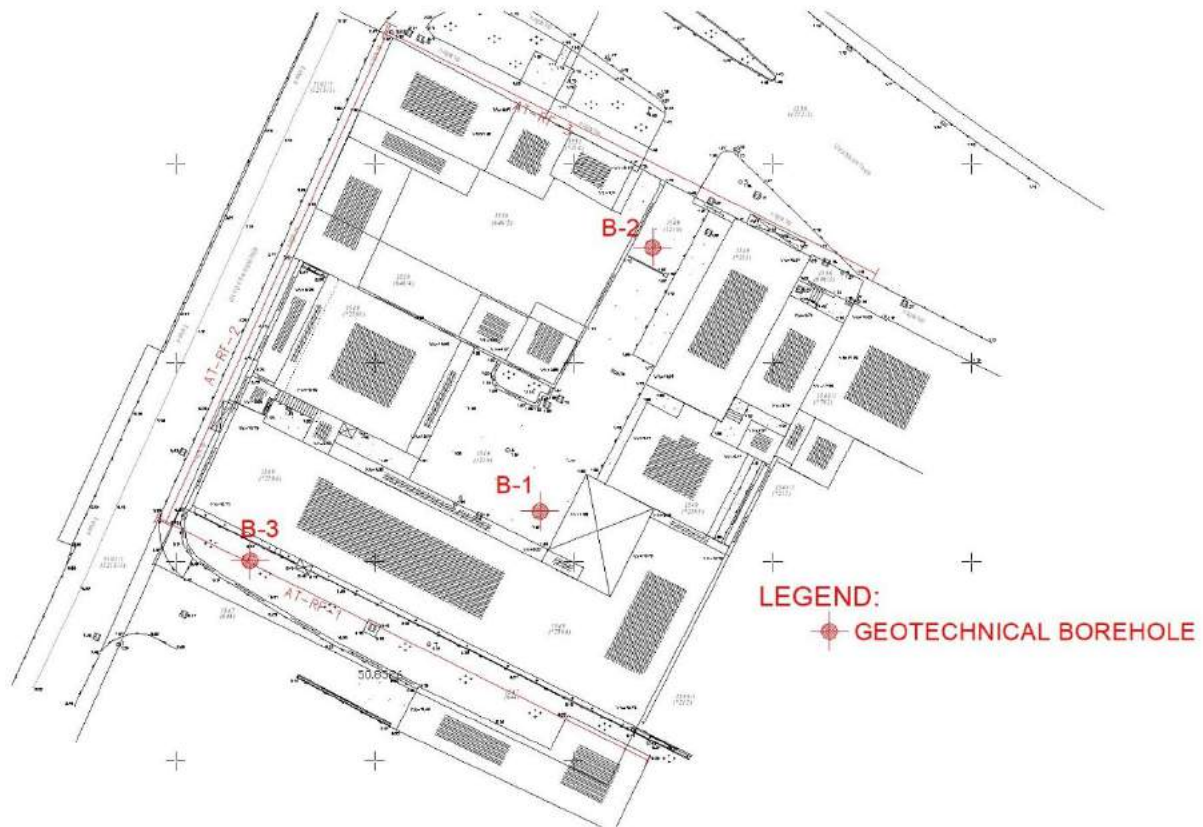


Figure 1. Area plan of geotechnical boreholes

2.2. Engineering Geographical Characteristics of Rock Mass

According to the geotechnical study, [5], it can be seen that the terrain is covered with topsoil made of rock blocks of different sizes and composition. In the lower part of the depth of 2.3 m and 2.5 m more often it is a reddish brown, high-plastic clay with minor dimensions' karsts. Topsoil extends to a depth of about 4.0 m. Top of the embankment is occasionally covered by asphalt. Positions of geotechnical boreholes are showed in Figure 1.

The ground is made of highly broken, upper cretaceous dolomitic breccia. In the central and southwestern part, the dolomite breccia is completely destroyed to the sand size. It is a poorly packed blend of fine grain and sharp-edged particles of sand. It often contains up to 5 mm fine sandy-silty concretions. Only short patches of about 1-2 m thick, with a very broken breccia and karst, 3-10 cm in size, occur only occasionally. In the central part at a depth of 7 to 11 m, there is a layer of sand with a higher share of silt size particles, mainly gray-brown to light-brown color. The mixture is generally weakly bounded, loose to medium compacted. Together with the soil layers described above, it belongs to the surface wear of bedrock.

Firmer rock mass occurs mostly in the northeast part of the B-2 borehole. Dolomite sand is present at a depth of 18.5 m. It is highly weathered (HW) rock mass, upper cretaceous (K_2^3 - mastriht). On rare solid blocks, discontinuities are observed of the inclination about 10 to 30 °, which would correspond to the contour planes. Cracks are around 75 °, mostly without filling, or filling is clay, but washed with drilling. The crack gap is larger than 5 mm. The cracks are mostly smooth to rough. RQD is low and ranges from 21% to 33%. There is cavern partially filled with clay that occurs at depths of 9.75 m to 11.45 m in borehole B-2.

The groundwater level in all boreholes was about 0.5 a.s.l. - 0.7 a.s.l., which corresponds to sea level.

3. DESIGNED PROTECTION OF CONSTRUCTION PIT

The design of the construction pit has these constructive elements

- Oblique support structure of secant piles with a nominal diameter of Ø90 cm placed in 65 cm spacing. Piles are drilled with protective casing in the surface layers (embankment and dolomite sand), and in the area of hard rock (dolomite breccia) without protective casing. This borehole diameter is approximately 80 cm, and overlaps of piles are ideally 25 and 15 cm. Large diameter piles have been selected to ensure sufficient overlap/water tightness. Every second pile is reinforced. Length of piles is 17 m, 19 m and 20 m.
- Pile cap dimensions are 95 x 60 cm.
- Three and four rows of self-drilling geotechnical anchors with yield force $F_{yd} > 290$ kN. The anchors ensure horizontal support of the secant pile wall and are installed at the angle of 20°. Horizontal anchor spacing is 1.3 m. Anchor length is 9 m, 12 m and 14 m, and they are designed as temporary, ie no special anticorrosive protection is needed. Anchors represent the tensile element of supporting structure which transfers soil pressures to the ground layers outside the active pressure zone. After installation, anchors are activated by a torque wrench, by force $P_0 = 50$ kN.
- 5-10 cm thick shotcrete and a reinforced mesh Q188 that serves as a base for laying waterproofing.
- Jet grouting and consolidation grouting below the bottom of the construction pit and around the pile on the inside of the pit (on the passive side) is designed, to reduce the groundwater inflow and secure excavation and structure of water uplift in construction

phase. Another equally important effect of jet grouting is increasing passive resistance to the piles on the passive side and the assurance of horizontal support.

The jet grouting procedure is in 4 phases: drilling, cutting, soilcreting and extending (Figure 2.).

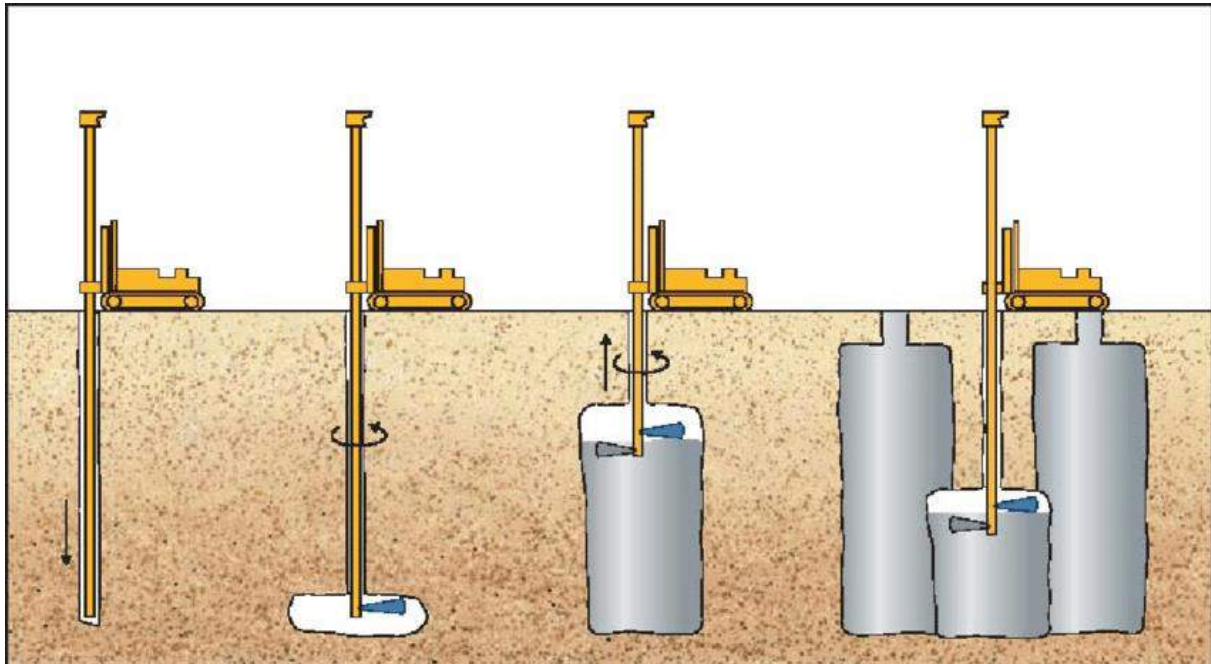


Figure 2. Order of execution of the jet grouting

- Six wells and drainage system are designed for water drainage ie maintaining a water level below the elevation of the bottom ground slab during construction phase.

This design of the construction pit ensures the stability and waterproofness of the construction pit's sides as well as securing the object from the buoyancy until the state of equilibrium is achieved under the weight of building.

4. GEOSTATIC CALCULATIONS

Internal and external stability control (ground stresses, displacements, bending moments and forces) and global stability of ϕ -c reduction, are made in accordance of references [6], [7] and [8], using Plaxis 2D software. The soil is modeled by a non-linear hardening soil model.

The calculation models are developed based on the geometry of the project and the assumed condition and characteristics of the soil, and are composed of two-dimensional finite element mesh. The distances between calculation models boundaries from the location of the largest stress variation were chosen according to the usual numerical modeling rules. Horizontal displacements are prevented in the vertical boundary nodes, while in the lower boundary node are prevented vertical and horizontal displacements. The groundwater level was set based on the geotechnical study, [5].

Based on data from geotechnical study, [5], the following characteristic of geotechnical parameters were defined in Main project – Construction pit protection, [2], [3]:

CROSS SECTION B - B

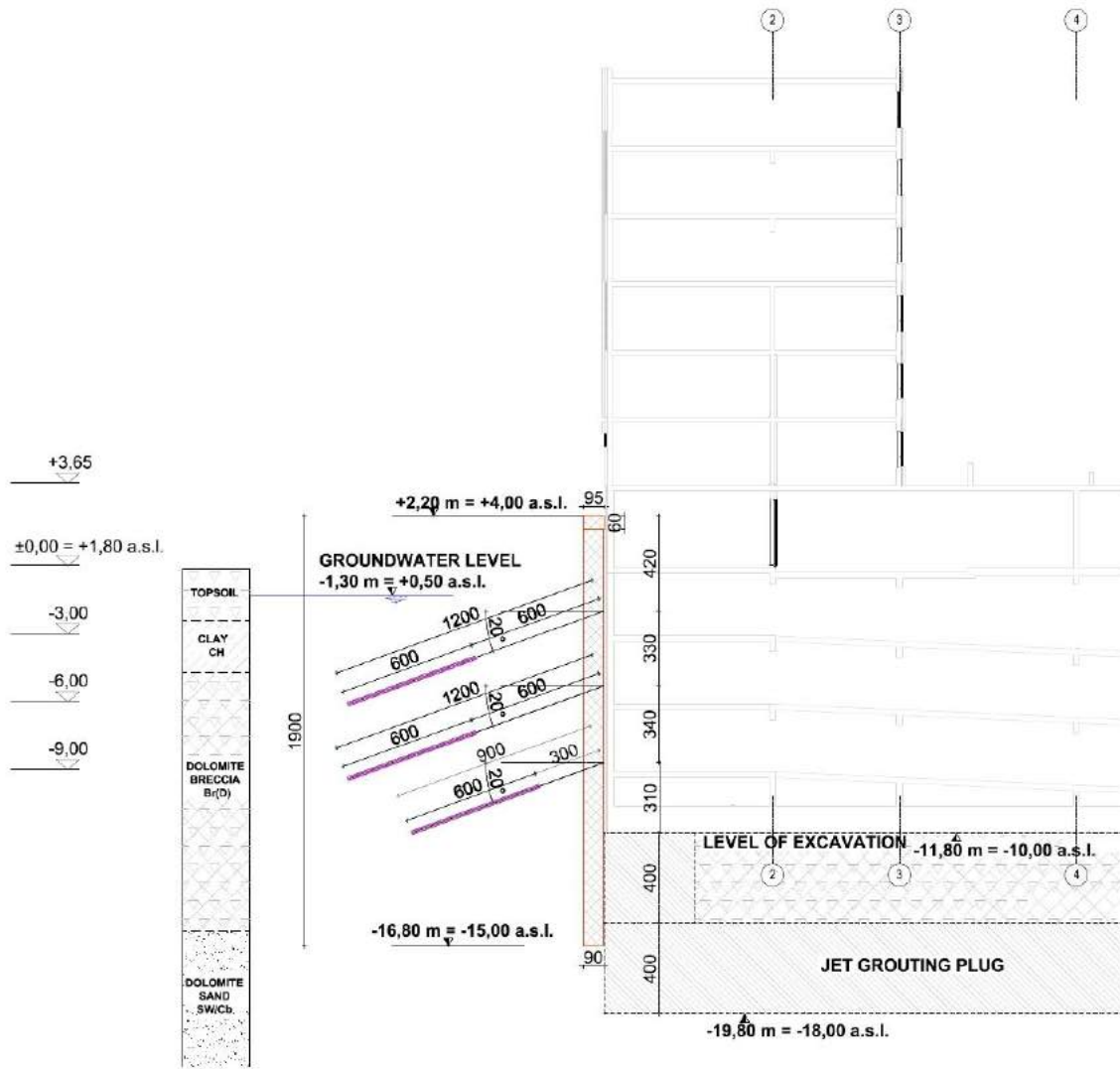


Figure 3. Cross section of construction pit

Table 1. Characteristic of geotechnical parameters

LAYER	E_{50ref} (kPa)	E_{oedref} (kPa)	E_{urref} (kPa)	ν_{ur}	c_{ref} (kPa)	ϕ (°)
1. TOPSOIL	20 000	20 000	60 000	0,2	20	30
2. CLAY	10 000	10 000	30 000	0,2	15	25
3. SAND	10 000	10 000	30 000	0,2	5	35
4. BEDROCK	300 000	300 000	900 000	0,2	50	40
5. JET GROUTING	1 000 000	1 000 000	-	0,3	60	40

Table 2. Tabular review of calculation results

Excavation mark	Last phase of calculation – Final excavation + Load 15 kPa					
	NE	NW	NW	NW	SW	SW
Pile lenght (m)	17	17	19	20	21	20
Maximum horizontal displacement (mm)	11,9	27,9	38,0	15,86	19,8	26,2
Phase horizontal displacement (mm)	0,76	1,58	3,70	0,73	0,4	1,7
Bending moment (kNm/m) Toward excavation	229,4	231,7	201,7	453,1	478,7	254,2
Toward ground	413,0	470,6	626,8	538,3	635,9	530,7
Anchors force (kN)						
1 st row Anchor	134,55	161,10	174,33	127,02	131,7	233,5
2 nd row Anchor	83,09	104,86	118,17	109,00	111,8	126,3
3 rd row Anchor	70,85	83,89	88,04	91,72	95,72	-
4 th row Anchor	-	-	-	86,79	90,42	-
Mobilized passive resistance (kN/m')	976	1030	1080	1070	1260	1000
Seepage in the construction pit (m ³ /day)	11,29	14,94	13,83	14,47	15,74	15,17

BENDING MOMENT DIAGRAM

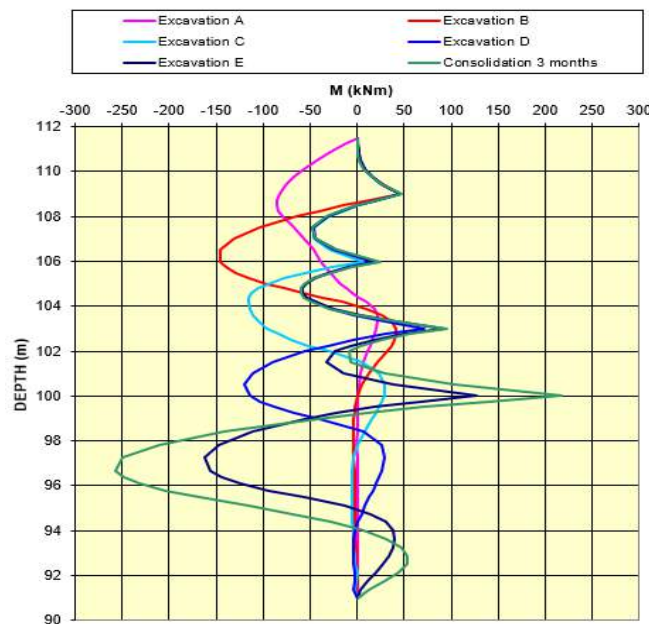


Figure 4. Bending moment diagram

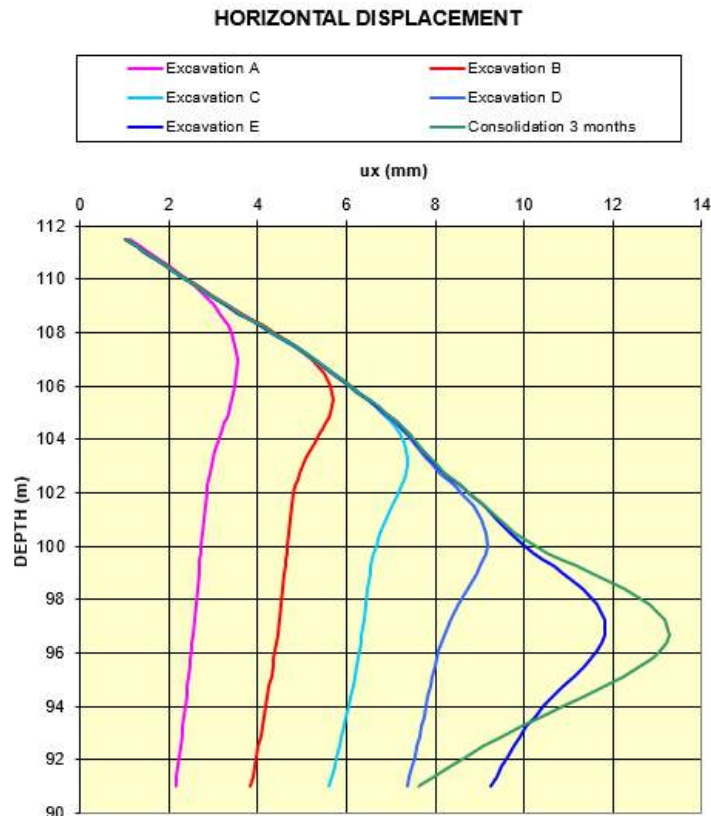


Figure 5. Horizontal displacement diagram

4. CONCLUSION

The protection of the construction pit is a very demanding task primarily due to the large groundwater control, during excavation and underground construction. The groundwater level in all boreholes was about 0.5 a.s.l. - 0.7 a.s.l., which corresponds to sea level.

Although the pile wall is designed as water-tight, some seepage is anticipated through imperfections on the joints. Considering the soil/rocks characteristics below the excavation zone, jet grouting will be applied, and on a smaller part, consolidation grouting. Jet grouting technology is suitable for ensuring the water-tightness of dolomite sand layers, and the consolidation grouting for dolomite breccia/bedrock layers. Protection of construction pit has temporary character. The durability of such constructions is normally estimated for a period of 2 years after the excavation is completed. Over time, there is strength loss in anchor and anchor corrosion and horizontal loads from soil and water pressure must be taken over by load-bearing structure of the building.

This design of the construction pit ensures the stability and waterproofness of the construction pit's sides as well as securing the object from the buoyancy until the state of equilibrium is achieved under the weight of building.

ACKNOWLEDGEMENT

I would like to express my very great appreciation to my mentor Krešimir Bolanča for his suggestions and useful critiques of this work.

REFERENCES

- [1] Kavurić T., 2018. *Main architecture project*, Project No: 18004
- [2] Bolanča K., 2018. “*Reconstruction of part of existing construction of Atlantska plovidba in business and residential building "Blok A"*”, *Main project – Construction pit protection*, Project No: 319-A/2018.
- [3] Bolanča K., 2018. “*Reconstruction of part of existing construction of Atlantska plovidba in business and residential building "Blok B"*”, *Main project – Construction pit protection*, Project No: 319-B/2018.
- [4] Federal Geological Institute Belgrade, 1971., *Basic geological map, the area of Dubrovnik*
- [5] Bolanča K., 2014. *Geotechnical study*, Project No: 050/2014.
- [6] EN 1536: 2015 – Execution of special geotechnical work – Bored piles
- [7] EN 1537:2013 – Execution of special geotechnical work – Ground anchors
- [8] EN 12716: 2018 – Execution of special geotechnical work – Jet grouting

GLOBAL STABILITY ANALYSIS OF REINFORCED EARTH RETAINING WALL FOR DUBROVNIK AIRPORT EXPANSION PROJECT

Ivan Mališa, *Geotehnički Studio d.o.o.*, ivan.malisa@geotehnicki-studio.hr

ABSTRACT

This paper provides a case study of geotechnical works performed to ensure the global stability of the reinforced earth retaining wall (Terramesh system) as a part of expansion of the Dubrovnik airport project, with emphasis on the additional stability analysis conducted especially for the purpose of this paper. All phases of the project are briefly here presented: geotechnical investigations, design, construction and supervision of the construction, field inspection of the jet grouting columns and laboratory testing on the samples taken from the field. The technical solution to ensure the global stability and foundation of the retaining wall consisted of foundation soil improvement with jet grouting columns and the construction of an anchored pile wall at the toe of the retaining wall. The purpose of the additional analyses was to model the jet grouting columns for different combinations of geometries (two approaches based on effective area and on effective bending resistance) and material models (Mohr-Coulomb and concrete) and consequently to examine the results of the analyses. The analyses were performed in Plaxis 2D. The advantages and disadvantages of different types of jet grouting columns modelling are discussed according to the results of numerical modelling while recommendations for similar problems modelling are given.

Keywords: Dubrovnik airport, Retaining wall, Jet grouting columns, Concrete material model, Stability analysis.

1. INTRODUCTION

The concrete material model, available in Plaxis 2D, allows the realistic modeling of jet grouting columns (“JGC”) behaviour constructed for the purpose of improving clayey ground. In this paper, an example of the application of the aforementioned material model is given for the assessment of the reinforced earth retaining wall stability of Terramesh type (“retaining wall”) which is constructed as part of the Dubrovnik airport expansion project. The retaining wall needs to be built because the existing condition on a portion of the “W” runway does not meet the requirements of the state regulations which requires that the minimum width of the airport runway with the reference code 4E is 47.5 m, measured from the central axis of the runway on each side separately [1]. This paper presents phases of investigation, design and execution of the southern retaining wall, while also showing the additional stability analyses with the application of the Mohr-Coulomb (“MC”) and concrete (“C”) material models.

1.1. Original Technical Solution According to the Main Design

According to the main design [1], south of the runway “W” a retaining wall with a maximum height of 18 m and length of 524 m was predicted [1]. A sinkhole resides in the central part of the retaining wall which is filled with a thick layer of terra rossa (5-8 m) and because of this reason, the project predicted that the retaining wall on this part must be founded on improved ground, which was done with the help of JGCs. The calculations in the project assumed the

JGCs are 80 cm in diameter, with a uniaxial compressive strength of 8 MPa and that the grid spacing between them is 2.5x2.5 m. The JGCs had to enter the rock to a depth of 0.5-1 m [1].

1.2. Adjustment of the Technical Solution According to the Main Design Modifications – Ensuring the Global Stability of the Retaining Wall

After the construction began in the sinkhole area and after control testing (see chapter 3), it was found that the original technical solution had to be adjusted to ensure the global stability of the retaining wall on that portion of the route. The adjustment of the technical solution was the subject of main design modifications [2].

Ensuring global stability of the retaining wall in the sinkhole area is divided into three characteristic zones: a) zone where the replacement of material or the ground improvement with ribs made of lean concrete takes place; b) zone where the anchored pile wall is constructed together with foundation ground improvement by JGCs and c) zone where the retaining wall is founded directly on rock [2].

In this paper, emphasis is on zone b), i.e. to additional analyses made on the calculation model of the zone b) to model the ground behavior and JGCs as realistically as possible, all with the purpose of estimating as close as possible the global stability at the stages of construction, exploitation, as well as during earthquake.

2. GEOTECHNICAL DATA

Geotechnical investigations for the construction of the southern retaining wall were done in April 2015. Geotechnical investigation works included the following: 1) exploration borehole drillings, 2) "in situ" testing in the boreholes, 3) laboratory testing of soil/rock samples, and 4) underground scanning with non-destructive geophysical methods – seismic refraction and geoelectrical tomography [3].

Based on the conducted investigations, two geotechnical mediums were identified in the foundation soil on site: embankment layer (consisting of rock fragments, construction waste and soil; medium dense), geotechnical medium 1 - natural cover (terra rossa, stiff to very stiff consistency) and geotechnical medium 2 - rock (limestone, different grades of weathering and fracturing) [3].

Figure 1 shows the longitudinal seismic refraction profile with the exploration boreholes position. Boreholes B-4 and B-5, which were executed approximately in the area of the sinkhole, are shown in Figure 2. As shown below, the depth of the natural cover (geotechnical medium 1) which is in bigger thickness (5-8 m) present in the central part of the investigated route (in the sinkhole area) can be seen. Also, Figure 2 shows the borehole B-1 which was executed outside the sinkhole area where the cover is much thinner [3].

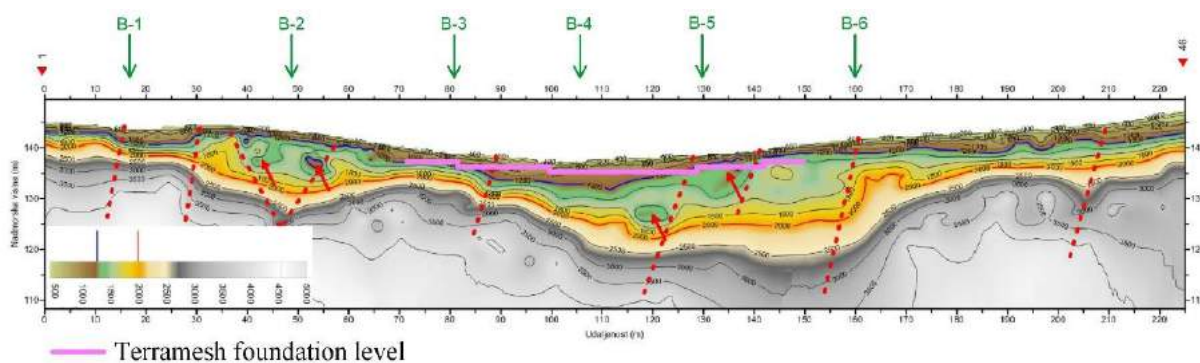


Figure 1. Longitudinal seismic refraction profile RF-1 [3]



Figure 2. Exploration borehole cores B-1 (left), B-4 (middle) and B-5 (right) [3]

3. CONSTRUCTION, SUPERVISION AND LABORATORY INVESTIGATIONS

Several activities were carried out during the supervision of foundation ground improvement with JGCs. For the purpose of this article, the following activities are important:

- a) Achieved diameter of the JGCs was controlled and it was established that the minimum achieved diameter is 60 cm (Figure 3) [2].
- b) Drilling through several JGCs was carried out in order to obtain representative samples for laboratory tests with the purpose of determining the uniaxial compressive strength and modulus of elasticity of JGCs. A total of 6 samples was collected. Laboratory tests showed that the mean value of the uniaxial compressive strength of the JGCs is 4 MPa and the mean value of the modulus of elasticity 1,844 MPa (Figure 4). The data obtained was of utmost importance during the design process [2].



Figure 3. Control of the achieved diameter of an executed JGC (left) and sample 2 taken from the investigation borehole B-26 before and after laboratory testing (right) [2]

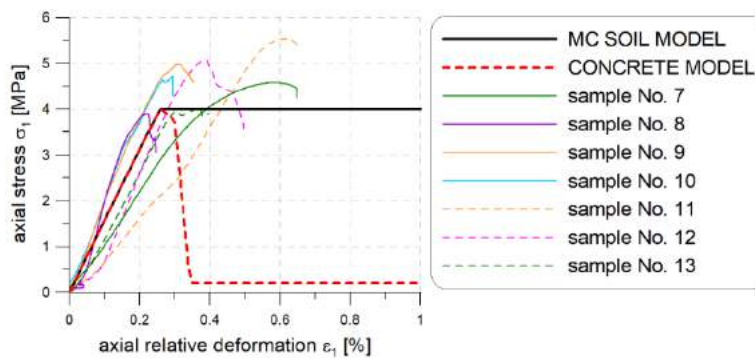


Figure 4. Work diagram of JGCs laboratory tested samples taken from the field and work diagram for MC and C material models used in the analyses

Since the calculations in the main design [1] were carried out with the assumption that the JGCs had a diameter of 80 cm and an uniaxial compressive strength of 8 MPa, on the basis of these findings, it was necessary to adjust the original technical solution according to the existing soil conditions and the possibility of execution of the JGCs.

4. NUMERICAL ANALYSES

The adjustment of technical solution is primarily referred to ensuring the global stability of the retaining wall which included the construction of the anchored pile wall in the toe of the retaining wall, as well as the improvement of the foundation ground with JGCs. In order to prevent the failure of already constructed JGCs and the excessive settlement of the retaining wall, the grid spacing between the JGCs has been changed from 2.5x2.5 m to 1.25x1.25 m. The chosen technical solution for ensuring the global stability of the retaining wall is shown on the characteristic cross section of the zone b) in Figure 5 [2].

The global stability of the retaining wall was calculated in Plaxis 2D. The calculation was carried out in phases (construction of JGCs, execution of the anchored pile wall, construction of the retaining wall, etc.).

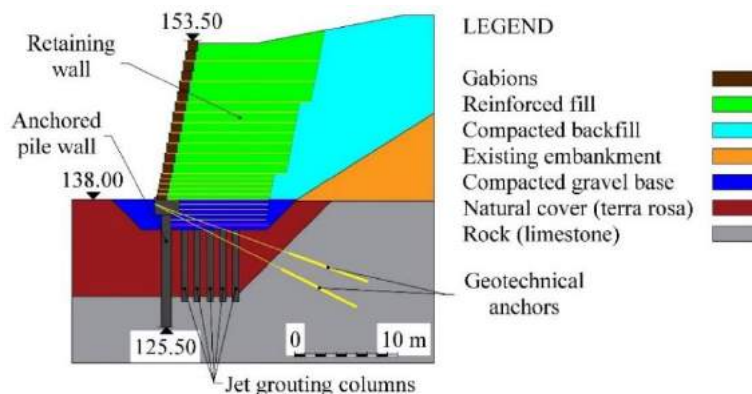


Figure 5. Technical solution for ensuring the global stability of the retaining wall [2]

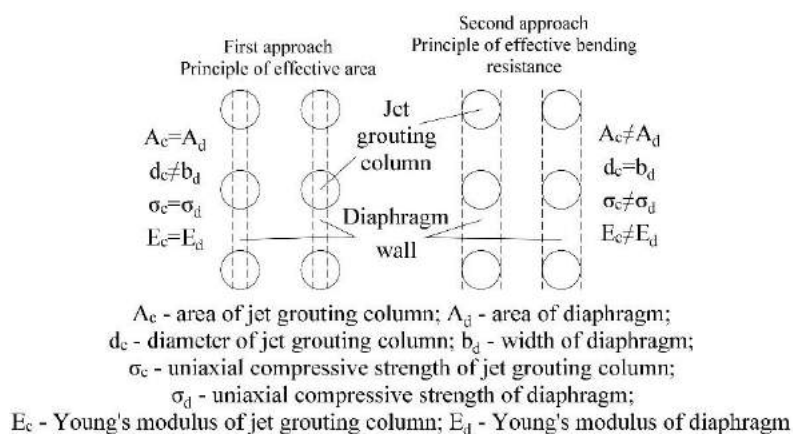


Figure 6. Two approaches to modeling the geometry of JGCs [2]

Since the JGCs are arranged in the space in a certain manner, a problem of modeling the JGCs arises, specifically, the transition from 3D to 2D space becomes problematic. Two approaches to modeling the geometry of the JGCs are considered (Figure 6). The first approach is the principle of effective area: the JGCs are reduced to a 'diaphragm wall' whose area per m' is

equal to the area of JGC per m², which implies that the thickness of the diaphragm is smaller than that of the JGCs; the mechanical parameters of the diaphragm remain the same as those of the JGCs [2]. The second approach is the principle of effective bending resistance: the JGCs are reduced to a 'diaphragm wall' whose thickness is equal to the thickness of JGCs, but the mechanical parameters of the diaphragm are reduced in relation to the JGCs because the area of the diaphragm is bigger than that of the JGCs.

For the purposes of the main design modifications [2], the JGCs in the program were modeled using the first approach and the MC material model. Before looking at how the global stability is influenced by different approaches to modeling the JGCs, a brief introduction to the C material model will be given. The C material model was developed specifically for the purpose of modeling the nonlinear behavior of concrete structures.

5. CONCRETE MATERIAL MODEL

In some cases, the non-linear behavior of the concrete structures needs to be modeled for the purpose of obtaining a reliable distribution of stresses and strains in the continuum. For the purpose of modeling this complex concrete behavior, the C material model was introduced. [4] The C material model is essentially an elastoplastic model through which this main feature of concrete can be simulated. [5]

Concrete shows different behaviors when subjected to deviatoric loading: in compression, the strength first increases non-linearly up until it reaches a peak value and then drops to a residual one; in tension, the strength increases linearly until it reaches the tensile strength and then drops to the residual value. [4] The normalized stress-strain curves for compression and tension, as defined in the C material model, can be seen in Figure 7.

Table 1. Summary of parameters for the C material model and their adopted values

Parameter	Name of the parameter	Adopted values	Unit
$\gamma_{\text{unsat}}/\gamma_{\text{sat}}$	Unsaturated/saturated unit weight	17	kN/m ³
Elastic parameters			
E_{28}	Young's modulus of cured concrete at t_{hydr}	1.6 (0.16)	GPa
ν	Poisson's ratio	0.30	-
Strength parameters			
$f_{c,28}$	Uniaxial compressive strength of cured concrete at t_{hydr}	4000 (680)	kN/m ²
f_{c0n}	Normalized initially mobilized strength	0.20	-
f_{cfn}	Normalized failure strength	0.95	-
f_{cun}	Normalized residual strength	0.01	-
$G_{c,28}$	Compressive fracture energy of cured concrete at t_{hydr}	2	kN/m
ϕ_{max}	Maximum friction angle	0.001	°
Ψ	Dilatancy angle	0	°
Strength in tension			
$f_{t,28}$	Uniaxial tensile strength of cured concrete at t_{hydr}	400 (68)	kN/m ²
f_{tun}	Ratio of residual vs. peak tensile strength	0	-
$G_{t,28}$	Tensile fracture energy of cured concrete at t_{hydr}	0.10	kN/m
Ductility			
$\epsilon_{cp,24h}^p$	Uniaxial plastic failure strain at 24h (negative value)	-0.0001	-
a	Increase of ϵ_{cp} with increase of p	1	-

The C material model involves a total of 25 parameters. Table 1 summarizes only the parameters which are considered for the analyses conducted in this article alongside their

adopted values (this adopted values were calibrated based on the laboratory tests conducted on field samples, as described in chapter 3). Other parameters were used by their default values (time-dependent effects such as shrinkage, creep and the change of compressive strength with time were not considered). The values of the parameters in Table 1 are given for the JGCs modeled using the first approach; those parameters for JGCs modeled using the second approach which differs from that modeled using the first approach are given in brackets [4]. The resulting stress-strain curve in compression for adopted parameters values of JGCs modeled using the first approach is shown in Figure 4 alongside the stress-strain curve for the MC material model and stress-strain curves obtained as a result of laboratory tests on samples of JGCs taken from the field.

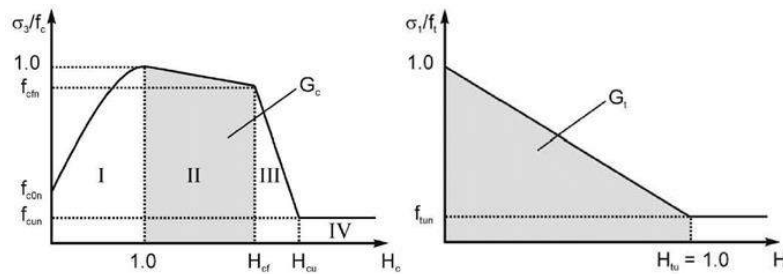


Figure 7. Normalized stress-strain curves in compression (left) and in tension (right) [4]

More detailed explanations and the theory behind the C material model can be found in references [4] and [5].

6. ADDITIONAL ANALYSES

For the purposes of this article, additional stability analyses have been made in relation to the main design modifications [2] which consider different approaches to JGCs modeling within the retaining wall. The columns were modeled using different combinations of geometry (two approaches described in chapter 4) and material models (MC and C). All analyses were carried out for undrained conditions of the natural cover.

Table 2. Additional stability analyses variants and results

VN	APW	JGC	GA	MM	ϕ -c	$\sum M_{stage}$ $a_x=0.05g$	$\sum M_{stage}$ $a_x=0.14g$
1	No	No	-	-	1.29	1.00	0.74
2	No	Yes	1.	MC	1.44	1.00	0.79
3	No	Yes	1.	C	1.45	0.96	0.35
4	No	Yes	2.	MC	1.45	1.00	0.93
5	No	Yes	2.	C	1.58	1.00	0.67
6	Yes	Yes	1.	MC	2.02	1.00	1.00
7	Yes	Yes	1.	C	2.01	1.00	1.00
8	Yes	Yes	2.	MC	2.00	1.00	1.00
9	Yes	Yes	2.	C	2.02	1.00	1.00

VN – variant number; APW – anchored pile wall; JGC – jet grouting columns; GA - approach for modeling the JGC geometry; MM – material model for JGC; ϕ -c – attained factor of safety from the ϕ -c analysis of the last calculation phase; $\sum M_{stage}$ – reached phase proportion during the pseudostatic (seismic) analysis for a given acceleration in the horizontal (x) direction

A total of 9 variants were considered. For result comparison, the earthquake load was used (pseudostatic analysis). These variants are shown in Table 2 together with the results obtained from the additional stability analyses. The incremental displacements for selected characteristic

variants are shown in figure 8. Based on the performed analyses, the following can be concluded:

- 1) Variant 1, although satisfactory in terms of global stability, does not achieve the required factor of safety (“FOS”) in the ϕ -c analysis (target FOS is 1.40) and does not pass the pseudostatic (seismic) analysis.

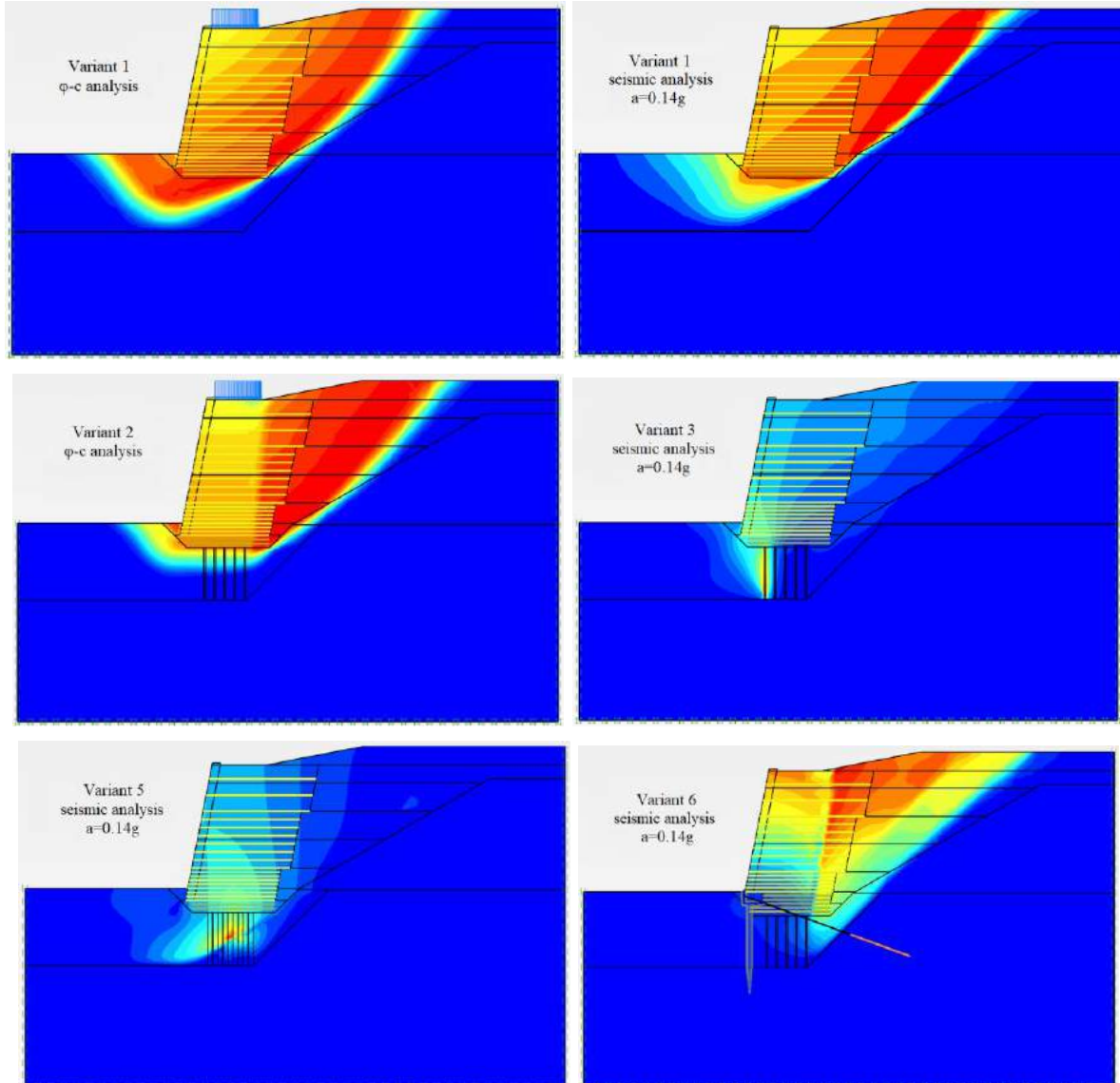


Figure 8. Incremental displacements for selected characteristic variants

- 2) In Variants 2 and 3, higher FOS is obtained in the ϕ -c analysis relative to the Variant 1 (FOS increased above the target value of 1.40) which is expected as the JGCs contribute to the global stability with their strength. Variants 2 and 3, however, do not pass the pseudostatic (seismic) analysis. It should be noted here that in variant 3, the collapse of the JGCs happens already during a small ground acceleration (0.05g), whereas that is not the case for Variant 2. The reason for the collapse can be attributed to the different approaches of JGCs modeling - in Variant 2, where the MC material model is used, the JGCs do not experience a brittle failure, but instead the plastic flow in the material continues indefinitely. On the other hand, in Variant 3, where JGCs are modeled with a C material model, at reaching the peak strength a brittle failure occurs (the JGC breaks at contact with

- the rock). Given that the JGCs are initially loaded in compression basically at their full capacity, the collapse happens already during a small horizontal force.
- 3) Variants 4 and 5 give similar FOS values in terms of ϕ -c analysis as Variants 2 and 3, but also do not satisfy the pseudostatic (seismic) analysis. Here, attention should be drawn to the collapse mechanism in Variant 5 during the earthquake; unlike Variant 3, which experiences failure at contact with the rock already at small values of ground accelerations (0.05g), the JGCs in Variant 5 are experiencing failure only at larger values (0.14g), during which the collapse occurs in the central zone of the JGCs.
 - 4) Variants 6 to 9 gives very similar values of FOS in the ϕ -c analysis (around 2.00) and satisfies the pseudostatic (seismic) analysis. These variants prove that the chosen technical solution satisfies in terms of stability for all cases of modeling the JGCs.

7. CONCLUSION

When using the MC material model for modeling materials characterized by brittle failure, it should be taken into consideration that the MC is an elasto-plastic material model in which the relationship between stresses and strain firstly linearly increases and then, when the peak strength of the material is reached, deformations continue to grow without increasing stress level (plastic flow). Unlike the MC material model, in the C material model after the peak strength is reached, the material, in general, experiences a brittle failure and the peak strength, after a certain level of plastic flow, drops to 0, i.e. to a very low residual value. The C material model is therefore a much better solution for modeling brittle materials since it far better approximates their real behavior.

It has been observed that the ϕ -c analysis gives the same results when JGCs are modeled either with the MC or C material model. The reason for this is that the strength of the MC model and the peak strength of the C model are the same and consequently, the ϕ -c analysis gives the same results. The ϕ -c analysis does not take into account the deformation-dependent strength reduction; therefore, it is not suitable for direct comparison of the results between MC and C material models.

ACKNOWLEDGEMENT

First, I would like to extend my gratitude to my mentor Igor Sokolić for his suggestions and guidelines during the writing of this paper. I would also like to thank my company Geotehnički studio for providing me with this opportunity. Also, special credits go to the Geotehnički studio laboratory staff for their diligent work and contribution during the whole project.

REFERENCES

- [1] Baždarić, S., 2016-2017. “*Reconstruction of structures inside the Dubrovnik airport – Dubrovnik airport development, Retaining wall - south, Structural design of mechanical resistance and stability*”, Main design, Transport Operational Programme 2007-2013., Project No: ZG 01-15.
- [2] Sokolić, I., 2018. “*Reconstruction of structures inside the Dubrovnik airport – Dubrovnik airport development, Retaining wall - south, Ensuring the global stability of the reinforced earth retaining wall of Terramesh type*”, Main design, Transport Operational Programme 2007-2013., Project No: 8914-P-18-39-77.
- [3] Šiša, P., 2015. “*Dubrovnik airport, Dubrovnik airport development, Retaining wall - south*”, Geotechnical report, Transport Operational Programme 2007-2013., Project No: 4665-2/15.GS.
- [4] Brinkgreve, R.B.J., Kumarswamy, S., Swolfs, W.M., Zampich, L., Ragi Manoj, N., 2019. “*PLAXIS Material Models Manual 2019*”, Plaxis bv, Bentley Systems, Incorporated, The Netherlands, 256 pages.
- [5] Schädlich, B., Schweiger, H.F., 2014. “*A new constitutive model for shotcrete*”, Eighth European Conference on Numerical Methods in Geotechnical Engineering, Volume I, pp. 103-108, 18-20 June 2014, The Netherlands.

INFLUENCE OF STRESS STATE AND STRESS HISTORY ON THE RATE OF SECONDARY DEFORMATION FOR A HIGH PLASTICITY PALEOGENE CLAY

Emil Mejlhede Kinslev*, *Technical University of Denmark, Department of Civil Engineering, emki@byg.dtu.dk and COWI A/S, Marine and Geotechnical engineering, emkv@cowi.com*

Ole Hededal, *COWI A/S, Marine and Geotechnical engineering, olhe@cowi.com*

Irene Rocchi, *Technical University of Denmark, Department of Civil Engineering, ireroc@byg.dtu.dk*

Varvara Zania, *Technical University of Denmark, Department of Civil Engineering, vaza@byg.dtu.dk*

ABSTRACT

An increasing demand for construction of high-speed railway systems in Northern Europe has led to increased focus on deformation prediction due to the low tolerances for settlement/heave in such projects. With a design lifetime exceeding 100 years, a detailed description of secondary deformation is essential for adequate prediction of long-term settlement/heave. The creep deformations of high plasticity Paleogene clays challenge currently planned Danish projects. These deposits have a high clay content with significant amount of smectite. Subsequent burial and erosion by Neogene deposits has led to a high level of overconsolidation, generating also fissures and slickensides. This complicated stress history along with active mineralogy influences the secondary deformation behaviour, which displays a significant stress state dependency. As a part of the tendering phase of the currently planned “Fehmarnbelt Fixed Link” project, connecting Denmark and Germany, an extensive laboratory campaign of 1D IL consolidation tests was carried out. The results from these tests were reanalysed in the current study, in order to assess the time dependent behaviour of folded Røsnæs Clay in compression and swelling. The results indicate that there is a nonlinear relationship between the primary and secondary compression, while a similar trend could not be as clearly identified for the swelling behaviour.

Keywords: Secondary Deformation, Overconsolidated Clay, High Plasticity Clay.

1. INTRODUCTION

The accurate prediction of long-term deformations in large infrastructure construction projects, where the design life exceeds 100 years, is essential for the evaluation of serviceability requirements and the life-cycle cost. Secondary deformation therefore plays an important part in the total deformations and should be accurately defined for the in-situ soil formations. In a number of planned Danish projects, the prediction of settlement/heave of Paleogene clays is associated with a high degree of uncertainty and therefore triggered engineering and research interest. One of these projects is the “Fehmarnbelt Fixed Link” (FFL), which aims to connect Denmark and Germany [1]. The geotechnical investigation campaign for this project has produced a large database of Incremental Loading (IL) 1D-consolidation tests on Danish Paleogene clay formations, providing an excellent opportunity for studying the characteristics of secondary deformation.

The Danish Paleogene clays, as defined by Heilmann-Clausen et al. [2], comprise of the Røsnæs Clay, Lillebælt Clay and Søvind Marl (oldest to youngest). They received a common name

“high plasticity Paleogene clays” taken from their extraordinary plasticity (IP of 58-168%, [3]) compared with other Danish clay formations. These formations were deposited in the North Sea basin, 56,0-33,9 million years ago. The sedimentation occurred well below the wave base resulting in a slow sedimentation (1mm/100years) of primarily clay minerals. The source material contained large amounts of volcanic ash (from the Icelandic Hotspot) that weathered into the clay mineral smectite, which therefore makes up a considerable part of the mineralogical composition [4]. The high plasticity is considered to originate from the high smectite content. The deposits from the Neogene period were generally eroded due to decreases and increases of the global sea level. Michelsen [5] describes the result of this as being a net deposition and then erosion of 250-1000 meters of material above the Paleogene clays depending on the geographical position in Denmark. These events lead to a high level of overconsolidation (preconsolidation pressure of several MPa compared to an in-situ stress of some hundreds kPa). Glaciotectonic activity from the Quaternary period resulted in remoulding of the shallowest parts of the Paleogene clays in the form of large thrust fault structures with folded parts, slickensides and micro fissures [6]. Krogsbøll et al. [7] and Okkels and Hansen [8] describe a particular implication of the geological history as the Danish Paleogene clays showing a gradual yielding in the compression plane or “loss of memory” of the preconsolidation pressure. Such behaviour is seen in some structured clays (see e.g. [9]) and may therefore be related to similar factors. Okkels and Hansen [8] presented an alternative explanation for the gradual yielding as gradual closing of fissures in the overconsolidated regime until the point where yield of the soil matrix starts.

The behaviour of clays in secondary deformation has received great attention the past decades. Most previous studies have analysed secondary compression of normally consolidated or slightly overconsolidated clays. Based on such clays along with different silts and peats, Mesri and Godlewski [10] suggested that the rate of secondary deformation ($C_{\alpha e} = \partial e / \partial \log(t)$) is related to the “local” tangent in the compression plane ($C_c = \partial e / \partial \log(\sigma'_v)$). They found, that the ratio $C_{\alpha e} / C_c$ may be approximated by a constant value, which depends on the soil type. Typical values for inorganic clays of $C_{\alpha e} / C_c$ are 0.04 ± 0.01 according to Mesri and Castro [11], whereas softer soil types attain a higher ratio and stiffer soil types a lower ratio. The soil type most comparable to Danish Paleogene clays studied by Mesri and Castro [11] is the Bearpaw Shale as it has comparable plasticity and preconsolidation pressure and also shows a gradual yielding. For this formation, a ratio $C_{\alpha e} / C_c = 0.029$ was observed. Powell et al. [12] observed a ratio of $C_{\alpha e} / C_c = 0.03$ also for Bearpaw Shale, thus backing up the observation by Mesri and Castro [11].

Although the $C_{\alpha e} / C_c$ concept originally was only applied to compression, Mesri et al. [13] and Powell et al. [12] used the same concept in swelling of reconstituted and intact shales respectively. Mesri et al. [13] observed an increase of $-C_{\alpha e} / C_s$ with increasing overconsolidation ratio (OCR) and much higher values of $-C_{\alpha e} / C_s$ (0.04-0.3) compared to compression, were observed at OCR close to 100. Powell et al. [12] on the other hand observed the trend for compression to fit swelling as well although with significant scatter compared to that presented by Mesri and his co-authors ([10], [11], [13]). Leroueil [14] and Leroueil et al. [15] also investigated the link between $C_{\alpha e}$ and C_c in normally consolidated soft clays. Instead of a constant value of $C_{\alpha e} / C_c$ they observed an increase of $C_{\alpha e} / C_c$ with increasing C_c .

The time dependent behaviour in compression and swelling of a Danish Paleogene clay named Røsnæs Clay is studied. A set of incremental loading test data from the FFL project has been made available and were re-interpreted to estimate the secondary deformation behaviour of Røsnæs Clay to form a hypothesis for modelling.

2. METHODOLOGY

In the geotechnical investigation for the FFL project in 2009-2010, Røsnæs Clay was the main Paleogene unit found along the alignment. It was subdivided into a “folded” and an “intact” part, based on whether influence from glaciotectonic activity was observed in the clay or not [16]. The folded part was subjected to the most intensive study by Femern A/S, [3] and [16], due to its close proximity to the seabed (starting between 5 and 35 meters below seabed and reaching down to maximum 75 meters below seabed) and thus high influence on the future structure. The 68 IL tests retrieved from 36 offshore and 12 onshore boreholes along the 18 km alignment form the basis for this study. The IL tests were performed on samples trimmed from high quality rotary cores (Ø100 mm). The testing complied with the ASTM [17]. Further, the added water had a similar salt composition (Cl^- , SO_4^{2-} , Na^+ , K^+ , Mg^{2+} and Ca^{2+}) and pH to that leached from 18 samples evenly distributed along the alignment to minimise osmotic and chemical effects. To re-establish the in-situ condition of the soil, the general testing procedure used loading to a low estimate of the preconsolidation pressure, followed by unloading to the in-situ stress from where further unloading or reloading occurred in some tests including multiple unloading reloading loops.

Although the geological description of the Danish Paleogene clays describes a very homogenous soil, the classification data from the samples by Femern A/S [3] display some variation of the initial water content, plasticity index and clay content, presented in Table 1.

Table 1. Classification parameters for folded Røsnæs Clay. From Femern A/S [3]

Parameter	Unit	Value
Initial water content (w_0)	%	29-43
Plasticity index (I_p)	%	58-168
Clay content (<2 μm) (CC)	%	53-89

The secondary deformation behaviour in loading, unloading and reloading of the folded Røsnæs Clay was re-analysed based on the series of IL test retrieved from the Femern database. Degago et al. [18] argued that creep rates should be evaluated based on void ratios to incorporate strain history, further they argued that interpretation based on load step deformation might lead to inaccurate determination of the end of primary (EOP) state and therefore influence subsequent interpretations. Based on these arguments, the time-curves from the tests from Femern A/S were reinterpreted based on void ratio as the original interpretations relied on volumetric strains. Along with this reinterpretation each time-curve was reassessed in terms of whether an appropriate identification of secondary deformation was possible and whether the load step ratio ($\Delta\sigma/\sigma$) in combination with the creep time would lead to inaccurate determination of stiffness properties as discussed by Mesri and Castro [11]. The load step ratio for the IL tests range between 0.04 and 2.93 in loading and -0.06 and -3.57 in unloading. The predominating load step ratios are $\pm 1/4$, $1/3$, $1/2$, $2/3$, $3/4$ and 1 with less than 10% smaller than 0.2 or higher than 2. The maximum allowed creep time was two log cycles. Two IL tests were excluded from interpretation based on combination of long creep time and low load step factor. The analysis of secondary deformation for unloading and reloading is restricted to include only the first unloading-reloading loops in order to clear the interpretation from effects of destructuration caused by multiple load cycles.

As described in Section 1, C_c and C_s are used as a reference to $C_{\alpha e}$. As described by Mesri and Castro [11] these indices only make a valid reference when they are determined from void ratios on the same time isotache (for instance from the EOP) and the corresponding $C_{\alpha e}$ is interpreted starting from that void ratio as well.

C_c and C_s should ideally represent the tangent to the stress-void ratio curve ($\partial e / \partial \log(\sigma'_v)$), but since an IL test is performed with finite stress increments, C_c and C_s can only be defined by a secant as the closest approximation of the local tangent. Figure 1 shows the method for defining the secant for a stress level “K” based on the previous and the next stress level (“J” and “L” respectively). When all three stress levels are loading points (Figure 1A), the secant related to K is defined as the inclination between J and L. When a stress path reversal occur after K (either going from loading to unloading or from unloading to loading) this method no longer makes sense, and the inclination between J and K is used instead (Figure 1B). When stress level K is at the boundary between reloading and loading (Figure 1C) the tangent is expected to change significantly and the inclination between J and L used for the definition of the secant may contain a larger amount of uncertainty compared to the other two cases (see [11]).

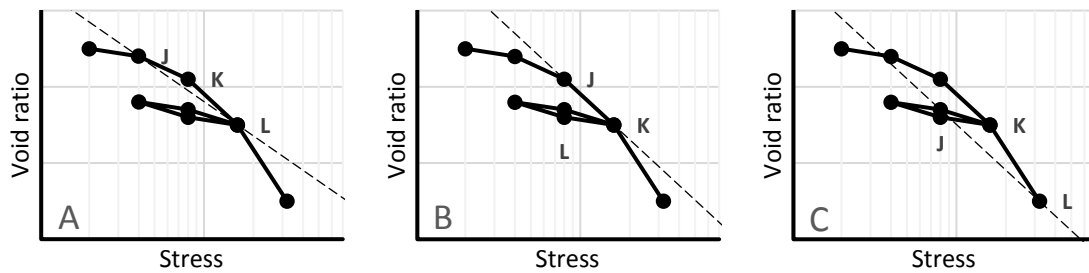


Figure 1. Method of interpreting C_c or C_s for a stress level (K), based on the previous (J) and next (L) stress level. Dashed line shows the slope used for defining the index.
 A) Interpretation for three consecutive loading stress levels. B) Interpretation at stress path reversal. C) Interpretation at the boundary between reloading and loading.

3. RESULTS AND DISCUSSION

One of the defining features of folded Rønæs Clay is the gradual yielding in the compression plane. Figure 2A shows that this feature appears as a stress dependant C_c both for virgin loading (in the laboratory) and reloading. Although with significant scatter, the stress dependency of C_c display a nonlinear development with the logarithm of vertical effective stress. If the concept of linking C_{ae} to C_c [10] applies to folded Rønæs Clay a similar development of C_{ae} with stress should appear. Figure 2B shows that C_{ae} indeed is stress dependent, though with more scatter

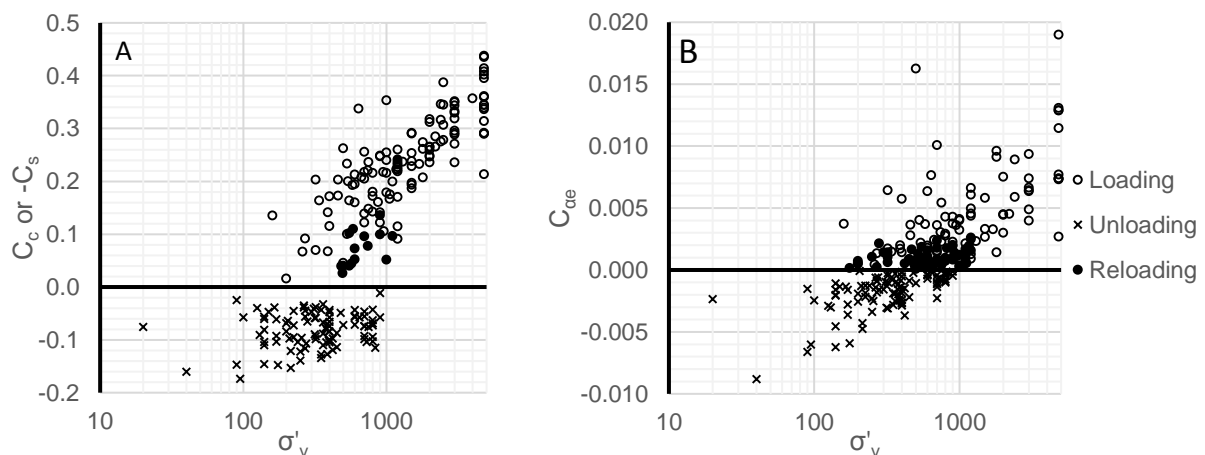


Figure 2. Compression and opposite signed swelling index (A) and rate of secondary deformation (B) based on vertical effective stress level.

and a more linear development compared to C_c . In swelling no stress dependency of C_s can be identified from Figure 2A. C_{ae} in swelling, on the other hand, show slight stress dependency,

though with significant scatter. The lack of stress dependency of C_s is in agreement with the observation by Kinslev et al. [19] that C_s for folded Røsnæs Clay relates to the unloading index (UI, defined in Equation (1)) rather than stress level, which is consistent with other studies [13].

$$UI = \sigma'_{unloading\ from} / \sigma'_v \quad (1)$$

The dependency of C_s on UI indicates that stress path changes have an important influence on the behaviour of folded Røsnæs Clay. A similar parameter to UI but for the reloading (RI) and loading (LI) indices (Equation (2) and (3)) is therefore defined to investigate this further. RI and LI increase at stress states further away from the point of stress path reversal in the same way as UI. The vertical effective in-situ stress ($\sigma'_{v,0}$) is chosen as the reference stress for the loading index, since the latest known geological process was unloading to the in-situ stress and a stress path reversal therefore occurs when loading the sample in the laboratory.

$$RI = \sigma'_v / \sigma'_{reloading\ from} \quad (2)$$

$$LI = \sigma'_v / \sigma'_{v,0} \quad (3)$$

Using the parameters LI, UI and RI, the development of C_c , C_s and $C_{\alpha e}$ with increasing distance to latest stress path reversal are shown in Figure 3. This slightly decreases the scatter in the development of C_c compared to Figure 2, while $C_{\alpha e}$ in compression still contains significant scatter. $C_{\alpha e}$ in swelling also show a less scattered trend and C_s , as expected, shows dependency on UI. Figure 3 shows, that C_c , C_s and $C_{\alpha e}$ all increase at increasing distance from latest stress path reversal. C_c show a slightly nonlinear trend to the logarithm of LI or RI while C_s and $C_{\alpha e}$ both show a trend closer to linearity. From Figure 3B, it may be seen that $C_{\alpha e}$ for a limited stress change after a stress path reversal (LI, UI or RI below 1.3) is very close to zero, suggesting that upon stress path reversal some amount of stress change is needed for the secondary response to activate. Unloading and reloading points display this behaviour most clearly. The reason for some of the loading points falling outside this trend may be caused by uncertainty in the determination of the in-situ stress along with influence for sampling.

Both Figure 2 and 3 show significant scatter. As discussed in Section 2, some amount of the scatter likely originates from the interpretation method for C_c and C_s as they are not determined from a continuous curve. Variation in classification parameters within the folded Røsnæs Clay could also explain the scatter. Figure 2 and 3 were sorted with I_p and initial void ratio, but did not produce any clear trends or correlations and are therefore not presented in this paper.

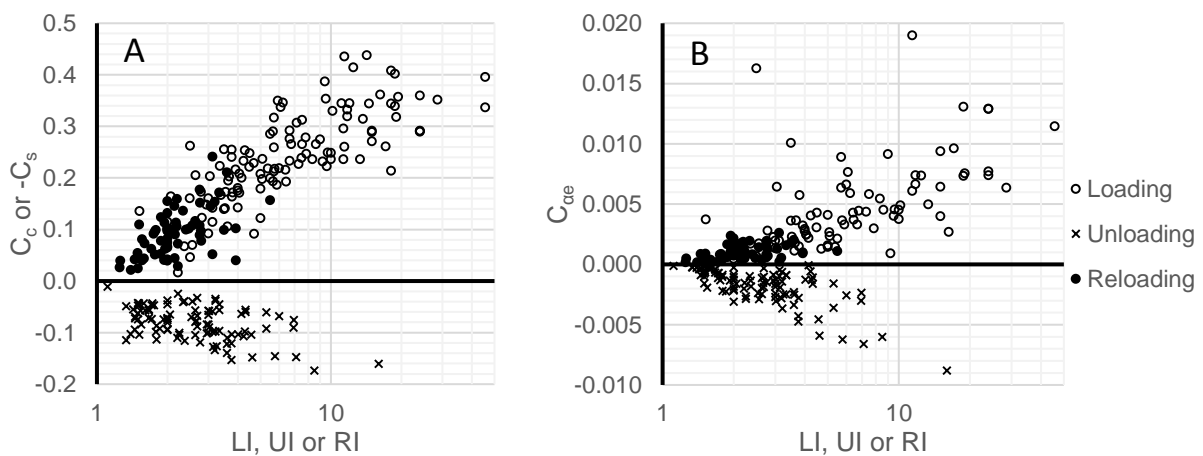


Figure 3. Compression and opposite signed swelling index (A) and rate of secondary deformation (B) based on LI, UI or RI.

As similar trending development of C_c or C_s and $C_{\alpha e}$ were observed in Figure 2 and particularly in Figure 3 a link between the primary and secondary response may indeed exist as the one observed by Mesri and Godlewski [10]. Figure 4 shows the development of $C_{\alpha e}$ with C_c or C_s .

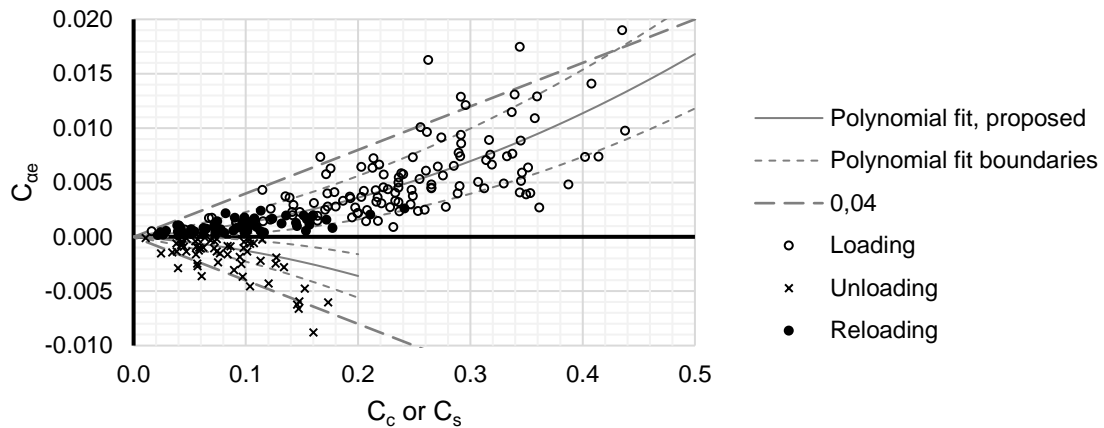


Figure 4. Relation between rate of secondary deformation and corresponding local compression or swelling index along with best polynomial fit (for compression) ± 0.01 on the linear term and the linear relation for inorganic clay by Mesri and Castro [11].

It may be seen from Figure 4 that the link between C_c and $C_{\alpha e}$ does not have as clear a trend as observed by Mesri and Godlewski [10] or Mesri and Castro [11], but it contains significant scatter. Mesri and Castro [11] found a variation of ± 0.01 for $C_{\alpha e}/C_c$ between different specific formations within one category of soil types (e.g. inorganic clays). Based on this observation folded Røsnæs Clay as a specific formation would be expected to show scatter less than ± 0.01 , but the scatter in Figure 4 exceeds these boundaries. Powell et al. [12] also observed a higher scatter for Bearpaw Shale than that reported by Mesri and Castro [11], who presents a smaller data set. This may suggest that structure and/or overconsolidation in clays and shales display an increased scatter since these features exist in both the folded Røsnæs Clay and the Bearpaw Shale. Mesri and Castro [11] particularly highlighted the difficulty in correctly identifying pairs of C_c and $C_{\alpha e}$ for soils with sudden changes in C_c such as structured clays.

The majority of the data points for the folded Røsnæs Clay has a lower $C_{\alpha e}/C_c$ ratio than observed by Mesri and Castro [11] and Powell et al. [12] for Bearpaw Shale. Only for $C_c > 0.3$ does a ratio of 0.03 seem to represent an approximate mean value. The 0.04 linear relation by Mesri and Castro [11] for inorganic clay is shown in Figure 4 to give a good representation of an upper boundary value for $C_{\alpha e}/C_c$ in folded Røsnæs Clay. The same linear fit, but with opposite sign, also makes a good representation of a boundary to the values of $C_{\alpha e}/C_s$.

From Figure 4 it may be seen that the link between $C_{\alpha e}$ and C_c for the folded Røsnæs Clay is not exactly linear as observed by Mesri, Powell and their co-workers ([10], [11] and [12]), but rather tend to increase with increasing C_c similarly to the observations by Leroueil [14] and Leroueil et al. [15]. A best polynomial fit between $C_{\alpha e}$ and C_c is therefore used to represent the development of $C_{\alpha e}$ with C_c . The polynomial fit is presented in Equation (4) and illustrated in Figure 4 along with 0.01 boundary lines of similar magnitude to the amount of variation within one type of soils found by Mesri and Castro [11].

$$C_{\alpha e} = 0.052 \cdot C_c^2 + (0.008 \pm 0.01) \cdot C_c \quad (4)$$

The polynomial trend along with the boundary lines seems to capture the general behaviour of the folded Røsnæs Clay in compression to a reasonable extent. By comparing the development

of C_c with that of $C_{\alpha e}$ in Figure 2 and 3, respectively, it may be realised that the nonlinearity in the development of $C_{\alpha e}$ with C_c (shown in Figure 4) is likely caused by the nonlinear development of C_c with both $\log(\sigma'_v)$ and LI or RI compared to $C_{\alpha e}$.

Due to the limited range of swelling indices for the data in Figure 4 it is not possible to determine a mathematical expression for this trend. If Equation (4) is used with opposite sign to represent the behaviour in swelling, a multiplication of the linear term by approximately three produces a trend that (including the boundary lines of ± 0.01) captures the data in swelling reasonably well. These observations on folded Røsnæs Clay therefore contradicts the observation by Powell et al. [12] that the same ratio is applicable in compression and swelling but confirms the observation by Mesri et al. [13] that a higher ratio applies in swelling compared to compression. Since C_s increases with UI (Figure 3A) and $C_{\alpha e}$ increases with C_s (Figure 4) for folded Røsnæs Clay, $C_{\alpha e}/C_s$ increases with UI. This is in agreement with the observation by Mesri et al. [13] of increasing $C_{\alpha e}/C_s$ with OCR for reconstituted Bearpaw Shale.

4. CONCLUSION

The IL consolidation tests on folded Røsnæs Clay performed as part of the geotechnical investigations for the Fehmarnbelt Fixed Link were re-analysed to improve the understanding of secondary deformation behaviour in this soil type and formulate hypotheses for future modelling of the observed behaviour.

Folded Røsnæs Clay is known to display a gradual yielding in the compression plane, which appears as a nonlinearly increasing C_c with both the $\log(\sigma'_v)$ and distance from latest stress path reversal (defined by the parameters RI and LI). C_s on the other hand shows no stress level dependency but instead depends on distance from latest stress path reversal (defined by the parameter UI). The secondary response of folded Røsnæs Clay shows dependency on both stress level and stress path reversal in compression as well as in swelling. It was observed that some amount of stress change after a stress path reversal is needed to activate the secondary response.

$C_{\alpha e}$ in compression shows a polynomial increase with C_c , which in combination with boundary lines of ± 0.01 on the linear term generally captures the data for folded Røsnæs Clay. The ratio $C_{\alpha e}/C_c$ suggested for inorganic clays by Mesri and Castro [10] defines a good estimate of upper boundary values for the behaviour of folded Røsnæs Clay in both compression and swelling. The non-linearity in the link between secondary and primary behaviour for folded Røsnæs Clay, is primarily generated by the non-linear relation between C_c and $\log(\sigma'_v)$ or LI and RI. Using the proposed polynomial fit from the compression data for swelling, reveals that there is a stronger dependency between the secondary and primary response in unloading.

The folded Røsnæs Clay displays significant scatter in the correlation between the secondary and primary response. Grouping with plasticity index and initial void ratio did not reduce this scatter. A primary source of the scatter is therefore believed to be generated by imprecise interpretation of C_c and C_s since they are defined from IL tests. More precise determination of C_c and C_s by constant rate of strain consolidation tests, along with grouping with other classification or state parameters may therefore be needed to reduce the scatter in the observed trends.

ACKNOWLEDGEMENT

Funding from Innovation Fund Denmark for the project 'Efficient performance of large infrastructure: a geomechanical approach towards sustainable design' – grant number 7038-

00203B – is gratefully acknowledged. The authors express gratitude to Femern A/S for providing the data.

REFERENCES

- [1] Femern A/S. “*The tunnel across Fehmarnbelt*”, Retrieved 8 July 2019 from <https://femern.com/en>.
- [2] Heilmann-Clausen, C., Nielsen O. B., Gersner, F., 1985. “*Lithostratigraphy and depositional environments in the upper Paleocene and Eocene of Denmark*”, Bulletin of the Geological Society of Denmark, 33:287-323.
- [3] Femern A/S, 2013. “*Advanced laboratory testing – Clays of Palaeogene origin*”, Geotechnical investigations for the Femern Fixed Link, GDR 18.0-005.
- [4] Nielsen, O. B., Rasmussen, E. S., Thyberg, B. I., 2015. “*Distribution of clay minerals in the Northern North Sea Basin during the Paleogene and Neogene: A result of source-area geology and sorting processes*”, Journal of Sedimentary Research, 85:562-581.
- [5] Michelsen, O., 1996. “*Late Cenozoic basin development of the eastern North Sea Basin*”, Bulletin of the Geological Society of Denmark, 43:9-21.
- [6] Pedersen, S. A. S., 2014. “*Architecture of Glaciotectonic complexes*”, Geosciences, 4:269-296.
- [7] Krogsbøll, A., Hededal, O., Foged, N. N., 2012. “*Deformation properties of highly plastic fissured Palaeogene clay – Lack of stress memory*”, Proceedings of the 16th Nordic geotechnical meeting, Denmark.
- [8] Okkels, N., Hansen, P. B., 2016. “*Swell pressure and yield stresses in Danish highly overconsolidated Palaeogene clays of extreme plasticity*”, Proceedings of the 17th Nordic geotechnical meeting, Iceland.
- [9] Cotecchia, F., Chandler, R. J., 2000. “*A general framework for the mechanical behaviour of clays*”, Géotechnique, 50:431-447.
- [10] Mesri, G., Godlewski, P. M., 1977. “*Time- and stress-compressibility interrelationship*”, Journal of the geotechnical engineering division, 417-430.
- [11] Mesri, G., Castro, A., 1987. “ *C_α/C_c concept and K_0 during secondary compression*”, Journal of geotechnical engineering, 113:230-247.
- [12] Powell, J. S., Take, W. A., Siemens, G., Remenda, V. H., 2012. “*Time-dependent behaviour of the Bearpaw Shale in oedometric loading and unloading*”, Canadian Geotechnical Journal, 49:427-441.
- [13] Mesri, G., Ullrich, C. R., Choi, Y. K., 1978. “*The rate of swelling of overconsolidated clays subjected to unloading*”, Géotechnique, 28:281-307.
- [14] Leroueil S., 2006. “*The isotache approach. Where are we 50 years after its development by Professor Šuklje*”, Proceedings of the 13th Danube European conference on geotechnical engineering, Slovenia.
- [15] Leroueil, S., Kabbaj, M., Tavenas, F., 1988. “*Study of the validity of a $\sigma'_v - \varepsilon_v - \dot{\varepsilon}_v$ model in situ conditions*”, Soils and Foundations, 28:13-25.
- [16] Femern A/S, 2014. “*Ground investigation report*”, Geotechnical investigations for the Femern Fixed Link, GDR 00.1-001.
- [17] ASTM D 2435-04, 2004. “*Standard Test Methods for One-Dimensional Consolidation Properties of Soils Using Incremental Loading*”, ASTM International, USA.
- [18] Degago, S. A., Grimstad, G., Jostad, H. P., Nordal, S., Olsson, M., 2011. “*Use and misuse of the isotache concept with respect to creep hypotheses A and B*”, Géotechnique, 61:897-908.
- [19] Kinslev, E. M., Hededal, O., Rocchi, I., Zania, V., 2019. “*Stress dependency and unloading-induced swelling behaviour of a high plasticity overconsolidated clay of Paleogene origin*”, Proceedings of the 7th International symposium on deformation characteristics of geomaterials, United Kingdom.

SCANDINAVIAN PRACTICES FOR CALCULATION OF SECOND-ORDER EFFECTS AND BUCKLING OF PRECAST CONCRETE PILES IN SOFT SOILS

Jakob Rahbek Udengaard, *Per Aarsleff A/S, jau@aarsleff.com*

ABSTRACT

The structural bearing capacity of concrete piles in soft soils is a complex problem. Lateral deflection and second-order effects of a pile element subject to axial load involves both soil mechanics and pile material characteristics. Scandinavian practices for treating this problem are examined and compared, along with discussion of the rules and recommendations of Eurocode 7 and approach to limit state analysis of structural bearing capacity of precast concrete piles with consideration of initial curvature and second-order effects.

In Denmark, it is common practice to disregard analysis of buckling and second-order effects on axially loaded foundation piles. Using a rule of thumb from a former Danish standard, DS 415, concrete pile foundations are designed to avoid exceeding a critical stress of 10 MPa on the cross-section of the concrete pile element when installed in soft soils. However, due to the soil conditions of Denmark, the bearing capacity of concrete piles are most often limited by the geotechnical bearing capacity, not the structural.

In Sweden and Norway, piles are frequently driven to bedrock, often making the structural bearing capacity decisive rather than the geotechnical bearing capacity. Buckling and second-order effects are calculated using analytical methods. The most significant factors of influence are the stiffness of the pile, the stiffness of the soil, and the initial curvature of the pile.

According to Eurocode 7, a check for buckling is normally not required when the piles are embedded in soils with a characteristic undrained shear strength, c_{uk} , that exceeds 10 kPa. However, this exemption is not safe when the initial curvature and the additional lateral deflection caused by second-order effects are considered.

Keywords: Buckling of Piles, Precast Concrete Piles, Slender Piles in Soft Soils, Limit State Analysis of Piles.

1. INTRODUCTION

Precast concrete piles are the most common type of pile foundation throughout Scandinavia, and the practices to pile design are relatively similar. This is however not the case for analysis of buckling and second-order effects. The common basis for the Scandinavian countries for analysis of piles is Eurocode 7 [1]. The standard only treats the buckling problem vaguely with two short statements – one is even unsafe. Second-order effects as well as the effects of initial curvature are not mentioned at all.

The deflection of a fully embedded pile under axial compression is described with a sine-function – see figure 1. In Norway buckling resistance is calculated using an analytical method accounting for initial curvature and limitation to lateral deflection of the pile. In Sweden the same formulation is used a step further to compute a load-effect curve, which represents the second-order moment in relation to the axial load.

The curve is compared to the resistance of the pile material to determine the resistance to buckling and second-order effects. In Denmark, analysis of buckling and second-order effects is omitted by using a rule-of-thumb for the lower limit of the structural resistance of the concrete pile.

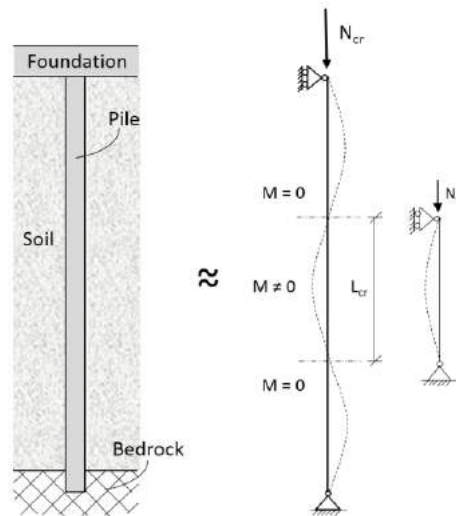


Figure 1. Deflection curve of fully embedded pile under axial compression

Structural bearing capacity according to Eurocode 2 [2] is determined by adding a partial safety factor to each material strength parameter, whereas geotechnical bearing capacity is in Scandinavia found by adding total safety to a calculated resistance. Instability analysis of piles however involves both concrete and soil parameters, causing doubt to which safety approach to use.

2. BUCKLING OF PILES ACCORDING TO SCANDINAVIAN CODES

Codes and standards dictate how engineers work with design and analysis of problems such as buckling of a pile. Eurocodes are the current rules in force in Denmark, Sweden and Norway for structural design, but each country have their own national annex (NA) and traditional calculation practice.

In Eurocode 7 chapter 7.8 [1] the two statements below can be found:

7.8(4)P Slender piles passing through water or thick deposits of extremely low strength fine soil shall be checked against buckling.

7.8(5) Normally a check for buckling is not required when the piles are contained by soils with a characteristic shear strength, c_u , that exceeds 10 kPa.

In the Swedish national annex, EKS 10 [4], the following general recommendation is found:

Chapter 7.1 article 3 When the exemption from verification in accordance with 7.8(5) in SS-EN 1997-1 is used, the shear strength should exceed 25 kPa.

Norwegian and Danish national annexes do not provide further description on the problem – not surprising since national choices for these two phrases is not allowed. However, in the former Danish code of practice, DS 415 [3], the following principle statement is found:

6.3.9(4)P For piles completely embedded in the ground, failure by buckling is not normally taken into account. In extremely soft deposits, for very slender steel piles and for reinforced concrete piles utilised for design concrete stresses above 10 MN/m², the risk of deformation shall be further analysed taking account of the deformation properties of the adjacent strata.

3. CALCULATION OF BUCKLING OF A FULLY EMBEDDED PILE

3.1. Danish Practice

The section from DS 415 is, even though the standard has been withdrawn, still widely used as a rule-of-thumb to avoid check for buckling and second-order effects for piles driven through thick deposits of soft soil e.g. peat and gyttja. Since such deposits often are the reason for choosing a pile foundation in the first place, it is often the case, that the rule-of-thumb acts as a safe side estimate of the design structural bearing capacity of piles in compression. For a 300 mm square precast concrete pile, we get:

$$N_{Rd} = 10 \frac{MN}{m^2} \cdot (0,3 m)^2 = 0,9 MN = 900 kN \quad (3.1)$$

In a typical Danish soil stratum, the geotechnical bearing capacity of precast concrete piles is often less than what can be computed from the rule-of-thumb. And because there is no analytical method presented in Danish literature which treats the problem of buckling, the rule of thumb is convenient to avoid complicated numerical modeling.

It is not rare to find thick deposits of peat and/or gyttja with c_{uk} far exceeding 10 kPa in Denmark, and because such organic soils deform significantly during consolidation, phrase 7.8 (5) from Eurocode 7 is unsafe and the DS 415 rule-of-thumb more relevant.

3.2. Swedish Method

Piles in Sweden are frequently driven to bedrock or firm moraine material through very thick deposits of weak clays. Risk of instability in the weak top-layers is always checked, and second-order effects are computed.

The Swedish Commission on Pile Research (Pålkommissionen) [5] suggests an analytical method for calculation of second-order effects and the instability load on a pile element passing through a thick layer of soft soil. The soil is modelled linear-elastic perfectly-plastic with the modulus of subgrade reaction k and the plastic resistance q_y at the deformation y_y with values for soft clay based on relations to the undrained shear strength. See figure 2a.

$$k = 200 \cdot \frac{c_u}{d} \quad \& \quad k = 50 \cdot \frac{c_u}{d} \quad \text{for short-term \& long-term conditions respectively} \quad (3.2a) \quad \& \quad (3.2b)$$

$$q_y = 9 \cdot c_u \quad \& \quad q_y = 6 \cdot c_u \quad \text{for short-term \& long-term conditions respectively} \quad (3.3a) \quad \& \quad (3.3b)$$

To account for plastic soil resistance along part of the critical length (for $y_0 > y_y$), but still use the linear relation $q = k \cdot y$ in the formulation, equivalent resistance q_e and -modulus k_e is determined by reducing with the factor Φ , which is computed from assumption of equivalent work of the curves in figure 2b.

$$\Phi = \frac{2}{\pi} \cdot (\alpha + 1,5 \cdot \sin(2 \cdot \alpha) - (\pi - 2 \cdot \alpha) \cdot \sin^2(\alpha)) \leq 1 \quad \text{where } \alpha = \arcsin\left(\frac{y_y}{y_0}\right) \quad (3.4)$$

$$k_e = \Phi \cdot k \quad \text{and} \quad q_e = k_e \cdot y \quad (3.5) \quad \& \quad (3.6)$$

$$N_{cr} = 2 \cdot \sqrt{k_e \cdot d \cdot EI} = 2 \cdot \sqrt{\Phi \cdot k \cdot d \cdot EI} \quad (3.7)$$

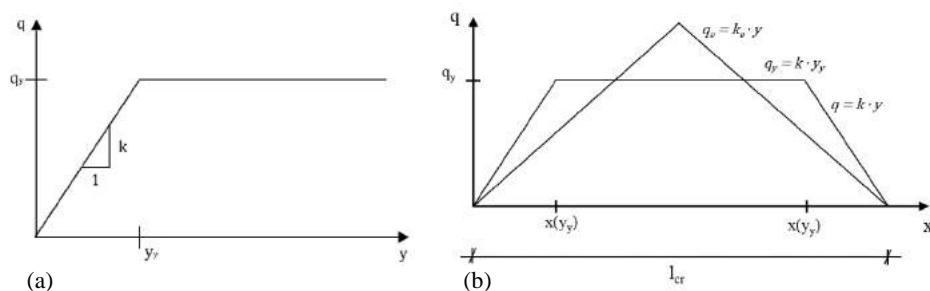


Figure 2. linear-elastic perfectly-plastic soil model

The lateral deformation of a fully embedded pile under axial compression is a sine-function.

The deflection curve $y(x)$ of one half-sine wave with the critical length l_{cr} is analysed, and the pile is assumed to have an initial curvature of the same sinusoidal form $\delta(x)$ with the amplitudes y_0 and δ_0 respectively. See figure 3.

$$y(x) = y_0 \cdot \sin\left(\frac{\pi \cdot x}{l_{cr}}\right) \quad (3.8)$$

$$\delta(x) = \delta_0 \cdot \sin\left(\frac{\pi \cdot x}{l_{cr}}\right) \quad (3.9)$$

The amplitude of the initial curvature δ_0 causes a first-order moment on the axially loaded pile, which increases the deflection of the pile, naming y_0 the additional deflection.

According to Pålkommissionen [5] δ_0 equals $l_{cr}/300$ for a single length pile and equals $l_{cr}/150$ for a segmental pile accounting for the angular deviation in a pile joint.

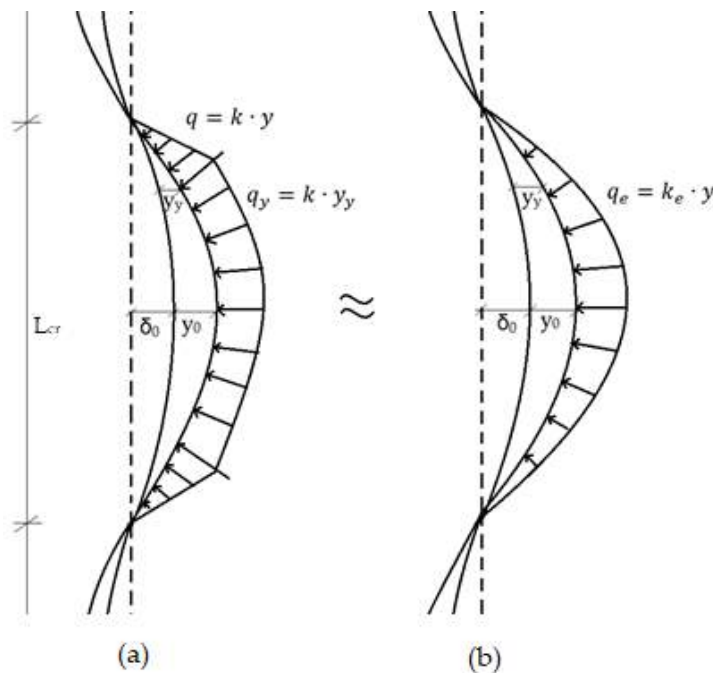


Figure 3. Initial curvature, δ_0 , and additional deflection, y_0 , with the distribution of soil resistance for $y_0 > y_y$: (a) soil resistance for linear-elastic perfectly-plastic distribution. (b) equivalent soil resistance distribution.

The additional deflection, normal force and second-order moment of a pile with an initial curvature δ_0 , is found from equation (3.10), (3.11) and (3.12) [5]. Since Φ depends on y_0 , iteration is required on y_0 to find its highest possible value for which the instability load can be computed.

$$y_0 = \frac{\delta_0}{\frac{N_{cr}}{N_E} - 1} \quad (3.10)$$

$$N_E = N_{cr} \cdot \frac{1}{1 + \frac{\delta_0}{y_0}} \quad (3.11)$$

$$M_E = N_E \cdot \frac{\delta_0 + y_0}{2} \quad (3.12)$$

3.3. Norwegian Method

The method presented by the Norwegian Geotechnical Society in [6] is similar to the Swedish method. For a straight pile, the buckling resistance is calculated equal to the critical load:

$$N_{b,R} = 2 \cdot \sqrt{k \cdot d \cdot EI} \quad (3.13)$$

For a pile with an initial curvature δ_0 , the total deflection y_{total} can be computed for a known load N_E . The additional deflection y_0 must be less than a critical deflection y_y to make sure that the soil can retain the deflection of the pile. The maximum buckling load on a pile with an initial curvature can therefore be found for the condition $y_0 = y_{total} - \delta_0 \leq y_y$.

$$y_{total} = \frac{\delta_0}{1 - \frac{N_E}{N_{b,R}}} \quad (3.14)$$

$$N_{b,R,max} = N_{b,R} \cdot \frac{1}{1 + \frac{\delta_0}{y_y}} \quad (3.15)$$

4. APPROACH TO LIMIT STATE ANALYSIS OF THE STRUCTURAL BEARING CAPACITY OF PRECAST CONCRETE PILES

In serviceability limit state (SLS) allowable deformation of elements and stresses in cross-sections are analysed using characteristic strength parameters with assumption of elasticity. For fully embedded piles, deflection limitations regarding appearance are not relevant, but lateral deflection shall be limited to avoid plastic deformations in the soil. Stresses in concrete and reinforcement cannot exceed limit values given in Eurocode 2.

Structural design of concrete piles in ultimate limit state (ULS) makes use of material factor approach (MFA), reducing material strength parameters with partial safety factors before calculating the bearing capacity assuming full utilisation (plasticity).

Analysis of the geotechnical bearing capacity of concrete piles in ULS is done using resistance factor approach (RFA) according to Eurocode 7 with Danish, Swedish and Norwegian NA's. In RFA bearing capacity is computed using derived strength parameters, and the design capacity in ULS is found by reducing the result with correlation- model- and safety factors.

Since buckling and second-order effects of piles involve both soil and concrete material characteristics, this causes controversy as geotechnical- and concrete engineers tend to use different safety approaches for analysis of precast concrete piles. There is no partial safety factor for soil stiffness in Eurocode 7, which makes it unclear how to deal with MFA for buckling of piles. On the other hand, RFA is not possible for analysis of the cross-sectional capacity according to Eurocode 2.

4.1. Calculation Example ULS – Swedish Method with Material Factor Approach

MFA is used in Sweden, and a design value of soil stiffness is determined according to a relation with the undrained shear strength of the weak clay. This enables addition of safety to the soil stiffness indirectly by reducing the undrained shear strength with the partial safety factor γ_{cu} .

The resistance of the concrete cross-section is calculated according to Eurocode 2, and the load-effect curve is computed for multiple increments of the normal force. The Structural bearing capacity for the pile in compression is determined as the load at buckling (failure in soil) or as the load at cross-section failure due to second-order effects cf. Figure 4.

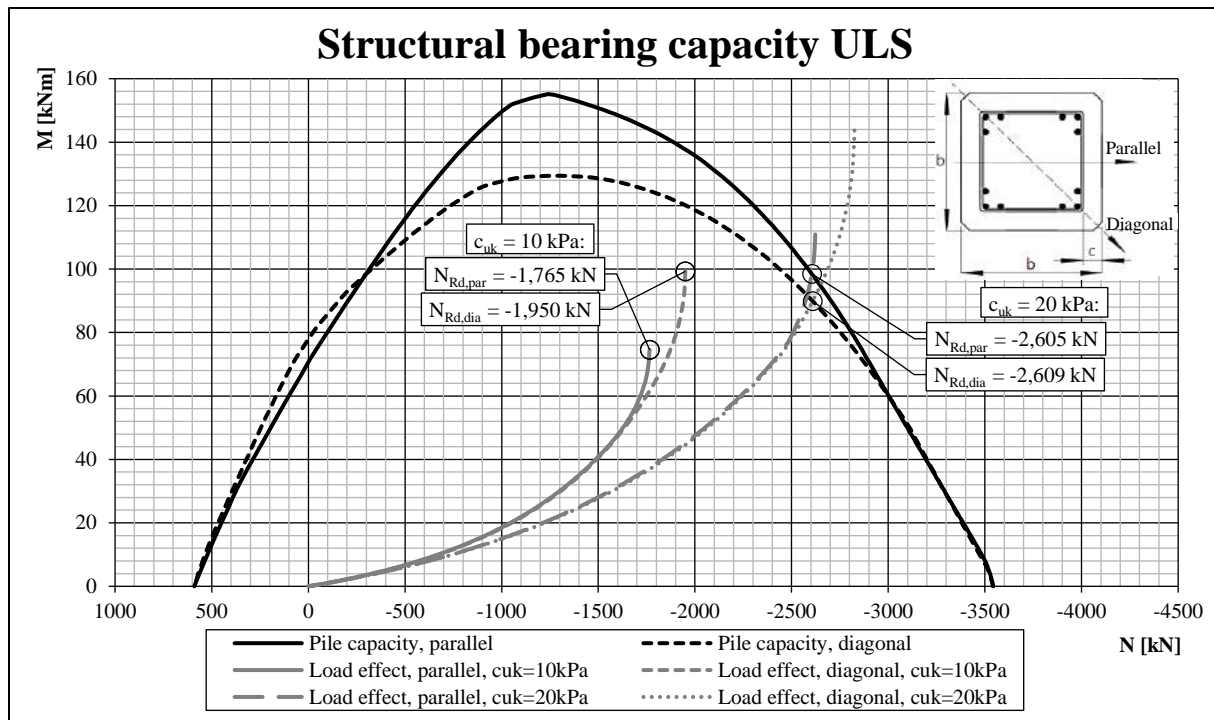


Figure 4. Calculation example – ULS. Swedish analytical calculation method with MFA, Partial safety factors according to recommendation in Eurocodes, $b = 300\text{mm}$, $c = 40\text{mm}$ to 5mm stirrup wire, concrete C50/60, reinforcement 12mm B500 with c-c distance 32mm, $\delta_0 = l_{cr}/300$.

In the calculation example above, we see that for $c_{uk} = 10\text{ kPa}$, buckling is critical rather than failure in cross section. Point of instability is reached at the top point of the load effect curve (where the tangent is vertical). For $c_{uk} = 20\text{ kPa}$, failure in cross-section occurs slightly below the point of instability. The risk for buckling is therefore present even for $c_{uk} = 20\text{ kPa}$, which justifies the recommendation in the Swedish national annex cf. section 2.

5. COMPARISON AND DISCUSSION

If we solely want to analyse the buckling load of the pile, it would be possible to use either MFA or RFA. The latter is used in Norway in calculation of the maximum buckling load. In the Swedish calculation method, the instability load is found as the top point of the load effect curve using MFA.

The Swedish calculation method as seen in figure 4, also provides the second-order moment indicated by the load-effect curve, for which we want to check the resistance of the pile cross-section. In this case it makes sense to use MFA for several reasons. One is, that resistance according to Eurocode 2 is computed with MFA. Also, there is no “*exposure safety factor*” available in the Eurocodes to add safety to the computed load effect in *resistance factor* approach (Note that the load effect is an output of the method to compute the resistance). Another reason for using MFA is, that it enables direct comparison of the design load effect and the design cross-section capacity as shown in figure 4 to give the design normal force resistance N_{Rd} at the intersection of the curves.

An important observation from figure 4 is that buckling may be critical in the present calculation example even for an undrained shear strength of twice the value stated in Eurocode 7 phrase 7.8 (5). The expression “*normally*” indicates that one can disregard buckling of any common pile dimension and type if $c_{uk} > 10\text{ kPa}$, but the calculation example is performed with a common pile dimension. Even in common soil conditions.

Danish, Norwegian and Swedish practices are compared in figure 5. For fair comparison MFA is used in both Norwegian and Swedish methods with partial factors according to recommendation in Eurocodes (no NA's applied), and with equal stiffness parameters of clay according to recommendations of Pålkommissionen [5]. The Danish rule-of-thumb gives the design resistance directly.

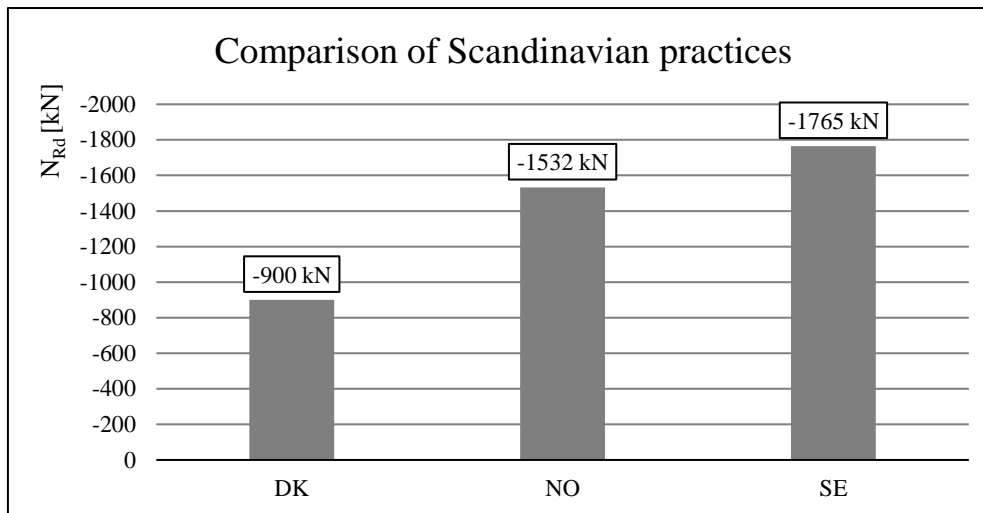


Figure 5. Comparison of Scandinavian practices – ULS, MFA, $c_{uk} = 10$ kPa, $b = 300$ mm, $c = 40$ mm to 5mm stirrup wire, concrete C50/60, reinforcement 12mm B500 with c-c distance 32mm, $\delta_0 = l_{cr}/300$.

The Danish practice stands on its own and is well on the safe side compared to Norwegian and Swedish methods, which uses the same formulation. The major difference is that the Swedish method contrary to the Norwegian method allows plastic soil resistance on part of the buckling length, considering that the soil still has some reserve strength to resist further deflection after the deflection reaches a level where it causes plastic resistance at the middle of the buckling length.

The described methods use a linear-elastic perfectly-plastic relationship between the deformation and resistance of the soil. This is however not true for soils, as they are only linear-elastic at very small strains and has irreversible deformations at the strain levels used for these methods. Nevertheless, it is very convenient for an analytical model to use linear-elastic perfectly-plastic modelling of the soil. More advanced soil modelling is not practicable for an analytical model and thus would require finite element modelling but would yield better accuracy.

6. CONCLUSION

The statements in Eurocode 7 regarding buckling of piles needs improvement. As shown in the calculation example, buckling can be critical for clays with undrained shear strengths exceeding 10 kPa. Eurocode 7 chapter 7.8 (5) is therefore misleading and unsafe. It should be removed or rephrased, and it should be supplemented by statements requiring analysis of second-order effects in case of high utilisation of the pile material, taking into consideration the initial curvature of the pile.

The Norwegian and Swedish calculation methods are convenient for analytical analysis of both second-order effects and buckling. The Danish rule-of-thumb can be used as a safe side estimate of the maximum structural capacity of concrete piles in cases where high utilisation of the pile material is not possible due to the soil strata.

It might be difficult (if not impossible) to convince concrete-engineers to use RFA, which leaves MFA as the only alternative for analysis of buckling and second-order effects. This has the advantage of direct comparison of second-order moment and resistance at any normal force but presents one problem: We need a partial safety factor for the soil stiffness moduli. It may be equal to γ_{cu} for clay respectively γ_{ϕ} for sand or it may be different, but it needs to be defined in Eurocode 7.

ACKNOWLEDGEMENT

Thanks to DGF (Danish Geotechnical Society) for the support and for providing me the opportunity to attend the 27th European Young Geotechnical Engineers Conference.

REFERENCES

- [1] CEN, DS/EN 1997-1:2007 & DS/EN 1997-1/AC:2010, “Eurocode 7: Geotechnical Design – Part 1: General rules”, Dansk Standard, Denmark.
- [2] CEN, DS/EN 1992-1-1 + AC:2008, “Eurocode 2: Design of Concrete Structures – Part 1-1: General Rules and Rules for Buildings”, Dansk Standard, Denmark.
- [3] DS, DS 415 Engelsk:2001, “Norm for Fundering”, Dansk Standard, Denmark.
- [4] Boverket, BFS 2015:6 EKS 10, “Boverket Mandatory Provisions Amending the Board’s Mandatory Provisions and General Recommendations (2011:10) on The Application of European Design Standards (Eurocodes), EKS”, Boverket (the Swedish National Board of Housing, Building and Planning), Sweden.
- [5] Bengtsson, Å. et al & Ehnåge, G. & Alén C. et al, 1998 & 2003 & 2011, “Dimensioneringsprincipper för pålar – Lastkapacitet”, Pålkommissionen (Commission on pile Research), Report 96:1 & supplement 1 & supplement 2, Sweden.
- [6] Simonsen, A. S. et al, 2012, “Peleveiledningen 2012”, Norsk Geoteknisk Forening – Den Norske Pelekomité, Norway.

CORRELATIONS BETWEEN SOIL CONDUCTIVITY AND GEOTECHNICAL PARAMETERS IN FINNISH CLAYS

Markus Haikola*, *Tampere University, markus.haikola@tuni.fi*

ABSTRACT

Due to the urbanization, a rising amount of construction needs to take place on areas with poor subsoil. This increases a need for a better knowledge of the soil conditions to assure safety and cost effectiveness of the constructions. This can be achieved by improving the quality of soil investigations. In order to accomplish this in Finland, Tampere University (TU) in association with Finnish Transport Agency (FTA) are conducting a research program, called Fincone. Aim of the project is to develop and promote the use of CPTU soundings in Finland. As a part of Fincone, a study was carried out to obtain the usability of the soil conductivity measurements. The results of this study are presented in this paper. Those compose of correlations between a set of geotechnical parameters and the soil conductivity. The measurements were conducted for a set of Finnish soft clays using the site investigation devices and geotechnical laboratory facilities of TU. The geotechnical parameters were obtained by using the test methods following mainly the national and European standards. In addition, the soil conductivity measurements were performed using a soil conductivity module attached behind a CPTU cone. The results show that the clearest correlation exists between the soil conductivity and the pore water salinity. In addition, the soil conductivity correlates weakly with the plasticity and liquidity indices, sensitivity, and remolded shear strength. Based on the results, the soil conductivity measurements are usable for the determination of the pore water salinity and the preliminary evaluation of the consistency and sensitivity of the soft Finnish clays. The soil conductivity measurements improve the quality of the soil investigations by providing additional data gathered from a CPTU test.

Keywords: Soil Conductivity, Clay, Geotechnical Parameters, Soil Investigations

1. INTRODUCTION

Due to the urbanization, increasing number of people gather at big cities. This influences on the land use, and more areas with poor subsoil have to take under construction. In order to use these areas, a wide knowledge of the subsoil properties needs to be collected. In addition, the cost of construction must remain reasonable. To fulfill these demands, the soil investigation methods need to be improved. In relation to previous, Tampere University (TU) is carrying out a research program, funded by Finnish Transport Agency (FTA), to develop soil investigations in Finland. The project, called Fincone, aims to promote CPTU and its use in Finland by collecting data and validating transformation models for determination of geotechnical parameters. Part of the project is to conduct an investigation of capabilities of soil conductivity measurements done simultaneously with CPTU. The goal is to find geotechnical properties correlating with the soil conductivity to increase the amount of information gathered from a single CPTU test. Electrical conductivity of soil is a complex property with several effecting factors. The main factors are porosity and pore water salinity when dealing with fully saturated soils [1,2]. However, when significant amounts of clay minerals are introduced into the soil mixture the complexity increases due to the electrical properties of clay particles [2,3,4].

Other factors effecting on soil conductivity are pore water chemical composition, soil structure and clay mineralogy [2,3,5,6]. In addition, measurement environment and technique has effects on the measured soil conductivity. Temperature has significant effect on soil conductivity as it decreases the viscosity of the pore water making it easier for current transporting ions to move. To avoid effects of different temperatures on measured conductivities, the measured results are usually normalized to the room temperature [7]. As the soil conductivity is usually measured using alternating current, the used frequency effects on the measurement. However, the soil conductivity is stated to be frequency independent in the range of 100–100,000 Hz [2,5].

Besides the pore water salinity has a major effect on the soil conductivity, it has been found to effect also on mechanical properties of clayey soils. The effect relates on the interaction between the electrically charged clay particles and ions of the pore water. High ion concentration in the pore water (salinity) helps the clay particles to attach to each other by decreasing the diffusion double layer (DDL) around the colloidal clay particles, which enables van der Waals forces between the clay particles become dominant. This increases the plasticity and strength of clayey soils. [3,8,9,10]

Long et al. [11] studied relationships between geotechnical parameters and soil resistivity in Norwegian clays. They concluded that pore water salinity and remolded shear strength correlate strongly with soil resistivity. They also found a trend of decreasing plasticity with increasing resistivity. However, the water content showed no correlation with the soil resistivity. Montafia [12] reported also similar results with Norwegian clays. However, the Norwegian clays differ from Finnish as those are formed in truly marine environment giving higher original pore water salinities. In addition, the clay content differs from the Finnish clays being significantly lower. In addition, the lower clay content decreases the plasticity of Norwegian clays compared to Finnish ones.

Extensive investigation of correlations between geotechnical properties and soil conductivity has not conducted for Finnish clays. However, in their report [13] Törnqvist et al. propose that the water content is the main factor effecting in resistivity in the Finnish clayey soils. However, the report did not gave any measured data for validation but only one explanatory graph of assumed relationship. In addition, Gardemeister [14] conducted an extensive study on Finnish clayey soils. There the basic geotechnical properties were examined and also formation time and mineralogy as well as pore water salinity was studied. However, the report gives no data about the conductivity of Finnish soils.

In this paper, the gap between the previous studies is closed. Representative amount of Finnish clayey soil deposits are extensively studied and basic geotechnical parameters are determined. In addition, the soil conductivity and pore water salinity are measured. The geotechnical properties effecting mainly on soil conductivity are determined based on correlations. In addition, the effect of soil conductivity on mechanical properties is studied.

2. MATERIALS AND METHODS

2.1. Testing Sites

In total of seven testing sites were chosen for correlations. The sites locate on the Southern Finland near the Baltic Sea except for the Murro site. All the sites are used for Fincone project and extensive site investigations were conducted in each of those. The Perniö, Sipoo, Paimio, Masku and Kotka 233 share similar subsoil features with around 1 m dry crust layer overlying 10 m thick soft clay layer. These sites locate under 20 km from the Baltic Sea coastline and the ground level is from 10 to 20 meters above the current sea level. While these sites share similar features, the Kotka 238 and Murro sites differ from those and each other.

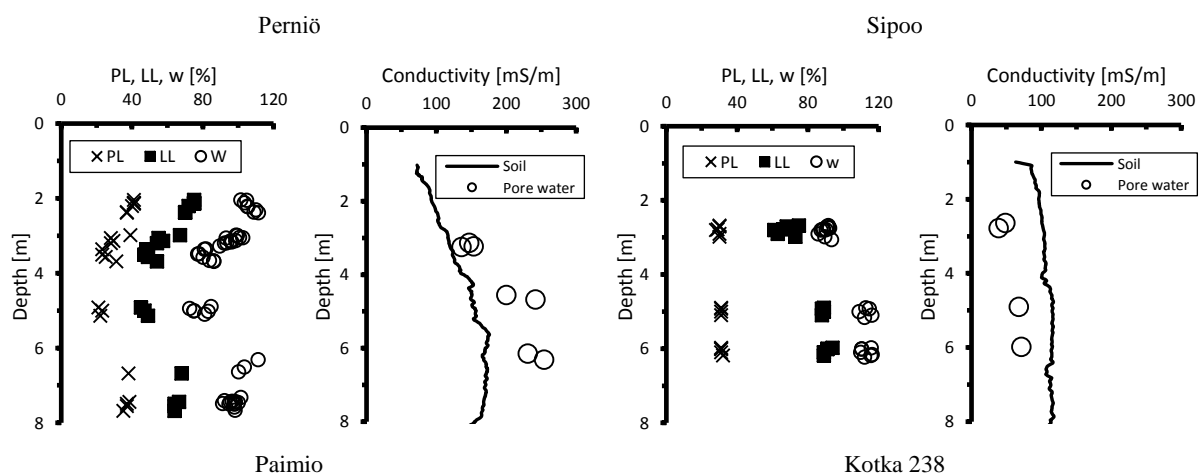
The Kotka 238 site locates only tens of meters from the coast and the ground level is only 1.6 m above the current sea level. The dry crust of the Kotka 238 site is very thin and the soft clay under it is organic. The Murro site locates away from coastlines. The subsoil there is highly organic and the clay content is low making the soil organic silt by definition. Even though the clay content is low, the water content of the Murro clay is high probably caused by the organic material. Initial water content and plasticity properties as well as conductivity properties of the sites can be seen from the figure 1.

The soil conductivities and the pore water salinities are low. This is due to the formation environment of the Finnish soils. Those are most likely formed in to the Baltic Sea basin after the last glacier. During that time, the salinity of the Baltic Sea water has been low, from fresh to about 8 g/l, causing low pore water salinities for Finnish soils. The highest salinity of the Murro site can be explained by the assumed formation environment when the salinity of the the Baltic Sea has been the highest. [14,15]

Table 1 completes the properties of the sites. The organic content is generally low and on the other hand, the clay content is relatively high in most of the sites. Activity yields low values implicating abundance of low active clay minerals.

Table 1. Additional properties of the sites

Site	PI	LI	Activity	Su	Sur	Sensitivity	Clay cont.	Org. cont.	Salinity
Perniö	21–41	1.6–2.5	0.34–0.79	9–20	0.2–1.6	7–72	52–89	0–2.1	0.7–1.4
Sipoo	33–63	1.2–1.8	0.50–0.72	15–18	0.3–1.2	16–45	64–94	0–1.4	0.2–0.4
Paimio	16–36	2.1–3.0	0.24–0.44	13–20	0.2–1.4	52–99	41–98	0–1.1	0.3
Kotka 238	16–55	1.2–2.2	0.30–1.7	11–29	0.3–1.2	15–38	32–87	0–4.9	1.9–2.3
Kotka 233	9–52	1.4–2.2	0.20–1.7	8–26	0.2–0.9	17–72	22–56	0–3.5	0.3–0.5
Masku	36–64	1.0–1.4	0.50–0.70	15–20	0.6–1.5	18–21	60–95	0.1–1.7	–
Murro	25–46	1.1–1.5	1.0–1.8	19–28	0.9–1.6	19–27	24–33	1.3–3.2	5.5–5.7



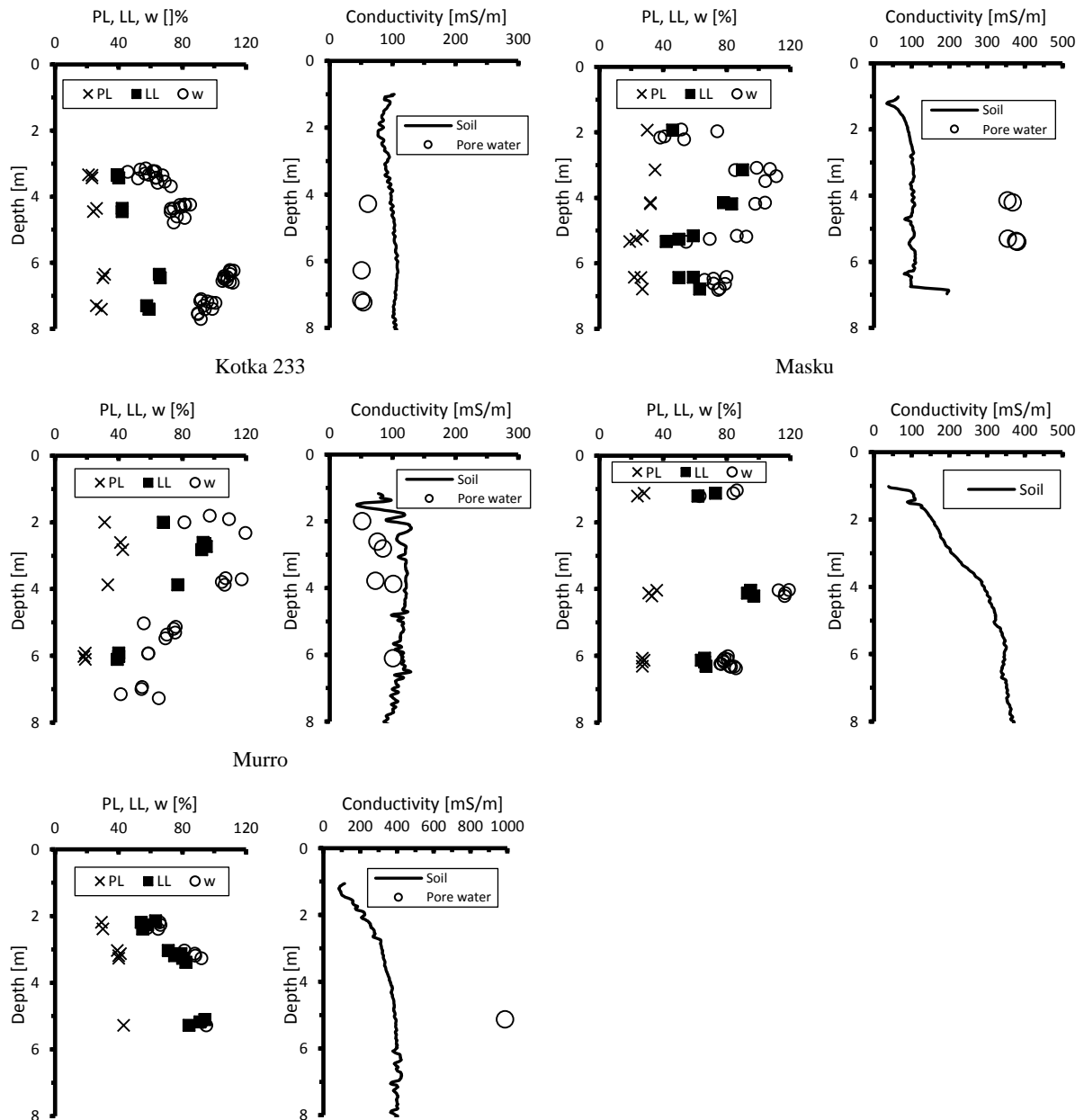


Figure 1. Initial water content and plasticity properties of the sites.

2.2. Test Methods

In-situ testing of the sites compose of soil conductivity measurements conducted with a conductivity module attached behind a CPTU cone. The conductivity module comprises four electrodes in a Wenner array where the outer most electrodes produces a current into the surrounding soil mass and the inner ones measure the voltage. The measurement is conducted by alternating the induced current to maintain a constant 50 mV voltage between the inner electrodes. The conductivity is determined from the current measurements based on the Ohm's law. Even though the measurements were conducted using guidelines of the manufacturer, the data handling process was developed during the project. The data handling composes of combining raw data measurements (3 measurements per site) and taking a sliding average of 8 cm in depth to balance the measurement deviation.

The conductivity module included also a temperature transducer and the temperature data was used to correct the conductivity measurements to the room temperature (25 °C) using equations (1) and (2) [7].

$$\sigma_{25} = f_T \sigma_T \quad (1)$$

$$f_T = 0.4470 + 1.4034e^{-T/26.815}, \quad (2)$$

where σ_{25} is the soil conductivity at 25 °C, f_T is the temperature correction factor at the temperature T and σ_T is the measured soil conductivity at the temperature T .

The laboratory tests were conducted according the standards used in Finland for geotechnical applications. The used standards are presented in the table 2.

Table 2. Margin settings for the paper

Property	Standard
Water content	SFS-EN ISO 17892-1
Plastic limit	CEN ISO/TS 17892-12:fi
Liquid limit (fc)	CEN ISO/TS 17892-12:fi
Particle size distribution	PANK-2103
Organic content	GLO-85
Intact strength (fc)	SFS-EN ISO 17892-6:2017
Remolded strength (fc)	SFS-EN ISO 17892-6:2017
Pore water salinity	-

(fc) = determined with the fall cone test

Standards for the particle size distribution and the organic content determination are used only in Finland but the methods are the commonly known hydrometer and furnace tests. The pore water salinity of the samples was determined by measuring the conductivity of the extruded pore water and determining the salinity by equation described in [16]. Changes in atmospheric pressure were not taken into account as it was evaluated to have little effect on the results. The pore water was extruded from the samples by forcing the water through a filter paper with pressurized air. The conductivity of the pore water samples was measured using the Consort conductivity meter.

3. RESULTS AND DISCUSSION

The results of the measurements are shown in figures where the different geotechnical properties are plotted against the soil conductivity from the corresponding depth. The results are not grouped according to the different sites, since the aim of this paper is to try to find general correlations for Finnish soft clays.

Figure 2 shows relations between the soil conductivity and the compositional properties of the tested clays. As it can be seen from the figure, the water content seems to have little effect on the measured soil conductivity. Similar results exist for the relation of the soil conductivity and the clay content. Neither of these seem to explain the soil conductivity values. However, a very clear, linear relation results for soil conductivity and pore water salinity. Since the salinity is determined based on pore water conductivity measurements, similar relation exists between the soil and pore water conductivities. Based on these results, the pore water salinity determines the electrical conductivity of the tested soils.

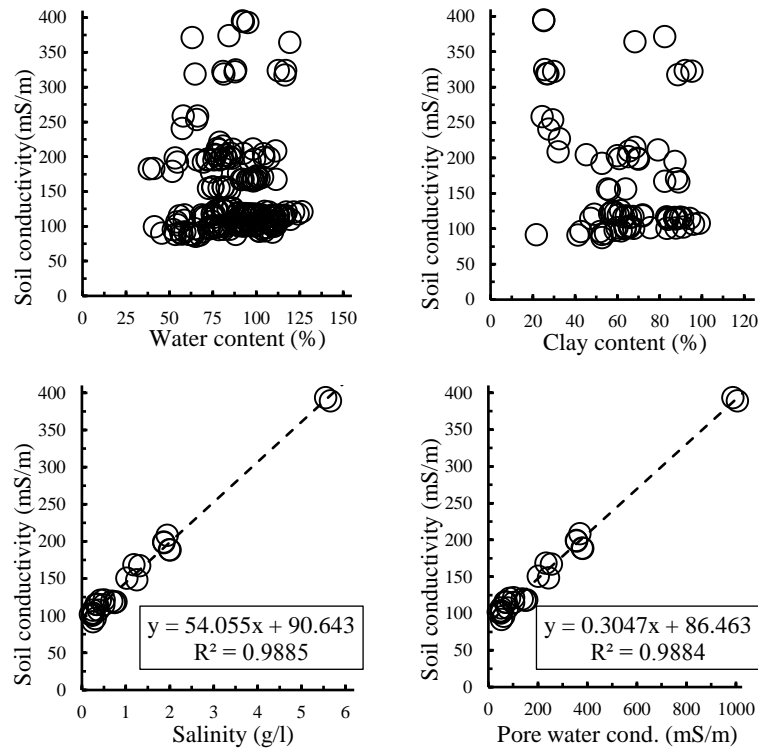
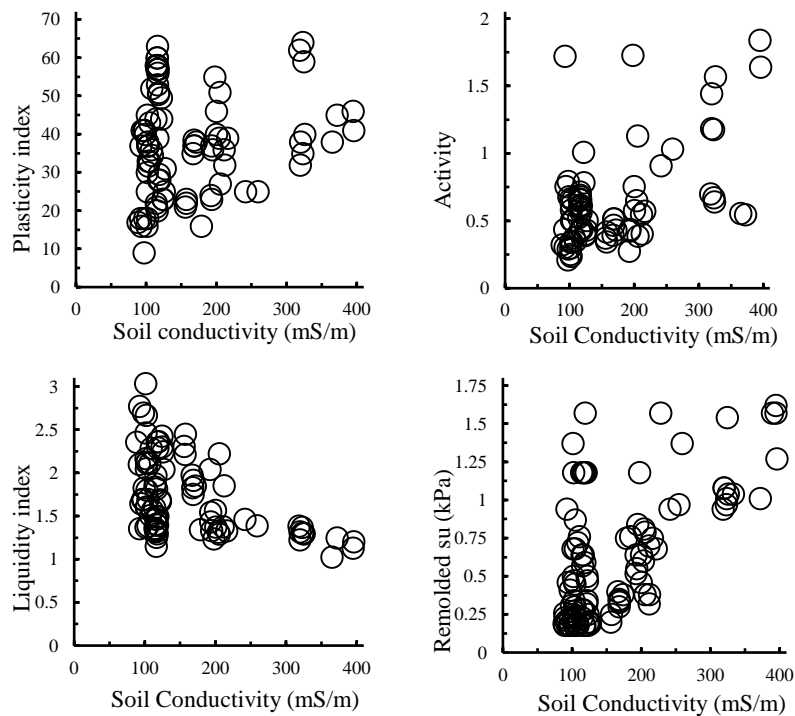


Figure 2. Soil conductivity against compositional properties.

Figure 3 presents the relations between the soil conductivity and some mechanical properties of the tested soils. The plasticity index and remolded shear strength seem to have weak positive correlation with the increasing conductivity. For both of those, a limiting lower boundary can be drawn. Activity shows somewhat similar relation compared to previous but it is even weaker. In contrast, the liquidity index and sensitivity decrease with increasing conductivity and an upper limit can be evaluated for these. Common feature for all of the relations presented in figure 4.2 is the behavior in low conductivities. The mechanical properties are not affected by the conductivity when it reaches low values (under 150 mS/m).



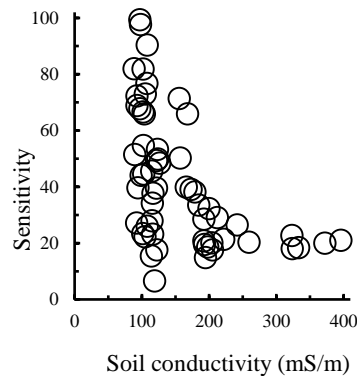


Figure 3. Soil conductivity against mechanical properties.

Results are in line with the previous studies and presented theory. Soil conductivity is at most effected by the pore water salinity as was concluded in Norwegian studies also. In addition, the water content has little effect on the soil conductivity. Increasing plasticity and remolded shear strengths as well as decreasing liquidity index and sensitivity support also the findings of the Norwegian clays and theories about the clay pore water interaction.

Based on this paper, the soil conductivity measurements can be used for the determination of pore water salinity in Finnish clays. In addition, a preliminary evaluation of the plasticity and liquidity indices as well as remolded shear strength and sensitivity can be performed in the case of over 150 mS/m conductivities.

4. CONCLUSION

In this paper correlations between the soil conductivity and geotechnical properties of soft Finnish clays were determined. In total of seven sites were extensively studied and correlations were compiled from those results. The studied correlations show that soil conductivity is dictated by the pore water salinity and other compositional properties have very little effect on it. Mechanical properties seem to correlate weakly with the soil conductivity when it reaches values over 150 mS/m. The plasticity index and remolded shear strength have a positive correlation with the soil conductivity while the liquidity index and sensitivity correlates negatively with it. The results are in line with theories concerning the clay-pore water-interaction and with studies made for the Norwegian clays. Based on the results the soil conductivity measurements can be used for the determination of the pore water salinity of Finnish clays and preliminary evaluation of mechanical properties.

REFERENCES

- [1] Archie, G.E., 1942. "The Electrical Resistivity Log as an Aid in Determining Some Reservoir Characteristics", Transactions of the AIME, 146(1):54-62.
- [2] Friedman, S.P., 2005. "Soil Properties Influencing Apparent Electrical Conductivity: A Review", Computers and Electronics in Agriculture, 46(1):45-70.
- [3] Mitchell, J.K., 1976. "Fundamentals of Soil Behavior", Wiley, USA, 422 p.
- [4] Waxman, M.H., Smits, L.J.M., 1968." Electrical Conductivities in Oil-Bearing Shaly Sands", Society of Petroleum Engineers Journal, 8(2):107-122.
- [5] Rinaldi, V.A., Cuestas, G.A., 2002. "Ohmic Conductivity of a Compacted Silty Clay", Journal of Geotechnical and Geoenvironmental Engineering, 128(10):824-835.

- [6] Fukue, M., Minato, T., Horibe, H., Taya, N., 1999. “*The Microstructure of Clay Given by Resistivity Measurements*”, *Engineering Geology*. 54:43-53.
- [7] Ma, R., Mc Bratney, A., Whelan, B., Minasny, B., Short, M., 2011. “*Comparing Temperature Correction Models for Soil Electrical Conductivity Measurement*”, *Precision Agriculture*, 12(1):55-66.
- [8] Bjerrum, L., 1954. “*Geotechnical Properties of Norwegian Marine Clays*”, *Géotechnique*, 4(2):49-69.
- [9] Rosenqvist, I.T., 1955. “*Investigations in the Clay-Electrolyte-Water System*”, Norwegian Geotechnical Institute, Norway, 125 pages.
- [10] van Olphen, H., 1977. “*An Introduction to Clay Colloid Chemistry for Clay Technologists, Geologists and Soil Scientists*”, Wiley, USA, 318 pages.
- [11] Long, M., Limacher, R., Donohue, S., L'Heureux, J.-S., Solberg, I.-L., Rønning, J.S., O'Connor, P., Sauvin, G., Rømoen, M., Lecomte, I., 2012. “*Relationship between Electrical Resistivity and Basic Geotechnical Parameters for Marine Clays*”, *Canadian Geotechnical Journal*, 49(10):1158-1168.
- [12] Montafia, A., 2013. “*Influence of Physical Properties of Marine Clays on Electric Resistivity and Basic Geotechnical Parameters*”, M.Sc Thesis, Norwegian University of Science and Technology, Norway, 150 pages.
- [13] Törnqvist, J., Laaksonen, R., Juvankoski, M., Vepsäläinen, P., Lojander, M., Takala, J., 2001. “*Tien jatkuvan painumaprofilin laskenta pikselimallilla*”, Tien pohja- ja päällysrakenteet tutkimusohjelma 1994–2001: Menetelmäkuvaus TPPT 19, Finland, 28 pages.
- [14] Gardemeister, R., 1975. “*On engineering-geological properties of fine-grained sediments in Finland*”, VTT, Finland, 91 pages.
- [15] Salonen, V.-P., Eronen, M., Saarnisto, M., 2002. “*Käytännön maaperägeologia*”, Kirja Aurora, Finland, 237 pages.
- [16] Fofonoff, N.P., Millard, R.C.J., 1983. “*Algorithms for Computation of Fundamental Properties of Sea Water*”, UNESCO technical papers in marine science, 44(61).

SOIL PERMEABILITY REDUCTION OF A DIKE BY INJECTING ORGANIC MATTER AND ALUMINUM: FIELD DATA ANALYSIS

Saara Lassila*, *Civil engineering, Aalto university, saara.lassila@ains.fi*

ABSTRACT

A field test was conducted in a leaking dike of a reservoir in order to create a flow barrier. Aluminum-organic matter precipitates were injected into the aquifer with the aim of reducing soil permeability. Pumping tests were conducted before and after the injection. The aim of the field data analysis was to study the effect of the treatment on the aquifer permeability. Changes caused by the barrier were analyzed qualitatively and quantitatively. Comparison of data before and after the implementation showed a change in hydraulic behavior. To quantify the change in permeability the Neuman method was applied by curve-fitting. This graphical approach did not provide quantitative results. This is due to the assumptions of the analytical solution and the manual curve fitting. The results and the field data indicated that the flow barrier is not only at the injection line but might be located further downstream. It is therefore recommended to investigate different analysis methods to get a better understanding of the location of the flow barrier.

Keywords: Unconfined Aquifer, Pumping Test, Neuman Method.

1. INTRODUCTION

High groundwater flow occurs when the hydraulic head gradient and the permeability of the porous medium are high. For engineering concerns, high groundwater flow can lead to leakage or endanger the stability of the structure. One way to mitigate the high flow issue is to reduce the permeability of the porous medium. The mitigation can be done by applying chemical grouting [1].

The soil permeability reduction method applied in this study is called SoSEAL (Soil Sealing by Enhanced Aluminum and DOM leaching). The main idea behind SoSEAL is to inject aluminum and organic matter to the ground, where the components form flocs that clog the pore spaces between grains of a porous soil (figure 1). This method developed in TU Delft is currently under testing and research. SoSEAL enables a quick and cost-efficient way to reduce soil permeability [2].

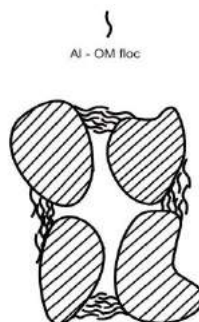


Figure 1. The flocs clog the pore spaces [3]

The goal of this study was to observe a change in soil permeability on a site where organic matter an aluminum was injected to a dike. Pumping test were conducted on site before and after the injection. The effect of the injection was defined qualitatively and quantitatively. The qualitative analysis was based on the change of the water level in the monitoring wells situated on the test site. The pumping test analysis method and tools chosen were as simple as possible to reduce the uncertainty linked to the method and parameter estimation. The Neuman (1975) method was chosen as the quantitative analysis method because of its quite well-suited assumptions and the curve-fitting tool that enabled a quick and simple estimation of aquifer parameters. The focus of this research was on the period close to the injection. The pumping tests analyzed were conducted from one week to one month after the injection. The long-term effect of the injection was not considered.

2. METHODOLOGY

2.1. The Test Site

A pilot was conducted in the summer 2018. The test site was a leaking dike of a fresh water reservoir. A part of the dike was remediated by injecting the mixture from the bottom of the aquifer to few meters above the water level (figure 2). The 100-m- long test site was divided into three zones (A, B and C) (figure 3).

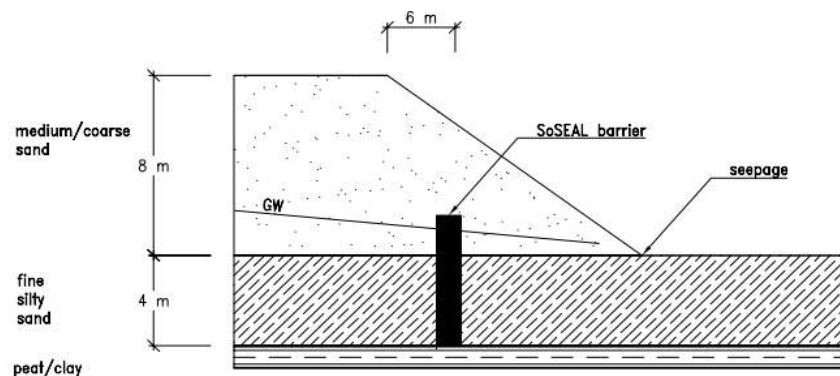


Figure 2. Model of the dike of the test site.

2.2. Data Collection

To monitor the water flow in the test site, monitoring wells were installed before the injection. The monitoring wells were installed on both sides of the planned injection line (figure 3). The monitoring wells reached from the bottom of the aquifer to the ground surface. A 2-meter-long filter was situated at the bottom of the monitoring well. For the data collection CTD-divers that measured pressure, temperature and electrical conductivity (EC) at a user defined time interval were used. To observe the change in water flow, baseline measurements were carried on the site during the months prior to the injection. In addition to data measured constantly from the site, pumping tests were conducted to monitor the change in head of the monitoring wells when water was pumped from a test well. The duration of the pumping tests varied from 10 minutes to 1 hour. Few longer pumping tests of more than 7 hours were experimented. The pumping rate varied mostly from 22 to 30 m³/d. During pumping, measurements were taken every 10 seconds. The pumping test were done mainly from zone C, since it gave most promising results in the preliminary analysis.

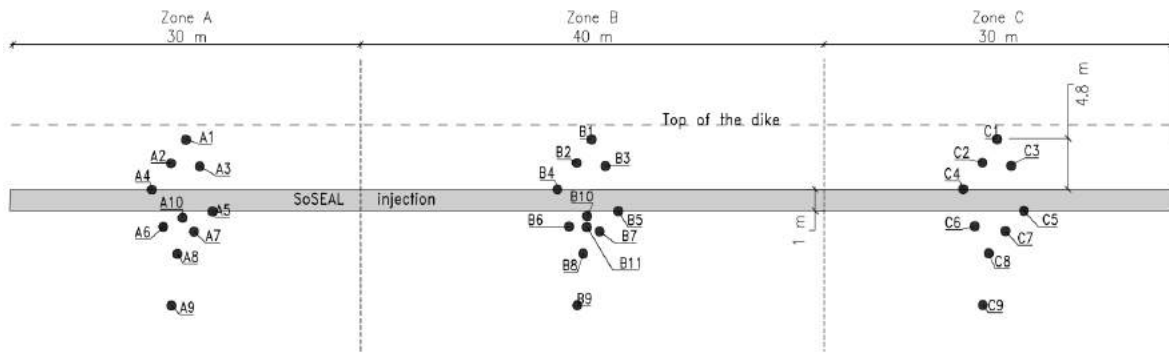


Figure 3. The positioning of the monitoring wells and the division into zones

2.3. Qualitative Analysis

The qualitative analysis aimed to observe the change in the water level in the dike. The divers were set to measure the water level in the monitoring wells at a 10 to 30 second interval for over few months before and after the injection. The water level of different monitoring wells was plotted at four different moments, two measurement sets before, and two measurements sets after the injection. The location of the injection line is indicated to observe a possible change in the water table in the injection region. The data was selected at moments that were not affected by the pumping tests to represent the water table naturally occurring in the dike.

2.4. The Neuman (1975) Method

The Neuman method is based on Theis method and it is developed for an unconfined aquifer [4]. The Neuman method assumes a homogenous aquifer where the water is immediately released from the storage when pumped [5]. The transmissivity T is assumed to be constant and specific yield (S_y) is assumed to be significantly bigger than specific storage (S_s) multiplied by the aquifer thickness (b) [4]. The theoretical time-drawdown curve of a pumping test analyzed with the Neuman method is S-shaped. It is composed of two Theis curves and a flat area between them (figure 4) [6]. The first Theis-curve is an early-time curve that represent the release of water from the elastic storage in the saturated zone. The storativity of the aquifer in the early-time curve is

$$S = S_s * b \quad (\text{Eq. 1})$$

The late time curve is a function of specific yield (S_y) and the drawdown occurs due to gravity drainage at the water table. [5] In this study the pumping tests were too short too reach the late-time curve.

The Neuman (1975) solution gives the drawdown at a given radial distance (Eq. 2). $W(u_A, u_B, \eta)$ is a well function that can be approximated by an infinite series but for simplicity tabulated values are used. [4]

$$h_0 - h = \frac{Q}{4\pi T} W(u_A, u_B, \eta) \quad (\text{Eq. 2})$$

Where u_A is the parameter for the early-time curve,

$$u_A = \frac{r^2 S}{4T(t-t_0)} \quad (\text{Eq. 3})$$

u_B is the parameter for the late-time curve,

$$u_B = \frac{r^2 S_y}{4T(t-t_0)} \quad (\text{Eq. 4})$$

And η is a dimensionless parameter,

$$\eta = \frac{r^2 K_z}{b^2 K_r} \quad (\text{Eq. 5})$$

The choice between the parameters u_A and u_B depends on whether the calculation is done for the early-time curve or is the late-time curve already reached. [4]

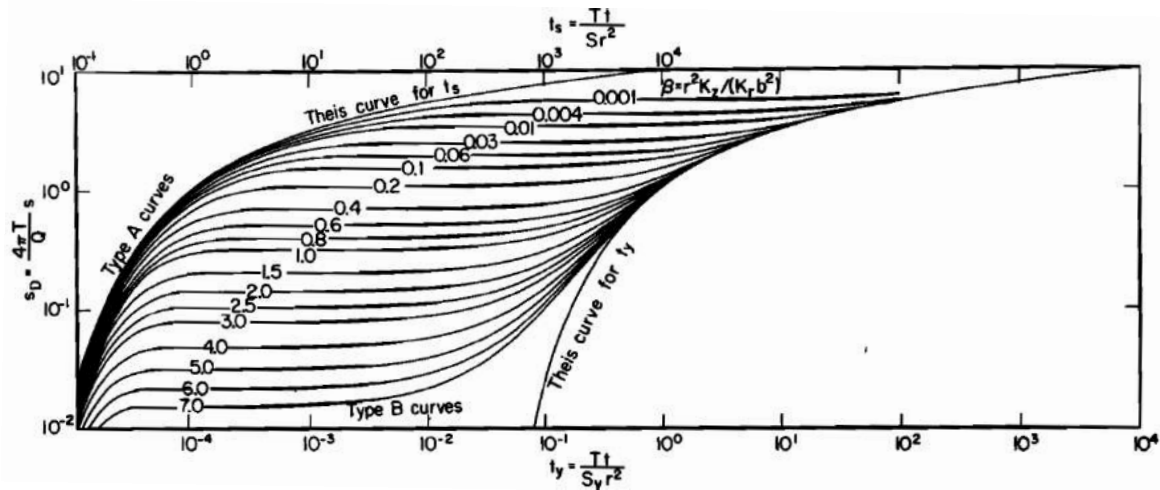


Figure 4. The Neuman (1975) method type curves. Type A curves are the early-time curves and type B curves are the late-time curves. t_s corresponds to $1/u_A$, t_y to $1/u_B$ and β to η . [7]

2.5. Curve Fitting

To estimate the transmissivity and storativity from the data a curve-fitting was introduced. The curve formed by the plotted measurement data is fitted to the type curve as precisely as possible to obtain the aquifer parameters. In this case the fitting was done with an Excel-tool created by Fitts (figure 5). The first step was to choose the best shape for the type curve by selecting the η -value. Secondly, the S and T values were adjusted to improve the fit. The values obtained from the best fit correspond to the aquifer parameters obtained with the equations of the Neuman (1975) method.

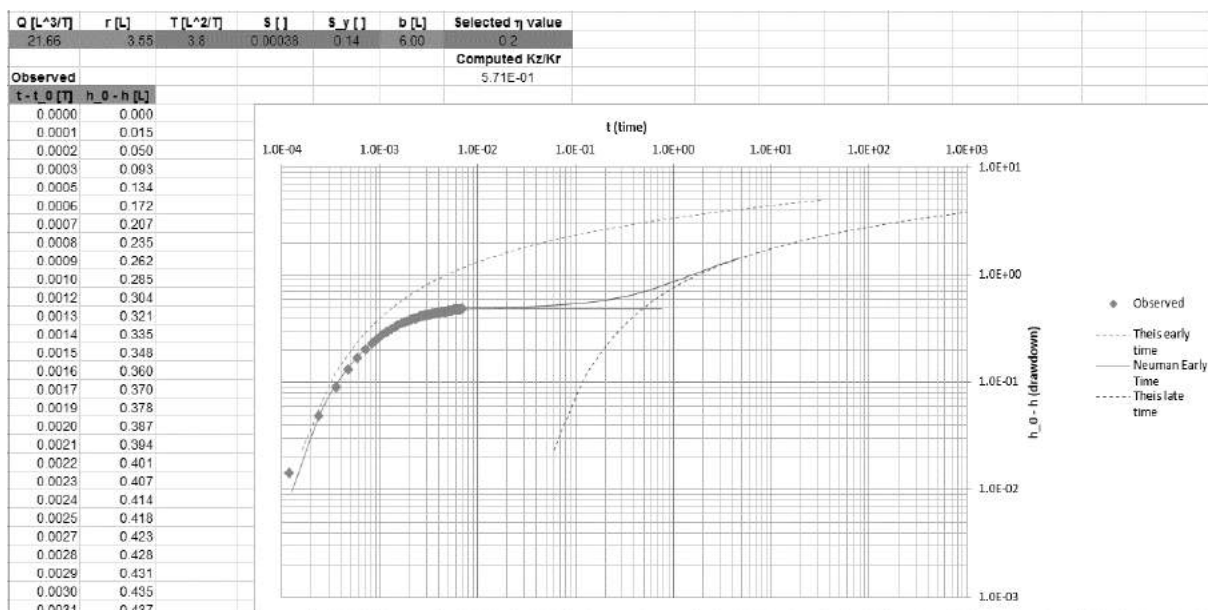


Figure 5. Curve fitting with the Fitts' Excel-tool.

3. RESULTS AND DISCUSSION

3.1 Qualitative Results

The pressure data gathered from the divers suggest that the shape of the water table changed after the injection (figure 6). The difference between the water level on the top part of dike (0-10 m) and the bottom part of the dike (15-20 m) increased after the injection. The injection in zone A was conducted from 21st June to 28th June 2018. The change in water table was not visible during the first weeks after the injection but after a month the water table seem to have settled to a steady level. The decrease in the water level does not occur at the injection line but from 3 to 5 meters from it.

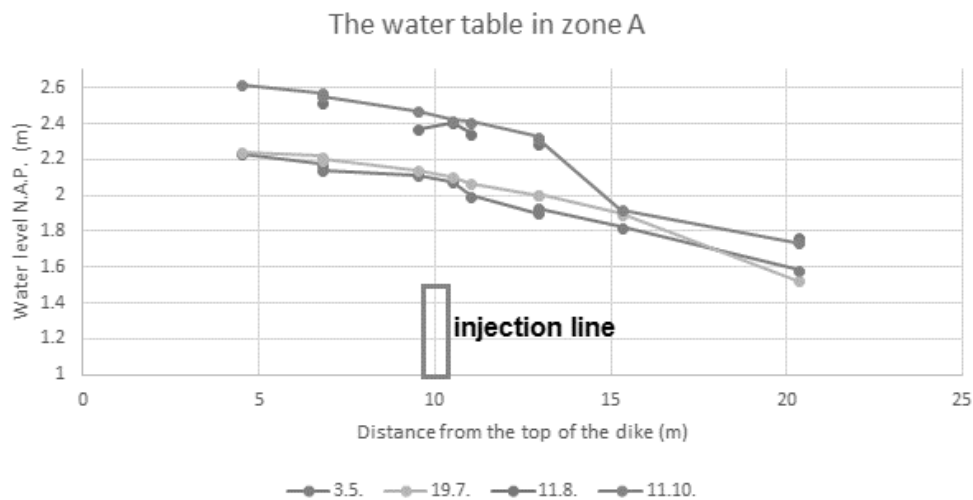


Figure 6. The water level in zone A before the injection (3.5. and 19.7., bottom lines) and after injection (11.8. and 11.10., upper lines).

3.2. Quantitative Results

The quantitative results obtained with the Neuman (1975) method by curve fitting show some variation in the before and after values of the aquifer parameters (table 1). However, the difference between the baseline measurements and the post-injection values is small and the values do not vary as a function of a location in a consistent way. The change in storativity was more significant than the change in hydraulic conductivity.

Table 1. A comparison of aquifer parameters obtained with the Neuman (1975) method by curve fitting in zone C

Well	K_{before} [m/d]	K_{after} [m/d]	K_{after}/K_{before}	S_{before}	S_{after}	S_{after}/S_{before}
C1	1.38	1.16	0.84	$7.0 \cdot 10^{-3}$	$1.1 \cdot 10^{-3}$	0.16
C3	1.51	2.13	1.41	$1.0 \cdot 10^{-3}$	$8.0 \cdot 10^{-4}$	0.80
C4	2.4	1.27	0.53	$8.9 \cdot 10^{-4}$	$6.0 \cdot 10^{-4}$	0.67
C5	1.97	1.68	0.85	$5.0 \cdot 10^{-4}$	$3.4 \cdot 10^{-4}$	0.68
C6	1.89	1.71	0.90	$4.2 \cdot 10^{-4}$	$1.0 \cdot 10^{-3}$	2.83
C7	2.27	1.99	0.87	$4.0 \cdot 10^{-4}$	$6.2 \cdot 10^{-4}$	1.55
C8	2.32	2.11	0.91	$3.0 \cdot 10^{-4}$	$5.7 \cdot 10^{-4}$	1.90
C9	5.27	3.21	0.61	$2.2 \cdot 10^{-4}$	$1.7 \cdot 10^{-4}$	0.77

3.3. Sources of Error

The change in water table demonstrated in the figure 6 might partly be due to the increased water table in the entire dike. However, it does not explain why the drop occurred few meters from the injection line, so the effect of the injection should not be neglected.

The water level in the monitoring wells was affected by the tidal effect of a nearby river. The wells situated the furthest from the test well experienced only a small decrease of water level due to pumping. The decrease or increase of the water level caused by the tide might have been of same magnitude which then either eliminated the effect of the pumping or doubled its effect depending on the direction of the tide. For the long pumping test, the tidal effect was partly eliminated with a reference data from a distant well (figure 7). For the tests lasting less than 1 hour, no elimination was done.

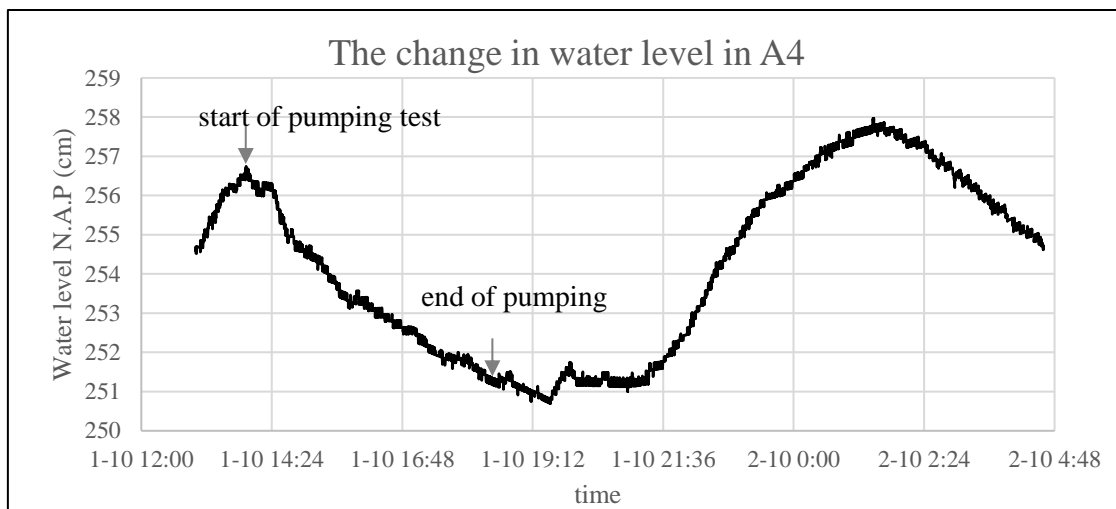


Figure 7. The variation of the water level in well A4 when C9 was pumped more than 80 m away. This data was used to eliminate the tidal effect.

The value of hydraulic conductivity seemed to correlate to the distance from the test well. To estimate the effect of the injection, the K values obtained with the Neuman method were compared as a function of distance and as a function of location regarding the injection line (table 2). The Eq 1. already considers the distance between the test well and the monitoring well. The pronounced effect of the distance might be due to the soil heterogeneity.

Table 2. The effect of the distance to hydraulic conductivity. The sample size (n) was small, before the injection n=6 and after the injection n=3.

Effect of		K_{before} [m/d]	K_{after} [m/d]
	all the wells	3	2.6
injection line	wells on the same side of the injection line	2.4	2.2
	wells on the other side of the injection line	3.4	3
distance	Distance from the test well less than 6 m	2	1.7
	Distance from the test well more than 6 m	3.2	3.4

One of the difficulties of the analysis method used was that the soil parameters were estimated as an average between the test well and the monitoring well. However, the soil studied was heterogenous and its properties varied in vertical and horizontal layers. The injection aimed to form a 1-m-thick low permeability zone in the aquifer layer. When a pumping test was analyzed with the Neuman method, the scope of the analysis was always much wider than just the injection zone. This causes the effect of the injection to seem insignificant. The ground investigation done at the site also suggests the presence of gravel layers. If preferential flow paths lead outside of the injection zone, the effect of the injected barrier is minimal.

The curve-fitting was done with the help of an Excel-tool. It is a biased system effect by the expert judgement. With some data sets, the choice of the type curve was tricky. The variation of parameter values obtained with two good fits with different type curves was significant ($T = 12 \text{ m}^2/\text{d}$ vs. $21 \text{ m}^2/\text{d}$).

4. CONCLUSION

The aim of the study was to show that there had been a reduction in soil permeability of the dike. The qualitative results suggest that the injection has changed the water level in different parts of the dike. After the injection, the water table drops few meters from the injection line (figure 6) which can be an indication that the flocs have migrated from the injection line.

The quantitative results fail to show a reduction in hydraulic conductivity. The Neuman (1975) assumes homogeneity and provides the aquifer parameters as an average over the soil between the test well and the monitoring well. The analysis showed a small decrease in overall hydraulic conductivity of the site, but the change was so small that it stays in the error range. An even simpler analysis method such as Theis (1935) could be applied by using more data and trying to estimate the effect of the soil heterogeneity [8].

To better understand the behavior of the mixture under the injection pressure, laboratory test simulating the injection could be enlightening. Soil samples from the injection line and from its surroundings, especially the bottom part of the dike could give an insight on the floc formation and their location. Instead of trying to observe a change in aquifer parameters, it could be interesting to study the change occurring in the shape of the cone of depression.

ACKNOWLEDGEMENT

I want to show my gratitude to the TU Delft SoSEAL research team that helped and supported me during my master thesis Prof. Timo Heimovaara, Dr. Susanne Laumann and Jiani Zhou.

A special thank you belongs to Suomen geoteknillinen yhdistys- Finnish Geotechnical Society that offered me the opportunity to participate to the EYGEC conference.

REFERENCES

- [1] Lietaert, B. Maucotel, F., 2012. “*Summary of the Short Courses of the IS-GI 2012 Latest Advances in Marine Grouting*”. Symposium on Ground Improvement IS-GI. ISSMGE TC211 p.3-72. 30 May- 1 June, Belgium.
- [2] TU Delft. “*SoSEAL: Soil Sealing by Enhanced Aluminium and Dissolved Organic Matter Leaching*”, Retrieved 26.3.2019 from <https://www.tudelft.nl/technology-transfer/development-innovation/research-exhibition-projects/soseal/>

- [3] Bonfiglio, C., 2016. “*Hydraulic Conductivity Reduction Induced by Precipitation of Aluminium-Organic Matter flocs in Porous Media*”, Master Thesis, Politecnico de Milano in co-operation with TU Delft, Italy, 69 pages.
- [4] Fitts, C. 2012. “*Groundwater Science*” (2nd edition), Academic Press Inc, USA, 692 pages.
- [5] Schwartz, F. W. and Zhang H., 2003. “*Fundamentals of Groundwater*”, John Wiley and Sons, USA, 592 pages.
- [6] Neuman, S. 1975., “*Analysis of Pumping Test Data from Anisotropic Unconfined Aquifers Considering Delayed Gravity Response*”. *Water Resources*, 11(2), 329–342, DOI: 10.1029/WR011i002p00329.
- [7] Bear, J., 1979. “*Hydraulics of Groundwater*”, McGraw-Hill Inc, USA, 567 pages.
- [8] Theis, C. V. 1935., “*The Relation Between the Lowering of the Piezometric Surface and the Rate and Duration of Discharge of A Well Using Ground - Water Storage*”, *Transactions of the American Geophysical Union*, 16(2), pages 519-524, DOI: 10.1029/TR016i002p00519.

CONSTRUCTION OF TWO STORM WATER BASINS IN THE SAND OF PLIOCENE

Lisa Miotti, *Project Hydrogeologist, FONDASOL, lisa.miotti@fondasol.fr*

ABSTRACT

The construction of two storm water basins at La Teste-de-Buch in the south-west of France started early 2018 with the objective to be operational late 2019. The excavation work is located nearby the Arcachon Basin: a costal lagoon partly surrounded by a mixed sand and gravel coastline. The project area is subject to water table rising to the ground level. The site dewatering management is a key issue to accomplish successfully the project. This paper presents the project hydro-geotechnical challenges and the methodology established to monitor and control the groundwater on site.

Keywords: Geotechnical Engineering, Hydrogeology, Groundwater Modelling, Dewatering.

1. INTRODUCTION

1.1. The Storm Water Basins Characteristics and Construction Techniques

The project consists in the construction of two storm water basins of 42 m and 60 m diameter each and 10 m deep, into the sand of the Pliocène geological time in the south-west of France. The basins are made of a 0.6 m thick diaphragm wall. Located 9 m below the bottom the basins, a 1.5 m thick low permeability concrete plug was designed to lower groundwater flow while dewatering and to face groundwater pressure pushing up the structure.

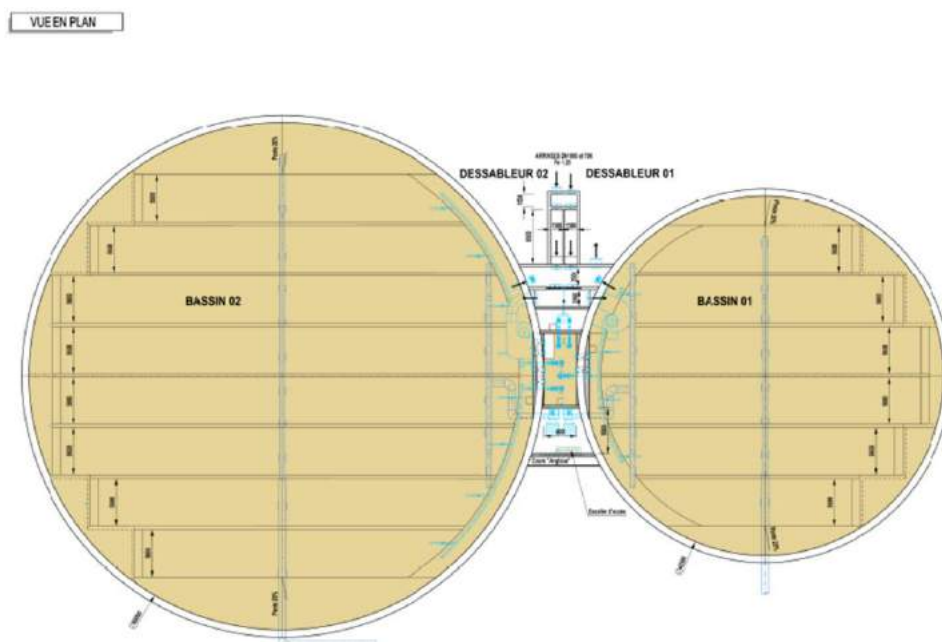


Figure 1. Schematic of the storm water basins

The construction phases of each storm water basins consist of:

- Phase 1: the construction of the diaphragm wall. The base of the wall sits at the elevation of 19 mbgl;
- Phase 2: the injection of the concrete plug at the base of the wall at 19 mbgl;
- Phase 3: the dewatering of the sand inside the structure. The dewatering target elevation is set to 1 m below the bottom of excavation to allow the excavation works at dry conditions;
- Phase 4: the excavation works to a depth of 10 mbgl.

The figure 3 presents the characteristics and phasing of the storm water basins construction.

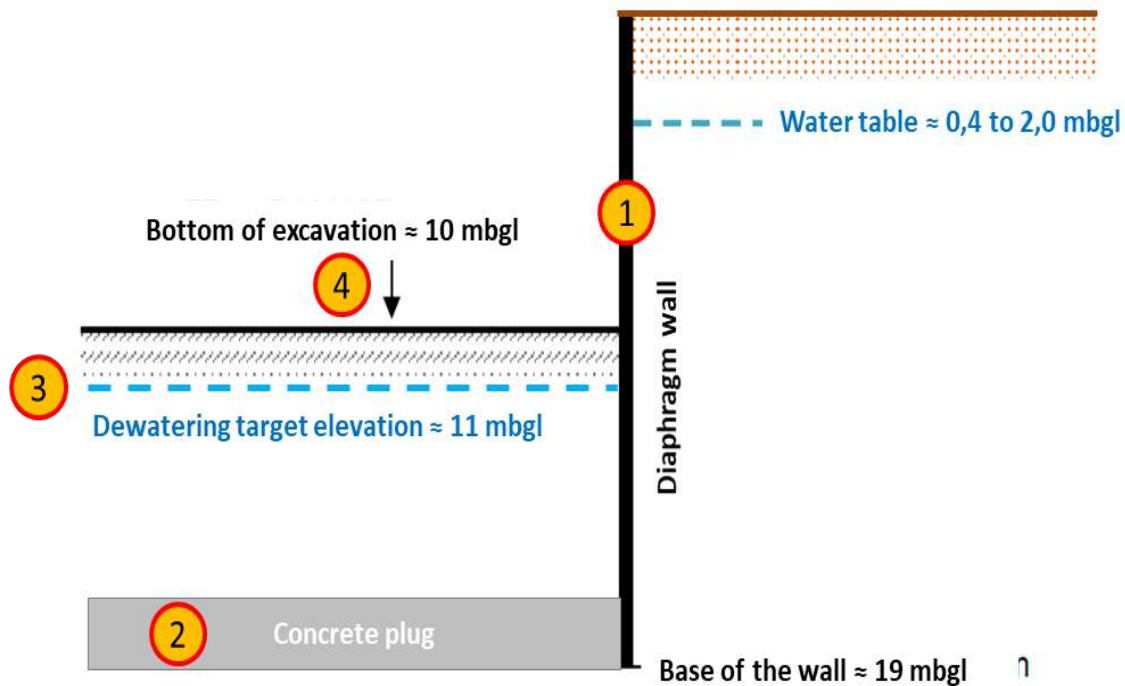


Figure 2. Characteristics and phasing of the storm water basins construction

1.2. Geological and Hydrogeological Context

The study is located on a coastline. The deposits here consist in the Sand of the Pliocène geological time.

The bore holes lithology logs realized on site indicates a sandy with clay lenses horizon from the surface down to 28 mbgl, then a compact sandy horizon down to 34 mbgl and finally a loose sandy horizon until the bottom of the holes (around 40 mbgl).

Prior to construction, the groundwater levels are measured between 0.4 and 2.0 mbgl on site.

In the project environment, the groundwater flows to the north-east, discharging in the Archon Basin.

Thank to pumping tests, the permeability of the sandy horizon intercepted by the project is measured around 1.10^{-5} m/s.

2. HISTORY

A first geotechnical study estimated the reference groundwater levels according to the Eurocodes.

These reference water levels are used to design the concrete plug in order to face the groundwater pressure pushing up the structure.

However, before the excavation starts, unexpected groundwater levels exceeded the reference values, putting the concrete plug stability efficiency in default.

Instead of resizing the plug, a more cost-effective option was decided, that consists in lowering the groundwater around the projected basins to ensure the stability requirements of the concrete plug.

3. METHODOLOGY

3.1. Field Measurements

Two existing piezometers record water levels inside the basins. A complementary piezometer was realized outside the basins with the objective to:

- monitor the groundwater outside of the basins while dewatering inside. A monitoring plan is defined to alert when the water table exceeds a critical level, causing a potential instability in the structure ;
- undertake in-situ pumping tests to verify the concrete wall sealing and the concrete plug low permeability.

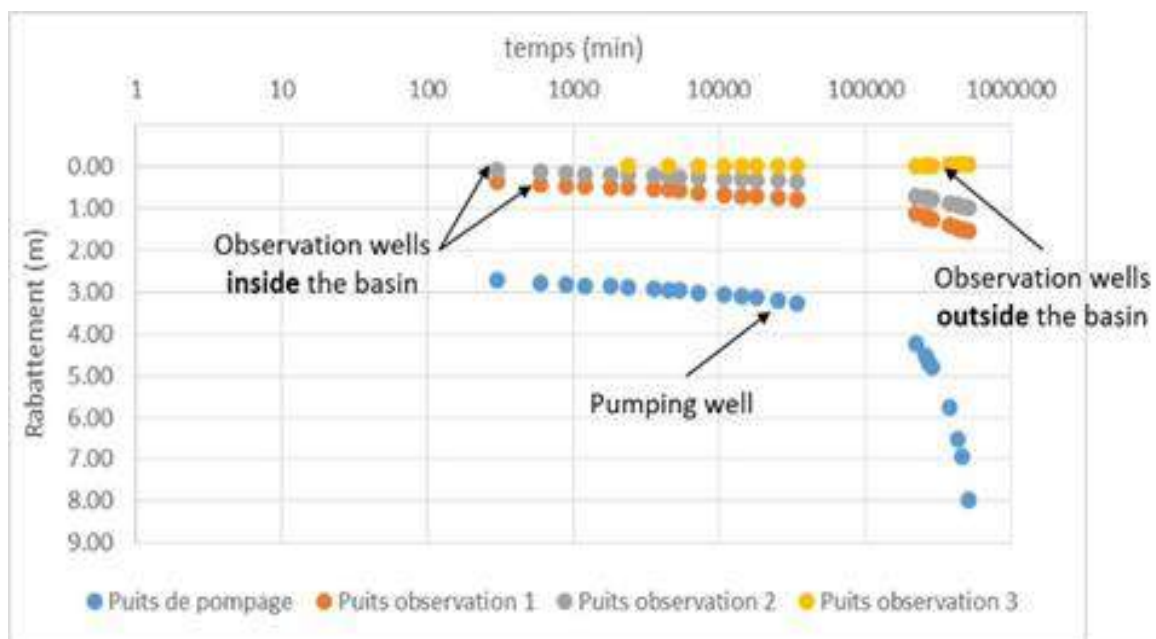


Figure 3. Water levels observed while pumping tests

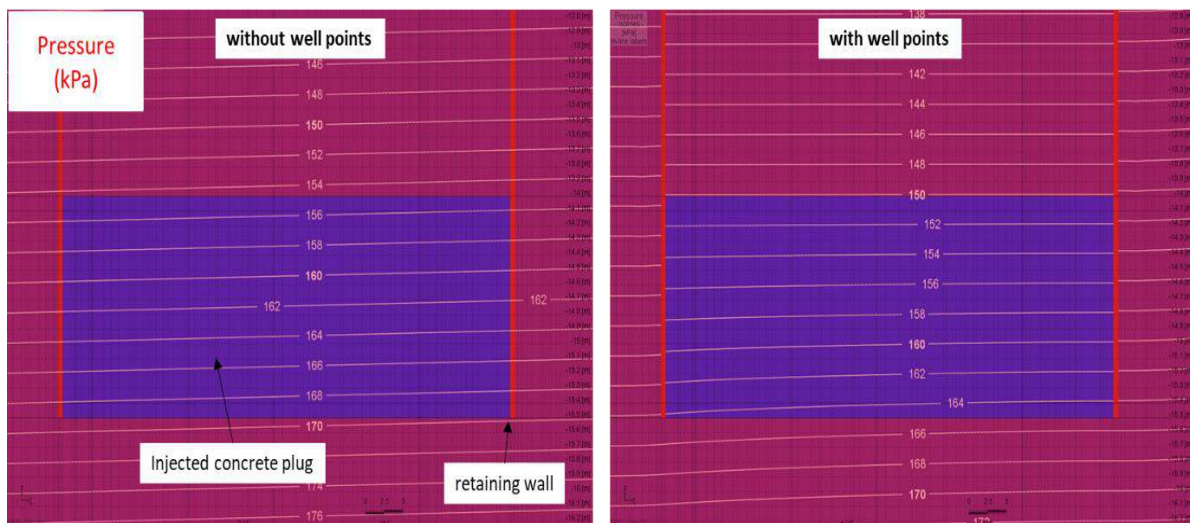
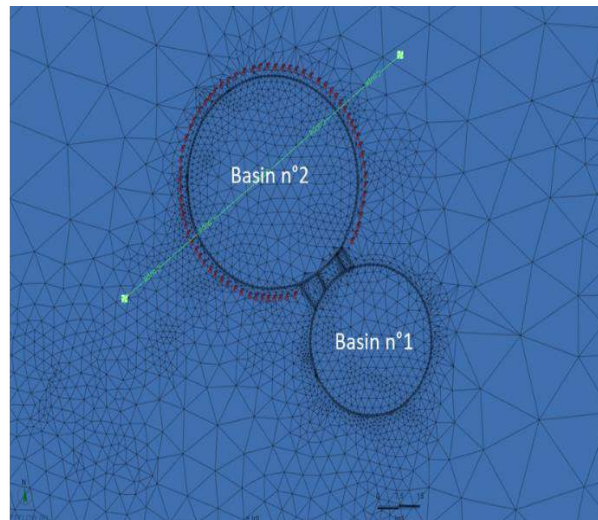
3.2. Numerical Modelling

A 3D groundwater flow model has been developed to estimate residual flow in excavations under water level, enclosed by a low permeability retaining wall embedded in a concrete plug.

The model also calculates the groundwater pressure around the basins structures, helping to verify their hydrogeological stability.

The numerical model allows to:

- assess the optimum dewatering plan taking into account the hydrological context (stream, ...);
- assess the groundwater drawdown on a local scale ;
- achieve a sensibility analysis of the concrete plug permeability on residual flow ;
- define an emergency drainage method by well points to lower the water table on site when exceeding the critical level (causing a potential instability in the structure).



* vertical exaggeration on the cross section

Figure 4. FEFLOW 3D groundwater model: the effect of active well points on pore pressure (isolines in kPa)

4. INSTRUMENTATION DURING CONSTRUCTION PHASE

During the works in winter and spring 2019, the project supervisor on site monitored the groundwater levels, which kept exceeding the critical stability level.

The emergency drainage plan was implemented: well points were installed around the basins to lower the groundwater level in the project area.



Figure 5. Operating well points on site while construction

4. CONCLUSION

Careful integration of hydrogeology into the geotechnical engineering study is allowing progressive optimization of water management on site, structures viability and obviously the costs.

LAGRUA – Radier OUVRAGES ANNEXES, remblai BAS1 et plancher haut BAS2 18 FEVRIER 2019



Figure 6. Picture of the construction phase

ACKNOWLEDGEMENT

The rewarding and constructive discussions with the client, The Etchart Engineering Company, were highly appreciated. I would also like to offer my special thanks to the Fondasol hydrogeology team and technical referent who worked with me on this project.

REFERENCES

[1] Miotti L., Joubert. J., 2018. “*Bassin de sécurité Lagrua – La Teste de Buch (33)- Diagnostic hydrogéologique : modélisation et dimensionnement des ouvrages de rabattement en phase travaux (Mission G5)*”.

[2] Bajolet M., Quirin L, Cardineau F, 2018. “*Bassin Lagrua – La Teste de Buch (33)- Note de calcul : paroi et bouchon injecté*”.

NEW 2D APPROACH TO ESTIMATE THE DISPLACEMENTS INDUCED BY TUNNEL BORING MACHINES

Nicolas Berthoz , *Engineering Geology and Geotechnical Design Department Centre for tunnels studies (CETU), Bron (France), nicolas.berthoz@developpement-durable.gouv.fr*

ABSTRACT

The estimation of the displacements induced by tunneling close to neighboring constructions (buildings, engineering structures, tunnels, networks, *etc.*) is an essential step in urban underground projects. From this estimate, important design choices can be deduced or adapted, such as the tunnel position or the control parameters of the TBM (face pressure, grouting pressure...). A new method based on two-dimensional numerical calculations with a phasing simulating the main sources of volume losses around the machine is proposed. This method is then validated thanks to its application on several tunnel projects.

Keywords: Tunnel, Numerical Modeling, Displacements Induced, Settlements.

1. INTRODUCTION

Urban sprawl and the increasing demand for mobility, coupled with the desire to limit environmental impacts, lead to an increasing use of the subsoil to develop underground infrastructures. In soft grounds, ubiquitous in urban sites, the need to limit mechanical stresses induced on neighboring buildings (buildings, engineering structures, tunnels, networks, *etc.*) leads to common use of Earth Pressure Balance Shields (EPBS) or Slurry Shields (SS).

On the whole, these excavation methods effectively help to limit impacts on neighboring constructions. However, the prediction of the displacements induced by them remains a delicate geotechnical problem due to: (i) the numerous sources of volume losses around the machine (lack of face pressure, overcut, taper of the shield tail, lack of annular void grouting...), (ii) the three-dimensional nature of the problem, (iii) the classical difficulties inherent to the mechanical behavior of soils and rocks (non-linear elasticity, plasticity, *etc.*). Consequently, an optimization of projects is possible through a reduction of technical constraints and / or a reduction of costs associated with the damages that could be generated by tunneling.

This issue has been the subject of numerous publications for some forty years, which can be grouped into three complementary categories: empirical approaches based on site data analysis [1, 2], physical modeling [3, 4] and theoretical, mainly numerical modeling [5, 6, 7].

A detailed literature review cannot be provided here due to lack of space. Let us simply remember that the current 3D numerical models presented in the scientific literature perform varied parametric studies but without application to a significant number of projects. In addition, these models are highly complex, making it difficult to use them in projects. As a result, 2D approaches are often used in practice. The excavation process is sometimes modeled with an imposed convergence: this type of approach is not physical because it can generate tensile stresses at the tunnel wall in the case of layers which have very different rigidities. Moreover, this method poses the difficulty of choosing the amplitude of the convergence according to the driving conditions of the machine. However, this approach may be useful in the particular case of homogeneous grounds with low shear strength, where the ground is in a

state of failure with displacements limited by the presence of the shield tail. Other approaches try to introduce an unconfinement ratio, corrected by the pressures exerted by the machine, but fail to take into account the pressure differences between the face, along the shield tail and the back of the shield tail, as well as the geometry of the shield tail.

The method presented in this article aims to allow the evaluation of the final displacements (far behind the face) generated in the ground by tunneling, in particular the final transverse profile of surface settlements and displacements in the cross section. This method does not focus on loads generated in the lining segments.

The choice of a 2D approach is motivated by the desire to have a method that is applicable from the initial design studies. Obviously less comprehensive than a 3D approach but much faster to implement, it can allow preliminary design, which will serve as a basis for more complete 3D approaches. The link between the "driving conditions" (Table 1) and the boundary conditions of the numerical model is formulated explicitly (§2). In order not to introduce bias related to a different interpretation of the mechanical characteristics of the grounds, the link between the "input data of the geotechnical model" (Table 1) and the constitutive law associated with the grounds in the numerical model is also explicit (§3). The results obtained with this method are then compared to measurements made on the Paris T6 tramway [8].

Table 1. Synthesis of input data needed by the numerical model.

	Description	T6-S1	T6-S3
Input data "driving conditions"			
D (m)	Excavation diameter	9.15	9.15
P_f (kPa)	Average face pressure in tunnel axis, including the cutting wheel ground supporting function [4]	290 (0.80.σ _{h0-axis})	320 (1.20.σ _{h0-axis})
P_j (kPa)	Average bentonite injection pressure along the shield tail (value in tunnel crown, where injections are physically made)	0	190 (0.60.σ _{v0-cle})
c_{max} (mm)	Maximale convergence allowed along the shield tail (= difference of radius between the cutter head and the end of the shield tail)	25	25
P_b (kPa)	Average grouting pressure in the annular void (value in tunnel crown, where injections are physically made)	270 (0.75.σ _{v0-cle})	320 (1.05.σ _{v0-cle})
Input data "geotechnical model"			
H (m)	Depth of the tunnel axis	22.9	19.8
litho	Depth of interfaces between the different grounds	Gravels and sands (Cf. Table 2)	Limes and clays (Cf. Table 2)
hydro	Depth of the different water tables		
γ (kN/m³)	Natural unit weight of each ground		
E_M (MPa)	Pressuremeter modulus of each ground		
k (m/s)	Permeability of each ground		
c'(kPa), φ'(°) c_u (kPa)	Cohesion and friction angle of permeable grounds, undrained cohesion of low permeability grounds		

The set of "input data" necessary for use of the method is listed in Table 1. Note that the associated values on two sections of the Paris-T6 project are also provided. It should be noted in particular that during the passage of the tunneling machine in these two sections, the face pressure P_f was of the order of the total horizontal stress $\sigma_{h0-axis}$ and that the injection pressure along the shield tail was zero or in the order of 60% of the total vertical stress in key σ_{v0-cle} .

The measurements used for the "validation" of the method concern the transverse profiles of surface settlements as well as the measurements carried out along inclinometers and extensometers. The maximum settlements on the surface s_{max} are 10.0 mm and 6.5 mm for the Paris-T6-S1 and Paris-T6-S3 sections. The transverse extension of the profile leads to parameters $k = i / H$ being respectively 0.40 and 0.42, where i is the distance between the axis of the tunnel and the point of inflection of the settlements profile. These values are consistent with [2]. Surface volume losses are therefore 0.35% and 0.20%, which are typical values for pressurized shields.

2. TUNNELING PROCESS

In order to obtain a correct estimate of the displacements induced on the surface and in the overburden, the numerical modeling procedure of the tunneling process has to reproduce the main sources of volume losses around the tunnel boring machine (at the face, along the shield tail and at the rear of the latter) as well as the three-dimensional nature of the problem. Volume losses located further back (retardation or creep of the grout, consolidation phenomena in fine soils, creep of joints between lining segments ...) are not considered here.

After a phase of initialization of the stresses, the volume losses at the face, along the shield tail and at the rear of the latter are generated and considered to be independent of each other (Figure 1). The loadings imposed in each step depend on: (i) machine pressures (P_f , P_j and P_b) modeled explicitly, (ii) the face distance introduced into the plane strain model via the "unconfinement ratio λ " of the Convergence/Confinement method [9]. These loads are described in the paragraphs below.

Step 1: Initialization of geostatic stresses:

The type of initial stress state to be used (total or effective) depends on the permeability of the ground with respect to the advance rate. If the excavation speed is important with regard to the permeability of the ground, it is reasonable to consider that excavation is conducted under undrained conditions (CU), which allows to reason in total stresses. In the opposite case, excavation takes place under drained conditions (CD), which makes it necessary to reason in effective stresses. Face stability studies carried out by [10] fix the limit between these domains with a permeability of the order of 10^{-7} to 10^{-6} m/s for an advance rate of the order to 0.1 to 1 m/h. This value corresponds to excavation speed: an advance rate of 1.8 m is made in 1h30 to 3h, with excavation accounting for 2/3 of this time and segment laying 1/3.

Step 2: Modeling of volume losses at the face:

The grounds corresponding to the interior of the tunnel are deactivated (numerically: a null Young modulus is assigned to them). The tunnel wall is then deconfined with a $\lambda_{eq-face}$ ratio. This unconfinement ratio aims to model the volume losses induced by the extrusion of the face and the preconvergence. It is considered that the extrusion and the preconvergence are mainly a function of the face pressure P_f . When P_f is of the order of the initial total horizontal stress in the axis, which is the case in the sections studied (see Table 1), we therefore consider that there is no volume loss at the face, *i.e.* $\lambda_{eq-face} \approx 0.0$. So this calculation step generates no displacements. The relation between $\lambda_{eq-face}$ and P_f is not immediate in the general case and needs to be specified by 3D or axisymmetric finite element calculations. Caution is advised as the settlement profile that could be obtained at the end of this calculation step in the general case ($\lambda_{eq-face} \neq 0.0$), will not be the "real" profile above the cutting wheel: it will simply be the contribution of volume losses at the face with regard to the total settlement profile.

Step 3 : Modeling of volume losses along the shield tail:

The volume losses generated along the shield tail are a function of: (i) the bentonite injection pressure P_j made therein, P_j being the value in the crown of the tunnel, (ii) the available space c_{max} induced by the overcutting and the conicity of the shield tail, (iii) the fictitious confining pressure associated with the report of a part of the soil weight on soils in the front of the face (enabled by longitudinal arching effects observed in all grounds, including in purely frictional soils [4]). If we consider that the injection pressure P_j is uniform over the length of the shield, these volume losses are maximum at the end of the shield tail (one diameter at the rear of the front), because here the annular space is the most important, and the effect of the face the weakest. Two loads are imposed simultaneously on the tunnel wall:

- (a) a total unconfinement ($\lambda = 1.0$), which is meant to be on the safe side from the settlements point of view, considers that the effect of the face is null at the end of the shield tail. Note that axisymmetric numerical calculations, carried out in parallel with this study, showed that the fictitious confinement pressure related to the effect of the face is between 85 and 95% of the initial radial stress for an homogeneous isotropic state stress and without radial confining pressure ($P_j = 0$ and no lining).
- (b) a pressure $P_j^*(z)$ evolving linearly with the depth (see Figure 1) calculated differently according to the studied case:
- In low permeability grounds (where the initial stresses are total stresses), without closure of the annular void (the convergence remaining lower than the sum of the overcut and the conicity of the shield tail, c_{max}): $P_j^*(z) = P_j + \gamma_{bentonite} \cdot z$ where $\gamma_{bentonite}$ is the unit weight of the bentonite injected, of the order of 15 kN/m^3 ,
 - In permeable grounds (where the initial stresses are effective stresses), without closure of the annular void: $P_j^* = P_j + \gamma_{bentonite} \cdot z - u_0(z)$ where $u_0(z)$ are initial pore pressures (hydrostatic). Indeed, it is considered that the bentonite forms a tight cake on the excavated wall. P_j is therefore opposed to total initial stresses. In drained conditions, only the "effective" part of the injection pressure limits the ground convergence, hence the need to subtract the pore pressures ($P_j - u_0$). This pressure P_j^* can not be negative: to say that $P_j = 0$ in case of absence of bentonite injections under water table (case of Paris-T6-S1 in Table 1) is not strictly true, one should write: $P_j = u_0$,

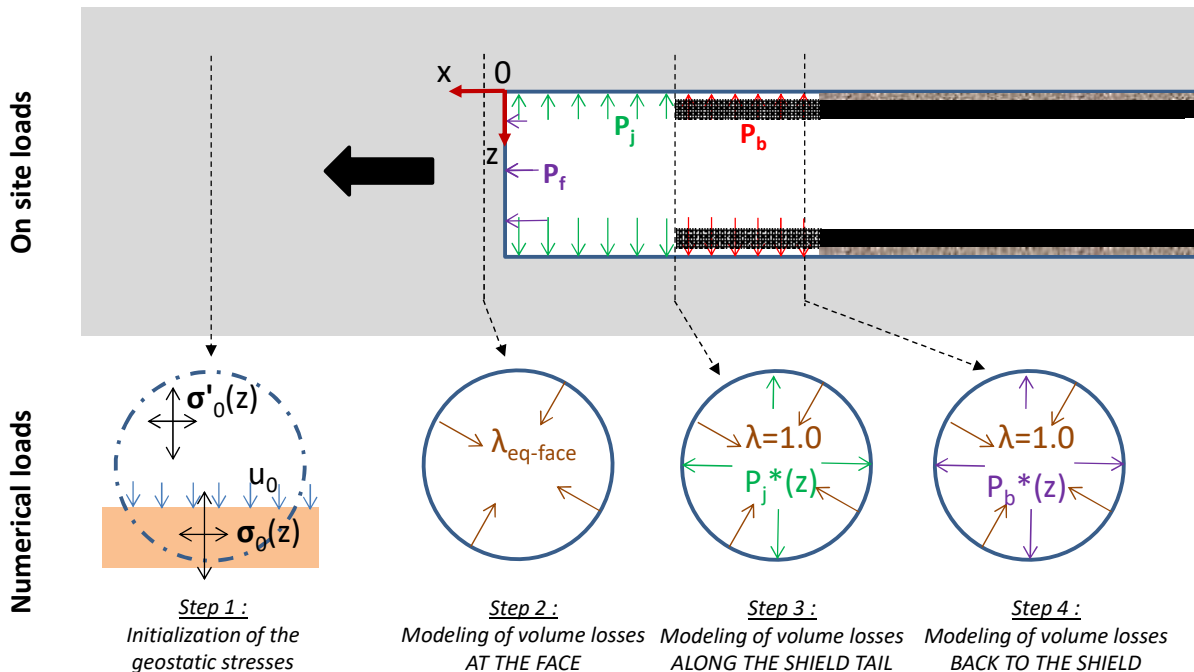


Figure 1. Phasing of the finite element model.

- If the convergences calculated with the preceding pressures are greater than the available annular space c_{max} : a fictitious pressure $P_{j\ bis}^* > P_j^*$ generating a convergence equal to c_{max} (total closure of the annular void) is calculated by iterative steps.

Step 4: Modeling of volume losses back to the shield:

These volume losses correspond to those generated during the grouting of the annular void between the ground and the lining. In the present case, it is considered that their amplitude depends only on the injection pressure of the grouting mortar P_b . This assumption implies two hypotheses considered reasonable in the short term: (a) that the tunnel wall is impervious and that there is no return of mortar forward along the shield tail (*i.e.* the annular void is a closed system), (b) the mortar is sufficiently liquid to actually exert a pressure on the wall. The volume losses generated during this step correspond so to the application of the following two loadings in the model:

- (a) a total unconfinement of the wall of the tunnel compared to the previous step to replace $P_j^*(z)$ with $P_b^*(z)$,
- (b) a pressure $P_b^*(z)$ evolving linearly with the depth, calculated in this way for the same reasons than previously: $P_b^*(z) = P_b + \gamma_{mortar} \cdot z$ in low permeability grounds, or $P_b^* = P_b + \gamma_{mortar} \cdot z - u_0(z)$ in permeable grounds, where γ_{mortar} is the volumetric weight of the mortar, considered equal to 23 kN/m³.

3. MECHANICAL BEHAVIOUR OF GROUNDS

The reliability of the estimation of the displacements induced by tunnelling depends on the capacity of the modeler to reproduce the tunnelling process (§2), but to the same extent, his/her capacity to reliably model the mechanical behavior of the grounds. The assumptions made to transpose the "geotechnical model input data" (Table 1) into mechanical characteristics in the numerical model are described below.

The initial state of stresses is generated by considering the natural or buoyant volumetric weights of the grounds. Their earth pressure coefficient at rest K_0 is evaluated as follows: $K_0 = (1 - \sin \varphi') \cdot OCR^h$ where φ' is their internal friction angle, OCR their overconsolidation ratio and h an exponent varying between 0.6 for very dense sands and 0.32 for highly plastic clays [11]. The grounds are then considered to be governed by the Hardening Soil Model HSM [12], commonly used in practice today. This 8-parameters elasto-plastic model includes in particular a non-linear elasticity with an unloading / recharging modulus E_{ur} different from the first loading Young modulus E_{50} , a dependence of these modules with the minor principal stress, and a deviatoric plasticity with hardening where the final plasticity surface is parameterized by a Mohr-Coulomb criterion. The associated hypotheses are as follows, and their application to Paris T6-S1 is given in Table 2:

- **First load Young modulus E_{50}^{ref} :** in permeable grounds (drained behaviour), it is assumed that $E_{50}^{ref} = 2 \frac{E_M}{\alpha}$ where α is the rheological coefficient of the ground [13] and E_M its pressuremeter modulus. The coefficient 2 is derived from the average value indicated in [13] for calculating the settlement of a shallow foundation. This coefficient should be reinforced for each practical case by correlations between triaxial tests and pressuremeter tests. In low permeability soils, $E_{50}^{ref} = \frac{9}{4} \cdot \frac{E_M}{\alpha}$ is considered to maintain a constant shear modulus G between the drained and undrained conditions,
- **Unloading / recharging Young Modulus E_{ur}^{ref} :** it is considered that $E_{ur}^{ref} = 3 \cdot E_{50}^{ref}$. This coefficient 3 is the average value observed during cyclic pressuremeter tests on line 12 of the Paris metropolitan (see the geotechnical synthesis report of the works contract) and should be reinforced by others tests,
- **Reference pressure p^{ref} :** this pressure is chosen equal to initial minor principal stress (here horizontal stress) at the middle of each ground layer, so as to have Young modulus

in the model which are equal to average measured values. In permeable grounds the effective stress is considered, whereas in low permeability grounds the total stress is considered,

- **exponent m:** this coefficient allows the evolution of the Young modulus with the minor principal stress. $m = 0.5$ is considered,
- **Poisson's ratio ν :** few measurements of the Poisson's ratio are done in practice. In the absence of specific data, an average value of 0.3 is considered for permeable grounds. Low permeability grounds are considered incompressible, *i.e.* $\nu = 0.499$,

Table 2. Example of mechanical ground parameters considered (Paris T6-S1).

Ground	Thick. (m)	Behaviour	γ (kN/m ³)	K_0 (-)	α (-)	E_M (MPa)	E_{S0ref} (MPa)	E_{urref} (MPa)	σ_v (kPa)	u (kPa)	P_{ref} (kPa)	m (-)	ν (-)	Ψ (°)	c' (kPa)	ϕ' (°)	c_u (kPa)	Rf (-)	
COLL	3	dry	18	0,8	0,5	8	32	96	27	0	22	0,5	0,33	-5	5	25	s.o.	1,0	
SF dry	7	dry	19	0,6	0,33	30	180	541	121	0	72			5	5	35			
SF sat	3	drained	19	0,6	0,33	30	180	541	216	15	120			5	5	35			
MH	5	drained	19	0,8	0,67	30	51	152	292	55	189			-5	50	25			
GV	2	undrained	19	1	0,67	11	19	56	358	90	358		0,5	0,5	0	s.o.	s.o.		80
MSG	14	undrained	19	0,8	0,67	25	42	127	510	170	442				130				
CSO	2	dry	19	0,7	0,5	30	120	360	662	0	463		0,33	0,33	0	20	30		s.o.
SB	2	dry	21	0,6	0,33	50	300	901	702	0	421				5	10	35		
MC	10	dry	20	0,6	0,5	50	200	600	823	0	494				4	25	34		
CG	10	drained	21	0,5	0,5	150	600	1800	1028	50	489				10	100	40		

4. APPLICATION ON SITE AND DISCUSSION

The application of this methodology to the sections of the tramway Paris T6 leads to the conclusions below. For the sake of brevity, only a few key figures illustrate these results. The detailed results will be published in a future article.

First, let us remember that in the vast majority of the cases studied, the volume losses induced by tunneling are generated integrally along the shield tail. Indeed, take for example the case of the Paris T6-S3 section. The face pressure P_f was of the order of the total initial horizontal stress in the tunnel axis, and the grouting pressure P_b was greater than the total vertical stress at the tunnel crown (Table 1). The 6.5 mm of settlements generated on the surface (Figure 2a) were thus integrally generated along the shield tail.

Moreover, the procedure for modeling the volume losses along the shield tail with a constrained boundary condition with a limitation of convergences to the available annular space (overcut and taper) gives correct results, as illustrated for example in Figure 3a. In this section (Paris T6-S1) where no bentonite has been injected along the shield tail, the limitation of the convergences to the value c_{max} leads to a good estimation of the maximal settlement.

The studies carried out also show the difficulty of precisely identifying the pressure conditions prevailing in the bentonite around the shield tail from field data. For example, considering the average value of the bentonite injection pressure 20 m on both sides of the studied section (190 kPa) leads to surface settlements three times lower than experimentally (Figure 2a). It is necessary here to consider the minimum value (70 kPa by Figure 2b) in the numerical model to reproduce the final amplitude of the settlements. This hypothesis is not absurd considering the fact that the injected volumes are very variable and remain much lower than the theoretical volume of the annular void (equal to 600 L/ring for a diametric convergence of the ground of 25 mm, corresponding exactly to the value associated with a pressure P_j of 70 kPa).

Concerning the transverse extension of the settlement profile, the models lead to satisfactory results when the plastic strains of the cover are important (case of Figure 2a). If the cover

remains mostly in the elastic domain, the profile obtained is too wide, so the volume loss is overestimated (case of Figure 3a). The increase of the ground dilatancy angle, the modification of their Young's modulus (E_{50} and E_{ur}) by $\pm 50\%$, or the variation of their pressure coefficients at rest K_0 by ± 0.2 , don't improve the accuracy of the modeling. To artificially tend to the experimental profile, it would be necessary to reduce the shear strength of the grounds and increase the pressure exerted along the shield tail P_j .

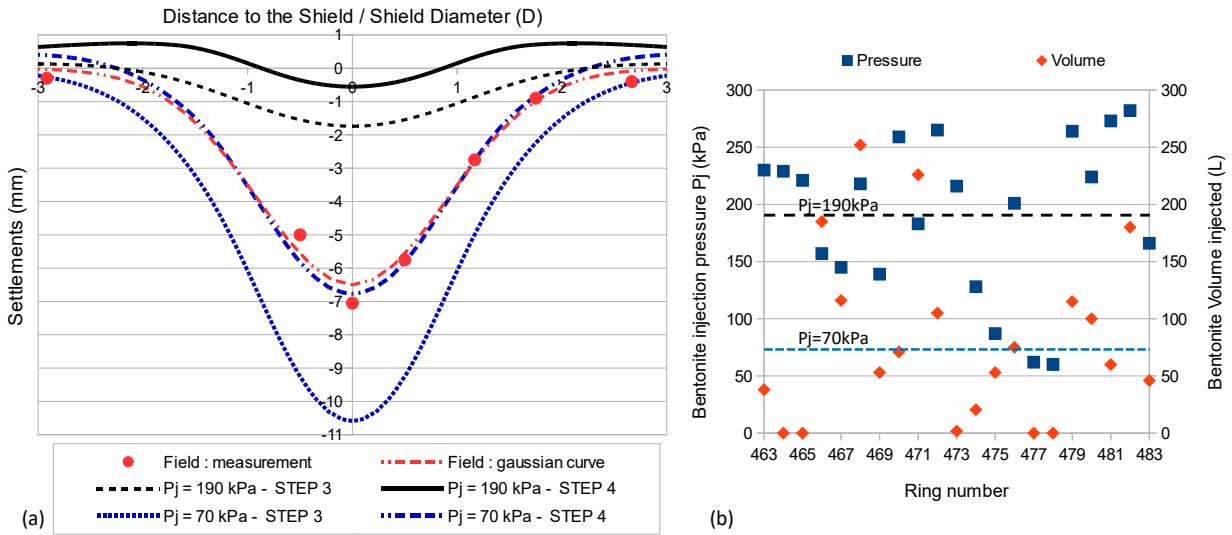


Figure 2. Paris T6-S3 model results: (a) transverse profile of settlements, (b) pressures and volumes of bentonite injected along the shield tail.

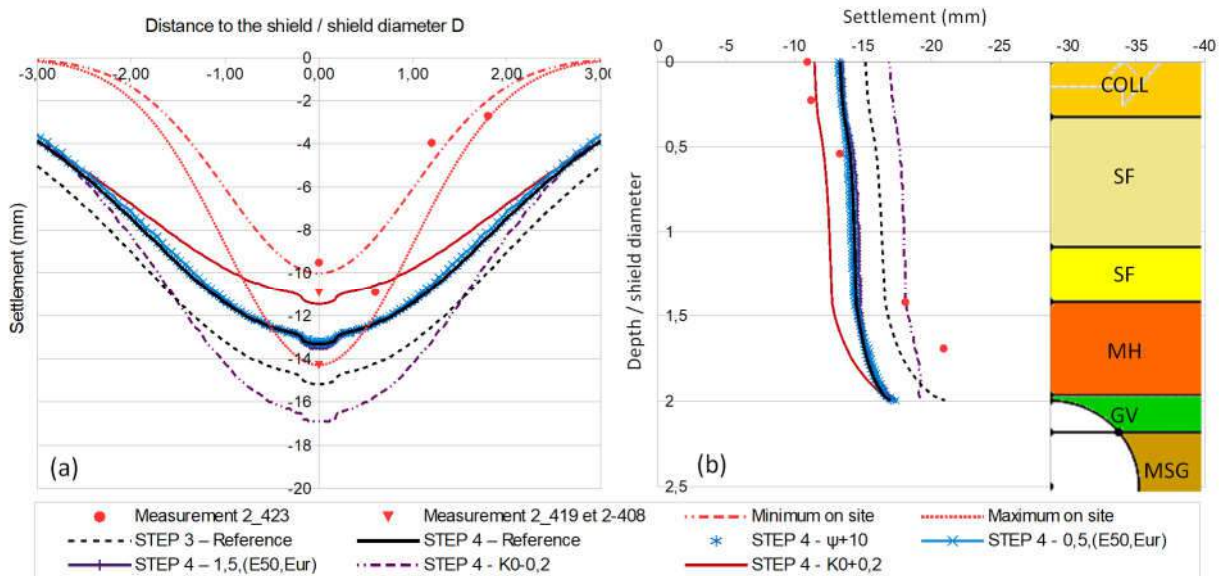


Figure 3. Paris T6-S1 model results: (a) transverse profile of settlements, (b) settlements along the extensometer E1 located above the tunnel axis.

Finally, the developed approach leads to an acceptable estimate of settlements in the overburden. The settlement at the tunnel crown is, however, slightly lower numerically than on site, but decreases less rapidly in the overburden (Figure 3b).

To conclude, the approach developed is an interesting tool for preliminary design and understanding, thanks to the explicit link between all the input data and the modeling assumptions. The validity of this approach remains to be confirmed thanks to:

- (i) Its application to other sites, where the actual conditions prevailing around the shield tail (crucial point of modeling) would be precisely known. As such, an upcoming publication will present the results obtained on the Paris L12, Lyon LB and Milan L5 metropolitans,
- (ii) Comparisons with 3D finite element calculations realized with exactly the same assumptions in order to quantify the error made in the 3D / 2D passage of the problem.

This approach is complementary to the 3D calculations but cannot replace them: the approach presented here will never allow studying, impact of tunnelling on piles for example.

ACKNOWLEDGMENTS

The authors would like to thank CD78, Egis Rail, and Eiffage for the data collected.

REFERENCES

- [1] Peck R.B, 1969. “*Deep excavations and tunneling in soft ground*”, Proceedings of the 7th ICSMFE, Mexico City, State of the Art Volume, pp. 225-290.
- [2] Mair R.J., Taylor R.N. 1997. “*Bored tunneling in the urban environment: State-of-the-art report and theme lecture*”, Proceedings of the 14th ICSMFE, pp. 2353-2385, Hamburg.
- [3] Atkinson J.H., Potts D.M., 1977. “*Subsidence above shallow tunnel in soft ground*”, Journal of the Geotechnical Engineering Division, ASCE GT4, 307-325.
- [4] Berthoz N., Branque D., Wong H, Subrin D., 2018. “*TBM soft ground interaction: Experimental study on 1g reduced-scale EPBS model*”, Tun. and Under. Space Tech., 72:189–209.
- [5] Finno R.J., Clough G.W., 1985. “*Evaluation of soil response to EPB shield tunneling*”, Journal of Geotechnical Engineering, 111-2:155-173.
- [6] Kasper T., Meschke G., 2004. “*A 3D finite element simulation model for TBM tunnelling in soft ground*”, International Journal of Numerical and Analytical Methods in Geomechanics, 28:1441-1460.
- [7] Dias D., Kastner R., 2013. “*Movements caused by the excavation of tunnels using face pressurized shields — Analysis of monitoring and numerical modeling results*”. Eng. Geo., 152:17-25.
- [8] Grave P., Dore V., Mordant E., 2012. “*Tramway T6 - Châtillon Viroflay link*”, Tunnels et Espace Souterrain, 234:533-541.
- [9] Panet M., 1995. “*Le calcul des tunnels par la méthode convergence-confinement*”, Presses des Ponts et Chaussées, Paris, 178p.
- [10] Anagnostou G., Kovari K., 1996. “*Face stability conditions with Earth Pressure Balanced Shield*”, Tunnelling and Underground Space Technology, 11:165-173.
- [11] Holtz, R., Kovacs, W., 1991. “*Introduction à la géotechnique*”, Presses de l’Ecole Polytechnique de Montreal, 808 p.
- [12] Schanz T., Vermeer P.A., Bonnier P.G., 1999. “*The Hardening Soil Model: Formulation and verification*”, Proceedings of the 1st Symposium on Plaxis, CRC Press, 328 p.
- [13] AFNOR, 2013. “*NFP94-261 – Justification des ouvrages géotechniques : normes d’application nationale de l’Eurocode 7 – Fondations superficielles*”, 126 p.

INVESTIGATION OF THE FLUIDISED ZONE IN DEEP VIBROCOMPACTION

Moritz Wotzlaw*, *Technische Universität Berlin, Chair of Soil Mechanics and Geotechnical Engineering, moritz.wotzlaw@tu-berlin.de*

ABSTRACT

Deep vibrocompaction is an established method for the improvement of loose sandy soils using deep vibrators. In a basic modelling concept, the area of the ground influenced by the vibrator is subdivided into three concentric cylindrical zones. According to that model, the compaction occurs only in some distance to the vibrator, since the acceleration amplitudes in the vicinity, the so-called fluidised zone, are considered too large. *Fluidisation* is defined and distinguished from *liquefaction*. Both phenomena can occur in the vicinity of the vibrator and so both have to be adequately considered in a simulation. A numerical model is developed and verified, while locally undrained conditions are applied in order to simulate liquefaction. Since mesh distortion becomes excessive, an MMALE-approach is being used.

Keywords: Soil Improvement, Vibroflotation, Numerical Modelling, MMALE, Large Deformations, Fluidisation, Liquefaction

1. INTRODUCTION

Since its invention by the German company Keller in the 1930s, deep vibrocompaction has become a widely used method for soil improvement [1]. The vibrator basically consists of a steel tube of about 3 m length, in which a rotating imbalance creates a centrifugal force causing a circular movement with a conoidal envelope (Fig. 1). It is connected to an extension tube via a joint and can be lowered to depths of up to 40 m. A basic modelling concept consists in subdividing the soil influenced by the vibrator into three concentric cylindrical zones (Fig. 2): Fluidised zone (A), compaction zone (B) and elastic zone (C).

First 2D attempts at modelling vibrocompaction numerically were carried out by [2], followed by [3] and [4]. More recently, full 3D-Simulations using the Coupled-Eulerian-Lagrangian (CEL) method (e.g. [5], [6]) were conducted, which seem to be rather unsuitable for a practical use due to the computational time necessary and the inability of the incremental constitutive law to correctly predict accumulated strains after a large number of cycles.

A more convenient solution is expected from a method, that has already been applied to vibratory pile driving ([7], [8]). In this two-step-scheme, a hypoplastic constitutive law [9] is used to determine the distribution of strain amplitudes, which then serve as the input data for the explicit calculation of accumulated plastic strains after 100s or even 1000s of cycles using the High Cycle Accumulation Model (HCA) [10].

A similar approach will be applied in this DFG-funded cooperation project of TUB, KIT and Keller Grundbau GmbH. While the authors task at TUB consists in the determination of strain amplitudes in the vicinity of the vibrator using Non-Lagrangian numerical methods, the researchers at the Karlsruher Institut für Technologie are involved in the enhancement of the HCA-Model for large strain amplitudes.

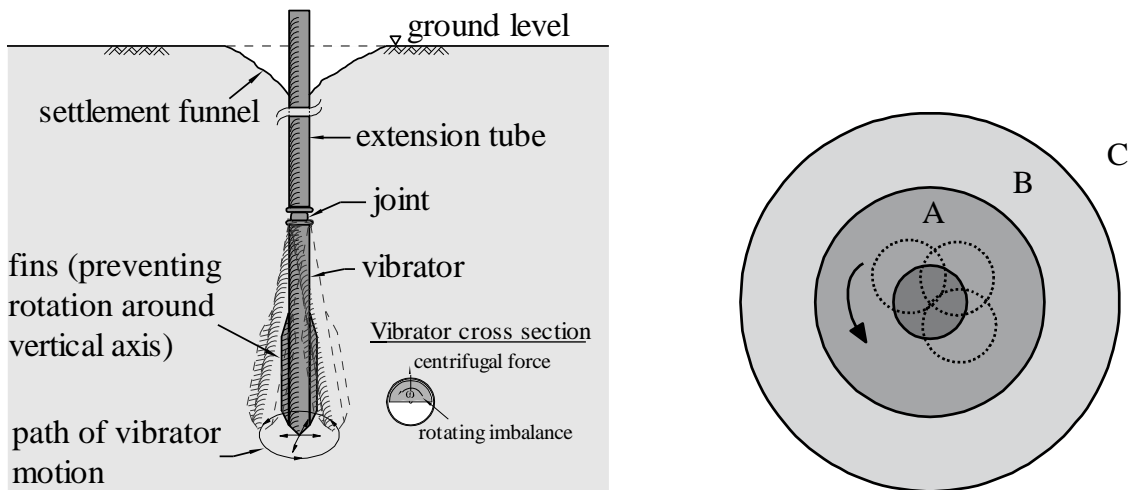


Figure 1. Schematic of deep vibrocompaction (left) and Modelling concept: fluidised zone (A), compaction zone (B) and elastic zone (C) (right, both after [1])

In-situ data obtained at construction sites by Keller Grundbau GmbH will be used for validating the numerical results.

2. MODELLING THE SOIL BEHAVIOR

In this chapter the theoretical background for the soil mechanical processes is briefly introduced.

2.1. Constitutive Model

The constitutive model applied in the numerical FE-simulations with explicit time integration is the well-known Hypoplasticity with intergranular strains [9]. The existing implementation by Mašin [12] was incorporated into the LS-DYNA UMAT using an interface written by Bakroon et. al. [13].

2.2. Locally Undrained Conditions

Since vibrocompaction is often used in soils where groundwater is present, a consideration of porewater is necessary. As stated in [14], *locally undrained* conditions are obtained by neglecting the porewater flow in a water-saturated soil, which means that volumetric strain occurs only due to a compression of the pore fluid.

With the rate form of Terzaghi's principle of effective stress, the locally undrained approach can be implemented into any material stress-point routine by simply adding the porewater pressure to the effective stress tensor $\dot{\boldsymbol{\sigma}}'$, computed with the given constitutive law:

$$\dot{\boldsymbol{\sigma}} = \dot{\boldsymbol{\sigma}}' + \dot{p}\mathbf{I} \quad (1)$$

With

$$\dot{p} = \dot{\varepsilon}_v \frac{K_f}{n} \quad (2)$$

being the rate of porewater pressure, calculated from the rate of volumetric strain $\dot{\varepsilon}_v$, the bulk modulus of the pore fluid K_f and the porosity n .

2.3. Liquefaction and Fluidisation

Two phenomena may strongly influence the soil behavior in Zone A and B: *Liquefaction* whenever pore water is present and *fluidisation* even if the soil is completely dry. While both of them are characterized by a decrease of shear strength and describe the fact that in this state the soil behaves like a viscous fluid, the mechanisms involved are not naturally the same.

Liquefaction is a rather well-understood phenomenon in a loose saturated granular soil under cyclic loading. The induced compactive grain rearrangement can't be directly transferred to a volumetric compression because of the present interstitial water and causes a decrease of effective stress and consequently of shear strength instead. Given that the total stress is constant, this leads to an increase of porewater pressure.

Fluidisation on the other hand is not well-established in the world of geotechnical engineering. It may be described as a reduction of shear strength and change of density caused by large acceleration amplitudes. Although it has been the subject of numerous experimental investigations in the past (an overview can be found in [16]) it has not yet been included in a constitutive law to be implemented into common numerical methods like the FEM. Besides the influence on shear strength it was found, that vertical vibrations with large accelerations cause dilation, while horizontally vibrations tend to compact the fluidised granular matter.

3. NUMERICAL MODEL

The current numerical model is a straightforward application of the modelling concept in Fig. 1. Since the essential soil mechanical processes are expected to occur in the horizontal plane, the soil is modelled as a pseudo-two-dimensional disc composed of 3D elements. According to [3] and [4] this is a justifiable compromise between full 3D- and oversimplified plane-strain-models.

3.1. Numerical Method

In the immediate vicinity of the vibrator, large soil deformations are expected. This is especially true, when the shear strength is decreased by liquefaction under undrained conditions. The application of numerical methods capable of handling large deformations is therefore necessary.

In a *Lagrange* formulation the material is fixed to the computational mesh and any material deformation causes mesh deformation. By contrast in a *Eulerian* formulation, the mesh is fixed in space and the material may move freely through it. ALE formulations combine the advantages of both views by introducing a reference domain, which is used to independently describe mesh and material motion [18].

In most numerical implementations, a three-step calculation scheme is applied, consisting of a Lagrange step (mesh deforms with material), rezoning step (mesh gets smoothed while the mesh topography is preserved) and advection step (the material "flows" relative to the rezoned mesh in order to retrieve the material state after the Lagrange step). ALE formulations are well suited for the application in geotechnical problems involving large deformations.

3.2. Geometry

The geometry is pictured in Fig. 2. For verification, the same geometry and model size as in [4] is being adopted. The disc has a radius of 15 m and a depth of 0.5 m. The inner hole containing the vibrator has a diameter of 0.4 m.

3.3. Soil Properties

The hypoplastic parameters for the soil in Tab. 1 are taken from [4] with an initial void ratio of 0.85. With a given grain density of 2.65 g/cm³, an initial dry density of 1.43 g/cm³ is obtained.

The initial stress state is taken as a K_0 -state with $K_0 = 0.463$.

Table 1. Parameters for Hypoplasticity with intergranular strains

φ_c	h_s in MPa	n	e_{d0}	e_{c0}	e_{i0}	α	β	R	m_R	m_T	β_r	χ
32.5°	591	0.5	0.577	0.874	1.005	0.12	1.0	10 ⁻⁴	2.9	1.45	0.2	6.0

3.4. Boundary Conditions

The soil disc is fixed in horizontal (x- and y-) directions. The horizontal boundary surfaces are provided with viscous boundaries following the approach of [15] for minimizing wave reflection.

Although the choice of the “correct” vertical boundaries is not obvious, for the sake of verifying the basic numerical model, pure stress boundaries are applied analogously to [4]. Since the modelled depth of the soil disc is 14.5 m to 15 m below ground level, the vertical stresses are given by $\sigma_{z,t} = 203 \text{ kN/m}^2$ at the top and $\sigma_{z,b} = 210 \text{ kN/m}^2$ at the bottom.

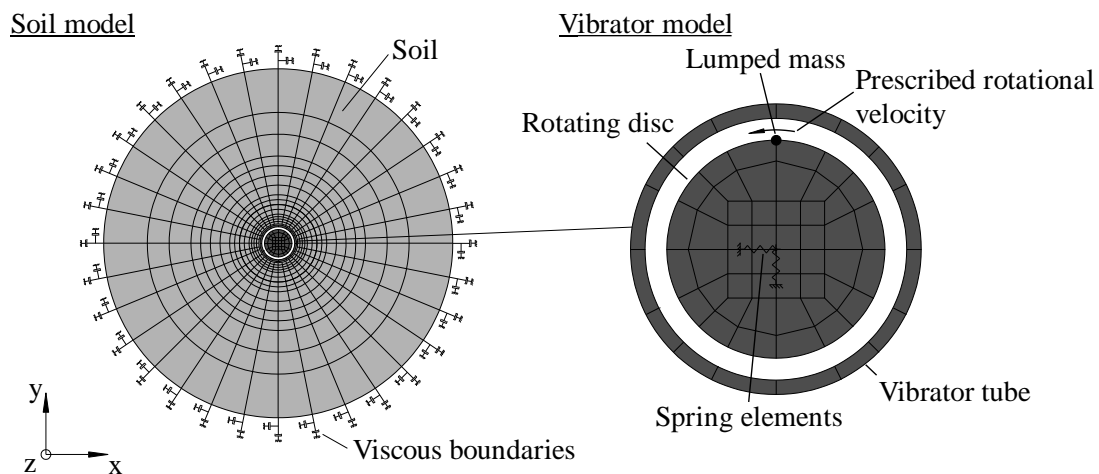


Figure 2. Disc shaped soil model (left, top view) and vibrator model with rotating imbalance (right)

3.5. Vibrator Model

For reproducing the in-plane movement of the vibrator as realistic as possible, it is modelled as a tube of rigid solid elements inside of which a lumped mass rotating on a disc composed of rigid shell elements causes a circular movement (Fig. 2, right). By coupling the translational DOFs from tube and the disc's middle node, this motion is transferred to the tube, reproducing the imbalance-driven motion of the vibrator.

Spring elements are attached to the vibrators center, restraining the movements to a circular path of a defined amplitude, which can be determined by the quotient of centrifugal force and spring stiffness.

With a centrifugal force of $F = 700 \text{ kN}$ and a spring stiffness of $k = 1 \cdot 10^5 \text{ kN/m}$ a displacement amplitude of $u_{vib} = 7 \text{ mm}$ (in the air) is obtained which is approximately the mean nodal displacement amplitude in [4].

Modelling the soil-vibrator interface is achieved via the use of a penalty contact algorithm.

4. NUMERICAL RESULTS

After verifying the Lagrange model, the influence of interface friction and the size of Zone A is discussed. Local undrained conditions are applied for modelling liquefaction.

4.1. Verification of Lagrange Model

For verifying the basic Lagrange model, it is compared to the results published in [4]. In their study, the authors applied circular nodal movements with a radius of 6.25 mm at the top and 7.5 mm at the bottom and a frequency of 30 Hz to the nodes at the inner boundary to simulate the vibrator impact. In a first step this vibrator model was adopted to test the models capability to reproduce the published results. The resulting void ratio distribution for the model verification (LS-DYNA with nodal movements vs. published results from [4]) is pictured in Fig. 3 on the left. It shows a fairly good agreement considering the fact, that the results were obtained using different FE-Codes and calculation schemes.

The results resemble the aforementioned 3-Zone-Model of Fig. 2: In the distance of more than ~5 m, the void ratio stays close to the initial value (Zone C). While the void ratio is reduced very fast in a distance between 0.5 and about 5 m (Zone B), it also remains at a rather high value in the region of <0.5 m distance from the vibrator (Zone A). This uncompacted zone is attributed to large shear strain amplitudes in [4]. Although that does explain the soil behavior in the hypoplastic model, it is not certain that this is also true in reality. Several authors (e.g. [19]) investigated the volumetric behavior of sand under cyclic large shear strain amplitudes and reported that, although the soil behaves dilatant during single cycles, the overall tendency is indeed compressive.

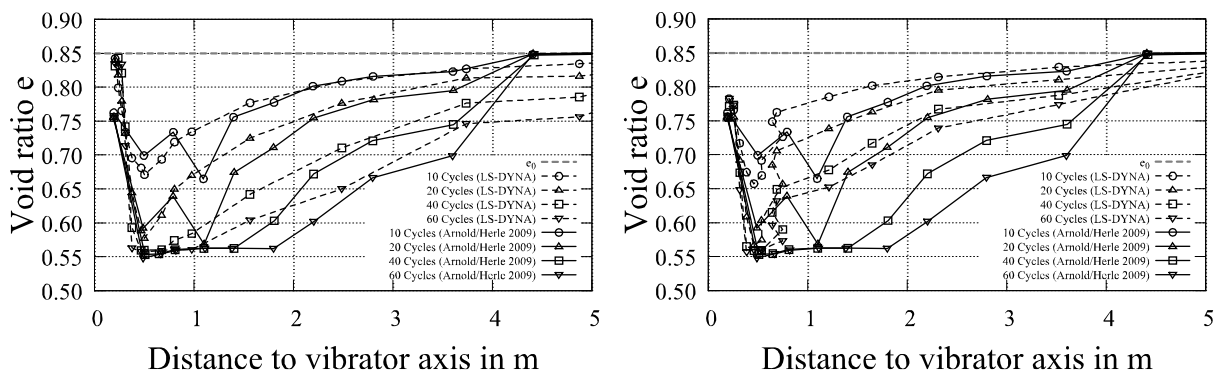


Figure 3. Void ratio distribution with nodal movement model (left) and imbalance model (right). Dashed lines: results obtained with LS-DYNA, solid lines: results taken from [4]

The diagram on the right-hand side of Fig. 3 shows the results obtained with the LS-DYNA imbalance model using a frictionless contact between vibrator and soil, compared to the results published in [4]. Although the results are similar in a qualitative way (formation of Zones A, B and C), a strong aberration is visible. This difference is mostly caused by the different assumptions for the soil-vibrator interface. In [4], the nodes in the contact surface move on a constant circular path so the radial and tangential amplitudes have the same size. This corresponds to a fully welded contact. In the imbalance model, the nodal movements are caused by the impact of the vibrator tube and since no friction was applied, only radial forces are transferred.

A very important input value for the latter simulations using the HCA-Model is the size of the fluidised zone. Following the initial model concept, one could consider the uncompacted region in the vicinity of the vibrator as fluidised, but as was pointed out before this doesn't fit the definition of fluidisation, since non-compactive behavior in the model is caused by large strain rather than large acceleration amplitudes.

The dimensionless amplitude of horizontal acceleration $\Gamma_h = a_h/g$ over a timestep of 0.4 s in different distances to the vibrator axis is given in fig 4. Following the suggestions in [1] the soil is considered fluidised for amplitudes between 1.5 and 3 g, so the fluidised zone would end in a distance of about 1.5 m to the vibrator axis. On the other hand, the reliability of this criterion is doubtful since the influence of a surcharge on the acceleration needed for fluidisation is present (as was pointed out by [16]) but not quantifiable, as no experimental results for large surcharges are available. In a more pragmatic approach for the following works, the outer boundary of zone A will be defined by the size of the largest strain amplitude ε_{ampl} that can be handled by the updated HCA-model.

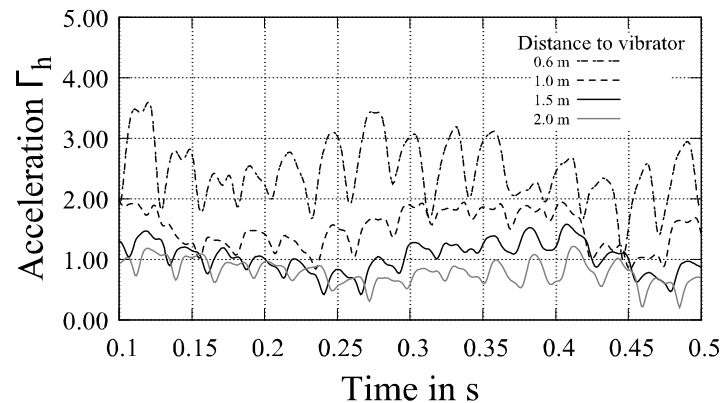


Figure 4. Acceleration amplitude Γ_h for different distances to vibrator (LS-DYNA imbalance model)

4.2. Influence of Interface Friction

A comparison of void ratio distributions for the nodal displacements model and imbalance model with a friction coefficient of $\mu = 1.0$, both obtained with LS-DYNA, is given in Fig. 5. The agreement is much better than without friction, especially for rather few cycles.

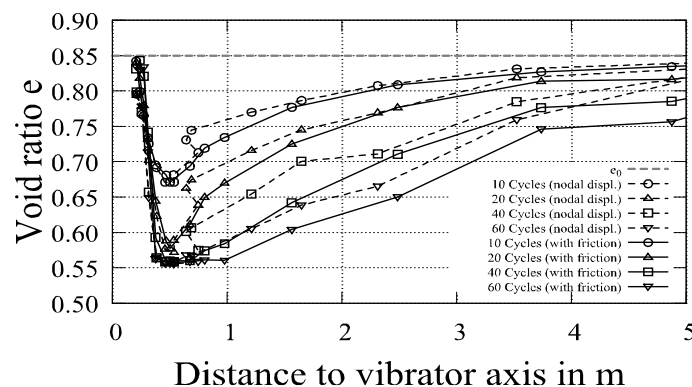


Figure 5. Void ratio distribution for LS-DYNA simulations using the nodal displacements model (dashed lines) and the imbalance model with friction coefficient of 1.0

This directly leads to the conclusion, that applying an unrealistically high interface friction or even fully welded contact, may cause a severe overestimation of the compaction zone's extension. More attention should therefore be put to the determination of realistic interface properties.

4.3. Locally Undrained Conditions

In a next step the locally undrained approach is applied. Because of the large deformations due to the reduction of shear strength, the calculation aborts after a few cycles in the pure Lagrangian model, so an MMALE-approach is used on a smaller model at first, to keep the computational time at a reasonable level.

Fig. 6 shows the evolution of the effective mean pressure distribution over time. While it monotonically drops to a very small value (compared to the initial stress level) in an annular region with an inner radius of 0.5 m, it oscillates on a much higher stress level in the vicinity. This corresponds well to the observation stated in section 4.1. concerning the distribution of void ratio, since the increase/decrease of pore water pressure, just like the change of void ratio, depends on the volumetric strain, i.e. the liquefied zone under water saturated and undrained conditions is part of the compaction zone under dry conditions. A similar observation was stated already in [7] and attributed to the inability of the hypoplastic model to correctly model the liquefaction behavior under cyclic shearing with large amplitudes in [17]. The outer radius reaches a value of about 2 m rather fast and essentially doesn't grow any larger.

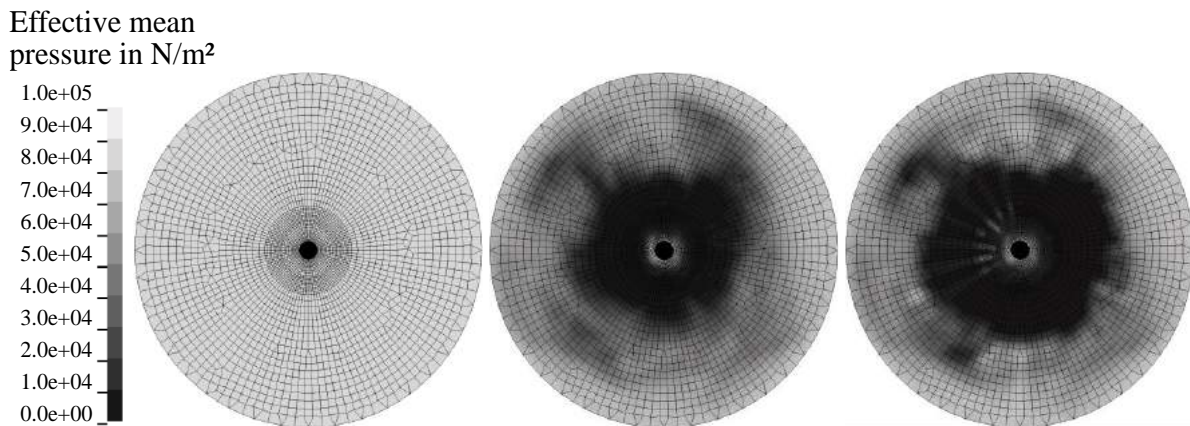


Figure 6. Distribution of effective mean pressure after 0 s, 0.1 s, 1 s

5. CONCLUSION

Since a physically realistic description of the fluidised material is not possible with the existing tools, a pragmatic definition for Zone A has to be found based on the capability of the used constitutive law. It was shown that the interface friction between soil and vibrator plays a most important role and unrealistic high values may cause an overestimation of the compactions zone extent. The application of an MMALE approach to the current model seems to be unnecessary in the case of dry sand. When applying locally undrained conditions, the deformations become excessive due to the vanishing of shear strength in the liquefied soil and calculations fail using the Lagrange model, while an MMALE model is able to produce plausible results.

Future work has to account for viscous material behavior of the liquefied and/or fluidised soil, as well as porewater flow.

It is also of greatest importance, that experimental data is obtained in order to validate the simulation results. In fact, in-situ and laboratory tests are being carried out by different institutions, but at present results are not available.

ACKNOWLEDGEMENT

Funded by the Deutsche Forschungsgemeinschaft (German Research Foundation) – Projectnumber 341427400.

REFERENCES

- [1] Kirsch, K., Kirsch, F., 2017. “*Ground Improvement by Deep Vibratory Methods*”, Second Edition, CRC Press/Taylor & Francis Group, USA, 234 pages.
- [2] Fellin, W., 2000. “*Rütteldruckverdichtung als plastodynamisches Problem*”, Ph.D. Thesis, University of Innsbruck, Institute of Geotechnics and Tunnelling, Austria, 194 pages.
- [3] Heibrock, G., Keßler, S., Triantafyllidis, T., 2006. “*On Modelling Vibro-Compaction of Dry Sands*”, In: *Numerical Modelling of Construction Processes in Geotechnical Engineering for Urban Environment*, Edited by T. Triantafyllidis, Taylor & Francis Group plc, London, 125-132
- [4] Arnold, M., Herle, I., 2009. “*Comparison of Vibrocompaction Methods by Numerical Simulations*”, *International Journal for Numerical and Analytical Methods in Geomechanics*, 33 (2009), 1823-1838
- [5] Henke, S., Hamann, T., Grabe, J., 2012. “*Numerische Untersuchungen zur Bodenverdichtung mittels Rütteldruckverfahren*”, 2. Symposium Baugrundverbesserung in der Geotechnik, 13.-14. September 2012, TU Wien
- [6] Heins, E., Grabe, J., 2015. “*Numerische Simulation einer Bodenverbesserungsmaßnahme infolge Rütteldruckverdichtung*”, In: *Numerische Methoden in der Geotechnik*, BAW Mitteilungen 98, 59-68
- [7] Osinov, V.A., Chrisopoulos, S., Triantafyllidis, T., 2013. “*Numerical Study of the Deformation of Saturated Soil in the Vicinity of a Vibrating Pile*”, *Acta Geotechnica* 8 (2013), 439–446
- [8] Osinov, V.A., 2013. “*Application of a High-Cycle Accumulation Model to the Analysis of Soil Liquefaction around a Vibrating Pile Toe*”, *Acta Geotechnica* 8 (2013), 675–684
- [9] Niemunis, A., Herle, I., 1997. “*Hypoplastic Model for Cohesionless Soils with Elastic Strain Range*”, *Mechanics of Cohesive-Frictional Materials*, Vol. 2 (1997), 279-299
- [10] Niemunis, A., Wichtmann, T., Triantafyllidis, T., 2005. “*A High-Cycle Accumulation Model for Sand*”, *Computers and Geotechnics*, Vol. 32, Issue 4 (June 2005), 245-263
- [11] von Wolfersdorff, P.-A., 1996. “*A Hypoplastic Relation for Granular Materials with a Predefined Limit State Surface*”, *Mechanics of Cohesive-Frictional Materials*, Vol. 1 (1996), 251-271
- [12] Mašin, D., 2017. “*Plaxis Implementation of Hypoplasticity Including Standalone Abaqus Umat Subroutines*”, 12th September 2017 from <https://web.natur.cuni.cz/uhigug/masin/plaxumat/>
- [13] Bakroon, M., Daryaei, R., Aubram, D., Rackwitz, F., 2018. “*Implementation and Validation of an Advanced Hypoplastic Model for Granular Material Behavior*”, 15th International LS-DYNA[®] Users Conference, 10th-12th June 2018 in Detroit, Michigan, USA
- [14] Aubram, D., 2019. “*Explicitly Coupled Consolidation Analysis Using Piecewise Constant Pressure*”, *Acta Geotechnica* (2019), <https://doi.org/10.1007/s11440-019-00792-z>
- [15] Lysmer, J., Kuhlemeyer, R., 1969. “*Finite Dynamic Model for Infinite Media*”, *Journal of the Engineering Mechanics Division*, 1969, Vol. 95, Issue 4, 859-878
- [16] Denies, N., Canou, J., Roux, J.-N., Holeyman, A., 2014. “*Vibrocompaction Properties of Dry Sand*”, *Canadian Geotechnical Journal*, 51 (2014), 409-419, dx.doi.org/10.1139/cgj-2012-0436
- [17] Wichtmann, T. 2016, “*Soil Behaviour under Cyclic Loading – Experimental Observations, Constitutive Description and Applications*”, Habilitation thesis, Veröffentlichungen des Institutes für Bodenmechanik und Felsmechanik am Karlsruher Institut für Technologie (KIT), Heft 181, 2016
- [18] Belytschko, T., Kam Liu, W., Moran, B., Elkhodary, K. I., 2014. “*Nonlinear Finite Elements for Continua and Structures*” Second Edition, John Wiley & Sons, UK, 804 pages.
- [19] Youd, T.L., 1972. “*Compaction of Sands By Repeated Shear Straining*”, *Journal of the Soil Mechanics and Foundations Division*, 1972, Vol. 98, Issue 7, Pg. 709-725

DEEP BOREHOLE DISPOSAL (3000 - 5000 M) OF SPENT NUCLEAR FUEL AND RADIOACTIVE WASTE - CONSIDERATIONS WITHIN A RESEARCH PROJECT

Tino Rosenzweig, *TU Bergakademie Freiberg, Institute of Mining and Special Civil Engineering, Tino.Rosenzweig@mabb.tu-freiberg.de*

Wilhelm Bollingerfehr, *BGE TECHNOLOGY GmbH*

Christin Dieterichs, *TU Bergakademie Freiberg, Institute of Drilling Engineering and Fluid Mining*

Maxi Herold, *BGE (federal company for radioactive waste disposal)*

Wolfram Kudla, *TU Bergakademie Freiberg, Institute of Mining and Special Civil Engineering*

Matthias Reich, *TU Bergakademie Freiberg, Institute of Drilling Engineering and Fluid Mining*

ABSTRACT

Currently, more than 30 countries throughout the world use nuclear energy to generate electricity. Almost all countries contemplate how to safely store and dispose of radioactive waste in the long term. In Germany, the disposal of heat-generating radioactive waste and spent fuel elements in a mine was favored from the very beginning. With regard to safety and licensing aspects, a mine solution was considered to be the most feasible of the disposal options. However, in several other countries, other disposal options have been considered. One of these options is the disposal of heat-generating radioactive waste and spent fuel elements in "deep boreholes". These are considered to be boreholes with a depth of 3,000 m to 5,000 m from ground level where the emplacement area is located in crystalline bedrock. Therefore a German research project on deep borehole disposal was initiated to provide knowledge necessary for the assessment of this disposal option especially in terms of technical feasibility and safety.

Keywords: Geotechnical Engineering, Conference, Young, ISSMGE, Turkey, Borehole, Disposal, Radioactive waste, Research project, Germany.

1. INTRODUCTION

Currently, more than 30 countries throughout the world use nuclear energy to generate electricity. Almost all countries contemplate how to safely store and dispose of radioactive waste in the long term. Repositories for low- and intermediate-level waste of various designs have been in operation throughout the world for decades. In 2015, Finland was the first country, however, that obtained a license to construct a repository for spent fuel elements. In Germany, the disposal of heat-generating radioactive waste and spent fuel elements in a mine was favored from the very beginning. With regard to safety and licensing aspects, a mine solution was considered to be the most feasible of the disposal options.

However, in several other countries, other disposal options have been considered. One of these considerations is the disposal of spent fuel elements in "deep boreholes". Within the scope of the research project CREATIEF (Investigations on the opportunities and risks of the disposal of heat-generating radioactive waste and spent fuel elements in deep boreholes, funded by the Federal Ministry for Economic Affairs and Energy of Germany), "deep boreholes" were

considered to be boreholes with a depth of 3,000 m to 5,000 m from ground level where the emplacement area is located in crystalline rock (crystalline bedrock - see figure 1).

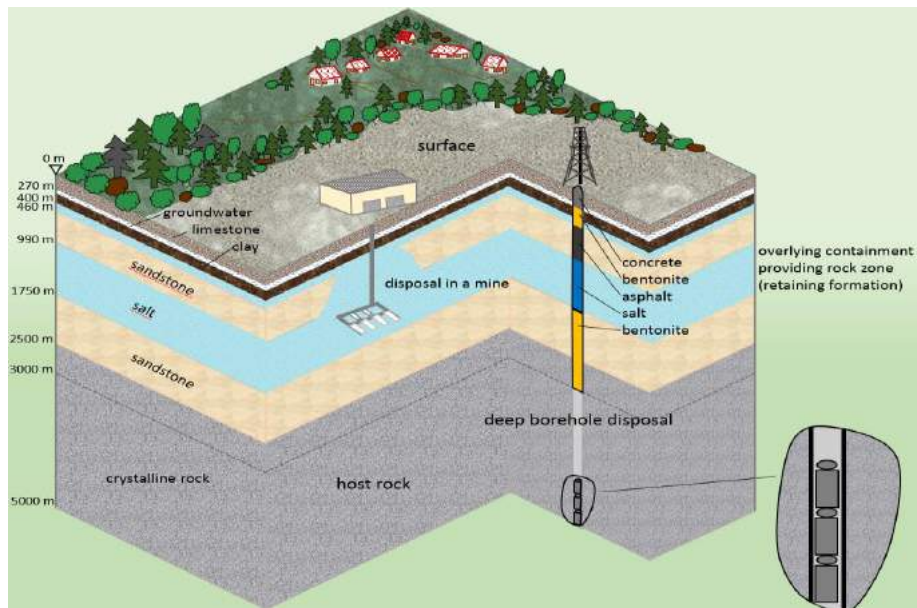


Figure 1. Schematic deep borehole disposal in crystalline rock

2. AIM OF THE RESEARCH PROJECT “CREATIEF”

The disposal of high-level heat-generating waste and / or spent fuel elements in boreholes with a depth of 3,000 m to 5,000 m is a disposal option that the "Endlagerkommission" [Commission on the Storage of High-Level Radioactive Waste] broached due to the discussion that has been underway in the USA in recent years [1]. Preliminary considerations and / or concepts regarding deep borehole disposal exist in Sweden and the USA and have been made in Germany by Gesellschaft fuer Anlagen- und Reaktorsicherheit (GRS). Within the scope of the research project CREATIEF, the option "disposal in deep boreholes" was studied further with the following three aims:

- 1) analysis and description of the assumptions made and boundary conditions used in previous research reports / studies (not further discussed in this paper),
- 2) description of the key aspects of deep borehole disposal and illustration of potential for improvement,
- 3) conceptual assessment of the opportunities and risks of deep borehole disposal.

3. ASSUMPTIONS ABOUT THE GEOLOGICAL CONDITIONS

Within the scope of this research project, two geologic profiles were derived, which served as references for geologic conditions that may be considered as candidates for final disposal in Germany (example in Figure 2). Disposal takes place at depths between 3,000 m and 5,000 m in presumably fractured crystalline rock. Just like for disposal in mines, it has to be demonstrated that radionuclides are not able to migrate from the disposal area at all or only in negligible amounts. Thus, when it comes to disposal in deep boreholes, the existence of a containment providing rock zone (CRZ) has to be demonstrated as well. As disposal takes place in probably fractured, crystalline rock, a CRZ can presumably only be accounted for in the form of a superimposing clay or rock salt layer (Type Bb according to the report of the Arbeitskreis

Auswahlverfahren Endlagerstandorte (AkEnd) [Working Group Selection Procedure for Repository Sites] [2]). The clay or salt layer must be so widespread (see figure 1) that even with circulation no or only negligible amounts of radionuclides can escape during the reference period of 1 million years (or, that they, in the case of Type Bb as defined by AkEnd, circulate the more flatly spread area of the CRZ). Especially in the area of the clay or salt layer, borehole seals have to be installed (see figure 1).

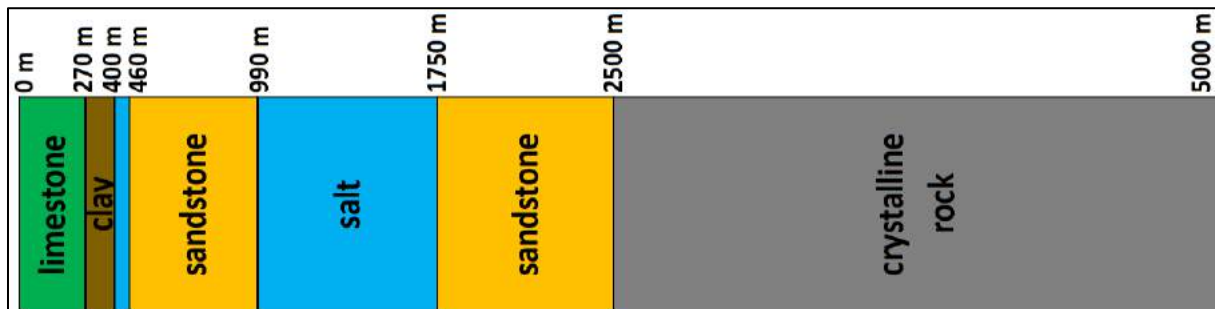


Figure 2. Generic model 1 for possible geologic conditions in Germany

4. STATE OF CONVENTIONAL DEEP DRILLING TECHNOLOGY

After the geologic profiles for Germany had been developed, the state of the art in the field of conventional deep drilling in the oil and gas industry for drillings to depths of 5,000 m with as wide a diameter as possible was investigated. In crystalline rock, boreholes can currently be drilled down to 5,000 m with diameters up to 17.5" (44.5 cm). For larger boreholes, larger roller bits would have to be developed. Alternatively, drilling techniques in hard rock (e.g., the electric impulse method) would have to be developed or further developed. It is assumed that a borehole diameter of about 35.4" (90 cm), as described as expedient in the GRS report [3], would reduce the number of boreholes to an acceptable amount (presumably 31). However, such large borehole diameters are currently not technically feasible. Adapting deep drilling equipment for drilling in hard rock and for diameters considerably larger than 17.5" (44.5 cm) as necessary for disposal boreholes with depths of 5,000 m would require considerable developmental and testing work. The particular challenges are to provide the large-sized bit with the necessary contact pressure (drill rod design), to continuously clean the cuttings from the borehole (capacity of the pumps), to manage the heavy drill string (development and engineering of a special deep drilling rig), and to develop a well design that can cope with a minimal drilling diameter in the first drilling section (lean casing drilling or mono bore method).

As far as the state of the art in deep drilling technology is concerned, it can be said that almost all previous developments aimed at developing and exploiting oil and gas deposits. Oil and gas can usually be found in the pores of sedimentary rock. The boreholes are optimized in such a way that - taking into account the high safety requirements - the costs are kept low, while at the same time, maximum extraction of the raw materials can take place without damaging the deposit. Typical final diameters in oil and gas drilling are thus between 4" and 8 1/2", i.e., approx. 10.2 cm to 21.6 cm.

For disposal in deep boreholes, all drilling work is finished before radioactive material is delivered for emplacement. Thus, the borehole can be drilled and inspected without radiation protection restrictions. Not until the quality of the borehole has been confirmed is the borehole approved for disposal. The emplacement building will then be erected above the drilling base. After this the radioactive waste will be delivered.

5. DISPOSAL CONTAINER

Based on the waste amounts to be disposed of which consists of:

- spent fuel of nuclear power plants,
- spent fuel of prototype and research reactors,
- vitrified waste from reprocessing of spent fuel of nuclear power plants,
- structural components of spent fuel of nuclear power plants

(taken from the National Waste Management Plan 2022 [4]), the disposal containers were considered. Regarding disposal at depths between 3,000 m and 5,000 m, the particular requirements for disposal containers are related to:

- tightness,
- robustness against all possible loads,
- temperature resistance,
- resistance to the drilling fluid in the borehole,
- requirements regarding the dimensions of the container due to the borehole diameter.

In the disposal area, temperatures between approx. 100 °C and 160 °C are to be expected. On account of the system, the temperature limit of 100 °C at the container surface as currently stipulated in the Standortauswahlgesetz (Site Selection Act) [5] cannot be met in deep borehole disposal. The pressure on the container as considered in the research project CREATIEF is a result of the load of the stacked containers (see figure 1) and the hydrostatic pressure of the liquid column (during operation, the borehole must be filled with fluid for stability reasons). The rock pressure is not taken into account in this concept, as it was assumed that the borehole casing together with the fluid-filled borehole will withstand the rock pressure until the borehole seal is fully functional. Based on the requirements listed above, the boundary conditions for a container were derived and used to roughly calculate the dimensions of the container. According to the calculations, the containers for a 17.5" borehole will have an outer diameter of 26.5 cm and an inner diameter of 17.5 cm. For a 35.4" borehole, the outer diameters will be 63.5 cm, the inner diameters 43.5 cm (see Figure 3).

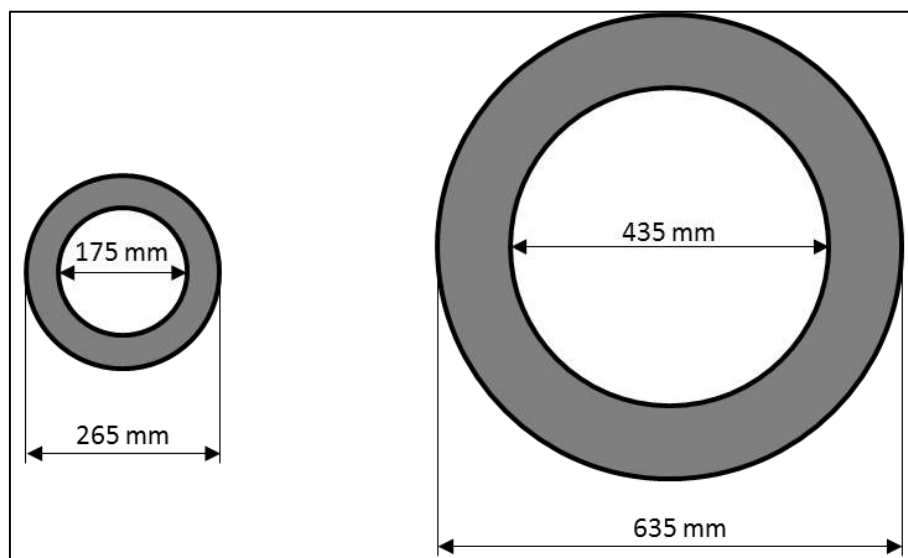


Figure 3. Inner and outer diameters of the container for the 17.5" borehole (left) and 35.4" borehole (right)

6. NUMBER OF BOREHOLES VERSUS BOREHOLE DIAMETER

Two concepts were considered for the disposal in deep boreholes. They are described below:

- Concept 1: Borehole diameter 17.5" (44.5 cm) at a depth of 5,000 m:

Taking into account a maximum borehole diameter of 17.5", the container may only have an outer diameter of 26.5 cm (inner diameter 17.5 cm) due to the necessary borehole casing and the required annular space (see Figures 3 and 4). The length of the container was assumed to be 5.6 m (based on the length of the fuel rods of spent fuel elements from power reactors). If the inner diameter is used to 70 % to 80 % to store fuel rods, the number of containers is expected to be between 23,000 and 27,000. If one borehole is filled with 180 containers, approx. 130 to 150 boreholes would be required. The containers described above can be stacked to a height of approx. 1,000 m. A larger stack height (e.g. 2,000 m) was not possible in the design, as this would have led to an excessive, meaningless wall thickness in relation to the inner diameter of the container. Here, there is potential for further optimization.

The advantage of concept 1 is that a further development of the drilling technology is not necessary and that the state of the art in deep drilling technology can be used. However, concept 1 has the disadvantage that a relatively large number of boreholes is required. Furthermore, concept 1 cannot accommodate the radioactive waste from reprocessing, which is already vitrified, as this would require that the containers have an inner diameter of at least 43 cm. Thus, only the fuel rods of spent fuel elements from power reactors could be emplaced and an additional repository for the waste from reprocessing would be required.

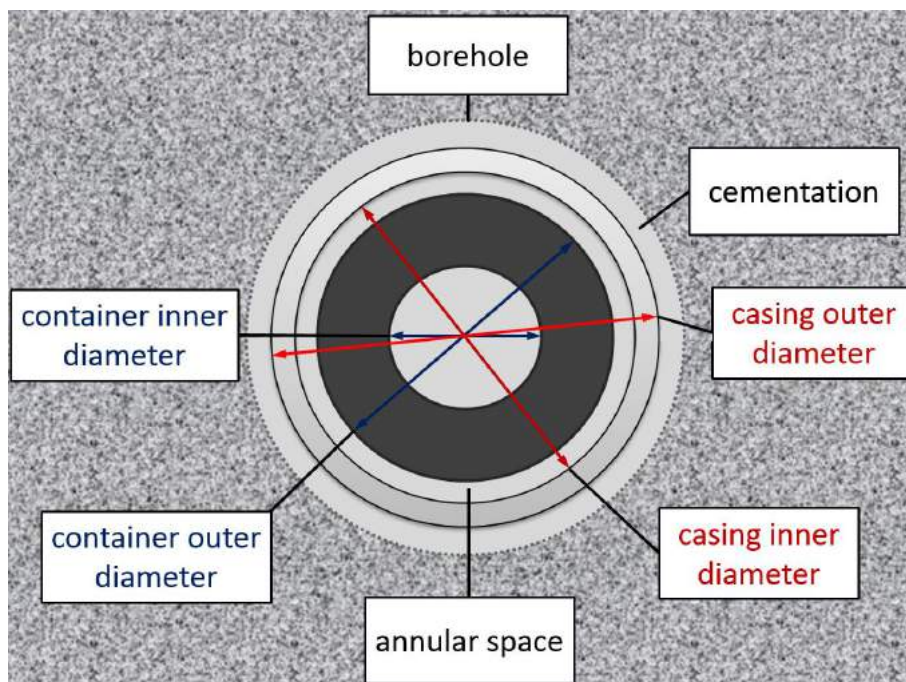


Figure 4. Schematic representation of interdependent diameters in the emplacement borehole

- Concept 2: Borehole diameter 35.4" (90 cm) at a depth of 5,000 m [3]:

For concept 2, a borehole diameter of 35.4" at a depth of 5,000 m was assumed. Taking into account the thickness of the borehole casing and the necessary annular space, the container can have an outer diameter of 63.5 cm (inner diameter: 43.5 cm) and can be stacked to a height of

2,000 m. The length of the container is 5.6 m. Based on these assumptions, a total of 11,000 containers would be required. If 363 containers were emplaced per borehole, 31 boreholes would be required.

The advantage of concept 2 is that with 31 holes, the number of boreholes is considerably lower than in concept 1. The disadvantage is that without considerable further developments in the deep drilling equipment, this concept cannot be implemented.

7. CONTAINMENT PROVIDING ROCK ZONE

In the case of disposal in deep boreholes, the existence of a CRZ has to be demonstrated just like in the case of disposal in a mine. As emplacement takes place in crystalline rock, which is very likely fractured, an overlying sealing layer of clay or salt is necessary (see figures 1 and 2). This CRZ corresponds to Type Bb according to AkEnd [2]. How the existence of a Type Bb CRZ is to be demonstrated (mathematically / through exploration), is yet unclear. This applies to both disposal in a mine and disposal in deep boreholes.

8. EMPLACEMENT AND RETRIEVAL CONCEPT

Furthermore, an emplacement and retrieval concept was developed. After the borehole has been completed, the drilling rig can be removed. Then, an emplacement plant is assembled on the surface. The emplacement plant has to include an emplacement device with shielding feature (lock) above the borehole. The disposal container is transported to the borehole inside a transfer case. There, it is placed above the emplacement borehole in vertical position (see figure 5). Throughout the entire process, the shielding device protects the personnel against radiation. The disposal container can then be emplaced in the borehole by means of rods or ropes made of steel or fibers (see figure 5).

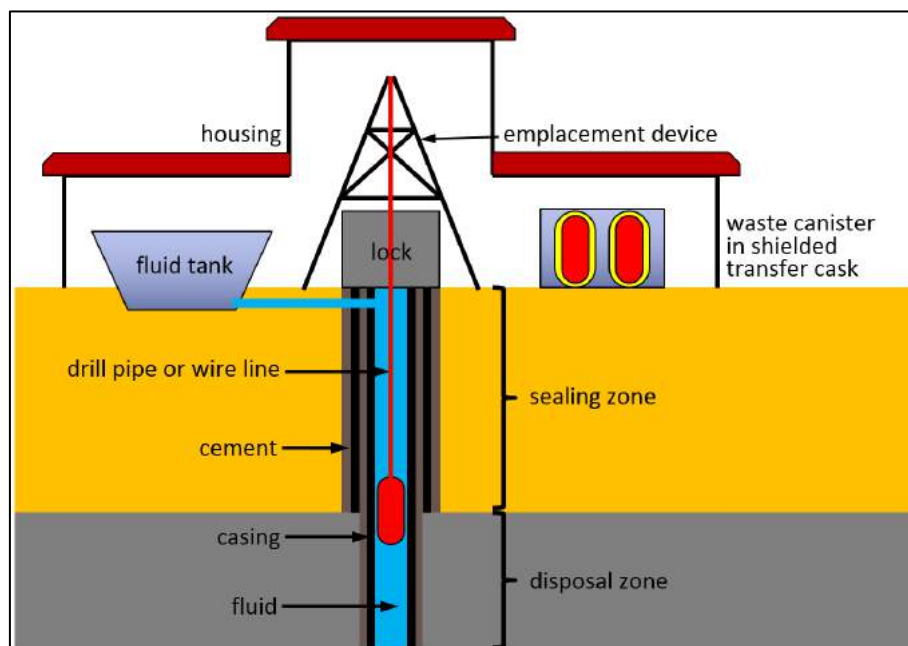


Figure 5. Schematic of emplacement of the disposal container

The processes related to retrieval are similar. While retrieval during the operating period of a borehole is considered to be possible in this concept, recovery of the disposal containers does not seem possible according to current information. Waste recovery means the retrieval of the waste after sealing and closure of the borehole. The period of time in which recovery is to be possible under current legal requirements is 500 years. Thus, it should be legally reassessed if the recovery requirement for the disposal in deep boreholes can be given up in the German rules and regulations.

9. SEALING AND CLOSURE OF THE BOREHOLES

Concerning the backfilling and closure of the emplacement boreholes, various possible materials have been listed in the research paper (see [6]). So far, concept studies (for example [7] und [8]) have mentioned bentonite, bitumen / asphalt, cement as well as salt suspensions and eutectic molten salt, and barite as backfilling or sealing materials. First considerations about how to feed the material into the boreholes or voids have been presented. However, all these technologies still need to be developed and tested with regard to the special conditions in repository boreholes. There are basically two options for installing the backfill materials:

- 1) The backfill materials are installed in the borehole fluid.
- 2) The borehole is pumped dry and the backfill materials are installed dry. Whether this possibility exists depends on the dimensioning of the casing.

10. CONCLUSION WITH OPPORTUNITIES AND RISKS

Subsequently, the opportunities and risks of disposal in deep boreholes were assessed. Some of them are described below:

- Opportunities:

The drilling fluid in the borehole has a shielding effect against radionuclides and a decelerating effect when the containers are emplaced, both of which are presumably positive for disposal in deep boreholes. Thus, it is allocated to the 'Chances' category. Compared with a repository mine, the total volume of voids to be excavated is much lower. Furthermore, sealing of the individual boreholes can start directly after the containers have been emplaced. In this case, it may well be possible to insert the borehole seal into a dry borehole. Drilling a borehole with a final diameter of 17.5" is feasible with the state of the art of deep drilling technology. In addition, the development of a technology for the sinking of boreholes with a larger diameter of up to 90 cm at depths of up to 5,000 m in crystalline rock is not excluded. However, this development would have to be funded by public resources, as there is no direct need for such a technology within the raw materials industry.

- Risks:

However, the assessment of the opportunities and risks shows significant risks for the disposal in deep boreholes. This includes the fact that, according to the current state of the art, not all heat-generating waste can be emplaced in a 17.5" (44.5 cm) borehole. The disposal of canisters (diameter: 43 cm) with waste from reprocessing (CSD-C, CSD-B and CSD-V) is not possible in deep boreholes with a final diameter of 17.5". Accordingly, a repository (e.g. in a mine) must also be built. The permanent presence of the drilling fluid, which must be selected specifically for the casing used and the repository containers, necessitates the choice of suitable corrosive-resistant container materials and the permanent tightness of all containers in a borehole until the borehole is sealed. Other risk topics like retrieval during the operating period or disaster

management require considerable research and development effort, the result of which is open. In addition, for the safety assessment of deep borehole disposal, temperature or criticality calculations are considered to be urgently necessary. As yet, no studies have been published.

From the consideration of the opportunities and risks, no statement can currently be made as to whether a final disposal in deep boreholes is a sensible alternative to final disposal in a mine and thus remains worth further investigating. There are too many open issues that would require very extensive and time-consuming research and development work. In addition, there are two points, the solution of which represents a very considerable challenge in each case and whose solution is considered rather unlikely by the project team even with generous financial support in the coming years. These two points concern:

- 1) Demonstration of containment providing rock zone Type Bb according to the AkEnd report (extensive overlying salt layer / clay layer):
- 2) Recovery of the high-level radioactive waste from deep boreholes during a period of up to 500 years after repository closure:

ACKNOWLEDGEMENT

The authors acknowledge the financial support by the Federal Ministry for Economic Affairs and Energy of Germany in the project CREATIEF (project numbers 02E11526A and 02E11526B).

Supported by:



on the basis of a decision
by the German Bundestag

REFERENCES

- [1] Kommission Lagerung hoch radioaktiver Abfallstoffe, 2016. “Abschlussbericht - Verantwortung fuer die Zukunft - Ein faires und transparentes Verfahren fuer die Auswahl eines nationalen Endlagerstandortes”, report, 683 pages, Berlin, Germany.
- [2] Arbeitskreis Auswahlverfahren Endlagerstandorte, 2002. “Auswahlverfahren fuer Endlagerstandorte - Empfehlungen des AkEnd - Arbeitskreis Auswahlverfahren Endlagerstandorte”, report, 272 pages, Cologne, Germany.
- [3] Bracke, G., Charlier, F., Geckeis, H., Harms, U., Heidbach, O., Kienzler, B., Liebscher, A., Mueller, B., Prevedel, B., Roeckel, T., Schilling, F., Sperber, A., 2016. “Tiefe Bohrloecher”, Gesellschaft fuer Anlagen und Reaktorsicherheit (GRS) gGmbH, report, 338 pages, Cologne, Germany.
- [4] Bundesministerium fuer Umwelt, Naturschutz, Bau und Reaktorsicherheit, 2015 “Programm fuer eine verantwortungsvolle und sichere Entsorgung bestrahlter Brennelemente und radioaktiver Abfaelle (Nationales Entsorgungsprogramm)”, report, 26 pages, Berlin, Germany.
- [5] German Law, 2017. “Gesetz zur Suche und Auswahl eines Standortes fuer ein Endlager fuer hochradioaktive Abfaelle (Standortauswahlgesetz - StandAG)”, Site Selection Act, Germany.
- [6] Bollingerfehr, W., Dieterichs, C., Herold, M., Kudla, W., Reich, M., Rosenzweig, T., 2018. “Untersuchungen zu Chancen und Risiken der Endlagerung waermeentwickelnder radioaktiver Abfaelle und ausgedienter Brennelemente in Tiefen Bohrloechern „CREATIEF“ - Abschlussbericht”, report, 182 pages, Freiberg, Germany.
- [7] Brady, P., Arnold, B., Freeze, G., Swift, P., Bauer, S., Kanney, J., Rechar, R., Stein, J., 2009. “Deep Borehole Disposal of High-Level Radioactive Waste”, Sandia National Laboratories, report, 75 pages, Albuquerque and Livermore, United States of America.
- [8] Brenner, R., Jedelhauser, P., 1989. “Technischer Bericht 89-26 - Bohrlochversiegelung: Konzept und Machbarkeitsnachweis”, Nationale Genossenschaft fuer die Lagerung radioaktiver Abfaelle, report, 149 pages, Baden, Switzerland.

A WINKLER TYPE APPROACH FOR THE DYNAMIC RESPONSE OF FLEXIBLE WALLS RETAINING INHOMOGENEOUS SOIL

Koutsantonakis A. Christos*, *Postgraduate Student, University of Patras, chkouts@yahoo.com*

Kanellopoulos G. Konstantinos, *Research Assistant, N.T.U.A., k.g.kanellopoulos@gmail.com*

ABSTRACT

An approximate solution is developed for the determination of the harmonic response of a flexible wall retaining a visco-elastic inhomogeneous soil medium, rested on a rigid base. The soil inhomogeneity of the backfill is considered in terms of shear wave velocity as a non-uniform function with depth. The analysis is carried out in the frequency domain, using a Winkler model, in which the backfill is replaced by linear elastic uncoupled translational springs of constant stiffness intensity, following the same variation with the shear modulus. The assumption of perfect-contact conditions at the wall-backfill interface is adopted to evaluate the response of the wall considering the kinematic Soil-Wall Interaction. Parametric analyses, using the Finite Element Method, which are conducted to validate the analytical solution, demonstrate the beneficial effects of wall flexibility and soil inhomogeneity, which combined can produce an extreme reduction of the imposed pressures on the wall, at least significantly lower than the usual proposal of Design Codes.

Keywords: Flexible Wall, Inhomogeneous Soil, Dynamic Soil Structure Interaction.

1. INTRODUCTION

Retaining structures are used widely at infrastructures and are necessary when the shear strength of the ground is so low that it cannot resist the design loads. Also, they are commonly used, when the soil deformations are required to be very small at the ground surface. Thus, retaining walls are structures of high importance in the field of Earthquake Engineering.

Despite these qualifications, the dynamic response of retaining structures is still at early stage and many misunderstandings remain, having a negative impact on the design codes. In order to understand the natural mechanisms that are developed, many features must be studied, such as the soil inhomogeneity, kinematic Soil-Structure Interaction (S.S.I.), geometric and soil nonlinearity, wall and foundation flexibility and frequency effects.

Recently, many researchers got on argue about the prioritization of the described impacts on the dynamic response of retaining systems, invoking experimental or numerical results and usually developing analytical solutions in order to describe the physics of these mechanisms. This paper intends to illustrate the available contributions at a brief state-of-the-art section and consequently to develop a simple, approximate closed-form solution which determines the response of a flexible wall retaining inhomogeneous viscoelastic soil.

2. STATE OF THE ART

The first effort for the development of a closed-form solution for the dynamic response of retaining walls, was made simultaneously and independently by [1] and [2], who considered the simplest model of a “bathtub” configuration [3]. These seminal solutions referred to the simple model of a pair of rigid fixed-base walls, founded on rigid bedrock. These mathematically rigorous methods provide quite complex expressions, while they result in extremely high values of induced thrusts, due to the imposition of such “intense” boundary conditions. As a consequence they quickly discarded by engineers.

On the other hand, the earlier proposal of [4] and [5], so-called as Mononobe-Okabe (M-O) method, had already begun to be used for the design of retaining structures. This type of limit-equilibrium method provides the pseudo-static (for zero frequency) total shear force, adopting the classical Coulomb-type method of a rigid soil wedge. The M-O solution, assumes simplifying approximations which are not justified adequately, such as the imposition of a known “static” inertial force and the required type of shear failure on a linear interface.

Later, [6],[7] and [8] proposed rigorous solutions for the dynamic response of rigid walls retaining homogeneous elastic soil, inhomogeneous embankment, and the influence of wavelength to wall height ratio (λ/H), respectively. These interpretations demonstrate different features of the system’s physics, which are confirmed by numerical and experimental results [8],[9],[10].

Also, many researchers studied the dynamic or quasi-static response of retaining walls using shaking table or centrifuge experimental data [11],[12],[13],[14]. Complementary, other researchers conducted various numerical solutions [15],[16], mainly using the Finite Element Method (F.E.M.), in order to validate both experimental and analytical investigations.

Recently, some researchers [17],[18],[19] concluded that soil nonlinearity holds the role of a counterpoise on the field of Soil-Structure Interaction (SSI). For high nonlinearity of the soil, the SSI effects are mitigated. This aspect is at a very early stage in order to be adopted entirely. Undoubtedly, the elasticity theory will provide an upper-bound for the response of the system, more rigorous than the conservative limit-equilibrium (pseudo-static) approach, such as M-O method which is adopted by Design Codes.

3. PROBLEM DEFINITION

The system under consideration is shown in Figure 1, where a viscoelastic inhomogeneous soil layer of constant thickness H , density ρ , variable shear modulus $G(z)$, Poisson ratio ν and damping coefficient δ , is retained by a cantilever wall of height H , thickness t_w and stiffness EI . Note that the inertial forces of the structure are ignored, as they can be considered in a separate analysis [20]. Also, the static response could be determined by a separated analysis, as the superposition principle is held. The solution is developed in the frequency domain assuming plane-strain conditions. A harmonic horizontal acceleration of constant amplitude X_g and frequency ω is imposed on the rigid bedrock. As a result vertical S-waves propagate through the soil. A Cartesian y - z coordinate system is defined, as shown in Figure 1, where u_y and u_z are the horizontal and vertical (relative to the rigid base) displacements, respectively. According to the recent study of [3], a distribution of shear modulus $G(z)=G_H f(z)$ is assumed, where G_H is the shear modulus at the base ($z=H$) and $f(z)$ is a known dimensionless function. Applying the theory of Elasticity and adopting a modified Vlasov-Leontiev’ model by [21], combining the validation of simplifying assumptions [22] of zero dynamic vertical normal stress and zero

variation of vertical displacement with respect to the horizontal direction ($\sigma_z=0, \partial u_z/\partial y=0$), the free-field displacements of the soil deposit are given by [3]:

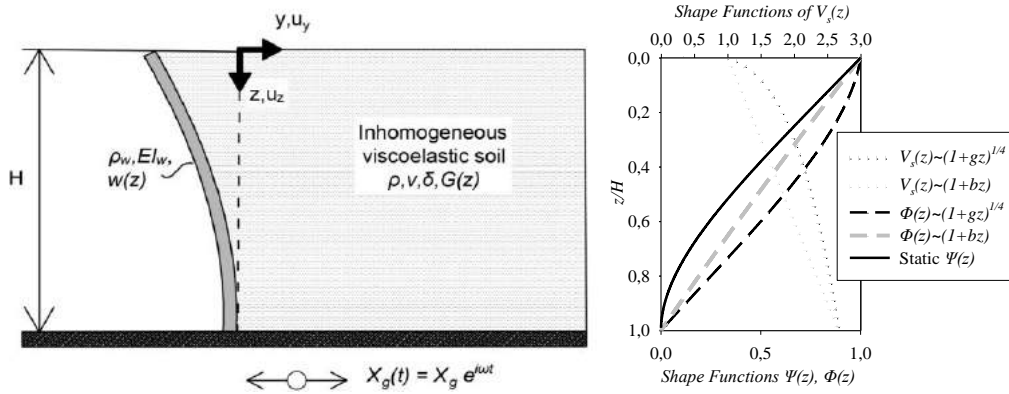


Figure 1. (left) Flexible wall retaining vertically inhomogeneous viscoelastic soil and variation of shear modulus with depth and (right) soil, wall and $V_s(z)$ shape functions

$$u_{ff}(z) = -\frac{\mathcal{L}}{b_{oc}^2 (a_{oc}^2 - a_o^2)} \frac{\rho H^2 X_g}{G_H} \Phi(z) = U_{ff} \Phi(z) \quad (1)$$

where $m = (b_{oc}^2 (a_{oc}^2 - a_o^2))^{1/2} / (H \psi_e)$, $a_o = \omega H / V_H$ a dimensionless excitation frequency, $V_H = (G_H / \rho)^{1/2}$ the corresponding shear wave velocity at the base, $\psi_e^2 = (2 - \nu) / (1 - \nu)$, $a_{oc}^2 = H^2 \int_0^H f(z) (\Phi'(z))^2 dz / \int_0^H \Phi^2(z) dz$ an approximate dimensionless cut-off frequency,

$\mathcal{L} = \int_0^H \Phi(z) dz / \int_0^H f(z) \Phi^2(z) dz$ a participation coefficient, $b_{oc}^2 = \int_0^H \Phi^2(z) dz / \int_0^H f(z) \Phi^2(z) dz$ is a multiplier relative to the heterogeneity of soil material and $\Phi(z)$ a known dimensionless shape function of the retained soil medium [3].

According to the Winkler model, the seismic load imposed on the retaining structure, is expressed as the difference between the wall deformations and the free-field displacements, multiplied by a stiffness factor:

$$\sigma_y(0, z) = k_{yH}(z) (u_{ff}(z) - w(z)) \quad (2)$$

The corresponding stiffness factor for the retained soil is produced by [3] and corrected by [16]:

$$k_y(z) = \frac{2}{\sqrt{(1-\nu)(2-\nu)}} \frac{G_H}{H} \sqrt{b_{oc}^2 (a_{oc}^2 - a_o^2)} f(z) = K_{yH} f(z) \quad (3)$$

This expression is similar to the shear-beam model used by [22] in order to determine the dynamic response of rigid walls retaining homogeneous elastic soil.

Assuming a classical Euler-Bernoulli type of beam for the retaining structure, the equation of equilibrium for an arbitrary element is given as:

$$EIw^{(4)}(z) + K_{yH} f(z) w(z) = K_{yH} f(z) U_{ff} \Phi(z) \quad (4)$$

where $I = t_w^3 / 12$. Equation 4 is an ordinary differential non-homogeneous equation of 4th order with variable factor and is very difficult to be solved rigorously for arbitrary types of inhomogeneity.

4. PROPOSED SOLUTION

2.1. Wall's Deformation

It is very difficult to provide a rigorous closed-form analytical solution for the differential Equation 4 of motion of the wall. Thus, an approximate analytical approach is provided, under the assumption for a known shape function of the retaining structure:

$$w(z) = W_o \Psi(z) \quad (5)$$

where W_o is the amplitude of wall displacements and $\Psi(z)$ a known dimensionless shape function, which in terms of modal analysis has been established in Structural Dynamics [23]. Substituting Equation 5 to Equation 4 of motion and integrating over the wall's height H , leads to:

$$W_o = \frac{K_{yH} U_{ff} \int_0^H f(z) \Phi(z) dz}{EI \int_0^H \Psi^{(4)}(z) dz + K_{yH} \int_0^H f(z) \Psi(z) dz} \quad (6)$$

Equation 6 provides the amplitude of wall displacements in order to satisfy the total equilibrium of the structure and not certifying the equilibrium at any depth. In other words, the wall displacement W_o , is expressed as the ratio of a generalized force and a generalized stiffness (including wall and soil stiffness) [16].

2.2. Soil and Wall Shape Functions

To determine the soil shape function $\Phi(z)$, the proposal of [24] is adopted. The following two profiles of variation for the S-wave velocity are considered [24]:

$$V_s(z) = V_{s0} (1 + gz)^{1/4} \quad (7a)$$

$$V_s(z) = V_{s0} (1 + bz) \quad (7b)$$

where g, b are known parameters with units of Length^{-1} . Note that for the limit values $g, b \rightarrow 0$, the case of a homogeneous soil profile is obtained, while Equation 7b represents a linear V_s profile against depth. The corresponding eigenmodes for the soil are given as [24]:

$$\Phi_n(z) = (1 + gz)^{1/4} \left(Y_{1/3} \left[S_n (1 + gH)^{3/4} \right] J_{1/3} \left[S_n (1 + gz)^{3/4} \right] - J_{1/3} \left[S_n (1 + gH)^{3/4} \right] Y_{1/3} \left[S_n (1 + gz)^{3/4} \right] \right) \quad (8a)$$

$$\Phi_n(z) = (1 + bz)^{-1/2} \sin \left[S_n \text{Ln} \left[\frac{1 + bH}{1 + bz} \right] \right] \quad (8b)$$

where $J_{1/3}[]$ and $Y_{1/3}[]$ are Bessel functions of the first and second kind of order 1/3 and $\text{Ln}[]$ is the natural logarithm function. These shape functions Φ are produced solving the equation of motion for a soil column and imposing the essential boundary conditions of zero shear stress at the free surface ($z=0$) and zero relative displacement at the base ($z=H$). The eigenperiods of the soil deposit (for $n=1,2,3,\dots$) are computed as:

$$T_n = \frac{8\pi}{3gV_{s0}S_n} \quad (9a)$$

$$T_n = \frac{4}{V_{s0}} \frac{\pi}{b(4S_n^2 + 1)} \quad (9b)$$

where S_n are the corresponding eigenvalues, determined by the so-called characteristic equation:

$$\frac{J_{1/3} [S_n(1+gH)^{3/4}]}{Y_{1/3} [S_n(1+gH)^{3/4}]} = \frac{2J_{1/3} [S_n] - 3J_{4/3} [S_n]}{2Y_{1/3} [S_n] - 3Y_{4/3} [S_n]} \quad (10a)$$

$$S_n \text{Ln}[1+bH] + \text{Arctan}[2S_n] = n\pi \quad (10b)$$

The corresponding dimensionless functions $f(z)$ for the soil inhomogeneity are $f(z)=[(1+gz)/(1+gH)]^{1/2}$ and $f(z)=[(1+bz)/(1+bH)]$, in order to provide the result of Equations 7, respectively. It is noticed that, according to [25] the shear modulus can be replaced by the complex $G^*(z)=G(z)(1+2i\delta)$ in order to consider a viscous type of damping.

For the wall shape function $\Psi(z)$, the “static” approach is examined. Applying a “static” inertial load, solving the equation of motion for the case of an Euler–Bernoulli beam and imposing the boundary conditions for a fixed–base cantilever wall, the corresponding shape function is given as [16]:

$$\Psi(z) = 1 - \frac{4}{3} \frac{z}{H} + \frac{z^4}{3H^4} \quad (11)$$

5. COMPARISON WITH 2D FEM RESULTS

For the verification of the proposed analytical solution, a numerical 2D Finite Element analysis was conducted using the Abaqus code. A finite grid was defined and a harmonic acceleration of constant amplitude was imposed on the rigid bedrock. The backfill had $H=5\text{m}$ height and $L=50\text{m}$ length, while a soil column representing the free–field was attached using viscous dampers at the right boundary of the soil stratum, as shown in Figure 2. This definition diminishes the reflection of waves at the boundaries of the soil medium.

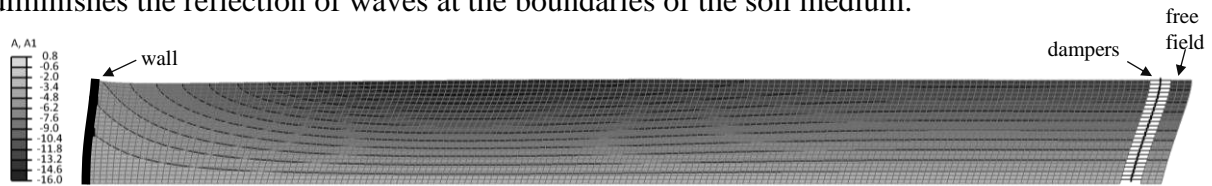


Figure 2. Considered model with Abaqus 2D – plot of accelerations (*S*–wave propagation)

In order to define the soil inhomogeneity, the soil deposit of $H=5\text{m}$ height, was divided into 25 equivalent homogeneous soil layers such that the considered profiles of shear modulus were identified. A Rayleigh–type of damping was applied, for $\delta=10\%$ at the frequencies of the imposed excitation. Also, the following parameters were selected: $V_s(0) = 80\text{m/s}$ is the S-wave velocity at the free surface, heterogeneity factors $b=0.33\text{m}^{-1}$ and $g=10\text{m}^{-1}$, mass $\gamma=2 \text{ ton/m}^3$, Poisson ration $\nu=0.33$ and acceleration of excitation $X_g=2.5 \text{ m/s}$, while various values of normalized wall flexibility $d_w=G_H H^3/EI$ are examined. Figure 3 depicts the distribution of normalized dynamic thrust against depth. The integration of the soil pressures profile provides the base shear force Q_b and the base moment M_b , while the ratio of M_b/Q_b leads to the height of elevation of the total shear force (h). Note that ω_I are given by Equations 9 for the two soil profiles, respectively.

As shown in Figure 3, a great agreement between the proposed solution and the numerical 2D FEM results is observed. A small deviation is observed at the base of the wall, due to the simplified assumptions of $\sigma_z=0$ and $\partial u_z/\partial y=0$. The linear soil profile, primarily, and the wall flexibility, secondarily, lead to more triangular distribution of soil pressures. Also, for high frequencies ($\omega/\omega_I \geq 1$) a more compliant wall leads to lower values of soil pressures at the top and higher values at the base, but this range is out of interest, as the predominant frequencies of earthquakes is much lower than the case of resonance. Note that the M–O method adopts a

linear profile of soil pressures against depth, with zero thrust at the top of the wall and commonly a normalized pressure about 2 at the base.

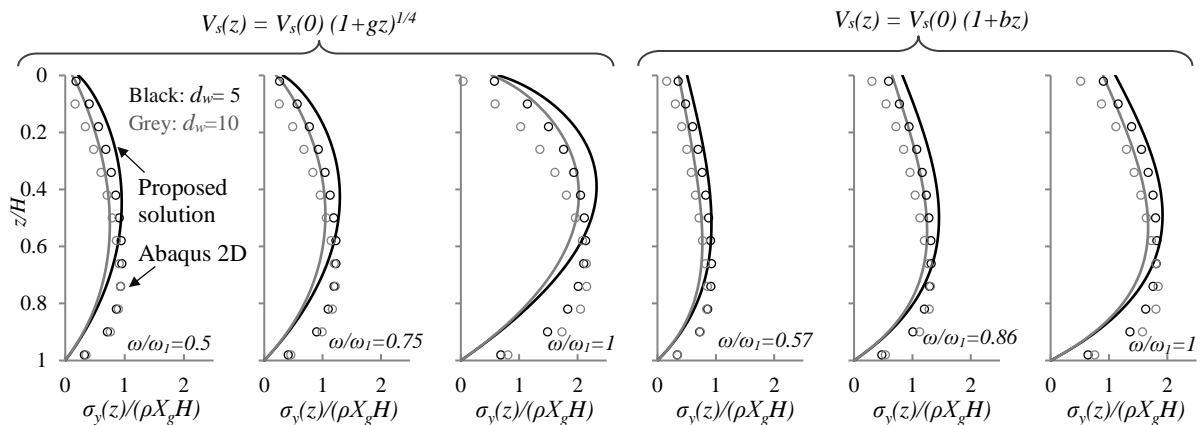


Figure 3. Distribution of normalized soil pressures against normalized depth.

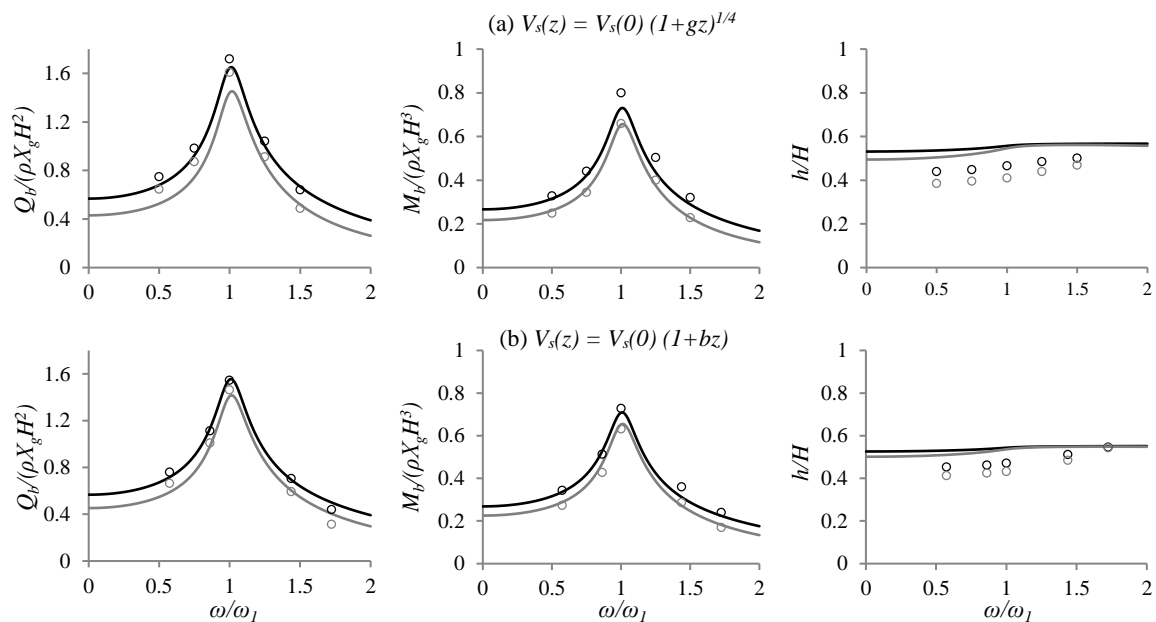


Figure 4. Normalized base shear force, moment and height of elevation against frequency.

Also, as observed in Figure 4, the differences for Q_b and M_b between the proposed analytical solution and the FEM results is about 10% for the case of resonance and less than 5% for other frequencies. The proposed solution provides a pseudo-static ($\omega=0$) normalized base shear force about 0.6, for $d_w=5$, and about 0.45, for $d_w=10$, for the inhomogeneity of Equation 7a, and 0.58 and 0.5 for Equation 7b, respectively, while the M–O commonly leads to values about 1 independently of the wall flexibility, soil heterogeneity, excitation frequency and material damping. Regarding the height of elevation of the total shear force h , the present solution provides almost 20% higher values. Consider that increasing the wall flexibility and the soil inhomogeneity, the higher modes become more significant than the case of a robust system. Also, Figure 3 and 4 demonstrate that the existence of the wall as a boundary, does not affect the fundamental frequency of the system, as it coincides with the free–field natural frequency ($\omega=\omega_1$). Note, finally, that a “dynamic” $\Psi(z)$ was also examined (the results are not plotted, due to lack of space), adopting the so–called fundamental eigenvector of a cantilever fixed–base wall [23], which provides almost constantly 10% lower values of Q_b and M_b than the “static” $\Psi(z)$ and the numerical results.

6. CONCLUSIONS

In the present study, an approximate closed-form analytical solution was presented for the determination of the seismic response of a flexible cantilever wall retaining an inhomogeneous viscoelastic soil. A numerical analysis performed, from which a great agreement between the analytical and the F.E.M. results was observed. The main conclusions of the present study are summarized in the following:

- (1) Small increments of wall flexibility can reduce up to 40% the base shear force and 30% the base moment for low excitation frequencies. As a consequence the height of elevation of the total shear force slightly increases.
- (2) The profile of soil inhomogeneity strongly affects the distribution of soil pressures with depth, leading to sharper shapes for the case of a linear soil profile. Also, the total base shear force and moment are reduced for a more heterogeneous soil material.
- (3) Frequency effects are also established to be important for the response of the system. For frequencies equal to the fundamental one of the soil stratum, leads to increased thrusts up to 60%.

As a closure notation, the elastic wave solutions, like the present, which consider S.S.I., frequency and soil inhomogeneity effects, provide considerably lower seismic loads on the wall. That fact nominates as crucially important the retirement of the conservative M–O method, which disregards all the above features and, yet, is predominant at the majority of Design Codes.

REFERENCES

- [1] Scott R.F., 1973, “*Earthquake-Induced Pressures on Retaining Walls*”, 5th World Conference on Earthquake Engineering, Vol.2 pp. 1611-1631. Rome, Italy.
- [2] Wood. J.H., 1973, “*Earthquake Induced Soil Pressures on Structures*”, Ph.D. Thesis, California Institute of Technology, CA, pp. 327.
- [3] Brandenberg S.J., Mylonakis G., Stewart J.P., 2017, “*Approximate Solution for Seismic Earth Pressures on Rigid Walls Retaining Inhomogeneous Elastic Soil*”, Soil Dynamics and Earthquake Engineering, 97: 468–477, <https://doi.org/10.1016/j.soildyn.2017.03.028>
- [4] Mononobe N., Matsuo M., 1929, “*On the Determination of Earth Pressures During Earthquakes*”, World Engineering Congress, vol 9. pp. 177–185, 29 October – 7 November, Tokyo, Japan
- [5] Okabe S., 1924, “*General Theory of Earth Pressure and Seismic Stability of Retaining Wall and Dam*”, Japanese Society of Civil Engineers, 10 (6): 1277–1323.
- [6] Papazafeiropoulos G., Psarropoulos P., 2010, “*Analytical Evaluation of the Dynamic Distress of Rigid Fixed-Base Retaining Systems*”, Soil Dynamics and Earthquake Engineering, 30 (12): 1446–1461, <https://doi.org/10.1016/j.soildyn.2010.05.004>
- [7] Vrettos C., Beskos D.E., Triantafyllidis T., 2016, “*Seismic Pressures on Rigid Cantilever Walls Retaining Elastic Continuously Non-homogeneous Soil: An Exact Solution*”, Soil Dynamics and Earthquake Engineering, 82: 142–153, <https://doi.org/10.1016/j.soildyn.2015.12.006>.
- [8] Brandenberg S.J., Mylonakis G., Stewart J.P., 2015, “*Kinematic Framework for Evaluating Seismic Earth Pressures on Retaining Walls*”, Geotechnical and Geoenvironmental Engineering, 141 (7): 10, [https://doi.org/10.1061/\(ASCE\)GT.1943-5606.0001312](https://doi.org/10.1061/(ASCE)GT.1943-5606.0001312)
- [9] Al Atik L., Sitar N., 2010, “*Seismic Earth Pressures on Cantilever Retaining Structures*”, Geotechnical and Geoenvironmental Engineering, 136 (10): 1324–1333, [https://doi.org/10.1061/\(ASCE\)GT.1943-5606.0000351](https://doi.org/10.1061/(ASCE)GT.1943-5606.0000351)

- [10] Ostadan F., 2005, “*Seismic Soil Pressure for Building Walls: An Updated Approach*”, Soil Dynamics and Earthquake Engineering, 7 (10): 785–793, <https://doi.org/10.1016/j.soildyn.2004.11.035>
- [11] Kloukinas P., Di Santolo A.S., Penna A., Dietz M., Evangelista A., Simonelli A.L., Taylor C., Mylonakis G., 2015, “*Investigation of Seismic Response of Cantilever Retaining Walls: Limit Analysis vs Shaking Table Testing*”, Soil Dynamics and Earthquake Engineering, 77: 432–445, <https://doi.org/10.1016/j.soildyn.2015.05.018>
- [12] Garini E., Tsantilas L., Gazetas G., 2016, “*Seismic Response of Cantilever Retaining Walls: Verification of Centrifuge Experiments*”, 1st International Conference on Natural Hazards and Infrastructures, 28–30 June, Chania, Greece.
- [13] Wagner N., Sitar N., 2016, “*On Seismic Response of Stiff and Flexible Retaining Structures*”, Soil Dynamics and Earthquake Engineering, 91: 284–293, <https://doi.org/10.1016/j.soildyn.2016.09.025>
- [14] Steedman R.S., Zeng W., 1990, “*Influence of Phase on the Calculation of Pseudo-Static Earth Pressure on a Retaining Wall*”, Geotechnique, 40 (1): 130–112, <https://doi.org/10.1680/geot.1990.40.1.103>
- [15] Athanasopoulos-Zekkos A., Vlachakis V.S., Athanasopoulos G.A., 2013, “*Phasing Issues in the Seismic Response of Yielding, Gravity-Type Earth Retaining Walls – Overview and Results From a FEM Study*”, Soil Dynamics and Earthquake Engineering, 55: 59–70, <https://doi.org/10.1016/j.soildyn.2013.08.004>
- [16] Koutsantonakis C., 2019, “*Contribution to Seismic Analysis of Retaining Structures*”, M.Sc. Thesis, University of Patras, Patras, (in Greek with extended description in English)
- [17] Kanellopoulos K., Gazetas G., 2019, “*Vertical Static and Dynamic Pile-to-Pile Interaction in Nonlinear Soil*”, Geotechnique, 1–51, <https://doi.org/10.1680/jgeot.18.p.303>
- [18] Bolisetti C., Whittaker A., Coleman J., 2018, “*Linear and Nonlinear Soil-Structure Interaction Analysis of Buildings and Safety – Related Nuclear Structures*”, Soil Dynamics and Earthquake Engineering, 107: 218–233, <https://doi.org/10.1016/j.soildyn.2018.01.026>
- [19] Sotiriadis D., Kostinakis K., Morfidis K., 2017, “*Effects of Nonlinear Soil-Structure-Interaction on Seismic Damage of 3D Buildings on Cohesive and Frictional Soils*”, Bulletin of Earthquake Engineering, 15 (9): 3581-3610, <https://doi.org/10.1007/s10518-017-0108-8>
- [20] Mylonakis G., Gazetas G., 2000, “*Seismic Soil-Structure Interaction: Beneficial or Detrimental?*”, Earthquake Engineering, 4 (3): 277–301, <https://doi.org/10.1080/13632460009350372>
- [21] Kloukinas P., Langousis M., Mylonakis G., 2012, “*Simple Wave Solution for Seismic Earth Pressures on Nonyielding Walls*”, Geotechnical and Geoenvironmental Engineering, 128: 1514–1519, [https://doi.org/10.1061/\(ASCE\)GT.1943-5606.0000721](https://doi.org/10.1061/(ASCE)GT.1943-5606.0000721)
- [22] Veletsos A., Younan A., 1994, “*Dynamic Soil Pressures on Rigid Vertical Walls*”, Earthquake Engineering and Structural Dynamics, 23: 275–301, <https://doi.org/10.1002/eqe.4290230305>
- [23] Karnovsky I., and Lebed O., 2000, “*Formulas for Structural Dynamics*”, McGraw-Hill, United States, 535 pages.
- [24] Gazetas G., 1982. “*Shear Vibration of Vertically Inhomogeneous Earth Dams*”, International Journal for Numerical and Analytical Methods in Geomechanics, 6: 219–241, <https://doi.org/10.1002/nag.1610060208>
- [25] Kramer S.L., 1996, “*Geotechnical Earthquake Engineering*”, Prentice-Hall, New Jersey, United States, 673 pages.

VISÉAN LIMESTONE, KARST AND THE N6 GALWAY CITY RING ROAD, WESTERN IRELAND

Megan J. Dolan* ^{1,2,3}, ¹*Civil Engineering, College of Engineering and Informatics*, ²*Earth and Ocean Sciences, School of Natural Sciences*, ³*Irish Centre for Research in Applied Geosciences (iCRAG), National University of Ireland, Galway*, *m.dolan16@nuigalway.ie

ABSTRACT

A c.100 m deep sediment-filled karst feature, discovered during the preliminary ground investigation for a proposed tunneled section of the N6 Galway City Ring Road in western Ireland, has prompted a research project to better understand the local and regional geology and geomorphology.

The geological investigation reported in this paper gives insight to the timing and style of formation of this large-scale feature. A large fault and numerous structural joints developed in the Carboniferous limestone govern the local hydrogeology and appear to have given rise to, and controlled the east-west orientation of, the deep enclosed depression. A combination of bedrock logging, petrography, palaeontology and geochemistry have helped to reconstruct the geological history of the local bedrock and highlight relationships between lithology and karstification. In the sediment, fluvial and lacustrine palaeoenvironments are interpreted while three phases of glaciation are potentially represented, with the oldest possibly dating to the Late Pleistocene or older. This information will prove invaluable to the detailed design of the tunnel.

Keywords: Karst, Palaeoenvironments, Hydrogeology, Cut-and-Cover Tunnel.

1. INTRODUCTION

Approximately half of the landmass of the Republic of Ireland is underlain by predominantly limestone bedrock [1], 70% of which appears to be sufficiently pure to encourage dissolution and can be referred to as “karstifiable” [2]. As a result, Ireland is host to many karst features, such as turloughs, springs, conduit networks, caves and dolines (enclosed depressions).

The presence and wide distribution of karst features poses significant challenges for the geotechnical engineering design of infrastructure projects; for example, in the west of Ireland, numerous karst features have been encountered along the route of the M17/M18 motorway (opened in 2017) and the N6 Galway City Ring Road project (planning decision expected in May 2019). During the site investigation for the latter project, a large (approximately 300 m long, 100 m wide, over 100 m deep) and unanticipated karst feature was discovered east of the river Corrib, between Galway City and Lough Corrib, adjacent to the inactive Coolough limestone quarry (Figure 1). In the original design, a bored tunnel was planned to pass through this area (starting from a quarry face), to avoid a local Special Area of Conservation located to the west of the quarry; however, the discovery of this sediment-filled depression will enable a section of the tunnel to be constructed using a less expensive cut-and-cover approach.

Such significant karst features are known to exist elsewhere in Ireland, but they have not been documented or subject to detailed geological investigation. This project aims to resolve the style and timing of formation of the Coolough karst landform. A better understanding of the geological history of this karst feature and its bedrock host will provide insight to the critical

relationship between karstification and carbonate lithologies, while also helping to inform future geotechnical projects in similar geological environments.

2. METHODOLOGY

The study involved analysis of (i) sediment from a deep rotary core borehole (BH03), west of Coolough quarry, (ii) pollen recovered from the BH03 core, (iii) the geological bedrock structures evident in the west quarry face and a fault transecting the quarry and (iv) petrography of bedrock samples from Coolough quarry. Relevant locations are shown in Figure 1.

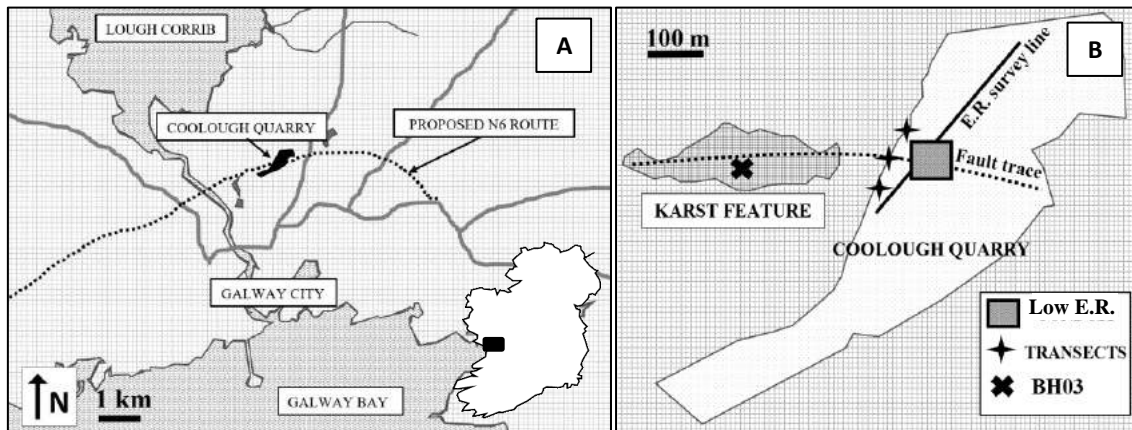


Figure 1. (A) Location of Coolough quarry (Galway) and proposed N6 route. (B) Location of large buried karst feature, trace of fault, electrical resistivity (E.R.) survey line, zone of low E.R., 10 m structural line transects and collar location of BH03.

2.1. BH03 Sediment Sequence

Core BH03 (109.9 m long) extracted from the large karst feature (Figure 1) was logged. A homogenous unit of fine-grained sediment occupying approximately 20 m of the length of the BH03 core was sampled for particle size distribution testing and the mineralogy was studied in thin section.

2.2. Pollen

Samples were taken for pollen analyses from four separate organic clay-rich horizons within core BH03. Sample preparation and pollen counting followed standard procedures as practised at the Palaeoenvironmental Research Unit, NUI Galway [3].

2.3. Bedrock Structure and Geophysics

All fractures intersecting three 10 m long horizontal line transects along the west quarry face adjacent to the deep karst feature (Figure 1) were measured for length, strike, inclination and dip orientation. These structural data were plotted on stereonet graphs in Stereonet 10.0 (version 10.1.1) [4]. Additionally, 2D electrical resistivity surveys were conducted across the quarry floor. Both Wenner-Schlumberger and dipole-dipole arrays were used to survey one 480 m line (“E.R. survey line” in Figure 1) with 10 m electrode spacing along the entire length and 5 m electrode spacing along the southern 240 m.

2.4. Petrography

The bedrock outcropping at Coolough quarry was logged and samples were extracted for (a) petrographic analysis of the limestones and (b) geochemical analysis of two prominent clay-rich units within the limestones, also known as clay wayboards (LQ2 at 14.3 m O.D. and LQ4 at 14.8 m O.D., roughly 20 m below ground surface). Limestone thin-sections were analysed

using a polarizing microscope. Element composition, oxide weight percentages and loss on ignition of the clay samples were determined at a local specialist laboratory.

3. RESULTS

3.1. BH03 Sediment Sequence

The summary log of core BH03 (Figure 2) indicates limestone at the base of the sequence, from 104.95 m to 109.9 m. These limestone blocks exhibit sub-vertical stylolites (horizontal solution planes) and are separated by a 40 cm interval of limestone gravel and a 30 cm horizon of soft, dark-brown clay from 108.3 m to 108.6 m. The latter clay contains sub-rounded limestone clasts. No core was recovered from 85.55 m to 104.95 m. Other younger sections of the core are also occupied by limestone, up to 1.65 m thick, and these appear to represent clasts. Boulder clay characterizes core BH03 at three distinct sections, from 73.15 m to 85.55 m, from 50 m to 62.2 m and again at the top of the core (between 12.2 m and 0 m). From 18.6 m to 37 m, a soft, light grey/brown and calcareous silty sand was found, composed of angular quartz with angular feldspars, mostly plagioclase, and amorphous limestone fragments.

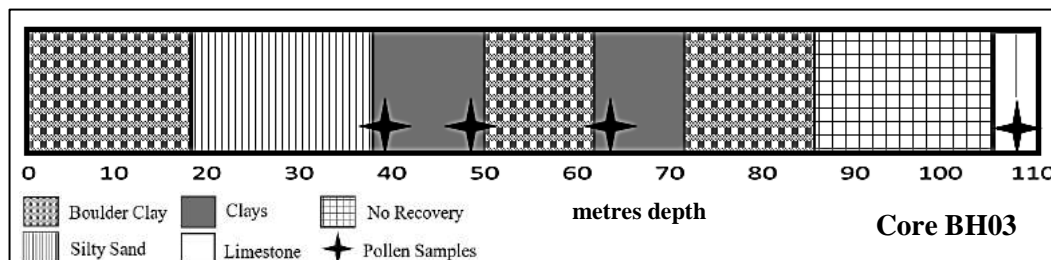


Figure 2. Simplified schematic sediment log of core BH03

BH03 contains several clay horizons of varying stiffness, texture, colour and calcium carbonate content. The clays are predominantly soft, sandy or silty, and contain limestone gravel and cobbles in some parts (generally angular and sub-angular). The clays are typically grey, brown or grey/brown in colour. Including the clay at ~108.5 m, six organic clay units were recorded within the clays of core BH03 ranging from 30 cm to 4.65 m in thickness. Most are firm and dark brown and some exhibit organic debris, particularly the 3.2 m thick organic unit from 62.5 m – 65.7 m depth which displays fragments of root, bark and leaves. Units of sand up to 1.5 m thick are interspersed in the clays.

3.2. Pollen

Samples from four of the six organic clay units were processed for pollen analyses (Figure 2) and each demonstrate disparate pollen assemblages. A pollen sum of 1000 was achieved per sample excluding aquatics and *Sphagnum* spores. The major flora (high pollen counts) of the 38.6 m sample is shown in an example pollen assemblage (Figure 3). This sample was composed of 8.9% organic matter (O.M.) and is dominated by pollen of *Pinus*, with relatively high levels of Cyperaceae pollen but low levels of *Ilex aquifolium* and *Isoetes lacustris* pollen. In the 47 m sample (6.6% O.M.) the pollen assemblage is dominated by *Sphagnum*, Poaceae, *Pinus* and *Typha latifolia*. Poaceae was the main contributor to the pollen assemblage at 63.8 m (8.0% O.M.). This sample contained no *Isoetes* and only very low levels of *I. aquifolium* and *I. lacustris* and *Sphagnum*. The 108.5 m sample contained the highest relative levels of *I. aquifolium* and *I. lacustris* and the lowest of *Sphagnum*. Overall the representation of *Betula* and Cyperaceae is higher in the two younger clay samples.

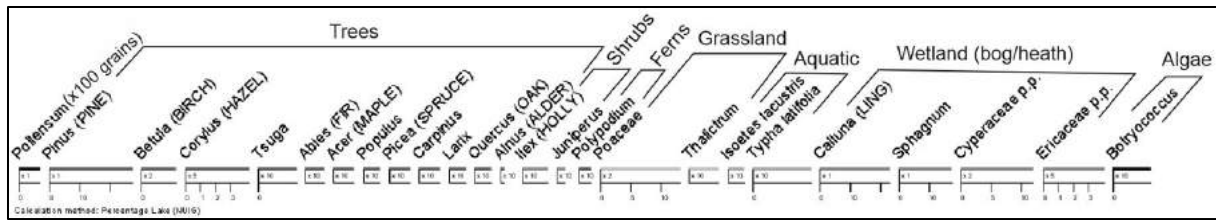


Figure 3. Example of pollen assemblage: major flora of sample from 38.6 m depth

3.3. Bedrock Structure and Geophysics

The Carboniferous (Mississippian) limestone bedrock is heavily fractured and demonstrates fractures from the millimeter scale with haphazard arrangement, some connecting to create a network, to major joints striking roughly 050 and 300 (Figure 4) which penetrate vertically/sub-vertically through all of the visible outcrop. A 2D resistivity profile generated from the E.R. data shows an area of low resistivity beneath the floor of Coolough quarry and is situated along the trend of the elongated axis of the large karst feature which also coincides with an E-W fault visible in the quarry (Figure 1).

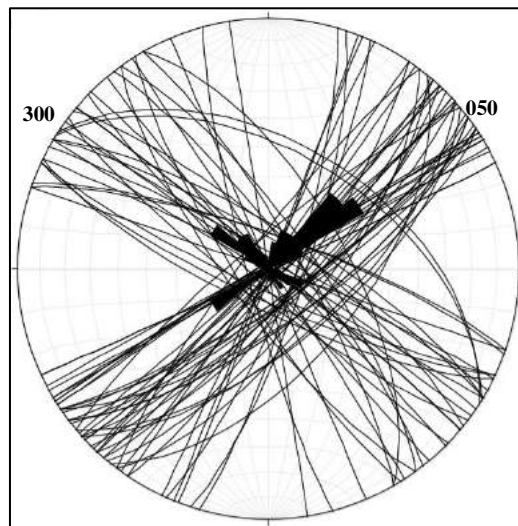


Figure 4. Stereonet [4]: major joint planes and calculated rose diagram

3.4. Petrography

The local bedrock consists of thickly-bedded, medium to light grey limestones, predominantly crinoidal packstones (grain-supported) and wackestones (mud-supported with >10% grains), with grains (typically bioclasts) becoming more sparse and less coarse towards the top of each bed. Occasional gastropods and brachiopods are discernible within some limestone units. The limestone microfossil assemblages are dominated by disarticulated crinoidal fragments, mostly crinoid ossicles. Various types of foraminifera are abundant, along with calcareous algae and skeletal and shelly fragments.

The two conspicuous clay wayboards (LQ2 and LQ4) are more than 25 cm thick on average around the quarry and are interbedded within the limestones. The clay material from LQ2 is light to medium grey in colour, very soft and pliable, argillaceous and non-calcareous. It exhibits pyrite stringers and coalified plant matter. Clay material from LQ4 is shaley, medium dark grey, calcareous, with a more fissile base and less fissile top than LQ2 and is less argillaceous overall. LQ4 contains at least two species of brachiopod.

Both LQ2 and LQ4 are largely geochemically disparate (Figure 5), but they do show some similarities, such as a similar SiO₂ content. LQ2 contains relatively lower percentages of Al₂O₃,

MgO, K₂O, Na₂O, TiO₂ and SrO but higher percentages of Fe₂O₃, MnO and P₂O₅, with the percentage of Fe₂O₃ being the greatest element oxide difference between the two samples. CaO, Cr₂O₃ and BaO are comparable in both samples. The loss on ignition of LQ2 clay is 18.5% and of LQ4 clay is 17.1%.

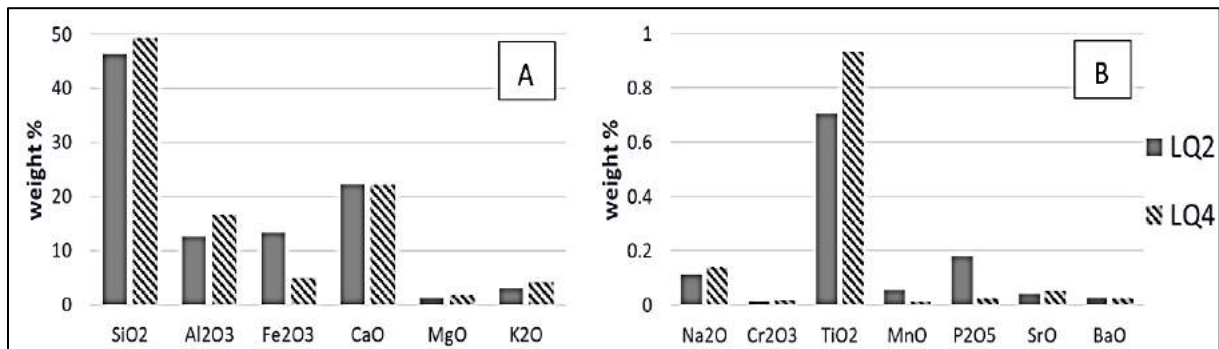


Figure 5. Geochemistry of clay horizons: major (A) and minor (B) element oxides

4. DISCUSSION

4.1. BH03 Sediment Sequence

The high angle stylolites observed in the limestone blocks towards the very base of core BH03 (between 104.95 m and 109.9 m) suggest that these blocks are perhaps allochthonous, remobilized due to rock failure which resulted in gravity and slab movement (with rotation). This suggests that the enclosed karstic depression formed (or opened) due to a collapse event. There is evidence of glacial, lacustrine and fluvial palaeoenvironments within the unconsolidated sediment that subsequently infilled the karst depression. Three distinct boulder clay units were deposited following perhaps discrete phases of glaciation. This strongly suggests that all sediment below the uppermost boulder clay is at least pre-Holocene in age. Following the various glacial periods, melt waters generated large lakes and rivers which transported and deposited abundant detrital sedimentary material. (Glacial) Lough Corrib appears to have enveloped the Coolough area more than once during the Cenozoic, leading to the formation of the lacustrine clays evident in core BH03. The various stiffnesses, textures, colours and calcium carbonate contents observed reflect changes within the lake environments, a consequence of fluctuating palaeoclimates. The geotechnical parameters of these clays are likely to vary significantly as seen in similar clays found in the nearby Terryland basin [5]. An 18.4 m silty sand unit within core BH03 suggests the presence of a river, possibly draining from Lough Corrib, as the sediment contains quite angular and texturally immature carbonate and igneous grains indicating a proximal source. Tributaries of modern Lough Corrib drain from the carbonate platform along the east and from the upland granites to the west. Satellite imagery of the region reveals other former river channels within the local topography which were apparently meandering and appear similar in nature to areas abutting Lough Corrib today.

4.2. Pollen

Warm climate species from the Oligocene/Miocene were not observed within the pollen recovered from BH03; hence the deposit is likely to be younger than *c.*5.3 Ma. Meltwaters waned during the Quaternary inter-glacials, creating prime opportunities for organic matter to accumulate.

The pollen assemblages from the 38.6 m and 47 m samples suggest a wooded landscape dominated by pine and hazel with lesser amounts of birch, fir, spruce, hemlock (*Tsuga*) and oak. Holly was also present. The presence of grasses and herbs such as meadow-rue imply an

open structure to the woodland. The high representation of birch and sedge pollen is reminiscent of Gortian type deposits dated to 302 ka – 428 ka ago [6,7], with the possibility that the 38.6 m sample may correspond to Gortian Stage Gn IV - Gn IIIb and the 47 m sample to Gn IIIb - Gn IIIa. However, both samples are missing a strong Alder (*Alnus*) pollen signature, a key component of the Gn III stages.

The pollen assemblage from the 63.8 m sample, dominated by grassland taxa and containing pollen of non-modern species such as a variety of hemlock (*Tsuga*), is comparable to Pliocene/Early Pleistocene (c.2.6 Ma) assemblages recorded at Pollnahalia some 20 km distant. However, the assemblage is also dissimilar, lacking pollen of several taxa evident at Pollnahalia such as hickory and members of the Cypress family. The Coolough clay at this depth was likely deposited in the Early Pleistocene but is relatively younger than the Pollnahalia deposit.

The 108.5 m sample was extracted from a void within the rotated limestone slabs at the bottom of core BH03 which also hosts rounded limestone clasts suggesting that this clay was deposited by groundwater within a conduit post collapse. The high proportion of pollen from lake quillwort (*I. lacustris*) in this sample is indicative of a lacustrine environment as the source of the clay sediment. The proximal Lough Corrib is a likely source.

4.3. Bedrock Structure and Geophysics

The major joint sets developed in the limestone aided karstification by channeling groundwater into the main fault structure transecting Coolough quarry, allowing more water to exploit this E-W lineament. As flow, and hence dissolution, was focused along the fault damage zone, a conduit developed and grew into an enlarged cavern which ultimately led to collapse when the overlying limestone bedrock roof, at the location of the large karst feature, became structurally unsound. Hence the long axis of the karst feature aligns with the fault, striking roughly east-west, and also with a deep subsurface conduit, implied by low E.R. values, which presumably connects to the karst feature. Dissolution of Irish limestones was intense throughout the warm and humid conditions of the Paleogene and Neogene Periods [9,10]; hence, local bedrock dissolution may date to the Early Pleistocene or earlier, in keeping with the timeline implied by the pollen assemblages.

4.4. Petrography

The petrography and palaeontology of the Carboniferous limestone bedrock indicate deposition in a moderate to high energy, shallow-water carbonate shelf environment. The limestone is lithologically similar, in several respects, to the Late Asbian Aillwee Member limestone of the Viséan (346.7 - 330.9 Ma) Burren Formation, which outcrops south of Galway Bay in County Clare [11]. Aillwee Cave is a karst network which is largely hosted within this particular member in the Burren region. It formed during intense dissolution of the Burren Formation and has been dated to >350 ka using alpha-spectrometer uranium series methods [12].

The Aillwee Member of the Burren Formation contains several distinctive clay wayboard horizons, which have been interpreted in the past as possibly volcanogenic in origin (i.e. as modified volcanic ash) [13,14]. Both of the clay wayboards from Coolough quarry were geochemically investigated using an element oxide discrimination technique [15], which indicates a detrital origin for these horizons (Figure 6). LQ2 contains coalified plant matter and pyrite, reflected in the geochemistry (high Fe₂O₃), suggesting a swampy and poorly oxygenated environment during the Carboniferous. LQ4 contains a brachiopod shell with spines still intact (buried on deposition) implying marine conditions with little or no post-mortem disturbance.

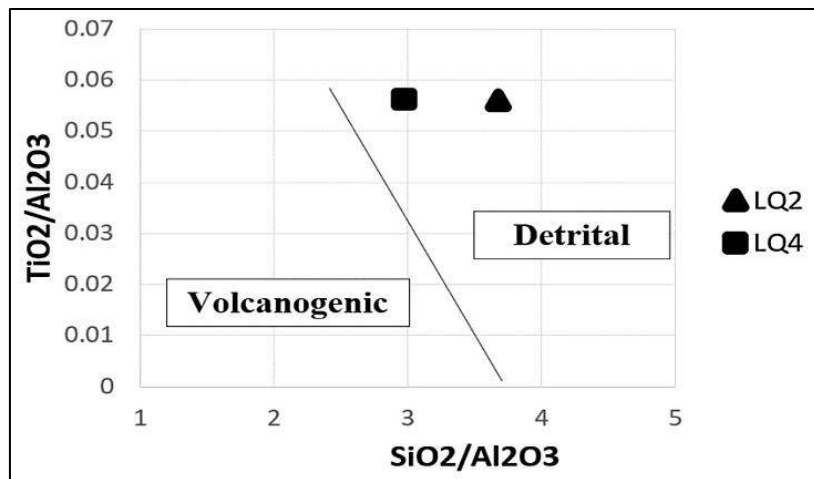


Figure 6. Discrimination chart [15] for origin of clay horizons

Both LQ2 and LQ4 have extremely low hydraulic conductivity values, and inhibit groundwater flow across them. Groundwater moving in the limestone bedrock thus flows preferentially along the top of these clay units. Conspicuous iron stains have developed on the quarry walls below these clay wayboards, particularly LQ2, as Fe₂O₃-rich groundwater emerges at these horizons. The bored tunnel will begin in the quarry face below LQ2 to mitigate groundwater disturbances and flooding issues. However, the E-W fault may have implications for the tunnel; groundwater could potentially flow vertically through the clay wayboards where they intersect the fault damage zone where their structural integrity has been compromised. Groundwater is seen to emerge from the west quarry face along the fault, both above and below the clay wayboards.

5. CONCLUSIONS

The c.100 m deep sediment-filled karst feature located in Coolough (County Galway) is a buried enclosed depression, most likely formed by enlargement of a deep-seated conduit. The infilling sediment and entrained pollen suggest that a collapse event occurred sometime between the Late Miocene and Late Pliocene, possibly during a warmer and more humid climatic phase. During this time, water exploited the principal structural lineaments developed in the local Carboniferous limestone bedrock; an E-W trending fault and two major joint sets (both continue to govern local groundwater movement today), leading to the formation of the large-scale karst feature. Petrography and microfacies analysis indicate that the massive and fossil-rich limestone hosting the karst feature is likely lithostratigraphically equivalent to the Aillwee Member of the Burren Formation. These Viséan limestones were deposited in a shallow tropical sea, in which the carbonate platform was periodically exposed, leading to the production of clay wayboards. It is hoped that this study will help inform the construction of the proposed tunnel and future geotechnical projects in similar geology.

ACKNOWLEDGEMENT

The author would like to gratefully acknowledge the support from MAppSc supervisors Dr. Bryan McCabe, Dr. John Murray and Dr. Tiernan Henry; the technical skills, input and training from Dr. Karen Molloy, Dr. Eve Daly, Shane Rooney and Dave O'Leary; and the data and guidance provided by Marie Fleming and Les Brown of Arup.

REFERENCES

- [1] Sevastopulo, G.D., Wyse Jackson, P.N., 2009. “*Carboniferous: Mississippian (Tournaisian and Viséan)*”, Holland, C.H. and Sanders, I.S. (eds) *The Geology of Ireland*, Dunedin Academic Press, 215–269.
- [2] Drew, D.P., Jones, G.L., 2000. “*Post-carboniferous pre-quaternary karstification in Ireland*”, *Proceedings of the Geologists' Association*, 111(4): 345-353.
- [3] Molloy, K., O’Connell, M., 2004. “*Holocene vegetation and land-use dynamics in the karstic environment of Inis Oirr, Aran Islands, western Ireland: pollen analytical evidence evaluated in light of the archaeological record*”, *Quaternary International*, 113(1): 41-64.
- [4] Allmendinger, R.W., Cardozo, N.C., Fisher, D., 2013. “*Structural Geology Algorithms: Vectors & Tensors*”, Cambridge University Press, 289.
- [5] Quigley, P., McCabe, B.A., Hunt, P., Rodgers, M., 2016. “*Some geotechnical characteristics of soft soil deposits along the Terryland River Valley, Galway*”, *Proceedings of Civil Engineering Research in Ireland (CERI, 2016)*, 439-444.
- [6] Heijnis, H., van der Plicht, J., 1992. “*Uranium/thorium dating of Late Pleistocene peat deposits in N.W. Europe, uranium/thorium isotope systematics and open-system behaviour of peat layers*”, *Chemical Geology*, 94: 161-171.
- [7] Dowling, L.A., Sejrup, H.P., Coxon, P., Heijnis, H., 1998. “*Palynology, aminostratigraphy and U-series dating of marine Gortian Interglacial sediments in Cork Harbour, Southern Ireland*”, *Quaternary Science Reviews*, 17(9–10): 945-962.
- [8] Coxon, P., Flegg, A., 1987. “*A Late Pliocene/Early Pleistocene Deposit at Pollnahallia, near Headford, County Galway*”, *Proceedings of the Royal Irish Academy, Section B: Biological, Geological, and Chemical Science*, 87B: 15-42.
- [9] Mitchell, G.F., 1980. “*The Search for Tertiary Ireland*”, *Irish Journal of Earth Science*, 3(1):13-33.
- [10] Mitchell, G.F., 1985. “*The Preglacial landscape*”, Edwards, K.J. and Warren, W.P. (eds) *The Quaternary History of Ireland*, 17-37.
- [11] Gallagher, S.J., McDermot, C.V., Somerville, I.D., Pracht, M., Sleeman, A.G., 2006. “*Biostratigraphy, microfacies and depositional environments of Upper Viséan limestones from the Burren region, County Clare, Ireland*”, *Geological Journal*, 41: 61-91.
- [12] Drew, D.P., Cohen, J.M., 1980. “*Aillwee Cave, Co. Clare, Ireland*”, *Proceedings of the University of Bristol Spelaeological Society*, 15.3: 227-240.
- [13] Vincent, P., 1995. “*Limestone pavements in the British Isles: A Review*”, *The Geographical Journal*, 161: 265-274.
- [14] Walkden, G.M., 1974. “*Palaeokarstic surfaces in Upper Viséan (Carboniferous) limestones of the Derbyshire Block, England*”, *Journal of Sedimentary Petrology*, 44(4): 1232-1247.
- [15] Batchelor, R.A., Jeppsson, L., 1994. “*Late Llandovery bentonites from Gotland, Sweden, as chemostratigraphic markers*”, *Journal of the Geological Society*, 151(5): 741-746.

OPTIMIZATION OF MONOPILE FOUNDATION FOR OFFSHORE WIND TURBINES THROUGH ADVANCED MODELLING

Soroosh Jalilvand*, *Head of Offshore, Gavin and Doherty Geosolutions, sjalilvand@gdgeo.com*

ABSTRACT

A significant challenge in reducing the cost of offshore wind turbines (OWTs) is the design of efficient and reliable substructures for turbines. Foundation structures for OWTs can represent up to 30% of the overall development cost. For OWTs with monopile foundation, the dynamic response of the structure is highly related to the foundation damping. It is generally accepted that soil damping is underestimated. However, it is already demonstrated that increasing the soil damping component in foundation design reduces fatigue loads and operational mudline moments which can cause significant cost savings. This paper investigates the benefit of a more accurate quantification of foundation damping using advanced numerical modelling and vibration analysis. A 3D Finite Element (FE) model of a representative OWT (DTU 10MW) is developed in Plaxis 3D. The soil-structure interaction model is developed using representative soil type, water depth and load levels. Contribution of foundation damping to the OWT overall damping is investigated. The analysis is performed using the HSS constitutive model which allows for capturing internal hysteretic material damping in the soil response. A time domain dynamic analysis is undertaken in Plaxis 3D and the foundation damping ratio is calculated from the time domain of a free vibration analysis. Furthermore, the relationship between the foundation damping and the mudline deflection and the monopile embedment depth is assessed. It is shown that for the same embedment length of the monopile, higher lateral loads result in larger mudline deflections, which in turn, contribute to increased foundation damping. Furthermore, increase in the overall fixity of the foundation is shown to reduce the monopile damping. Damping is shown to converge to a unique backbone curve if adequate embedment length is provided. It is concluded that the current industry practice of adopting constant-value foundation damping is conservative, and additional cost savings can be realized (especially under extreme loading conditions) using advanced soil-structure-interaction models that consider the collective influence of monopile geometry, loading levels, and site-specific soil conditions.

Keywords: Offshore Wind, Monopile, Damping

1. INTRODUCTION

The offshore wind energy sector is expected to play a key role in mitigating climate change impact and achieving ambitious carbon emission targets set by various judiciaries in recent years. The UK has recently announced zero emission target for 2050, and it is projected that 50GW of offshore wind energy is required to be installed to achieve these goals. Similar targets have been announced by governments worldwide with both mature and emerging offshore wind sectors. The US is expected to install up to 9GW of offshore wind by 2030, while China is aiming for an ambitious installed capacity of 100GW within the same timeline. Other countries in Asia such as Taiwan, India, Vietnam, South Korea, and Japan have also shown strong appetite for development of multi-Gigawatts of offshore wind capacity in the next decade, with

Taiwan having a pipeline of 5.5 GW to be installed by 2025, and India aiming for ambitious goal of 30GW offshore wind installed by 2030

The rapid growth in the offshore wind sector is in large part owed to the significant cost reductions realized in mature markets across Europe over the past decade. The cost reduction trends is apparent in the UK's past Cost for Difference (CfD) allocation rounds where the requested support level by developers has continuously reduced over the past few years. Germany was the first market to announce winners of a subsidy free tender for offshore wind in 2017. The Netherland's zero-subsidy bids in 2018 and 2019 are other landmark developments in the continuous cost reduction success story for the offshore wind. The Holland Kust Zuid is expected to be the first offshore wind project to be installed by 2022 without subsidies.

The continuous cost reduction in the offshore wind industry is related to technological advances that have enabled construction of larger wind turbines and associated benefits from the economy, as well as, improved efficiency in the supply chain. Larger wind turbines require the installation of more massive substructures, which in turn, pose significant engineering and installation challenges to the project. The design approaches adopted in the oil & gas sector, or for the assessment of smaller sized wind turbine substructures may no longer be valid, and therefore, revised and optimized solutions that account for unique characteristics of these substructures need to be developed.

Monopiles are the most commonly installed type of foundation in the offshore wind sector due to each of fabrication and quick installation time, which reduces the time required for offshore work. While the monopile behavior is adequately understood for small diameters and large embedment depth to diameter ratios (typical of oil & gas jacket piles), there are still several knowledge gaps in understanding the static and dynamic behavior of large diameter monopiles (with small ratio of embedment depth to the pile diameter), which are becoming increasingly common in the offshore wind industry. In particular, the damping response of large monopiles is poorly understood, which results in conservative estimation of fatigue loads on the structure. The damping response in the wind turbine structure can be associated with a combination of sources including (i) aerodynamic damping, (ii) hydrodynamic damping, (iii) structural damping, (iv) foundation (soil) damping, and (v) external dampers including passive and active concepts, which can be linearly super-imposed to obtain the total damping. Among these sources, the foundation damping is poorly understood and is associated with one of the main sources of uncertainty in the estimation of the overall damping of offshore wind turbine structures [1].

Several studies have been undertaken to quantify the damping in offshore wind turbine structures [2]. A series of measurements were undertaken by Versteijlen et al. [3] at Orsted's (formerly Dong Energy) Burbo Bank offshore wind farm in the Irish Sea to quantify damping under rotor-stop condition. The study included installation of several accelerometer and strain gauges along the tower to assess the free decay response of the structure. In a sperate measurement campaign, Devriendt et al. [4-5] investigated the impact of wind speed and vibration amplitude on the damping was investigated. It was shown that the total damping of the wind turbine structure varied between 1.1 and 2.6% of critical damping depending on the wind speed. It was shown that a three-fold increase in the maximum wind speed could result in approximately 30% additional damping in the structure. Further attempts in the quantification of foundation and structural damping include the study undertaken by Bajric et al. [6] that adopted modal identification techniques to estimate the damping under non-operation condition. The average damping in these studies was reported in the range 0.7 and 1.2% of the critical damping.

The foundation damping was also investigated using laboratory scale tests in Kaolinite by Lombardi et al. [7]. The tests involved application of horizontal cyclic loading to the model monopile structure and estimation of damping using the logarithmic decrement approach. The analysis suggested that higher damping ratios can be expected at higher strain levels. The foundation damping has also been investigated using numerical modelling. Carswell et al. [8] investigated soil damping using lumped parameter model, which include a rotational dashpot at mudline level. The study suggested foundation damping in the range 0.17% to 0.28% of critical damping using logarithmic decrement approach. In particular, it was shown that the incorporation of foundation damping could result in 7-9% reduction in the maximum mudline moment applied to the monopile.

In this paper the results of advanced 3D Finite Element modelling for a large diameter monopile supporting the generic 10MW DTU turbine is provided. The analysis shows the stress distribution in the vicinity of a monopile and the stress mobilized along the soil plug varies between the pile toe level and the mudline. Furthermore, the results of free vibration of the wind turbine structure are presented and the associated foundation damping quantified using logarithmic decrement approach. A high-level discussion is finally provided on the relationship between the amplitude of vibration, the pile embedment length and the rate of decay in the RNA displacement.

2. METHODOLOGY

The offshore wind turbine structure was modelled using Finite Element package (Plaxis 3D). Only half of the model was considered due to symmetry. The size of the model was selected in such a way to avoid boundary conditions [9]. The model size was taken as approximately $20 \times D$ and $5 \times D$ in directions parallel and traverse to loading, respectively. The schematic of the wind turbine structure is show in Figure 1.

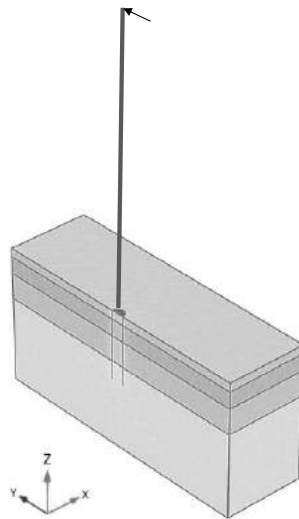


Figure 1. 3D FE model.

2.1. Wind Turbine Structure (DTU 10MW)

The tower structure and hub height/mass were modelled using the DTU 10-MW reference wind turbine [10]. The tower and monopile above mudline were modelled using linear elastic beam elements with representative cross sections. The embedded section of the monopile was modelled using plate elements which allow interaction with ten-node tetrahedral elements used for modelling of soil material. The beam elements were connected to the plate structure using a rigid link. The RNA mass was assumed as 675 Tonne.

Water depth is assumed as 45m relative to MSL level. Table 1 summarises the main elevations along the wind turbine structure. Table 2 summarizes the monopile geometry used in the current study.

Table 1. Tower Properties and Interface Levels

Property	Elevation (m MSL)	Cross Section (m ²)
RNA	119	0.3443
MP-Tower Interface	0	0.9863
MP Kink Point (start of tapered section)	-7.5	1.1197
MP Kink Point (end of tapered section)	-22.5	1.4967
Mudline	-45	1.4967

Table 2. Monopile Properties

Analysis ID	Diameter (m)	Thickness (mm)	Embedment Length (m)	L/D
1	8	80	30	3.75
2			35	4.38
3			40	5.0

2.2. Material Properties

The pile and tower structure were modelled using linear elastic material with Young's Modulus, 210 GPa, Poisson's ratio of 0.3 and steel unit weight of $\gamma = 77\text{kN/m}^3$, which eliminates the structural damping in the analysis. The soil was modelled using small strain Hardening Soil model (HSS). The HSS model considers stress dependency in the soil stiffness values and allows for modelling stiffness degradation as a result of accumulation of shear strain [9]. The latter is the source of hysteretic damping.

Table 3 summarizes the soil profile used in the current study [2]. The soil model is representative of ground condition encountered in the North Sea area. The soil parameters including unit weight (γ), friction angle (ϕ), angle of dilation (ψ), and small strain shear modulus (G_0) are also provided in Table 3.

Table 3. Soil properties

Layer	From (mBML)	To (mBML)	γ (kN/m ³)	ϕ (deg)	ψ (deg)	G_0 (GPa)
1	0	5	17	36.2	3.9	57.8
2	5	15	17	35.5	3.0	119.0
3	15	30	17	34.9	2.3	125.6
4	30	80	17	34.4	1.7	166.8

2.3. Logarithmic decrement approach

The logarithmic decrement approach was used to estimate the damping from the time history response of free vibration analysis. The logarithmic decrement is defined as the natural logarithm of the ratio of the amplitudes of two peaks (A_0 and A_n) separated with n periods in the time history response:

$$\delta = \frac{1}{n} \ln \left(\left| \frac{A_0}{A_n} \right| \right) \quad (1)$$

The current study uses successive positive peaks (e.g. A_1 and A_2 , A_2 and A_3 , etc.) in the calculation of damping. The damping calculated from the logarithmic decrement approach can be converted to the damping ratio ξ (damping as % of critical damping) can be calculated as a function of δ by:

$$\xi = \frac{1}{\sqrt{1 + \left(\frac{2\pi}{\delta} \right)^2}} \quad (2)$$

3. RESULTS & DISCUSSION

The analysis was conducted in two phases. First, the wind turbine structure was laterally loaded at the Rotor Nacelle Assembly (RNA) level to achieve a pre-defined displacement at mudline level. This was performed using a static analysis. The structure was subsequently unloaded and the free decay response of monopile and tower structure recorded using dynamic time history analysis. Figure 2 shows the effective horizontal stress (σ'_{yy}) in the soil at the onset of dynamic unloading. It can be observed that passive earth pressures (shown with dashed lines) are mobilized on opposite faces of the pile at mudline and toe levels, while K0 condition (earth pressure at rest) is identified around the point of rotation. It is also evident that the internal soil plug contributes to the overall pile resistance, with the highest internal stress levels identified at the pile toe level.

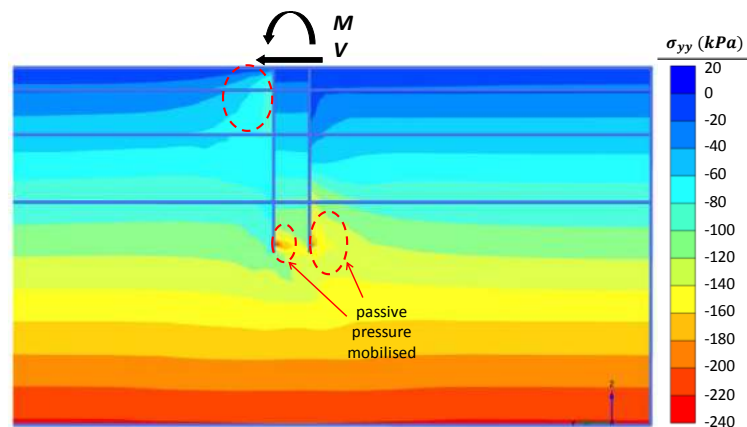


Figure 2. Stress distribution in the soil at the onset of free decay analysis

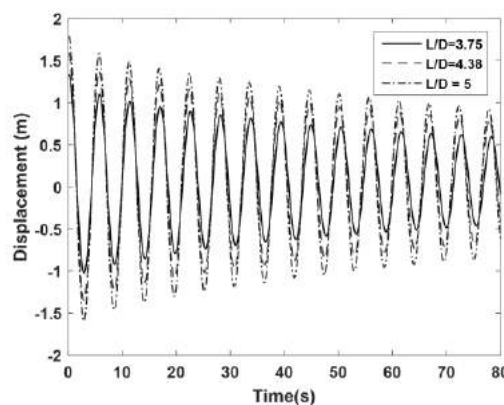


Figure 3. The free decay response at RNA level.

Shows the time history of RNA displacement for monopiles with L/D of 3.75, 4.38, and 5. The mudline deformation at the onset of all analyses is set to 32mm, which is representative extreme loading events. This corresponds to RNA displacement levels of 1.34m, 1.59m, and 1.79m for monopiles with L/D of 3.75, 4.38, and 5. The first natural frequency of the offshore wind turbine structure was assessed for the three monopiles using Fast Fourier Transform (FFT). A similar frequency of 0.183 was calculated for all three piles irrespective of the embedment ratio.

The time history response in Figure 3 shows that the amplitude of vibration decays over time. This is entirely associated with soil damping in the model as all other sources of damping are excluded and the structural elements are modelled using linear elastic model with no damping contribution. In order to calculate the damping for each analysis, the peak displacements were first identified. The logarithmic decrement damping was subsequently calculated between successive peaks, starting with the second peak.

It can be observed that the damping in each case is highest at the onset of free vibration analysis and gradually decreases with time. Suggesting a correlation may exist between damping values and the amplitude of vibration. The highest damping values are observed for the monopile with the shortest embedment length ($L/D = 3.75$), ranging between 2% and 7.5%. In contrast, notably similar damping values were obtained for monopile with L/D of 4.38 and 5, ranging between 2% and 6.25%.

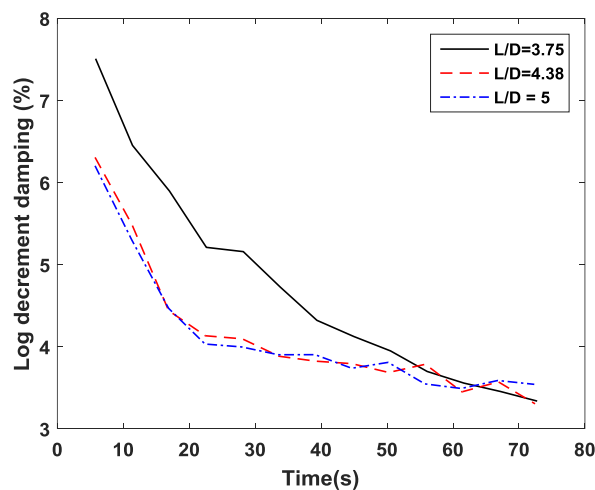


Figure 4. Logarithmic damping at different time steps.

4. CONCLUSION

The current study assessed the monopile foundation damping using advanced 3D Finite Element Modelling. The generic DTU 10MW turbine structure was adopted for this study. The wind turbine structure was modelled using combination of beam and plate elements for sections above and below the mudline.

The soil was modeled using advanced HSS constitutive model which enables consideration of stiffness degradation and damping as a result of accumulation of shear strain.

Three analysis cases were considered including monopiles with diameter of 8m and embedment ratio (L/D) of 3.75, 4.38, and 5. The monopile in each case was statically loaded to a prescribed mudline deflection level and then dynamically unloaded to undergo free vibration.

The time history response with decaying vibration amplitude was subsequently assessed to calculate the logarithmic decrement damping. Damping values ranging between 2% to 7.5% were calculated for all cases.

It was shown that the logarithmic decrement damping reduces as a result of reduction in vibration amplitude for all case considered. The comparison of monopiles with embedment ratios of 3.75 and 4.38 suggested that the damping reduces with increase in the fixity of the monopile.

No further reduction in damping was observed with additional embedment to L/D of 5. The findings allow for justification of larger damping ratios for offshore wind turbines through the use of advanced 3D FE modelling, while providing unique insights into the damping response of monopiles with different embedment ratios.

ACKNOWLEDGEMENT

The author wishes to acknowledge the financial support provided by Geological Survey Ireland (GSI) for participation in the conference. The author also wishes to acknowledge support from colleagues at Gavin and Doherty Geosolutions, Abdollah Malekfarajian, David Igoe, and Paul Doherty, who provided expertise and intellectual discussions that assisted in development of ideas for this paper.

REFERENCES

- [1] Versteijlen, W.G., Renting, F.W., Van Der Valk, P.L.C., Bongers, J., Van Dalen, K.N. and Metrikine, A.V., 2017. “*Effective Soil-Stiffness Validation: Shaker Excitation of An In-Situ Monopile Foundation*”, Soil Dynamics and Earthquake Engineering, 102: 241-262.
- [2] Malekfarajian, A., Jalilvand, S., Igoe, D. and Doherty, P., 2019. “*On the Estimation of Foundation Damping of Mono Pile-Supported Offshore Wind Turbines*”, Vibroengineering PROCEDIA, 23, pp.7-12, 25-26 April 2019, Slovakia.
- [3] Versteijlen, W.G., Metrikine, A., Hoving, J.S., Smidt, E.H. and De Vries, W.E., 2011. “*Estimation of the Vibration Decrement of an Offshore Wind Turbine Support Structure Caused by its Interaction with Soil*”, EWEA Offshore 2011 Conference, 29 November-1 December 2011, The Netherlands.
- [4] Devriendt, C., El-Kafafy, M., Sitter, G.D. and Guillaume, P., 2012. “*Damping Estimation of Offshore Wind Turbines on a Monopile Foundation Using State-Of-The-Art Operational Modal Analysis Techniques*” International Conference on Noise and Vibration Engineering, pp. 2647–62, 17-19 September 2012, Belgium.
- [5] Devriendt, C., Weijtjens, W., El-Kafafy, M. and De Sitter, G., 2014. “*Monitoring Resonant Frequencies and Damping Values of an Offshore Wind Turbine in Parked Conditions*” IET Renewable Power Generation, 8(4): 433-441..
- [6] Bajrić, A., Høgsberg, J. and Rüdinger, F., 2018. “*Evaluation of Damping Estimates by Automated Operational Modal Analysis for Offshore Wind Turbine Tower Vibrations*” Renewable Energy, 116: 153-163.
- [7] Lombardi, D., Bhattacharya, S. and Wood, D.M., 2013. “*Dynamic Soil-Structure Interaction of Monopile Supported Wind Turbines in Cohesive Soil*” Soil Dynamics and Earthquake Engineering, 49: 165-180.

- [8] Carswell, W., Johansson, J., Løvholt, F., Arwade, S.R., Madshus, C., DeGroot, D.J. and Myers, A.T., 2015. “*Foundation Damping and the Dynamics of Offshore Wind Turbine Monopiles*” *Renewable energy*, 80: pp.724-736.
- [9] Bak, C., Zahle, F., Bitsche, R., Kim, T., Yde, A., Henriksen, L.C., Hansen, M.H., Blasques, J.P.A.A., Gaunaa, M. and Natarajan, A., 2013. “*The DTU 10-MW Reference Wind Turbine*” Danish Wind Power Research, 27-28 May 2013, Denmark.
- [10] Murphy, G., Igoe, D., Doherty, P. and Gavin, K., 2018. “*Computers and Geotechnics 3D FEM Approach for Laterally Loaded Monopile Design*” *Computers and Geotechnics*, 100: 76-83.

NUMERICAL MODELLING OF CONSOLIDATION PROCESSES OF FINE-GRAINED DREDGED SEDIMENTS: THE CONTAINMENT FACILITY OF THE PORT OF GAETA

Armando de Lillis*, *Sapienza University of Rome*, armando.delillis@uniroma1.it

Giada Maria Rotisciani, *Sapienza University of Rome*, giada.rotisciani@uniroma1.it

Salvatore Miliziano, *Sapienza University of Rome*, salvatore.miliziano@uniroma1.it

ABSTRACT

Fine-grained dredged sediments can be efficiently handled by filling coastal confined containment facilities and then reclaim their area to integrate it into the port infrastructure. When large soil volumes are excavated, the dredging is typically performed hydraulically, transporting the soil as a slurry and depositing it into the containment facility. The dredged mud then settles at high void ratios before experiencing great volume reductions due to the self-weight consolidation. To investigate these processes, the numerical model presented herein was developed accounting for all the main phenomena involved, such as the variability of the soil hydromechanical behavior from very low to medium stress levels, the gradual filling and the large-strain consolidation. The model was then validated against a challenging case-study. Finally, a set of sensitivity analyses was performed to evaluate the influence of the soil parameters whose experimental determination suffers the most uncertainties. The results confirm the effectiveness of the proposed model and remark the great influence of the soil behavior at low stress levels on the overall response.

Keywords: Numerical Modelling, Large-Strain Consolidation, Hydraulic Dredging.

1. INTRODUCTION

Dredging activities near ports grew continuously over the course of the last few decades to meet the needs dictated by the increase in ships size and traffic, emphasizing the importance of finding adequate management options for huge amounts of dredged material. An environmentally-friendly way to dispose of the dredged soil is to re-use it to fill coastal confined containment facilities whose areas, once the soil has been properly improved, can easily be reclaimed and integrated into the port's infrastructure.

When large volumes of fine-grained soils are involved, the dredging is usually carried out hydraulically. The excavated soil is transported through pipes as a slurry, characterized by high volumetric water:to:solid ratios, and then deposited inside the containment facility where it experiences a combined sedimentation-consolidation process, with the former far quicker than the latter. Hence the soil settles at low stress levels (high void ratios) before its volume is greatly reduced by the development of effective stress associated with the self-weight consolidation.

Numerous contributions to the understanding of these phenomena have been recently proposed focusing on the experimental determination of the hydromechanical soil properties starting from very low stress levels (e.g. [1], [2], [3], [4], [5]) or on the numerical modelling of the entire boundary value problem (e.g. [6], [7], [8]).

This study focuses on the development of a numerical model apt to describe the distinctive features of this class of problems, such as the gradual filling of the containment facility, the variability of the soil hydromechanical behavior from very low to medium stress levels and the large-strain consolidation process.

The main objective of this work is to propose a robust and effective numerical tool that can be useful both at the design stage – for the determination of the maximum volume occupied by the dredged soil, for instance – and during works. To this end, the model has been validated simulating a well-documented case study, briefly described in paragraph 2, comparing numerical results and monitoring data (paragraph 3). Moreover, a sensitivity analysis, also reported in paragraph 3, has been carried out to investigate the influence of the hydromechanical soil parameters whose experimental determination suffers the most uncertainties.

2. DESCRIPTION OF THE CASE STUDY

The expansion project of the port of Gaeta (center Italy) included a 60 000 m² containment facility to be filled with fine-grained dredged material and then reclaimed to enhance the port infrastructure. Since the containment facility's volume was small with respect to the dredging volume (roughly 300 000 m³ against 370 000 m³), even without accounting for the increase in volume associated with the hydraulic dredging, an elaborate sequence of operations was designed in order to i) guarantee the deposition of all the dredging soil into the facility; ii) rapidly make the front pier fully operational with the new deeper seabed; iii) enable a quick reclamation of the area.

Prior to the start of the operations, prefabricated vertical drains were installed into the fine-grained foundation soils and hydraulically connected to a horizontal draining geo-composite placed on top of them. Then, the dredging was divided into three sub-phases of roughly equal volume. After the first and the second filling sub-phases, two further horizontal drainage layers, made of 4 m spaced micro-fissured pipes embedded in a geo-composite, were installed (Fig. 1). Once each layer was covered by roughly 1 m of dredged mud, the drainage pipes were connected to a system of vacuum pumps able to exert suction up to 60÷70 kPa. This is an atypical application of the classic vacuum consolidation technique originally proposed by [9].

This procedure allowed to i) accelerate the consolidation process and ii) increase the effective stress state of the dredged mud. This caused the dredged mud to quickly reduce its volume right after deposition – while the dredging was still underway – and therefore increased the capacity of the containment facility, allowing the whole dredging soil to be deposited. Further details about the project are reported in [10].

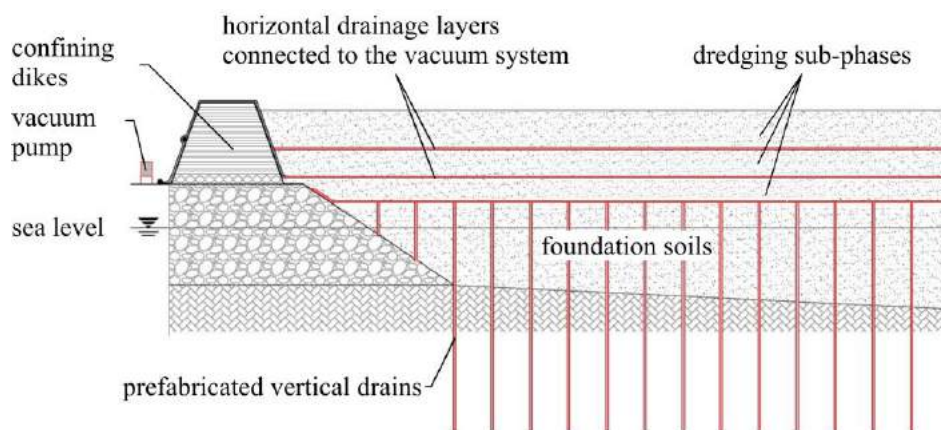


Figure 1. Construction scheme (modified from [10]).

3. NUMERICAL MODELLING

The boundary value problem was simulated adopting the finite element code Abaqus/Standard. The developed model is one-dimensional and accounts for all the distinctive features of the problem; geometric non-linearities associated with the large-strain consolidation processes are also considered.

Since the bottom is about coincident with the sea level, and hydraulically connected to it via the vertical drains, a zero-pore pressure condition is imposed. The vacuum pressures (60 kPa) are switched on over the course of 3 days once the corresponding drainage layer is covered by 1 m of dredged soil. At the upper boundary, a ponding surface condition is applied for the entire duration of the filling operation, consistently with the hydraulic filling of the containment facility. 30 days after the dredging completion, a 60 kPa suction is applied to the top over the course of 1 month, simulating the upwards propagation of the vacuum pressure associated with the evaporation of the ponding water.

The soil mechanical behavior was described adopting the well-known Modified Cam-clay model. To describe the high compressibility at low stress levels, a double Normal Consolidation Line (NCL), whose slope λ depends on the current void ratio, e , with respect to the one associated with the liquid limit, e_L (corresponding to an effective vertical stress, $\sigma'_v = 8$ kPa [11]), was introduced. Moreover, a strongly non-linear void ratio:permeability relation was formulated as $k = C \cdot e^D$, following [12]. Both constitutive relations were calibrated based on experimental data, as shown in Figure 2, where the variations adopted for the sensitivity analyses are also reported. The corresponding parameters are listed in Table 1. To account for site effects, the permeability coefficient was increased 5-fold when analyzing the boundary value problem.

The soil state is initialized at a post-sedimentation state, having $\sigma'_v = 0.1$ kPa and $e = 4.5$, as determined through laboratory sedimentation tests [10]. The gradual filling of the containment facility was simulated by creating the whole soil column at the start of the analysis and then exerting gravity on each element according to the actual rate of filling recorded during works. Between each filling sub-phase, a time interval is considered for the installation of the drainage system. The main phases of the simulation are listed in Table 2.

3.1. Results

The numerical results, expressed in terms of height of dredged soil, are reported in Figure 3 and compared with monitoring data recorded during the entire dredging campaign and the subsequent consolidation process.

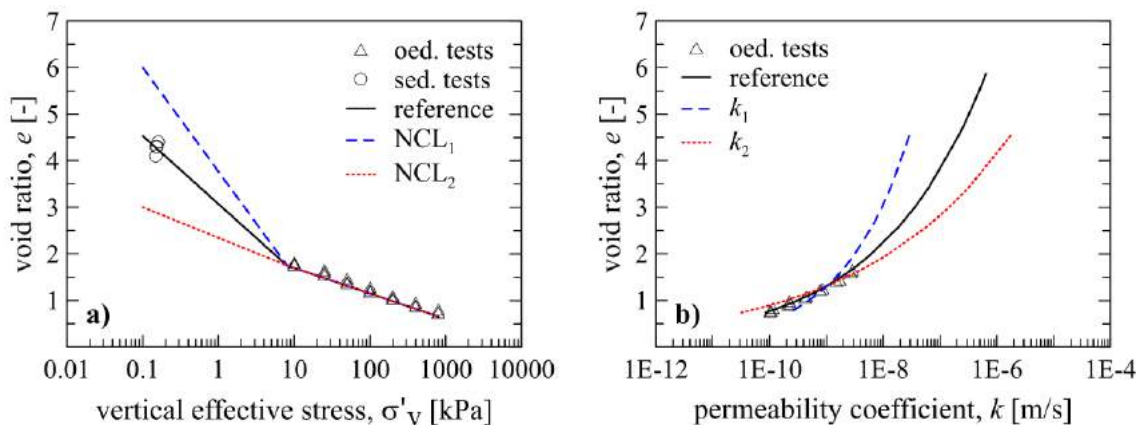


Figure 2. Constitutive relations: a) compressibility law; b) permeability law.

Table 1. Constitutive parameters.

Analysis	$\lambda_1 (e > e_L)$	$\lambda_2 (e < e_L)$	C [m/s]	D
Reference	0.634	0.239	$3.2 \cdot 10^{-10}$	4.3
NCL ₁	0.970		$3.2 \cdot 10^{-10}$	4.3
NCL ₂	0.285		$3.2 \cdot 10^{-10}$	4.3
k_1	0.634		$5.0 \cdot 10^{-10}$	2.7
k_2	0.634		$2.0 \cdot 10^{-10}$	6.0

Table 2. Phases of the simulation.

Phase	I fill	I drain install	II fill	I vacuum	II drain install	III fill	II vacuum	filling ends	top suction	final condition
Time [d]	0	16	60	65	84	129	137.5	154	186	330

Overall, the comparison confirms the effectiveness of the developed numerical model in reproducing the main phenomena involved (namely gradual filling, complex hydro-mechanical behavior, large-strains). Still, the numerical prediction overestimates the soil height during the whole process; the overestimation is equal to 57%, 19% and 11% at the end of the first, second and third dredging sub-phases respectively, and tends to reduce during the consolidation phases. In drained conditions the overestimation is about 10%. Since the effective stress state at the final drained conditions is at least 60 kPa, and the experimental determination of the related branch of the compressibility curve is quite reliable, the final difference is likely due to a misestimate of the in-situ void ratio of the dredging soil or to a not-negligible spill of dredged mud during filling.

3.2. Sensitivity Analyses

In order to investigate the differences between numerical results and field data, a set of sensitivity analysis was carried out focusing on the constitutive parameters whose determination suffers the most uncertainties. Hence, four further analyses were performed tweaking the permeability curve (k_1 and k_2) and the slope of the low-stress branch of the NCL (NCL₁ and NCL₂). The results are reported in Figure 4 and Figure 5, respectively.

To differentiate the hydraulic behavior between high and low void ratios, the permeability curve was changed applying a rotation. Adopting k_2 the permeability at low stresses is high enough to allow for the dissipation of the majority of excess pore pressures while the filling is taking place; vice versa, using k_1 , excess pore pressures accumulate rapidly during the filling stage causing the soil to reach greater heights and the subsequent consolidation process to be more pronounced.

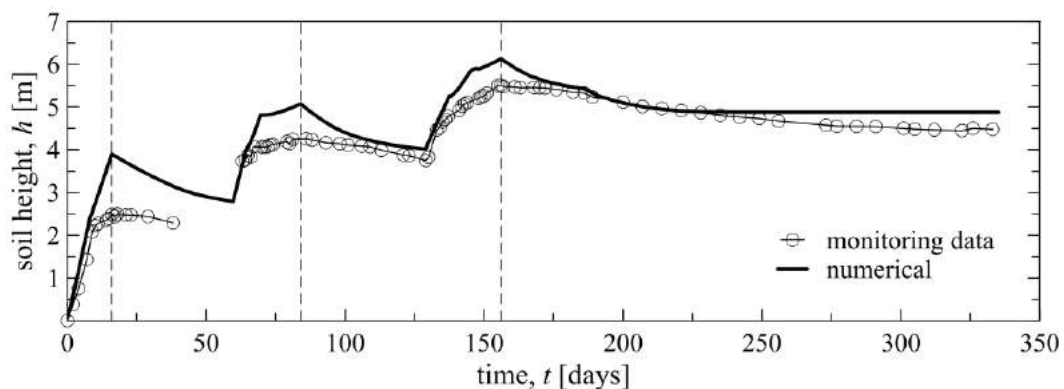


Figure 3. Comparison between numerical results and monitoring data.

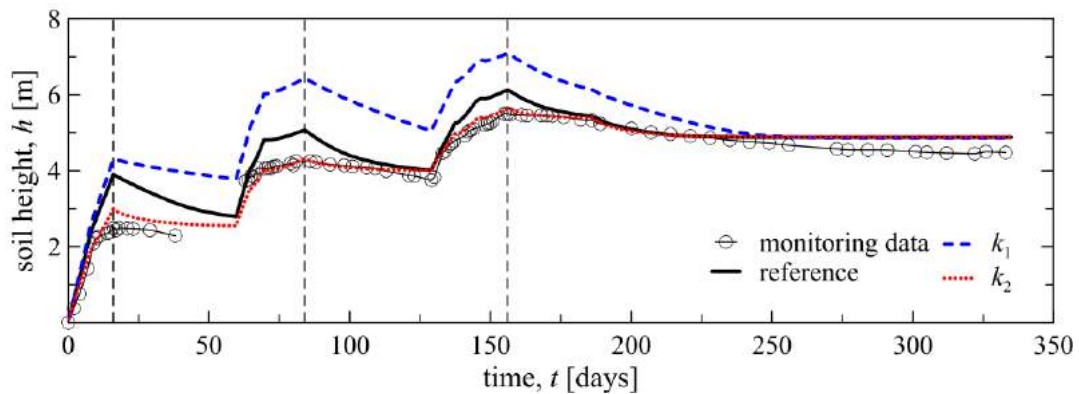


Figure 4. Parametric analyses: effects of the variation of the permeability curve.

At the end of the analysis, obviously, the three numerical curves coincide. The comparison shows a very good agreement between the k_2 -analysis and the monitoring data, except for the difference in drained conditions discussed above.

Adopting different NCLs, the dredged mud is deposited inside the containment facility at different void ratios; it is worth noting that, using the same permeability law, this implies different permeability for equal stress states.

The results of the NCL_1 -analysis show that the higher permeability of the dredged mud allows for a much faster consolidation rate. In fact, the dissipation of excess pore pressures is such that the height evolution in time follows closely that of the reference analysis even during the filling phases, when soil accumulation and consolidation processes occur at the same time. Adopting the NCL_2 , the dredged mud settles at a lower void ratio, hence occupying a lower volume inside the containment facility, and then consolidates at a slower rate due to its smaller permeability. The results compare rather well with the monitoring data, even though the best fit is obtained with the k_2 -analysis.

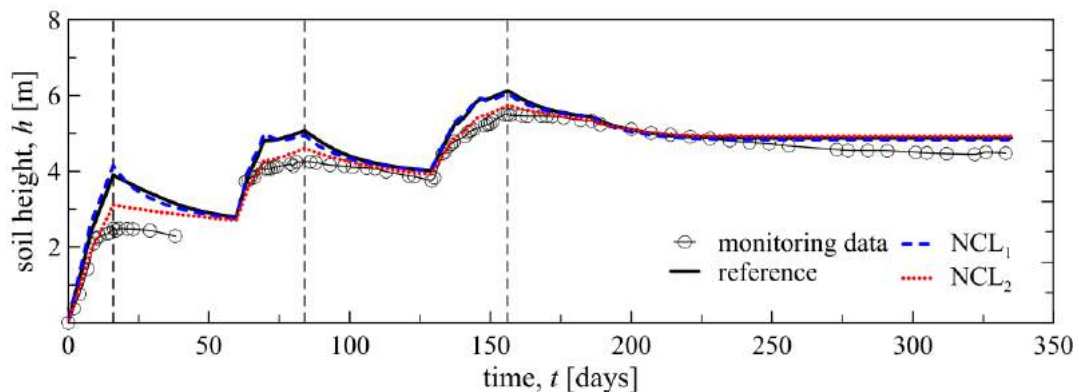


Figure 5. Parametric analyses: effects of the variation of the low-stress branch of the NCL.

4. CONCLUSIONS

This study focused on improving the understanding of the major phenomena involved in the behavior of fine-grained dredged sediments hydraulically placed in containment facilities, such as the gradual filling, the variability of the soil hydromechanical behavior starting from very low stress levels and the large-strain consolidation process.

To this aim, an advanced numerical model was developed and validated simulating a challenging and well-documented case study obtaining overall satisfactory results even though the numerical prediction overestimated the soil height evolution throughout the process.

To further investigate the difference between numerical results and monitoring data, a set of sensitivity analyses was performed focusing on the soil parameters whose experimental determination suffers the most uncertainties. This allowed to better understand the great influence of the soil behavior at very low stress levels on the overall response.

The numerical results confirm the effectiveness of the proposed model and remark its usefulness, both as a design tool and during works, especially in cases of small containment facilities, where unconventional procedures must be adopted.

REFERENCES

- [1] Stark, T.D., Choi, H., Schroeder, P.R., 2005. “*Settlement of Dredged and Contaminated Material Placement Areas. II: Primary Consolidation, Secondary Compression, And Desiccation of Dredged Fill Input Parameters*”, *Journal of Waterway, Port, Coastal and Ocean Engineering*, 131(2): 52-61.
- [2] Berilgen, S.A., Berilgen, M.M., Ozaydin, I.K., 2006. “*Compression and Permeability Relationships in High Water Content Clays*”, *Applied Clay Science*, 31(3-4): 249-261.
- [3] Chong, S.H., Santamarina, J.C., 2016. “*Soil Compressibility Models for a Wide Stress Range*”, *Journal of Geotechnical and Geoenvironmental Engineering*, 142(6): 06016003.
- [4] Ma, J., Qian, M., Yu, C., Yu, X., 2018. “*Compressibility Evaluation of Reconstituted Clays with Various Initial Water Contents*”, *Journal of Performance of Constructed Facilities*, 32(5): 04018077.
- [5] Felici, M., Domizi, J., Fratolocchi, E., 2018. “*Consolidation of Dredged Sediments in a Confined Disposal Facility: Hydraulic Conductivity Constitutive Relations*”, 8th International Congress on Environmental Geotechnics, pp. 288-294, Singapore.
- [6] Agapito, L. A., Bareither, C. A., 2018. “*Application of a One-Dimensional Large-Strain Consolidation Model to a Full-Scale Tailings Storage Facility*”, *Minerals Engineering*, 119: 38-48.
- [7] de Lillis, A., Miliziano, S., Flora, A., Fasano, G., 2017. “*Reclamation of a Containment Area: Measurements and Back Analysis of the Height of Dredged Mud*”, 19th International Conference on Soil Mechanics and Geotechnical Engineering, pp. 2965-2968.
- [8] Indraratna, B., Rujikiatkamjorn, C., Ameratunga, J., Boyle, P., 2011. “*Performance and Prediction of Vacuum Combined Surcharge Consolidation at Port of Brisbane*”, *Journal of Geotechnical and Geoenvironmental Engineering*, 137(11): 1009-1018.
- [9] Kjellman, W., 1952. “*Consolidation of Clayey Soils by Atmospheric Pressure*”, *Conference on Soil Stabilization*, pp. 258-263, Boston.
- [10] de Lillis, A., Miliziano, S., 2016. “*Geotechnical Aspects of the Design of the Containment Area of the Port of Gaeta*”, *Italian Geotechnical Journal*, 50(4): 3-22.
- [11] Skempton, A.W., 1969. “*The Consolidation of Clays by Gravitational Compaction*”, *Quarterly Journal of the Geological Society*, 125: 373-411.
- [12] Krizek, R.J., Somogy, F., 1984. “*Perspectives on Modelling Consolidation of Dredged Materials*”, *Symposium on Sedimentation-Consolidation Models: predictions and validation*, pp. 296-332.

SEISMIC BEHAVIOUR OF LATERALLY DISCONNECTED SHALLOW FOUNDATIONS

Viviana Mangraviti*, *Politecnico di Milano, viviana.mangraviti@polimi.it*

Orazio Casablanca, *Università di Messina, ocasablanca@unime.it*

Giovanni Biondi, *Università di Messina, gbiondi@unime.it*

Claudio di Prisco, *Politecnico di Milano, claudio.diprisco@polimi.it*

Ernesto Cascone, *Università di Messina, ecascone@unime.it*

ABSTRACT

Taking into consideration the dynamic interaction between structure and foundation soil is generally recognized to allow a beneficial reduction in the forces acting on the superstructure, since the natural period of superstructure plus foundation soil is longer than that of its fixed-base counterpart. An additional beneficial contribution is given by plastic strains developing in the “near field” causing a not negligible reduction in the energetic content of the input.

The paper examines, in case of embedded foundations, the effects of removing the lateral ground on the dynamic soil-structure interaction. The proposed lateral disconnection produces a change in both the stiffness and the damping ratio of the overall system. It also causes a parasite effect: a shrinkage of the foundation interaction domains and an increase in base rotations. All these factors are taken into account in the paper and a procedure is presented to design the trenches to be excavated. A parametric analysis is carried out by varying (i) the dimensions of the lateral disconnection; (ii) the stiffness of the soil. The obtained results are presented and discussed in the paper, focusing on the effectiveness of the proposed lateral disconnection. In a series of specific cases, it is demonstrated that a proper selection of the lateral disconnection width allows a suitable increase in the natural period of the soil-structure system significantly reducing the seismic actions on the superstructure, so improving the performance of existing buildings under seismic conditions.

Keywords: Soil-Structure Interaction, Earthquake Engineering, Foundations Engineering.

1. INTRODUCTION

The structural damages occurred during the last earthquakes in Central (2016-2017) and Northern Italy (2012) are reminders that despite the modern achievements in earthquake engineering technology, many existing masonry structures and historical buildings (widespread in zones that have been recently identified as seismic) are not safe under seismic conditions.

Theoretically, an earthquake resistant design should allow to minimize, regardless both the magnitude and the epicentre location, earthquakes induced damages. To achieve this goal, since the 1960s, both Structural (SSI) and Geotechnical (GSI) Seismic Isolation systems have been developed. However, conventional SSI systems can be quite expensive to implement and maintain. As a consequence, only strategic structures are commonly provided by these devices.

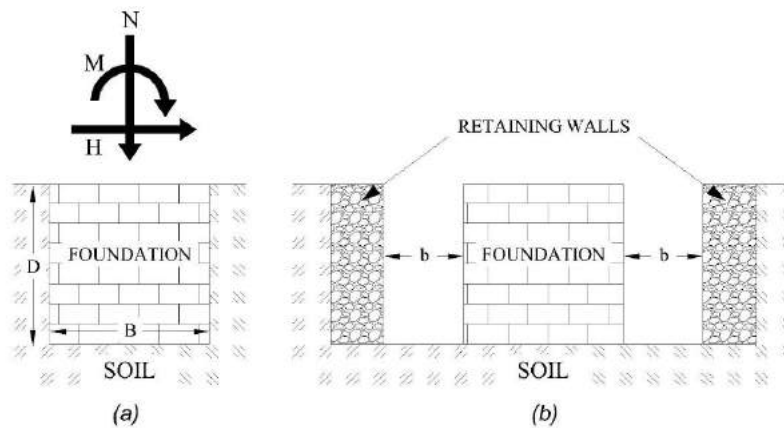


Figure 1. (a) Connected foundation and acting forces; (b) Disconnected foundation

In contrast, to the commonly used SSI systems ([1], [2], [3]) in which either the sliding or flexible interfaces are positioned between structure and foundation, the GSI systems directly operate as artificial seismic barriers by employing natural earth materials and/or man-made reinforced earth materials [4].

When the dynamic input comes from the superstructure, isolation systems are commonly designed by employing of vibration screening, initially proposed by Woods [5] and then developed to intercept, scatter, and diffract surface waves by means of barriers such as trenches [6], sheet-pile walls [7], and piles [8]. Most of this kind of interventions are nowadays successfully employed as wave barriers to mitigate ground vibrations from railways and machine foundations. More recently, subsoil interventions as seismic isolators have been proposed by Kirtas et al [9] [10], Lombardi et al. [11] and Flora et al. [12].

This paper intends to analyse the effectiveness of lateral disconnections in reducing the actions on the superstructure induced by earthquakes. The excavation of a trench around an existing foundation proposed herein aims at increasing the natural period of the soil-foundation-structure system rather than operate as wave barrier, leading to an increase in natural period of overall system. The idea of physically disconnecting the foundation arises from the possibility of combining the effectiveness of a reduction in the horizontal loads affecting the superstructure under seismic conditions with the simplicity of application of this technical solution for existing structures. However, together with the advantageous reduction in seismic actions, the removal of the ground adjacent to the foundation is unfortunately associated with both a reduction in the foundation bearing capacity and in an increase in rotation under horizontal loads. The disconnection will be a successful isolation system if its net effect is beneficial in terms of both seismic safety conditions and post-seismic serviceability of the structure.

2. METHODOLOGY

To describe the approach proposed by the Authors, hereafter a strip footing B wide and placed at a depth D from the ground surface (Figure 1.a) has been considered. For the sake of simplicity, the dynamic effect of the superstructure on the foundation has been reduced to the equivalent generalized forces N , H and M (denoting respectively vertical and horizontal forces and overturning moment) statically applied. With the aim of studying the effectiveness of the lateral disconnection b wide (Figure 1.b), the theoretical procedure considers: (i) the reduction in stiffness of the overall soil-foundation-structure system; (ii) the reduction in bearing capacity

due to the removal of the lateral soil; (iii) a push-over curve for the foundation in terms of overturning moment.

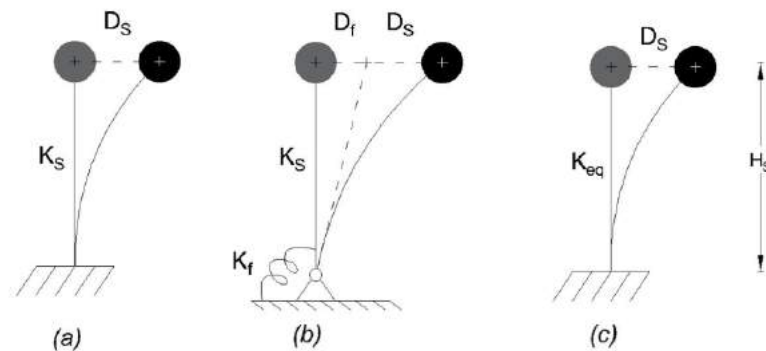


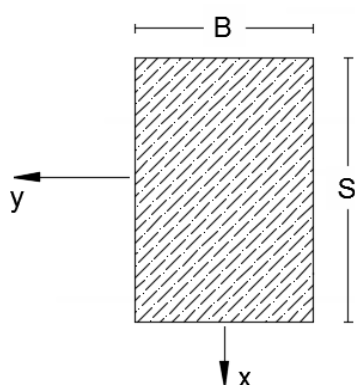
Figure 2. (a) structure perfectly fixed to the base; (b) structure free to rotate at the base; (c) structure with equivalent stiffness perfectly fixed to the base [13]

2.1. Reduction in the Overall Stiffness

Frequently, the capability of the soil foundation to deform under seismic loading is disregarded by considering a fixed base model (Figure 2.a). In order to account for the possibility of base rotation due to both the soil compliance and the realized disconnection, a flexibly-supported structure can be considered (Figure 2.b). According to Wolf [13] if K_f denotes the stiffness of the soil-foundation system to the rotational mode, an equivalent fixed-base system of stiffness K_{eq} can be defined (Figure 2.c):

$$K_{eq} = \frac{K_S D_S}{D_S + D_f} = \frac{K_S}{1 + H_S^2 \cdot K_S / K_f}, \quad (1)$$

in which K_S is the shear stiffness of the structure; D_S stands for the structural horizontal displacement; D_f for the lateral displacement due to the rotational capability of the foundation and H_S for the height of the equivalent SDOF system (Figure 2.c). The procedure to evaluate K_S is well established. Owing to the non-linear behaviour of the foundation soil when subject to dynamic loads, the stiffness K_f depends on: (i) the nature and the stiffness of the supporting soil and (ii) the geometry and the inertia of the foundation. To take into account all these factors the solutions proposed by Gazetas [14] are adopted herein (**Error! Reference source not found.**).



$$K_{f,sur} = \frac{G}{1 - \nu} I_{bx}^{0.75} \left(\frac{S}{B} \right)^{0.25} \left(2.4 + 0.5 \frac{B}{S} \right)$$

$$K_{f,emb} = K_{f,sur} \cdot \mu_{r0x}$$

$$\mu_{r0x} = 1 + 1.26 \frac{2D}{B} \left(1 + \frac{2D}{B} \sqrt{\frac{B}{S}} \right) \text{ stiffness ratio}$$

I_{bx} area moment of inertia of the foundation-soil contact surface around the x axis

Figure 3. Gazetas' formulas for foundations with perfect contact between sidewall and soil

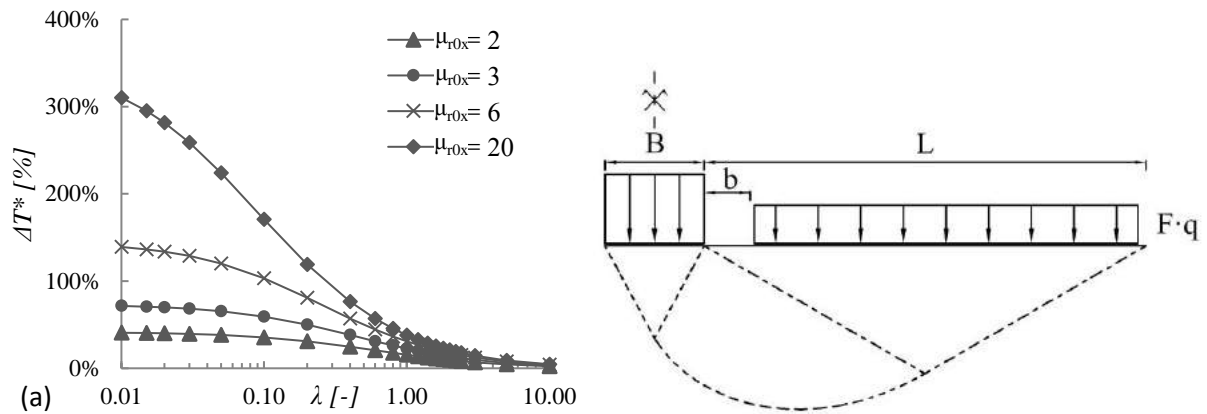


Figure 4. (a) Increase in natural period for fixed μ_{r0x} by varying the interaction ratio (λ) (b) Removal of lateral load (q) on the failure mechanism through the reduction factor (F)

The soil-foundation stiffness for shallow foundations is denoted as $K_{f,sur}$, whereas $K_{f,emb}$ is the stiffness of embedded foundations. Herein, in the disconnected case $K_{f,sur}$ is employed ($K_{f,dis} = K_{f,sur}$) whereas in the connected case $K_{f,emb}$ has been used ($K_{f,con} = K_{f,emb}$). In the solution proposed by Gazetas the soil-foundation stiffness depends on (i) shear modulus G and Poisson ratio ν of the foundation soil; (ii) moment of inertia I_{bx} of the foundation-soil contact area around x -axis; (iii) shape (S/B) and depth (D/B) ratios that influencing stiffness ratio μ_{r0x} . Since $\mu_{r0x} > 1$, $K_{f,dis} < K_{f,con}$, therefore the disconnection causes an increase in the natural period of the equivalent system ($T_{dis} > T_{con}$). By using the Wolf's model (Figure 2 **Error! Reference source not found.**) and the Gazetas' formulas (**Error! Reference source not found.**):

$$\Delta T^* = \frac{T_{dis} - T_{con}}{T_{con}} = \sqrt{\mu_{r0x} \frac{(\lambda + 1)}{\mu_{r0x} \cdot \lambda + 1}} - 1, \quad (2)$$

where $\lambda = K_{f,dis} / (H_s^2 K_s)$ is the interaction ratio. The dependence of ΔT^* on λ for different stiffness ratios is plotted in Figure 4.a. The range of variation of μ_{r0x} is evaluated by considering $S/B = 1 \div 10$ and $D/B = 0,1 \div 3$.

2.2. Reduction in Bearing Capacity

In order to determine the failure mechanism loci, for both the connected and the disconnected soil foundation systems, the non-dimensional representation proposed by di Prisco et al. [15] is used:

$$\left(\frac{H}{N_{max} - N_{min}}\right)^2 + \left(\frac{M}{B(N_{max} - N_{min})}\right)^2 - \left[\frac{N}{N_{max} - N_{min}} \left(1 - \frac{1}{\mu}\right)\right]^{2\delta} \left[1 - \frac{N}{N_{max} - N_{min}} \left(1 + \frac{1}{\psi}\right)\right]^{2\epsilon} = 0, \quad (3)$$

where δ , ϵ , μ and ψ are static numerical coefficients defining the shape of the interaction domain. N_{max} and N_{min} are, respectively, the bearing capacity under positive and negative values of vertical loads for $H = M = 0$. The static interaction domains described by Eq. 3 have been improved by considering the inertia forces acting within the soil foundations due to the seismic actions [16] for homogeneous foundation soils. Accordingly, N_{max} has been calculated as follows:

$$N_{max} = B \left(\frac{1}{2} \gamma B i_\gamma s_\gamma d_\gamma N_\gamma + q i_q s_q d_q N_q F \right), \quad (4)$$

where γ is the soil unit weight, q is the lateral surcharge, i_γ and i_q are the inclination factors, s_γ and s_q are the shape factors, d_γ and d_q are the depth factors, N_γ and N_q are the bearing capacity

factors directly depending on soil friction angle φ' , horizontal (k_h) and vertical (k_v) seismic acceleration coefficients.

By considering the failure mechanism plotted in **Error! Reference source not found.**b, the lack of the soil adjacent to the foundation causes a reduction in the lateral load (L wide) assumed to be applied aside the foundation when disconnection is not realized. Coefficient F (Eq. 5) takes into account the reduction in the bearing capacity of the footing due to a disconnection b wide and, for the sake of simplicity:

$$F = \frac{L-b}{L} \quad (5)$$

F is equal to 1 in case of connected foundations. When $b > L$ the reduction coefficient (F) is equal to 0, causing a strong reduction in the bearing capacity of the foundation. For this reason, the designer is expected to properly modify b to optimize the intervention. L is calculated by means of the characteristic lines method. By varying the value of N_{\max} and N_{\min} (nil for disconnected foundations) the interaction domains in H - N , M - N and H - M planes for connected and disconnected systems are evaluated.

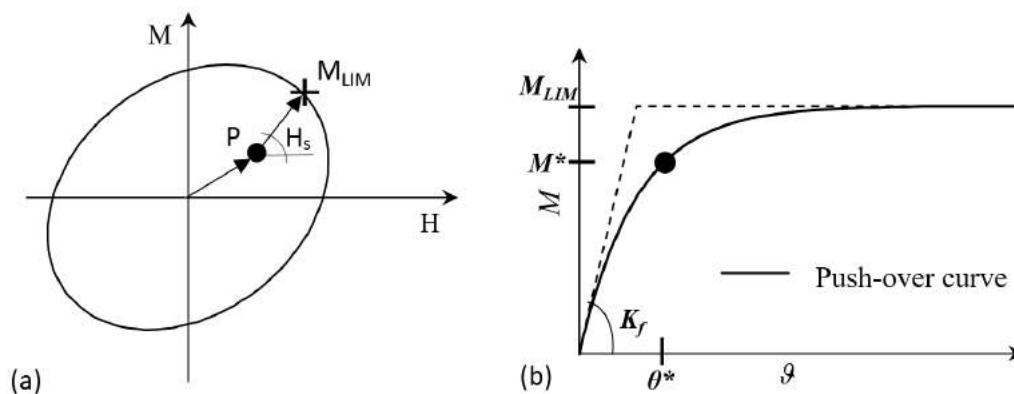


Figure 5. (a) limit value of the bending moment evaluated on the interaction curve for fixed static load configuration; (b) push-over curve evaluated by means of Butterfield's interpolation

2.3. Increase in Base Rotation

In order to calculate the rotation at the foundation level, a push-over analysis in terms of M and ϑ (foundation rotation) is performed. Once the interaction domain is assigned (§ 2.2) and, in particular, its H - M domain is obtained (Figure 6.a), the push-over curve for the foundation can be obtained by using the Butterfield's law [17] interpreted in terms of M and ϑ :

$$M/M_{LIM} = 1 - \exp(-K_f \cdot \vartheta/M_{LIM}) . \quad (6)$$

The shape of the push-over curve is directly related to K_f (Figure 3) and to the limit bending moment, M_{LIM} . This latter has been evaluated by starting from the static load acting on the foundation (point P in Figure 5.a) and by individuating on the failure locus as is suggested in **Error! Reference source not found.**Figure 6.a. The generalized stress path is inclined of H_s since seismic loads are considered to be applied at the top of the equivalent SDOF in Figure 2.c. Once the push-over curve is obtained and the maximum seismic action transmitted by the superstructure to the foundation (M^*) is known, the corresponding rotation (θ^*) can be evaluated by means of Figure 5.b.

3. EXAMPLES

For the sake of brevity, in order to verify the effectiveness of the intervention, the proposed procedure has been applied to the case of a one-story building based on isolated plinths. The geometry of the overall system has been maintained unaltered. In particular, at the foundation level, μ_{r0x} has been fixed by setting $D/B = 1$, $S/B = 1$, $B = 1$. Both the soil and the design spectrum parameters reported in Table 1 have been assumed to be constant. On the contrary different values for shear modulus G and disconnection width b have been considered in cases 1 and 2 (Table 2).

Table 1. Stiffness ratio, soil properties and design spectrum parameters (NTC18 [17])

μ_{r0x} [-]	c' [kPa]	φ' [°]	ν [-]	γ [kN/m ³]	a_g [g]	F_0 [-]	T_c^* [s]	q [-]
8.6	0	30	0.3	18	0.215	2.482	0.341	4.0

Table 2. Cases 1 and 2: shear modulus G , b/B ratio, interaction ratio λ and natural period of the connected (T_{con}) and disconnected (T_{dis}) system

Case	G	b/B	λ	T_{con}	T_{dis}
1	192.0 MPa	0.5	1.52	0.21 s	0.27 s
2	11.5 MPa	0.3	0.1	0.31 s	0.71 s

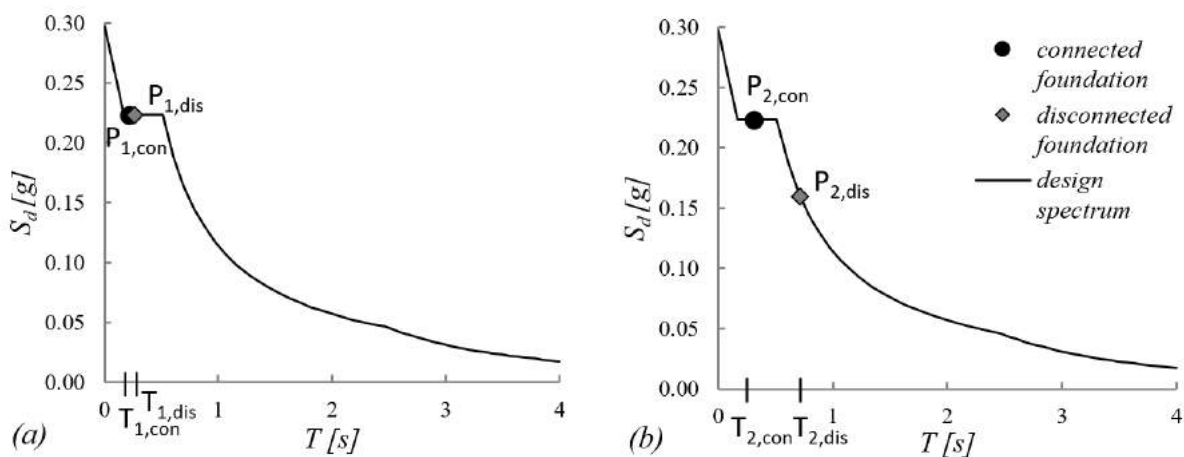


Figure 6. Design spectrum and seismic actions corresponding to connected and disconnected foundation: (a) case 1; (b) case 2.

As is evident from Figure 6 and Table 2, in case 1 the high value of λ leads to a small variation in the period (Eq. 2) and, since P_{1dis} is placed on the plateau of the spectrum, a nil variation in the seismic input is obtained. In this case, the lateral disconnection has no effect on the actions but reduces the bearing capacity of the foundation. For this reason, the intervention is not beneficial. By contrast, in case 2 a marked variation in the natural period causes a relevant reduction in the input acceleration (Figure 6**Error! Reference source not found.**b). This induces a significant reduction in both the horizontal and bending moment acting on the

foundation (Figure 7.a). The disconnection causes also a slight reduction in the interaction domain (dashed line in Figure 7.a). In this case, the net effect of the proposed intervention is positive. This is emphasized by Figure 7.b where the overturning moment associated with $P_{2,con}$ is larger than the maximum overturning moment can be applied to the foundation, whereas, when the disconnection is realized, the maximum footing rotation is equal to $0,3^\circ$.

4. CONCLUSIONS

A procedure to evaluate the effects induced by lateral disconnections on shallow foundations under seismic actions has been described. The results put in evidence that the effectiveness of this intervention is closely related to (i) the initial period of the overall system and the shape of the design spectrum; (ii) the interaction ratio related to the soil and the super structure stiffness; (iii) the size of the disconnection width.

The use of the proposed intervention can provide an alternative way of taking advantage of both the non-linear behaviour of the soil and the increase in the period of the soil-foundation-structure system.

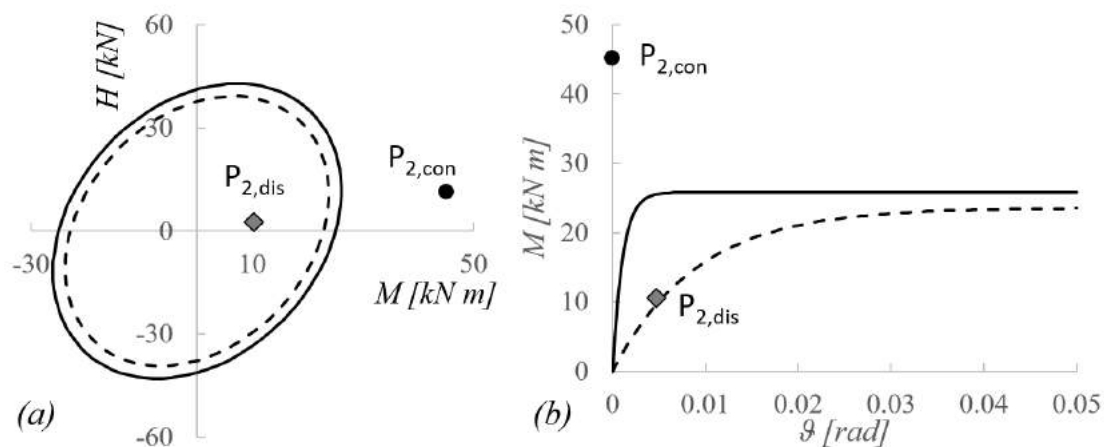


Figure 7. Case 2 results: (a) interaction domain M - H and current actions on both connected (solid line and point $P_{2,con}$) and disconnected (dashed line and point $P_{2,dis}$) foundation; (b) push over curves and acting moment in case of both connected (solid line and $P_{2,con}$) and disconnected foundation (dashed line and point $P_{2,dis}$).

REFERENCES

- [1] Skinner, R.I., Robinson, W.H., Mc Verry, G.H. 1993. "Seismic Isolation", Chichester, England: Wiley.
- [2] Naeim, F., Kelly, J.M. 1999. "Design of Seismic Isolated Structures: From Theory to Practice". New York, U.S.A.: Wiley
- [3] Kelly, J.M. 1997. "Earthquake-resistant Design with Rubber". (2nd ed.) London, U.K.: Springer.
- [4] Tsang, H-H, Lo, S.H., Xu, X., Neaz Sheikh, M. 2012. "Seismic isolation for low-to-medium-rise buildings using granulated rubber-soil mixtures: numerical study". Signal Eng Struct Dyn 41: 2009–2024.
- [5] Woods, R.D. 1968. "Screening of surface waves in soils". Journal of the Soil Mechanics and Foundations Division (ASCE), 94(SM4): 951–979.

- [6] Beskos, D.E., Dasgupta, B., Vardoulakis, I.G. 1986. “*Vibration isolation using open or filled trenches*”. Computational Mechanics. 1: 43-63.
- [7] Andersen, L. & Liingaard, M. 2005. “*Environmental Vibrations: Prediction, Monitoring, Mitigation and Evaluation*” (ISEV 2005). In H. Takemiya (eds.). Vibration screening with sheet pile walls: 429 – 437 United Kingdom: Taylor & Francis/Balkema.
- [8] Liao, S. & Sangrey, D.A. 1978. “*Use of piles as isolation barriers*”. Journal of the Geotechnical Engineering Division (ASCE) 104 (GT9): 1139–1152.
- [9] Kirtas, E., Rovithis, E., Pitilakis, K. 2009a. “*Subsoil interventions effect on structural seismic response. Part I: validation of numerical simulations. Journal of Earthquake Engineering*”. 13 (2): 155–169.
- [10] Kirtas, E. & Pitilakis, K. 2009b. “*Subsoil interventions effect on structural seismic response. Part II: parametric investigation*”. Journal of Earthquake Engineering. 13 (3): 328–344.
- [11] Lombardi, D., Flora, A., Lirer, S., Silvestri, F. 2014. “*Soil grouting for the seismic protection of existing buildings*”. Proceedings of the Institution of Civil Engineers: ground improvement. 167(3):206–218.
- [12] Flora, A., Lombardi, D., Nappa, V., Bilotta, E. 2018. “*Numerical analyses of the effectiveness of soft barriers into the soil for the mitigation of seismic risk*”. Journal of Earthquake Engineering. 22 (1), 63-93.
- [13] Wolf, J. P. 1985. “*Dynamic Soil-Structure Interaction*”. Englewood Cliffs, N. J., U.S.A.: Prentice Hall.
- [14] Gazetas G. 1991. “*Foundation vibrations*”. Chapter 15. Foundation Engineering Handbook (2nd edition). Fang H-Y (ed.). New York: Van Nostrand, Reinhold.
- [15] di Prisco, C., Nova, R., and Corengia, A. 2004. “*A model for landslide-pipe interaction analysis*”. Soils and foundations 44 (3): 1-12.
- [16] Cascone, E. & Casablanca O. 2016. “*Static and seismic bearing capacity of shallow strip footings*”. Soil Dynamics and Earthquake Engineering. 84: 204-223.
- [17] Butterfield, R. 1980. “*A simple analysis of the load capacity of rigid footings on granular materials*”. Géotechnique. 44: 128-134.
- [18] NTC18, 2018. Italian Standards: “*Normativa Tecnica delle Costruzioni*”.

LIQUEFACTION HAZARD ASSESMENT AND ZONIING BASED ON IN-SITU INVESTIGATIONS – CASE STUDY

Chaneva Jordanka*, *MSc, Institute of Earthquake Engineering and Engineering Seismology, Skopje, dance@iziis.ukim.edu.mk*

Bojadjieva Julijana, *PhD, same as above, jule@iziis.ukim.edu.mk*

Sheshov Vlatko, *PhD, same as above, vlatko@iziis.ukim.edu.mk*

Edip Kemal, *PhD, same as above, kemal@iziis.ukim.edu.mk*

Kitanovski Toni, *MSc, same as above, tonik@iziis.ukim.edu.mk*

ABSTRACT

A liquefaction potential zoning of a selected area of interest is presented in this paper. The case study location is the city of Ohrid, Southwest Macedonia. Situated on the Coast of Ohrid Lake, the soil for this location is characterized with high groundwater tables and complex geology, consisting of relatively loose saturated sand layers, with low to high content of fines. Based on available SPT in-situ investigations, the susceptibility and potential for liquefaction of representative soil profiles were defined. For this purpose, the deterministic and probabilistic relations proposed by Boulanger and Idriss were used. As for the seismic hazard, Ohrid is located in an area appointed with medium level seismicity. Two seismic scenarios by means of PGA and Mw were selected for evaluating the CSR (cyclic stress ratio) as the dynamic input for each soil layer. The liquefaction potential was then evaluated as an Fs (factor of safety against liquefaction) and PL (probability of liquefaction). A proper methodology for local zoning was made, and four liquefaction potential maps were obtained as the final result – Fs and PL maps for the two selected seismic scenarios.

The results led to several conclusions related to the soil conditions and characteristics, the advantages of the in-situ methods, the need for additional on-site investigations as well as comparison between deterministic and probabilistic approaches. Moreover, the necessity for this type of investigations as a preventative measure for urban planning, was commented as well.

Keywords: Liquefaction, Hazard, Mapping, SPT

1. INTRODUCTION

The simplified procedures based on in-situ investigations (SPT, CPT) for liquefaction potential assessments can be considered as the dominant approach for liquefaction potential assessment when analyzing a larger area. Their advantages are mainly related with the difficulties and costs associated with good quality undisturbed sampling for high-quality laboratory testing. Moreover the same factors that affect the SPT/CPT resistance of soils, affect the liquefaction resistance (i.e. overconsolidation, non-uniformity, density, fines content etc.) as well.

There are several simplified procedures that are used in practice (Youd et al. 2001, Cetin et al. 2004, Idriss and Boulanger 2006, 2010, 2014). The methodologies are empirical relations based on a selected data base of case histories. Both deterministic and probabilistic empirical

approaches based on SPT investigations, proposed by Idriss and Boulanger (2010), were used for the purpose of the research presented in this paper.

Being the most common in-situ investigation in the engineering practice in Republic of Macedonia, along with the fact that it is “favored” in EUROCODE 8 for this type of assessment, is mostly why the SPT method was chosen for the presented case study.

The liquefaction potential can be expressed as a factor of safety against liquefaction (F_s) or as a probability for liquefaction (PL). The probabilistic liquefaction triggering models are crucial for developing the relatively new framework for evaluating liquefaction hazards - the Performance-based liquefaction assessment procedure (Kramer et al., 2006).

Up until this research, a relatively small number of investigations and assessment of this type were performed in Macedonia, (Cubrinovska, 2009, Sheshov et al. 2012, Bojadjieva et al. 2013, Bojadjieva et al. 2016) and for smaller areas (building sites of prospective structures of a higher importance class), fully based on deterministic approaches. The case study area is considered as a location with complex geological conditions, with soil layers susceptible to liquefaction and relatively high ground water tables. Moreover, the newest seismic hazard maps for R. Macedonia (Figure 3), upgraded the seismicity level of the region, from an area with moderate level of seismicity to relatively high level seismicity. Even with these unfavorable factors, the recent history of an array of earthquakes (the highest magnitude $M_w > 5$), was not followed with recorded liquefaction phenomena occurrences. The last fact imposed the question of the probability of liquefaction for this location and a parallel assessment of deterministic and probabilistic approaches for deriving the final results.

2. STUDY AREA

The case study location is the city of Ohrid, located in southwest Macedonia, on the coast of the Ohrid Lake. Along with the Ohrid Lake it is accepted as Cultural and Natural World Heritage by UNESCO (1979 and 1980 respectively). Thus it has been always considered as a city of a great importance. Available geological investigations and state maps show that the soil in and around the city is generally composed of surface Quaternary and deep Pliocene sediments (Figure 1).

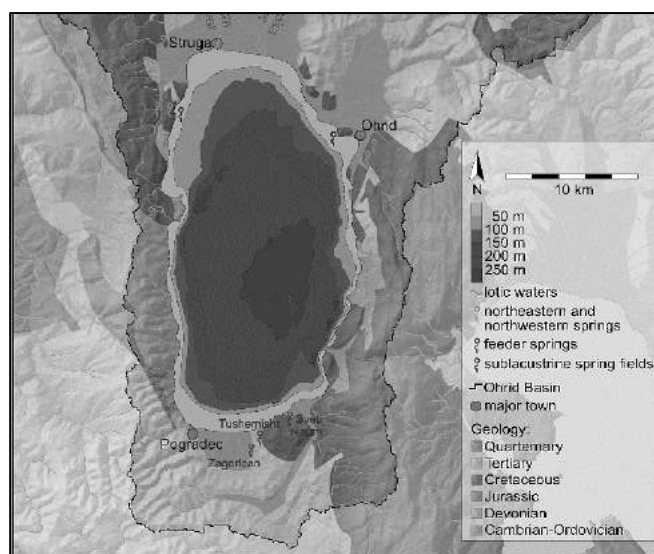


Figure 1. Map of the Ohrid basin showing major hydrological and geological features. (Hauffe et al. (2011)).

The Quaternary sediments are composed of silty materials composed of fine gravel and sand as well as organic clays and silty sand. The thickness of the Quaternary sediments reaches down to a depth of 20 m. These sediments are of a heterogeneous nature and are characterized by unfavourable physical-mechanical characteristics. The Pliocene sediments are composed of clays, sands and gravels characterized by much better physical-mechanical characteristics than those of the Quaternary sediments. The thickness of these sediments reaches down to a depth of 100 m. The underground water level is generally high in most of the investigated locations due to the vicinity of the Ohrid Lake. SPT and additional geotechnical investigations were performed (GEING Krebs und Kiefer International, Skopje) and available for 16 locations (Figure 2).

For each location, the liquefaction susceptibility of each layer was primarily assessed. Most of the soil profiles were consisted of one (to max 2) liquefiable layers, thus the liquefaction potential assessment was carried out with the purpose to obtain the critical layer. Therefore, the interpolation for the local zoning later on was based on the obtained values for F_s and PL for the critical layer of each location, instead of a liquefaction potential index map (LPI), mostly used for this type of mapping.

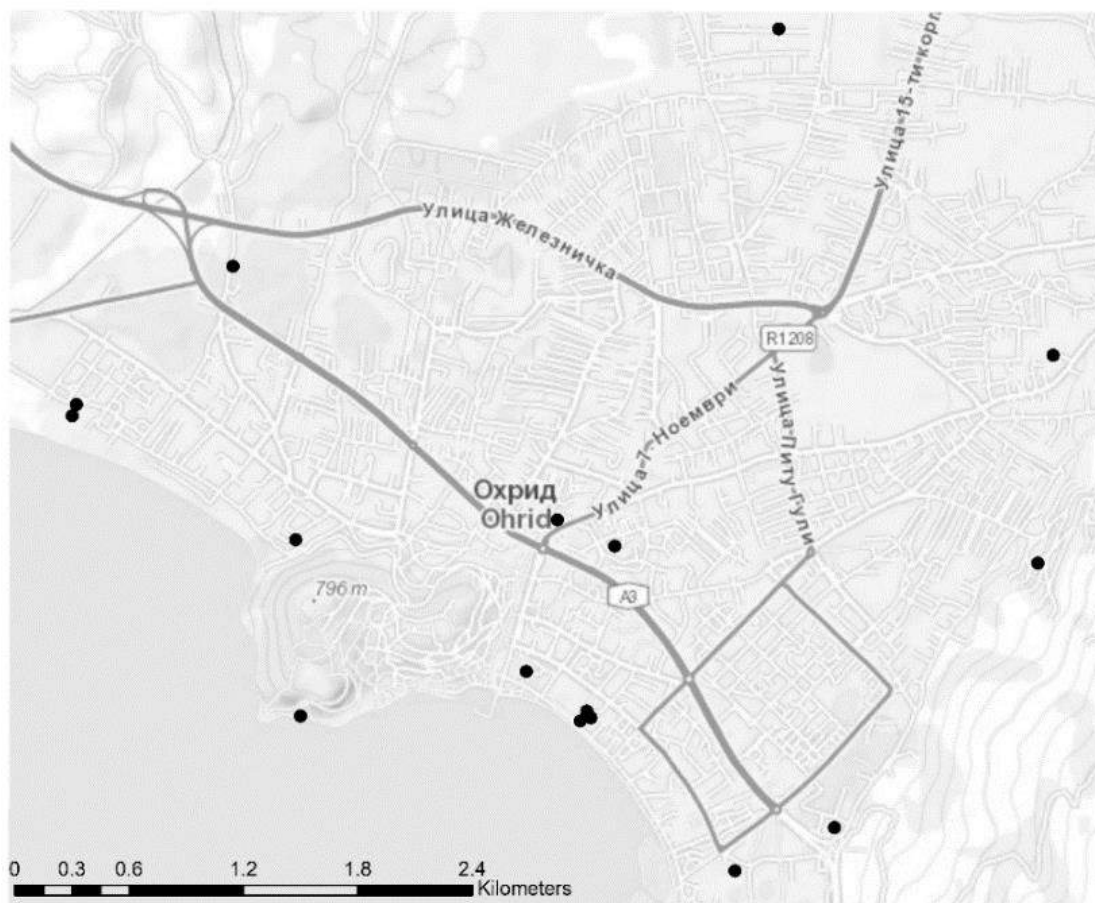


Figure 2. Locations of SPT investigations

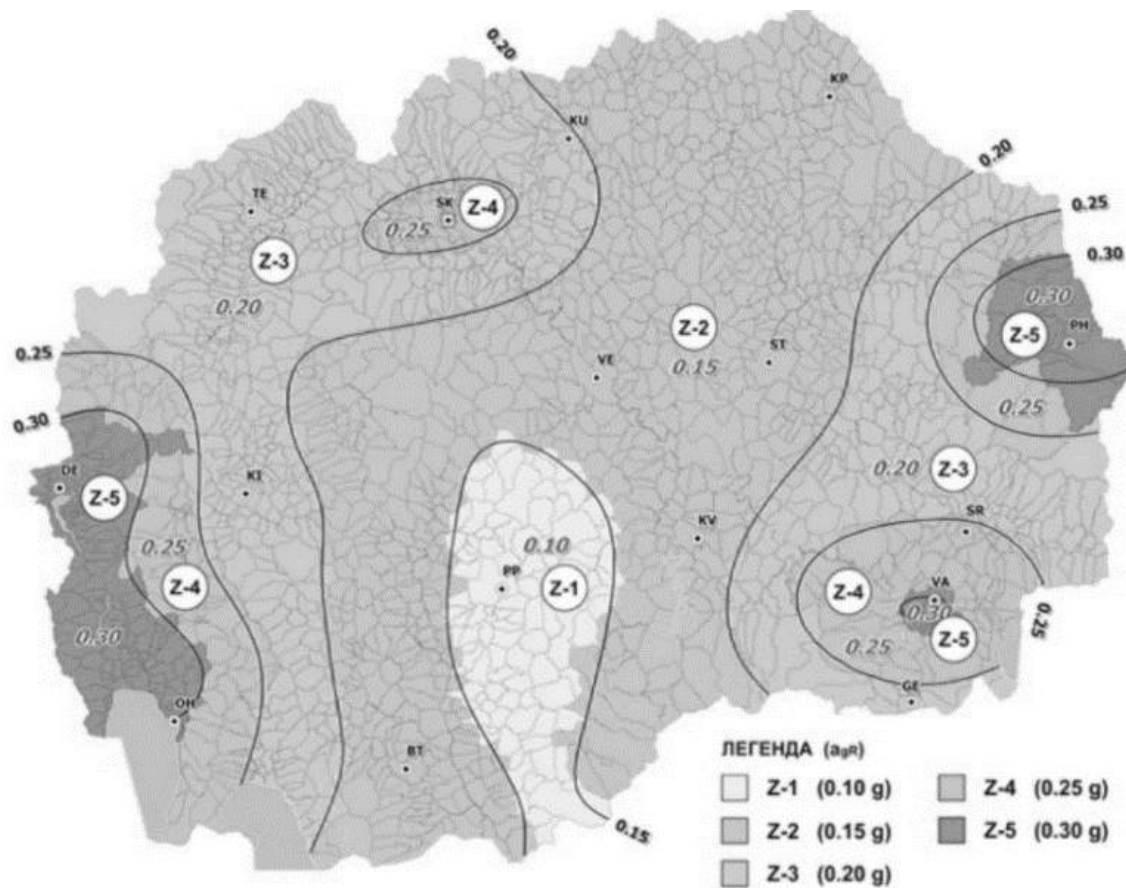


Figure 3. Seismic hazard map (PGA) for Macedonia, Soil Type A, (Milutinovikj, Shalijkj et al. (2016))

3. LIQUEFACTION POTENTIAL ASSESSMENT

3.1. Applied Methodology

Figure 4 illustrates the applied methodology for obtaining the final liquefaction potential zoning maps. It should be noted that two characteristic seismic scenarios were selected, with PGA values for soil type A, and due to lack of seismic hazard maps for other soil types for the country, a “SHAKE” type analysis for obtaining the CSR was necessary.

The liquefaction susceptibility of the layers was obtained depending on the available data for the soil profiles of the 16 locations, by means of PI, content of fines, gradation criteria etc. The liquefiable layers were submitted to the Boulanger and Idriss (2010) deterministic and probabilistic relations for obtaining the CRR. In the end, the selected critical layer from each soil profile was used as a base point (F_s and PL) for zonation of the maps. The average depth from the ground level of the critical layers at the location was around 4.5m. The range of the global thickness of the liquefiable layers is from 2 meters up to 7 meters.

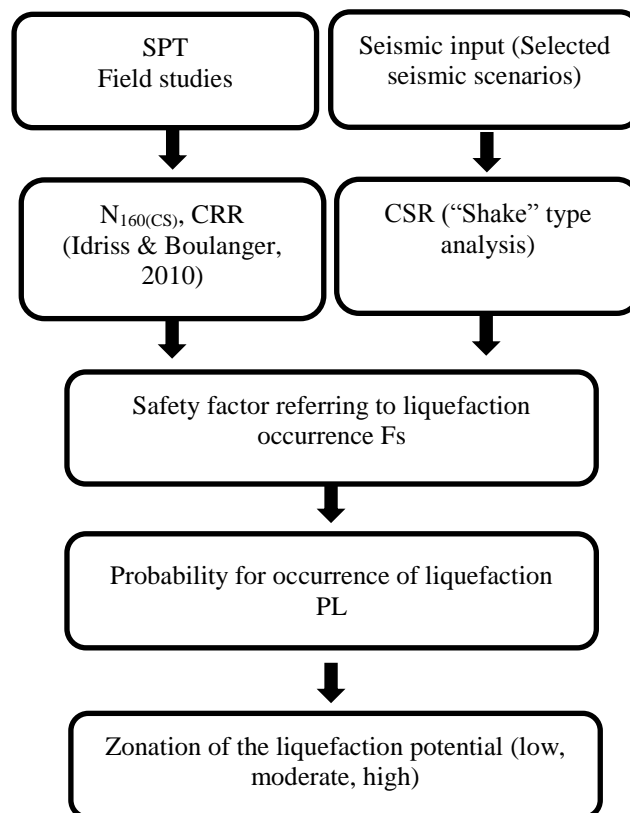


Figure 4. Applied methodology for obtaining the liquefaction hazard maps

The soil was found to be expressively heterogeneous, with loose and soft layers present even at greater depths. Generally, the location is characterized by low bearing capacity soil with low compactness of the soil layers. The bedrock is located relatively deep, which combined with the low mechanical/geophysical characteristics results in large amplification of the input seismic excitation. This affects the liquefaction potential very unfavorably. Yet, sandy, water saturated layers of considerable thickness that are very slightly granulated are relatively scarce in the considered sites. The percentage of fine particles in the sandy layers of the greater number of soil profiles is high. In addition, clayey, silty and layers with organic intercalations are very much present, which is favorable from the aspect of susceptibility to liquefaction. Generally, those sandy layers that have a small percentage of fine particles are well granulated, as well. All this affected the evaluation of the susceptibility to liquefaction for which a large number of layers of the considered soil profiles were excluded in further analysis.

3.2. Zoning Classification

In Table 1 the classification of zones for the Factor of Safety maps (F_s) is presented. The classification is according to the recommendations given in EUROCODE 8 (EN 1998-5-2004 (E)) Article 4.1.2.: *The liquefaction potential is small and no soil improvement is needed, for a $F_s > 1.25$* Table 2 presents the zone classification for the Probability of Liquefaction (PL) maps.

Table 1. Zonation of the factor of safety for liquefaction potential

$F_s \leq 1$	Locations with very high liquefaction potential	(Red zone)
$1.01 \leq F_s \leq 1.25$	Locations with moderately high liquefaction potential	(Yellow zone)
$F_s \geq 1.25$	Locations with low liquefaction potential	(Green zone)

Table 2. Zonation of the probability for liquefaction (PL)

Probability [%]	Factor of safety	Zoning
PL < 10	F _s < 1,03	
10,01 < PL < 50	1,03 – 0,87	
50,01 < PL < 70	0,87 – 0,82	
70,01 < PL < 95	0,82 – 0,70	
95,01 < PL < 100	0,70 – 0,50	

I should be noted that 16 locations are a small number to correctly cover the area when interpolating the F_s and PL values. A higher base density would be more suitable, and in situ investigations to cover the matter are currently on-going.

The final product from the research are the 4 maps presented in Figure 4 and 5:

1. F_s (against liquefaction) for seismic scenario – M_w = 5, a₀ = 0.15g;
2. F_s (against liquefaction) for seismic scenario – M_w = 6, a₀ = 0.25g;
3. PL (probability of liquefaction) for seismic scenario – M_w = 5, a₀ = 0.15g;
4. PL (probability of liquefaction) for seismic scenario – M_w = 6, a₀ = 0.25g.

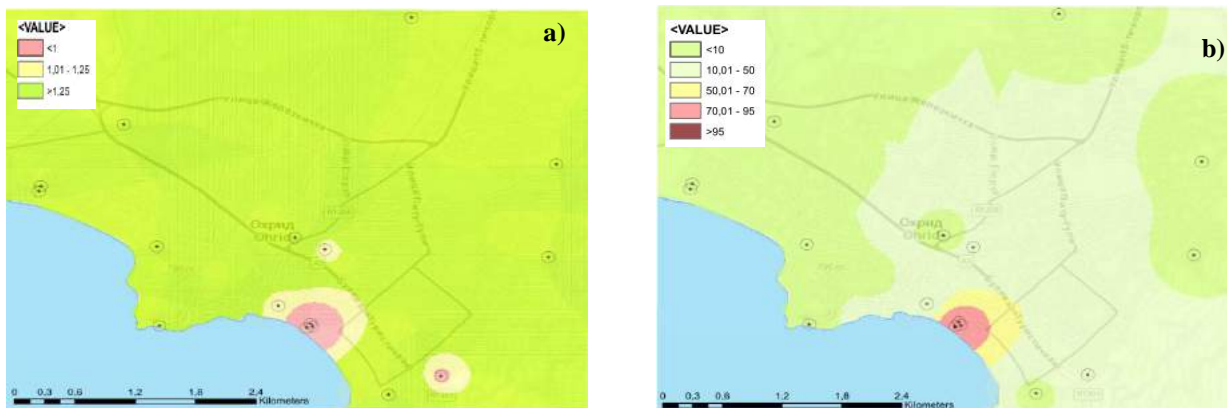


Figure 4. (a) Factor of safety against liquefaction map (b) Probability of liquefaction map for Ohrid, Macedonia for seismic scenario M_w=5, a₀=0.15g

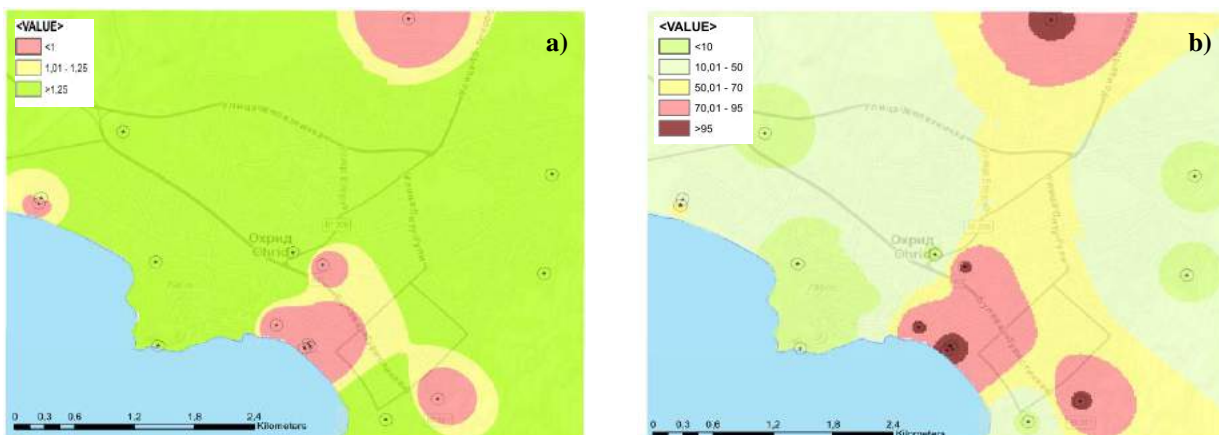


Figure 5 (a) Factor of safety against liquefaction map (b) Probability of liquefaction map for Ohrid, Macedonia for seismic scenario M_w=6, a₀=0.25g

4. CONCLUSIONS

Several groups of conclusions were derived by the end of this research. The parallel between the deterministic and probabilistic approaches will be highlighted in the following paragraphs.

It can be observed that the probabilistic models insert the factor of probability for liquefaction where values of $F_s < 1.2$. In other words, they enable further zoning classifications where the deterministic ones indicate a red zone (Tables 1 and 2). For the selected study location, recently affected by a series of earthquakes (the maximum being with a $M_w=5.2$), with no record of liquefaction occurrence, the results from the probabilistic approach seems to correspond more, and the deterministic one can be considered as the upper bound (Ulmer 2015).

This indicates that probabilistic models should not be excluded by default, especially in the decision making process for higher importance class structures.

The advantages of the in-situ methods for this type of assessment are evident, but in general, these maps should serve as indicators of the red zones of liquefaction potential. Depending on the acceptable risk for a potential structure, additional laboratory and numerical analyses are recommended.

Finally it should be noted that, the SPT investigations were found to be not completely unified at all locations. The main aim to the research was to develop the methodology and locate the weak points and shortcomings in the country's engineering practice. Regarding this, the on-going follow up research is consisted of CPT based liquefaction assessments that would hopefully ratify and refine the above presented one.

5. REFERENCES

- [1] Bojadjieva J., V. Sheshov, K. Edip. 2016. "A Case Study of Liquefaction Assessment for Business Center in City of Skopje" ACUUS, Ss. Petersburg, Russia, 2016.
- [2] Cetin K.O., Seed R. B., Der Kiureghian A., Tokimatsu K., Harder Jr. L. F., Kayen R. E., Moss R.E.S., "Standard Penetration Test-Based Probabilistic and Deterministic Assessment of Seismic Soil Liquefaction Potential".
- [3] Chaneva J, (2018) "Application of in-situ methods for liquefaction hazard assessment", Master's thesis, UKIM-IZIIS;
- [4] Chaneva, J., Bojadjieva, J., Sheshov, V., Edip, K. and Kitanovski, T. (2018), Application of deterministic and probabilistic - SPT based liquefaction assessment triggering models. *ce/papers*, 2: 603-608. doi:10.1002/cepa.736.
- [5] Cubrinovska, E., (2009), "Foundation of Structures in Urban Media with Liquefaction Potential", Master's thesis, UKIM-IZIIS.
- [6] Cubrinovski M., September (2013), "Liquefaction-Induced Damage in the 2010-2011 Christchurch (New Zealand) Earthquakes", 18th Int. Conf. ISSMGE.
- [7] Cubrinovski M., McManus K., Anderson K., (2013), "Earthquake Geotechnical Engineering Practice, Module 3: Identification Assessment and Mitigation of Liquefaction Hazards", New Zealand Geotechnical Society and Ministry of Business Innovation Employment Earthquake Geotechnical Engineering.
- [8] Hauffe, T. et al., 2011, "Spatially explicit analysis of gastropod biodiversity in ancient Lake Ohrid" *Biogeosciences*, 8, 175–188, doi:10.5194/bg-8-175-2011.

- [9] Idriss I. M., Boulanger R. W., December 2010, “SPT-BASED LIQUEFACTION TRIGGERING PROCEDURES” Report no. UCD/CGM-10/02 University of California at Davis.
- [10] Kramer, S. L., Mayfield, R. T., & Huang, Y. M. (2006). Performance-based liquefaction potential: a step toward more uniform design requirements. In Proceedings of the US-Japan workshop on seismic design of bridges. Bellevue, WA.
- [11] Sheshov, V et al., (2012), “ Analysis of Stability and Technical Solution for Strengthening (Partially Strengthened) Structural System of the Structure of Surgical, Gynecological-Obstetrics and ORL Clinics”, (in Macedonian), Public Health Institute – General Hospital – Ohrid - Evaluation of Seismic Parameters and Geophysical Field Studies, IZIIS Report 2012-02
- [12] Sheshov V., Edip K., Cvetanovska J., September, 2012, “Evaluation Of The Liquefaction Potential by In-Situ Tests And Laboratory Experiments in Complex Geological Conditions”, 15th World Conference on Earthquake Engineering, Lisbon, Portugal, 24 – 28.
- [13] Talaganov K., Petrovski J., Mihailov D., 1981, “Soil Liquefaction Seismic Risk Analysis Based on Post 1979 Earthquake Observations in Montenegro”, First International Conference on Recent Advances in Geotechnical Earthquake Engineering & Soil Dynamics, Missouri University of Science and Technology.
- [14] Ulmer K. J., (2015), “Development of a simplified performance based procedure for Assessment of liquefaction triggering using liquefaction loading maps”, Master thesis Brigham Young University.
- [15] Youd et. al., April 2001 – “Liquefaction Resistance of Soils: Summary Report from 1996 NCEER/NSF Workshops on Evaluation of Liquefaction Resistance of Soils”, Journal of Geotechnical and Geoenvironmental Engineering.

INFLUENCE OF SPATIAL VARIABILITY OF SHEAR STRENGTH PARAMETERS ON RELIABILITY-BASED ASSESSMENT OF DYKES

Divya Varkey*, *Section of Geo-Engineering, Faculty of Civil Engineering and Geosciences, Delft University of Technology, D.Varkey@tudelft.nl*

Michael A. Hicks, *Section of Geo-Engineering, Faculty of Civil Engineering and Geosciences, Delft University of Technology, M.A.Hicks@tudelft.nl*

Philip J. Vardon, *Section of Geo-Engineering, Faculty of Civil Engineering and Geosciences, Delft University of Technology, P.J.Vardon@tudelft.nl*

Abraham P. van den Eijnden, *Section of Geo-Engineering, Faculty of Civil Engineering and Geosciences, Delft University of Technology, A.P.vandenEijnden@tudelft.nl*

ABSTRACT

The Dutch dyke network includes 14,000 km of regional dykes that are regularly assessed in order to reduce the risk of flooding. The current strategy for maintenance and/or upgrading of existing dykes is based on safety assessments using partial factors and reliability-based characteristic values of material properties, interpreted from Eurocode 7 (EC7). In this paper, an historic dyke in the Netherlands has been analysed for stability using two methods: (a) based only on the point statistics of the material properties, as is widely adopted in Dutch practice based on a simplified interpretation of EC7, and (b) based on both the point and spatial statistics of the material properties, using a probabilistic approach in line with the full requirements of EC7. The results of safety assessments by the two methods show that a consideration of the spatial variability leads to a narrower range of possible responses, and thereby to a higher computed factor of safety at the target reliability of 95%. Moreover, for the dyke section considered, it results in much reduced remedial action compared to that suggested as a consequence of using the simplified approach, and thereby to a more economic design and reduced environmental impact.

Keywords: Dykes, Eurocode 7, Reliability, Spatial Variability.

1. INTRODUCTION

The factor of safety against instability is often expressed as the ratio of resisting to disturbing forces or moments. However, a deterministic analysis does not allow for a quantifiable assessment of the impact of uncertainties on the calculated factor of safety. The three primary sources of geotechnical uncertainty are: the inherent variability of soil arising due to a combination of various geological, environmental and physico-chemical processes; measurement errors caused by equipment and/or procedure followed; and transformation errors introduced when field or laboratory measurements are transformed into soil properties using empirical equations or other models [1]. Although the relative contribution of these components to the overall variability is dependent on various conditions, the latter two, i.e. the measurement and transformation errors, can be reduced by quality control and/or taking other measures. Hence, only the inherent spatial nature of variability of soil properties will be considered in this paper.

Various reliability-based methods have been developed to account for the inherent variability of soil parameters in performance assessments of geotechnical structures; for example, the first order reliability method, stochastic response surface method and random finite element method (RFEM) [2]. RFEM has proven to be an effective and versatile method due to it not making any prior assumptions regarding the shape of the failure mechanism, and accounting fully for the spatial nature of inherent variability. Much research has been done to understand the influence of spatial variability in mechanical and hydraulic parameters on the reliability of geotechnical structures in 2D, i.e. assuming an infinite correlation between the parameters in the third dimension. Moreover, a limited amount of research has been done in 3D slope reliability analysis, which has shown the importance of considering the finite correlation length of soil parameters relative to the slope length in the third dimension. However, in practice, the performance of geotechnical structures is usually assessed using a deterministic analysis, i.e. by ignoring the spatial variability of soil parameters, and often results in the over-designing of structures in order to meet safety requirements.

This paper illustrates the advantages of incorporating spatial variability of soil parameters in the reliability-based assessment of one section of a dyke ring in the Netherlands. A representative cross-section of the dyke has been analysed for slope stability using two methods: (a) based only on the point statistics of the material properties, as widely adopted in Dutch practice and based on a simplified interpretation of Eurocode 7 (EC7) [3], and (b) based on both the point and spatial statistics of the material properties, using a stochastic RFEM analysis satisfying the requirements of EC7. The practical implications of the latter approach are illustrated by the relative extent of remedial actions suggested by the two methods in order to meet the required safety level.

2. DYKE SAFETY ASSESSMENTS IN THE NETHERLANDS

Stability assessments of regional dykes in the Netherlands are based on the EC7 [3] philosophy of partial factors defined by the code and characteristic values of soil properties chosen by the engineer, often through a simplified interpretation of the statistical approach proposed in EC7. The derivation of characteristic soil property values according to EC7 is revisited in the following sub-section, and the implication of using a simplified interpretation of EC7 is illustrated by the reliability-based assessment of a dyke section.

Table 1. Clause (11): Extract from Section 2.4.5.2 of Eurocode 7 [3]

-
- (11) If statistical methods are used, the characteristic value should be derived such that the calculated probability of a worse value governing the occurrence of the limit state under consideration is not greater than 5%.

NOTE: In this respect, a cautious estimate of the mean value is a selection of the mean value of the limited set of geotechnical parameter values, with a confidence level of 95%; where local failure is concerned, a cautious estimate of the low value is a 5% fractile.

2.1. Characteristic Value According to EC7

Table 1 states Clause (11) from Section 2.4.5.2 of EC7, which gives guidelines for when statistical methods are used in deriving characteristic values. From the table it can be inferred that the characteristic value should be selected so as to give a structural reliability (relative to the limit state under consideration) of at least 95%.

However, this appears to be contradicted by the footnote, in that the first part of the footnote refers to a mean value and the second part refers to the 5% fractile of the soil property distribution. However, Hicks [4] and Hicks and Nuttall [5] demonstrated that the clause and the footnote are entirely consistent, and can be explained by considering the scale of fluctuation (θ) of the property values (i.e. the distance over which they are significantly correlated) relative to the size of the problem domain (D). They demonstrated that by selecting the 5 percentile of a modified “effective” property distribution (back-figured from the response of the structure) as the characteristic value, the requirements of EC7 would be fully satisfied.

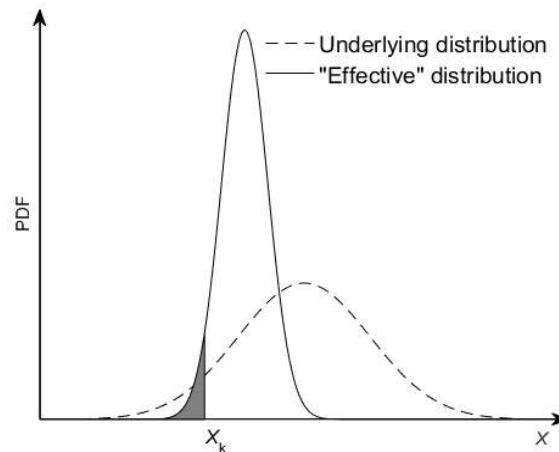


Figure 1. Characteristic value satisfying Eurocode 7 (based on [4,5])

For three possible scenarios of θ/D (i.e. very large, very small and intermediate values), there exist three scenarios for the “effective” property distribution relative to the underlying property distribution, although it is intermediate values of θ/D that are generally encountered in practice. For a soil property X modelled by a normal distribution (as illustrated by the underlying probability density function (PDF) in Figure 1), the resulting “effective” property distribution for the general case, i.e. for intermediate values of θ/D , is shown. It is seen that the mean and standard deviation of the effective distribution are lower than those of the underlying distribution, due to the tendency for failure to be attracted to semi-continuous weaker zones and due to the averaging of soil property values over the failure surface, respectively. Consequently, the 5 percentile of the “effective” property distribution, representing the characteristic value (X_k), is generally greater than the 5 percentile of the underlying property distribution. However, for reasons of simplicity and/or conservatism, Dutch practice often uses the 5 percentile of the underlying property distribution as the characteristic value.

2.2. Problem Description and Analysis Methodologies

The Starnmeer polder, situated in the Dutch province of North Holland, lies within a 13 km dyke ring managed by the water board Hollands Noorderkwartier (HHNK). Stability assessments of 10 dyke sections based on the characteristic values derived from the simplified interpretation of the statistical approach (i.e. based on the 5-percentile soil property values) revealed that 5 sections did not meet the safety requirements. Moreover, for one particular dyke section, a factor of safety (F) as low as 0.5 was reported [6], for which, a re-design was proposed by HHNK to meet the safety requirements. This re-design presented a significant economic burden due to the large volume of material required, as well as having a considerable impact on neighbouring property. Hence, the stability of the dyke section was reassessed [7] by using a stochastic approach that is entirely consistent with the requirements of EC7.

The two methodologies adopted herein for the safety assessment of the dyke section can be summarised as follows:

- Method (I) - safety assessment using 5-percentile soil property values and partial factors, as adopted in Dutch practice, based on a simplified interpretation of the statistical approach proposed in EC7.
- Method (II) - safety assessment using the point and spatial statistics of soil properties and partial factors, based on a stochastic approach fully consistent with the requirements of EC7.

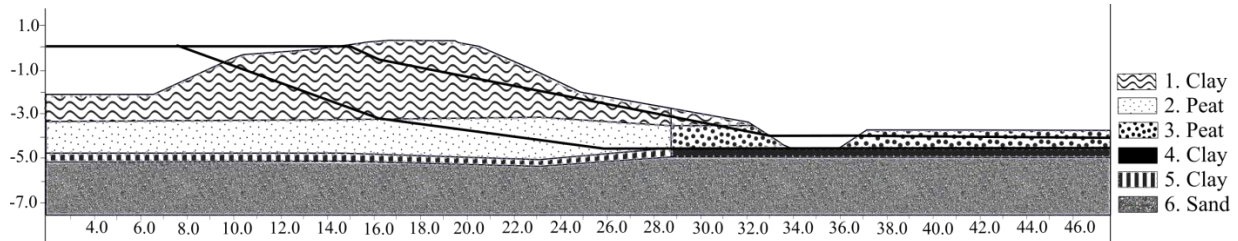


Figure 2. Dyke cross-section (scale in metres)

Table 2. Unit weights and strength parameter values used in analysis of dyke cross-section:

(a) Layers 1–6

Layers	γ (kN/m^3)	c'				$\tan \phi'$			
		Mean (kPa)	COV	Partial factor	Design value (kPa)	Mean	COV	Partial factor	Design value
1	13.9*	4.4	0.773	1.20	0.917	0.580	0.081	1.15	0.429
2	9.9	3.2	0.656	1.20	0.833	0.398	0.058	1.15	0.310
3	9.8	2.0	0.775	1.20	0.417	0.358	0.145	1.15	0.241
4	15.0	4.5	0.544	1.20	1.417	0.559	0.012	1.15	0.465
5	15.0	5.4	0.352	1.20	2.417	0.601	0.007	1.15	0.503
6	20.0	0.0	0.000	-	0.000	0.637	0.000	1.20	0.531

* $\gamma = 6.9 \text{ kN/m}^3$ above the phreatic surface

(b) Layers 7–8

Layers	γ (kN/m^3)	c'				$\tan \phi'$			
		Mean (kPa)	COV	Partial factor	Design value (kPa)	Mean	COV	Partial factor	Design value
7	17.0	6.2	0.773	1.20	1.333	0.531	0.081	1.15	0.403
8	20.0	0.0	0.000	-	0.000	0.637	0.000	1.20	0.531

2.3. Results and Discussions

Figure 2 shows a cross-section through Dyke Section 8 at Starnmeer. The unit weight (γ) and shear strength properties of the various material layers are summarised in Table 2(a). The coefficients of variation (COV) of cohesion (c') and tangent of friction angle ($\tan \phi'$) have been back-calculated using the respective mean and 5-percentile values reported in [6]. Note that the lognormal distribution has been adopted to model each soil property for each material layer in order to avoid the possibility of negative values, especially for properties with higher values of COV. Also listed in the table are the design soil property values that have been calculated by dividing the 5-percentile soil property values with their respective partial factors.

Figure 3 shows the results obtained by re-evaluating the stability of the dyke section using an in-house finite element software using the strength reduction method. The value of $F = 0.54$ obtained by using Method (I) is based on analysing the stability of the dyke section using the design soil property values from Table 2(a); that is, it does not consider the spatial nature of soil variability and is not consistent with the intention of EC7 (Table 1).

The cumulative distribution function (CDF) of F using Method (II) has been obtained by analysing the dyke section using the design soil property distributions (generated by scaling down the distributions for c' and $\tan \phi'$ by the respective partial factors listed in Table 2(a)), but additionally, for each soil property and each material layer, vertical (θ_v) and horizontal (θ_h) scales of fluctuation have also been considered by using a fully stochastic RFEM.

The RFEM combines random fields (i.e. the mathematical representation of spatial variability) of soil property values with finite elements within a Monte Carlo framework. The random fields have been generated by covariance matrix decomposition using the Markov autocorrelation function (see [8] for details). As insufficient spatial data were available for the cross-section, $\theta_v = 0.5$ m and $\theta_h = 6.0$ m were assumed for each soil property and each material zone, which would result in a conservative estimate based on the range of values of θ_v reported [9] for similar soils and based on the results obtained with other values of θ_h [7].

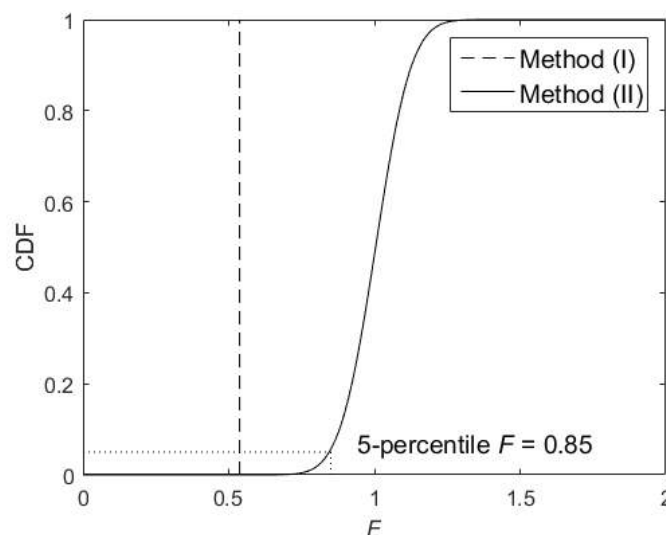


Figure 3. Comparison of F calculated by the two methods

Figure 3 shows that for a 95% reliability (R) of the dyke section, $F = 0.85$ is obtained by using Method (II), which is significantly higher than the value of F computed using Method (I). Note that characteristic soil property values have not been calculated explicitly in Method (II); instead, the reliability-based factor of safety has been calculated directly, and is this value that is needed in the safety assessment. Hicks et al. [7] have shown (via a simple re-analysis) that, for this particular dyke section, the characteristic soil property values correspond to the 34 percentiles of their respective underlying distributions.

2.3.1. Re-designing the dyke section

Although the results obtained by Method (II) represent a 57% increase in the computed value of F , some upgrading of the dyke section is needed as it is still less than the required $F = 0.95$ (the limit of $F = 0.95$ includes partial factors and is dictated by the standard [6]). Figure 4 shows the initial re-design of the dyke section proposed by HHNK, following on from the estimate of F obtained using Method (I).

This involves moving the ditch further away from the dyke, infilling the original ditch, and construction of a clay berm to increase resistance against failure. The value of F obtained by analysing the re-designed dyke section using the in-house finite element software (with the unit weights and shear strength properties of the sand infill and clay berm listed in Table 2(b)) using Method (I) is also shown in Figure 4, demonstrating that the proposed upgrade of the dyke section would be over-conservative and uneconomical since the calculated F is significantly greater the required F of 0.95.

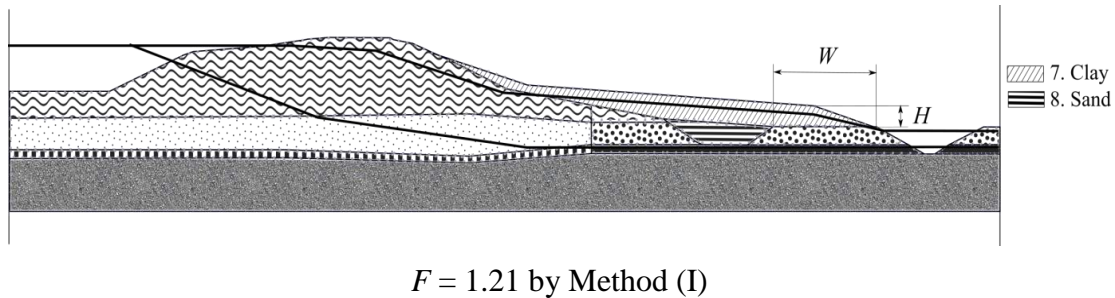


Figure 4. Initial re-design for dyke cross-section and the value of F obtained by Method (I)

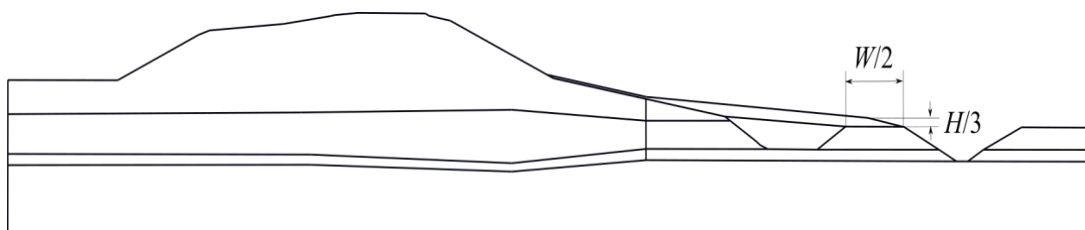
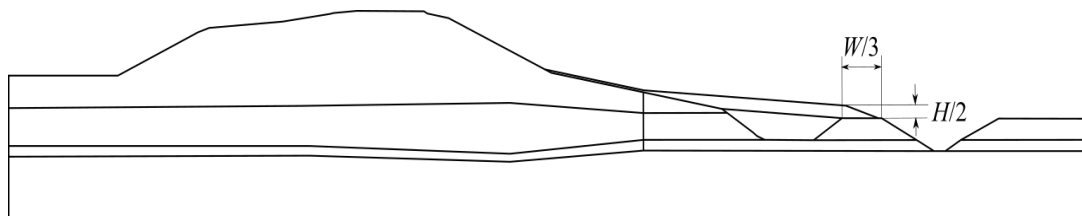


Figure 5. Proposed alternative re-designs for the dyke cross-section, the value of F calculated by Method (I) and the value of F at $R = 95\%$ calculated by Method (II)

Therefore, further analyses have been carried out for re-designing the dyke section using Method (II), for a range of berm heights and inter-ditch spacings. Figure 5 shows two of the alternative proposals: these are (a) constructing a berm of half the initially proposed height and reducing the inter-ditch spacing to 1/3 of its original dimension, and (b) constructing a berm of 1/3 of its initially proposed height and reducing the inter-ditch spacing to half of its original dimension.

Both give a factor of safety satisfying the safety requirement ($F > 0.95$ with a 95% confidence) when analysed using Method (II). Also shown in Figure 5 are the values of F obtained by analysing the stability of the alternative re-designs using Method (I). The comparisons for F obtained by the two methods show that accounting for spatial variability in the reliability-based safety assessment is important as it results in a significant saving relative to the original proposed re-design.

3. CONCLUSIONS

An historic dyke section in the Netherlands has been analysed by two methods. The first is based only on the point statistics of the material properties, and is an approach which is widely adopted in practice and based on a simplified interpretation of Eurocode 7. The second is based on the point and spatial statistics of material properties, and is an approach which is fully consistent with the requirements of Eurocode 7. The results of the safety assessments by the two methods show that a consideration of the spatial variability leads to a narrower range of possible responses, and thereby to a higher computed factor of safety at the target reliability of 95% (approximately 57% higher than the factor of safety computed using the former approach for the dyke section, although still lower than the safety requirement). An initial proposal for re-designing the dyke had been suggested based on analysis using the former approach. However, it has been shown that, through a proper consideration of spatial variability of soil properties, the extent of the upgrade can be significantly reduced, thereby resulting in economy of design and reduced environmental impact.

ACKNOWLEDGEMENTS

This work is part of the research programme Reliable Dykes with project number 13864 which is financed by the Netherlands Organisation for Scientific Research (NWO), and was carried out on the Dutch National e-infrastructure with the support of SURF Foundation. The authors are grateful for the assistance of Henk van Hemert (STOWA) and Niels Tenhage (HHNK).

REFERENCES

- [1] Phoon, K.-K., Kulhawy, F.H., 1999. “*Characterization of Geotechnical Variability*”, Canadian Geotechnical Journal, 36:612–624.
- [2] Fenton, G.A., Griffiths, D.V., 2008. “*Risk Assessment in Geotechnical Engineering*”, John Wiley & Sons, New York.
- [3] CEN, 2004. “*Eurocode 7: Geotechnical Design. Part 1: General Rules, EN 1997-1*”, European Committee for Standardisation.
- [4] Hicks, M.A., 2012. “*An Explanation of Characteristic Values of Soil Properties in Eurocode 7*”, In: Arnold, P., Fenton, G.A., Hicks, M.A., Schweckendiek, T., Simpson, B. (Eds.), *Modern Geotechnical Design Codes of Practice: Development, Calibration and Experiences*, IOS Press, 36–45.
- [5] Hicks, M.A., Nuttall, J.D., 2012. “*Influence of Soil Heterogeneity on Geotechnical Performance and Uncertainty: A Stochastic View on EC7*”, Proceedings of 10th International Probabilistic Workshop, pp. 215–227, 15–16 November 2012, Stuttgart, Germany.
- [6] Kames, J., 2015. “*Veiligheidstoets Boezemkaden*”, Technical Report 14.0046944, Hollands Noorderkwartier.

- [7] Hicks, M.A., Varkey, D., van den Eijnden, A.P., de Gast, T., Vardon, P.J., 2019. “*On Characteristic Values and the Reliability-Based Assessment of dykes*”, Georisk: Assessment and Management of Risk for Engineered Systems and Geohazards, under review.
- [8] van den Eijnden, A.P., Hicks, M.A., 2017. “*Efficient Subset Simulation for Evaluating the Modes of Improbable Slope Failure*”, Computers and Geotechnics, 88:267–280.
- [9] de Gast, T., Vardon, P.J., Hicks, M.A., 2017. “*Estimating Spatial Correlations Under Man-Made Structures on Soft Soils*”, Proceedings of 6th International Conference on Geotechnical Safety and Risk, pp. 382–389, 4–6 June 2017, Colorado, USA.

A NUMERICAL STUDY UPON THE EFFECT OF CRACKS ON THE STABILITY OF DIKES

Maria Luisa Taccari*, *Department of Flood Defences, Deltares, MariaLuisa.Taccari@deltares.nl*
Maria Konstantinou, *Department of Flood Defences, Deltares, Maria.Konstantinou@deltares.nl*
Arno Rozing, *Department of Flood Defences, Deltares, Arno.Rozing@deltares.nl*

ABSTRACT

Cracks are often observed in dikes after a long period of drought, severe external loads, reduced stability, or as effect of differential settlement. Cracks can occur along the slope, at the crown and at the toe of the dike. Cracks can be shallow or they can reach a couple of meters depth. They are usually dry but, due to the effect of wave overtopping, water overflow or extreme precipitation, they can also be filled up with water. The aim of the research is to evaluate whether longitudinal cracks have a negative influence on the macro-stability for flood defences and if they should be part of the formal regular safety assessment. To quantify the influence of cracks, a series of numerical analyses using the Finite Element Method are carried out on a river dike section in the Netherlands which is made anonymous due to privacy reasons. Several scenarios are examined which take into account different location and depth of the cracks within the dike, and a different saturation state of the cracks; dry or fully saturated with water. The results are compared with the outcome of stability analyses performed without the presence of cracks.

Keywords: Dikes, Stability, Finite Element Method, Drought, Cracks.

1. INTRODUCTION

Flood defences provide protection against catastrophic events to the large and growing concentration of human population living in low-lying coastal zones [1]. In the Netherlands, the strength of the primary dikes must fulfill stringent requirements. According to The Water Act, dike administrators must regularly test whether their dikedikes fulfill the standards, which have been drawn up by the Ministry of Infrastructure and Water Management. The new standards by 1st January 2017 are based on the maximum permissible probability of flooding.

Climate change predictions for the Netherlands indicate an increased frequency or intensity of extreme events and changes on precipitation and temperature [2]. The temperature keeps increasing, i.e. milder winters and hotter summers will happen more frequently. There will be more often dry periods, also in combination with changes in rain and evaporation. This will lead to an increase of potential evaporation, which depends on temperature and solar radiation. The increasing temperature, average amount of precipitation, drought events and increasing intensity of e precipitation are major effects that are likely to affect the stability of dikes [3]. An overall increase in temperature and prolonged periods of drought can cause long-term soil drying. Evaporation of water can result in soil volumetric shrinkage and desiccation cracking. Desiccation cracking can induce severe problems for geotechnical applications. The presence of tension cracks due to desiccation may badly influence the stability of natural slopes, and dams [4].

Due to the increasing frequency of extreme drought, soil desiccation cracking will likely be more frequent and it will need increased attention in the future. While various studies provide general insight in the effects of sea-level rise for coastal defences to relative sea-level rise, there is a clear gap in the state of our knowledge in terms of characterizing and quantifying the impacts of extreme drought events under a changing climate on earthen dikes.

This study provides a method to estimate the effect of cracks on geotechnical macro-stability of dikes. A series of numerical analyses using the Finite Element Method are carried out on a river dike section in the Netherlands which is made anonymous due to privacy reasons. Several scenarios are examined considering different location and depth of the cracks within the dike, and a different saturation state of the cracks; dry or fully saturated and filled with water. The results are compared with the outcome of stability analyses performed without the presence of cracks.

2. SHRINKAGE CRACKS

2.1. Initiation and Propagation

Climatic conditions as temperature and rainfall highly influence crack initiation and propagation. High temperatures during dry seasons can lower the water table to considerable depth in the soil profile. The unsaturated area dries out due to evaporation and plant transpiration, volume change/shrinkage occurs as its water content decreases (Figure 1(a)). Due to volume shrinkage and increase of suction, the tensile stresses in the dehydrated soil increases (Figure 1(b)) and when it exceeds the tensile strength of the material, shrinkage cracks initiate (Figure 1(c)). As rainwater infiltrates less easily into the dehydrated soil, shrinkage continues, and cracks grow deeper (Figure 1(d)). The process stops when the soil reaches its shrinkage limit and the void ratio remains constant with reduction in moisture content [5].

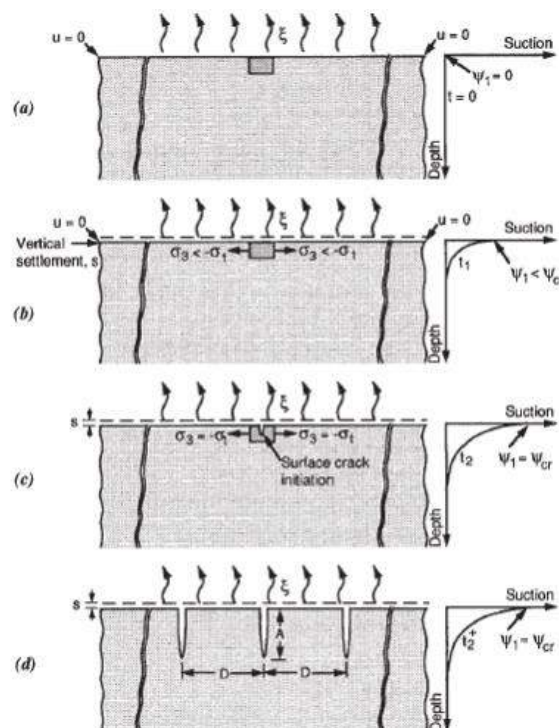


Figure 1. Illustration of cracking [5]

Cracks are not only caused due to shrinkage but also as effect of differential settlement [6], severe external loads and reduced stability. Marginal stability of the embankment, heavy traffic load and differential settlement between crown, inner slope or roadside can generate relatively large tensions in the substrate with consequential deformation and cracks occurrence. In case of cracking caused by deformation, the cause lies deeper into the substrate and so also the process of crack formation.

The initiation and propagation of shrinkage cracks depend on several factors, such as initial water content, mineral composition, clay content and plasticity index, layer thickness and size, surface vegetation cover, cyclic change of the climate [7].

Desiccation due to exposure with atmosphere let shrinkage cracks start from the soil surface. Cracks develop mainly vertically, being the horizontal deformation usually constrained. Cracking concentrates at larger cracks, because the growth of smaller cracks is retarded and eventually suppressed by the deeper ones. Theoretically, cracks develop in parallel, square or hexagonal patterns. In real situations, the observed cracks have irregular, orthogonal and hexagonal crack patterns [5]. In flood defenses, five types of patterns are usually observed: long cracks at the crest or on the higher part of the slope, diagonal cracks in the embankment, crackle cracks at its toe, cracks around trees and cracks along hard elements [6]. The present work is limited to continuous longitudinal cracks at the crest of the embankment or at the upper part of the slope, since this is the most observed type of crack and it has the highest impact on the stability of the flood defense.

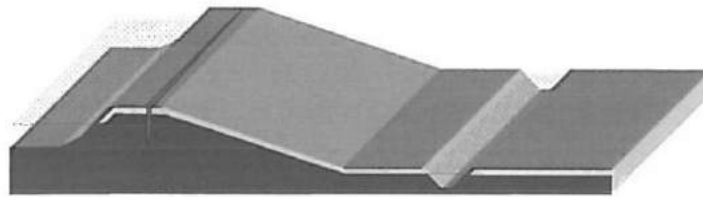


Figure 2. Longitudinal cracks at the crest of a dike

2.2. Impact on Earthen Dikes

Soil mechanical and hydraulic characteristics are significantly modified by the presence of desiccation cracks. The hydraulic conductivity increases, sometimes as large as three orders of magnitude [7]. Water infiltration into open cracks can occur more rapidly, pore pressures increase and the effective stress and corresponding soil strength decreases [4]. Cracks also affect soil compressibility and consolidation rate of the soil [8].

The performance of geotechnical structures reduces because of cracks. Due to extreme drought, in 2007, more than 1,200 reservoir dams in Chongqing, China, presented deep desiccation cracks. When it rained, the rapid groundwater recharge caused instability of several dams [4]. Similarly, after long-term drought events in 2008 and 2009, multiple locations of the riverbanks of the Murray River in Australia failed due to extensive desiccation cracks along the crest of the sloped riverbanks [9]. In August 2003, after a prolonged drought season, the Wilnis Dike in the Netherlands failed [10]. The peat soil presented extensive desiccation cracks which were among the principal causes for horizontal translation of the dike. The largest cracks were found at the crest of the dike, with direction parallel to the dike [11].



Figure 3. Horizontal Failure of the Wilnis Dike in the Netherlands, (August 26, 2003) [12]

There are various mechanisms for which cracks weaken a flood defense, such as damage of the clay cover or wash-out of the inner sand core (micro-instability). Cracks can have a significant negative impact on the overall stability of a dike, according to the International dike Handbook (ILH) [13]. The sliding surface follows the path of least resistance. If an open crack, which has no shearing resistance, is located near the most likely sliding surface (without cracking), the sliding surface can follow the crack and lead to failure. In United States and France stability analyses consider a vertical crack at the crest of the dike and the sliding surface ends at the point where it reaches the bottom of the crack [13].

3. NUMERICAL MODEL

3.1. Modelling Approach

The present work focuses on the influence of cracks on the macro-stability of a primary flood defence in the Netherlands (clay dike) [16]. To that end, a series of finite element analyses are carried out on a river dike section in the Netherlands. To obtain a representative case, data obtained from practice have been used. A selection of scenarios is applied to the calculations in terms of different crack locations and depths. Finally, the impact on macro stability has been investigated in case of cracks filled with water or when the phreatic level rises, because of wave overtopping, overflow or extreme precipitation.

The calculations are done using the Finite Element package, PLAXIS 2D, version 2017 [14]. A plane strain model with 15-noded elements is considered in all simulations. The model uses a 4 m high embankment with a slope of 30 degrees. To minimize the influence of the boundary conditions, the model is 60 meters wide and 20 meters deep. An FE mesh consisting of 3,000 fifteen-noded triangular elements is employed to discretize the soil material. The mesh is refined at the core of the embankment.

The core material consists of clay, covered by a 150 cm sand top layer. The analysis uses the Shansep material model with undrained parameters. The stability analyses have been carried out by modeling cracks at the crest and along the slope of the embankment, with a ranging depth from 1 to 4 m below the ground level (see cracks A, B, C as shown in Figure). For each meter

of crack depth, calculations have been performed. The cracks are modelled by a so-called *interface* in the calculation model, which presents very low strength and drained behaviour. In case of cracks filled with water, this method creates numerical instability and cracks are therefore modelled as a 20 cm wide opening. Further calculations give equal results for both methods for the situations without water-filled cracks and it can be assumed that the modelling method with a 20cm opening produces sound results for water-filled cracks.

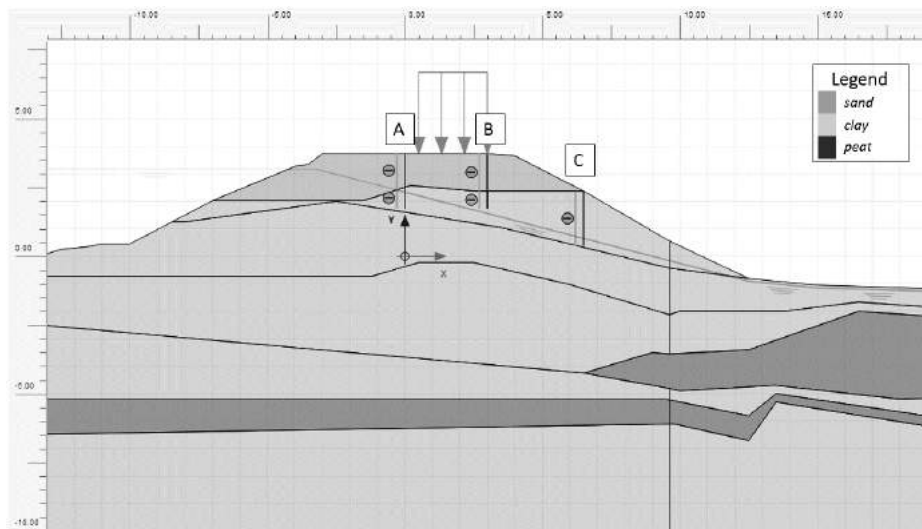


Figure 4. Dike profile used for numerical calculations

3.1. Modelling Approach

The calculations consider several cracks scenarios at the crest and along the slope of the embankment. The impacts of cracks are compared in terms of factor of safety, which is the ratio of the average shear strength of the soil and the average shear stress exhibited along the critical slip plane.

In the case without any crack, the sliding surface reaches four meters depth below ground level. The stability factor is equal 1.70. Calculations with cracks show a decrease in stability with crack depth, though the decrease is not larger than 2.5% (cracks A3 and A4) compared to the calculation without cracks. As it may be expected, crack A (at the crest of the dike) has the largest influence on the overall stability of the dike, since it intersects the sliding surface, while shallower cracks slightly influence it. The decrease of stability when a crack is present depends on both its depth and its location compared to the sliding plane for the situation without cracks.

In the calculations with water-filled cracks, the decrease of safety factor is more. The largest decrease is around 4% for cracks A3 and A4, which are the cracks closest to the sliding surface in the situation without cracks.

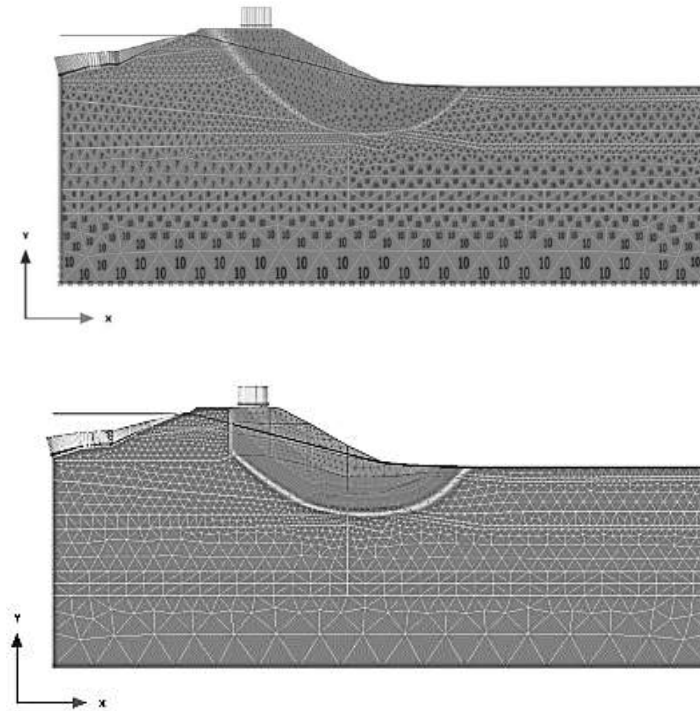


Figure 5. Indication of sliding surface in a calculation without crack (above) and with crack A4 (below)

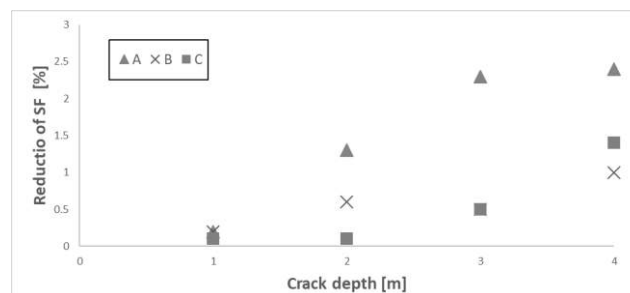


Figure 6. Results in terms of safety factor for the three cracks at several depths

Cracks can also facilitate infiltration of water to the dike core. The phreatic level in the dike can rise due to infiltration by wave overtopping, overflow or extreme precipitation. When considering an increase of one meter of the phreatic level, the decrease the stability factor is approximately 6%. These results suggest that the cracks mainly decrease the stability of a dike not due to the local reduction of strength but mainly due to the easier infiltration of water inside the dike body. Desiccation cracking facilitates the infiltration of water, leading to significant decreases in the effective stress and corresponding soil strength.

The change to the hydraulic properties due to the presence of cracks should be modelled in order to assess their influence on stability. Hydraulic conductivity tests performed on cracked specimens after drying cycles show that hydraulic conductivity increases due to cracking, sometimes as large as three orders of magnitude [15]. After determining the hydraulic and mechanical properties of the uncracked and cracked soil, fully coupled hydro-mechanical analyses under unsaturated condition can estimate the effect of cracks on the stability of the dike. In a previous work carried out at Deltares [3], the hydraulic properties of the soil of the dike are described with Soil-Water Characteristic Curve (SWCC) and Hydraulic Conductivity Function (HCF) and the presence of cracks is simulated by increasing the hydraulic conductivity by one order of magnitude. The resulting safety factor reduces by 15% .

The influence of cracks on the stability of a flood defence is quite complex. From one side, the higher hydraulic conductivity facilitates the infiltration of water. On the other side, higher temperature and prolonged periods of drought do increase soil suction. Depending on the hydraulic conductivity of the material, the reduction of hydraulic conductivity with higher suction may reduce the infiltration of water and lead instead, after a extreme precipitation event, to erosion of the slope of the embankments.

4. CONCLUSION

The study provides a method to estimate the effect of cracks on geotechnical stability of flood defences, leading to the following conclusions:

- The deeper a crack is, the more influence it has on the stability of a dike. Shallower cracks have less influence on the overall stability.
- For large dikes with large height (primary defenses) where, in absence of cracks, the sliding surfaces are large, the impact of cracks will be lower than for small dikes or dikes with smaller sliding surfaces.
- The most critical cracks are the closest ones to the sliding surface of the situation without cracks. In the case under analysis that corresponds to cracks located at the crest of the dike.
- The calculations carried out show that when a crack develops at the crest of a dike with a depth of 3 or 4 meters, the safety factor decrease not more than 2.5%. When these cracks are filled with water, the safety factor decrease at maximum by 4%. However in case of all the other cracks, the decrease of safety factor is very low and in almost all cases less than 0.5%.
- This indicates that considering only the local reduction of strength due to presence of cracks is not sufficient to quantify the reduction of safety that cracks induce to a flood defense.
- Cracks can facilitate infiltration of water into the dike core. When the phreatic plane in the dike rises by one meter due to infiltration by wave overtopping, overflow or extreme precipitation, the decrease the stability factor is approximately 6%.
- Cracks do change the hydraulic properties of the soil: the hydraulic conductivity increases sometimes as large as three orders of magnitude. With fully coupled hydro-mechanical analyses under unsaturated condition, the presence of cracks is simulated by increasing the hydraulic conductivity by one order of magnitude. For an earlier other case the resulting safety factor reduces by 15% .
- Due to the increasing frequency of extreme drought, soil desiccation cracking will likely be more frequent. However, not much is known in terms of quantifying the impacts of extreme drought events on earthen dikes. For this reason, at Deltares we are currently attempting to fill in this knowledge gap.

ACKNOWLEDGEMENT

This research was performed as part of the work reported by A.Rozing (2018) [16]. The authors would like to thank Water Board Waterschap Rivierenland for making the soil data available.

REFERENCES

- [1] Small, C. and Nicholls, R.J., 2003. “A global analysis of human settlement in coastal zones”, *Journal of Coastal Research*, 19(3), 584–599.
- [2] Koninklijk Nederlands Meteorologisch Instituut. KNMI’14, s.l. : KNMI, 2015 klimaatscenario’s voor Nederland.
- [3] Taccari, M.L., Galavi, V., Tehrani, F.S., Elkadi, A.S. 2019. “Resilience of Road Embankments under Changing Climate: A Numerical Study”, PIARC World Road Congress.
- [4] Tang C, Shi B, Lui C, Gao L, Inyang H. s.l. : J Mat 2011. “Experimental investigation of the desiccation cracking behavior of soil layers during drying”, *Civ. Eng. Vols.* 23(6), 873 – 878.
- [5] Wijesooriya, Rathnayaka Mudiyansele Sasika Dilrukshi, 2017. “Modelling of desiccation crack depths in clay soils”, figshare Thesis.
- [6] Lubking P., 2006. “Veenkadeonderzoek Deelproject 3; invloed scheuren op faalmechanisme. Onderdeel A: Scheurvormingsprocessen”, GeoDelft rapport 415341-003-v02.
- [7] Albrecht B. A., Benson, C. H. s.l., 2011. “Effect of desiccation on compacted natural clay”, *Journal of Geotechnical and Geoenvironmental Engineering*. Vols. 127(1), 67–75.
- [8] Morris, P.H., Graham, J., Williams, D.J., 1992. “Cracking in drying soils”, *Canadian Geotechnical Journal* 29(2): 263-277.
- [9] Hubble, T., De Carli, E. 2015. “Mechanisms and processes of the millennium drought river bank failures: Lower Murray River, South Australia”, Tech. Rep. Series No. 15/5, Goyder Institute for Water Research, Adelaide, SA, Australia.
- [10] Van Baars, S. 2005. “The horizontal failure mechanism of the wilnis peat dyke. Géotechnique 55(4):319 – 323.
- [11] Robinson, J.D., Vahedifard, F. 2016. “Weakening mechanisms imposed on California’s levees under multiyear extreme drought”, *Climatic Change*, 137(1-2).
- [12] Anonymous. Retrieved 28 May, 2019 from <https://www.deltaproof.stowa.nl>.
- [13] CIRIA. 2013. “The International Levee handbook”, C731, CIRIA 2013, RP957, ISBN: 978-0-86017-734-0.
- [14] Brinkgreve, R.B., Kumarswamy, S., Swolfs, W.M. 2016. “PLAXIS”, Delft, The Netherlands : s.n.
- [15] Albrecht B.A., Benson, C.H. s.l. 2011. “Effect of desiccation on compacted natural clay”, *Journal of Geotechnical and Geoenvironmental Engineering*. Vols. 127(1):67-75.
- [16] Rozing A. 2018. “Scheuren in dijken, Invloed scheuren op macrostabiliteit in primaire keringen, (kleidijken)”, KPP 2018. Deltares report 1202189-008-ZWS-0004, August 2018.

LEVELLING OF SKIRTED SUBSEA STRUCTURES AND SUCTION BUCKET JACKETS BY APPLICATION OF SUCTION OR OVERPRESSURE IN PLAXIS 3D

Jesper Bjerre*, *Multiconsult Bergen, jesb@multiconsult.no*

Erik R. Sørli, *Multiconsult Oslo, erik-s@multiconsult.no*

ABSTRACT

Offshore structures such as subsea foundations and jackets are normally characterized by restricted installation tolerances. For structures with multiple suction piles, application of suction or overpressure in two adjacent suction piles is a beneficial tool to achieve results within the installation tolerances. However, the procedure should be well analysed and planned to accomplish a successful levelling without soil plug failure and avoiding damage to the main structure or the individual suction pile.

Application of levelling, the applied suction or overpressure must first exceed the soil skin friction and afterwards the soil resistance that is required to rotate the foundation in the soil volume. Rotation of the foundation will result in reaction forces in the structural elements that may be critical for design. The magnitude of these two contributions (soil skin friction + rotational resistance) will increase with the penetration depth and thereby the adjustment possibilities will generally decrease during the installation.

In this paper, PLAXIS 3D has been used to determine the required suction and associated overturning moment in the main structure for different rotations and penetration depths. The levelling resistance is used to evaluate the allowable rotation as a function of penetration depth. The analysis is based on a typical subsea foundation with four suction piles in high plastic soft clay.

Keywords: Levelling, Suction, Overpressure, Offshore structures, PLAXIS 3D

1. INTRODUCTION

Offshore structures such as subsea foundations and jackets are design within a specific installation tolerance. Exceeding the installation tolerance may be crucial for the structure's performance and can result in undesirable actions such as reinstallation.

Levelling by application of suction or overpressure is a beneficial tool for foundation solutions consisting of three or more (typically four) suction piles to achieve results within the installation tolerance. These foundation systems are relevant for several structures e.g. skirted subsea structures and jackets with suction piles.

An important aspect in the levelling assessment is associated to the increasing levelling resistance with depth, which is a function of:

- Soil skin friction and tip resistance of the skirts.
- Soil resistance that is required to rotate the foundation in the soil volume.
- The structural stiffness, where a larger stiffness will increase the levelling resistance.
- The structural weight.

The reaction forces in the structural elements caused by levelling may be critical for design. Considering suction piles with diameter of $\text{Ø}6\text{-}8$ m and length of 10-15 m the structural foundation frame is usually very flexible compared to the soil body influenced by the rotation. To avoid soil plug failure, damage to the main structure or the individual suction pile, the levelling procedure should be well analysed and planned to accomplish a successful installation. It is essential that the restrictions for the levelling procedure is outlined in the installation framework used by the installation contractor.

Reviewing the offshore standards and recommendations the demand of levelling analyses are limited. Some recommendations slightly touches the topic such as in DNVGL-RP-N103:

“(6.3.2.2): *The procedure should be well planned, and the necessary suction and or overpressure to accomplish the levelling should be calculated*” [1].

A recommended calculation procedure are not given in the DNVGL RP.

This paper presents a calculation methodology to determine the levelling resistance using the FE-software PLAXIS 3D, and explains how the results (restrictions) can be incorporated in the installation procedures.

1.1 Concept of Levelling

Before the concept of levelling is described in further details, a simple introduction to installation of suction piles will be highlighted.

The installation principle of one suction pile is presented in Figure 1. At phase one, the suction pile is landing onto the seabed followed by a self-weight penetration into the soil. During this phase the mudmat hatches are open to allow water seepage out from the skirt compartment. At the time where the tip resistance and side friction along the skirt wall are equal to the weight of the structure, the forces are in equilibrium and the penetration stops. At phase three, the mudmat hatches are closed and controlled suction is applied until the foundation has reached the target penetration depth.

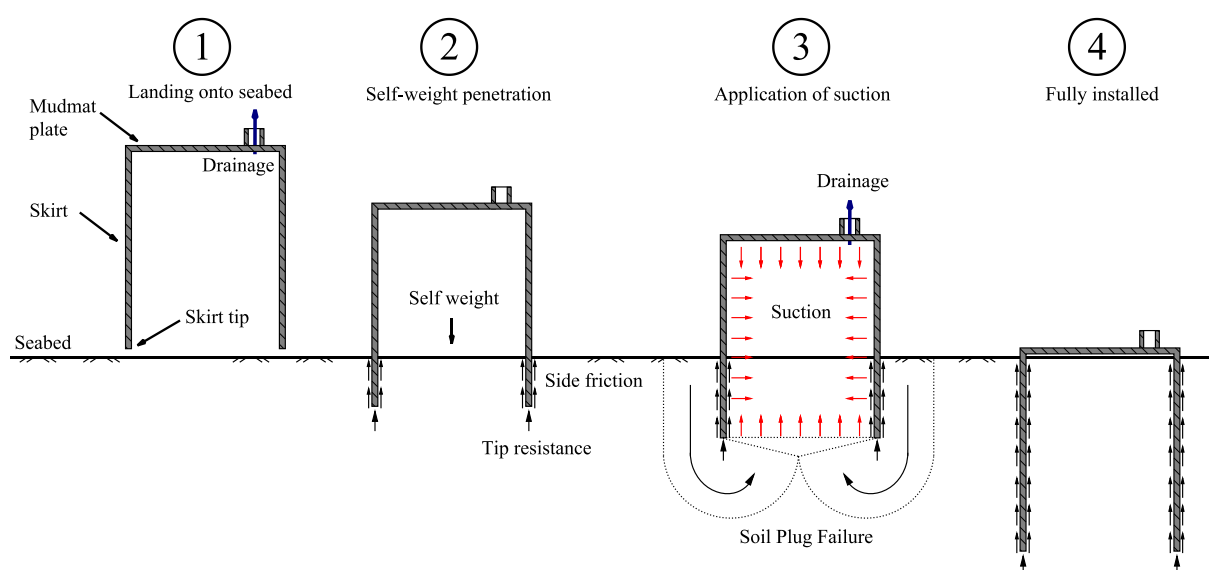


Figure 1. Suction pile - Installation principle

The installation procedure of structures with multiple suction piles is relative complex and several aspects may lead to an undesired installation inclination during the installation phase:

- After self-weight penetration, the structure tends to be inclined in the same direction as the seabed inclination.
- Inclined lifting of the structure during the lowering phase influence the inclination after self-weight penetration.
- An off-set in the CoG of the structure.
- Local variation in the soil conditions and difference between the four suction pile.
- Turn-back effects after levelling operations, which leads to a structure that partly rotates back due to elastic properties of both the structure and the soil. The levelling operations may be performed by over-compensate the tilt, in order to limit the inclinations after the turn-back effects have taken place.
- Difference in pressure loss in the piping between the four suction piles, which gives a different suction pressure between the four suction piles.
- Other effects, such a boulder impact, geometrical imperfections.

Levelling operations occur during phase three with respect to Figure 1 and can be relevant several times during the installation, either by application of suction or overpressure. The levelling principle is presented in Figure 2 where levelling is applied by suction in two adjacent suction piles. At the time where the decided structure inclination is achieved, suction will be applied on all four suction piles as shown in phase three.

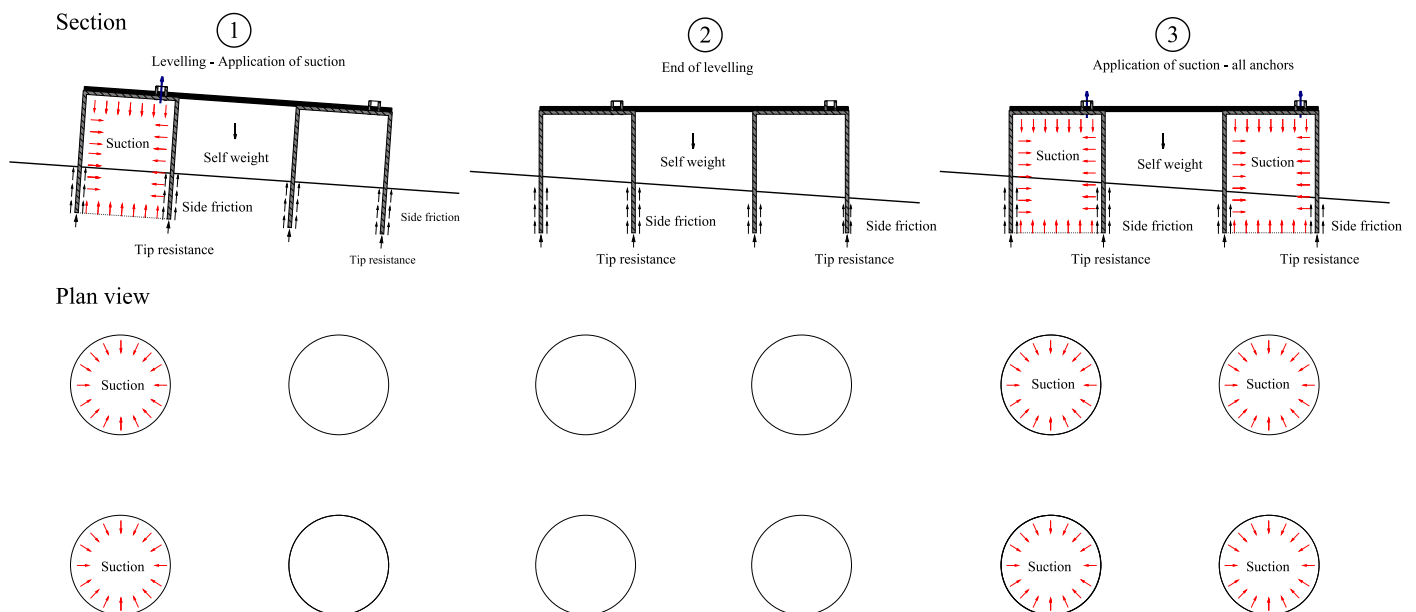


Figure 2. Foundation with four suction piles - Levelling principle

2. LEVELLING METHODOLOGY IN PLAXIS 3D

PLAXIS is a finite element program developed mainly for geotechnical aspects e.g. deformation and stability analysis [2]. PLAXIS 3D are able to capture the soil-structure interaction, flexibility of the foundation system and complex groups effect etc. PLAXIS allows the user to pick between several soil models. The chosen soil model should be calibrated to advanced laboratory tests.

The methodology in PLAXIS to evaluate the levelling resistance is outlined in the following:

1. Establish a model consisting of the relevant soil layers, the suction piles and the structure between the suction piles. If applicable, symmetry may be used.
2. Apply the submerged weight of the structure in the model.
3. Apply suction for two of the four suction piles, and evaluate the corresponding rotations and moment in the frame for different suction pressures.
4. Repeat step 1-3 at different penetration depths. Depending on the geometry three penetration depths are normally sufficient.
5. The results can be interpolated between these penetration depths.
6. Based on the results in step 4, establish a relationship between levelling resistance with depth. The levelling resistance in terms of applied suction and moments in the frame should be given for different rotations e.g. 0.25, 0.5, 1.0 and 2.0 degrees.

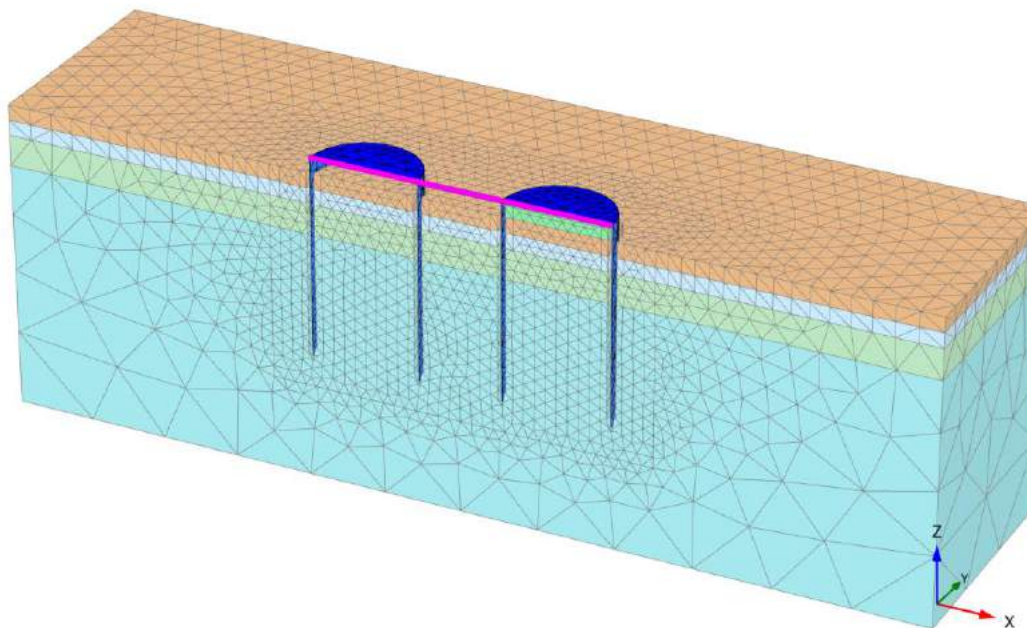


Figure 3. PLAXIS 3D - Model setup. Symmetry exploited

2.1 Important Factors in the PLAXIS Model

Following aspects should be considered for the levelling assessment in PLAXIS:

- The levelling resistance is mainly govern by the stiffness and strength of the soil. To ensure conservative results, the levelling assessment is normally design for high estimated soil properties.
- The sensitivity of the soil is an important aspect, which is used to take into account the remoulded shear strength along the skirts.

- The mesh quality is very important aspect in finite element. A mesh sensitivity analysis should be performed to ensure reliable results and avoid mesh locking effects.
- Only half of the structural stiffness should be used if symmetry is exploited. The member forces should be multiplied with a factor of 2 for the same reason.
- To model the effect of the entrapped water in the passive suction pile a linear elastic soil body with unit weight close to water with a very low shear modulus and a relatively high bulk modulus is used to connect the mudmat plate to the soil.
- The rotation is simply determined by comparing the vertical displacement at the centre of the top plate between the two suction piles.
- The forces and moments are taken from PLAXIS at the edge of the mudmat plate, and converted to an equivalent overturning moment at the centre of the mudmat. The shear force is transfer into an equivalent moment by multiplying half of the diameter of the suction pile and added to the moment at the edge.

3. CASE STUDY

3.1 Soil Conditions

The case study is based on a typical offshore soil profile dominated by homogeneous, soft very plastic clay with increasing shear strength with depth. The high estimate strength profile is defined as $s_{uDSS} = 5.0\text{kPa} + 2.5\text{ kPa/m}$. The material is slight overconsolidated, with an upper firmer crust in the upper 1.0 m. The basis soil index properties are presented in Table 1. The analyses is performed using an anisotropic soil model in terms of both strength and stiffness.

Table 1. Case study – Basic soil index properties

Parameter	Value	Unit
Unit weight	15	[kN/m ³]
Plasticity index	50	[-]
Water content	70	[%]
s_{uDSS}/p_0'	0.7 - 0.5	[-]
OCR	1.8 - 1.3	[-]
Sensitivity	4	[-]

3.2 Results

Based on PLAXIS analyses three curves can be assembled as presented in Figure 4 to Figure 6.

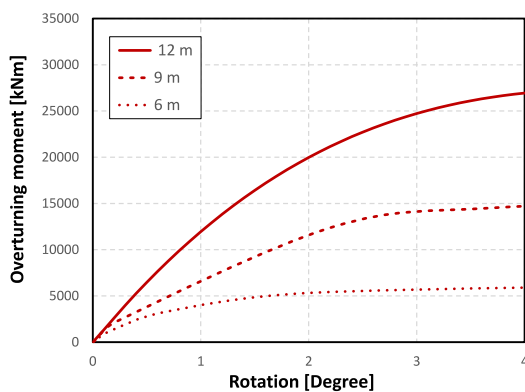


Figure 4. Overturning moment vs. rotation

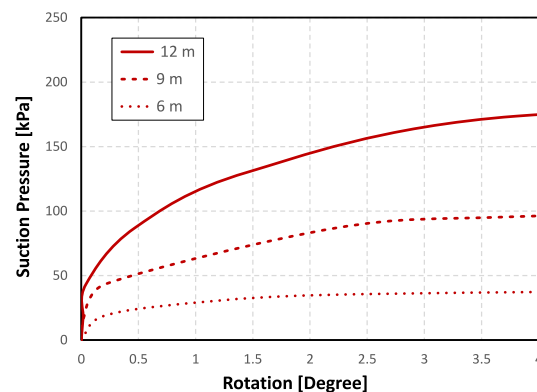


Figure 5. Suction pressure vs. rotation

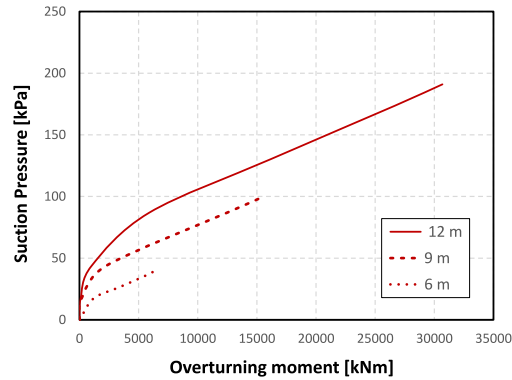


Figure 6. *Overturning moment vs. suction pressure*

The analysis to determine the structural capacity is left out for this article but should be evaluated in collaboration with the structural discipline. Imaginary capacity of the structural frame and the buckling capacity of the suction pile are presented in Table 2 with realistic magnitude.

Table 2. *Properties of the foundation system – Case study*

Moment capacity of the frame	Buckling capacity (depth dependence)			
	Penetration [m]	6	9	12
22000 kNm	Suction [kPa]	60	90	110

Combining and rearranging the output from PLAXIS 3D and the foundation properties in Table 2, Figure 7 and Figure 8 can be assembled. In addition, the capacity for soil plug failure is presented as well.

From Figure 7 one may observed that soil plug failure (orange line) is not critical for this particular case. The buckling capacity (red line) introduces a restriction of allowable suction and thereby obtainable rotation of the structure at specific depths. From Figure 8 the frame capacity (blue line) introduces a moment restriction and thereby obtainable rotation of the structure at specific depths.

The case for overpressure is left out but can simply be assembled from Figure 7 by adding twice the applied structure weight divided by the total suction area.

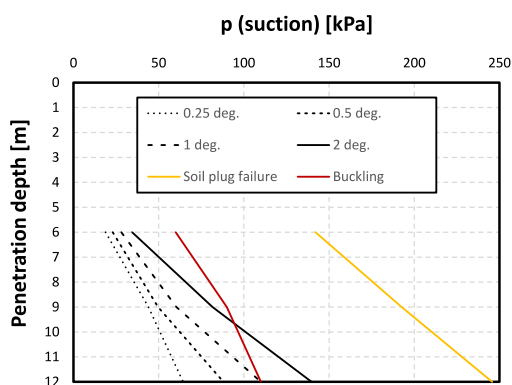


Figure 7. *Suction pressure vs. depth*

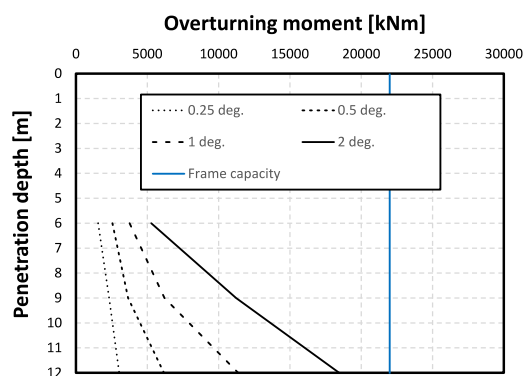


Figure 8. *Moment vs. penetration depth*

The final results are presented in Figure 9 as allowable rotation with respect to either suction/(overpressure) or overpressure by combined Figure 7 and Figure 8. The overpressure is only driven by the frame capacity and soil-plug failure where the suction also need to take into account the buckling capacity.

Figure 9 should be outlined in the installation framework. In this way, the installation contractor can easily see what allowable rotation can be obtained by either method at a given penetration without avoid damaging the foundation or causing soil plug failure.

A typical vulnerability assessment is to compare Figure 9 with a conservative self-weight penetration. A high self-weight penetration may be crucial since it may result in restrictions for the allowable rotation. For instance if the penetration depth is determined to 9.0 m, the foundation is allowed to rotate up to 2.8 degree by suction alone. However, for overpressure alone there is no restrictions for this particular case. For greater penetration depth, the allowable rotation will be less.

At the final penetration depth, the foundation has limited levelling performance. Meanwhile, the levelling should be performed at shallow penetration depths to ensure that only minimum adjustments are needed at deeper penetration depths. As a general recommendation, the allowable levelling should at least be 0.5 degree at the final penetration depth.

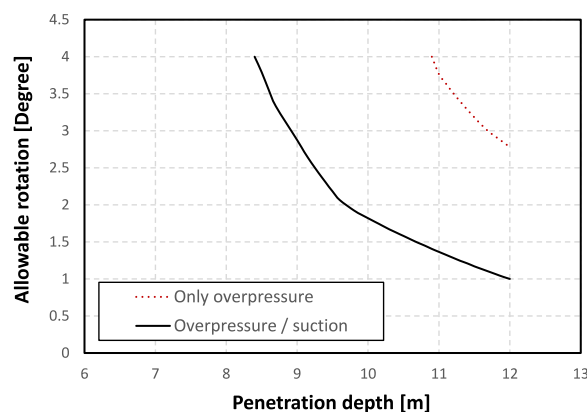


Figure 9. Allowable rotation vs. penetration depth

3.3 Validation Using Limit State Principles

The overturning moment in the structural frame determined in the PLAXIS 3D model can be verified through limit state principles assuming rigid body motion. According to [3], the ultimate moment capacity for rigid body can be formulated as:

$$M_{ult} = N_m \cdot H_{ult} \cdot L \quad (1)$$

where L = length, H_{ult} = the ultimate lateral capacity and N_m = empirical capacity factor related to the failure mode. In addition, the ultimate lateral capacity can be formulated as:

$$H_{ult} = N_p \cdot s_{u,average} \cdot L \cdot D \quad (2)$$

where D = Diameter, $s_{u,average}$ = the average undrained shear strength and N_p = empirical capacity factor related to the failure mode. For aspect ratios $L/D > 2$, N_p is usually in the range of 7-11 while N_m is usually in the range of 0.20-0.24 [4].

Table 3 summarises the validation and where good agreement between PLAXIS and hand-calculations are found.

Table 3. Validation using limit state principles

	Length = 6 m	Length = 9 m	Length = 12 m	Unit
M_{plaxis}	6300	15400	27900	kNm
N_p	7.0	7.0	7.0	-
N_m	0.24	0.22	0.20	-
$S_{u,average}$	13	17	19	kPa
H_{ult}	3822	7497	11172	kN
M_{ult}	5504	14844	26813	kNm
M_{plaxis}/M_{calc}	1.13	1.04	1.04	-

4. CONCLUSION

Levelling of skirted subsea structures by application of suction or overpressure is a beneficial tool to achieve results within the installation tolerance.

Application of levelling, the applied suction or overpressure must first exceed the soil skin friction and afterwards the soil resistance that is required to rotate the foundation in the soil volume. Rotation of the foundation will result in reaction forces in the structural elements may be critical for design. Meanwhile, the offshore standards and recommendations slightly touches the topic of levelling and do not present a recommended calculation procedure.

This paper presents a calculation methodology to determine the levelling resistance using the FE-software PLAXIS and how to incorporate the results (restrictions) in the installation procedures have been presented and assembled into one single figure.

ACKNOWLEDGEMENT

The authors wish to acknowledge the financial support to R&D project provided by the Geotechnical Division in Multiconsult. The contribution of colleagues through fruitful discussions is also gratefully acknowledged.

REFERENCES

- [1] DNVGL-RP-N103, 2017 July. “Modelling and analysis of marine operations”. DNV GL AS, Norway.
- [2] PLAXIS 3D version 2017. Delft University of Technology and PLAXIS bv, The Netherlands.
- [3] Sørli, E. R., Bendzovski, R., Athanasiu, C., Bye, A., Giese, S., 2019. “A modified modal earthquake analysis of caisson foundations”, The XVII European Conference on Soil Mechanics and Geotechnical Engineering, 1-6 September 2019, Reykjavik.
- [4] Sørli, E. R., 2013. “Bearing capacity failure envelope of suction caissons subjected to combined loading”, M.Sc Thesis, Department of Civil and Transport Engineering, Norwegian University of Science and Technology, June 2013.

CONCRETE STRESS-STRAIN BEHAVIOR AND ELASTIC MODULUS DETERMINATION IN FOUNDATION PILE LOAD TEST INTERPRETATION

Mateusz Wiszniewski*, *Faculty of Civil and Environmental Engineering, Gdansk University of Technology, Poland, mateusz.wiszniewski@pg.edu.pl*

Adam Krasinski, *Faculty of Civil and Environmental Engineering, Gdansk University of Technology, Poland, adam.krasinski@pg.edu.pl*

ABSTRACT

Static load tests on instrumented piles are conducted in order to determine force distribution along the shaft, load transfer mechanism and characteristics of soil-structure interaction (unit resistance curves t - z , q - z). Currently available instrumentation techniques focus on direct strain measurements in concrete piles. Using basic elastic relations measured strains can be converted into axial forces. However, proper determination of that forces requires the exact value of pile material stiffness (EA), which is subjected to various impacts (uncertainties). Due to difficulties in determination of that stiffness, additionally hampered by the practical lack of knowledge about the pile shafts real geometry, very often the interpretation results of instrumented load tests are inadequate and can be subjected to significant errors.

Two static load tests on instrumented piles were performed. After carrying out the load test, piles were extracted from the ground to perform detailed geometry measurements. Concrete samples were taken from several sections for elasticity modulus determination. Investigation has shown some significant imperfections in pile core stiffness evaluation (changes in pile cross section area and elasticity modulus variability along the shaft). Both, field and laboratory tests have shown a nonlinear characteristic of concrete stress-strain behavior that should be considered in the results interpretation. Possible methods of concrete core stiffness determination and its influence on the final load distribution along the pile shaft are also presented in the paper.

Keywords: Pile Instrumentation, Static Load Test, Strain Gauge, Pile Load Distribution, Elastic Modulus

1. INTRODUCTION

Static load tests on instrumented piles, equipped with strain measuring devices to determine the axial force distribution along the pile shaft are regularly performed. Popularity of these studies steadily increases. They are usually conducted for scientific and cognitive purposes. Compared to a standard load capacity test, instrumented pile measurements provide a number of new, detailed and quantitative information that deepens the knowledge of interaction between various technology piles and the soil. Mobilization of soil friction can be assessed, what is useful especially for testing the behavior of a new drilling auger and its impact on the soil condition. Foundation designer may also verify his assumptions regarding soil bearing capacity, what shows high economic benefits of such a testing. That shows why structure monitoring market (Intelligent Structures) grows so fast. The test results are also used for verifying and calibrating numerical models of axially loaded piles and load transfer mechanism.

Instrumentation may also be used for pile condition control – presence of any imperfections and discontinuities. General principle of static load test on instrumented pile is to insert a measuring instruments into the pile core to determine the axial deformation of the shaft [1,2]. Several measurement techniques are currently available, most of which benefit from the use vibrating wire extensometers (global strain extensometers – retrievable or local strain gauges - embedded), also special optical fiber cables (embedded). Older measurement methods, such as pile embedded rods or electro-resistive strain gauges, have been virtually abandoned due to high workload, low measurement accuracy, and high sensitivity to other factors, such as temperature and humidity [3,4]. Based on the pile shaft deformation measurements, carried out at various depths (several to several dozen locations) the values of axial forces are calculated on the basis of the Hooke's law formula (Eq.1) [5,6].

$$Q_i = \varepsilon_i \cdot E_{t,i} \cdot A_{t,i} \quad [\text{kPa}] \quad (1)$$

where:

ε_i – axial strain in section 'i' of the pile core

$E_{t,i}$ – elasticity modulus (Young modulus) of the pile material in section 'i'

$A_{t,i}$ – pile cross section area in in section 'i'

Experience has quickly shown that the apparently simple formula is fraught with many factors that may significantly influence the value of Q_i [7,8,9]. The lowest influence has the axial strain ε_i measurement. Currently available techniques (vibrating wire or fiber optics) allow accurate strain measurements at the level of $10^{-6} \div 10^{-5}$. Due to high precision of the measurement, instrumentation should be installed in the pile with the utmost care and meticulousness also apparatus itself should be characterized by high reliability. Failing in this matter often disqualify the whole work [10]. Parameters $E_{t,i}$ and $A_{t,i}$, are subjected to various impacts (uncertainties). Concrete that serves as main material for pile construction is not homogeneous and its strain-stress characteristics may highly differ depending on age, curing conditions, location in the ground and strain range. Therefore, taking a single value of elastic modulus (often based only on concrete type) may lead to serious inaccuracies in stress determination for particular structure sections. Deviations of the pile cross section area depend mainly on the technology of the pile. In the case of cast in-situ piles, necking, widening or weakening of the shaft, caused by other technological and geomechanical factors may occur.

Works of Sinnreich [11], Fellenius [9] and Pine [12] address the issue of concrete modulus determination. They presented some ideas how to consider nonlinear pile stiffness in the strain readings interpretation. Some possible differences of modulus are shown in Fig.3. Methods like Transformed Area Method, Implicit Method, Linearly Elastic Method (Incremental Method), Secant Modulus Method, Tangent Modulus Method have been introduced. However, they all have significant limitations and can be used only in very specific situations, eg. TMM requires sufficient pile settlement and full mobilization of soil friction for all pile sections. Lam and Jefferis [13] presented a critical review of those methods.

2. SCREW DISPLACEMENT PILES

As part of the research task, two screw displacement piles equipped additional strain measurement instruments were constructed. Static load tests were conducted, after which piles were extracted from the ground in order to determine pile core stiffness. Diameter was recorded and concrete samples were taken for testing the elastic moduli on individual sections of the pile. Piles and research work were carried out in cooperation with the Menard company on the experimental plot next to the construction being carried out at that time. Pile length was: A -

5.55 m and B - 5.45 m. Piles were made at a distance of about 2 meters from each other. Class C30/37 concrete was used. Ground conditions were analyzed and presented in the form of CPT probing chart in Figure 6. Up to about 1.2 m below the surface was medium compacted sand, then irrigated silt (organic soil) with poor mechanical parameters, and from about 4 m a layer of medium compacted sand.

Piles were excavated from the ground after about 30 days (Figure.1.) Small necking was found in both piles (about 3-4 cm), more or less in the middle of their length (2.20 - 3.40 m). Piles were divided into 5 sections, from each 3 cylindrical samples were taken (core drilling). Samples were then stored in the laboratory for approximately 30 days at constant temperature and full water saturation.



Figure 1. Piles excavated from the ground and pile sections prepared for concrete sampling.

3. CONCRETE MODULUS OF ELASTICITY TESTING

Cylindrical samples with a diameter of 10 cm and a height of 20 cm were tested. The surfaces (upper and lower) were properly aligned and smoothed. A total of 29 samples out of 30 were tested (1 sample was damaged during preparation). For local measurement of strain, steel hoops with a spacing of 10 cm and 3 inductive displacement sensors with an accuracy of 0.001 mm were used. The load was set at a constant speed in 10 steps using a Zwick testing machine with a maximum pressure of 10 tons. The course of the test itself, i.e. the range of the stress to be applied, was based on the polish standard PN-EN 12390-13: 2014-02. The standard gives the range from 0.5 MPa to $0.33 f_{cm}$, where f_{cm} is the average compressive strength of concrete measured on cylindrical samples with a diameter of 150 and a height of 300 mm. For C30/37 concrete it is respectively a range from 0.5 to 9.9 MPa, while the actual range used in the work was 0.64 to 10.8 MPa. On this basis, a standard modulus of elasticity (tangent) could be determined. This value, however, does not reflect the real behavior of concrete in the stress-strain relationship ($\sigma - \epsilon$). As mentioned earlier, the modulus of elasticity changes with the deformation and it is not a fully linear relationship. Therefore, the following types of modules can be distinguished: E_p - initial module, occurs in the range of very small deformations and is characterized by a much higher value than the average module; E_s - secant modulus, changes with deformation; E_{st} - tangent module, can be determined for any range of deformations.

4. RESULTS ANALYSIS AND DISCUSSION

Test results of cylindrical concrete samples were presented in the form of $\sigma - \epsilon$ graphs in Figure 2. In both cases (for all samples) two zones can be determined that characterize the behavior of the material. In the first phase (I), relatively low deformation values are registered for a constant stress increase, which results in high values of the elastic modulus - this is the so-called initial module. These values may be due to the unspecified property of the concrete structure, the

uneven distribution of cross-sectional forces and the initial stiffness and inertia of the measurement system. After exceeding 50 $\mu\epsilon$, the slope $\sigma - \epsilon$ stabilizes, thus entering the second zone (II) of the material characteristics, where it is approximately linear.

29 analyzes were carried out, 15 for pile A and 14 for pile B. The graphs in Figure 2 clearly show the heterogeneity of the material being tested - for the same stress value different values of measured deformations were achieved, which is especially visible for pile A. For the stress $\sigma = 10.8$ MPa, the strain values range from 228 to 336 $\mu\epsilon$, so it is a difference of 32%, which directly translates into values of the elastic modulus. For pile B this difference is smaller and amounts to 12%.

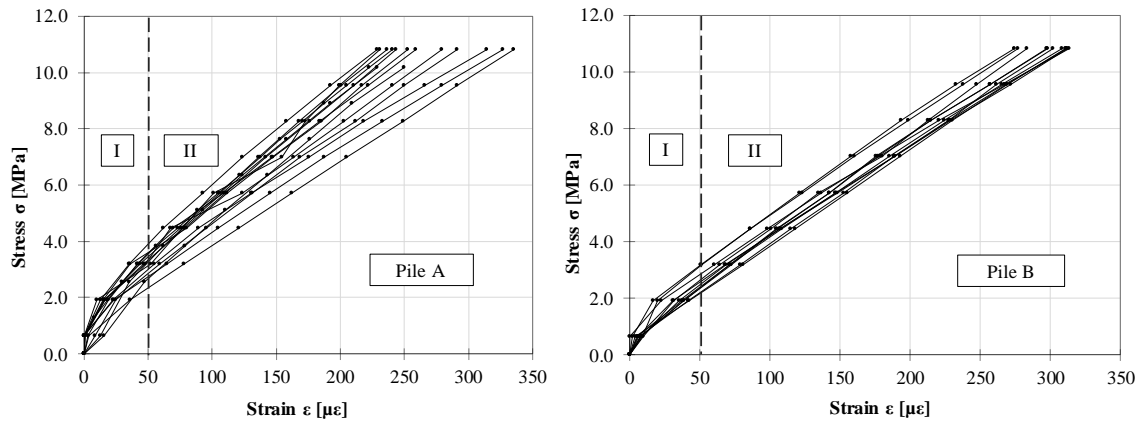


Figure 2. Stress - strain relation ($\sigma - \epsilon$) for pile A and B.

Figure 3. shows the variation of the secant modulus in relation to the deformation. The change was described by power functions for two piles, they reflect the concrete behavior quite well. In the range of small deformations (up to $\epsilon = 100 \mu\epsilon$), the E modulus decreases significantly with increasing deformation - from 128 GPa to about 50 GPa for pile A and from 112 GPa to around 45 GPa for pile B. At larger strains, above 100 $\mu\epsilon$, the modulus continues to decrease systematically, but much more slowly and this relationship can be described as linear. Laboratory results showed an analogy to the field measurements of the concrete modulus, where a similar relationship $E - \epsilon$ was found, which can also be described by power function [1, 2]. The secant modulus method and its variability create some interpretation problems for later analysis of the stress occurring in the structure. The high variability along with the deformation and additionally the material heterogeneity along the pile length (especially the spread of results in the range of small deformations) can generate significant errors when estimating the cross-sectional forces in the initial pile load or at significant depth where the deformations are small. According to the national standard, the initial measurements, i.e. up to a stress value of 0.5 MPa, should be omitted. In the case of the analyzed material, this value was insufficient. The characteristics of $\sigma - \epsilon$ stabilized at 10 - 36 $\mu\epsilon$ (pile A) and 17 - 39 $\mu\epsilon$ (pile B), which corresponded to a pressure equal to 2.0 MPa. This may have been partly caused by a too high step in the increase of stress, with a denser measurement grid, it might be possible to achieve stabilization at a slightly lower stress value.

In further analysis, only the results above 50 $\mu\epsilon$ were considered (zone II, Figure 2). For each sample, a new distribution of the "stabilized" secant modulus E_{stab} and its variability depending on the deformation (total strain including also the initial zone) were determined. The results are shown in Figure 4. Also a certain spread of results was obtained for individual samples, but it

is much smaller, i.e. for pile A, the initial values of the module for individual samples range from 30 to 42 GPa, and for pile B from 32 to 39 GPa. What is more important in such a method of analysis, the variation of the secant modulus is much smaller and amounts on average 2.5 GPa for about 210 $\mu\epsilon$ (comparing to earlier over 10 GPa for 250 $\mu\epsilon$). In addition, this variability can be described by a simple linear function while maintaining a high correlation coefficient. In both cases (pile A and B) a similar average characteristic of this variability was obtained, i.e. 1.181 and 1.185 GPa per 100 $\mu\epsilon$.

The application of the standard rule, omitting the initial measurements (the initial modulus of elasticity) in the analysis of the results seems to be justified. The standard, however, lacks information about the variability of the module along with the deformation, and this relationship can be of significant importance when interpreting the measured values in the pile tests. Fellenius [14] in his work on the distribution of forces in the pile wrote about ignoring measurements smaller than 100 $\mu\epsilon$ in the determination of the module E, in his opinion they are burdened with too large errors and give unreal results. Nevertheless, it is necessary to determine the correct value of the module also in the area of small deformations. In the case of pile tests, stress transmitted to the pile decrease along with the depth causing less and less deformation, so at the pile base very slight deformations are common.

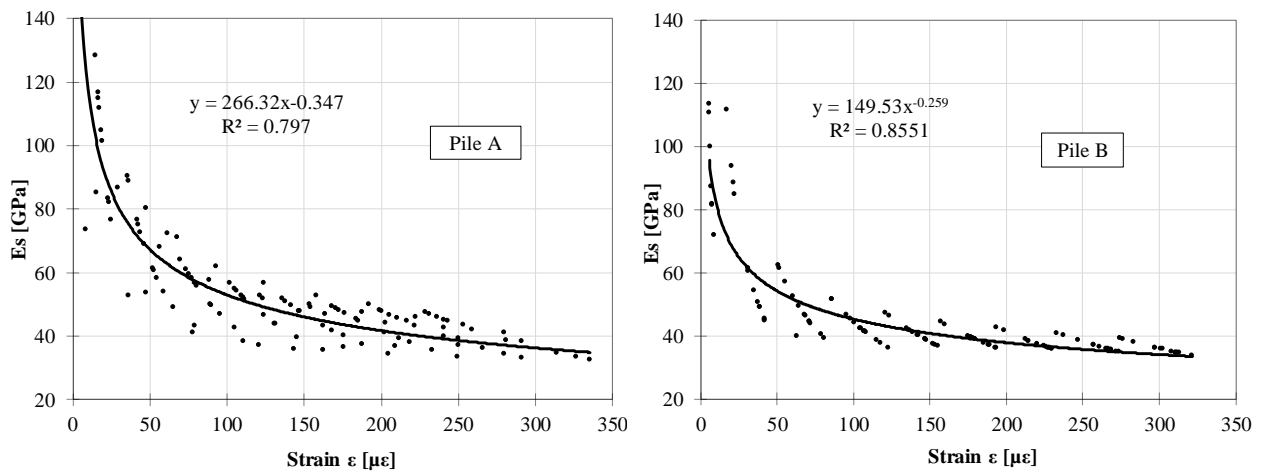


Figure 3. Distribution of secant modulus of elasticity (E_s).

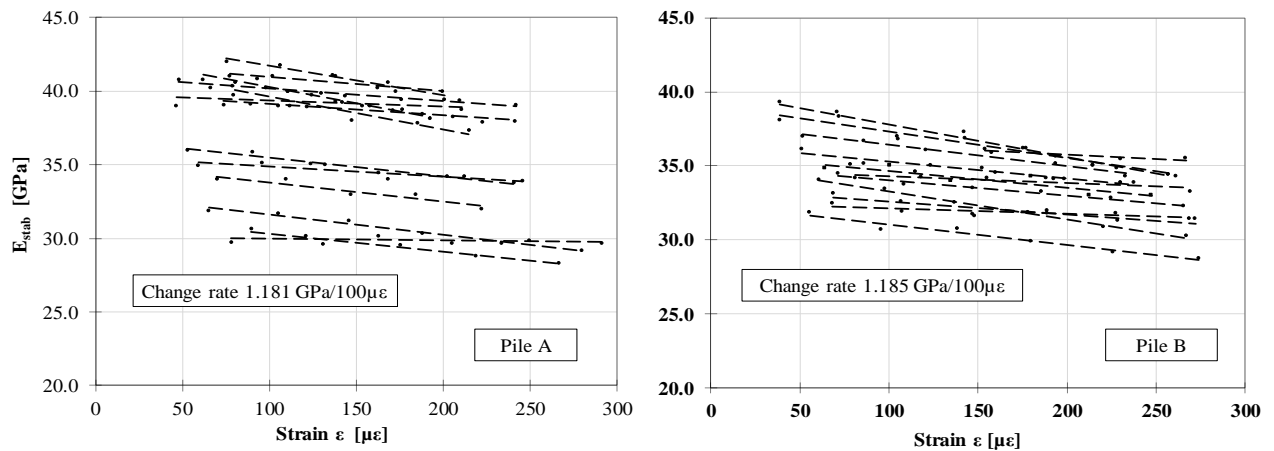


Figure 4. Distribution of the "stabilized" secant modulus (E_{stab}).

For all 29 samples, in zone II of $\sigma - \varepsilon$ relation (Fig. 2), i.e. omitting measurements of strains lower than $50 \mu\varepsilon$, the averaged modulus of elasticity (tangent modulus for the considered range of deformations) was determined. The literature value of the modulus for concrete class C30/37 is 32-33 GPa. The values of tangent modulus obtained from the tests are presented in Figure 5. In both cases, the module values are heterogeneous over the pile length and range from 28.8 to 39.1 GPa for pile A and from 30.3 to 34.3 GPa for pile B. Values at similar depths differ by an average of 6.5% (for the last segment the difference is 16.2%). Attention should be paid to the reduced E value (28.8 and 30.3 GPa) at a depth of about 2.80 m, for both pile A and pile B. At this depth, small necking was also noted. Piles were at a distance of about 2.0 meters from each other, so they were made in practically identical ground conditions, the narrowing occurred in the layer of compressible (organic) silt saturated with water. The reason for the narrowing could be the increased pressure of the silt layer on fresh concrete and the tendency of the pile hole to partially close. This process could be spread over time and break the structure of curing concrete. Amir et al. [15] showed in their work that the modulus of elasticity of concrete in the pile increases with depth. In the analyzed case, it is difficult to conclusively state such a dependence. It should be emphasized that in the cited work the length of piles was 70 m and the authors had more data, which allowed for more precise characterization of the material. Certainly, however, it is possible to determine the variability of the modulus on the length of the pile and this variability should be taken into account in the analysis and interpretation of deformation measurements of the concrete pile shafts.

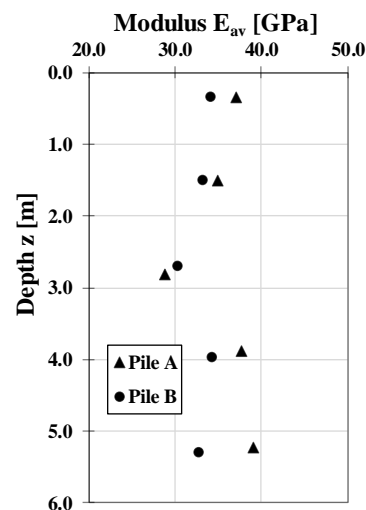


Figure 5. Values of the average modulus of elasticity E_{av} at certain depths.

The results of pile A load test are shown in the Figure 6. below. The first graph shows distribution of force along the side surface for a constant pile core stiffness value, i.e. a constant modulus of elasticity (33 GPa) and a constant cross-sectional area. In the first measurement section unrealistically high force values are visible (higher than those set on the top). In the upper part of the pile, the highest deformations occur, so according to earlier findings, the modulus will achieve its lowest value here. Assuming a constant (inflated) value of the modulus, we get inflated force values. The opposite situation occurs at the pile base, where, firstly, the modulus can achieve higher value due to the depth and secondly, the slightest deformation will occur here (possibly less than $50 \mu\varepsilon$, therefore in the range of large initial modulus values). In the central pile section, another disturbance caused by reduced stiffness is

visible (reduced cross-section area and reduced elastic modulus). Force in the pile shaft cannot increase with depth, just the opposite, soil resistance takes over part of the load, and therefore force value must decrease. The second graph presents a correct force distribution during the pile load test, for which stiffness variations have been taken into account (cross section area measured after the test and elastic modulus determined from laboratory tests). The differences are significant, especially for unit shaft resistance analysis. Load transferred to the ground under the pile base in the first scheme equals to 166 kN, for second it is 209 kN, so there is 26 % difference. Performed analyzes clearly indicate the need of accurate pile core stiffness determination the stiffness in order to obtain a correct load distribution during the test.

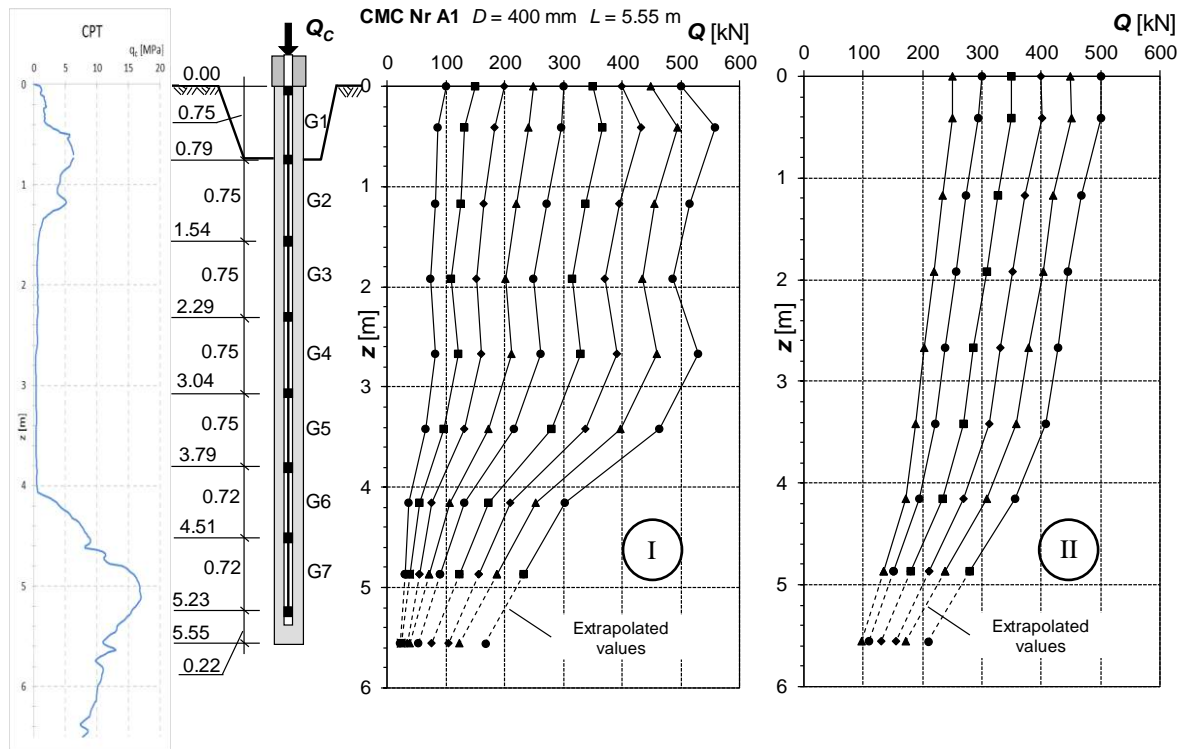


Figure 6. Force distribution during a static pile load test. I - constant pile core stiffness.
 II - variable pile core stiffness (calculated).

5. CONCLUSIONS

- The value concrete modulus of elasticity depends on many factors, therefore it should be determined for each analyzed material, it cannot be taken directly from tables based on the declared compression strength class;
- The elasticity modulus changes along with the deformation, it decreases with its increase. For zone II (stabilized) a linear decrease was determined at about 1.18 GPa per 100 $\mu\epsilon$;
- Tests also confirmed heterogeneity of the material (concrete modulus) along the pile length, modulus reduction at the cross-section narrowing was found in the case of both piles. The analyzed piles were too short to unambiguously assess the increase in the modulus along with depth described in some literature;
- Adopting a constant value of the concrete modulus to interpret deformations measured in the pile can lead to significant errors in load distribution estimation.

ACKNOWLEDGEMENT

Authors would like to thank Menard company for the help in carrying out research tasks, technical and financial support in organizing the experimental plots. This work was supported by the Polish National Science Center under Preludium Grant No 2017/27/N/ST8/02179.

REFERENCES

- [1] Krasiński A., Sieńko R., 2010. „*Pomiar pionowego rozkładu siły w palu podczas testów statycznych*” [The measurement of vertical force distribution in the pile during a static load tests]. 56 Konferencja Naukowa Kielce – Krynica 19-24.09.2010. Poland. (In Polish).
- [2] Krasiński A., Sieńko R., 2010. „*Wykorzystanie pomiaru pionowego rozkładu siły w palu do interpretacji testów statycznych*” [Use of vertical force distribution measurement in pile to interpret static tests]. *Magazyn Autostrady*, 11/2010: 24-28. (In Polish).
- [3] Kim, S.R., Chung, S.G., and Fellenius, B.H., 2011. “*Distribution of residual load and true shaft resistance for a driven instrumented test pile*”. *Canadian Geotechnical Journal*, (48) 4: 583-598.
- [4] Fellenius, B.H., Kim, S.R. and Chung, S.G., 2009. “*Long-term monitoring of strain in strain-gage instrumented piles*”. *ASCE Journal of Geotechnical and Geoenvironmental Engineering*, 135(11): 1583-1595.
- [5] Fellenius B.H., 2002. “*Determining the resistance distribution in piles, Part 1: Notes on of no-load reading and residual load. Part 2: Method for determining the residual load*”. *Geotechnical News Magazine*. 20(2): pp. 35-38 and 20(3): 25-29.
- [6] Sahajda, K., 2015. “*Siły rezydualne w ocenie nośności i osiadań żelbetowych pali wbijanych*” [Residual forces in the assessment of bearing capacity and settlement of reinforced concrete driven piles]. PhD Thesis. Warsaw University of Technology, Poland (In Polish).
- [7] Fellenius, B.H. 1989. “*Tangent modulus of piles determined from strain data*”. The ASCE Geotechnical Engineering Division Foundation Congress, Vol. 1:500-510.
- [8] Fellenius, B.H., Brusey, W.G., Pepe, F. 2000. “*Soil setup, variable concrete modulus, and residual load for tapered instrumented piles in sand*”. ASCE Specialty Conf. on Performance Confirmation of Constructed Geotech. Facilities, University of Massachusetts, Amherst, USA, April 9-12, 2000.
- [9] Fellenius, B.H., 2002. “*Determining the true distributions of load in instrumented piles*”. ASCE International Deep Foundation Congress, Orlando, Florida.
- [10] Siegel, T.C. and McGillivray, A., 2009. “*Interpreted residual load in an augered cast-in-place pile*”. 34th Annual Conference on Deep Foundations, Deep Foundations Institute, 173-182.
- [11] Sinnreich J., 2011. “*Strain Gage Analysis for Nonlinear Pile Stiffness*”, *Can. Geotech. J.*, 35, No. 2
- [12] Pine T. L., 2016. “*Measurement and prediction of the load distribution and performance of continuous flight auger piles*”. MSc. Thesis at University of Western Australia, Australia
- [13] Lam C., Jefferis S. A., 2011. “*Critical assessment of pile modulus determination methods*”. *Canadian Geotechnical Journal*, Vol. 48, No. 10: 1433-1448.
- [14] Fellenius, B.H., 2001. “*From Strain Measurements to Load in an Instrumented Pile*”. *Geotechnical News Magazine*, Vol. 19, No. 1: 35 - 38.
- [15] Amir, J. M., Amir E. I., Lam C., 2014. “*Modulus of elasticity in deep bored piles*”. DFI/EFFC International Conference on Piling and Deep Foundations, Stockholm, Sweden.

LABORATORY TESTING AND NUMERICAL MODELLING OF THE DYNAMIC BEHAVIOUR OF TAGUS RIVER SAND

Luís Miranda*, *MSc, Laboratório Nacional de Engenharia Civil, lmiranda@lnec.pt*

Laura Caldeira, *PhD, Laboratório Nacional de Engenharia Civil, laurac@lnec.pt*

João Serra, *PhD, Laboratório Nacional de Engenharia Civil, biles@lnec.pt*

André Barbosa, *PhD, Oregon State University, andre.barbosa@oregonstate.edu*

ABSTRACT

In the framework of a third Tagus River crossing, through an immersed tunnel, advanced laboratory tests were performed on its highly liquefiable foundation sand, namely cyclic undrained torsional tests. The Manzari-Dafalias model, which allows simulating liquefaction on the Tagus River sand and is, therefore, central in the tunnel design, as well as the numerical work to calibrate the model and identify its most relevant parameters, are presented. Model parameters, their respective reference values and tests performed to determine directly most of the parameters, are introduced. A parameter sensitivity analysis, conducted through numerical simulation of triaxial monotonic drained tests and of cyclic undrained torsional tests, implemented both for the pre-liquefaction and liquefaction phases, is described. Finally, some parameters are determined by fitting the model to the laboratory results.

Keywords: Advanced Laboratory Tests, Constitutive Model, Numerical Simulation, Liquefaction, Immersed Tunnel.

1. INTRODUCTION

Design of a third Tagus river crossing is currently being considered downstream of 25 de Abril Bridge in Lisbon, Portugal, between Algés and Trafaria, corresponding to an immersed tunnel with a length of approximately 2.4 km.

Many immersed tunnels are built on alluvial formations in earthquake zones and one of the main issues in their safety design is precisely their resistance to foundation liquefaction. As a matter of fact, displacements of an immersed tunnel resulting from a seismic event depend largely on the behaviour of the surrounding ground, namely its stiffness [1]. These displacements may be amplified by liquefaction and can lead to ground failure if significant loss of soil strength occurs. Consequences of liquefaction may include loss of lateral or vertical support, differential movements or rotations, movements due to shake-down settlement effects (where granular material naturally densifies due to loss of structure) and floatation of the tunnel. Likewise, its uncontrolled movement is undesirable and could lead to overstressing and damage of the structure or leakage of the tunnel joints.

This paper summarizes the laboratory and numerical work to calibrate a chosen constitutive model, the Manzari-Dafalias (M-D) model, to the Tagus river sand properties, with the goal of enabling its future application in the scope of the immersed tunnel crossing design.

2. TAGUS RIVER SAND

The immersed tunnel is supported on alluvial Tagus river sands, with a maximum thickness of around 50 m, overlaying Miocenic layers of increasing stiffness and strength with depth and a basalt bedrock (Figure 1). The river maximum depth is about 30 m.

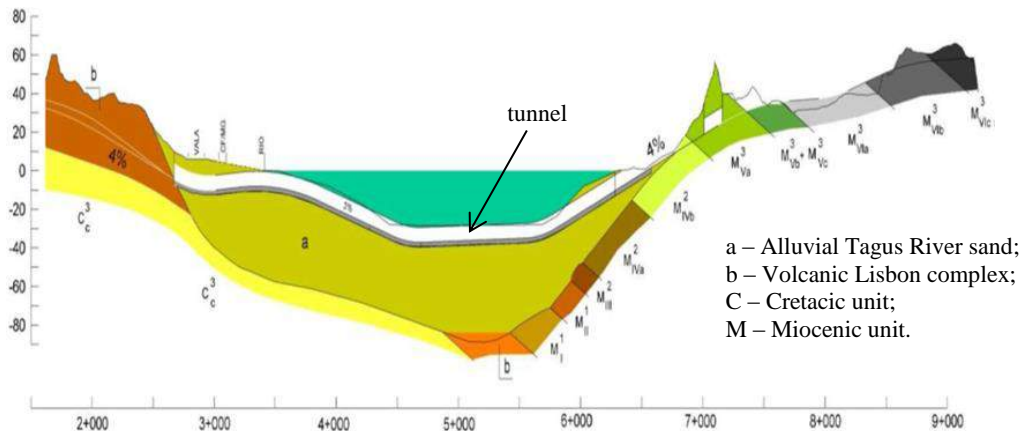


Figure 1. Third Tagus River crossing geologic profile

Tagus River sand is a siliceous, clean and poorly graded sand, classified as SP. Its physical characterization included: a grain size analysis; determining the solid particles density, G_s ; and obtaining the maximum, $\gamma_{d,max}$, and minimum, $\gamma_{d,min}$, dry unit weight. Some physical indexes are presented in Table 1.

Table 1. Physical indexes of Tagus River sand

D_{10}	0.20 mm	D_{50}	0.36 mm	$\gamma_{d,max}$	17.12 kN/m ³
D_{30}	0.28 mm	G_s	2.70	$\gamma_{d,min}$	14.32 kN/m ³

The in-situ relative density, D_r , of Tagus River sand was determined by using a correlation with SPT values, which were obtained for different boreholes and depths, mainly in the north shore of the river. Similar SPT values were assumed at the centre of the river as, at the tunnel site, flow velocities near the bed of the waterway are small. A D_r of 70% was then obtained. Admitting a maximum depth of 30 m for liquefaction triggering, effective confining pressures, p_{conf} , ranging from 100 to 300 kPa, were set. Additionally, $D_r = 60\%$ ($p_{conf} = 100 \text{ kPa}$) and $D_r = 80\%$ ($p_{conf} = 300 \text{ kPa}$) were adopted to analyse the effect of varying the relative density. All stresses herein defined are effective stresses.

3. CYCLIC UNDRAINED TORSIONAL TESTING

Actuation of the earthquake generates primarily an increase of shear stresses, which can be well simulated in a cyclic torsional test. Thus, the main goal of these tests was to characterize stress-strain behaviour of the sand under cyclic loading, in the medium to large range of strains, including liquefaction, and to obtain parameters for the constitutive model, related with dynamic behaviour of the soil.

Therefore, LNEC's (Laboratório Nacional de Engenharia Civil) torsional shear device [2] was used to perform five cyclic undrained torsional tests (CUTT) on hollow cylindrical specimens. Table 2 includes dimensions of the specimens, H_0 , $r_{e,0}$ and $r_{i,0}$, as well as their dry unit weight, γ_d , relative density, D_r , and void ratio after preparation, e_0 ; the chosen effective consolidation pressure, p_{conf} , and void ratio after consolidation phase, e_{conf} .

Table 2. Cyclic undrained torsional tests data

Test	After specimen preparation						After consolidation	
	H_0 (m)	$r_{e,0}$ (m)	$r_{i,0}$ (m)	γ_d (kN/m ³)	D_r (%)	e_0	p_{conf} (kPa)	e_{conf}
CUT_Dr70_p300	0.1431	0.0354	0.0147	16.15	68.9	0.640	300	0.551
CUT_Dr70_p200	0.1433	0.0354	0.0148	16.17	69.8	0.637	200	0.581
CUT_Dr70_p100	0.1431	0.0355	0.0147	16.18	70.0	0.637	100	0.627
CUT_Dr60_p100	0.1431	0.0355	0.0147	15.92	60.9	0.664	100	0.652
CUT_Dr80_p300	0.1433	0.0355	0.0147	16.51	80.6	0.605	300	0.539

After the saturation phase, specimens were isotropically consolidated. All tests were subjected to shear by controlling strain. Strain amplitude, $\gamma_{\theta z}$, was increased progressively seven times, using each of the following values during 10 cycles of 1 s ($f = 1$ Hz): $\gamma_{\theta z} = \pm 5 \times 10^{-4}$, $\pm 1 \times 10^{-3}$, $\pm 3 \times 10^{-3}$, $\pm 6 \times 10^{-3}$, $\pm 1.0 \times 10^{-2}$, $\pm 2.0 \times 10^{-2}$, $\pm 3.0 \times 10^{-2}$.

External and internal confining pressures were kept constant as well as axial force. Changes on the mean effective confining stress were exclusively due to pore pressure variation. Additionally, the final excess pore pressure value corresponded approximately to the initial mean effective confining stress, which meant liquefaction was attained in all cases.

Figure 2 to Figure 4 illustrate the obtained results for test CUT_Dr70_p100, with a D_r of 70% and the lowest p_{conf} of 100 kPa. Initial liquefaction was considered to have occurred when excess pore pressure was 95% of the initial effective consolidation pressure, thus in this test at cycle 47 ($\gamma_{\theta z} = \pm 0.01$ - Figure 4).

In Figure 2, it can be observed that, for the first cycles, the curves are very close together, but as the specimen approaches liquefaction strains increase and hysteresis loops' open up quickly, tending to the horizontal, with their hysteresis area increasing considerably.

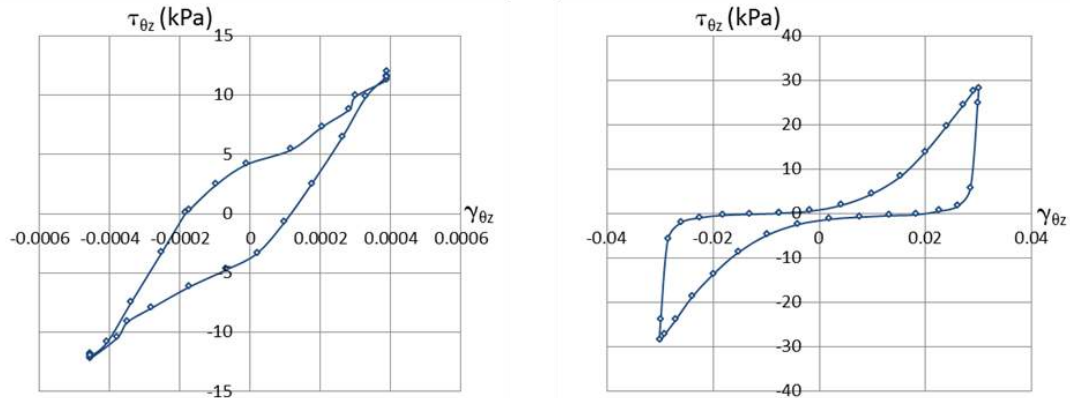


Figure 2. Shear stress $\tau_{\theta z}$ (kPa) vs shear strain $\gamma_{\theta z}$ (left - cycle 6 (pre-liquefaction); right - cycle 66 (liquefaction))

Concerning Figure 3, the left plot reflects the gradual build-up of pore pressure (Figure 4) as the effective mean stress reduces. Before initial liquefaction, for each imposed strain, the decrease in p , as well as the rate of excess pore water pressure accumulation, is higher during the first cycle than during the subsequent cycles, where it is almost constant. This behaviour has been associated with particle rearrangement and elimination of local instabilities at the contact points [3].

The specimen starts failing, as the stress path approaches the critical stress ratio. As seen on the right plot of Figure 3, the shape of the stress path changes completely and becomes "hooked" towards the later stages of the test. The specimen reaches the critical stress ratio at

low q values, because of the high pore pressures generated, but as strain increases dilation tendency moves the stress path up the critical state line (CSL). When stress reverses, dilation tendency ceases and volumetric contraction tendency drives the stress path back down towards the origin, until the critical stress ratio is encountered in the opposite direction. Moreover, for each cycle of imposed shear strain, there are two cycles of excess pore pressure, which decreases in the dilation phase and, after strain (and stress) reversal, increases in the contraction phase in both directions.

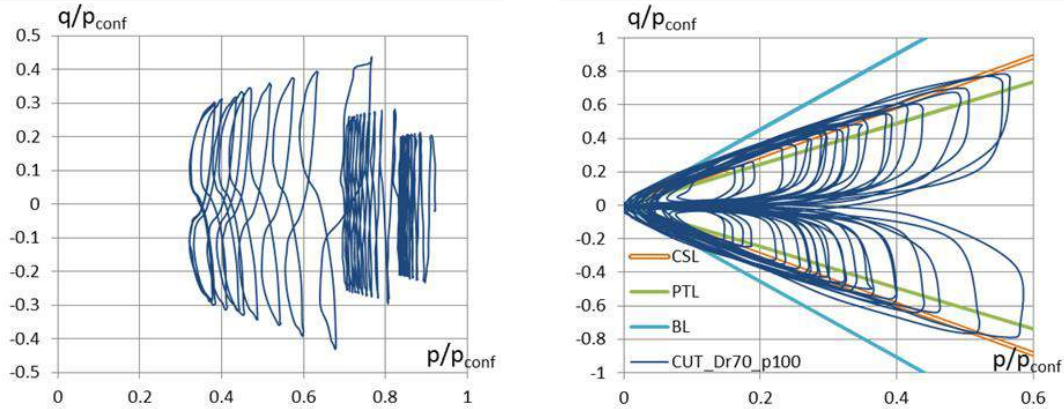


Figure 3. q/p_{conf} vs p/p_{conf} (left – cycles 1 to 30 (pre-liquefaction); right - after initial liquefaction; CSL – critical state line, PTL – phase transformation line, BL – bounding line)

After cycle 20, when a shear strain amplitude of $\pm 3 \times 10^{-3}$ was imposed, sand began to become significantly soft and pp/p_{conf} , at the end of the last cycle with this amplitude (cycle 30), exceeded approximately 65% (Figure 4).

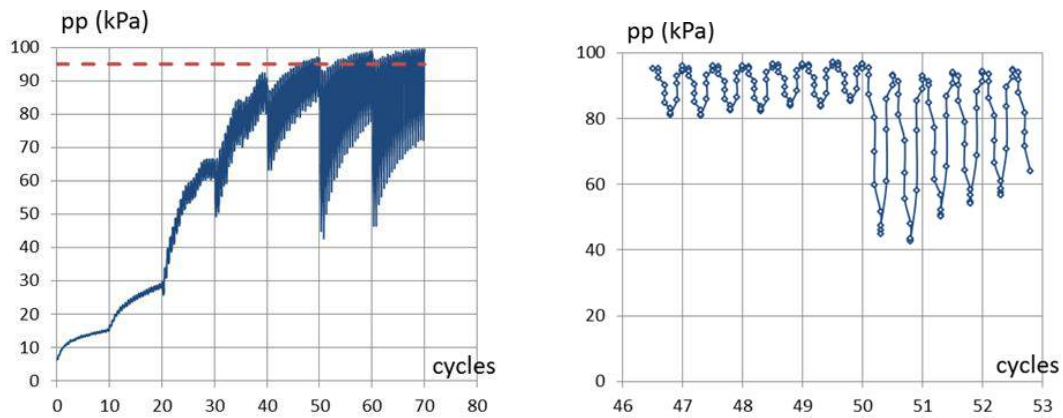


Figure 4. Excess pore pressure pp (kPa) vs number of cycles (left – full test; right - detail after initial liquefaction)

4. NUMERICAL MODELLING OF THE LABORATORY TESTS

4.1. Constitutive Model

The Manzari-Dafalias (M-D) model was chosen. This bounding surface model builds upon previous work by [4], which was extended to account for the effect of fabric changes during loading [5]. In the formulation in triaxial stress space, the yield surface represents a “wedge” in p - q space, with an opening value of $2mp$ and whose bisecting line has a slope α (Figure 5). α and m are stress ratio quantities. The dilatancy line, where there is a zero volumetric rate response, separates the contractant (below the line) from the dilatant (over the line) response.

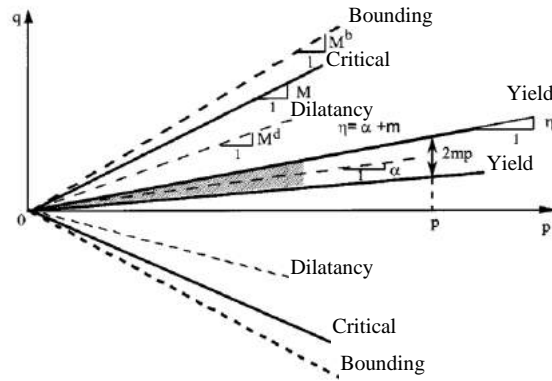


Figure 5. Yield, critical (CSL), dilatancy (PTL) and bounding lines (BL) in p - q space [5]

The model parameters and respective reference values, which correspond either to laboratory tests results ([lab]) or to published data in several references about the M-D model ([5], [6], [7], [8]), plus tests commonly used to determine the parameters, are summarized in Table 3.

The following parameters of the M-D model were directly determined from MDTTs: $G_0 = 125$ and $\nu = 0.3$ (elasticity parameters); $M_{f,c} = 1.46$, $c = 0.67$, $e_{p0} = 0.014$, $\lambda_c = 0.78$ and $\xi = 1.15$ (related with the critical state); $n^b = 3.5$ (related with the plastic modulus) and $A_0 = 0.932$ and $n^d = 1.5$ (related with dilatancy).

Table 3. Manzari-Dafalias model parameters, reference values and published data

Category	Parameter	Reference value	Test
Physical	γ_d	16.21 kN/m ³ [lab]	Physical testing
	e_0	0.634 [lab]	Physical testing (Dr = 71.3%)
Elasticity	G_0	125 [lab] [8]	RCT (small strain measurements), MDTT
	ν	0.3 [lab] (0.2 to 0.4 in [7])	MDTT, $\nu = \frac{K_0}{1+K_0}$, $K_0 = 1 - \sin\phi$
Critical state	$M_{f,c}$	1.46 [lab] (1.20 to 1.32 in [7])	MDTT
	c	0.67 [lab]	MDTT ($c = M_{f,e}/M_{f,c}$)
	λ_c	0.014 [lab] (0.01 to 0.03 in [7])	MDTT that approach critical state
	e_{p0}	0.78 [lab] (0.72 to 0.90 in [7])	Void ratio at $p_c = 1kPa$. MDTT that approach critical state
	ξ	1.15 [lab] (0.7 for most sands [6])	MDTT that approach critical state
Yield surface	m	0.015 [8] (0.02-0.05 in [6] and 0.06-0.07 in [7])	Fitting (MDTT)
Plastic modulus	h_0	7.05 [8]	Fitting (MDTT)
	c_h	0.968 [8]	Fitting (MDTT)
	n^b	3.5 [lab] (1.1 in [5])	$n^b = \ln(\frac{M}{M^b})/\Psi^b$, where Ψ^b and M^b are the values of Ψ and η at a drained peak stress ratio state
Dilatancy	A_0	0.932 [lab] (0.704 in [5])	MDTT – good quality stress dilatancy data – volumetric strain vs deviatoric strain in a constant p drained triaxial test (before z is activated $A_0 = A_d$)
	n^d	1.5 [lab] (3.5 in [5])	$n^d = \ln(\frac{M}{M^d})/\Psi^d$, where Ψ^d and M^d are the values of Ψ and η at a phase transformation state
Fabric-dilatancy tensor	z_{max}	4 [8] (4-5 for most sands in [6])	Fitting (CUTT) – η must exceed M^d so that the evolution of z is activated
	c_z	600 [8]	Fitting (CUTT) - η must exceed M^d so that the evolution of z is activated

MDTT - monotonic drained triaxial test; RCT - resonant column test; CUTT - cyclic undrained torsional test.

4.2. Sensitivity Analysis

Before calibrating the remaining parameters, related to monotonic and cyclic behaviour, a sensitivity analysis was carried out in order to better understand the relevance of each model parameter. The selected parameters were namely those that couldn't be obtained directly by laboratory tests (m , h_0 and c_h) as well as some parameters that, though obtained directly through laboratory tests, don't have a straight physical meaning (n^b , A_0 and n^d). G_0 was also considered due to its relevance in the response, particularly in the pre-liquefaction phase.

Numerical simulations of laboratory tests, MDTTs and CUTTs, were performed using an existing OpenSees constitutive driver [8], where the Manzari-Dafalias model governing equations had been implemented. The numerical model was built to perform the described sensitivity analysis, using a $1 \times 1 \times 1 \text{ m}^3$ SSPbrickUP 3D element with 8 nodes. This element can be used in dynamic analysis of saturated porous media with a mixed displacement-pressure ($u - p$) formulation, based upon the work of Biot as extended by [9].

A variation of $\pm 20\%$ of the reference value was defined for the selected parameters (except for parameter m , for which, according to several references, 0.015, 0.03 and 0.06 were chosen). This $\pm 20\%$ variation was believed adequate to avoid instabilities and non-convergence of the model. Only the main results of the sensitivity analysis through numerical simulation of MDTTs are presented next, since it is described in more detail in [10].

4.2.1. Parameter sensitivity analysis through numerical simulation of MDTTs

Results of the sensitivity analysis for each model parameter pointed out that the parameters that cause a greater variation of the response are: c_h concerning peak shear strain ε_s , n^b regarding peak shear stress ratio η and finally A_0 concerning peak dilatancy and volumetric strain at the critical state ε_v . Then, two related parameters (A_0 with n^d concerning dilatancy and c_h with h_0 regarding the plasticity modulus) were varied simultaneously. It was shown that when parameters c_h and h_0 are varied simultaneously, ε_s variation is fairly greater than when only one of them is changed. Finally, pairs of the most relevant parameters (A_0 with c_h , A_0 with n^b and c_h with n^b), were also varied simultaneously. It was concluded that joint variation of parameters c_h and A_0 causes larger variation than when only one of the parameters is changed.

4.2.2. Parameter sensitivity analysis through numerical simulation of CUTTs

First, specific boundary conditions for the SSPbrickUP 3D element had to be defined. At the base of the element two of the four nodes were free in each horizontal direction (x or y) and one was free in both horizontal directions. The top nodes were all free. During the consolidation phase, concentrated forces representing an all-around confining pressure p_{conf} (100, 200 or 300 kPa) were applied at the free nodes. Then, in the shear phase, pore pressure was set free at all nodes and top nodes were fixed in the horizontal direction (y). Displacements were applied at the four top nodes in the x horizontal direction, according to a cyclic sine function, with a frequency of 1 Hz and which amplitude increases progressively up to $\pm 0.03 \text{ m}$ ($\pm 1 \times 10^{-5}$, $\pm 5 \times 10^{-5}$, $\pm 1 \times 10^{-4}$, $\pm 5 \times 10^{-4}$, ± 0.001 , ± 0.003 , ± 0.006 , ± 0.01 , ± 0.02 and $\pm 0.03 \text{ m}$).

Parameters c_z and z_{max} weren't considered in the *pre-liquefaction phase* because they only have influence on liquefaction response. From the analysis of 3 cycles gradually approaching liquefaction, it was concluded that the most relevant parameters for cyclic response in this phase are G_0 , m , h_0 and c_h . In Figure 6, the normalized stress path q/p_{conf} vs p/p_{conf} for the pre-liquefaction phase and the pore pressure ratio change during the shear phase are shown, considering the effect of changing parameter G_0 in the response.

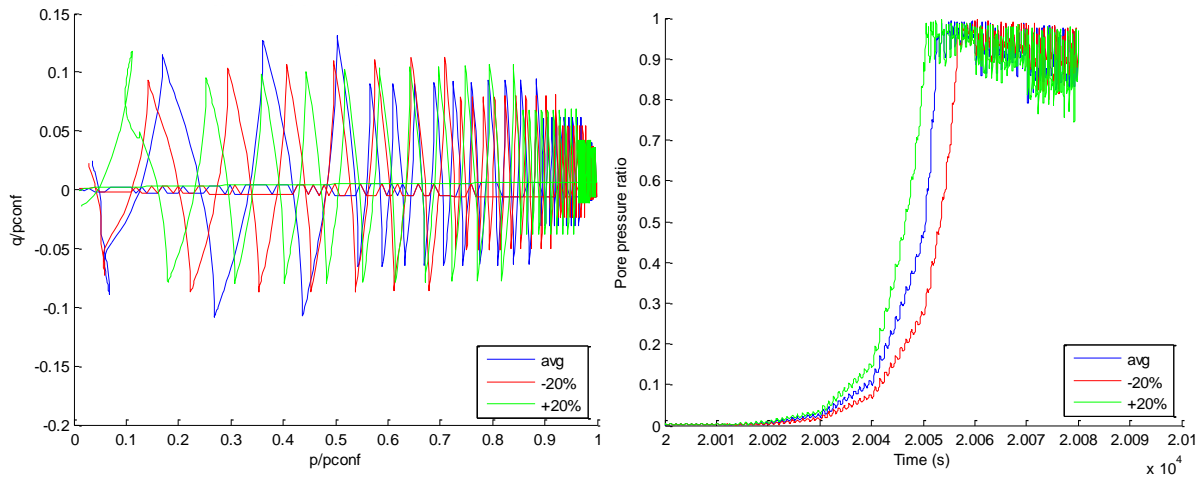


Figure 6. q/p_{conf} vs p/p_{conf} paths (pre-liquefaction) and pore pressure ratio time history (shear phase) considering variation of G_0

In Figure 7, the normalized stress path q/p_{conf} vs p/p_{conf} for 3 cycles in the liquefaction phase (corresponding to different applied shear strain levels, respectively ± 0.01 , ± 0.02 and ± 0.03) is presented, considering the influence of varying c_z in the response. In the liquefaction phase, in each cycle, the pore pressure ratio should reach a value near one and shear strain should follow the applied cyclic displacements. However, due to convergence problems of the M-D model, the pore pressure ratio varies significantly, with its maximum value decreasing and moving away from one and shear strain doesn't follow the applied cyclic displacements (Figure 7). Thus, it wasn't possible to determine the relative importance of c_z and z_{max} in cyclic response. Further improvements in the M-D model are deemed necessary, namely for the liquefaction phase.

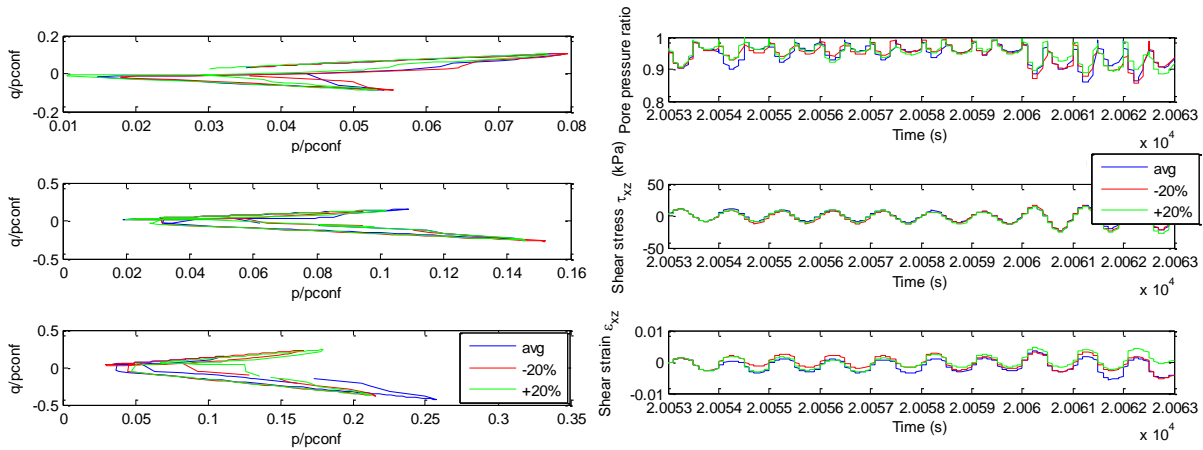


Figure 7. q/p_{conf} vs p/p_{conf} paths (liquefaction) and pore pressure ratio, shear stress and shear strain time history (after initial liquefaction) considering variation of c_z

4.3. Fitting the Model to the Laboratory Results

Hence, the value of parameters h_0 , c_h and m still had to be determined. This was done by fitting the numerical model to the MDTT results. From the sensitivity analysis, the most relevant of these parameters was c_h and then h_0 . Due to its irrelevant influence on the response for the monotonic sensitivity analysis, the used value of m was the reference value in Table 3. Therefore, parameter c_h was fitted first, followed by h_0 . Small adjustments in n^b and A_0 were made as well. As a result, the chosen values for the parameters were: $c_h = 1.33$, $h_0 = 6.05$, $n^b = 4.50$ and $A_0 = 1.25$.

5. CONCLUSION

An immersed tunnel case-study, supported on liquefiable alluvial Tagus river sands, was presented, providing context to this work. MDTTs were executed to characterize stress-strain behaviour of Tagus river sand and calibrate the M-D model. CUTTs were also performed, highlighting the dynamic behaviour of the sand.

Some parameters of the M-D model were directly determined from triaxial tests, while others (h_0 and c_h) were determined by fitting the model to the laboratory results, after carrying out an extensive sensitivity analysis. From this sensitivity study, the most significant parameters to consider for monotonic loading were c_h , n^b and A_0 and, in a joint sensitivity analysis, c_h and h_0 , as well as c_h and A_0 . Regarding cyclic loading, before initial liquefaction, the most relevant parameters were G_0 , m , h_0 and c_h .

Both the calibration framework and the results of the sensitivity analysis presented here can provide designers with an understanding of the model parameters effects' on its performance and guide them in implementing a complex model into their designs.

ACKNOWLEDGEMENT

Luís Miranda was supported by “Fundação para a Ciência e Tecnologia” (FCT), through PhD scholarship SFRH/BD/99581/2014. Available geotechnical information from various surveys, namely borehole logs and SPTs, was kindly provided by Administração do Porto de Lisboa.

REFERENCES

- [1] Ingerslev, C., Kyiomya, O., 1997. “*Earthquake Analysis*”, Tunnelling and Underground Space Technology, 12(2):157–162.
- [2] Serra, J. B., 1998. “*Caracterização experimental e modelação numérica do comportamento cíclico de solos não coesivos. Aplicação à engenharia sísmica*”, Ph.D. Thesis, Universidade Técnica de Lisboa, Instituto Superior Técnico, Portugal, 282 pages.
- [3] Georgiannou V. N., Tsomokos A., Stavrou K., 2008. “*Monotonic and cyclic behaviour of sand under torsional loading*”, Géotechnique, 58(2):113–124.
- [4] Manzari M. T., Dafalias Y. F., 1997. “*A critical state two-surface plasticity model for sands*”, Géotechnique, 47(2):255–272.
- [5] Dafalias, Y. F., Manzari, M. T., 2004. “*Simple Plasticity Sand Model Accounting for Fabric Change Effects*”, J Eng Mech, 130(6):622–634.
- [6] Cheng, Z., Dafalias, Y. F. and Manzari, M. T., 2013. “*Application of SANISAND Dafalias-Manzari model in FLAC 3D*”, Continuum and Distinct Element Numerical Modeling in Geomechanics, Paper 09-03, 22-24 October 2013, Hangzhou, P.R. China.
- [7] Papadimitriou, A. G., Bouckovalas, G. D., Dafalias, Y. F., 2001. “*Plasticity model for sand under small and large cyclic strains*”, J Geotech Geoenvironmental Eng, 127(11):973–983.
- [8] University of Berkeley, California. OpenSees, retrieved from <http://OpenSees.berkeley.edu/>.
- [9] Zienkiewicz, O. C. and Shiomi, T., 1984. “*Dynamic behavior of saturated porous media; the generalized Biot formulation and its numerical solution*”, Int J Num Methods Geomech, 8:71-96.
- [10] Miranda, L., Barbosa, A., Serra, J., Caldeira, L., 2017. “*Parameter sensitivity analysis of the Manzari-Dafalias model for modelling the cyclic response of a sand*”, 16th WCEE, 9-13 January 2017, Santiago, Chile, <https://goo.gl/zhngnq>.

LABORATORY RESEARCH ON THE PHYSICAL AND MECHANICAL PROPERTIES OF SOILS IMPROVED WITH CEMENT BY DEEP MIXING. LONG-TERM BEHAVIOUR

Oana Carasca, *M. Sc., Civ. Eng.*; *Technical University of Civil Engineering Bucharest, Geotechnical Engineering and Foundations Department*, oana.carasca@yahoo.com

ABSTRACT

Soil treatment and improvement by mixing is an economic and eco-friendly method that has more and more applicability worldwide in order to improve soft soils that are available for construction works, given the need to exploit sites with poor characteristics in terms of bearing capacity.

An increased knowledge of the properties and behavior of the resulted material is important in order to replace classical foundation methods and to be able to optimize the design of the mixing process and technologies. Therefore, for developing the mixing methods, it is necessary to extend and develop more laboratory researches.

The overall objective of the research presented in this paper is to contribute to the understanding of some physical and mechanical properties of soils improved with cement. Artificial soils were created in the laboratory, consisting of ten recipes of mixes made of kaolin clay and Fontainebleau sand treated with cement, having different but controlled contents of clays, and two dosages of cement. The ten mixes have been initially tested at 7 and 28 days of curing to determine the unconfined compressive strength, flexion strength, porosity, density and dynamic modulus. Then, at approximately 1000 days from the preparation stage, tests were carried out in order to determine the unconfined compressive strength and the dynamic elasticity modulus. Moreover, on the hardened material, the density and its influence on the final behavior was determined.

The paper briefly presents an analysis of the influence of the clay content on the physical and mechanical characteristics of the stabilized soils and the evolution of the physical and mechanical parameters on long term (after over 1000 days of curing).

Keywords: Soil Mixing, Soil Treatment, Binder, Unconfined Compressive Strength, Long Term Behavior.

1. INTRODUCTION

The Deep Soil Mixing technology is based on mixing stabilizing agents in different states into the soil, using specialized equipment, in order to improve the physical and mechanical properties thereof, such as strength, permeability and volume stability. The pores in the structure of the soil get filled with additive, so the particles and the aggregates get closer to each other, reducing the initial void volume and so developing better mechanical strengths [1].

This soil improvement technology can be used for a wide range of applications, such as: shallow foundations, excavation support, offshore platforms, dams, slope stability and seismic applications, being in the same time economic and environmental friendly [2].

The most commonly used binders are cement and lime, but there are many other materials that can be used as stabilizing agents, such as: bentonite, volcanic ash, grinded furnace slag, bitumen, silica fume etc. Usually, the Deep Soil Mixing technology is based on stabilizing agents in dry or slurry formula, the state and proportion of these agents being assigned after studying the behavior of several different mixtures by laboratory tests [3].

In order to achieve a better understanding of the performances of the new soil-binder material, this paper aims to present a research program based on laboratory tests, which was conducted in order to assess the influence of the clay quantity over the main characteristics of the improved soil. The aim of the research is to analyze as well, besides the influence of the clay content on the physical and mechanical characteristics of the stabilized soil, the variation of the physical and mechanical parameters on long term (at approximately 1000 days of curing).

2. METHODOLOGY

2.1. Research Program

The research was conducted both at Université de Cergy-Pontoise, France, at L2MGC (Laboratoire de mécanique et matériaux du génie civil), being part of an ERASMUS+ research program for doctoral studies, and in the Geotechnical Laboratory of the Technical University of Civil Engineering Bucharest. Artificial soils were created in the laboratory, with different but controlled contents of clays, and mixed with different doses of cement which have been initially tested at 7 and 28 days from the preparation stage, respectively at 1000 days. Ten soil mixes with five controlled clay content and two doses of cement were created, containing 0, 10, 25, 40 and 50% kaolin clay, the rest of the volume being occupied by the Fontainebleau sand (Table 1).

Table 1. Summary of the artificial soil mixes created for this research

Formulation	Kaolin clay	Cement	Kaolin clay	Sand	Water	Cement/ Water ratio	Water content
	%	kg/m ³ material			Mixing	%	
K0/C200	0	200	0	1534	352	0.57	20.29
K10/C200	10	200	125	1144	451	0.44	30.69
K25/C200	25	200	243	743	557	0.36	46.94
K40/C200	40	200	318	487	625	0.32	62.20
K50/C200	50	200	347	353	664	0.30	73.70
K0/C150	0	150	0	1589	349	0.43	20.07
K10/C150	10	150	128	1178	455	0.33	31.22
K25/C150	25	150	255	781	556	0.27	46.85
K40/C150	40	150	336	514	625	0.24	62.49
K50/C150	50	150	366	373	667	0.23	74.97

Each material was poured into labeled cylinder-shaped cardboard molds, then cured until the desired age for being tested (Figure 1). The tests carried out on the soil-mix samples at the age of curing of 7 days and 28 days were: determination of the density, porosity, unconfined

compressive strength, flexion strength and dynamic modulus, whereas the tests carried out at the age of curing of 1000 days were: determination of the unconfined compressive strength and of the dynamic elasticity modulus. Moreover, on the hardened material, the density and its influence on the final behavior was determined.



Figure 1. Material samples after curing, removing the mold and labeling

2.2. Testing Methods for the Cured Material at the Age of 1000 Days

The determination of the density in wet state consisted in cutting the surface of the sample, weighing and measuring each sample right after taking it out of the storage environment, as shown in Figure 2 below.



Figure 2. Operations for determining the density of the material in wet state

Determining the P-waves velocity and the dynamic elasticity modulus consists in creating longitudinal waves through impulse, by the means of an electro-acoustical type transducer device, which makes a firm contact with the surface of the material. After it goes through the whole length of the sample, the wave is captured and transformed in an electrical signal, by the means of a second transducer, as described in the norm EN 12504-4: 2004 (Figure 3) [4].



Figure 3. Equipment and method for determining the P-waves velocity and the dynamic elasticity modulus

The Unconfined Compressive Strength (UCS) describes the behavior of a material regarding its peak resistance and the deformation modulus. Tests have been carried out on cylindrical samples of 5 cm diameter and 10 cm height (ratio of 2 regarding height/diameter), by means of two mechanical presses [5].

3. RESULTS AND INTERPRETATION OF THE TESTS

3.1. Density

The density of the fresh and hardened material was measured in wet and dry state. It can be observed that adding cement in the soil has as effect the increase of the density. The density decreases with the increase of the Kaolin clay content (Figure 4).

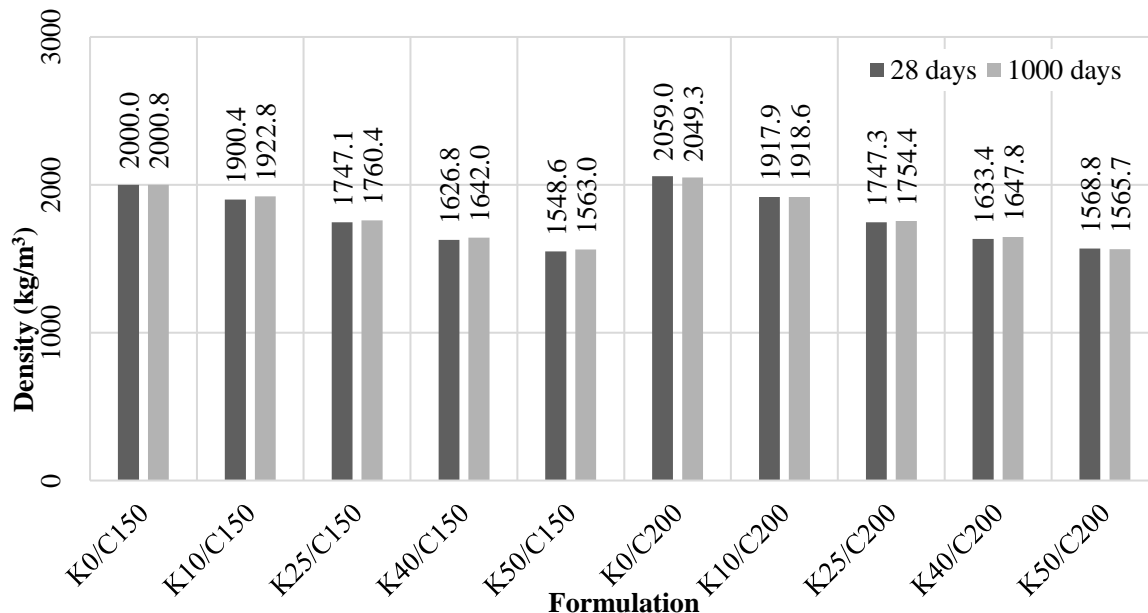


Figure 4. Variation of density in wet state (28 days vs. 1000 days)

The density of the materials in wet state, ρ , suffered insignificant modifications over time (a mean increase of 0.5%), the variations between the curing ages of 28 and 1000 days ranging between 0.5% and 1.2%, as shown in Figure 5.

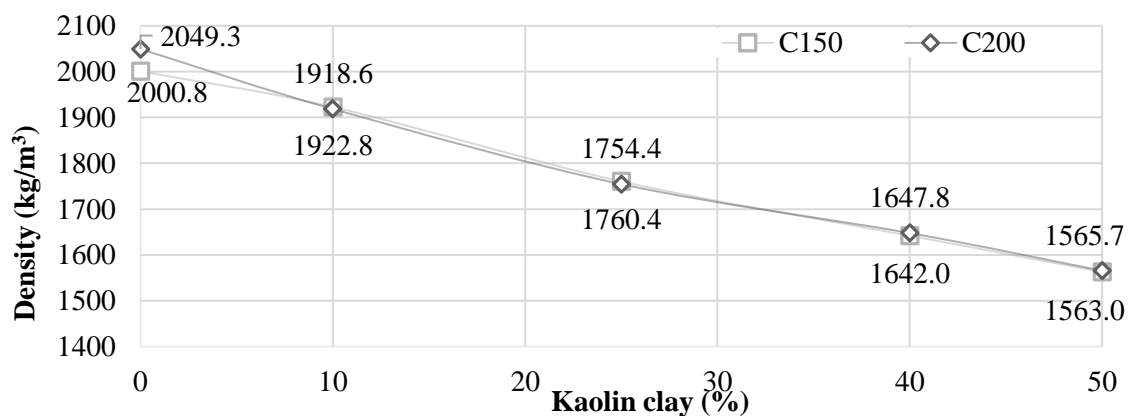


Figure 5. Variation of the density in wet state with the content of clay - 1000 days

3.2. P-Wave velocity

The P-waves velocity, V_P , has increased over time (mean increase of +16%), between 28 days and 1000 days, the increase ranging between +5.8% and +30.6% (Figure 6). The variation of the P-waves velocity is also influenced by the content of Kaolin clay, decreasing with it (Figure 7).

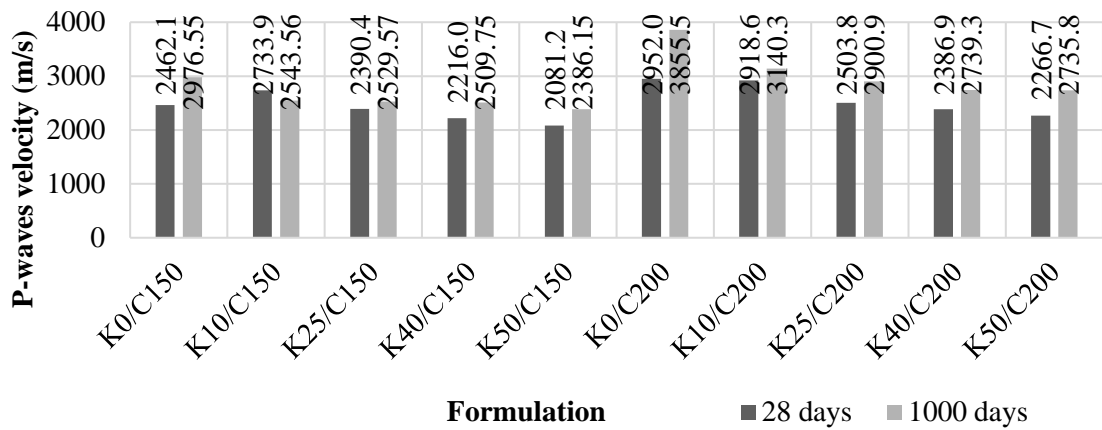


Figure 6. Variation of the P-waves velocity V_P (28 days vs. 1000 days)

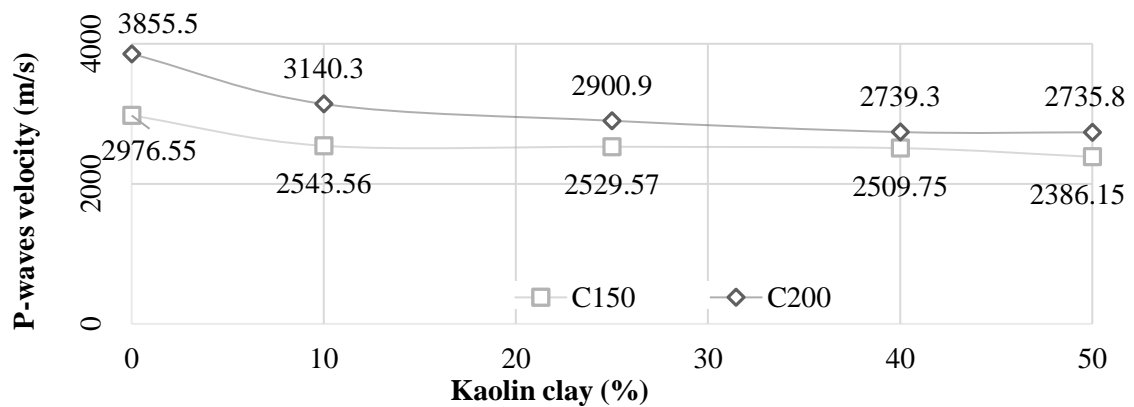


Figure 7. Variation of the P-waves velocity with the clay content - 1000 days

3.3. Dynamic Elasticity Modulus

Being strongly connected to the P-waves velocity, the dynamic elasticity modulus E_d has increased over time (mean increase of +39%) between the age of 28 days and 1000 days, the variation ranging between +16% ... +73%, as shown in Figure 8 below. The variation of the dynamic elasticity modulus is influenced by the clay content, as it decreases once with the increase of Kaolin clay (Figure 9).

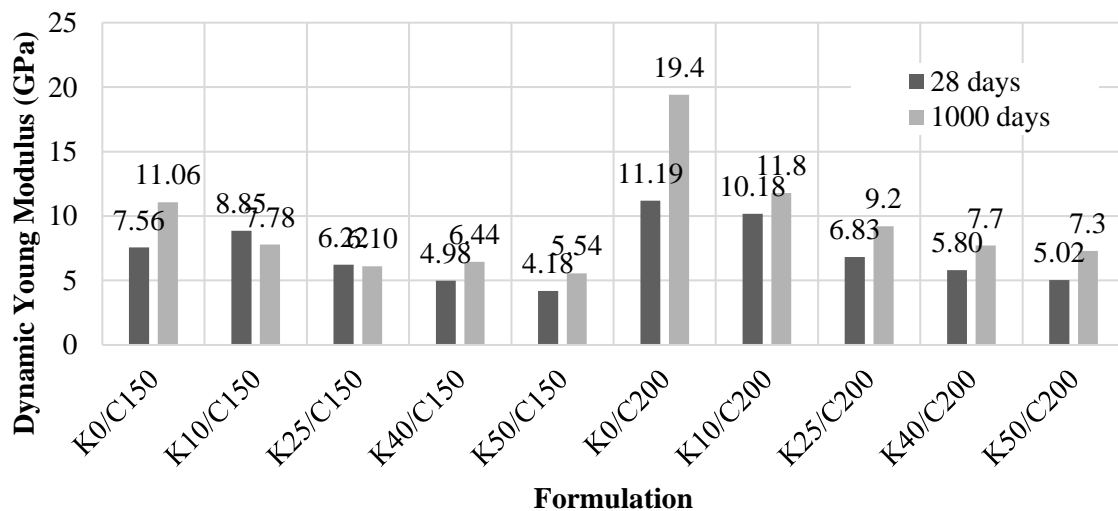


Figure 8. Variation of the Dynamic Young Modulus (28 days vs. 1000 days)

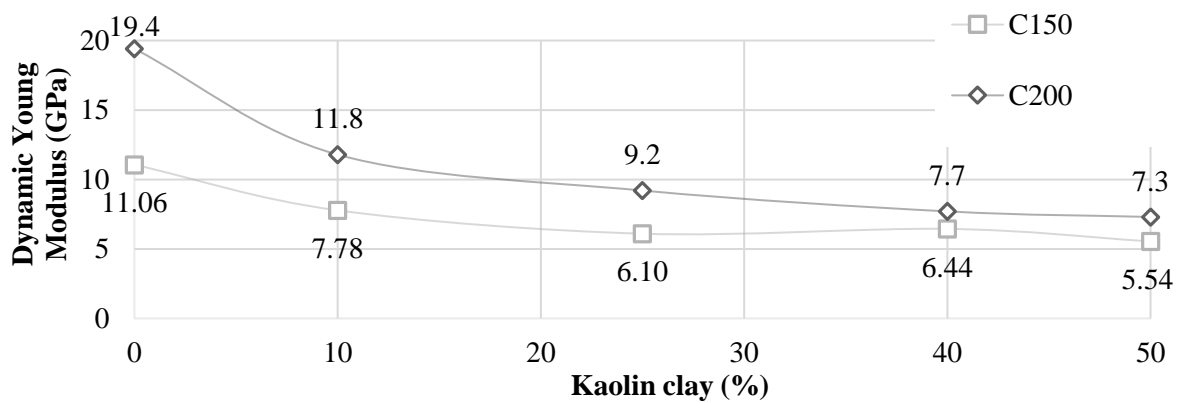


Figure 9. Variation of the Dynamic Young Modulus with the clay content - 1000 days

3.4. Unconfined Compressive Strength (UCS)

The unconfined compressive strength UCS has increased over time (with a mean of +45%) between 28 days and 1000 days, the variation ranging between +11% +75% (Figure 10). Exceptions made the formula K25/C150 which recorded a decrease, respectively the formula K0/C200 which showed a significant increase.

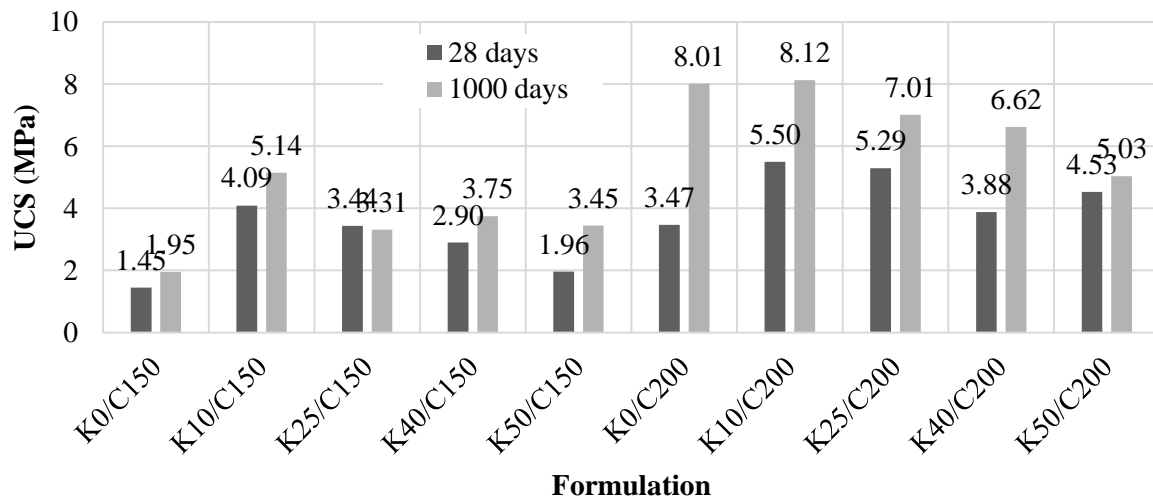


Figure 10. Variation of the unconfined compressive strength UCS (28 days vs. 1000 days)

The best values of the unconfined compressive strength were obtained on the samples having a 10% Kaolin clay content (8 MPa for a cement dosage of 200 kg/m³), so the optimum dosage of Kaolin clay for developing a good resistance is approximately 10%, as show in Figure 11.

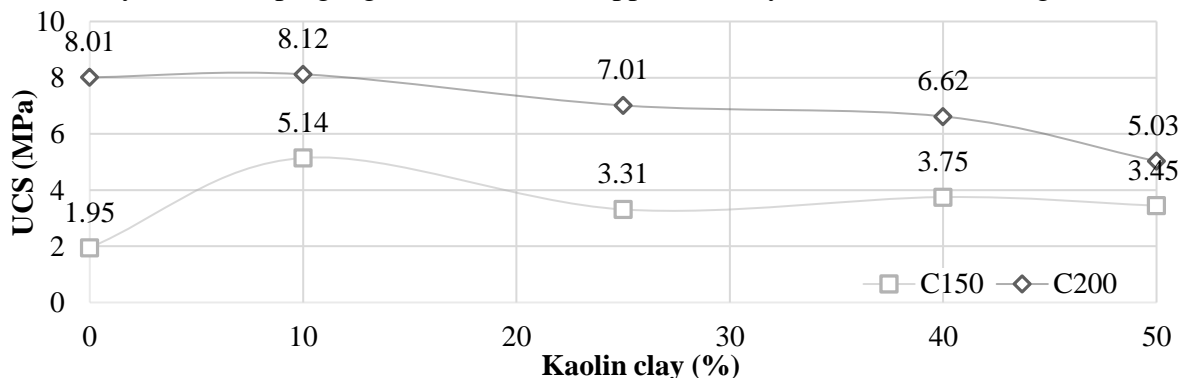


Figure 11. Variation of the unconfined compressive strength with the clay content - 1000 days

The most abrupt increase was recorded on the K0/C200 formulation, which also had the highest value of the dynamic modulus, and the lowest increase rate was determined on the K50/C200 formulation. In terms of Binder content (cement), adding cement in the soil leads to an increase of the unconfined compressive strength of the material. The differences between UCS at 1000 days, for the same content of clay and different dosage of cement, showed variations between +46% and +76% with a mean increase of almost +60%.

4. CONCLUSIONS OF THE RESEARCH

The overall objective of this research was to study the long-term physical and mechanical characteristics of soil-binder materials. Since these are a particular type of material, the mechanical behavior thereof is still poorly known, especially due to the non-standardized applied test methods [7]. For the experimental program, several testing methods for concrete and mortar have been used, which required adaptations and modifications to meet the new requirements. The information presented in this report follows the same trends as other previous research, confirming a certain repeatability of the results [3, 6].

The density decreases with the increase of the Kaolin clay content, as the samples with a higher content of Kaolin clay need more water to achieve the same workability (a spread of the slump of 32 cm). The densities in a hardened, wet state at 1000 days of curing, have values between 1560 kg/m³ and 2050 kg/m³, being relatively constant compared to the age of 28 days.

The P-waves velocity obtained at 1000 days have values between 2385 m/s and 3855 m/s, increasing over time (mean increase of +16%). This increase directly confirms the fact that the higher the cement dosage, the higher quantity of hydrates is created [6].

The values of the dynamic elastic moduli determined through correlation, taking into consideration a value of the Poisson ratio of 0.35, have values between 5.5 GPa and 19.5 GPa. The highest values of the dynamic Young modulus were obtained for the samples without Clay content. For the formulations having a content of 50% Clay, the elastic moduli are relatively low, depending on the cement content. Adding cement to the soil has as an effect an increase of the dynamic elastic modulus of the material. The variation of the dynamic elasticity modulus is also influenced by the content of clay as it decreases once with the increase of the Kaolin clay content. The differences of the dynamic elastic modulus determined at 1000 days for the same content of clay, showed a mean increase of 46%.

Adding cement to the soil leads to an increase of the unconfined compressive strength of the material. The unconfined compressive strength determined at the age of 1000 days varies between 2 MPa and 8.1 MPa. The best values for the compressive strength were obtained on the samples having a kaolin clay content of 10% (approximately 5.1 MPa for a cement dosage of 150 kg/m³, 8.1 MPa for a cement dosage of 200 kg/m³). For the formulations having 50% clay content, the unconfined compressive strength ranges between 3.4 MPa and 5 MPa, depending on the cement dosage. The differences between the UCS determined at 1000 days for the same content of clay and different dosage of cement, showed an increase of almost 60%. It is outlined the fact that the strength of the mixtures with a clay content of 10% are with 50-60% higher than the strength of the mixtures with a 50% content of clay.

ACKNOWLEDGEMENT

This research was partially carried out at Université de Cergy-Pontoise, France, at L2MGC (Laboratoire de mécanique et matériaux du génie civil). I express my appreciation to Assoc. Prof. PhD Eng. Anne-Lise Beaucour and PhD Eng. Olivier Helson, who assisted the research

carried out during the ERASMUS+ doctoral stage. I have to thank as well Assoc. Prof. PhD Eng. Constantin Dorinel Voinitchi from the Building Materials Laboratory of Technical University of Civil Engineering Bucharest, for helping me carry out some of the tests.

REFERENCES

- [1] Ahnberg, H., Holmen, M., 2011. “*Assessment of stabilized soil strength with geophysical methods*”. Ground Improvement, 164 (3):109-116.
- [2] Carasca, O., 2016. “*Soil improvement by mixing: techniques and performances*”. Energy Procedia, 85:85-92.
- [3] Helson, O., 2017. “*Comportement thermo-hydro-mécanique et durabilité des bétons de sol: influence des paramètres de formulation et conditions d'exposition*”, Doctoral Thesis, Université de Cergy-Pontoise, France, 230 pages.
- [4] EN 12504-4:2004, 2004. “*Testing concrete. Part 4: Determination of ultrasonic pulse velocity*”, European Committee for Standardization, EU.
- [5] Chung, P., 2018. “*Testing of cores taken from cement stabilized soil*”, Seminar on the latest development in Construction Materials Testing, Inspection and Certification, Hong-Kong, January 2018, Retrieved 30 September, 2018 from <https://www.hkctc.gov.hk/en/doc/>
- [6] Helson, O., Beaucour, A. L., Eslami, J., Noumowé, A., 2015. “*Caractérisation du comportement mécanique des bétons de sol*”, Rencontres Universitaires de Génie Civil Bayonne, 27-29 May 2015, France.
- [7] Terashi, M., a., 2015. “*Deep Mixing – Four Decades of Experience, Research and Development*”. Deep Mixing Conference, pp. 781-800, 2-5 June 2015, San Francisco, USA.

SOME ASPECTS REGARDING THE EFFECT OF FOUNDATIONS SYSTEM ON DEFORMATION BEHAVIOR FOR BUILDINGS ON SLOPED TERRAIN. CASE STUDY

O.C. Mureșan *, *Technical University of Cluj-Napoca, Romania, olimpiu.muresan@dst.utcluj.ro*

V. F. Chiorean, *Technical University of Cluj-Napoca, Romania, olimpiu.muresan@dst.utcluj.ro*

ABSTRACT

In this paper, the response of foundation system to soil-structure interaction is analyzed for buildings on slope terrain conditions. The case study presents the different response of foundation ground, depending on the foundation system, isolated foundations for columns and raft foundation, to a downstream excavation, respectively the change of stress in the soil body mass. There was performed a plain stain FEM analysis in order to predict the soil-structure response. The interaction between the soil and the structure is considered using zero thickness interface elements. The results obtained were compared with the in-situ measurements and observations. Despite some differences (in terms of magnitude), the numerical modeling analysis indicate a similar behavior observed also in site, at real scale.

Keywords: slope, excavation, finite element method, zero thickness interface, post-failure.

1. INTRODUCTION

The expansion of human settlements involves, in many cases, the placement of buildings on natural slopes. In such situations, the natural slopes equilibrium (in terms of stresses) is modified. The chronological sequence of slope interventions (different building processes) is one of the principal factors which could trigger the loose of stability or could trigger significant slope displacements as a result of field stresses redistribution.

Thereby, such as behavior is analyzed in this case study. The area is situated on the South-Eastern side of Cluj-Napoca City, in the western part of Romania, on a sloped terrain, situated under a forest fringe at the South of National Road 1. The case study implies two existing civil buildings disposed on the slope. The executed buildings are situated at about 20,00 m from the forest fringe and are extended on two built terraces, following natural slope of the terrain. When the built terraces change the level, the buildings are separated by settlement joints disposed continuously (in structure and foundation system) on the normal direction to the slope inclination.

The foundation system for the analyzed buildings is different: raft foundation for Building B, (Figure 1) and isolated foundations for Building A, (Figure 1). The raft foundation was executed partially to an equalization concrete with variable thickness (Figure 2, b), in order to transmit the foundation pressure to the good foundation ground. Both buildings structural system is made from reinforced concrete frames, with masonry panels and reinforced concrete slabs. The buildings are separated by a settlement joint with spread along building length on the slope direction (Figure 1). Downstream of these buildings was executed an excavation (app. 8.00 depth) in order build a new civil building (Figure 1). This operation involves a major and suddenly stresses field modification on slope profile, and thereby the upstream buildings record

major displacements. In order to evaluate the stress and strain field modification, the phenomenon is modeled using FEM (finite element method), in plane strain analysis. The magnitude and evolution of the technical event is revealed by site observations and measurements. Previous investigations regarding slope behavior as a response to local excavation are made in [1] and previous studies regarding buildings response to an urban excavation are performed in [2].

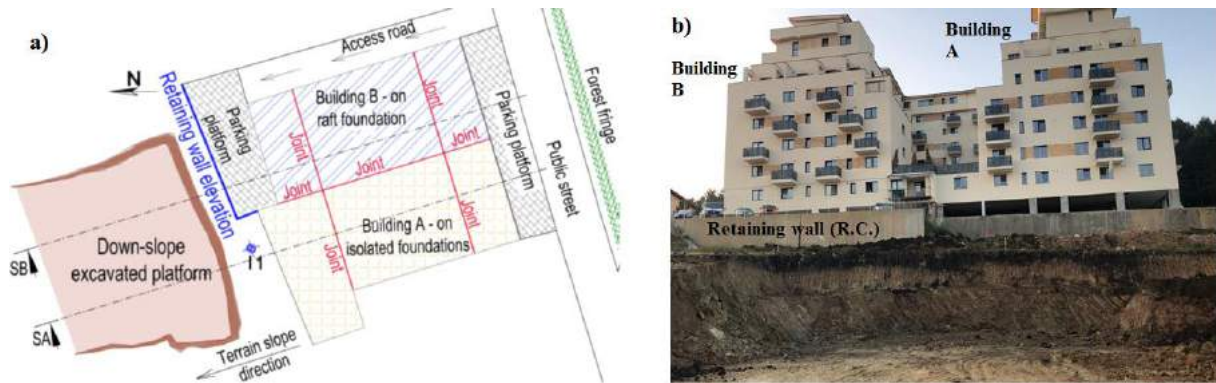


Figure 1. a) Overall site plan; b) Upstream view from excavated platform

2. ASPECTS REGARDING ANALYSIS MODEL

Real geotechnical engineering applications represents complex problems in terms of analysis domain geometry, complex border conditions (including groundwater), complex material (soil) behaviour and not at least interaction problems of two dissimilar materials with different behaviour. D. M. Potts [3] pointed out the major role of the anteriorly listed aspects in order to reduce the difference between numerical FEM predictions (in terms of stresses and deformations) and real behaviour of a geotechnical engineering system. The analysis domains were build based on geological profile sections, topology of the slope and buildings configuration. Builing A was investigated on section SA profile and Builing B was investigated on section SB (Figure 1 and 2). The excavation was simulated in stage analysis sequences. Ground water table (GWT) was local lowered as the excavation stages get down to the initial GWT (Figure 2).

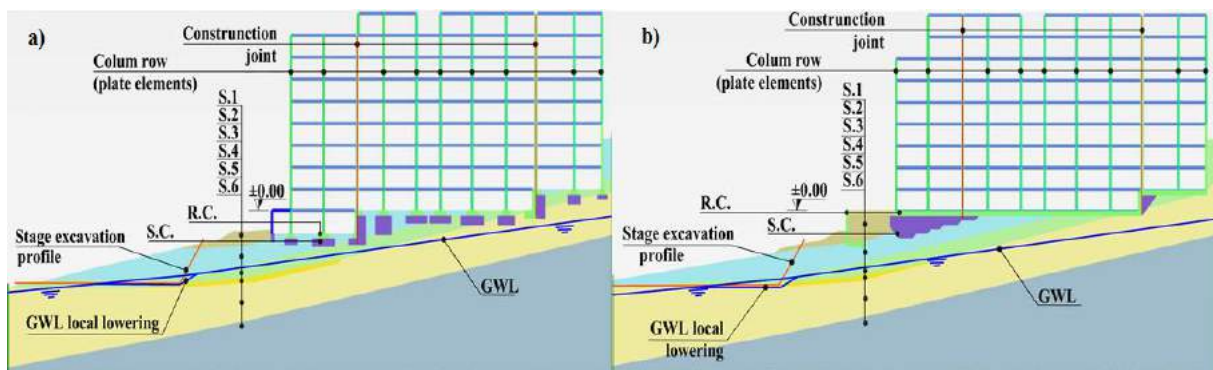


Figure 2. Analysis domain: a) Section SA; b) Section SB

Soil, foundation system, solid diaphragms from the sides of construction joint and existing retaining wall were modeled using continuum plane elements. Structural members like columns rows or slabs were modeled by linear elements (plate elements, [4]). Interaction at soil-foundation system level and interaction at construction joint level was modeled by interface ``zero thickness elements``,[4].

2.1. Soil and Continuum Material Modeling

Soil was modeled adopting 15 node plane triangular finite elements mesh (T15), with 15 nodes per element and 12 Gauss integration points (stress points) per element,[4]. Regarding material behavior, the soil was assumed to behave linear elastic – perfect plastic with Mohr-Coulomb (MC) failure criterion, in addition to tension cut-off criterion in agreement with PLAXIS 2D, [4]. Thereby for MC was adopted a six parameters model: E_s - effective Young modulus of the soil, ν_s - effective soil Poisson's ratio, ϕ_s - effective internal friction angle of the soil, c_s - effective soil cohesion, ψ_s - soil dilation angle and unit weight of the soil ($\gamma_{unsat}/\gamma_{sat}$). For reinforced concrete (R.C.) and simple concrete (S.C.) regions modeled with continuum elements (raft foundation, retaining wall, isolated foundations, and equalization concrete) was adopted a linear elastic material (LE), described by unit weight (γ), Young modulus (E) and Poisson's ratio (ν). Continuum material properties are assigned to sections according to Figure 2 with properties presented in Table 1.

2.2. Structural Members Modeling

In order to simulate bending and axial behavior of superstructure elements (columns rows and slabs) were used used plate elements with 5 node, compatible with plane T15 elements. The behaviour of plate elements is linear elastic, [4]. Equivalence of structural row elements as plate elements is accomplished by equalization techniques (per unit width) for bending and axial stiffness,[5]. Thereby, the whole behavior of superstructure was reduced as a linear elastic frames behaviour. The slabs were equalized in behavior with plate elements with axial stiffness $EA= 6200000 \text{ kN/m}$, flexural stiffness $EI= 20666.7 \text{ kNm}$, and $\nu=0.2$. The column rows behavior was equalized in behavior with plate elements with $EA=1291670 \text{ kN/m}$, $EI=5381.9 \text{ kNm}$, and $\nu=0.2$. Along vertical construction joint were modeled diaphragms modelled with plane elements and with no weight LE material assigned. In that way, vertical interface elements are flanked on both sides by continuum elements.

Table 1. Continuum material model parameters

Mat. ID	Type	Unsaturated / saturated unit weight [kN/m ³]		Deformation properties		Strength properties			K_0	R_{inter}
		γ_{unsat}	γ_{sat}	E_s [kPa]	ν_s [-]	ϕ_s [°]	c_s [kPa]	ψ_s [°]		
S.1	MC	19.24	19.90	6284	0.335	14.2	17	0	0.71	0.7
S.2	MC	19.24	19.90	6284	0.335	14.2	17	0	0.71	0.7
S.3	MC	19.9	20.02	13490	0.37	19.7	25.9	0	0.66	0.75
S.4	MC	19.67	20.15	18860	0.37	25	30	0	0.56	0.75
S.5	MC	19.7	20	1700	0.3	29	1	0	0.52	0.9
S.6	MC	19.75	20.4	29300	0.35	26.1	42.2	0	0.56	0.8
R.C.	LE	25.00		$31 \cdot 10^6$	0.15	-	-	-	-	-
S.C.	LE	24.00		$24 \cdot 10^6$	0.15	-	-	-	-	-

The actions of the existing buildings on the slope are simplified to vertical linear loadings acting at the foundations base. The vertical pressure is obtained by simplified equivalence considering that one building storey acts vertically with 18 kN/m^2 . The foundation base pressures were

obtained by summing procedure and simple frame distribution scheme. Note that the equivalence procedure does not take into account foundation and superstructure FEM elements self-weight and in according with this procedure the self-weight of the superstructures and foundations elements was neglected (to avoid double weight adding).

2.3. Interaction Modeling

Interaction at contact surface level is modeled using 10 nodes zero thickness interface elements, compatible with T15 plane elements and 5 nodes plate elements, [4]. Zero thickness interface elements are composed by 5 node pairs which share the same location. The formulation of interface elements is based on node pair's relative normal (δ_n) and tangential (δ_t) displacement and normal (σ_n) and tangential (τ) stress. Considering maximum shear stress noted as: τ_{lim} , the behavior at interface level could be described in specific states as: adhesion ($\delta_n \leq 0$ and $\tau \leq \tau_{lim}$); sliding ($\delta_n \leq 0$ and $\tau > \tau_{lim}$); separation ($\delta_n > 0$ and $\tau = 0$) and re-bonding, after separation occurs anteriorly ($\delta_n \leq 0$). The maximum shear admitted at interface level is evaluated by Mohr-Coulomb friction criterion considering interface friction angle (φ_i) as a fraction of φ_s , and interface adhesion (c_i) as a fraction of c_s , [6],[7]. The interface elements are described by Mohr-Coulomb elastic-perfect plastic model for shearing behavior in addition to tension cut-off for normal behavior, [4]. The elastic behavior is defined by elastic tangential stiffness (k_{ss}) and elastic normal stiffness (k_{nn}), and the plastic behavior is evaluated using incremental numerical analysis based on a yield function and plastic potential function,[8],[9]. Interface properties, are evaluated from surrounding soil properties by an automatic procedure based on virtual interface thickness, t_i , (imaginary dimension based on mesh parameters) and interface strength reduction factor (R_{inter}). The elastic stiffness of interface elements are evaluated: $k_{nn} = [(R_{inter})^2 \cdot E_s \cdot 5.5] / [t_i \cdot (1 + \nu_s)]$ and $k_{ss} = [(R_{inter})^2 \cdot E_s] / [2 \cdot t_i \cdot (1 + \nu_s)]$. Evaluation of interface strength parameters is achieved in function of soil strength parameters and R_{inter} : $\varphi_i = \tan^{-1}[\tan(\varphi_s) \cdot R_{inter}]$, $c_i = c_s \cdot R_{inter}$. Interaction between foundations elements and soil is ensured by interface elements defined in function of surrounding soil material and R_{inter} , according to Table 1. The real interaction between buildings bodies is accomplished by a narrow layer of polystyrene (vertical construction joints see Figure 2). The vertical joints are modeled by interface elements with: $k_{nn} = 130 \text{ kN/m}^3$, $k_{ss} = 30 \text{ kN/m}^3$, $c_i = 0.3 \text{ kN/m}^2$, $\varphi_i = 3^\circ$, $\psi_i = 0^\circ$ and tension cut-off condition activated. The values assumed to construction joint interface elements ensure numerical stability and are in engineering acquiescence with extruded polystyrene material behavior (construction joint material).

3. RESULTS AND DISCUSSIONS

3.1. Section SA- Isolated Foundations Building Body (Building A)

According to the numerical analysis, excavation induces a deformation profile of the slope presented in Figure 3-a. Horizontal displacement profile reveals a possible slip surface (Figure 3-b) denoted also by plastic points distribution (Figure 4-a), and shear strain profile (Figure 4-b). A possible slip surface (band), tends to form from local point of horizontal displacement concentration and the point situated at foundation level under the construction joint (Figure 3, 4). The concentration of horizontal displacement estimated by numerical analysis, corresponds in real observed behavior with some cracks mobilized in quasi-horizontal direction at the base point of the excavated upstream slope (Figure 5-a).

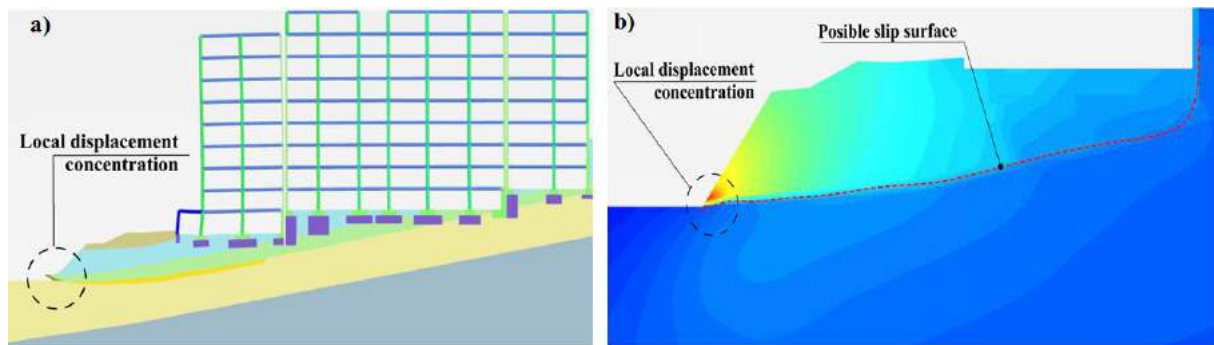


Figure 3. Section SA: a) Exaggerated deformed shape of the slope (scale factor:45);
 b) Horizontal displacement profile

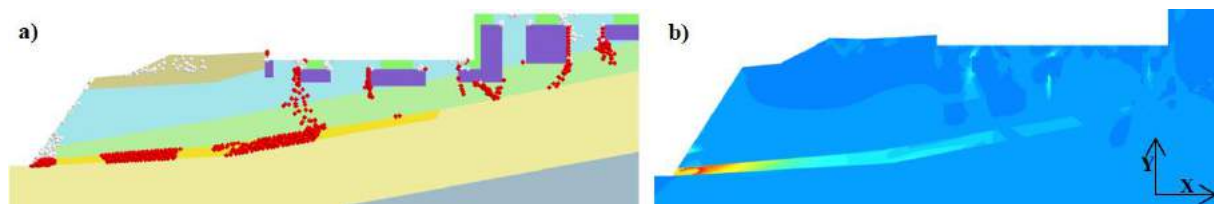


Figure 4. Section SA: a) Plastic points distribution; b) Shear strain distribution, γ_{xy}

Another aspect observed from numerical results is the deformed shape of the vertical construction joint. In that way the joint opening describes a “V” shape, interface elements are in de-bonding mode and the joint opening spread with height from 0.5 cm to 1.53 cm, Figure 5-b. The real joint opening measurements indicate slightly superior values against numerical predictions (Figure 5-b versus Figure 5-c).

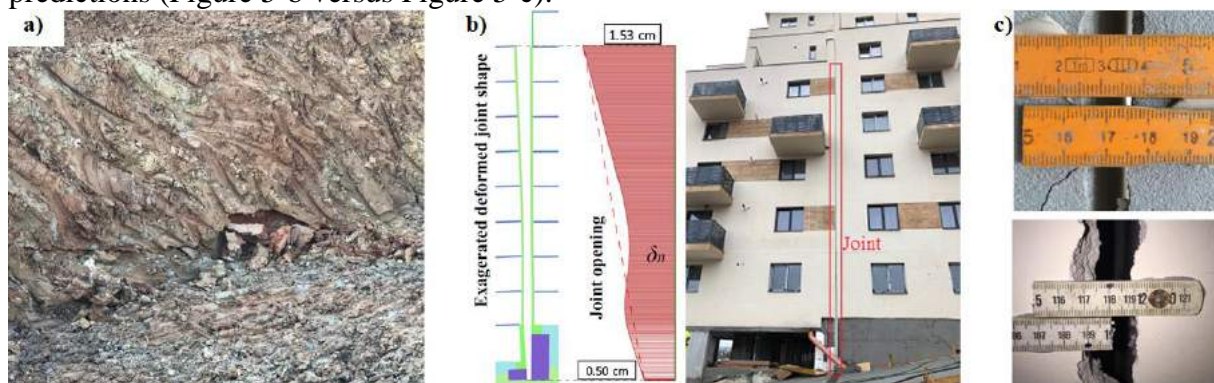


Figure 5. a) Base local cracks on excavated upstream slope; b) Joint deformation for Building A: numerical prediction versus reality; c), Real construction joint opening

3.2. Section SB -Raft Foundation Building Body (Building B)

According to the numerical analysis, excavation induces a deformation profile of the slope presented in Figure 6-a. Horizontal displacement profile reveals a possible slip surface (Figure 6-b) denoted also by plastic points distribution (Figure 7-a), and shear strain profile (Figure 7-b). A possible slip surface (band), tends to form from local point of horizontal displacement concentration and the point situated at foundation level under the construction joint (Figure 6, 7). Another aspect observed from numerical results is the deformed shape of the vertical construction joint. In that way the joint opening describes an inverse “V” shape, interface elements are in de-bonding mode, with joint opening decreasing with height. In superior region of the construction joint, last interface elements are in adhesion (sliding) state according to Figure 8-a. Maximum, predicted joint opening is recorded at the foundation level (0.97 cm).

At superior region of the building, relative normal displacement of the joint record negative value (-0.017 cm), indicating compression interaction at interface elements level.

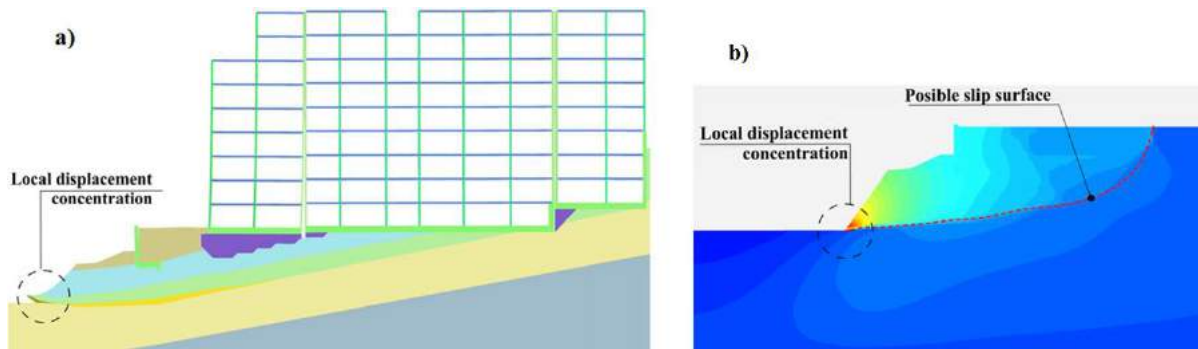


Figure 6. Section SB: a) Exaggerated deformed shape of the slope (scale factor:45);
 b) Horizontal displacement profile

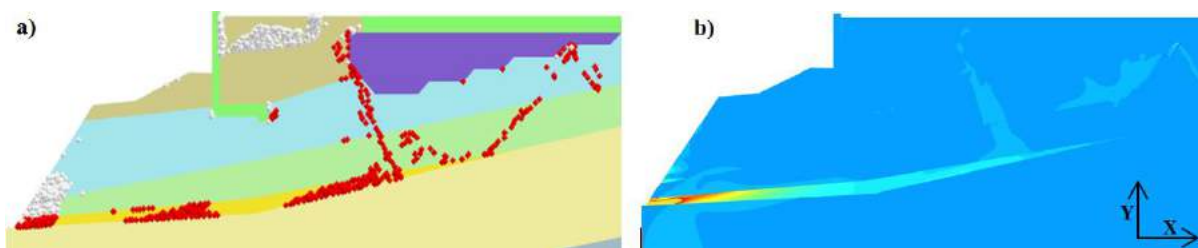


Figure 7. Section SB: a) Plastic points distribution; b) Shear strain distribution, γ_{xy}

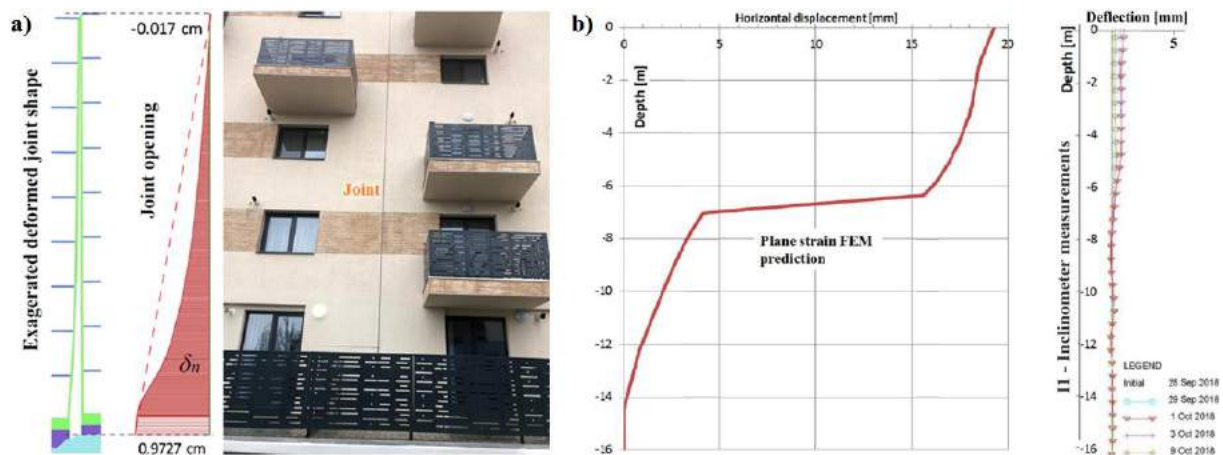


Figure 8. a) Joint deformation for building numerical prediction versus reality;
 b) Soil horizontal deformation: FEM prediction versus inclinometer measurements

3.3. Discussions

The plastic stage analysis (FEM) was performed on two analysis domains according to sections: SA (Figure 2-a) and SB (Figure 2-b). The estimated slope buildings response to downslope excavation platform is slightly different in terms of superstructure deformation (SA: Figure 3-a and SB:Figure 6-a). The deformation profile of the soil, denotes a possible slip surface on both sections (SA- Figure 3-b and SB:Figure 6-b). Regarding soil profile deformation one of the first difference in FEM predictions is the maximum horizontal displacement recorded. In this way, for SA analysis, it was encountered a maximum 6.8 cm horizontal displacement at the local displacement concentration zone (Figure 3-b) and for SB analysis it was encountered a maximum 8.5 cm horizontal displacement (Figure 6-b). Despite of these differences it is necessary to admit that both analysis (SA and SB) predict a moving soil body mass spreading

from local displacement concentration zone (Figure 3-b, Figure 6-b, Figure 5-a) in upstream area till the first vertical construction joint. In that way the closest building body to the excavated platform is subjected to lateral (horizontal) and vertical displacement. This behaviour is confirmed by observations on real site slope behaviour and by inclinometer measurements for I1 tube (Figure 1-a). Numerical estimations and inclinometer measurements confirmed that the deformed soil body mass spread in depth to a value around 7.00 m, Figure 8-b. The magnitude of the phenomenon is revealed with largely differences from FEM prediction and inclinometer measurements (approximately 5 times greater in FEM prediction). The sources of non-convenience could be some of the listed above:

A) Inclinometer measurements are made to a limited period (28 sept. – 4 dec. 2018), insufficient for the slope system to reach effective stress equilibrium as the effect of excavation.

B) Real soil behavior is not close to the assigned behavior (linear elastic-perfect plastic model). In that way it is necessary to use more sophisticated constitutive models, in order to evaluate the nonlinear hardening / softening soil behavior.

Buildings superstructure interaction at vertical joint level exhibits different normal deformation profiles for SA and SB analysis. Joint normal deformation profile estimation exhibits a ``V`` shape for SA profile analysis (isolated foundations building body), according to Figure 3-a and Figure 5-b. Neglecting expectations, for SB profile analysis, joint normal deformation profile estimation exhibits an inverse ``V`` shape, according to Figure 6-a and Figure 8-a. Thereby, it could be pointed out that for this case study de foundations system affects the interaction mode at superstructures construction joint.

The difference propagation sources could be related to model calculation assumptions (plane strain FEM) and unrelated to model calculation assumptions. The distortion sources unrelated to model calculation assumption refer to building geometrical differences in SA and SB profile, slope topology aspects (for SA and SB), soil stratigraphy aspects (for SA and SB) and not ultimately loading transfer mechanism in different foundations systems (SA- isolated foundations and SB – raft foundation).

The distortion sources related to model calculation assumption refer to plane strain analysis FEM model limitations (2D). Thereby stress and strain distribution are estimated on a bi-dimensional section (analysis domain). Following this aspect, the effect of 3D stress and strain state is not taking into account including here 3D slope local excavation influence, 3D interaction between constructions bodies and 3D soil-structures interaction aspects. Another ignored aspect is the 3D behaviour of superstructures regarding columns, beams and slabs.

Thereby the real 3D behaviour was estimated through various equalization techniques to an ``equivalent`` bi-dimensional model behaviour. Following this, column rows were evaluated as plate linear elements, isolated foundations were ``idealized`` to a 2D plane strain behaviour, etc. Near the limitations of plane strain analysis method, many assumption made inside the model formulation could enlarge the range between real behaviour and estimated behaviour. For this case study, the inside model ``contaminating`` assumptions could be enumerated below: superstructure is assumed to behave purely linear elastic with no self-weight or supplementary vertical loading at every storey; the building effect on slope profile is evaluated by an equivalent vertical pressure applied at foundation base contact level; foundation material is assumed to behave linear elastic; the soil is assumed to behave linear elastic-perfect (without nonlinear or strain – softening/hardening aspects accounted).

4. CONCLUSIONS

Despite all the above elements one important aspect should be noted. The FEM 2D predictions denote a behaviour observed in the real slope site . The FEM interaction procedure (interface elements) reveal a non-continuous strain distribution profiles along analysis domains. This aspect is confirmed by site observations and in situ measurements Figure 5-c, Figure 8-b. Besides this, both FEM estimations and inclinometer measurements revealed that the mobilized soil body moving mass spread in depth up to 7.00 m, Figure 8-b. Accordingly, a possible slip surface could occur and thereupon the soil will experience large strains and shift to residual strength properties. In order to ensure the safety of the slope and buildings it is necessary to adopt a retaining structure.

ACKNOWLEDGEMENT

The first author would like to acknowledge the financial support by the Romanian Society for Soil Mechanics and Geotechnical Engineering for attending the 27th European Young Geotechnical Engineers Conference.

REFERENCES

- [1] Troncone A., 2005. “*Numerical analysis of a landslide in soils with strain-softening behaviour*” , Geotechnique , 55(8): 585-596.
- [2] Ou C.-Y., Liao J.-T., Cheng W.-L., 2000. “*Building response and ground movements induced by a deep excavation*”, Geotechnique , 50(3): 209-220.
- [3] Potts D. M., 2003. “*Numerical analysis: a virtual dream or practical reality?*”, Geotechnique , 53(6) : 535-573.
- [4] Brinkgreve R.B.J., Kumarswamy S., Swolfs W.M., Zampich L., Manoj N. G.,2019.“*Plaxis 2D 2019 Manuals*”, Plaxis bv.
- [5] Ellis E.A., Springman S.M.,2001.“*Modelling of soil-structure interaction for a piled bridge abutment in plane strain FEM analyses*”, Computers and Geotechnics, 28(2):79-98.
- [6] Potyondy J.G.,1961.“*Skin friction between various soils and construction materials*”, Geotechnique, 11(4): 339-353.
- [7] Aksoy H.S., Inal E., Gor M., “*Skin Friction between Soil and Pile Materials*”, 12th International Congress on Advances in Civil Engineering (ACE 2016), 21-13 September,2016, Istanbul, Turkey.
- [8] Boulon M., Garcia P., Vermeer P.A., 1995. “*Soil-structure interaction: FEM computations*”, Studies in Applied Mechanics, 42:147-171.
- [9] Van Langen H., 1991.“*Numerical analysis of soil-structure interaction*”, PhD Thesis, TU Delft, Nederland, 153 pages.
- [10] NM Ilies, VS Farcas, RV Cot, IM Moldovan, „*The Control of Natural Disaster Caused by Slopes Sliding by Means of Stepped Buildings*”, 9th International Conference on Interdisciplinarity in Engineering (Inter-Eng)., Tirgu Mures, INTER-ENG 2015 Book Series: Procedia Technology Volume: 22 Pages: 391-398
- [11] Moldovan, I.M & Ilies, N.M. 2014 „*Stabilization of a potentially sliding slope with the aid of an underground house*”, Journal of Applied Engineering Sciences, Vol. 4 (17) issue 2. Oradea: University of Oradea Publishing House.

HOEK - BROWN FAILURE CRITERION AND IMPORTANCE OF TRIAXIAL TESTING IN A PROJECT OF DEEP GEOLOGICAL REPOSITORY

Mgr. Radek Onysko, *SG Geotechnika, a.s., radek.onysko@geotechnika.cz*

ABSTRACT

The goal of this paper is to define Hoek – Brown (HB) failure criterion for granodiorite samples from the possible site of the Czech Deep Geological Repository (DGR) – Brezovy potok. This paper includes triaxial testing, description of the HB failure criterion for intact rocks, rock massif and the evaluation of available data. Other methods used for the description of the HB failure criterion parameters (e.g. GSI and m_i) are also explored. The paper is concluded with a simple numerical model which is using results from laboratory tests and literature reviews.

Keywords: Hoek – Brown failure criterion, Deep Geological Repository, Triaxial test, ISSMGE

1. INTRODUCTION

The project of the Czech Deep geological repository (DGR) is underway that means an ongoing and rigorous laboratory testing. Up to this date, a final repository site has not been chosen. Therefore, for purposes of this paper, one of the potential sites – Brezovy potok – was used for defining the complete Hoek – Brown (HB) failure criterion for intact rock and rock massif. A simplified numerical model was created using the defined parameters.

1.1 Geology

Brezovy potok site lies in the main body of the Central Bohemian Plutonic Complex (CBPC) of the Bohemian Massif (see Fig.1 – number 2). The CBPC was created during the Variscian orogeny and is quite complex. The main rock types of the CBPC are gabbros, hornblendites, tonalites, granodiorites, mela-syenites to mela-granites, and granites. On studied site, the main occurring rock type was amphibole – biotite granodiorite of Blatna type. The estimated age of these rocks is 346 ± 2 Ma [1].

The archive drill cores in the area confirmed, that the granodiorite pluton is homogenous to a depth of at least 150 meters.

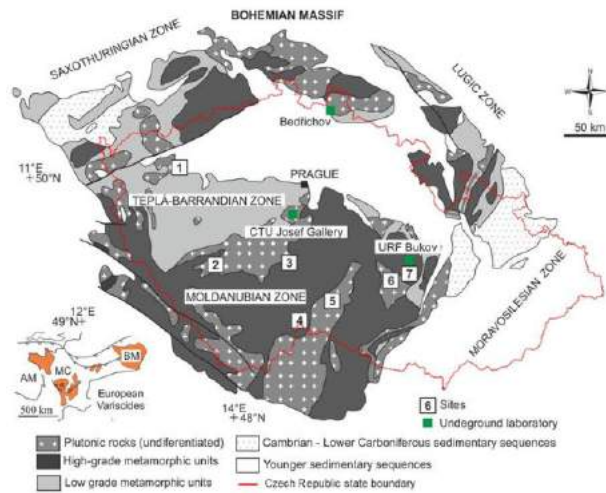


Figure 1. Bohemian massif and possible sites for Czech DGR (Deep geological repository); 1 – Certovka, 2 – Brezovy potok, 3 – Magdalena, 4 – Cihadlo, 5 – Hradek, 6 – Horka, 7 – Kravi hora; by Slovak [2]

2. METHODOLOGY

2.1 Rock Testing

The laboratory tests are based on work done by Petruzalek in 2017 [3] which consists of the uniaxial compressive strength tests (UCS), the Brazilian strength tests (BTS) and one set of the triaxial tests ($\sigma_1, \sigma_2 = \sigma_3$) with a chamber pressure of 13 MPa. Another triaxial tests, with a chamber pressure of 6,3 MPa, 33,5 MPa, and 81,4 MPa, were carried out by the author in 2018. The Brazilian strength tests were used to calculate the direct tensile strength (DTS) using Eq. (1) by Read and Richards [4].

$$DTS = BTS * 0,9 \quad (1)$$

All triaxial tests were carried out at the Institute of Geology of the Czech Academy of Sciences, using a hydraulic press (MTS 815) and triaxial cell (Ergotech).

2.2 Hoek – Brown Failure Criterion – Intact Rock

The Hoek – Brown failure criterion defines all allowable states a rock can be in without a failure. It is described by Eq. (2). The greek sigma one and three denotes maximum and minimum effective stresses at failure, respectively [5], σ_{ci} denotes uniaxial compressive strength.

$$\sigma'_1 = \sigma'_3 + \sigma_{ci} \left(m_i \frac{\sigma'_3}{\sigma_{ci}} + 1 \right)^{0,5} \quad (2)$$

Material parameter m_i and its determination are of utmost importance. This parameter is affected by rock mineralogy, cementation, and its micro-mechanics of failure [6;7;8]. There are two basic approaches to determining m_i : the statistical regression and the indirect estimation.

For statistical regression, are needed data from the DTS tests, the UCS tests and at least 3 to 4 triaxial datasets with σ_3 (chamber pressure) up to UCS/2. The requirement of maximal chamber pressure up to UCS/2 was laid down by Hoek [5]. The lower chamber pressures are critical for precise estimation of m_i as it was proved by Shen and Karakus [9]. At lower pressures (σ_3),

growth in rock strength is steeper [10]. The value of m_i is also affected by the fitting method. In this paper, the statistical regression (fitting), was done by RocLab by Rocscience.

Table 1. m_i chart by rock type; Hoek 2001 - edited

Rock type	Class	Group	Texture				
Sedimentary	Clastic		Coarse Conglomerates 21 ± 3 Breccias 19 ± 5	Medium Sandstones 17 ± 4	Fine Siltstones 7 ± 2 Greywackes 18 ± 3	Very fine Claystones 4 ± 2 Shales 6 ± 2 Marls 7 ± 2	
		Non-Clastic	Evaporites Carbonates	Crystalline Limestones 12 ± 3	Gypsum 8 ± 2 Spartic Limestones 10 ± 2	Anhydrite 12 ± 2 Mieritic Limestones 9 ± 2 Coal* 8-21	Dolomites 9 ± 3 Chalk 7 ± 2
	Organic					Quartzites 20 ± 3	
	Metamorphic	Non-foliated		Marble 9 ± 3	Hornfels 19 ± 4 Metasandstone 19 ± 3		
Igneous	Slightly foliated		Migmatite 29 ± 3 Gneiss 28 ± 5	Amphibolites 26 ± 6 Schists 12 ± 3			
	Plutonic	Light	Granite 32 ± 3 Gneodiorite 29 ± 3	Diorite 25 ± 5	Phyllites 7 ± 3	Slates 7 ± 4	
		Dark	Gabbro 27 ± 3 Norite 20 ± 5	Dolerite 16 ± 5			
	Hypabyssal Volcanic	Lava	Porphyries 20 ± 5			Diabase 15 ± 5 Dacite 25 ± 3 Basalt 25 ± 5	Pefidotite 25 ± 5 Obsidian 19 ± 3
			Pyroclastic	Agglomerate 19 ± 3	Breccia 19 ± 5	Tuff 13 ± 5	

Indirect methods of m_i estimation are advantageous because they do not require triaxial rock testing. There are several methods. One of them is a chart by Hoek [11] (Tab. 1). Next method is the so-called “R – index” used by many authors [12;13;14;15;16;17]. The method uses a ratio between the UCS and the DTS (Eq. 3) to estimate m_i value.

$$m_{it} \approx \frac{UCS}{DTS} = R \quad (3)$$

Last two methods are the UCS – based model, and the TS – model developed by Shen and Karakus [9], and Wang and Sheng [6], respectively. These two models use artificial constants determined by laboratory testing and field praxis. The UCS – based model (Eq. 4) uses constants “a, b” and the UCS to estimate m_i . The TS – model (Eq. 5) uses “A, B” and the DTS.

$$m_i = a\sigma_{ci}^{b+1} \quad (4)$$

$$m_i = A\sigma_t^B \quad (5)$$

Both models are limited in use because of the constants. The constants for both models and various rock types are listed in Tab. 2.

Table 2. Constants for UCS and TS-based methods; Shen and Karakus [9] - edited, Wang and Sheng [6] - edited

Rock types	a	b
Coal	120	-1.70
Granite	100	-1.20
Limestone	22	-1.15
Marble	100	-1.55
Sandstone	50	-1.26
Monzonite	120	-1.40
Monzogranite	87	-1.14
Hybrid rocks	387	-1.67

Rock types	A	B
Coal	22	-0.48
Granite	75	-0.46
Limestone	23	-0.28
Marble	40	-0.66
Sandstone	25	-0.27

2.3 Hoek – Brown Failure Criterion – Rock Massif

The HB failure criterion of rock massif (Eq. 6 – 9) differs slightly from the HB failure criterion for intact rock. Parameters GSI and D reduce the parameter m_i , and thus the actual state of rock massif (weathering, discontinuities, etc.) and its strength can be estimated.

$$\sigma_1' = \sigma_3' + \sigma_{ci}' \left(m_b \frac{\sigma_3'}{\sigma_{ci}'} + s \right)^a \quad (6) \quad m_b = m_i * e^{\left(\frac{GSI-100}{28-14D} \right)} \quad (7)$$

$$s = e^{\left(\frac{GSI-100}{9-3D} \right)} \quad (8) \quad a = \frac{1}{2} + \frac{1}{6} \left(e^{\frac{-GSI}{15}} - e^{\frac{-20}{3}} \right) t \quad (9)$$

Both parameters (D and GSI) must be evaluated in-situ (excavation pit, tunnel, etc.). The parameter D expresses the impact of an excavation/drilling method on rock massif itself, e.i. secondary crack development. Its value can be assessed using the chart listed by Hoek et al. [18]; for this paper, the value of D is 0. Czech DGR (Deep geological repository) should be excavated using a tunnel boring machine (TBM) and thus impact on massif itself should be minimal [19].

The geological strength index (GSI) is a mean to describe mechanical rock properties of a rock massif. The GSI translates laboratory data (e.g. strength) to real in-situ conditions (Eq. 7). There are many ways to assess the GSI value. In this case, archive drill cores data (RQD and geological description of discontinuities) were used to determine the possible GSI range using Eq. 10 [20].

$$GSI = 2JCond_{76} + \frac{RQD}{2} t \quad (10)$$

2.4 Numerical Modelling

The main goal of the numerical model was to answer a question of whether it is necessary to have a precise value of m_i or if the estimated value is enough. The modelling was done using Plaxis 2D plain-strain analysis with custom stress field. The tunnel geometry was a circular tunnel face with a diameter of 5 meters, bare walls, and without lining. The custom stress field was based on data by Souček et al. [21] from underground rock laboratory URF Bukov and edited to cover all possible ranges of the stress field. The custom stress field tensor consisted of overburden ($S_v = 13,29$ MPa), maximum ($S_H = 16 - 26$ MPa) and minimum ($S_h = 11,6 - 13$ MPa) stress component with its ranges. The maximum and minimum stress components are perpendicular to each other. With four sets of input data, 18 scenarios were calculated. Input data are listed in Tab. 3. It is important to note, that reduction of m_i to m_b was made automatically by Plaxis.

Table 3. Data for the numerical model; γ – bulk density, E – young's modulus, ν – Poisson's ratio, σ – uniaxial compressive strength, m_i – material parameter, GSI – geological strength index, D – parameter of disturbance

	HB - estimated		HB - fully defined	
	Intact	Weathered	Intact	Weathered
γ [kN/m ³]	25,66	25,66	25,66	25,66
E [GPa]	58,70	33,40	58,70	33,40
ν [-]	0,28	0,28	0,28	0,28
σ [MPa]	157,60	157,60	157,60	157,60
m_i [-]	29,00	29,00	21,93	29,00
GSI [-]	100,00	62,00	100,00	62,00
D [-]	0,00	0,00	0,00	0,00

3. RESULTS AND DISCUSSION

3.1 Triaxial Tests and m_i

By using formulas introduced in chapter 2, the material parameter m_i was predicted and then calculated from measured data by using statistical regression. Used methods and parameters are summarized in Table 4.

Table 4. Laboratory data and method comparison for m_i

Laboratory data			Method comparison		
Type	σ_3 [MPa]	σ_1 [MPa]	Method	m_i value [-]	Difference [%]
DTS	-7,50	0,00	Regression	21,93	-
UCS	0,00	157,60	R index	21,01	4
Triaxial data	6,30	224,60	UCS model	36,35	65
	13,00	249,70	TS model	29,68	35
	33,50	432,50	Hoek's chart	29±3	19-46
	81,40	659,81			

It is necessary to mention that in the case of UCS and TS models, the constants for granite were used due to their absence for granodiorites.

The value obtained by the method of R index was exact in this case, with only 4% difference. Even charted value by Hoek yielded good value with an average difference of 32,5 %. It needs to be said, that granodiorite from Brezovy potok site is homogenous, and these conclusions are tied to this specific spot.

Precise calculation of m_i is time-consuming and costly, due to the high price of triaxial tests. Except for uniaxial compressive strength and direct tensile, at least four sets of triaxial tests (8 test samples) are needed to obtain a single value. Moreover, any location could consist of several rock types. However, it cannot be denied that there is no other way to precisely calculate m_i . Value of m_i calculated by using regression should be credible; the only downside is the sample origin. Granodiorite samples came from the old quarry, which is situated at Brezovy potok site. Samples from target depth would be indeed better.

3.2 Rock Massif and GSI

GSI value was estimated using archive drill cores data. Five drill cores were in proximity of Brezovy potok site [22], another three came from a location close by [23]. GSI value was derived from the last 20 meters of drill cores. In Tab. 5 we can see all available data for GSI calculation. The final GSI value was obtained using Eq. (10), and its range was set to be 100 – 62.

Table 5. Archive drill cores and derived GSI

Location	Drill core number	Designation	Length [m]	RQD [%]	Used interval [m]	JCond ₇₆	GSI - min.	GSI - max
Vicinity	1	V10	50,5	98,6	50,5 - 30,6	25 - 12	73,3	99,3
	2	V11	55,3	100	55,3 - 30,6	25 - 12	74,0	100,0
	3	V12	50,0	100	50,0 - 30,2	12 - 6	62,0	74,0
	4	V13	50,0	100	50,0 - 28,3	25 - 12	74,0	100,0
	5	V14	50,0	100	55,0 - 35,0	25 - 12	74,0	100,0
Distant ones	6	HV1	150,2	100	150,2 - 130,6	12 - 6	62,0	74,0
	7	HV2	115,5	86,9	115,5 - 93,6	12 - 6	55,5	67,5
	8	HV3	70,0	89,1	70,0 - 48,9	12 - 6	44,6	68,6

This range should cover all possible situation considering rock massif, even though the lower boundary of 62 is low value and rock massif in depth of approximately 500 meters should be in better condition. It should be noted that GSI values were derived from shallow archive drill cores. Longer drill cores or exploratory tunnel at target depth would be better.

3.3 Hoek – Brown Failure Criterion

With all parameter fully defined, we can construct a complete HB failure criterion envelope for intact rock and rock massif. The graphical representation of 4 HB failure envelopes is in Fig. 2. Each method of calculating m_i has two failure envelopes, one for GSI value of 100 and one for GSI value of 62.

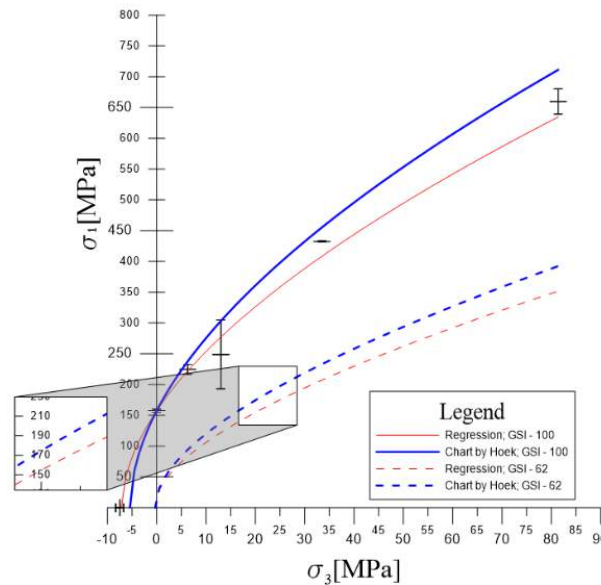


Figure 2. HB failure criterion for intact rock and rocks massif

Laboratory data are shown with their statistical deviation. As we can see, at lower values of σ_3 differences could be as much as 20 MPa. Differences of tensile strength prediction (negative side of the graph) are noticeable too. Failure envelopes were calculated using the “D” value of zero, as it was stated in chapter “Hoek – Brown failure criterion – Rock massif”.

3.4 Numerical Modelling

Results of numerical modelling were evaluated using the so-called characteristic points. These points were along the tunnel wall in positions twelve, three, six and nine o’clock. In Tab. 6 we can see that value of absolute deformation of characteristic points (convergence) is very much identical between HB – estimated ($m_i = 29$) and HB – calculated ($m_i = 21,93$). Scenarios 8_1 and 16_1 led to tunnel collapse due to high horizontal stress (stress was “above” HB failure envelope). Additional scenarios 8_2 and 16_2 found out that upper boundary for horizontal stress is 23 MPa for HB – estimated and 21 MPa for HB – calculated. In these additional scenarios, values of absolute deformation differ, due to the occurrence of plastic deformation. The author is aware of the simplicity of the model, but for the purpose of this paper, it is considered to be sufficient. We can see, that value of m_i is of lower importance for the numerical model than for example value of stress tensor (S_v, S_H, S_v) or GSI.

Table 6 - Numerical modelling, absolute deformation (convergence) of characteristic points

Scenario	m_i value	Vertical stress [MPa]	Horizontal stress [MPa]	Point 1 [mm]	Point 2 [mm]	Point 3 [mm]	Point 4 [mm]	Commentary
1	29,00	13,29	11,60	0,756	0,588	0,763	0,588	-
2	29,00	13,29	13,00	0,723	0,697	0,730	0,697	-
3	29,00	13,29	11,60	1,044	1,349	1,053	1,349	-
4	29,00	13,29	13,00	1,230	1,288	1,241	1,287	-
5	29,00	13,29	16,00	0,652	0,930	0,659	0,930	-
6	29,00	13,29	26,00	0,419	1,707	0,423	1,707	-
7	29,00	13,29	16,00	1,177	1,670	1,188	1,670	-
8 1	29,00	13,29	26,00	-	-	-	-	Tunnel collapse
8 2	29,00	13,29	21,00	1,036	2,353	1,018	2,353	Upper limit for horizontal stress is 23 MPa
9	21,93	13,29	11,60	0,756	0,588	0,763	0,588	-
10	21,93	13,29	13,00	0,723	0,697	0,730	0,697	-
11	21,93	13,29	11,60	1,044	1,349	1,053	1,348	-
12	21,93	13,29	13,00	1,232	1,289	1,242	1,288	-
13	21,93	13,29	16,00	0,653	0,930	0,659	0,930	-
14	21,93	13,29	26,00	0,418	1,707	0,418	1,707	-
15	21,93	13,29	16,00	1,179	1,670	1,190	1,670	-
16 1	21,93	13,29	26,00	-	-	-	-	Tunnel collapse
16 2	21,93	13,29	21,00	1,033	2,367	1,040	2,367	Upper limit for horizontal stress

4. CONCLUSION

The full Hoek – Brown failure criterion was defined with the usage of statistical regression. The value of the material parameter m_i equals to 21,93; the parameter of disturbance D equals to 0. Based on the archive drill cores range for GSI (Geological strength index) was set to 62 up to 100. In case of insufficient triaxial data, method of “R index” is a viable way of defining m_i and it may appropriate to consult the “Hoek’s chart” as well. In terms of the laboratory data, it would be more suitable if the samples were from the target depth. As it was stated in chapter 3.2, available data for determining GSI are not ideal. For numerical modelling, the precise value of m_i is not required, and thus, the expensive laboratory may not be necessary. The stress tensor, GSI and other parameters are much more critical. It is important to emphasize that in general, triaxial test are still necessary to determine the precise value of m_i and are considered to be the only reliable way.

ACKNOWLEDGEMENT

I would like to thank Mgr. Matej Petruzalek Ph.D. for his assistance and advice, without his help triaxial testing would not be possible. Thanks to Institute of Geology of the Czech Academy of Sciences on whose premises triaxial testing took place.

REFERENCES

- [1] Janoušek, V., Wiegand, B., Žák, J., 2010. “Dating the onset of Variscan crustal exhumation in the core of the Bohemian Massif: new U-Pb single zircon ages from the high-K calc-alkaline granodiorites of the Blatná suite, Central Bohemian Plutonic Complex”, Journal of the Geological Society London, 167, pp. 347–360.
- [2] Slovák, J., 2016. “Progress of the Czech Deep Geological Repository Program”, In: Faybishenko, B., Birkholzer, J., Sassani, D., Swift, P., (eds.), 2016. *International Approaches for Nuclear Waste Disposal in Geological Formations: Geological Challenges in Radioactive Waste Isolation - Fifth Worldwide Review*.
- [3] Petružálek, M., 2017. “Stanovení mechanických vlastností hlavních petrografických typů na potenciálních lokalitách HÚ”, TZ 88/2017, GIÚ AV ČR, v. v. i., 76 s
- [4] Read, S. A. L., Richards, L. R., 2015. “Guidelines for use of tensile data in the calculation of the Hoek Brown constant m_i ”, Proceedings of ISRM Congress, Montreal, pp. 10-13, Quebec, Canada.
- [5] Hoek, E., Brown, E.T., 1997. “Practical estimates of rock mass strength”, International Journal of Rock Mechanics and Mining Sciences, 34-8, pp. 1165-1186. ISSN 1365-1609.

- [6] Wang, W., Shen, J., 2017. “*Comparison of existing methods and a new tensile strength based model in estimating the Hoek-Brown constant m_i for intact rocks*”, Engineering Geology, 224, pp 87-96. ISSN 0013-795.
- [7] Zuo, J., Li, H., Xie, H., Ju, Y., Peng, S., 2008. “*A nonlinear strength criterion for rock-like materials based on fracture mechanics*”, International Journal of Rock Mechanics and Mining Sciences, 45-4, pp. 594-599. ISSN 1365-1609.
- [8] Zuo, J., Liu, J., Li, H., 2015. “*A theoretical derivation of the Hoek–Brown failure criterion for rock materials*”, Journal of Rock Mechanics and Geotechnical Engineering, 7-4, pp. 361-366. ISSN 1674-7755.
- [9] Shen, J., Karakus, M., 2014. “*Simplified Method for Estimating the Hoek-Brown Constant for Intact Rocks*”, Journal of Geotechnical and Geoenvironmental Engineering, 140-6.
- [10] Singh, M., Raj, A., Singh, B., 2011. “*Modified Mohr–Coulomb criterion for non-linear triaxial and polyaxial strength of intact rocks*”, International Journal of Rock Mechanics and Mining Sciences, 48-4, pp. 546-555. ISSN 1365-1609.
- [11] Hoek, E., 2001. “*Rock mass properties for underground mines*”, in: Hustrulid, W. A., Bullocks, R.L(eds): *Underground Mining Methods: Engineering Fundamentals and International Case Studies*.
- [12] Cai, M., 2010. “*Practical Estimates of Tensile Strength and Hoek–Brown Strength Parameter m_i of Brittle Rocks*”, Rock Mechanics and Rock Engineering, 43, pp. 167-184.
- [13] Hoek, E., Brown, E.T., 1980. “*Empirical strength criterion for rock masses*”, J. Geotech. Engng Div., pp. 1013-1035.
- [14] Mostyn, G., Douglas, K., 2000. “*Strength of intact rock and rock masses*”, GeoEng 2000-1.
- [15] Sari, M., 2010. “*A simple approximation to estimate the Hoek-Brown parameter ' m_i ' for intact rocks*”, ISRM International Symposium - EUROCK 2010.
- [16] Read, S. A. L., Richards, L., 2011. “*A Comparative Study of m_i , the Hoek-Brown Constant for Intact Rock Material*”, International Society for Rock Mechanics and Rock Engineering.
- [17] Read, S. A. L., Richards, L. R., 2014. “*Correlation of direct and indirect tensile tests for use in the Hoek-Brown constant m_i* ”, International Society for Rock Mechanics and Rock Engineering.
- [18] Hoek, E., Carranza-Torres, T., Corkum, B., 2002. “*Hoek-Brown failure criterion - 2002 Edition*”.
- [19] SÚRAO, 2017. “*Zprávy ze Správy*”, 2017(4). ISSN 2533-5073.
- [20] Hoek, E., Carter, T., Diederichs, M., 2013. “*Quantification of the Geological Strength Index Chart*”, 47th US Rock Mechanics / Geomechanics Symposium 2013, 3 pp. 1757-1764.
- [21] Souček, K., Vavro, M., Staš, L., Vavro, L., Waclawik, P., Konicek, P., Ptáček, J., Vondrovic, L., 2017. “*Geotechnical Characterization of Bukov Underground Research Facility*”, Procedia Engineering, 191, pp.711-718. ISSN 1877-7058.
- [22] Bárta, J., Bašta, J., Lipold, O., Malá, J., Ottová, M., Suková, H., Unzeitig, M., Vach, J., Vondra, J., 1986. “*ZAVERECNA ZPRAVA UKOLU SLATINA - SUROVINA: DEKORACNI KAMEN - ETAPA PRUZKUMU: PODROBNA - STAV KE DNI: 31.12.1985*”, Geoindustria, Praha.
- [23] Bašta, J., Morvicová, L., Suková, H., Špaček, K., 1976. “*Závěrečná zpráva úkolu Defurovy Lažany II. Surovina: kámen štěpný a dekorační (blatenská žula). Etapa průzkumu: předběžná. Stav ke dni: 22.1.1975*”, Geoindustria, závod Stříbro.

VULNERABILITY OF TRAFFIC EMBANKMENTS TO LIQUEFACTION-INDUCED DEFORMATIONS

Aleš Oblak*, *University of Ljubljana, Faculty of Civil and Geodetic Engineering, Chair of Geotechnical Engineering, Ljubljana, SLOVENIA, aoblak@fgg.uni-lj.si*

Janko Logar, *University of Ljubljana, Faculty of Civil and Geodetic Engineering, Chair of Geotechnical Engineering, Ljubljana, SLOVENIA*

Sebastjan Kuder, *University of Ljubljana, Faculty of Civil and Geodetic Engineering, Chair of Geotechnical Engineering, Ljubljana, SLOVENIA*

Antonio Viana Da Fonseca, *CONSTRUCT-GEO, Faculty of Engineering, University of Porto (FEUP), Porto, Portugal*

ABSTRACT

Liquefaction-induced deformations on traffic embankments were studied using software package FLAC in combination with advanced material model PM4Sand in order to simulate the liquefaction phenomenon. A parametric study was carried out, where the geometry of the embankment and soil profile was varied. In addition, numerical analyses were performed for two sets of material properties of the liquefiable sandy layer – medium dense and loose state. On the basis of numerical results, fragility curves were derived in terms of crest settlement as damage state parameter and Arias intensity or peak ground acceleration as intensity measure.

Keywords: Embankment, Liquefaction, FLAC, Vulnerability Analysis.

1. INTRODUCTION

Soil liquefaction is a phenomenon where soil loses its shear strength and stiffness due to rearrangement of solid particles, which leads to a pore pressure build-up during dynamic loading, such as earthquakes. Most often, liquefaction occurs in loose saturated sandy to silty sandy soils. The development and extent of the consequences of this complex phenomenon depend on many factors. Initially, properties of a liquefiable layer, ground motion characteristics and site conditions (thickness and depth of layers susceptible to liquefaction, ground water level, ground inclination, etc.), along with other circumstances associated with the effects of human activities in the ground near the site under consideration.

According to literature ([1], [2] and [3]), earth dams, embankments and river levees are very vulnerable to seismic shaking and liquefaction occurrence under foundations. Within this study, attention was given to traffic embankments built on liquefiable ground, since they are of vital importance and represent links between assistant institutions and affected areas. A parametric study of an embankment was conducted using 2D finite difference program FLAC. Numerical simulation of liquefaction process in the ground was achieved using advanced PM4Sand material model [4]. Individual combination of model geometry and material properties was shaken by 30 ground motions with at least 8 different peak ground acceleration levels in order to derive fragility curves.

2. MODEL DESCRIPTION

2.1. Model Geometry and Material Properties

The earthquake-liquefaction-induced deformations of traffic embankment were observed on a simple numerical model for four different soil profiles – S1, S2, S4 and S5. Soil profiles S1, S4 and S5 contain a liquefiable sandy layer of various thicknesses (7, 2 and 4 m, respectively), which lie between 24 m thick base stiff clay layer and 1 m thick clayey crust layer on top, while soil profile S2 was modelled with a 7 m thick liquefiable layer without crust. Ground water level was placed at one meter depth.

Considering embankment geometry, slope inclination was set to 1:2 (vertical:horizontal) and remained constant through all analyses. Additionally, embankment height was varied from 2 to 8 m by steps of 2 m and was analysed in combination with all soil profiles and 24 m wide embankment crest, whereas the effect of crest width (6, 12 and 24 m) was considered only for soil profile S1 and 4 m high embankment.

Basic model variables are presented in Figure 1 and Table 1.

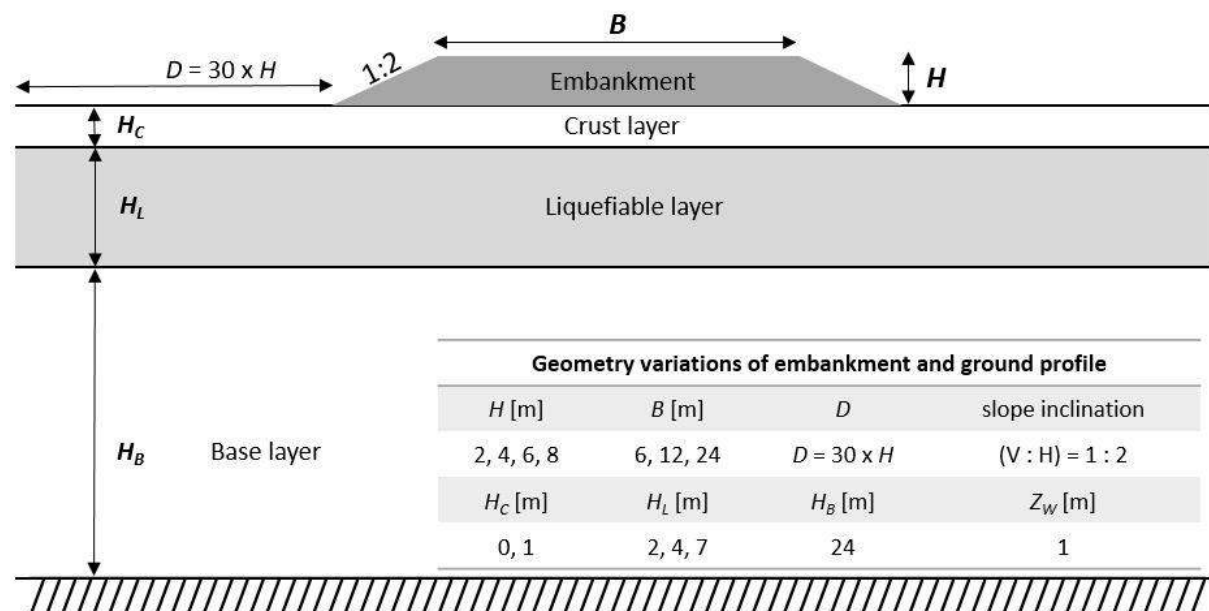


Figure 1. Model geometry.

Table 1. Soil profiles.

Soil ID	H_C – thickness of crust layer [m]	H_L – thickness of liquefiable layer [m]	H_B – thickness of base layer [m]
S1	1	7	24
S2	0	7	24
S4	1	2	24
S5	1	4	24

The numerical model was constructed in several phases. Firstly, free field initial stresses were calculated after the geometry, material parameters, pore water pressure distribution and boundary conditions for static analysis had been assigned to the model. Then followed the construction of the embankment and the replacement of the material model. It was assumed that only sandy layer can liquefy; thus, PM4Sand model was assigned to that layer only. Other layers were modelled by Mohr-Coulomb material model throughout the analysis. In the next

phase, seismic load was applied to the model. For this purpose, free field boundary condition at lateral edges and compliant base at the bottom of the model was set. Ground motion was transformed into shear stress history and applied at the compliant base.

Since numerical analyses were carried out for hypothetical ground conditions, all secondary input parameters for PM4Sand material model were kept at their default values. The three main input parameters (relative density – D_r , shear modulus coefficient – G_0 and Contraction rate parameter – h_{po}) were selected on the basis of real soil tests.

Material properties for three soil layers and embankment are presented in Table 2.

Table 2. Material properties.

Layer	Dry density	Bulk modulus	Shear modulus	Undrained shear strength	φ'	c'	PM4Sand		
	kg/m ³	MPa	MPa	kPa	°	kPa	D_r [/]	G_0 [/]	h_{po} [/]
Crust	1784	64	30	80	-	-	-	-	-
Liquefiable “loose”	1486	57.3	43	-	30	0	0.6	760	0.55
Liquefiable “medium”	1486	77	77	-	30	0	0.35	476	0.5
Base	1436	227	105	150	-	-	-	-	-
Embankment	1800	83.3	38.5	-	35	5	-	-	-

Two sets of sandy layer characteristics were analysed within this study, depending on the density of the liquefiable layer – medium dense and loose state, with relative density equal to 0.6 and 0.35, respectively. Liquefiable layer was underlain by stiff clay with undrained shear strength of 150 kPa.

2.2. Ground Motions

A selection of 30 real acceleration time histories recorded on rock outcrop were used as dynamic loading in numerical calculations. Ground motions (GM) were collected from PEER (Pacific Earthquake Engineering Research Center) database in such manner that the mean spectrum of the selected ground motions matches sufficiently well the EC8 spectrum for soil class A, taking into account peak ground acceleration (PGA) of 0.25 g. All of 30 GMs were subsequently modified to different intensity levels for the derivation of fragility curves. In case of medium dense sand, eight intensity levels (0.25 g, 0.375 g, 0.5 g, 0.625 g, 0.75 g, 1.0 g, 1.25 g and 1.5 g) were used. For the loose case, three to four extra PGA levels were added (0.1 g, 0.2 g, 0.3 g and in some cases even 0.15 g). With these extra intensity levels, the whole range of fragility curves is sufficiently well covered by numerically calculated points, even in cases where crest deformations, and consequently the number of cases exceeding certain limit state, increase rapidly with increasing PGA at bedrock by small increments.

3. VULNERABILITY ANALYSIS AND RESULTS

Based on the results of numerical calculations, a vulnerability assessment of the traffic embankments was performed. The probability of exceedance of a certain limit state for the embankments in question is expressed by the means of fragility curves. Various approaches for the derivation of fragility curves can be found in literature, from empirical [5] and analytical [6] procedure to expert judgement or hybrid method. Within this study, analytical

approach was used due to the repeatability of numerical analyses on the same model subjected to different ground motions. In this way, the impact of uncertainties originating from the earthquake source is decreased.

Soil-structure interaction is very complex in case of traffic embankments underlain by liquefiable layer leading to several possible failure mechanisms – lateral spreading, subsidence of the crest, slope instability or hydraulic heave through cracks [7]. Since crest settlement is still widely used among geotechnical engineers due to its simple comparisons with field measurements, it was selected as engineering damage state parameter in this study, as well as in other relevant researches [8]. Permanent vertical displacement was obtained at the midpoint of embankment model. On the other hand, two different intensity measures were chosen – peak ground acceleration and Arias intensity. The first one is more commonly used in practice due to numerous correlations with other engineering parameters, while the latter more specifically describes the released energy during ground movement.

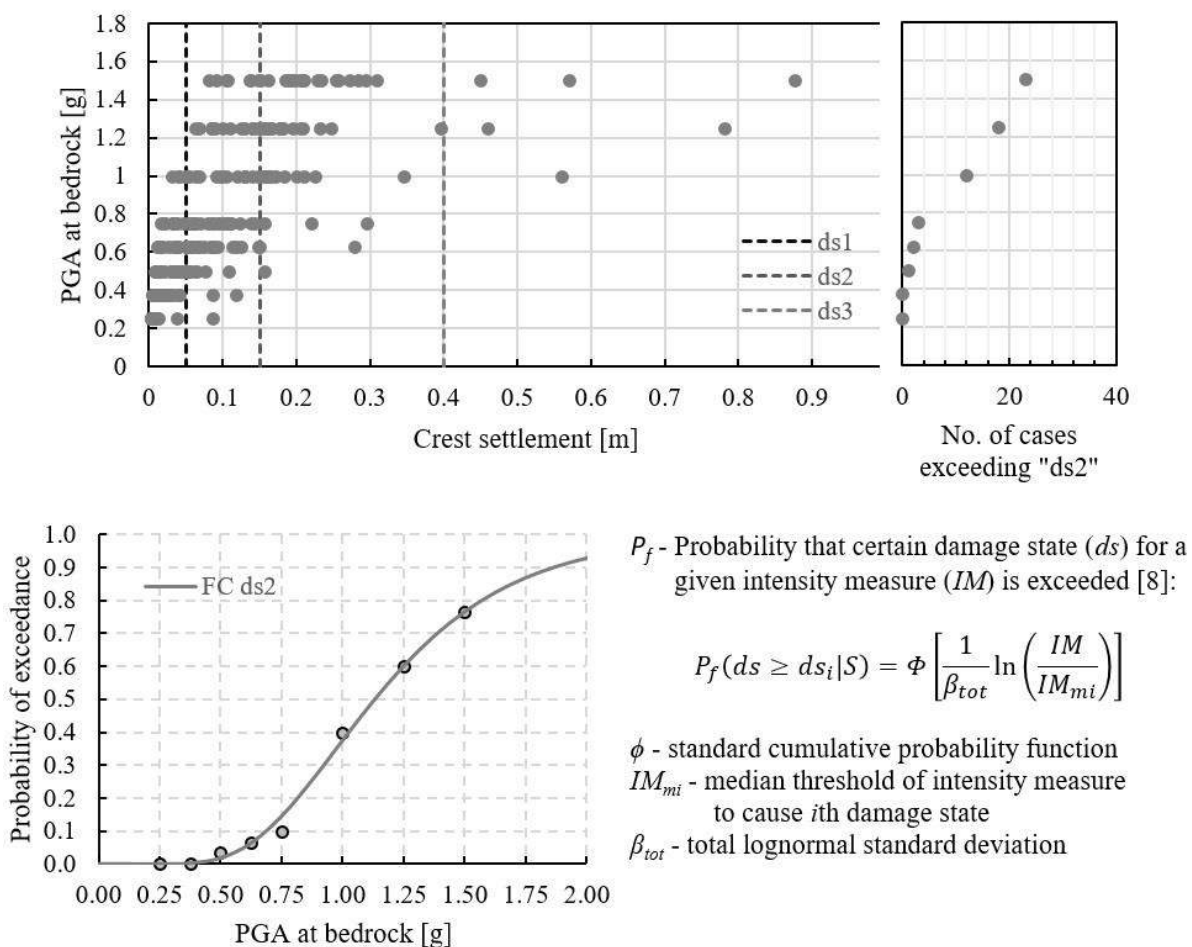


Figure 2. Multiple Stripe Analysis procedure.

Numerical analyses were performed following the principle of Multiple Stripe Analysis method [9], where calculations were executed at discrete intensity measure levels for a set of selected ground motions (see the example in Figure 2). The probability of exceedance was calculated as a number of cases exceeding certain limit state divided by the number of all performed analyses at i -th intensity level. Maximum of likelihood function was used for fitting procedure. Threshold values for the limit state parameter were gathered from literature [10] and are presented in Table 3.

Table 3. Threshold values of damage states for highway and railway embankments [10].

Damage state	Permanent vertical ground displacement [m] – highway			Damage state	Permanent vertical ground displacement [m] – railway		
	min	max	mean		min	max	mean
ds1 – minor	0.02	0.08	0.05	ds1 – minor	0.01	0.05	0.03
ds2 – moderate	0.08	0.22	0.15	ds2 – moderate	0.05	0.10	0.08
ds3 – extensive	0.22	0.58	0.40	ds3 – extensive	0.10	0.30	0.20

Typical numerical results in terms of permanent displacements at final calculation step, progress of crest settlements through dynamic time, are introduced in the subsections below. Furthermore, the effects of different model variations (embankment height, crest width, thickness of liquefiable layer, presence of crust layer and density state of liquefiable layer) are presented through fragility curves below.

3.1. Numerical Results – Embankment Displacements

Typical distribution of the embankment's displacements at the end of analysis and advancement of crest settlement at midpoint with time are shown in Figure 3. The figure below represents a case with 6 m high embankment, underlain by crust layer and 7 m thick medium dense liquefiable layer (soil profile S1), subjected to dynamic loading with PGA at bedrock equal to 1.0 g. Actual values of calculated displacements depend on selected ground motion, because earthquake records with various frequency compositions and time durations are considered within the set of 30 GMs.

Generally, rotational slip surface at both sides, crest subsidence and lateral spreading in horizontal direction due to dynamic excitation and consequent foundation's liquefaction, were observed in the majority of numerical calculations. Similar failure mechanism was noticed in literature [11, 12]. The detailed exploration of all deformed shapes of the analysed embankments is beyond the scope of this paper.

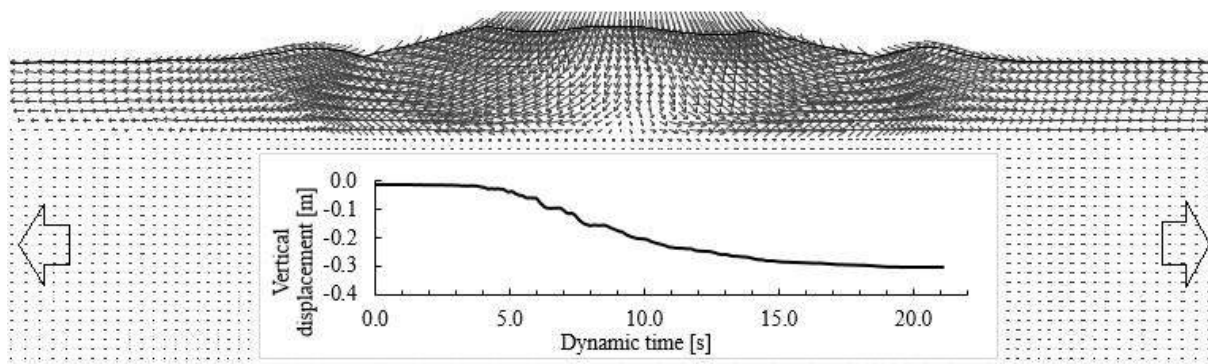


Figure 3. Typical deformed shape of the embankment and settlement vs. time during shaking.

3.2. Fragility curves

The outcomes of the vulnerability analysis of traffic embankments are expressed through fragility curves (see Figure 4 to Figure 7). Fragility curves under this study were derived based on permanent vertical crest settlements in the midpoint of the model, where mean threshold values of damage states for traffic embankments from Table 3 were used. Three limit states were considered – minor (ds1), moderate (ds2) and extensive (ds3).

With the aim of achieving sufficient clarity in the figures containing fragility curves, different line types are used to differentiate between model variations (crest width, embankment height, thickness and density state of the liquefiable layer), while the damage states differ in colour, namely ds1 (light grey), ds2 (dark grey) and ds3 (black).

In addition, Figure 4 and Figure 5 are based on damage states for highways, while Figure 6 and Figure 7 present fragility curves for railways. Regardless of the choice of threshold values for limit states, the trends of various effects related to the model variations are the same, only the curves move to the left, due to more rigorous criteria for railways.

3.2.1. Influence of crest width

According to Figure 4, lower settlements in the middle point are expected with increasing crest width, based on three examined cases (6 m, 12 m and 24 m). Analyses were performed on a case with a 4 m high embankment underlain by soil profile S1 with medium dense sandy layer.

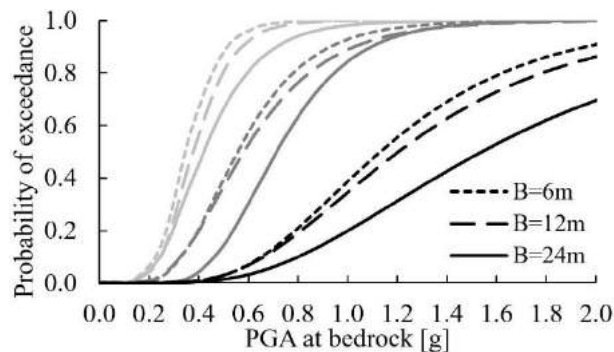


Figure 4. Effect of crest width on fragility curves (highway criteria) – *ds1*, *ds2* & *ds3*.

3.2.2. Influence of embankment height

The impact of the height of embankment was analysed on the model with 24 m wide crest, where embankment was built on soil profile S1. Both Figure 5a and Figure 5b show that vulnerability of the embankment rises with increasing embankment height, since the curves move to the left.

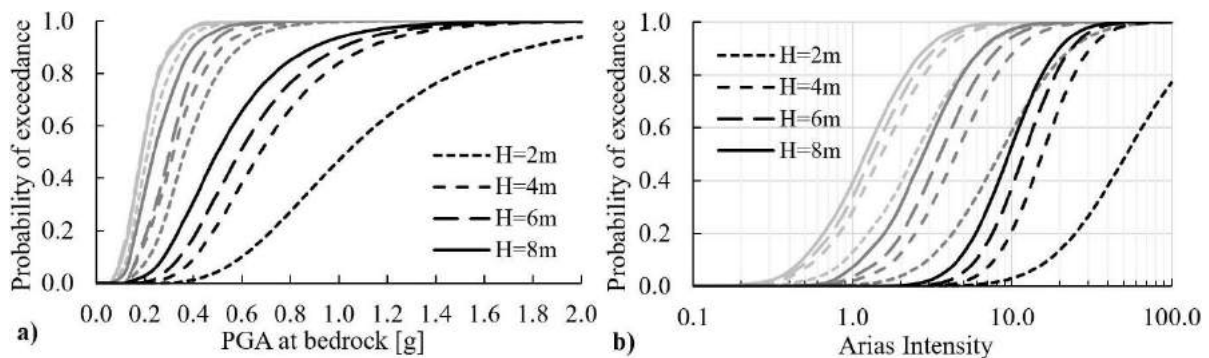


Figure 5. Effect of embankment height on fragility curves (highway criteria) for a) PGA and b) Arias Intensity – *ds1*, *ds2* & *ds3*.

3.2.3. Influence of thickness of liquefiable layer

The effects of the thickness of liquefiable layer and the presence of crust layer were studied on a model with 6 m high embankment and 24 m wide crest. Moreover, soil properties related to the medium dense case were assigned to the sandy layer.

Initially, larger settlements were expected with increasing thickness of liquefiable layer. Figure 6 clearly shows that this is partially true, because the probability of exceeding certain limit state is greater in the case of a 7 m than in the case of a 4 m thick liquefiable layer. Even larger probability was calculated for the case without crust layer and 7 m thick sandy layer. Nevertheless, greater vulnerability was obtained for the case with soil profile S4 ($H_L = 2$ m) compared to S5 ($H_L = 4$ m) for this particular model variation.

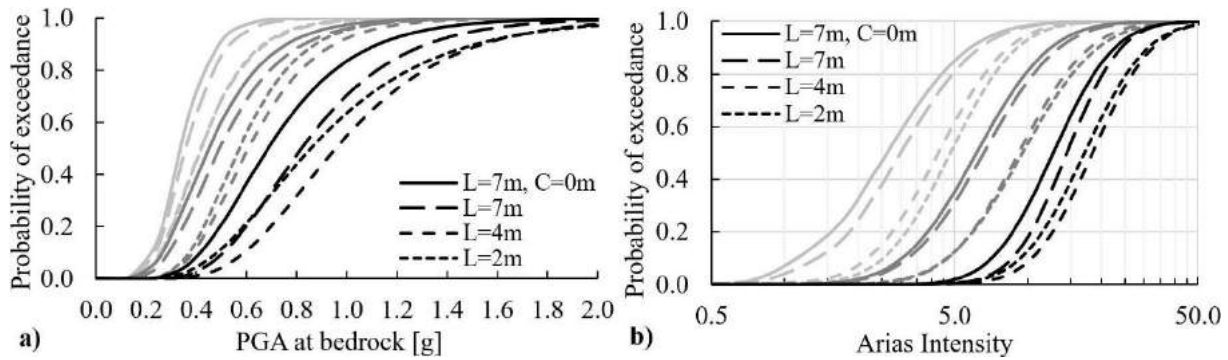


Figure 6. Effect of thickness of liquefiable layer (railway criteria) for a) PGA and b) Arias Intensity – *ds1*, *ds2* & *ds3*.

3.2.4. Influence of density of liquefiable layer

Model with a 6 m high embankment and 24 m wide crest, lying on soil profile S2, was used for the comparison between loose and medium dense state of the liquefiable layer. The result is presented in Figure 7, where larger crest settlements were calculated for the loose case.

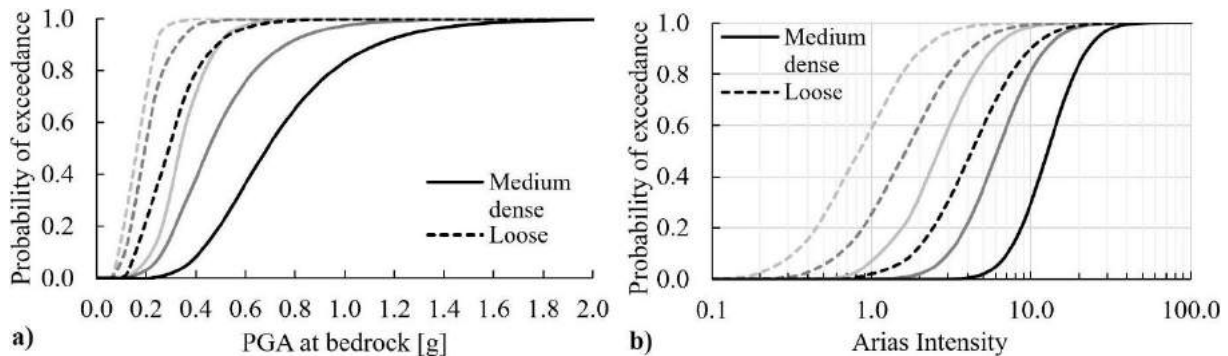


Figure 7. Effect of soil density on fragility curves (railway criteria) for a) PGA and b) Arias Intensity – *ds1*, *ds2* & *ds3*.

4. CONCLUSION

A comprehensive set of numerical calculations of the traffic embankment built on liquefiable ground was made using 2D FLAC software in order to perform the vulnerability analysis. The soil behaviour during liquefaction was captured with advanced PM4Sand material model. Attention was given to the deformation of the embankment crest, more precisely, permanent vertical displacement at midpoint was used as damage state parameter for the derivation of fragility curves. Fragility curves were determined for different variations of the model parameters, among which crest width, embankment height, presence of crust layer, density state and thickness of liquefiable layer were varied. Uncertainties related to earthquake excitation were decreased using a set of 30 ground motions recorded on rock outcrop. Depending on the case, ground motions were scaled to at least 8 intensity levels until the entire range of the fragility curve was reasonably well covered. On the basis of numerical calculations and figures presented above, it was found out that the probability of exceeding certain limit state for the studied range increases with increasing embankment height (2 m, 4 m, 6 m and 8 m) or with decreasing crest width (6 m, 12 m and 24 m). Furthermore, depending on the density state of the liquefiable layer, greater deformations at the embankment crest are expected for looser sand. The effect of thickness of the liquefiable layer is not so straightforward, since it turned out that the embankment is more vulnerable if built on soil profile S4 ($H_L = 2$ m) than on soil profile S5 ($H_L = 4$ m), but less than on soil profile

S1 ($H_L = 7$ m). Nonetheless, absence of crust layer causes larger crest settlement, when comparing embankment deformations built on soil profiles S1 and S2. Fragility curves were derived based on damage criteria from literature [10] for highway and railway embankments. Additional information can be found in [13].

ACKNOWLEDGEMENT

This study is a product of the LIQUEFACT project, funded by the European Union's Horizon 2020 research and innovation programme under grant agreement No GAP-700748.

REFERENCES

- [1] Siyahi, B., Arslan, H., 2008. "Earthquake induced deformation of earth dams", Bulletin of Engineering Geology and the Environment, 67(3):397-403, DOI: 10.1007/s10064-008-0150-5.
- [2] Wu, G., 2014. "Seismic Design of Dams", Encyclopedia of Earthquake Engineering, 1-18, DOI 10.1007/978-3-642-36197-5_96-1.
- [3] Argyroudis, S., Mitoulis, S., Kaynia, A.M., Winter, M.G., 2018. "Fragility Assessment of Transportation Infrastructure Systems Subjected to Earthquakes", Geotechnical Earthquake Engineering and Soil Dynamics V GSP, 174-183, 10-13 June 2018, Austin, Texas, USA.
- [4] Boulanger, R.W., Ziotopoulou, K., 2017. "PM4Sand (Version 3.1): A sand Plasticity Model for Earthquake Engineering Applications", Report No. UCD/CGM-17/01.
- [5] Maruyama, Y., Yamazaki, F., Mizuno, K., Tsuchiya, Y., Yogai, H., 2010. "Fragility curves for expressway embankments based on damage datasets after recent earthquakes in Japan", Soil Dynamics and Earthquake Engineering, 30(11): 1158-1167, doi.org/10.1016/j.soildyn.2010.04.024.
- [6] Khalil, C., Rapti, I., Lopez-Caballero, F., 2017. "Numerical Evaluation of Fragility Curves for Earthquake-Liquefaction-Induced Settlements of an Embankment", Geo-Risk 2017, pp. 21-30, 4-7 June 2017, Denver, Colorado, USA.
- [7] Rapti, I., Lopez-Caballero, F., Modaressi-Farahmand-Razavi, A., Foucault, A., Voldoire, F., 2018. "Liquefaction analysis and damage evaluation of embankment-type structures", Acta Geotechnica, 13(5): 1041-1059, doi.org/10.1007/s11440-018-0631-z.
- [8] Argyroudis, S., Kaynia, A.M., 2015. "Analytical seismic fragility functions for highway and railway embankments and cuts", Earthquake Engineering & Structural Dynamics, 44(11): 1863-1879.
- [9] Baker, J.W., 2015. "Efficient Analytical Fragility Function Fitting Using Dynamic Structural Analysis", Earthquake Spectra, 31(1): 579-599, doi.org/10.1193/021113EQS025M.
- [10] Ptilakis, K. (project coordinator), Kaynia, M.A. (report editor), 2009-2013. "Fragility curves for all elements at risk", Systemic Seismic Vulnerability and Risk Analysis for Buildings, Lifeline Network and Infrastructures Safety Gain (SYNER-G), Project N°: 244061, Call N°: FP7-ENV-2009-1.
- [11] Maharjan, M., Takahashi, A., 2014. "Liquefaction-induced deformation of earthen embankments on non-homogenous soil deposits under sequential ground motions", Soil Dynamics and Earthquake Engineering, 66: 113-124, DOI: 10.1016/j.soildyn.2014.06.024.
- [12] Oka, F., Tsai, P., Kimoto, S., Kato, R., 2012. "Damage patterns of river embankments due to the 2011 off the Pacific Coast of Tohoku Earthquake and a numerical modeling of the deformation of river embankments with a clayey subsoil layer", Soils and Foundations, 52(5): 890-909, doi.org/10.1016/j.sandf.2012.11.010.
- [13] Viana da Fonseca et al. (2018). "Methodology for the liquefaction fragility analysis of critical structures and infrastructures: description and case studies", LIQUEFACT Deliverable D3.2, Horizon 2020 EU funding for Research & Innovation Project ID: 700748 (www.liquefact.eu).

BEARING CAPACITY CORRECTION FACTORS FOR SOILS AND ROCKS

Ana Alencar*, *Technical University of Madrid (UPM)*, *at.santos@alumnos.upm.es*

Svetlana Melentijevic, *Complutense University of Madrid (UCM)*, *svmelent@ucm.es*

Rubén Galindo, *Technical University of Madrid (UPM)*, *rubenangel.galindo@upm.es*

ABSTRACT

In the field of soil mechanics, the calculation of the bearing capacity is well developed, there are various correction coefficients published by different authors that are used to take into account diverse hypothesis regarding self-weight, foundation type, foundation roughness, etc. However, in rock mechanics the application of these correction coefficients developed in soil mechanics can lead to erroneous results, so it is still necessary to carry out more research in order to know further the influence of multiple parameters of the rock mass on the bearing capacity of shallow foundation to estimate it with more accuracy applying different correction factors. Based on the limitations of different analytical solutions for the estimation of the bearing capacity of shallow foundation on rock mass, the numerical modeling of the shallow foundation by finite difference code FLAC is performed over a great number of cases. The purpose of that numerical modelling is to study the influence of geometrical and geotechnical parameters (foundation width, rock type, uniaxial compressive strength and geological strength index) on the bearing capacity of foundations on rock mass under different hypotheses of the self-weight of material, the footing shape and the roughness of the base interface. In this paper a summary of a comparison between the influence of different correlation coefficients in soils and rocks is presented in order to determine which parameter is more conditioning in each type of material and the mechanical behavior observed, analyzing quantitatively those differences as well.

Keywords: Correction Factors, Bearing Capacity, Shallow Foundation, Soils, Rocks, Analytical Method, Numerical Modeling.

1. INTRODUCTION

For the study of the ultimate bearing capacity several methods of analysis have been used: limit equilibrium method, slip line method, limit analysis method, numerical method, etc.

The traditional analytical solutions for the estimation of the ultimate bearing capacity in soils [1], [2] were developed for the linear Mohr-Coulomb failure criterion that depends on the cohesion and internal friction angle of the material. Since the development of the non-linear Hoek and Brown failure criterion [3], [4], [5] for rock masses, in the majority of the calculation of the bearing capacity of rock masses the equivalent strength parameters of the Mohr-Coulomb failure criterion (cohesion and friction angle) are deduced for the corresponding stress level of the rock mass, for its introduction into the traditional formulations. The non-linear Hoek & Brown failure criterion [5] is applicable for the rock mass with a homogeneous and isotropic behavior, meaning that by inexistence or by abundance of discontinuities has the same physical properties in all directions.

Merifield et al. [6] observed that the use of Mohr-Coulomb's equivalent strength parameters overestimates the bearing capacity of strip footing up to 157% in the case of a good quality rock mass.

In the last decades, some methods were developed for the estimation of the ultimate bearing capacity of rock masses based on the parameters that define the failure criterion.

The analytical method that solves the internal equilibrium equations combined with the failure criterion was proposed by Serrano & Olalla [7] and Serrano et al. [8] applying the Hoek and Brown [3] and the modified Hoek and Brown failure criterion [4] respectively. It is based on the characteristic line method [9], under hypotheses of weightless rock, strip footing and associative flow law.

This paper is based on the limitations of the analytical solutions, for the estimation of the bearing capacity of shallow foundation on rock mass considering the hypothesis that employ. The analysis in this study is focused on the analysis of the influence of the self-weight of material, the footing shape and roughness of base interface on the bearing capacity determined by the numerical model developed by the finite difference method (FLAC code).

Considering the influence of the self-weight of the rock material, it is important to emphasize that the self-weight of the material works as a confining load that displaces the Mohr circle to the right in the Mohr-Coulomb failure diagram, increasing the stress level at the failure. In the case of soils, as it is generally assumed that the geotechnical parameters do not change with the stress level, because the Mohr-Coulomb failure criterion is linear, therefore the cohesion and friction angle are constant and independent of the stress level. In the field of rock mechanics, the behavior changes according to the stress level, so the failure parameters change if the self-weight of the rock mass is considered. Besides that, for both soil and rock the consideration of the self-weight of material increases the bearing capacity, because to reach the failure under this hypothesis it is necessary to apply a load that exceeds the material resistance and the load due to the weight.

In relation to the influence of the footing shape and interface roughness on the bearing capacity of shallow foundations on rock mass, it can be emphasized that these two issues have not been studied a lot, considering few references encountered for the footing shape ([10], [11], [12], [13], [14]) and no literature was found for the foundation base roughness influence on bearing capacity on rock masses. In contrast, in soil mechanics, the influence of these factors is broadly studied, taking into account different correction factors published for specific soil type, for example in relation to the footing shape can be emphasized the studies performed by Meyerhof [15], De Beer [16] and Brinch Hansen [1]; while concerning the interface roughness Terzaghi [2], Meyerhof [17] and Hjjaj et al. [18] have made significant contributions.

In the case of the rock mass, the analytical solution [8] can't contemplate the base roughness of the footing due to not taking into account the displacements of the footing nor the footing stiffness effect in its theoretical formulation. However, the results are very similar to obtained by the abacus of Merifield et al. [6] under the assumption of rough interface

2. NUMERICAL ANALYSIS

A total of 192 cases was analyzed under different hypothesis, these cases are resulting from the combination of four influential parameters in the bearing capacity (rock type (m_o), foundation width (B), uniaxial compressive strength of the rock (UCS), geological strength index (GSI)). The values of these parameters are given in Table 1 that covers a wide variety of types and states of rock masses.

Numerical calculations were developed by the finite difference code FLAC employing 2D models and applying the plane-strain condition to represent a strip footing and the axisymmetric condition to simulate a circular footing. The axisymmetric model uses a cylindrical coordinate system that allows to represent objects with axial symmetry, as is the case of a circular footing. In the case of the plane-strain condition, a symmetrical model is used, where only half of the strip footing is represented. The axisymmetric grid is viewed as a unit-radian sector [19]. The boundaries of both models are located at a distance that does not interfere in the result.

Table 1. Summary of the parameters adopted in the study

m_o	B (m)	UCS (MPa)	GSI
5	4.5	5	10
12	11	10	50
20	16.5	50	85
32	22	100	

It is important to note that in the numerical calculations the model is usually simplified by adopting a footing as a load (velocity increments) applied directly on the ground surface. Thus, it is not necessary to define strength parameters for the footing, neither for the interface between the ground and the structure. To simulate a perfectly smooth or rough interface, the nodes where the load is applied are loose or fixed, allowing or not the displacement.

In the cases studied, the vertical load is applied by velocity increments, if the nodes where the load are applied are fixed in two perpendicular directions ("x" and "y") the interface is perfectly rough. While, when the movement in the horizontal direction ("x") is not restricted, a perfectly smooth interface is simulated, because there is no resistance to the horizontal movement.

From the basic cases, four different calculation hypotheses are implemented adopting plane strain and axisymmetric model, weightless or considering the self-weight of the material, rough or smooth interface, resulting in a total of 768 cases. In all simulations the associative flow rule and the unit weight of 26 kN/m³ are adopted.

Numerically, it is assumed that the bearing capacity is reached when the continuous medium does not admit more load, because an internal failure mechanism is formed. In FLAC the load is applied through velocity increments, and the ultimate bearing capacity is determined from the relation between stresses and displacements of one of the nodes (in this case the central node of the foundation is considered).

A convergence study is carried out consisting in the analysis of values of the bearing capacity obtained under different increments of the velocity that is used, with the decrease in the value of velocity increments the result converges towards the final value by the upper limit in the theoretical method. For each case with different combination of geometrical and geotechnical parameters (Table 1) a convergence study is carried out with different values of velocity increments.

3. RESULTS AND DISCUSSION

Due to the common soil failure criterion that is linear and the rock failure criterion non-linear, the variation of the friction angle and cohesion are different in each material. In the case of granular soil, a low internal friction angle is associated with a low quality material.

Regarding the rock mechanics, it is known that the instantaneous friction angle depends on the stress level. Figure 1 shows how the instantaneous friction angle under foundation (ρ_2) [8] varies depending on the GSI value. From Figure 2 can be deduced that for lower value of GSI the ρ_2 is greater, because the failure occurs associated to low stress status, where the instantaneous friction angle is higher. Therefore, poor quality rock mass (related to low GSI values) shows high instantaneous friction angles.

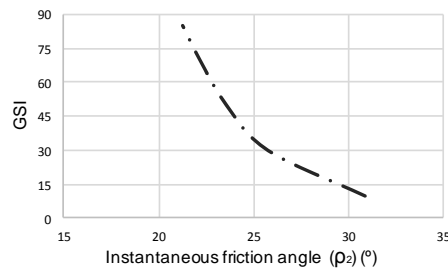


Figure 1. Instantaneous friction angle as function of GSI for $m_o = 20$.

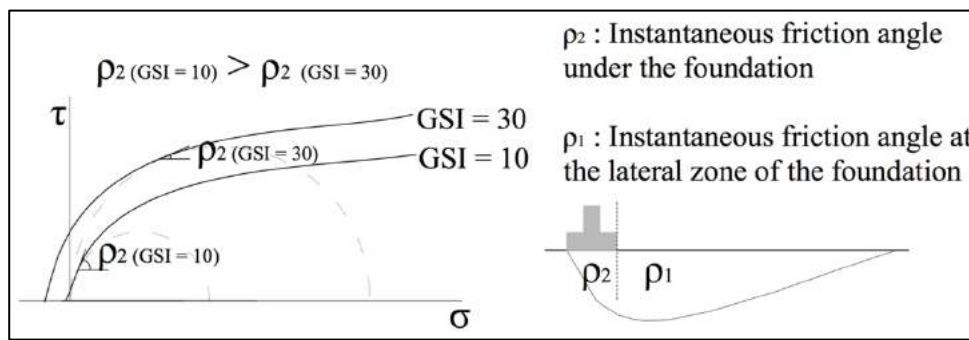


Figure 2. Instantaneous friction angle schedule adapted from Serrano et al. [8].

3.1. Self-Weight of Material

In the field of soil mechanics, the classical self-weight coefficient is represented in eq. (1), the coefficients of the eq. (2) and eq. (3) are those recommended by Vesic [20]. N_γ depends on the value of the friction angle of the material, in Figure 3 can be observed that with the increase of the friction angle the influence of the self-weight of material in the bearing capacity increases as well.

$$(1) \frac{\gamma \cdot B \cdot N_\gamma}{2} \quad (2) N_\gamma = 2 \cdot (N_q + 1) \cdot \tan \phi \quad (3) N_q = e^{\pi \cdot \tan \phi} \cdot \tan^2 \left(\frac{\pi}{4} + \frac{\phi}{2} \right)$$

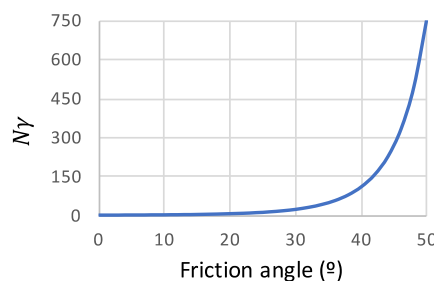


Figure 3. N_γ as function of the friction angle.

In the field of rock mechanics, the same conclusion is observed. As previously stated, the bearing capacity of shallow foundations on rock mass with low GSI presents high values of instantaneous friction angle. Comparing the results obtained considering the self-weight of the rock mass (P_{hsw}) with those under the assumption of weightless material (P_{hWL}) as function of

the GSI (Figure 4), it can be concluded that the cases associated with low GSI are the most conditioned by the consideration of the self-weight of the material, being similar to the behavior observed in soils.

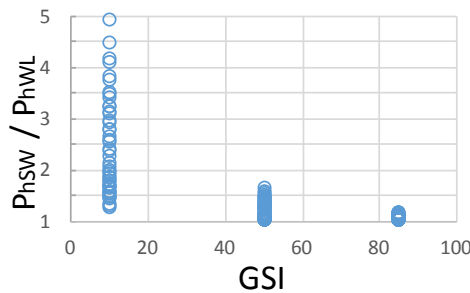


Figure 4. P_{hSW} / P_{hWL} as function of the GSI.

3.2. Footing Shape

As it is generally known, the circular footing supports more load than the strip footing of the same width (considering the diameter of the circular foundation equal to the width of the strip foundation). This is due to the fact that the resistant mechanism of the circular footing is developed in 3-D. Under the plastic hypothesis a behavior of the strip footing can be simulated by several rectangles placed one next to each other, resulting in the overlapping of the bulbs of pressure reaching greater depths, these pressure bulbs depth differences can be expected at failure.

In the soil mechanics, the shape coefficient is commonly used. According to Vesic [20] the engineering approach for the evaluation of the effect of foundation shape on the bearing capacity of soils is mostly semi-empirical, because the mathematical difficulties in obtaining solutions are considerable. The shape factors proposed by this author are the following (in the case of circular footing B is equal to L (length)):

$$(4) \quad S_c = 1 + \left(\frac{B}{L}\right) \cdot \left(\frac{N_q}{N_c}\right) = 1 + \left(\frac{N_q}{N_c}\right) \quad (5) \quad S_q = 1 + \left(\frac{B}{L}\right) \cdot \tan\phi = 1 + \tan\phi \quad (6) \quad S_\gamma = 1 - 0,4 \cdot \left(\frac{B}{L}\right) = 0,6$$

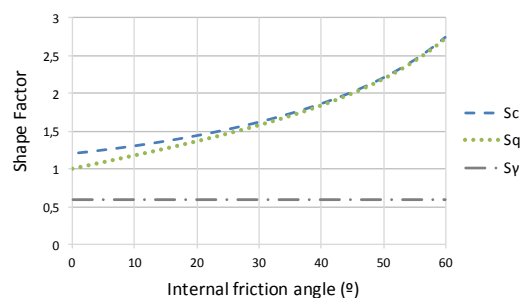


Figure 5. Shape factor as function of the friction angle.

In Figure 5, it can be observed how the value of shape factors changes depending on the friction angle. It is well known that the Terzaghi equation can be divided in 3 parts, the first related to the cohesion, the second with the friction and the third part is in function of the self-weight of the material depending on the footing width. Therefore, S_c affects the part associated to the cohesion, in a usual soil if the cohesion is high the friction angle is low, where the S_c show a small influence on the bearing capacity, because when the S_c value is elevated, it is multiplied by a low cohesion value. On the other hand, S_q is the shape factor that most influences the bearing capacity, once that affect the part related to the friction. S_γ is constant, being equal to 0.6, this factor interferes the bearing capacity in cases with great width, considering the usual footing width the decrease of bearing capacity caused by this factor is overcome by the increase

induced by the other. Finally, it can be concluded that the shape factors influence more the bearing capacity of non-cohesive soils.

In the field of rock mechanics, according to the analysis performed, the most influential parameter in the relationship between the results of bearing capacity obtained with the axisymmetric model (P_{hCF}) (circular footing), and the results under plane strain conditions (P_{hSF}) (strip footing), is the GSI. This fact can be justified because the instantaneous friction angle is heavily dependent on the GSI, and in soil mechanics the friction is one of the parameters used to estimate the shape factor [16].

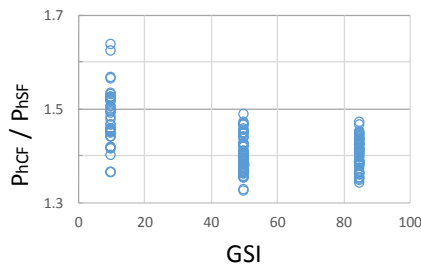


Figure 6. P_{hCF} / P_{hSF} as function of the GSI.

Figure 6 shows that for lower GSI the variation between P_{hCF} and P_{hSF} is the greatest. With $GSI=10$ the range of dispersion varies from 35 to 65%, while for medium and higher values of GSI, the range is between 35 and 50%.

3.3. Roughness

In previous studies in soil mechanics, Meyerhof [17] showed that theoretically in cases under the assumption of weightless material the bearing capacity is independent to the interface roughness. The interface roughness is associated to the consideration of the self-weight of the material because the friction of the surface changes the shape and the size of the wedge [17], [18]. Therefore, depending on the interface type the failure affects a different amount of material. Hjiatj et al. [18] observed that in cases of cohesionless material the size of the wedge for a smooth footing is smaller than that for an equivalent rough one. According to Jahanandish et al. [21], for the frictional soils with relatively high internal friction angles, the bearing capacity of the foundation with the rough base is approximately two to three times higher than those for the foundation with the smooth base with stress level consideration. It is emphasized that the influence of the interface roughness on the bearing capacity, in the soil material, depends on the embedment depth [17], [22]. With the increase of the embedment depth, the influence of the base interface reduces, and the lateral interface becomes more important. Considering that, under the hypothesis of the footing supported on the ground surface the maximum influence of the base interface is obtained.

In cases of the rock mass, the numerical results obtained under the assumption of plane-strain condition, associative flow law, self-weight rock mass, and two interface type: (A) rough base (P_{hRB}) and (B) smooth base (P_{hSB}) demonstrated once again that the GSI is the most determinant parameter.

In Figure 7 a decrease in the dispersion range is observed with the increase of GSI. The bearing capacity of poor quality rock mass ($GSI = 10$) varies between 20 to 33% depending on the interface type. However, for average and very good rock mass quality the dispersion range is between 4 to 19%.

As it is generally known, the circular footing supports more load than the strip footing of the same width (considering the diameter of the circular foundation equal to the width of the strip

foundation). This is due to the fact that the resistant mechanism of the circular footing is developed in 3-D. Under the plastic hypothesis a behavior of the strip footing can be simulated by several rectangles placed one next to each other, resulting in the overlapping of the bulbs of pressure reaching greater depths, these pressure bulbs depth differences can be expected at the failure.

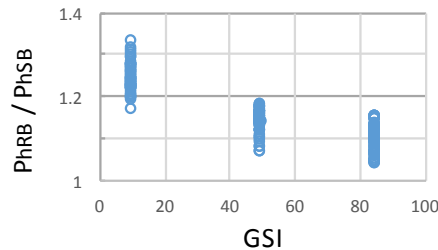


Figure 7. P_{hRB} / P_{hSB} as function of the GSI.

4. CONCLUSIONS

Taking into account the comparison described in previous sections regarding numerical results of the bearing capacity of shallow foundations on rock masses obtained through the finite difference code FLAC and the literature about the correction factors for soils, the following can be concluded:

- In the field of soil mechanics, the correction factors due to the self-weight of material, the footing shape and the roughness of the interface, are very dependent on the internal friction angle.
- In the rock mechanics, the parameter that most influences the bearing capacity correction factor is the GSI, this influence decreases with the increase of the GSI value. It is emphasized that the instantaneous friction angle depends on the GSI, because in cases of low GSI the failure occurs associated to the low stress status, where the instantaneous friction angle is higher.
- Comparing the influence of the friction observed in soils, it is important to emphasize that granular soils of low quality present a low internal friction angle, so the influence of the correction factors is small. However, poor quality rock mass (related to low GSI values) shows higher instantaneous friction angles, so in cases of rock mass, the influence of the correction factors on the bearing capacity is more significant for highly weathered rock mass.
- According to the numerical results obtained, the influence of the self-weight of the rock mass on the value of the bearing capacity may be less than 5% or exceed as much as 400% for very low values of GSI; the influence of footing shape on the bearing capacity of rock mass can exceed up to 60%; and the influence of the interface roughness on the bearing capacity of rock mass exceeds 20% only in the cases of poor quality rock mass (e.g. GSI = 10).

ACKNOWLEDGEMENT

This research has been funded by Fundación José Entrecanales Ibarra.

REFERENCES

- [1] Brinch Hansen, J.A. (1970). "Revised and extended formula for bearing capacity." Bulletin N° 28, Danish Geotechnical Institute Copenhagen, pp. 5-11.

- [2] Terzaghi, K. (1943). *“Theoretical soil mechanics.”* New York: Wiley.
- [3] Hoek, E., and Brown, E. T. (1980) *“Empirical strength criterion for rock masses.”* J Geotech Eng Div ASCE. 106(9):1013–1035.
- [4] Hoek, E., Brown, E. T. (1997) *“Practical estimates of rock mass strength.”* Int J Min.34(8):1165–1186.
- [5] Hoek, E., Carranza-Torres, C., Corkum, B. (2002) *“Hoek-Brown failure criterion – 2002 Edition.”* In Hammah R, Bawden W, Curran J, Telesnicki M, editors. Proceedings of NARMS-TAC 2002, Mining Innovation and Technology. Toronto – 10 July, pp. 267–73.
- [6] Merifield, R.S., Lyamin, A.V., Sloan, S.W. (2006) *“Limit analysis solutions for the bearing capacity of rock masses using the generalised Hoek–Brown criterion.”* Int J Rock Mech Min Sci 43:920–37.
- [7] Serrano, A., and Olalla, C. (1994) *“Ultimate bearing capacity of rock masses.”* Int. J. Rock Mech. Min. Sci. Geomech. Abstr.31:93-106.
- [8] Serrano, A., Olalla, C., González, J. (2000) *“Ultimate bearing capacity of rock masses based on the modified Hoek-Brown criterion.”* Int. J. Rock Mech. Min. Sci. 37:1013–1018.
- [9] Sokolovskii, V. V. (1965). *“Statics of soil media.”* London: Butterworths Science; (Translator R. Jones & A. Schofield).
- [10] Carter, J. P., and F. H. Kulhawy. (1988) *“Analysis and Design of Foundations Socketed into Rock.”* Report No. EL-5918. Empire State Electric Engineering Research Corporation and Electric Power Research Institute, New York, NY, p. 158.
- [11] Clausen, J. (2013). *“Bearing capacity of circular footings on a Hoek–Brown material.”* International Journal of Rock Mechanics and Mining Sciences. 57. 34–41. <https://doi.org/10.1016/j.ijrmms.2012.08.004>.
- [12] Ramamurthy, T. (2014) *“Engineering in rocks for slopes foundations and tunnels”*, 3rd ed., PHI Learning, Delhi
- [13] Chakraborty, M., and Kumar, J. (2015) *“Bearing capacity of circular footings over rock mass by using axisymmetric quasi lower bound finite element limit analysis.”* Computers and Geotechnics, Volume 70, Pages 138-149
- [14] Keshavarz, A., and Kumar, J. (2018) *“Bearing capacity of foundations on rock mass using the method of characteristics.”* Int J Numer Anal Methods Geomech; 42:542 - 557.
- [15] Meyerhof, G. G., (1963). *“Some recent research on the bearing capacity of foundations.”* Can. Geotech. J. 1 (1), 16–26.
- [16] De Beer, E. E., (1970). *“Experimental determination of the shape factors and the bearing capacity factors of sand.”* Géotechnique 20 (4), 387–411.
- [17] Meyerhof, G. G. (1955) *“Influence of roughness of base and ground-water conditions on the ultimate bearing capacity of foundations.”* Geotechnique 5, No. 3, pp. 227-242
- [18] Hjiiaj, M., Lyamin, A. V., Sloan, S. W. (2005) *“Numerical limit analysis solutions for the bearing capacity factor N_γ .”* Int J Solids Struct;42(5–6):1681–704.
- [19] FLAC (2007) *“User's Manual”*, Itasca Consulting Group Inc. Minneapolis.
- [20] Vesic, A. S. (1973) *“Analysis of ultimate loads of shallow foundations”*. J. of the Soil Mechanics and Foundations Division, American Society of Civil Engineers, Vol. 99, No. SMI, pp. 45-73
- [21] Jahanandish, M., Veiskarami, M., Ghahramani, A. (2012) *“Effect of Foundation Size and Roughness on the Bearing Capacity Factor, N_γ , by Stress Level-Based ZEL Method.”* Arab J Sci Eng 37: 1817.
- [22] Benmebarek, S., Saifi, I., Benmebarek, N., (2017) *“Depth factors for undrained bearing capacity of circular footing by numerical approach”*, J of Rock Mech and Geo Eng, 9(4), Pages 761-766

RESIDUAL SHEAR STRENGTH OF AN OVERCONSOLIDATED CLAY: BACK ANALYSIS AND LABORATORY TESTS

Natalia S. Montero Cubillo*, *PhD Candidate, Universidad Politécnica de Madrid - Fundación Agustín de Betancourt, ns.montero@upm.es*

José Estaire Gepp, *Head of CEDEX Track Box, Laboratorio de Geotecnia, CEDEX, Jose.Estaire@cedex.es*

ABSTRACT

Residual shear strength of hard overconsolidated soils, like the so called Guadalquivir Blue Clays formation, takes relevant importance because it is usually the real acting strength on discontinuities, shear zones, fissures and clay reorientation zones along which landslides occurs. Different conditions of the sample state and failure modes in shear tests enable to simulate accurately the field conditions at laboratory. The main objective of this investigation is the comparison between the values obtained by back analysis and the strength parameters achieved through different shear strength tests. An accurate back analysis of a landslide in a overconsolidated clay provided the most reliable result of cohesion and frictional angle along the failure plane. To compare this result with the values reached in laboratory the following tests were carried out: direct shear tests with undisturbed samples; after each of the previous tests, the shear box was returned to its original position at five times and the specimen was tested again; direct shear tests with remoulded specimens prepared at their liquid limit; and ring shear tests with remoulded specimens prepared at their both liquid and plastic limits. To determine the most accurate test to predict the strength parameters in real failures, a comparison was made between this study and others in literature with cases of similar conditions. The main conclusions are: the ring shear test with remoulded samples was found to be the best method in laboratory to reach the back analysis strength parameters; a new range of brittleness index is given taking advantage of the high effective stresses used in the tests performed in this study; and an alternative test procedure is proposed that combines the methods set in ASTM and EN standards.

Keywords: Residual Shear Strength, Slope Stability, Overconsolidated Soils, Direct Shear Test, Ring Shear Test.

1. INTRODUCTION

Guadalquivir Blue Clay is a Miocene clayey formation with marine origin which is located at the Guadalquivir Basin (Spain). A great number of slope stability problems appear in these materials, similar to other soft rocks and overconsolidated clayey soils (e.g. well known London clay), so their geotechnical properties have been studied by several authors [1-3]. The formation consists on an overconsolidated clay with a pronounced brittleness behaviour. Residual strength of Guadalquivir blue clays is very important since it is the actual strength that appears along discontinuities, shear zones, and clay reorientation and fissures zones. The residual friction angle of this material usually ranges between 10 and 15°, very similar to the stable natural slopes in the area.

2. SLOPE STABILITY CASE

2.1. Preliminary Data and Geotechnical Characterization

The laboratory and field data of an embankment stability case founded on overconsolidated marls of the “Guadalquivir Blue Clays” Formation, enabled to carrying out this research. The problems in the embankment, located on a slope with an angle of about 11°, appear one month after one of the rainiest of the last 30 years.

Field campaign consisted of mechanical rotating drilling boreholes with continuous sample extraction and Standard Penetration Tests (SPT), sampling of undisturbed material and Dynamic Probing Super Heavy (DPSH) tests. Some of the boreholes were equipped with inclinometric tubes, which allowed detecting the movements of the ground in depth, as it can be seen in Figure 1 that shows the clear existence of horizontal movements at a depth of about 12 m. The parameters obtained are shown in Table 1.

Table 1. Geotechnical parameters of studied overconsolidated marls

Parameter	Number of tests	Value		
		Average	Min.	Max.
Fine content (%)	4	70	50	98
Liquid limit (%) ^a	24	43	26	58
Plasticity Index (%)	24	16	4	32
Specific gravity of the solid particles	20	2.61	2.47	2.72
Carbonates content, CaCO ₃ (%)	14	38	32	45
Natural moisture (%)	18	17	13	24
Dry density (g/cm ³)	23	1.8	1.6	2.2
Uniaxial compressive strength (MPa) ^b	15	18	8	27

Notes: ^a9 of the 24 samples were no plastic due to possible matches with frequent sandy levels. Most samples are classified as CL (USCS classification); and ^bThe values of uniaxial compressive strength indicate a cementation and competition much greater than that presented by [1-3], more characteristic of a mudstone or shale.

2.2. Back Analysis

Figure 1 shows one of the two geological-geotechnical profiles where four geotechnical units were defined. To carry out the back analysis (BA), the water level depth indicated in Figure 1 was used, which comes from the data obtained in the boreholes during a very rainy period. The geometry of the assumed failure surface was defined thanks to the inclinometers and to the direct observation of failure points and subsidence zones in the road, in the embankment slope and in a transversal drainage work. It is a deep-seated slip, whose failure surface has a first circular shape on its way through the units classified as soil and next, it follows a planar surface at a depth of about 12-14 m, within the brown marl unit. The coincidence of these depths with sandstone levels leads to the hypothesis that water circulating favourably through those levels has softened the lower contact between the sandstone and the marl, generating in the latter a plane of weakness. The results of the back analysis calculations performed by limit equilibrium methods reveal residual strength conditions in the marls, characterized by zero cohesion and an angle of friction of about 10-11°.

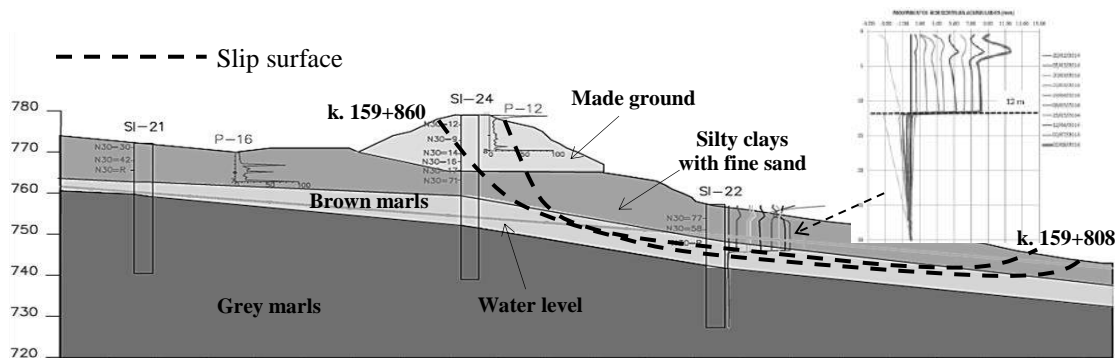


Figure 1. Representative geotechnical-geological profile

3. LABORATORY SHEAR STRENGTH TESTS

3.1. Direct Shear Tests with Undisturbed Samples

Seven drained direct shear tests (DST) with undisturbed samples were carried out. The normal stresses applied ranged between 98 and 1079 kPa. These higher values were used to compensate the swelling pressures of some samples, with values up to 700 kPa. The shear stress-displacement curves reveal a pronounced brittle behaviour. Figure 2a shows a very characteristic pattern of the tested specimens: i) a steep rise in shear stress until reaching the peak strength at a low value of relative displacement, ii) a rapid and strong reduction of shear stress (post-rupture), and iii) a more gentle shear stress reduction to residual strength (named as first cycle in this investigation). The peak strength is usually reached for displacements between 0.5 and 1.5 mm (Figure 2b), without apparent relation with the applied normal stress, as mentioned by Alonso and Gens [4].

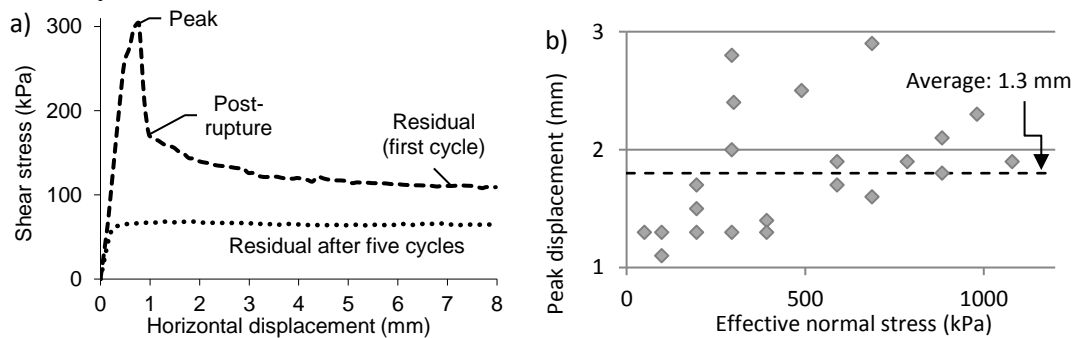


Figure 2. a) Direct shear test with undisturbed sample. b) Peak displacement

A different residual strength was determined through the manual performance of ten changes of shear box direction (five cycles), using a higher velocity than in the previous test, to clearly generate the shear plane. Once this operation was carried out, the specimen was left at rest for 24 hours to establish the pressure equilibrium, and a new direct shear test was carried out in the usual manner. In this way a second residual strength of the soil was obtained, with values lower than those of the first shear, due to a greater reorientation of the clay minerals in the direction of the applied shear stress. It should be noted that the new European standard of direct shear test (EN ISO 17892-10 [5]) explicitly includes this test procedure.

Figure 3a reveals the difference between the achieved results of peak strength in terms of cohesion and friction angle. Cohesion varied between 120 and 520 kPa and friction angle between 35 and 58°, with an average value of 225 kPa and 47°, respectively (see Figure 3a).

The residual strength obtained according to the first cycle can be represented by null cohesions and friction angles between 23 and 45°.

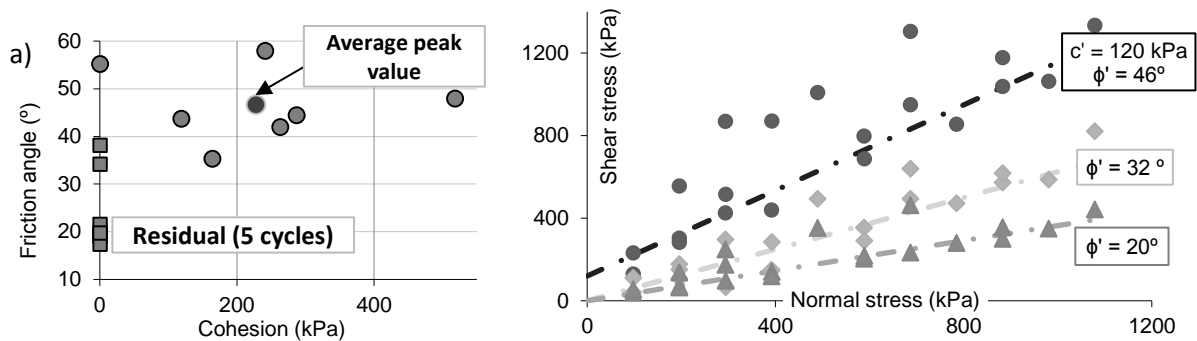


Figure 3. a) Peak and residual strength parameters. b) Global analysis: direct shear tests

The friction angles achieved with the tests after several cycles of the shear box are also presented in Figure 3a, ranging between 17 and 38 ° (with null cohesions). The individual strength results of each tested specimens are represented in Figure 3b with the aim of carrying out a global analysis, resulting in a peak friction angle of 46° and a cohesion of 120 kPa. The first and the second residual angles are 32 and 20 °, respectively, both with null cohesions.

3.2. Direct Shear Tests with Remoulded Samples

An additional method was used to evaluate the residual strength of the soil at laboratory. Three samples remoulded at their liquid limit (WL) were tested in the direct shear equipment.

Figure 4 shows the shear stress-displacement curves resulting from the direct shear and ring shear tests with one of the remoulded samples prepared at their liquid limit. Both group of curves are similar and show a constant residual strength practically from the beginning of the test. The friction angles deduced from the ring shear test, ranging between 17 and 26 °, are similar to those obtained from the direct shear test, ranging between 23 and 25 °.

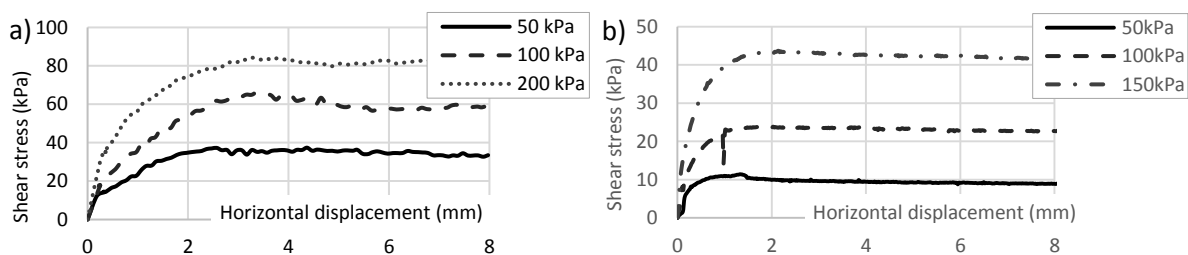


Figure 4. Shear stress-displacement curves of the same sample: a) Direct shear test, b) Ring shear test

3.3. Ring Shear Tests

Ring shear tests (RST) were carried out with the seven undisturbed samples tested in the direct shear and three additional samples (3.2. section). The Bromhead ring shear apparatus is used following a combined test procedure from ASTM and BS standards (ASTM D 6467-06a [6] and BS 1377-7 [7]).

Specimens were prepared by crushing (or ball-milling if necessary) an air-dried representative sample, passing it through a 0.4 mm sieve and adding water until a water content near the liquid limit. In order to avoid a relevant soil extrusion (see Figure 5c), different specimens were used for each of the normal stresses applied (25, 50 and 75 kPa). As reported by Stark and Vettel [8],

as the top porous stone settles into the specimen container, the possibility of the extruded soil becoming trapped between the container and porous stone becomes greater. This may also lead to an increase in shearing strength as the top platen settles. These authors suggest a new test procedure fixing the settlement of the plate to 0.75 mm. In the present study, around 1.5 mm settlements were recorded during the pre-shearing process. In this case soil extrusion can also be more pronounced due to the specimen swelling.

The tests begin consolidating the specimens to the desired normal stress, placing the load in steps, to reduce the soil extrusion between the walls of the container and the top plate. Then, the shear surface is created rotating the ring shear base, with a velocity of 28°/min during 10 minutes. After observing the same pattern of irregularities in the results and excesses of soil extrusion in the first three tests it was decided to unload the specimen to the lowest desired normal stress (procedure recommended in ASTM D 6467-06a [6]) during the pre-shearing process. The relocation of the total normal load was carried out immediately after the pre-shearing, with time intervals of ten minutes between each load, until the pressure equilibrium (following up dilation curves). Following this procedure, lower soil extrusions were achieved. The appropriate displacement rate selected to minimize shear-induced pore water pressure was 0.003 mm/min (note that ASTM D 6467-06a [6] recommends a displacement rate of 0.02 mm/min for a CH soil) during the shearing process.

As previously mentioned, in the first tests carried out, peaks were observed in the failure curves that were repeated at a more or less constant frequency of displacement, and which, at times, greatly deviated the normal tendency of the curves. It was thought that one of the reasons for the repetition of these jumps was that the generated shear surface was in the boundary between the sample and the upper plate of the annular ring, given that the thickness of the sample is small (8-9 mm) and the excessive soil extrusion during consolidation. This caused that in the later tests, it went to the search of the shearing surface. In certain specimens such as the one in Figure 5b, external marks of a possible shearing plane were observed which, however, did not continue in the cross section, where a clearer reorientation should be observed (not even under a microscope). Therefore, no conclusive facts were found at this respect despite the fact that the strength parameters obtained in the present study, derived from this test, agree with those presented by other authors for this Formation. In this sense, it should be noted that there are authors such as Feda [9] and Zhang et al. [10], among others, whose tests clearly show the formation of the shear surface, perhaps due to the use of other ring shear equipment.

The friction angles derived from these tests ranged between 6 and 20°, with null cohesions. The average value of friction angle and the value derived of the global analysis are very close, as can be seen in Figure 5a. It should be mentioned that a sample from the failure surface detected by the inclinometers was tested, obtaining a friction angle of 15° and zero cohesion.

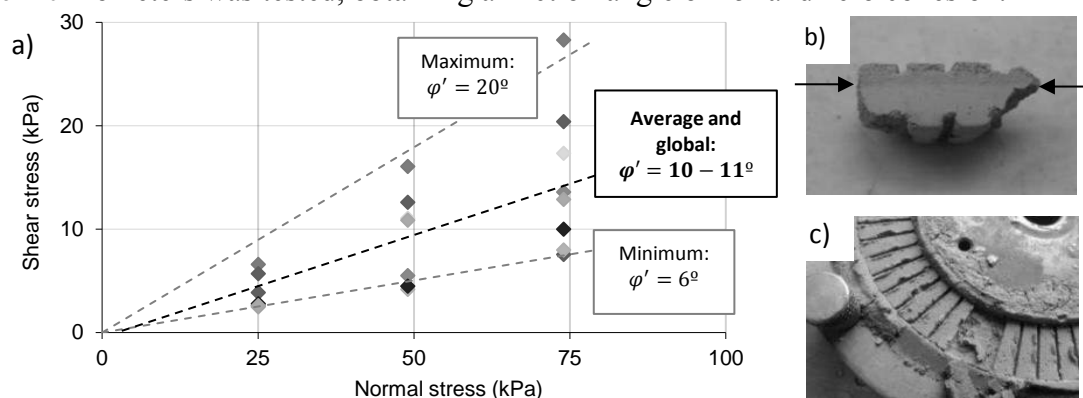


Figure 5. a) Global analysis: ring shear tests, b) External marks of possible shear surface in air-dried specimen, c) Specimen container with excess of soil extrusion

To have a global picture of the problem, five samples, previously used, were prepared at their plastic limit (WP) following the described procedure. As can be expected, these results were always higher than the previous ones. The results obtained are compared in the following section.

4. RESULTS AND DISCUSSION

4.1. Residual Strength Comparative

Remarkable different friction angles can be achieved through the previous shear strength lab tests performed with different sample conditions: direct shear test at peak strength condition (DST peak), at residual strength condition after the first cycle (DST residual), after 5 cycles (DST 5 cycles), with remoulded specimens prepared at their liquid limit (DST WL), ring shear test with remoulded specimens prepared at their plastic limit (RST WP) and at their liquid limit (RST WL). These results and the values derived of back analysis are compared in Figure 6a. The residual strengths achieved in the ring shear test, with remoulded specimens, both prepared at their liquid and plastic limits, seem to be the closest to the back analysis values ($\phi' = 10-11^\circ$). Peak and residual values obtained in the conventional direct shear test (DST peak and residual) differ greatly from those provided by back analysis.

Failures cases in similar formations as the landslides of Carambolo, S.Sadurní, El Bierzo, La Riba and Cortes (Alonso [11]), and Aznalcóllar (Alonso and Gens [4]) are compared with the values resulting from the global analysis of the present research in Figure 6b, including values reported by Tsige [1]. As can be expected for the same Formation, a good correlation is observed between the Aznalcóllar study and the current one in relation to the disposition of the strength results provided by the different methods studied; in both cases the failure friction angle (obtained in back analysis) was slightly underestimated by the values obtained in the ring shear tests with remoulded specimens prepared at their liquid limit. Comparing the obtained results with those discussed by Alonso [11], in similar formations, it can be seen that peak values obtained in direct shear tests always overestimate the values at failure or provided by the retrospective analysis of landslides in this materials type (hard soil-soft rock). In the case studies by Alonso [11], the angles obtained from the direct shear tests on the failure surface are the closest to those derived from the retrospective analysis (especially in the case of landslides in favor of bedding planes) and, in some cases, also those provided by the ring shear test and by the residual direct shear.

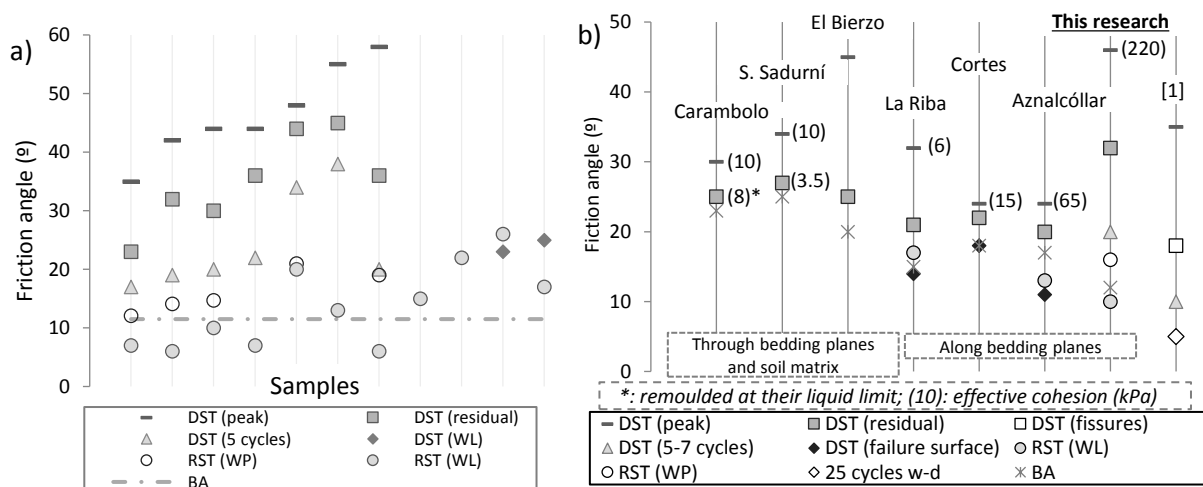


Figure 6. a) Friction angle values depending on the applied test method. b) Results of friction angles according to the test or applied method and comparison with other landslides.

According to Tsighe [1] and this research, the brittleness of the formation and the importance of disturbed grade and failure mechanism in laboratory are highlighted in Figure 6b. The former due to the difference between the peak (35 and 46 °, respectively) and the minimal residual angle (5 and 10 °), and the latter, in accordance to the pronounced difference between the achieved residual angles.

4.2. Brittleness Index

Progressive failure is frequently mentioned [12-14] as a mechanism that leads to the instability of overconsolidated clays; the importance of this phenomenon is greater as the brittleness increases. At this respect, Figure 7 compares the brittleness index (I_B), obtained as Bishop [15], of the studied formation with that of other English clay formations (Bishop et al. [16]) and Guadalquivir Blue Clays studied by Alonso and Gens [4] in the Aznalcóllar dam failure case. The figure reveals: a) a reduction of I_B with an increase of applied normal stress is observed; b) the values obtained in this study agree with those published for the Guadalquivir Blue Clays in the study of the Aznalcóllar failure and are similar to the values deduced for the disturbed London blue clays, and c) due to the high applied stresses, additional information is available on the variation of the brittleness index with the normal stress, with a certain asymptote around 40%.

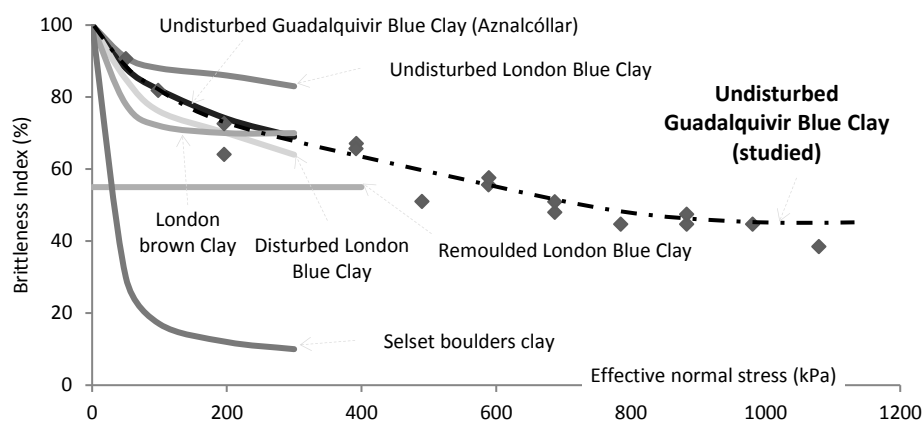


Figure 7. Comparison of brittleness index with other values reported by Alonso and Gens [4] and Bishop et al. [16]

5. CONCLUSION

Landslides in which the failure mechanism is the softening of a layer of marls by accumulation of water and generation of a favourable weakness surface, are clearly governed by the residual strength of the material. It has been concluded that the ring shear test with specimens prepared at their liquid limit is the most approximate method to determine the failure strength, when compared with that derived from the retrospective stability analysis. It's worth to note that the direct shear test with undisturbed specimens after several cycles and with specimens prepared at their liquid limit, also seem to offer an acceptable result. Regarding the ring shear test, improvements are observed in terms of results and less sample extrusion when using the lower vertical stress discharge procedure during the pre-shear process (ASTM D 6467-06a [6]). The brittleness index of the formation studied is between that of the Aznalcóllar blue clay and the disturbed London Blue Clay, obtaining an asymptotic value close to 40% for very high effective normal stresses (almost 1000 kPa).

ACKNOWLEDGEMENTS

The authors would like to thank Mauro Muñiz and José L. Toledo from Laboratorio de Geotecnia (CEDEX), especially for the thorough performance of the laboratory campaign. This research was financially supported in part by the Ministry of Economy and Competitiveness of Spain from the framework of the 2016 challenge – collaboration (RTC-2016-5755-4). This support is greatly appreciated.

REFERENCES

- [1] Tsige, M., 1998. “*Microfábrica y mineralogía de las Arcillas Azules del Guadalquivir y su influencia en las propiedades geotécnicas*”, M.Sc Thesis, Universidad Complutense de Madrid, Spain, 313 pages.
- [2] Olalla, C., Cuéllar, V., 2001. “*Failure mechanism of the Aznalcóllar Dam, Seville, Spain*”, *Géotechnique*, 51 (5): 399-406.
- [3] Galera, J. M., Checa, M., Pérez, C., Williams, B., Pozo, V., 2009. “*Caracterización de detalle de las margas azules del Guadalquivir mediante ensayos in situ y de laboratorio*”, *Ingeopres*, 186: 16-22.
- [4] Alonso, E. E., Gens, A., 2006. “*Aznalcóllar dam failure. Part 1: Field observations and material properties*”, *Géotechnique*, 56 (3): 165-183.
- [5] EN ISO 17892-10, 2018. “*Geotechnical investigation and testing - Laboratory testing of soil - Part 10: Direct shear tests*”, ISO.
- [6] ASTM D 6467-06a, 2006. “*Standard Test Method for Torsional Ring Shear Test to Determine Drained Residual Shear Strength of Cohesive Soils*”, ASTM International, USA.
- [7] BS 1377-7, 1990. “*Methods of test for soils for civil engineering purposes. Shear strength tests (total stress): 6. Determination of residual strength using the small ring shear apparatus*”, BSI, UK.
- [8] Stark, T. D., Vettel, J. J., 1992. “*Bromhead Ring Shear Test Procedure*”, *Geotechnical Testing Journal*, 15: 24-32.
- [9] Fedá, J., 1992. “*Creep of soils and related phenomena*”, Elsevier, New York, 423 pages.
- [10] Zhang, M., Yueping, Y., Ruilin, H., Shuren, M., Yongshuang, Z., 2011. “*Ring shear test for transform mechanism of slide-debris flow*”, *Engineering Geology*, 118: 55-62.
- [11] Alonso, E., 2005. “*Parámetros de resistencia en cálculos de estabilidad*”, VI Simposio Nacional sobre Taludes y Laderas Inestables, pp. 1-65, 21-24 June 2005, Valencia.
- [12] Skempton, A.W., 1964. “*Long-term stability of clay slopes*”, *Géotechnique*, 14: 77-101.
- [13] Bjerrum, L., 1967. “*Progressive failure in slopes of overconsolidated plastic clay and clay shales*”, *Journal of Soil Mechanics & Foundations Div.*, ASCE, 93: 3-49.
- [14] Bishop, A.W., 1971. “*The influence of progressive failure on the choice of the method of stability analysis*”, *Géotechnique (Technical Notes)*, 21 (2): 168-172.
- [15] Bishop, A.W., 1967. “*Progressive failure: with special reference to the mechanism causing it. Panel discussion*”, *Proceedings of the Geotechnical Conference on shear strength properties of natural soils and rocks*, Vol. 2. pp. 152, Oslo.
- [16] Bishop, A. W., Green, G. E.; Garga, V. K., Andresen, A., Brown J. D., 1971. “*A new ring shear test apparatus and its application to the measurement of residual strength*”, *Géotechnique*, 21 (4): 273-328.

INTERNAL EROSION AND DAM STABILITY

Arthur Jedenius, *Geotechnical Engineer, Luleå University of Technology,*
arthur.jedenius@ramboll.se

ABSTRACT

One of the subjects dam owners of embankment dams have to consider is internal erosion. This phenomenon is induced by the movement of fine particles within the dam due to seepage forces. A dam in Sweden has presented recurring incidents related to internal erosion within the core. To analyze the affect the increased flow has, Finite Element Analysis (FEA) was used.

FEA models simulate the in situ stresses in the dam and calculate the strength. It also enables the analysis of changing hydraulic conductivity and how it affects the overall effective strength due to changing pore pressure. The in situ stresses are initially calculated using gravity loading. Then, through a set of phases, zones where erosion is assumed to have occurred are changed to have a higher hydraulic conductivity and will thus affect the pore pressures in the dam following Darcy's law with hydraulic conductivity through a set medium.

The increased hydraulic conductivity is set to follow an increased void ratio due to loss of fine material in the core. How this increase of void ratio affects the hydraulic conductivity is investigated through a newly proposed equation for calculating hydraulic conductivity.

The increase of the hydraulic conductivity in the eroded zones of the core did not seem to impact the strength of the dam in much regard. The phreatic surface and thus the pore pressure did not change significantly to influence the overall effective strength of the dam. It raises the question if the stability of an earth-rock fill dam will be affected by increased pore pressure at all due to its draining properties and if it would rather show instability due to increased seepage forces. Or maybe the zone considered with internal erosion is located in a zone that does not affect the stresses significantly.

Keywords: Internal Erosion, Stability, Seepage, Void Ratio, FEA.

1. INTRODUCTION

As environmental concerns rise, a growing interest of sustainable power resources grows with it. Hydroelectric power being such a resource brings a lot of attention to existing dams built. Sweden has over 2000 dams where a majority are classified as embankment dams [1].

Embankment dams can furtherly be designated as earthfill and rockfill dams. By using an impermeable section in the construction named 'core' the embankment can be sufficiently impermeable to withstand the stress brought by the reservoirs hydrostatic pressure. In Sweden the core is usually constructed using glacial till. This pressure, in combination with unstable gradation of the core material and/or low stress in the soil matrix due to low compaction, has in some instances triggered the initiation of a deterioration process called internal erosion. This process involves the movement of fine particles in the dam. If the filter is poorly designed, the dam core may not self-heal. When the filter is not capable to stop the migration of fine particles, internal erosion may continue until the dam breaks, thus it is an important aspect that is studied in dam safety.

This article presents the analysis of stability, in terms of safety factor, of a hydropower embankment dam that has shown signs of internal erosion or suffusion. The analysis was conducted using the finite element program Plaxis2D by applying a steady state analysis.

A previous study was performed which focused on an overall safety analysis of the dam. The study concluded that the dam was assigned as class 1 which is the next to highest classification [2]. This means that the risk of loss of human lives or damage to person cannot be neglected. This also means that the environmental impact will be significant as well as having a substantial economic effect if the dam would break. Since internal erosion is one of the most common failure modes for an embankment dam it proves the importance of further analysing the effects on this dam, since it has a history of increased turbidity downstream, meaning a loss of finer material in the dam [3].

Since the construction of the dam there have been two sinkhole occurrences. In both instances they were repaired with more material and grouting. They were also situated near the vicinity of the cross section used in this report. The dam has later been added with a berm made of rockfill material downstream to increase the stability of the dam.

2. METHODOLOGY

2.1. The Dam

The embankment was built using four different zones which are shown in Figure 1 and where the parts are explained below. The figure shows a section from the first design of the dam.

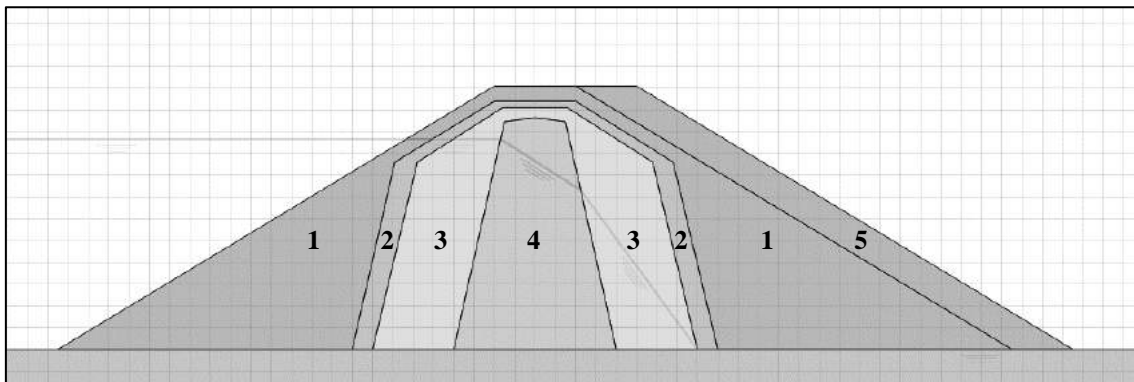


Figure 1. Model used for the iterative lowering of parameters in Plaxis2D.

1. Rock fill shell – Composed of blasted rock from a nearby constructed canal.
2. Coarse filter – Macadam material (gravel).
3. Filter – Sandy material.
4. Core – Well graded till.
5. Berm – Constructed berm to increase stability of the dam.

2.2. Parameter Evaluation

The strength parameters used for the analyses also was estimated by an iterative process followed from input parameters from the previously performed stability analysis on another dam [4]. The parameters are shown in Table 1.

Table 1. Parameters used in previous stability analysis.

Material	Friction angle ϕ (°)
Core	38
Filter	34
Coarse filter	34
Shell	42

The stability analysis performed was done to calculate if the dam, with an added berm, is following the guidelines set by Swedish dam safety guidelines. During a rapid drawdown the upstream safety factor must be at the least 1,3 and while being a full reservoir a safety factor of 1,5 downstream needs to be achieved.

As the initial parameters are set, an iterative lowering of the dam's friction angle performed with the resulting safety factor shown in Figure 2. This is done with the aim of finding the lowest possible friction angle of the dam. The analysis was performed with a steady state analysis of a full reservoir as well as a rapid draw down (RDD) analysis in both GeoStudio SLOPE/W as well as Plaxis2D to make a comparison. The results are shown in Figure 2.

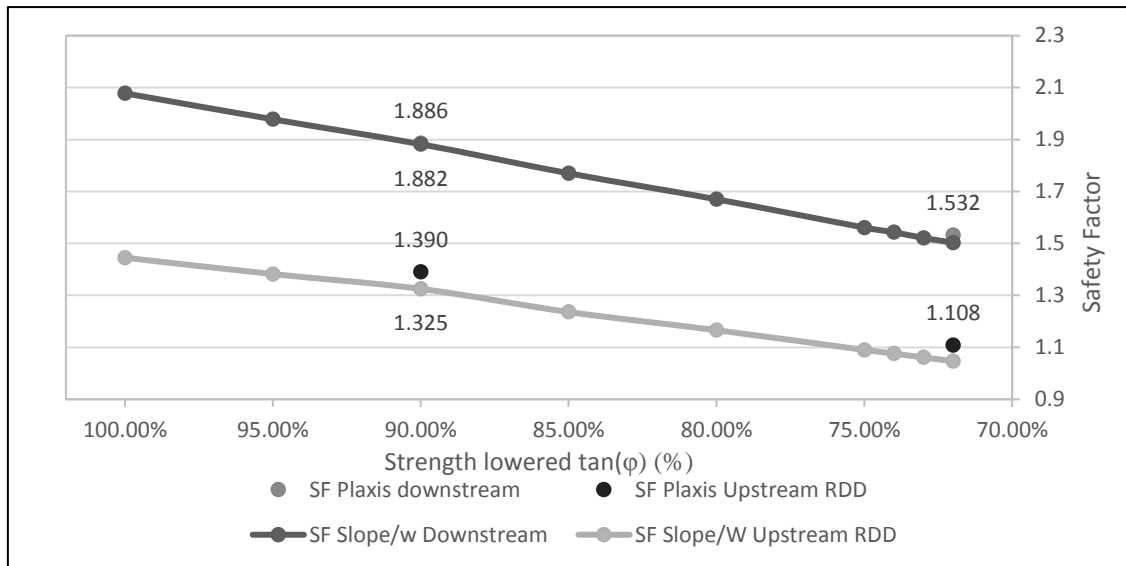


Figure 2. Iterative lowering of the overall strength in the dam.

When the GeoStudio analysis received a safety factor of 1.325 the strength parameters are as shown in Table 2 as well as the unit weight parameters.

Table 2. Strength after iterative lowering of parameters.

Material	Friction angle ϕ (°)	Dry unit weight (kN/m ³)	Saturated unit weight (kN/m ³)
Core	35	21,4	23,2
Filter	32	18,0	21,0
Coarse filter	32	22,0	23,4
Fill	39	17,0	20,4

3. HYDRAULIC CONDUCTIVITY AND VOID RATIO

3.1 Calculating Hydraulic Conductivity

Hydraulic conductivity of soils is a fundamental subject when constructing an embankment dam, thus it is important to understand the behaviour of seepage. Seepage is often explained with Darcy's law through a porous medium as

$$q = Aki \quad (1)$$

Where A is the area from where the area of the section where water is transported, k the hydraulic conductivity of the medium, i the hydraulic gradient and q the measured flow.

For a medium such as soil there is a close relation between the void ratio and the hydraulic conductivity. The higher the porosity the higher the hydraulic conductivity is the general rule, which is also the case for the Kozeny-Carman relation:

$$k = C_F \frac{1}{S_s^2} \frac{\gamma_w}{\mu \rho_m^2} \frac{e^3}{1+e} \quad (2)$$

Where C_F is a dimensionless constant, k is the calculated coefficient for the permeability, S_s is the specific surface for the material, γ_w the unit weight for the water, μ the coefficient for the fluid's viscosity, ρ_m the density of the soil and e the void ratio. The void ratio in this case is the total void ratio of the medium, meaning that there is the assumption of total use of the pores for fluid flow. The fact is that the Kozeny-Carman equation works well for coarse materials like sand and gravel but loses its coherency for finer soils such as silt and clay due to the total pore volume is used for fluid transportation. In the work of Ren et al. [5] a new concept is introduced called effective void ratio (e_e) and ineffective void ratio (e_i). Effective void ratio being the parts of the pore which enables transport of water to take place while the ineffective void ratio is pore volume which does not contribute in the transport of fluid. The total pore volume is represented by

$$e_t = e_e + e_i \quad (3)$$

Ren et al. [5] suggested the following relation to calculate the hydraulic conductivity of the soil

$$k = C \frac{e_t^{3m+3}}{(1+e_t)^{\frac{5}{3}m+1} * [(1+e_t)^{m+1} - e_t^{m+1}]^{\frac{4}{3}}} \quad (4)$$

Where C is explained by

$$C = \frac{1}{C_F} * \frac{\gamma_w}{\mu \rho_m^2} * \frac{1}{S_s^2} \quad (5)$$

3.2 Internal Erosion

When considering flow inside a medium like cohesionless soil, seepage forces will act on the grains. If not well compacted or well graded, a loss of fines will occur, meaning they will follow the flow and cause suffusion. There are different types of internal erosion where as in this study suffusion is being studied [6].

The following assumptions are used:

- The internal erosion mechanism is only localized in the core and occurred in defined horizontal layers.
- A plane strain assumption of the erosion is used.
- No self-healing of the core.
- No subsidence occurs when lowering the void ratio.

- Only fine particles (particles <0,075mm) will erode from the soil matrix.

With the assumption that only particles smaller than 0,075mm will erode, the test is set to where the fine material has totally eroded, which is approximately 39% of the mass. The iterative process was started where the specific surface was decreased to resemble a sandy material (mass has eroded, and thus specific surface has decreased) going from 0,1 to 0,01m²/g. This was performed with the constant m as well going from 1,175 to 0 which resembles sandy material. The results of this assumed study are shown in Figure 3.

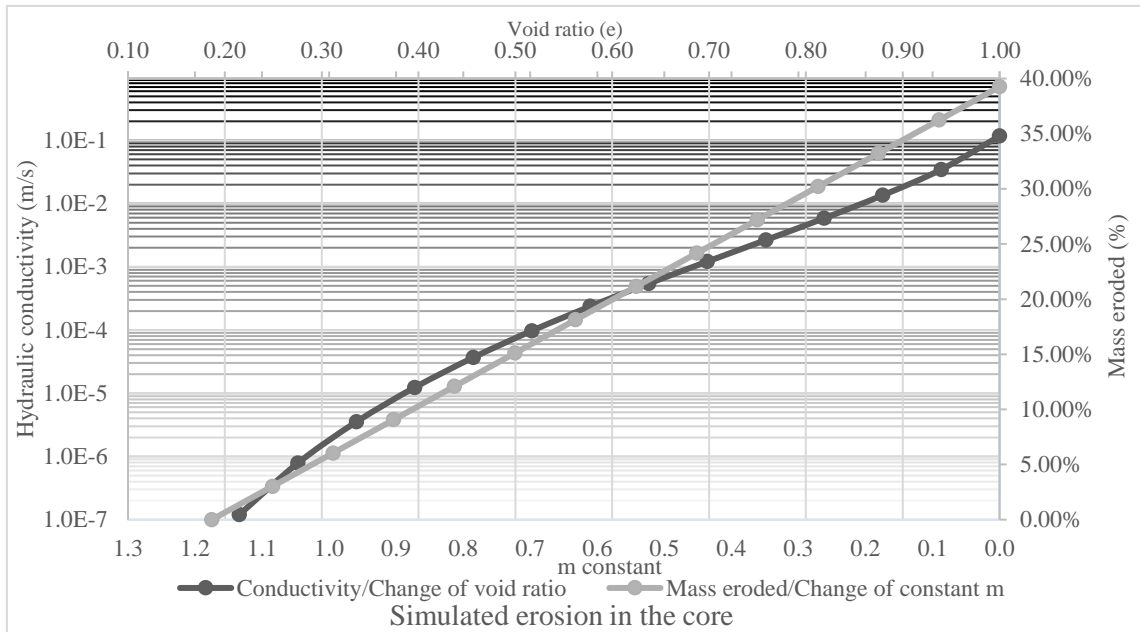


Figure 3. Conductivity change with change of void ratio and how much mass has been eroded.

By regarding Figure 3 it is possible to extrapolate parameters for conductivity of the eroded zones which are shown in Table 3.

Table 3. Parameters changed in the core for different void ratios.

e	-	0,215	0,25	0,3	0,35	0,4	0,94	1
k	m/s	1,2E-07	7,0E-07	1,1E-06	5,0E-06	1,2E-05	3,5E-02	1,2E-01
m	-	1,175	1,15	1,07	0,95	0,84	0,090	0,00
mass eroded	%	0,00	0,8	3,5	7,52	11,2	36,2	39,3

4. ANALYSIS

An example of a finished model for the Plaxis2D analysis is shown in Figure 4.

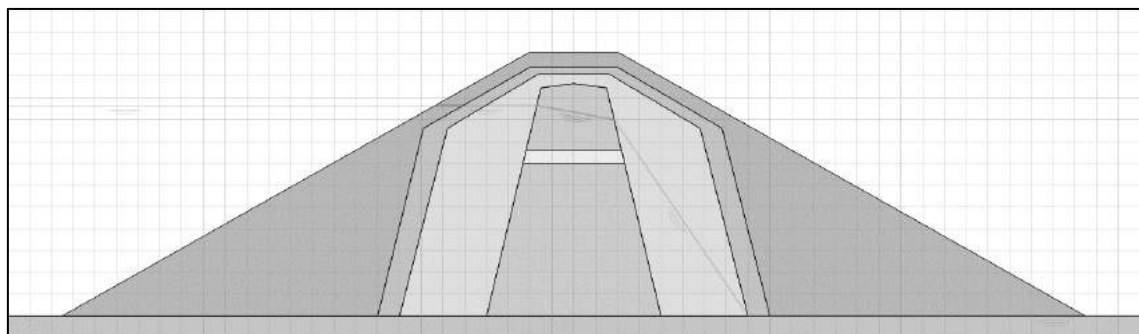


Figure 4. Initial conditions as they are designed in Plaxis2D.

4.1 Internal Erosion

The internal erosion phase was calculated using the plastic calculation and seepage analysis where the internal erosion analysis was performed on three different depths in the core where suffusion has occurred. The material loss was done in regards to loss of mass with increasing void ratio. By using the different permeabilities shown in Table 3 the increased hydraulic conductivity in that part of the core will simulate the internal erosion. The volume of the area affected by suffusion was also increased ranging from 50-500 mm in diameter.

4.2 Safety Analysis

New pore pressures have been calculated in the internal erosion phase and thus the last step is to calculate the safety factor by using the “c/phi-reduction”-method on the new stress situation. This method for safety analysis measures the difference between lowered strength parameters and initial parameters until the model calculates a failure.

5. RESULTS AND DISCUSSION

An example of a seepage analysis shown in Figure 5.

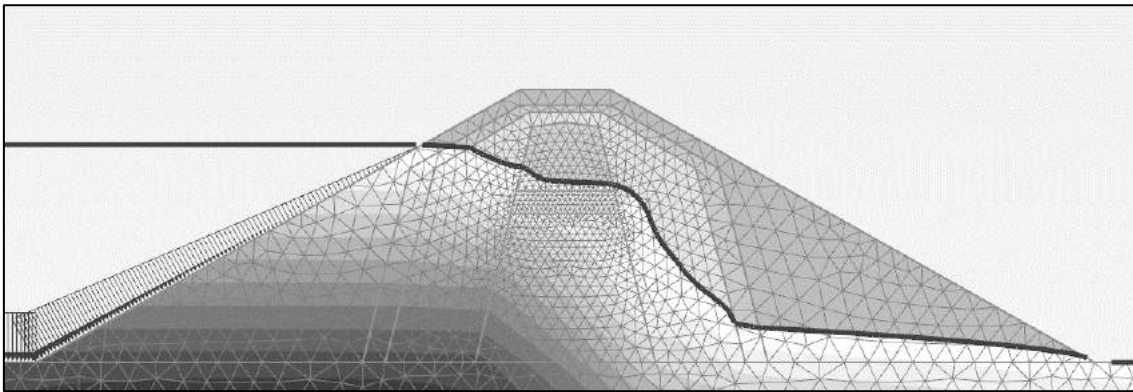


Figure 5. Example from the results of a seepage analysis with internal erosion occurring at 5 meters depth.

The overall stability was investigated for the dam with different dimensions on the pipe shown in. An example of a safety analysis is shown in Figure 6. Results from the stability analysis are shown in Table 4. Calculations that were not able to converge in their integration are presented with (-).

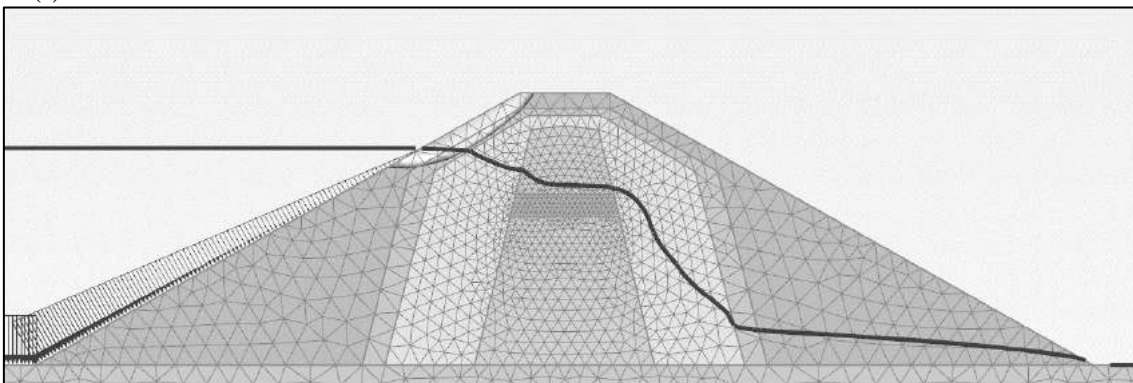


Figure 6. Example of a stability analysis with c/phi-reduction.

Table 4. Results from the stability analysis.

Safety Calculation		Void ratio (e)				
		0,25	0,3	0,35	0,4	1
Depth from crest (m)	Thickness layer with internal erosion (mm)	Safety Factor (Σ Msf)				
5	50	1,365	1,365	-	-	-
	100	1,369	-	-	1,38	-
	200	-	-	-	-	-
	300	1,37	1,37	-	1,37	-
	400	1,375	1,375	-	-	-
	500	1,376	1,373	1,374	1,375	-
8	50	1,378	1,376	1,377	1,377	1,384
	100	1,377	1,373	1,378	1,375	1,395
	200	1,379	-	-	-	1,389
	300	-	-	1,425	1,45	-
	400	1,381	1,382	1,382	1,378	1,388
	500	1,375	1,375	1,376	1,377	1,391
11	50	1,381	1,376	1,381	1,376	1,386
	100	1,381	1,38	1,381	1,381	1,39
	200	-	1,369	1,373	1,377	1,38
	300	1,375	1,377	1,376	1,377	1,388
	400	-	-	-	-	1,379
	500	-	1,373	1,373	1,373	1,373

All models shown in Table 4 has had their critical shear surface upstream which would not be a concern to the guidelines set by RIDAS [2] since this consider as critical condition for a full reservoir, the downstream slope and minimum safety factor required is 1,5. It is also observed that the shear surface tend to be located on materials with less strength than the rockfill (the filters).

It is observed that the safety factor gradually becomes slightly higher in almost all simulations with higher void ratio. This is due to the lowering of the pore pressure upstream which yields higher effective stresses and thus shear strength. and void ratio. The most critical surface changed to be downstream where a higher pore pressure is built as well as seepage forces affecting the slope.

6. CONCLUSION

The impact of internal erosion on hydraulic conductivity show that the approach made to calculate the different changes in hydraulic conductivity was a plausible method since the reached value corresponded with materials of the same sort.

The variations of the calculated factor of safety in the model including layers with internal erosion is changing but only to a minimal degree. This since local changes of hydraulic conductivity does not affect significantly the effective strength in the slopes both downstream and upstream of the dam.

The viability of using a FEM program can be questioned. It should still be considered that FEM is incapable of creating an eroded zone itself due to the reliance of continuum mechanics. In a

calculation where change of material properties of a cluster is required, it is recommended to use a combined numerical (seep) and analytical approach (stability) instead.

REFERENCES

- [1] ICOLD, 2017. “*Database Presentation*”, Retrieved 23 May, 2017 from https://www.icold-cigb.org/GB/world_register/database_presentation.asp
- [2] Svenska Energi, 2012. “*RIDAS*”, Svensk Energi, Sweden.
- [3] Silva, I., Lindblom, J., Viklander, P., Laue, J., 2017. “*Assessment of internal erosion behavior in glacial till core of a Swedish dam*” Department of Civil, Environmental and Natural Resources Engineering Luleå University of Technology, Sweden.
- [4] Vahdati, P., 2014. “*Identification of soil parameters in an embankment dam by Mathematical Optimisations*” Department of Civil, Environmental and Natural Resources Engineering Luleå University of Technology, Sweden.
- [5] Ren, X., Zhao, Y., Deng, Q., Kang, J., Li, D., Wang, D., 2016 “*A relation of hydraulic conductivity – void ratio for soils based on Kozeny-Carman Equation*” Faculty of Engineering China University of Geosciences, China.
- [6] Sibille, L., Marot D., Sail Y., 2015 “*A description of internal erosion by suffusion and induced settlement on cohesionless granular material*”, Springer Verlag, France.

ON EVALUATING SLOPE STABILITY IN SENSITIVE CLAY -A COMPARISON OF METHODS THROUGH A CASE STUDY

Carolina Sellin, *Chalmers University of Technology, Architecture and Civil Engineering,*
carolina.sellin@chalmers.se

ABSTRACT

This paper presents a comparison of four methods of analyses for slope stability for drained and undrained conditions with Mohr-Coulomb failure criteria, applied on a simplified slope along Göta River, Sweden. In addition to Limit Equilibrium Method (LEM), the methods include Discontinuity Layout Optimization (DLO), Finite Element Limit Analysis (FELA) and Finite Element Analysis (FEA), using both Strength Reduction Method (SRM) and Gravity Increase Method (GIM). The results showed very good correlation between all methods for undrained analyses, whereas the drained analyses showed a noticeable discrepancy in both the safety factor and the failure mode for small cohesion intercept between SRM and LEM. Results from the drained analyses performed with GIM were >100% higher than with SRM, or did not result in the development of a full failure mode. The main conclusions drawn from this comparative study are: 1) LEM is the least conservative method for all drained scenarios, and thus should be used with caution; 2) The failure mode for small cohesion intercepts c' varies between the methods, implying an uncertainty in the application of the methods; 3) The use of GIM requires further study.

Keywords: Slope Stability Analysis, Strength Reduction Method, Gravity Increase Method, Limit Equilibrium Method, Finite Element Limit Analyses

1. INTRODUCTION

Stability of slopes in cohesive soil has an important role of spatial planning of today, with both densification of urban areas as well as continuous maintenance of existing and construction of new infrastructure. The most commonly used methods for slope stability analyses are based on either kinematical or statical assumptions, such as limit equilibrium method and limit analysis, and are most often only applicable for isotropic material models, even though in some programs built-in functions to account for anisotropy of the limiting strength exist. A more rigorous way to model the behaviour of the soil is to use the displacement-based FEA (Finite Element Analysis), with the benefit of having the ability to include advanced anisotropic material models and strain softening, as needed for modelling sensitive clays.

This paper presents a case study where four methods of analyses for slope stability are applied for drained and undrained analyses with Mohr-Coulomb failure criteria. The case study is the initial result of a research project where numerical tools are planned to be developed to account for the effects of the climate change on the response of slopes in sensitive clay.

2. METHODS FOR SLOPE STABILITY ANALYSES

Stability of slopes is commonly evaluated by the Limit Equilibrium Method (LEM) where an assumed sliding mass is discretized in to vertical slices for which force and/or moment

equilibrium is calculated for each slice and the total mass, e.g. [1, 2]. The value of the stability in LEM is then defined as the ratio of the shear strength along the slip surface over the shear stress for at the same surface, the Factor of Safety (FoS), as defined by [3]. This method requires an iterative process to identify the size and location of the most critical slip surface. However, the method only considers circular (or pre-defined) slip surfaces, and assumes a constant mobilized shear strength along the slip surface of each slice. This could lead to an over- or underestimation of the stability, as well as the critical slip surface may be overlooked.

Other methods of analyses have been recently developed to for slope stability. This study will look at three alternatives to LEM: Discontinuity Layout Optimization (DLO), Finite Element Limit Analysis (FELA) and displacement-based Finite Element Analysis (FEA). The three methods simulate the soil mass either as a continuum (FEA, FELA), or by representing the soil with a large number of sliding blocks connected by nodes (DLO) [4-5, 7].

DLO is based on the upper bound theorem of plasticity, according to which the safety factor is described as the rate of work due to external loads over the simultaneous work done by internal stresses [4]. FELA on the other hand, allows for calculation of both the upper and lower bound to obtain an interval for the safety factor, where the lower bound is defined as the static equilibrium of the soil [5], and the upper bound considers the kinematics. Both DLO and FELA are simple but effective methods that have shown good agreement in previous comparison with LEM, e.g. [6], for undrained analyses.

The failure mode in FEA is dictated by the material model and the (effective) stress state, resulting in a slip surface being located where the mobilized shear strength is lower than the applied shear stress. This method automatically fulfils both the static and kinematic conditions, in contrast to DLO and LEM. Another advantage of using FEA over LEM, DLO and FELA is the ability to adopt advanced material models that can include the development of effective stresses and mobilized strength in the slope, as discussed by [7-8], as a function of time, or as a result of the changing environmental conditions due to the climate change.

The safety factor is calculated in the three methods above (DLO, FELA and FEM) by adjusting the properties of each cell or sliding block until failure by either: (1) reducing the cohesion and friction angle simultaneously with the Strength Reduction Method (SRM) or (2) increasing the gravitational loads with the Gravity Increase Method (GIM). As a result, SRM gives a safety factor, similar to LEM, whereas GIM gives the gravity multiplier required for failure. The main benefit of SRM and GIM is the lack of assumption of the shape or location for the critical slip surface. However, GIM is the only method that does not require specified strength parameters, and thus can work with any constitutive model.

The material models used in this study are based on the models available in the commercial software used, where LEM with Morgenstern-Price method (GeoStudio 2019 version 10.0.1.1733), DLO (LimitState:GEO version 3.4.a.20820), FELA (OptumG2 version 2019.02.12) and FEA (PLAXIS 2018) are all performed with Mohr-Coulomb failure criteria for drained and undrained analyses. Software-specific anisotropic functions have not been considered, as well as strain softening of the sensitive clay is not modelled at this stage in order to keep the results directly comparable.

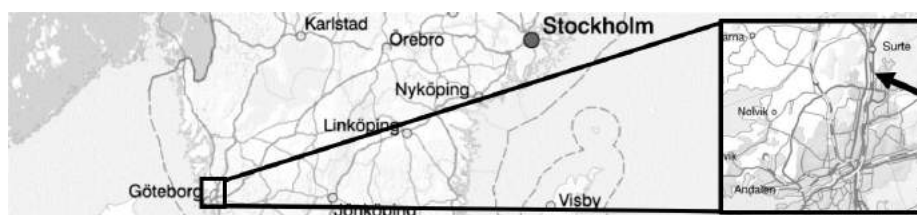


Figure 1. Location of slope of interest, 10 km north of Gothenburg. (map from Lantmäteriet)

3. DESCRIPTION OF CASE STUDY

The chosen slope is located by highway E45 at Göta River in the West of Sweden (Figure 1) with an inclination of 2H:1V and 13H:1V, of which the steepest part is partially located under water (Figure 2). Field investigations suggest a homogenous sulphide-bearing clay to >45 m depth with a sensitivity of 14-16. The pore pressure head is simplified in the model to be hydrostatic, at 1 m below the surface at the crest. The river is assumed to be 3 m deep. Material properties have been evaluated from fall cone tests, vane tests, direct simple shear tests and triaxial tests, of which the results are presented in Karlsson & Karstunen [9]. The friction angle has been assumed to be 36° for all soil layers, and the in situ coefficient of earth pressure at rest, K_0 , have been evaluated by the combining Jaky's simplified formula with the empirical relation of Schmidt [10], assuming $m = 0.6$. The horizontal and vertical hydraulic conductivity assumed to be $k_x = k_y = 0.001$ m/day and the drained analyses have been performed for three cohesion intercepts, $c' = 0.1$ kPa, $c' = 0.5$ kPa and $c' = 5$ kPa.

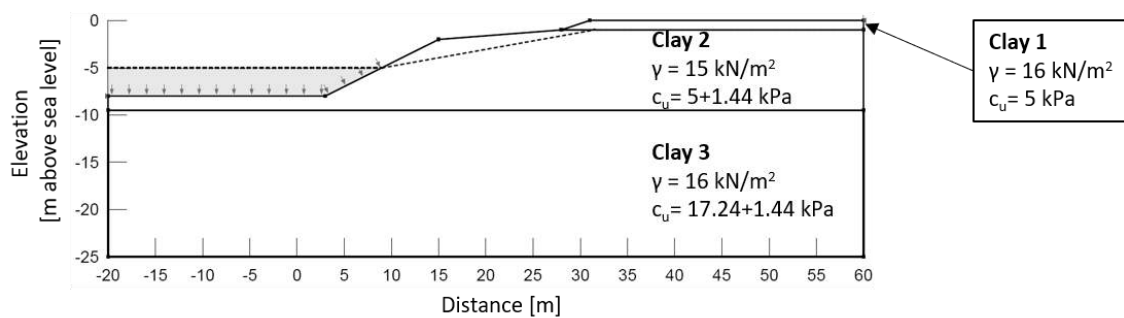
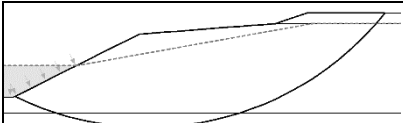
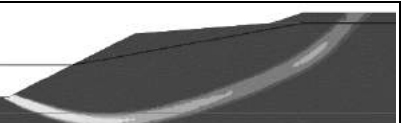
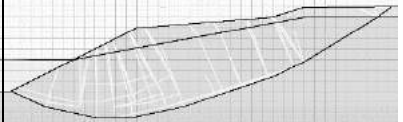
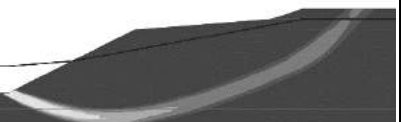


Figure 2. Geometry, stratification, density and undrained shear strength of the slope

4. RESULTS AND DISCUSSION

The calculations have been performed with GIM and SRM for DLO, FELA and FEA, in addition to LEM. Results from the undrained analysis with the methods show good correlation for both the size and the location of the critical slip surface, as seen in Table 1 where a selection of the results are presented. The average obtained safety factor is 1.16 with a variation of up to 3%, which is considered to be most acceptable.

Table 1. Critical slip surface with corresponding safety factor for undrained conditions.

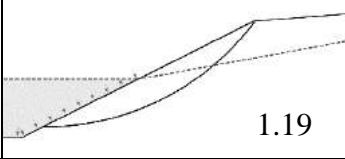
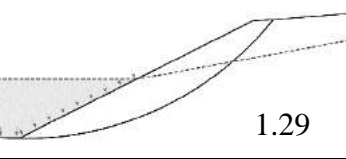
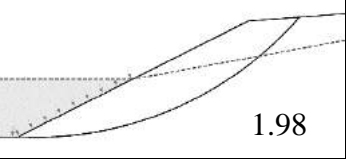
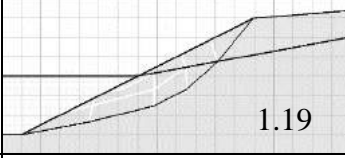
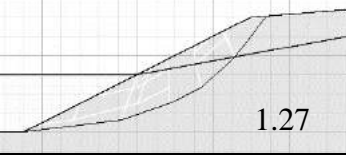
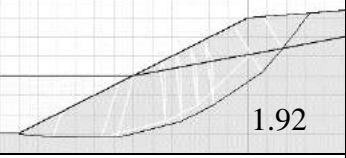
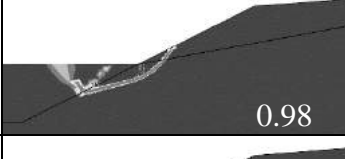
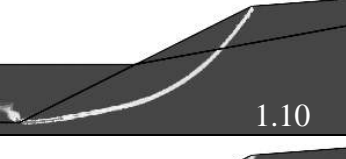
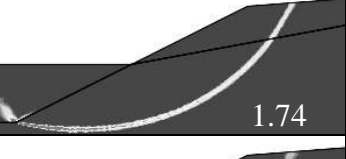
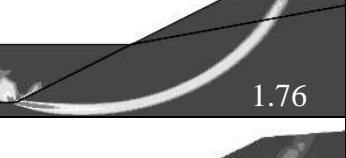
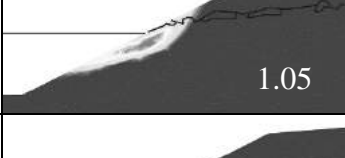
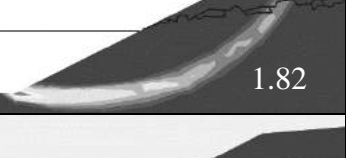
		
LEM, M-P: 1.19	FELA-LB-SRM: 1.16	FEA-SRM: 1.17
		
DLO-SRM: 1.18	FELA-UB-SRM: 1.17	FEA-GIM: 1.15

An overview of the results from the drained analyses with LEM and the SRM-implemented methods is presented in Table 2 together with the assumed values for the shear strength. Higher values are expected from FELA and FEA in a real case scenario, as in the analyses here, the two methods are applied without suction, in order to get comparable results with LEM and DLO. Furthermore, with FEA and FELA the slope stability analyses cannot be performed with

zero apparent cohesion, as the resulting mobilised strength at the surface would be zero. Thus, we investigated how much the assumed value for the cohesion intercept affects the results. The results in Table 2 indicate that one needs to be careful with the value chosen, as c' affects for example the mechanism and the volume of the failure mass. LEM and DLO show very similar result for all three scenarios. Systematically, LEM and DLO predict higher factors of safety than the FE -based methods (FELA and FEA). In terms of the mode of failure, the results by LEM and DLO are similar to FELA and FEA for higher values of c' , even though the predicted factors of safety differ.

Results from FEA-GIM in drained analysis showed discrepancy of >100% from the other methods, and despite of ever increasing the coefficient of gravity, no full slip surface was developed to results in global failure. Similar performance was observed by Swan & Seo [8] and Sternik [11] when GIM was combined with Mohr-Coulomb and slopes of < 20-30 m of height in effective stress analysis. The phenomenon is associated with shallow depths, where the increase of gravity increases the shear strength of the soil rather than the loads bringing the slope to failure. In our case, the unit weight of the water in the river, which is a counterbalancing force, also increases. Modelling the river water as a load, however did not help. The same performance, i.e. no initiations of a clear failure mode, was also seen for FELA-GIM as well as DLO-GIM, which by definition of the failure criteria did not give a result.

Table 2. Critical slip surface with corresponding safety factor predicted with SRM for drained conditions.

Method	$c'=0.1$ kPa, $\phi'=36^\circ$	$c'=0.5$ kPa, $\phi'=36^\circ$	$c'=5$ kPa, $\phi'=36^\circ$
LEM, M-P	 1.19	 1.29	 1.98
DLO	 1.19	 1.27	 1.92
FELA, LB	 0.98	 1.10	 1.74
FELA, UB	 0.99	 1.11	 1.76
FEA, SRM	 1.05	 1.13	 1.82
FEA, GIM	 No failure	 No failure	 No failure

5. CONCLUSIONS

This paper describes a comparison between Limit Equilibrium Method (LEM), Discontinuity Layout Optimisation (DLO), Finite Element Limit Analysis (FELA) and displacement Finite Element Analysis (FEA) for undrained and drained analyses for a slope. The slope represents a typical case of a slope on sensitive clay along Göta River, Sweden. The study was performed with Mohr-Coulomb failure criteria, thus assuming the soil to be isotropic as commonly done in industry today. The safety factors for DLO, FELA and FEA was calculated with both Strength Reduction Method (SRM) and Gravity Increase Method (GIM). The latter has the advantage that it can be combined with any constitutive model. The results showed good correlation between the methods for total stress analyses (i.e. undrained analyses), but up to 20% difference between the four methods with SRM for drained analyses. The safety factors from FELA-GIM and FEA-GIM were unrealistically high, a behaviour that has been confirmed by previous literature [8, 11].

The main conclusions drawn from this comparative study are: 1) LEM is the least conservative method for all drained scenarios, and thus should be used with caution; 2) The failure mode for small cohesion intercepts c' varies between the methods, implying an uncertainty in the application of the methods; 3) The use of GIM requires further study. In the next stage, for the same slope, GIM will be applied in conjunction with an advanced constitutive model, as needed for representing the stability of a sensitive clay slope.

The study highlights the danger of implementing advanced climate-scenarios in calculation methods with in-built assumptions of failure mode or implementation of material models without cap model, as the safety factor varies substantially already without climate scenarios.

Effective stress analyses with advanced material models are essential to capture the climate-induced changes in strength of the soil, and its effect on the future slope stability. Such analyses cannot be done by exploiting the conventional LEM, which just like FELA and DLO suffer from the inability to account for changes in the soil response due to environmental loads. The latter include, in addition to pore pressure changes and erosion, in the Nordic situation also cyclic weather conditions affecting the dry crust and the shallow part of the slope. Phenomena such as extreme precipitation, increased number of yearly freeze-thaw and drying-wetting cycles, as well as the effect of vegetation or the lack of it, will affect the properties of the soil. A multi-physic approach will be needed, combined with probabilistic techniques.

The future research will initially look at six independent scenarios; 1) external erosion, 2) flooding, 3) changes in pore pressure due to precipitation, 4) freezing-thawing, 5) drying-wetting and 6) changes in temperature. Points 4) – 6) are of particular concern, as their cyclic nature is likely to affect the water content and soil fabric, and thereby increasing the depth or frequency of cracks in the upper part of the soil.

ACKNOWLEDGMENTS

Financial support by Swedish Geotechnical Society, FORMAS (2016-00834) and the Swedish Transport Administration (TRV 2016/106280) are greatly acknowledged.

REFERENCES

- [1] Bishop, A.W., 1955. “*The use of the Slip Circle in the Stability Analysis of Slopes*”, *Géotechnique*, 5(1):7-17, <https://doi.org/10.1680/geot.1955.5.1.7>.
- [2] Morgenstern, N.R., Price, V.E., 1965. “*The Analysis of the Stability of General Slip Surfaces*”, *Géotechnique* 15(1):79-93, <https://doi.org/10.1680/geot.1965.15.1.79>.
- [3] Fellenius, W., 1926. “*Jordstatiska beräkningar med friktion och kohesion (adhesion) och under antagande av cirkulär cylindriska glidytor*”. Kungl. Väg- och Vattenbyggarkåren 1851-1926, festskrift, Stockholm 22/12:79–127.
- [4] Smith, C., Gilbert, M., 2007. “*Application of discontinuity layout optimization to plane plasticity problems*”, *Proceedings of the Royal Society, Series A*, 463:2461-2484, <https://doi.org/10.1098/rspa.2006.1788>.
- [5] Sloan, S.W., 2013. “*Geotechnical stability analysis*”, *Géotechnique* 63(7):531-571, <https://doi.org/10.1680/geot.12.RL.001>.
- [6] Hernvall, H., 2017. “*Clay slopes and their stability: An evaluation of different methods*”, M.Sc Thesis, Chalmers University of Technology, Sweden, 64 pages.
- [7] Zienkiewicz, O.C., Humpheson, C., Lewis, R.W., 1975. “*Associated and non-associated viscoplasticity and plasticity in soil mechanics*”, *Géotechnique* 25(4):671–689, <https://doi.org/10.1680/geot.1975.25.4.671>.
- [8] Swan, C.C., Seo, Y-K., 1999. “*Limit state analysis of earthen slopes using dual continuum/FEM approaches*”, *International Journal for Numerical and Analytical Methods in Geomechanics*, 23:1359-1371, [https://doi.org/10.1002/\(SICI\)1096-9853\(199910\)23:12<1359::AID-NAG39>3.0.CO;2-Y](https://doi.org/10.1002/(SICI)1096-9853(199910)23:12<1359::AID-NAG39>3.0.CO;2-Y).
- [9] Karlsson, M., Karstunen, M., 2017. “*On the Benefits of Incorporating Anisotropy in Stability Analyses in Sensitive Clays*”, In: *Advances in Natural and Technological Hazards Research*, 46:259-266, Springer, Netherlands, https://doi.org/10.1007/978-3-319-56487-6_23.
- [10] Schmidt, B., 1966. “*Earth Pressures at Rest Related to Stress History*”, *Canadian Geotechnical Journal* 3(4):239-242, <https://doi.org/10.1139/t66-028>.
- [11] Sternik, K., 2013. “*Comparison of slope stability predictions by gravity increase and shear strength reduction methods*”, *Czasopismo Techniczne. Środowisko*, R. 110, z. 1-Ś:121-130.

INFLUENCE OF GRAIN SIZE AND SHAPE ON EVALUATION OF SHEAR ZONE GEOMETRY

Candaş Öner*, *MSc Candidate in Boğaziçi University, Institute of Graduate Sciences in Science and Engineering, candasoner95@hotmail.com*

Çağdaş Arda, *Ph.D Candidate in Boğaziçi University, Institute of Graduate Sciences in Science and Engineering, cag_arda@hotmail.com*

Özer Çinicioglu, *Assoc. Prof. Dr. in Boğaziçi University, Institute of Graduate Sciences in Science and Engineering, ozer.cinicioglu@boun.edu.tr*

ABSTRACT

Shear band geometry is an important design parameter, especially in the era of retaining structures backfilled with granular materials. In the literature, there exist several theories relating the geometry of the shear band to soil arching, soil-wall interface behavior and backfill density. Indeed, backfilled soil layer is prone to both externally and internally physical actions. Surcharge pressure, grain size distribution and shape of the considered layer are the major actions mentioned previously. All these factors contribute to the dilatant behavior of the backfilled soil, which has an influence on the geometry of the shear band surface. In this paper, an attempt is made to investigate the effects of these factors on controlling geometry to the failure planes. With the help of a rigid retaining wall model, physical model tests are performed to simulate the active failure state in which the constructed rigid wall is translated outwards, resulting in a decrease in the confining stress. PIV (Particle Image Velocimetry) technique is used to illustrate the displacement field. The displacement field categorizes the amount of displacement, and creates sections marked with different colors according to the amount of the displacement on the specific point. In this way, the shear band surface is illustrated. By testing different types of soils (in terms of grain shape and gradation) under different relative density surcharge conditions, a numerical formula that stands for the shear band is tried to be obtained and comparison is done between the actual results with the existing numerical functions that predicts the geometry of the shear band.

Keywords: Physical Modelling, Retaining Wall, PIV Analysis, Shear Band Geometry.

1. INTRODUCTION

One of the pioneering works regarding with the failure surface formation behind retaining walls was done by Rankine [7]. In his work, the slope of the failure surface is considered to be linear, and it is a function of internal friction angle. In this work, friction from the surface of the wall is disregarded. However, the linear failure surface formation proposition is refuted by the future research (Fang and Ishibashi [3], Paik and Salgado [6]), in which it is observed that for granular backfills, the geometry of the shear band is non-linear due to the wall interface and arching mechanism. Interpretation of the arching mechanism with the help of numerical modelling is tedious to solve, and an actual geometry of the failure surface cannot be explained by theoretical assumptions. This is why, physical modelling tests are required to observe the behavior of failure surfaces.

Advances in graphics affected all areas as well as geotechnical engineering. The most recent advance in the era of geotechnical engineering is particle image velocimetry method (PIV), in

which a reference image is been selected, and corresponding movements according to the reference image are plotted in terms of displacements or strains by the flow of grains between the reference image and the other images (White et al. [9]). For example, Niedostatkiewicz et. al. [5] used the PIV method to illustrate the failure surface of cohesionless soils for both active and passive cases. Also, by testing samples having different relative densities, the effect of relative density to the failure surface was tried to be observed. Likewise, Altunbas et. al. [1] conducted physical model tests on samples having different relative density ranges to find out the effect of dilatancy and proposed a parabolic equation of failure surface. Although it is true that relative density is a part of dilatant behavior, as samples having different initial stress values did not tested, effect of dilatancy on the failure surface geometry was not fully revealed. To have an accurate parabolic equation which defines failure surface geometry, parameters that affect dilatancy (grain size, grain shape, void ratio, and initial stress state) should be changed repeatedly while conducting physical model tests and the effect of each parameter to the dilatancy should be found separately.

This work has started with a manufacturing process of the physical model of a retaining wall, which is inspired by the test box presented by Lesniewska and Wood [4]. Tests are conducted under three different relative density ranges (loose, medium dense, dense) and different induced surcharge pressure values (0-50-100kPa). Afterwards, keeping the relative density and surcharge pressure constant, soil samples having different grain size distribution and grain shape are tested. After each test, a failure surface is obtained by PIV analysis. Differences among these failure surfaces are evaluated by a linear regression model in SPSS, which will be explained in detail in the Results and Discussion sections.

2. METHODOLOGY

Two different granular soils are selected in this study, namely Çerkezköy sand, and Kilyos Sand. Both sands are silica sands. Also Glass Beads having a particle diameter between 400-600 μ m are used. The reason of using Glass Beads is to have a sample having perfect sphericity, which permits this study to reveal the effect of particle shape to dilatancy. Laboratory tests are conducted to ascertain necessary physical properties of the test samples, which are in accordance with ASTM standards [12-15]. Figure 1 illustrates granulometry graphs for the granular soils used in the tests. To propose a relationship between granulometry and dilatancy, Çerkezköy sand is separated into two groups, being, poorly graded(SP) and well graded(SW). Also, to compare the effect of grain shape to dilatancy, median particle size of the poorly graded Çerkezköy sand is selected as equal to the Glass Beads. In this way, only thing (neglecting the mineralogy of the samples) differentiates these two samples becomes their grain shape. Lastly, to determine average particle shape values, 50 pictures are taken for each sand type by MShot brand digital light microscope. By processing this pictures using the ImageJ software (Cox [12]), average sphericity and roundness (R_{ave}) values are determined. Also, to make a comparison, grain shape charts proposed by Krumbein and Sloss [10] are used. Properties of these granular soils are summarized in Table 1.

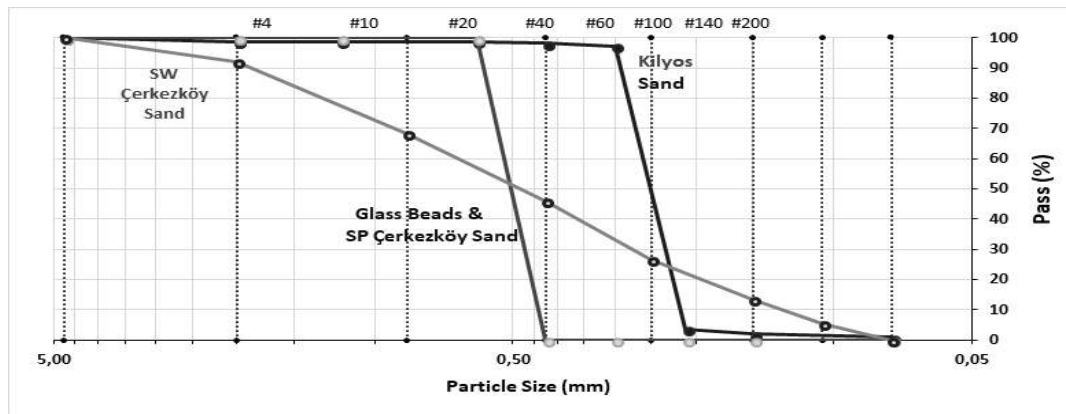


Figure 1. Grain size analysis of sands used in experiments

Table 1. Physical Properties of Sands Used in Experiments

Property	Glass Beads 400-600 μ m	Kilyos Sand	SP Cerkezko y Sand	SW Cerkezko y Sand
Classification	SP	SP	SP	SW
Median particle size (D_{50})	0.50	0.26	0.60	0.48
Uniformity Coefficient (C_u)	1.23	1.24	1.43	6.00
Coefficient of Gradation (C_c)	0.89	0.97	0.94	1.08
Specific gravity (G_s)	2.45	2.66	2.62	2.62
Maximum Void Ratio (e_{max})	0.67	0.77	0.92	0.77
Minimum Void Ratio (e_{min})	0.34	0.44	0.56	0.38
Average Sphericity (S_{ave})	0.95	0.743	0.548	0.569
Average Roundness (R_{ave})	0.98	0.759	0.718	0.741

As mentioned in the last paragraph of the introduction section, a physical retaining wall model inspired by Lesniewska and Wood [4] is constructed. (Figure 2) This model box has the dimensions of 20cm and 25cm for height and length respectively. Width of the model is chosen as 15cm to avert possible arching, which affects shear band geometry. Retaining wall model is made out from aluminum. Lateral movement of the wall is provided by a rotating wheel attached to it. In the tests, rate of the displacement of wall is kept constant and is approximately 0.5mm/s. Front and rear sides of the physical model is transparent plexiglas so that particle movements during wall transition may be seen and photographed. Pictures of this transition are taken by a high resolution camera placed on a tripod. As a minor difference may trigger the evaluation of the failure surface mechanism, special care is given not to change the model system. (focus of the camera, height of the tripod, etc.) The black points in the plexiglas surface are control points. The use of this points will be mentioned in “Analysis with PIV method” section. Necessary surcharge pressure induced on backfill material is provided via five pneumatic pistons placed at the top of the frame. These pistons have the ability to apply same vertical pressure, but at the same time they can move separately, which enables them to distribute the vertical stress evenly. Also, there are two stress transducers (vertical and horizontal) placed inside the model box to record the pressure change while the test is ongoing. Besides, this stress transducers permits authors to check whether there is an arching or not, by applying a surcharge pressure on the top, and reading the pressure values from the vertical sensor located at the bottom. Vertical stress (σ_1) and horizontal stress readings (σ_3) are recorded by imcSTUDIO from at rest condition until failure state.

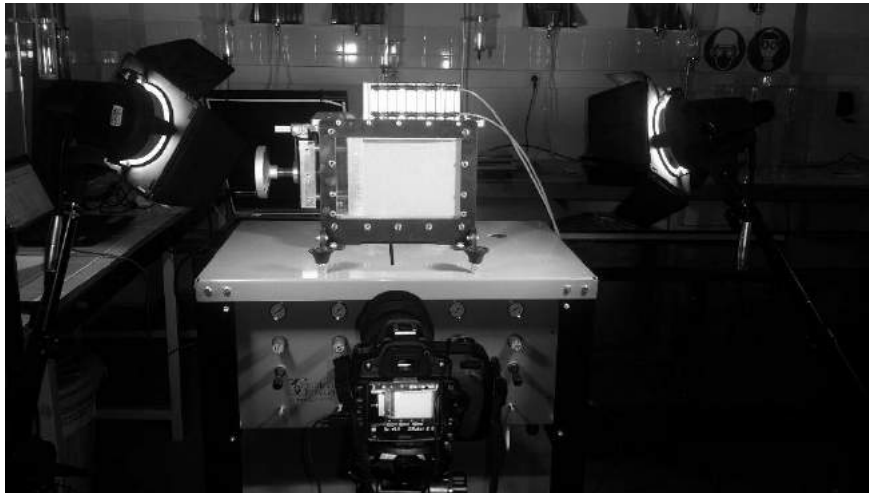


Figure 2. General view of physical retaining model prior testing

3. TEST PROGRAM

Tests are conducted at three different relative density and surcharge ranges for all the sands and glass beads (Table 2). Compaction of glass beads to 75-85% relative density could not be obtained due to perfect circularity of glass beads, so tests having 75-85% relative density for glass beads are skipped.

Table 2. Program of the physical model tests for all soil samples

Experiment No	Relative Density Range(%)	Applied Vertical Stress(kPa)
1	25-35	0
2	25-35	50
3	25-35	100
4	45-55	0
5	45-55	50
6	45-55	100
7	75-85	0
8	75-85	50
9	75-85	100

4. ANALYSIS WITH PIV METHOD

To be able to illustrate failure surface geometries, pictures taken from at-rest state until reaching the failure state, are analyzed by geoPIV-RG software, which is an image analysis module for MATLAB (Stanier et. al. [8]). PIV method evaluates the difference between the reference image (image from at-rest condition) and sequence of the other images taken while the transition of the wall. This evaluation is done by dividing the initial image into subgroups, and by comparing the differences of each subgroup with the adjacent picture, a displacement vector is created. Also, program permits users to visualize the differences in terms of volumetric and shear strain maps where the strain intensity is embodied by colored pixels. In this way, failure surface geometry is depicted. (Figure 3). After PIV analysis, it is seen that experiments

conducted under high surcharge pressure tend to have a wider and scattered failure surface, and high relative density results in steeper failure surface. This observation is compatible with the stress-dilatancy theories of Bolton [2]. As the failure surfaces obtained by PIV analysis are in terms of pixel coordinates, PlotDigitizer program is used, which enables authors to make the necessary conversion from pixel coordinates to SI units. (Huwaldt [16]). With the use of control points, which have predetermined distances among one another, calibration is done between pixel units and SI units. Averagely, all results show 1 cm = 200 pixels because camera distance, focus and height are kept constant and stable for all tests. The borders of the slip surface are picked manually using PlotDigitizer and the obtained x-y coordinate of these points are normalized with the wall height in both axes to obtain unitless parameters. Finally, these points are plotted in Microsoft Excel to visualize the geometry of the failure surface for each test.

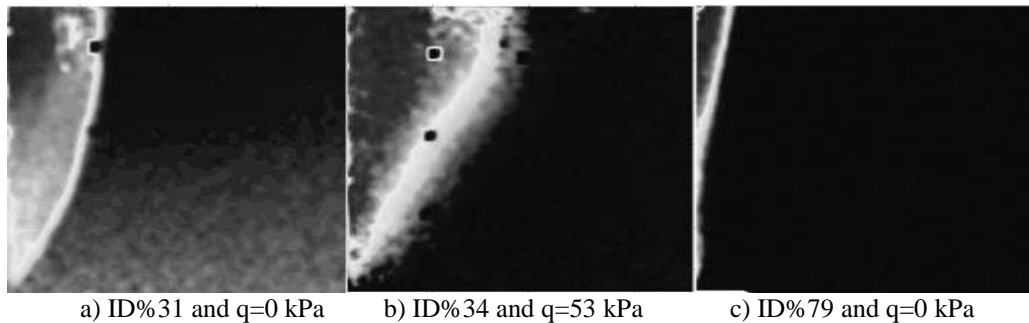


Figure 3. Displacement distribution generated by PIV analysis behind retaining of SP Cerkezkoey Sand Sample

5. RESULTS & DISCUSSION

Altunbas et al. [1] proposed a parabolic function to define the actual shear geometry based on their physical model tests:

$$z = aB^2 + bB + c \quad (1)$$

where,

$$a = [(a_b - 1)/(a_b^2 H_w)] \tan^2(\alpha) \quad (1a)$$

$$b = -\tan(\alpha) \quad (1b)$$

$$c = H_w \quad (1c)$$

In equation 1, H_w stands for wall height, B_f stands for distance of shear band to wall at ground surface, X stands for the distance of the extrapolated line, which is tangent to initial part of shear band at toe level, to the wall at ground surface, α stands for inclination of the bottom part of shear band, z is the vertical coordinate and B is the horizontal distance from the retaining wall to the failure surface at a particular depth z . Positions of those variables are illustrated in Figure 4. a_b is the ratio of B_f/X , and according to the findings of Altunbas et. al. [1], it is constant and equal to 0.67.

In their study (Altunbas et. al. [1]), failure surface created by the proposed parabolic equation coincides with the actual failure surfaces obtained by PIV analysis. However, as their model box does not include pneumatic pistons, obtained values are valid under low surcharge conditions. Besides, influence of grain size and grain shape on failure surface could not be investigated as only one type of soil is tested.

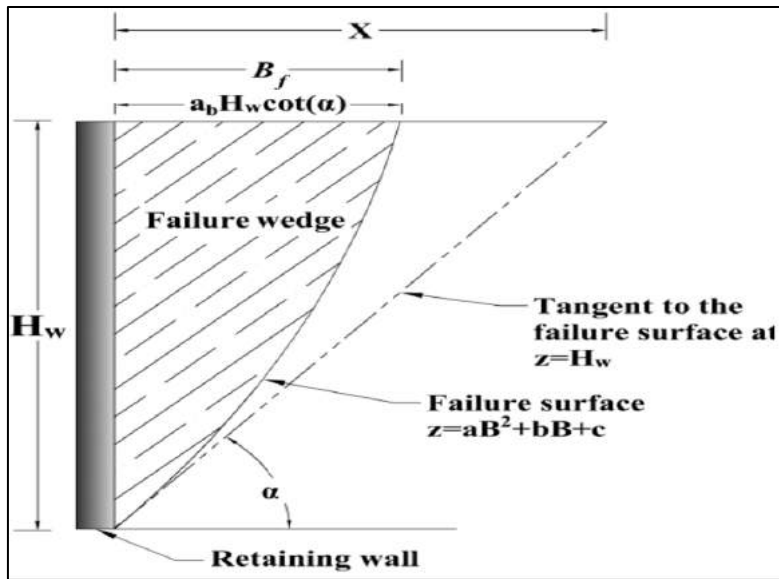


Figure 4. Geometric properties of shear band and the influence of dilatancy at failure surface (Altunbas et. al.,)[1]

Therefore, a comparison is done among the actual failure surface generated by PlotDigitizer, traditional Rankine solution, and the parabolic equation proposed by Altunbas et. al. [1] to demonstrate the effects of surcharge pressure, grain size, and grains shape to the failure surface geometries.(Figure 5).

From Figure 5, it can be seen that failure surface created by the formula proposed by Altunbas et. al. [1] is a good estimator for tests under zero surcharge pressure. However, with the increase in the surcharge pressure, a deviation is seen. This deviation is different for different sand types, primarily due to grain size and grain shape influence. For glass beads, which is completely circular, there is not much deviation seen. Conversely, with the increase of the angularity of particles, difference between actual failure surface and failure surface obtained by Altunbas et. al. [1] formula becomes more obvious. Also, effect of granulometry can be seen when comparison is done between SP and SW Çerkezköy sands tested under 100 kPa surcharge pressure. Interpreting the results, it can be proposed that higher coefficient of uniformity (C_u) causes a more convex shaped slip surface.

To consider those effects, an amendment is tried to be made on the proposed formula of Altunbas et. al. [1]. This amendment, which is shown below (Equation 2), is a function of shape factor, gradation of the granular soils, and surcharge pressure.

$$z' = z + \left(n * \left(\frac{S_{ave} + R_{ave}}{2} \right) * (C_u) * B \right) \quad (2)$$

where, S_{ave} is the average sphericity and R_{ave} is the average roundness of the soil (grain shape parameters). C_u is the coefficient of uniformity and is added to the formula in order to consider the effects of gradation. z and B is the same geometric properties proposed by Altunbas et. al. [1]. z' is the actual vertical coordinate found from PIV analysis.

From Figure 5, it is seen that difference between the values obtained from Altunbas et. al. [1] and the actual values are not constant. Therefore a grouping is done by dividing the tests into nine groups, and a specific ' n ' value is assigned to each of the groups (Table 3). The ' n ' values are obtained by processing a linear regression analysis in SPSS software. In the analysis, R^2 value is greater than 0.9, which means that the proposed amendment may be used conveniently.

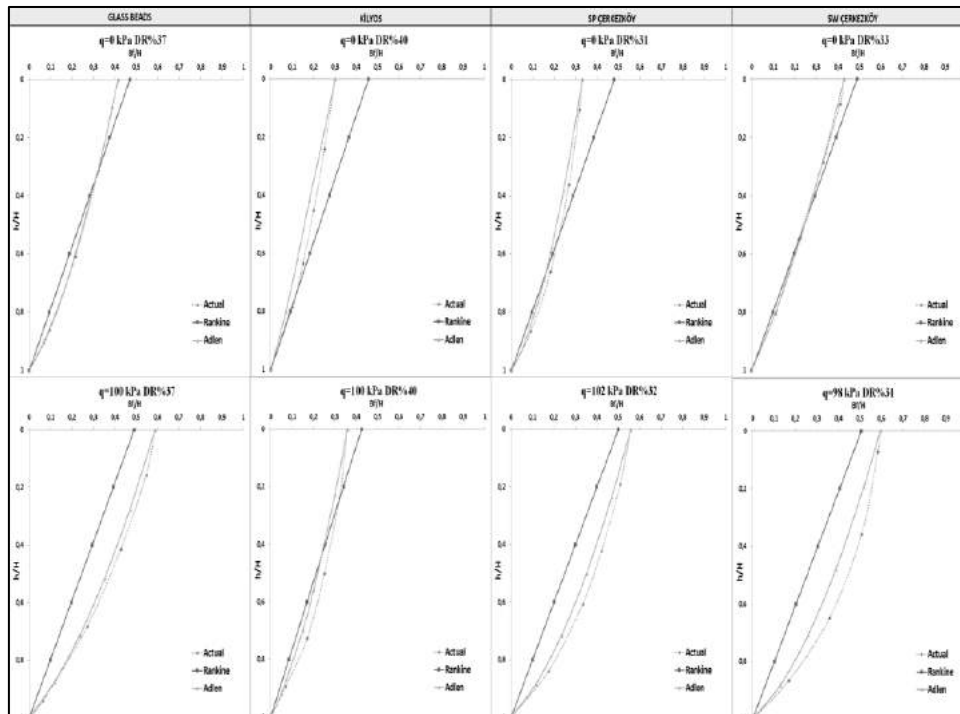


Figure 5. Actual versus calculated failure surface geometries for a particular density range of different sand types and surcharges

Table 3. Derived ‘n’ coefficient values from SPSS analysis for different density and surcharge ranges

	no surcharge (q=0 kPa)	q=50kPa surcharge	q = 100 kPa surcharge
	<i>n</i>	<i>n</i>	<i>n</i>
Loose	0.040	0.087	0.091
Medium Dense	0.029	0.072	0.073
Dense	0.011	0.045	0.050

Because of the nature of amendment, it is not valid for the top point where the failure surface touches to the ground surface. For the sake of accuracy, the use of this amendment for the points where B/Bf is higher than 0.95 is not recommended. From Table 3, it can easily be seen that regardless of the induced surcharge pressure on tested soils, the “n” coefficient tends to decrease as the relative density of the soil increases. Also, if the relative density of the soil kept constant, increase in surcharge pressure leads to an increase in the “n” coefficient. Therefore, it can be proposed that there is an inverse proportion between the ‘n’ coefficient and dilatancy.

6. CONCLUSION

In the design of soil-retaining structures, one of the most-widely accepted theories is Rankine’s [7] theory. This theory is based on limit-equilibrium method which do not consider wall interface, soil arching and dilatant behavior. Many research during 20th century revealed the influence of these parameters on the shape and geometry of shear bands.

Provided that the effects of wall-soil interface and soil arching due to model geometry is eliminated, the only function that influences the shear band geometry is dilatancy. As proposed

by stress-dilatancy theories available in literature, soil relative density and the stress at failure state are two main functions of dilatancy. However, recent research revealed that macro-scale physical properties such as grain size and shape also have an important influence on dilatant behavior. Physical model tests, by means of recent advances in photogrammetry, are convenient and appropriate to visualize and reveal the actual slip surface geometries during wall transition. Therefore many researchers adopted physical model studies to investigate the parameters effecting shear band evaluation. However, the models failed to comprise all variables influencing the formation of shear bands due to either physical restrictions of the model box or the variety of soil samples. Therefore, in this study a physical retaining wall model has been manufactured that is capable of applying surcharge pressure to backfill. Next, tests are conducted on glass beads and sands of different grain shape or granulometry so that the coupled influence of physical soil properties into dilatant behavior is revealed.

7. REFERENCES

- [1] Altunbas, A., Soltanbeigi, B., Cinicioglu, O., 2017. “*Determination of Active Failure Surface Geometry for Cohesionless Backfills*”, Geomechanics and Engineering, Vol.12, No.6, 983-1001.
- [2] Bolton, M.D., 1986. “*Strength and dilatancy of sands*”, Geotechnique 36(1), 65-78.
- [3] Fang, Y.S., Ishibashi, I., 1986. “*Static Earth Pressures with Various Wall Movements*”, Journal of Geotechnical Engineering, Vol.112, Issue 3.
- [4] Lesniewska, D., Wood, D.M., 2009. “*Observations of stresses and strains in a granular material*”, Journal of Engineering Mechanics.
- [5] Niedostatkiewicz, M., Lesniewska, D., Tejchman, J., 2011. “*Experimental Analysis of Shear Zone Patterns in Sand During Earth Pressure Problems using Particle Image Velocimetry*”, Strain, Vol 47, 218– 231.
- [6] Paik, K.H., Salgado, R., 2003. “*Estimation of active earth pressure against rigid retaining walls considering arching effects*”, Geotechnique 53, No. 7, 643-653.
- [7] Rankine, W.M.J., 1857. “*On Stability of Loose Earth*”, Philisophic Transactions of Royal Society, London, Part I, 9-27.
- [8] Stanier, S.A., Blaber, J., Take, W.A. and White, D.J., 2015. “*Improved image-based deformation measurement for geotechnical applications*”, Canadian Geotechnical Journal.
- [9] White, D.J., Take, W.A., Bolton, M.D., 2003. “*Soil Deformation Measurement using particle image velocimetry (PIV) and photogrammetry*”, Geotechnique 53, No. 7, 619-631.
- [10] Krumbein, W.C., Sloss, L.L., 1963. “*Stratigraphy and Sedimentation*”, Freeman, San Francisco.
- [11] Cox, M.R., 2008. “*The Influence of Grain Shape on dilatancy*”, PhD. Thesis, The University of Arizona.
- [12] ASTM D422-63, 2014. “*Standard Test Method for Particle-Size Analysis of Soils*”, ASTM International, USA.
- [13] ASTM D854-14, 2014. “*Standard Test Methods for Specific Gravity of soil Solids by Water Pycnometer*”, ASTM International, USA.
- [14] ASTM D4253-00, 2006. “*Standard Test Methods for Maximum Index Density and Unit Weight of Soils Using a Vibratory Table*”, ASTM International, USA.
- [15] ASTM D4254-00, 2008. “*Standard Test Methods for Minimum Index Density and Unit Weight of Soils and Calculation of Relative Density*”, ASTM International, USA.
- [16] Huwaldt, J.A., 2015. <http://plotdigitizer.sourceforge.net/>.

INFLUENCE OF CRUST THICKNESS IN RELATION TO SLIP BAND DEVELOPMENT BENEATH EMBANKMENTS

Zülal Akbay Arama*, *Istanbul University-Cerrahpasa, Engineering Faculty, Civil Engineering Department, zakbay@istanbul.edu.tr*

S. Feyza Çinicioglu, *Özyeğin University, Engineering Faculty, Civil Engineering Department, feyza.cinicioglu@ozyegin.edu.tr*

ABSTRACT

In this paper, lower bound plasticity theory is used together with a limit state equilibrium approach to determine the depth and propagation of possible slip band development. Slip bands are envisaged as the band of critical slip surfaces. The term critical refers to the possible slip surfaces for which safety factor is smaller than or equal to unity by the application of the methodology proposed in this paper. Based on the observations regarding the collapse of embankments on soft clays slip circle development is envisaged as starting from the toe and propagating towards the center line. In accordance with this, a limit equilibrium mechanism is developed along the slip lines encircling the toe and evolving towards deeper and also laterally further away from the toe. Undrained and axi-symmetrical conditions were assumed. The method searches for the safety factor variation beneath an embankment of a specific height. A parametric application of the proposed method with differing embankment heights was carried out to evaluate propagation level and the thickness of the slip bands with respect to the change in the height of the embankment. The effect of the presence of a crust layer was also worked out in this context. The results are compared with those of well accepted limit equilibrium software to evaluate the applicability and distinctions of the proposed approach.

Keywords: Embankment, Slip zone, Critical Slip Surface, Lower Bound Plasticity Theory.

1. INTRODUCTION

Strength and deformability properties of the soils beneath the embankments have a major role in the design and construction of the embankments. Especially if there are soft clays beneath embankments both of these concerns need special attention in relation to providing stability and satisfactory performance of embankments. Safety emerges as the principal concern in soft clays due to their limited strength capacity, despite the indisputable importance of the deformability in the same context. This is the main concern of this paper which proposes a limit equilibrium method based on lower bound plasticity theorem.

Various types of methods are available in the literature, applying different procedures either theoretical, numerical or experimental for the evaluation of the stability of embankments (Chen and Davidson, 1972; Michalowski, 1983; Michalowski and Shi, 1993; Atkinson and Bransby 1978; Chen, 1975; Krabbenhoft and Damkilde, 2002). Despite the general popularity of limit equilibrium methods, they generally lack the capacity to model the working conditions. Limit analysis methods are generally restricted to applying average stress states defined as a function of limit strength parameters and moreover most of them fail to take different modes of failure into account. Finite element methods are referred to eliminate these problems, but on the other

hand, they usually require significant time and is more complex with regard to choosing the problem parameters compared to limit equilibrium methods (Duncan, 1996).

One of the typical problems in the design of the embankments is the rotation in the principal stress directions along any considered slip plane (Bjerrum, 1972; Jardine and Smith, 1991; Nishimura et al., 2007; Kiziewicz and Lechowicz, 2013). This consideration is usually not taken into account in existing limit equilibrium methods. These considerations are also related to the strength anisotropy, but neither the general purpose limit analyses methods nor the typical FE methods take strength anisotropy into account.

All these considerations bring out the need for a middle way method which has the practicality of the limit equilibrium methods and also capacity of the FE methods to take into account the working stress conditions. This paper proposes a new method developed by Akbay Arama (2016) and Akbay Arama and Cinicioglu (2019). The method presents a middle way, because it takes into account the stress axis rotation effect in terms of stress distributions along the possible slip lines and also is capable to consider possible modes of failure. Although undrained stress anisotropy is not considered in the present applications, the method has the capacity to be modified in a way to take this consideration into account. Lower bound plasticity theorem was used in the development of the method. Slip fans are used to create meshes to calculate the changing values of stresses all along the possible slip lines. Failure zones are envisaged to start from the toe and evolve towards the deeper zones. These failure meshes are formed by the slip lines crossing each other and as these zones enlarge they encompass a greater portion of the foundation soils eventually covering the whole foundation width. Comparisons of the failure zones with the field observations and FE modelling results indicated the competency of the envisaged failure mechanisms.

2. METHODOLOGY

The proposed method checks for the stability of an embankment of a specific height and geometry embankment by starting from the toe regions and all along the evolving slip lines. In this way the foundation soils are scanned through the evolving slip lines. During this operation safety values are continuously found by applying the limit equilibrium method on the failure wedge which was specifically developed for the method presented in this paper. The zones which gives safety values below or equal to one are taken in the slip band and those which give safety values greater than one are considered safe. As the slip lines enlarge the limit equilibrium wedge also enlarges and through this process all of the regions are methodically controlled. Undrained conditions are assumed, as this is the critical case in terms of safety consideration.

The general layout of an axi-symmetrical embankment and the shape of the evolving failure zones can be seen in Figure 1. In Figure 1, the height of the embankment is given as h_e , the apex angle of the slip fan is θ_f , angles covered between successive radial slip planes are $\delta\theta$ and θ_a shows the change of angle of major principal stress. The radius of the circumscribed semicircular slip zone is represented by r . The number of radial discontinuities can be represented by n and selected in accordance with the desired level of sensitivity of the calculations. The angles of the slip fan system is dependent on the selected number of discontinuities and the main relationship between the identified parameters are given in Equations 1 and 2. These equations identify the boundaries of the incipient slip fans and probable slip zones.

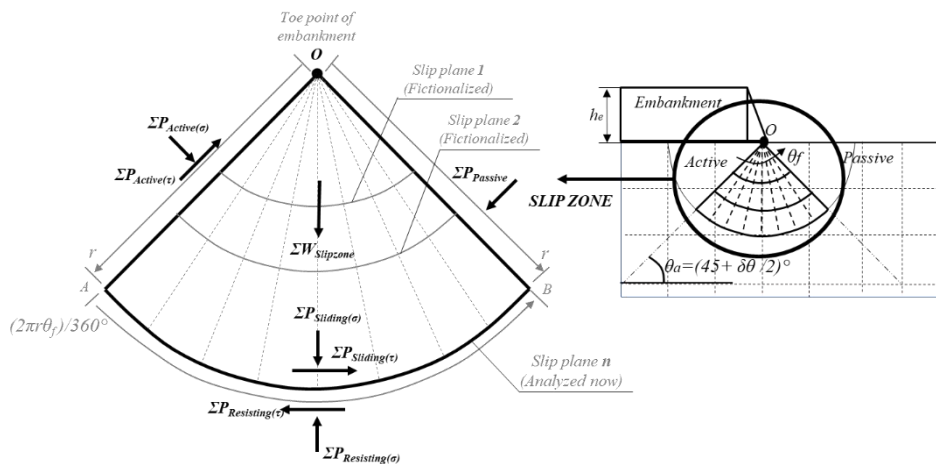


Figure 1. Slip zones limit equilibrium conditions of the proposed method

$$\theta_f = (n - 1)\delta\theta = \left(\frac{n-1}{n}\right)\Delta\theta \quad (1)$$

$$\theta_a = \left(45 - \frac{1}{2}\delta\theta\right) \quad (2)$$

The change of a stress values across a single discontinuity can be determined by Equation 3 (Atkinson, 1981). Δs is the total change of stresses and c_u is the undrained shear strength of clayey soil. The equation is simplified for a single discontinuity in Equation 4 and simplified for a stress fan in Equation 5.

$$\Delta s = n\{2c_u \sin\delta\theta\} = n\{2c_u \sin[\theta_f/(n - 1)]\} \quad (3)$$

$$\delta s = \pm 2c_u \sin\delta\theta \quad (4)$$

$$\frac{ds}{d\theta} = \pm 2c_u \quad (5)$$

Figure 1 also shows the envisaged limit equilibrium mechanism that is used for the determination of safety levels in different depths. Mobilized total active normal and shear forces along the OA plane are given as $\Sigma P_{active(\sigma)}$ and $\Sigma P_{active(\tau)}$ respectively. In the calculations given in this paper, the self-weight of embankment is evaluated by taking into account the slope gradient and the total load is propagated as a distributed load with the use of 2/1 method. Stress axis rotation calculations are started from the centerline of the embankment. The stress axis rotation effect is twofold in the calculation of the presented solution and for this reason two successive slip fans are used. The first one is to carry the stress state from the centerline to the toe region and encompasses the half-width of the base of the embankment and the other one is to take care of the stress axis rotation effect inside the limit equilibrium wedge. The dual stress fan system is seen in Figure 2. Undrained shear strength variation with depth in the soft clay layers is taken into account in the calculations. The limit equilibrium wedge shown in Figure 2 is activated by the forces developed by the thrust action caused by the embankment loads. The thrust action causes shearing effect inside the wedge and these stresses can only be resisted by the passive reaction mobilized on the outward side of the wedge. Total passive force that affects OB plane is found as $\Sigma P_{passive}$. Self-weight of limit equilibrium wedge is found as $\Sigma W_{slipzone}$ of course, takes its value according to the depth and width it extends. Considering the opposite action of total sliding, $\Sigma P_{sliding}$ and resisting, $\Sigma P_{resisting}$ and all effective stresses, equilibrium state of the considered wedge is analyzed.

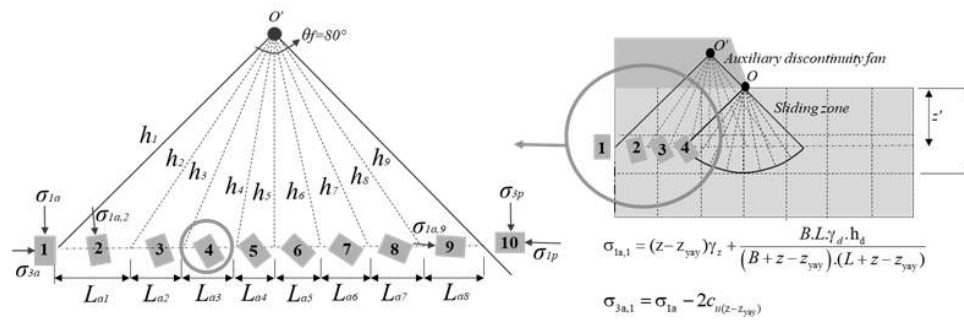


Figure 2. Dual stress fan system and principal axes rotations

Equilibrium condition is written for all selected depths with the determination of above mentioned forces and the vertical-horizontal force equilibrium and moment equilibrium (from point O) is written between sliding and resisting forces for all sliding zones. In addition to these equations, safety levels can be evaluated for all the defined levels of soil deposits. This condition not only leads to know the critical slip zone of the interacted system but also helps to understand the influence of loading stages to all the affected soils. Typical four cases are selected to show the application of proposed method in this paper. The cases are named depending on the height of embankment. Selected embankment heights are 1 meter, 2 meters, 3 meters and 4 meters for the cases 1, 2, 3 and 4 respectively. Two kinds of foundation soil profiles are selected to compare the effects of stratification of soil medium to the development of slip zones. The first profile is consisted of homogenous soft clay layer by taking into account the increase of undrained shear strength along the depth. The critical state soil mechanics framework and stress path application are made use of to determine the variation in the undrained shear strength values with respect to increasing depth levels. The second foundation soil profile is made up of two layers. A crust layer of 1 meter thickness tops the soft clay layer. The geotechnical parameters that are used at the solution procedure is given in Table 1. The base and platform width of the embankment is constant for all cases and takes the values of 24 meters at base and 20 meters at platform.

Table 1. Geotechnical parameters of example

Property	Soft clay	Crust	Embankment
γ (kN/m ³)	14.2	17	21
ν_0	4.2	2.0	-
κ	0.085	0.017	-
λ	0.75	0.12	-
M	1.03	1.29	-
Φ (°)	26	32	35

3. RESULTS AND DISCUSSION

A parametric survey was made by applying the proposed method with four embankment heights and two types of soil profile. The embankment heights were chosen to be ranging between one and four meters with one meter intervals. These analyses were repeated with two soil profiles, one is made up of a thick soft clay deposit and the other is the same clay layer topped with a crust layer of one meter thickness. In the application of the method for these cases nine discontinuity planes ($n=9$) were selected to generate the slip fan system. Radial slip planes were

arranged with 0.1 meter intervals to cross the slip lines. The apex angle of the stress fan is calculated to be 80° and the angle between two successive discontinuity planes is evaluated as 10° .

To define the failure zone, successive calculations are carried out at all depths giving a safety factor less than or equal to 1.0, until safe values ($FoS > 1.0$) are reached. In the figures, the subheading (a) represents homogenous soft clay foundation profile and subheading (b) represents stratified foundation profile with 1 meter thick crust above soft clay layer. The symbol, r' shows the outer and r , the inner boundary of slip zone. It is assumed that during sliding, the embankment attended to collapse behavior with the same width as the radius of the outer boundary of the obtained slip zone. It can be seen in Figure 3 that, one meter high embankment causes soft soil profile to slide through the planes propagating up to 2.8 meters depth from the ground surface.

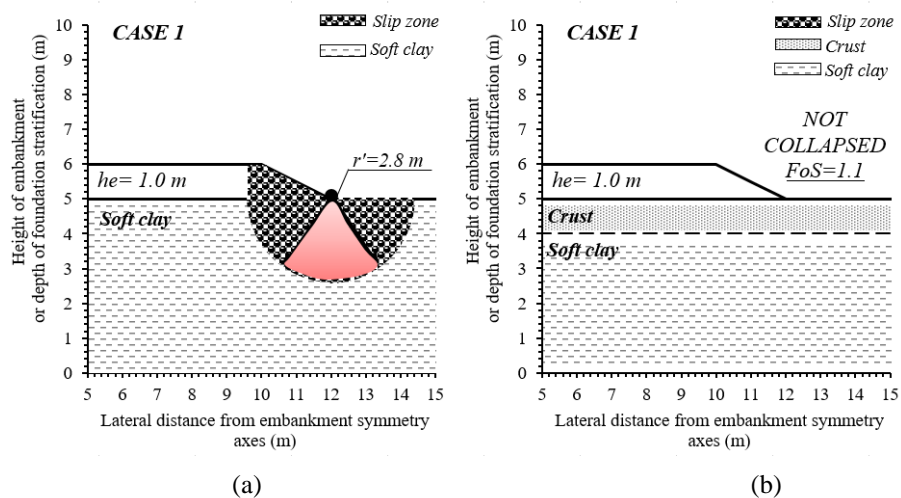


Figure 3. Slip zone development beneath 1 meter high embankment

On the other hand, however, had there been a one meter of crust at the surface of the same soft clay deposit, no collapse condition would be encountered. The safety factor would increase to 1.1 in case with the presence of a crust layer. Using the same thick soft clay deposit with two meters embankment height, the failure zone reached up to 4.2 meters depth as seen in Figure 4 (a).

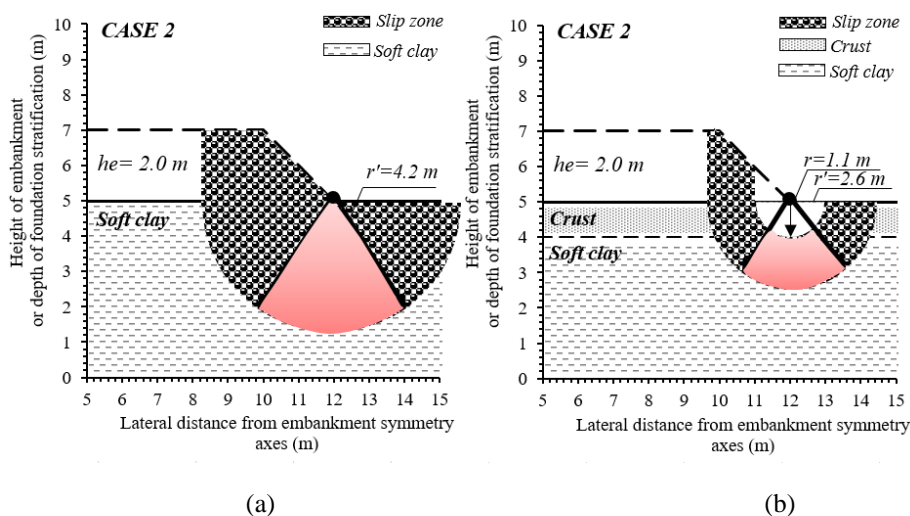


Figure 4. Slip zone development beneath 2 meter high embankment

However, the presence of a one meter thick crust layer changed both the shape and the depth of the failure zone. The failure zone in the second case as seen in Figure 4 (b) the crust layer pushes away the failure zone. The failure zone, in this case, is basically confined to the soft clay zone between the slip planes located at 1.1-2.6 meters. The depth of the failure zone has also been reduced to 2.6 meters compared to 4.2 meters in case without crust layer. This trend is the same with increasing embankment heights as seen in Figures 5 and 6.

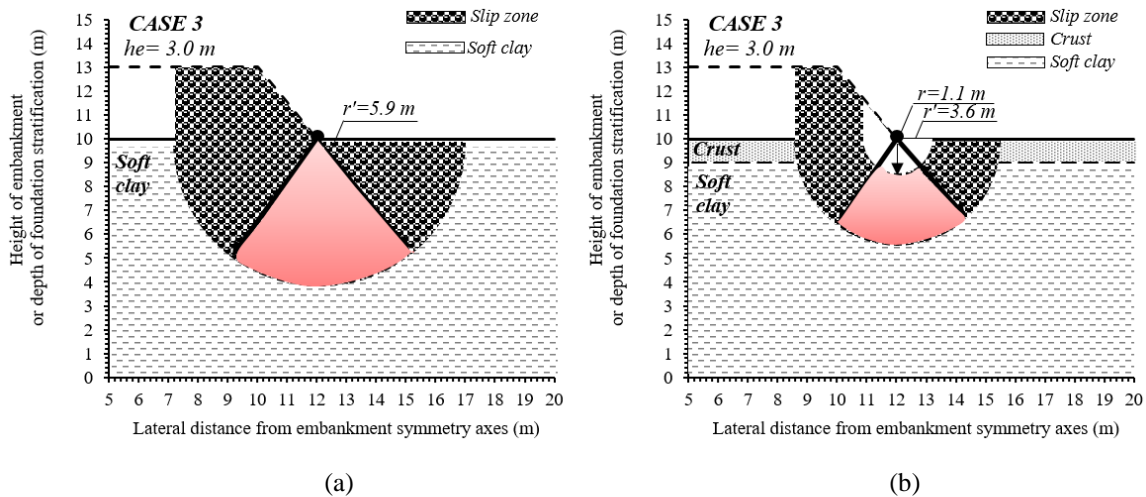


Figure 5. Slip zone development beneath 3 meter high embankment

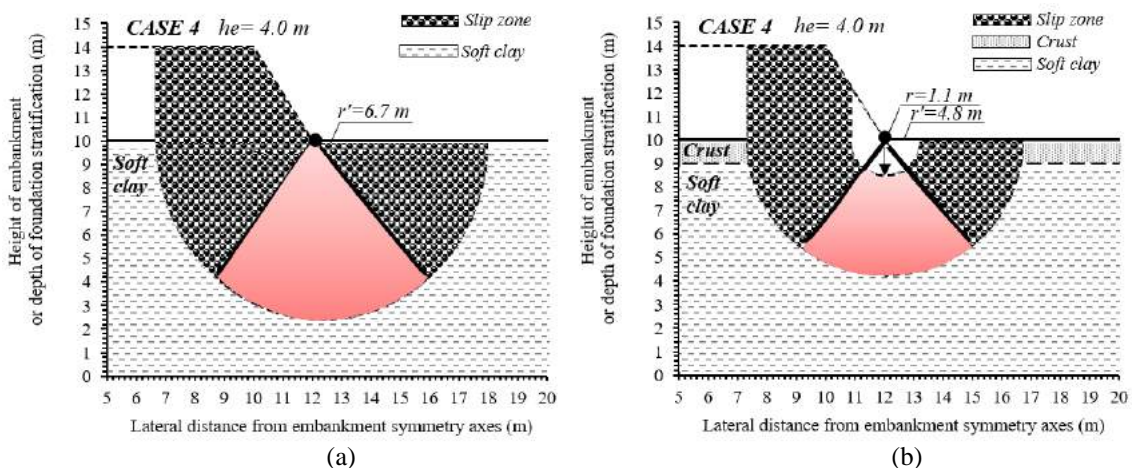


Figure 6. Slip zone development beneath 4 meter high embankment

Comparisons of analysis with different foundation soil profiles and with various software's were also performed to verify the results of the proposed method. The results of the comparisons are presented in Table 2. It can be seen that the failure depths are found to be similar.

Table 2. Depth of slip zones for homogenous foundation soil profile

h_e (m)	Depth of slip zones (m)	
	Proposed Method	Slope/W (Morgenstern Price)
1	2.8	3.0
2	4.2	4.6
3	5.9	5.9
4	6.7	6.8

The role of the thickness of the crust layer or the case with a stiffer layer at the top followed by a soft soil deposit is also investigated by giving increasing thickness values to the crust layer and the results are listed in Table 3, 4 and 5. This analysis is also serves as to refer the application of the proposed method in case of stratified soils.

Table 3. Depth of slip zones for stratified foundation soil profile (1 m crust layer)

h_e (m)	Depth of slip zones (m)	
	Proposed Method	Slope/W (Morgenstern Price)
1	Not collapsed (FoS=1.1)	Not collapsed (FoS=1.3)
2	2.6	2.7
3	3.6	3.9
4	4.8	4.9

Table 4. Depth of slip zones for stratified foundation soil profile (2 m crust layer)

h_e (m)	Depth of slip zones (m)	
	Proposed Method	Slope/W (Morgenstern Price)
1	Not collapsed	Not collapsed (FoS=1.359)
2	Not collapsed	Not collapsed (FoS=1.109)
3	0.3	0.5
4	0.8	1.1

Table 5. Depth of slip zones for stratified foundation soil profile (3 m crust layer)

h_e (m)	Depth of slip zones (m)	
	Proposed Method	Slope/W (Morgenstern Price)
1	Not collapsed	Not collapsed (FoS=1.369)
2	Not collapsed	Not collapsed (FoS=1.109)
3	0.3	0.5
4	0.8	1.1

4. CONCLUSIONS

A new working stress based method is developed for the design of embankments on soft clays. The method has a distinct advantage of considering both the regional and total collapse conditions and scanning both the embankment and the foundations soils thoroughly in terms of safety. Moreover stress axis rotation can be taken into account at least in terms of stress propagation and the method has the capacity to integrate strength anisotropy if necessary strength data is implemented. Lower bound plasticity theory is used in combination with a newly developed limit equilibrium scheme in the development of the method. In order to verify the method the results are compared with the results of the methods which gained general acceptance. The comparisons indicated the remarkable strength of the method as a limit state method with an additional capacity of reflecting the working stress conditions.

REFERENCES

- [1] Chen, W. F., Davidson, H.L., 1972. "Bearing Capacity Determination by Limit Analysis", Fritz Engineering Laboratory Department of Civil Engineering Lehigh, University Bethlehem, Pennsylvania, DOI: 10.1007/s10409-013-0018-1
- [2] Michalowski, R. L., 1983. "On the Solution of Plane Flow of Granular Media for Jump Non-homogeneity", International Journal for Numerical and Analytical Methods in Geomechanics, 485-492, DOI: 10.1002/nag.1610070409
- [3] Michalowski, R.L., Shi, L., 1993. "Bearing Capacity of Nonhomogeneous Clay Layers Under Embankments", Journal of Geotechnical Engineering, 119, 2284, [https://doi.org/10.1061/\(ASCE\)0733-9410\(1993\)119:10\(1657\)](https://doi.org/10.1061/(ASCE)0733-9410(1993)119:10(1657))
- [4] Atkinson, J. H, Bransby, P. L., 1978. "The Mechanics of Soils: An Introduction to Critical State Soil Mechanics", Mc Graw Hill, England, ISBN: 0-07-084077-6.
- [5] Chen, W. F., 1975. "Limit Analysis and Soil Plasticity", Elsevier Scientific Publishing Company, New York.
- [6] Krabbenhoft, K. and Damkilde, L., 2002. "Lower Bound Limit Analysis of Slabs with Nonlinear Yield Criteria", Computers & Structures 80(27):2043-2057, [https://doi.org/10.1016/S0045-7949\(02\)00269-9](https://doi.org/10.1016/S0045-7949(02)00269-9), [https://doi.org/10.1016/S0045-7949\(02\)00269-9](https://doi.org/10.1016/S0045-7949(02)00269-9)
- [7] Duncan, J.M. 1996. "State of the Art: Limit Equilibrium and Finite-Element Analysis of Slopes". Journal of Geotechnical Engineering, 122, 577-596.
- [8] Bjerrum, L., 1972. "Embankments on Soft Ground: State of the Art Report", Proceedings of the American Society of Civil Engineering Speciality Conference on Performance of Earth and Earth Supported Structures, New York, 2, 1-54.
- [9] Jardine, R. J. and Smith, P. R. 1991. "Evaluating Design Parameters for Multi-stage Construction", Geo-coast'91. International Conference Yokohama Port & Harbour Res. Inst. Yokosuka, 1, 197-202.
- [10] Nishimura, S., Minh, N. A. and Jardine, R. J., 2007. "Shear Strength Anisotropy of Natural London Clay", Geotechnique, 57(1): 49–62, <https://doi.org/10.1680/geot.2007.57.1.49>
- [11] Kiziewicz D., Lechowicz Z., 2013. "Anizotropia Wytrzymałoci na Ćcinanie bez odpáywu Gruntów Spoistych w Cylindrycznym aparacie skrĆtnym", Budownictwo i InĹynieria ģrodowiska 4(2): 119–126
- [12] Akbay Arama, Z. 2016, "Yumuşak Zeminler Üzerinde Yer Alan Genişletilmiş Yol Dolgularının Teorik ve Nümerik Analizi", İstanbul Üniversitesi, PhD thesis.
- [13] Akbay Arama, Z. and Ćinicioġlu, S. F. 2019. "Yumuşak Zeminler Üzerinde Dolgu İnşasında Temel Zemini Göçmesine Dayalı Tasarım Yaklaşımı", Teknik Dergi, 30(5), <https://doi.org/10.18400/tekderg.393971>
- [14] Atkinson, J.H., 1981. "Foundations and Slopes: An Introduction to Applications of Critical State Soil Mechanics", Mc Graw-Hill Book Company, 375.

GROUND MOVEMENT DUE TO SHAFT CONSTRUCTION

Joseph Newhouse, *Mott MacDonald (formerly Imperial College London), British Geotechnical Association, joseph.newhouse@mottmac.com*

ABSTRACT

Ground movement due to shaft construction can damage surrounding assets. A comprehensive synthesis of case studies of ground surface movement due to the excavation of circular shafts is presented herein. The data highlight the importance of considering shaft construction method when making empirical predictions.

After subtracting significant settlement due to dewatering, two shafts at Crossrail's Limmo Peninsula Tunnelling Site have been added to the existing data set. This has confirmed that when wall installation occurs prior to excavation, shafts typically experience less ground surface settlement than when installation and excavation are concurrent.

New design lines which differentiate between construction method are presented.

Keywords: Ground movement, Shaft construction, Limmo Peninsula.

1. INTRODUCTION

High-quality predictions of ground movement due to circular shaft construction are of importance for projects in urban environments. Such movement can result in unacceptable damage to surrounding structures and utilities, and so one must understand which assets are at risk. However, overestimation of movement can lead to the implementation of unnecessary and costly mitigation measures.

Empirical formulae are a key tool for making predictions in line with best practice guidelines such as Crossrail's Civil Engineering Design Standards [1]. However, for circular shafts, historically the data set of case studies on which predictions may be based has been very small, with a single shaft underlying the formula presented by New & Bowers [2], which for many years was the primary tool for empirical predictions. Subsequent formulae have been developed to take account of shaft geometry (Mott MacDonald [3]; McNicoll [4]; Pairaudeau [5]; GCG, [6]), but the limited number of case studies has prevented a detailed assessment of the influence of construction method.

However, a growing body of case studies, including two shafts at Limmo Peninsula Tunnelling Site presented herein (and expanded upon by Newhouse [7]), has offered the opportunity to update and improve current prediction methods.

2. CATEGORIES OF SHAFT AND CAUSES OF GROUND MOVEMENT

Following Faustin et al. [8], three categories of shaft may be defined:

1. Pre-lined; the wall lining is installed prior to excavation e.g. secant, sheet pile and diaphragm walls.

2. Concurrently-lined; installation of the wall lining and excavation are concurrent e.g. caisson, underpinning and sprayed concrete lining (SCL).
3. Combined; the upper portion of the shaft is pre-lined and the lower portion is concurrently-lined.

There are three general causes of ground movement due to shaft construction that encompass these categories; installation of the wall, excavation in front of the wall, and changes in groundwater regime. When concurrently-lined, movement due to installation and excavation are coincidental.

The focus of the present study is on the maximum vertical ground surface movement due to circular shaft excavation. Details of other facets of ground movement, including settlement trough extent, are presented by Newhouse [7].

3. SYNTHESIS OF CASE STUDIES

The body of case studies has grown significantly over the last five years, with both Mott MacDonald [3] and Schwamb [9] presenting details of the increasing catalogue. These, along with subsequent case studies, are summarised by Newhouse [7]. The 19 case studies are primarily located in London, UK, and have predominantly competent ground conditions that typically comprise stiff clays.

For each of the case studies, a ‘best-estimate’ at excavation depth, H , of the maximum vertical ground surface movement due to excavation, $\delta_{v,max}$, has been defined for the available settlement data. $\delta_{v,max}$ has then been normalised by the excavation depth, H , to give α ($= \delta_{v,max}/H$). Categorised by shaft construction method, the values of α are plotted against shaft internal diameter, D , in Figure 1, and against D/H , in Figure 2. Values of α for the Main Shaft and Auxiliary Shaft at Limmo Peninsula Tunnelling Site (Section 4) at the completion of excavation ($H = H_{final}$) are included in Figure 1, and throughout their excavation in Figure 2.

The following may be observed:

1. In Figure 1, the data are presented against the design line proposed by GCG [6] for the Crossrail project. The line is close to an upper limit of the data. Thus, in most cases, it would overpredict ground surface settlement. For pre-lined shafts, the overprediction would be considerable.
2. Construction method is shown to be of key importance. For common values of D , or D/H , concurrently-lined shafts (e.g. underpinning or caisson, with SCL follow-on) show the greatest values of α . Pre-lined shafts (e.g. secant pile or diaphragm walls) show the smallest values of α . Combined shafts (e.g. jet grout, secant pile, or sheet pile walls, with SCL follow-on) lie between the two extremes.
3. Considering separately pre-lined shafts, and concurrently-lined shafts, the geometry of a shaft clearly has an impact on the observed ground movement; greater values of D and D/H typically exhibiting larger values of α .

In Figure 1 and Figure 2, new design lines for pre-lined and concurrently-lined shafts are tentatively presented. The design lines represent moderately conservative upper and lower extents of the limited data sets, as well as an average between these two thresholds.

4. OVERVIEW OF LIMMO PENINSULA TUNNELLING SITE

Two shafts were constructed in London, UK, at Crossrail’s Limmo Peninsula Tunnelling Site; the Main Shaft and Auxiliary Shaft. Structural and simplified geological details for the shafts are presented in Table 1, and are shown along with details of the site hydrogeology, and dewatering and piezometric installations in Figure 3.

The site lends itself to the analysis of ground movement, as movement is anticipated to have been relatively unaffected by historic or existing structures. However, extensive dewatering during construction resulted in significant ground settlement, obscuring movement due to excavation. Piezometric level data collected during the shaft construction are presented in Figure 4. Key points of note are listed below. The data these points refer to are indicated in Figure 4 adjacent to a corresponding arrow:

1. A pumping test was conducted using the External Chalk Wells, prior to the excavation of the shafts.
2. Drawdown in the Lower Aquifer was primarily a response to dewatering from the seven External Chalk Wells (2a), and drawdown in the Middle Aquifer was primarily a response to dewatering from the six External Thanet Wells (2b).
3. Piezometric levels gradually fell in the low permeability London Clay, in response to the drawdown in the Middle Aquifer.
4. There was no dewatering, and consequently no drawdown, in the Upper Aquifer.
5. Varying instruments exhibit gaps in readings (for example 5a), termination of changeable readings (5b), erratic behaviour (5c), and sudden spikes (for example 5d). These were all accounted for in the analysis described below.

Table 1. Details of the shafts at Limmo Peninsula Tunnelling Site
 (with reference to DSJV [10], Crossrail [11] and Crossrail [12])

Shaft	Generalised geological stratigraphy	Construction method	Wall depth (m)	Primary lining wall thickness (m)	Final excavation depth, H_{final} (m)	Internal diameter, D (m)
Main Shaft	13.5 m Made Ground, Alluvium and River	Diaphragm wall	55	1.2	44.3 (39.1*)	30.2
Auxiliary Shaft	Terrace Deposits 30 m London Clay 1 m Harwich Formation 17.5 m Lambeth Group 26.5 m Thanet Sand Chalk	16.8 m Sheet pile 22 m SCL	38.8	SCL 0.6 to 0.8	38.8	27

* Depth reached prior to pause in excavation; final depth considered in the analysis presented herein.

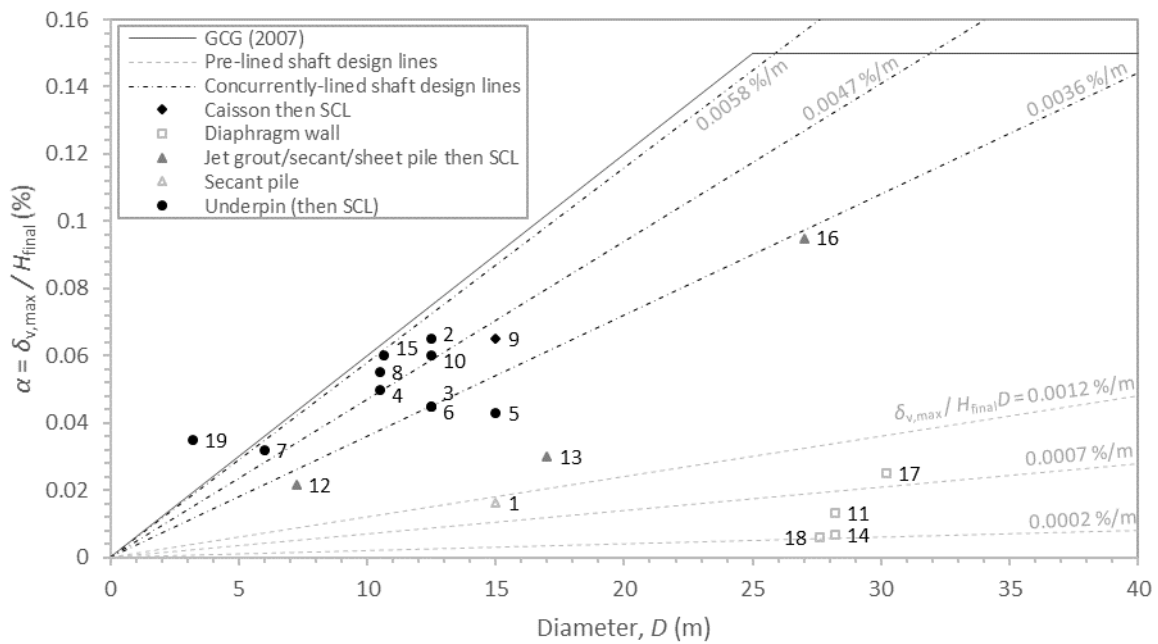


Figure 1. Settlement at the end of shaft excavation against diameter

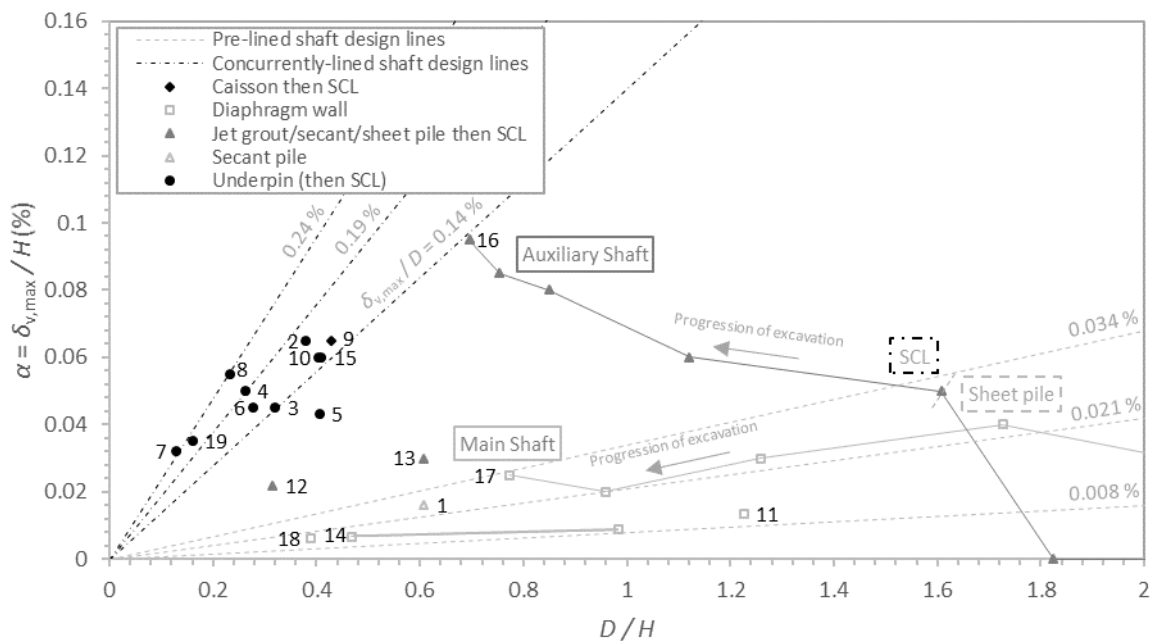


Figure 2. Settlement against diameter normalised by current excavation depth

Key: (1) Farringdon in Faustin et al. [8]; (2) Channel Gate Road, (3) Eade Road, (4) Earls Court, (5) Highbury, (6) St John's Wood 1, (7) St John's Wood 2, (8) St Pancras, (9) Wandsworth and (10) Willesden in McNicoll [4]; (11) Cambridge Heath in Mott MacDonald [3]; (12) and (13) confidential shafts in Mott MacDonald [13]; (14) Musashino in Muramatsu & Abe [14]; (15) Heathrow Express Trial Tunnel in New & Bowers [2]; (16) Limmo Peninsula Auxiliary Shaft and (17) Limmo Peninsula Main Shaft in Newhouse [7]; (18) Abbey Mills Shaft F in Schwamb [9]; (19) Terwilligar in Wong & Kaiser [15].

Note: Values of α characterised by solid data point markers represent movement due to installation and excavation, whereas hollow data point markers represent movement due to excavation only.

Note: Points joined by a solid line represent different stages of excavation for the same shaft.

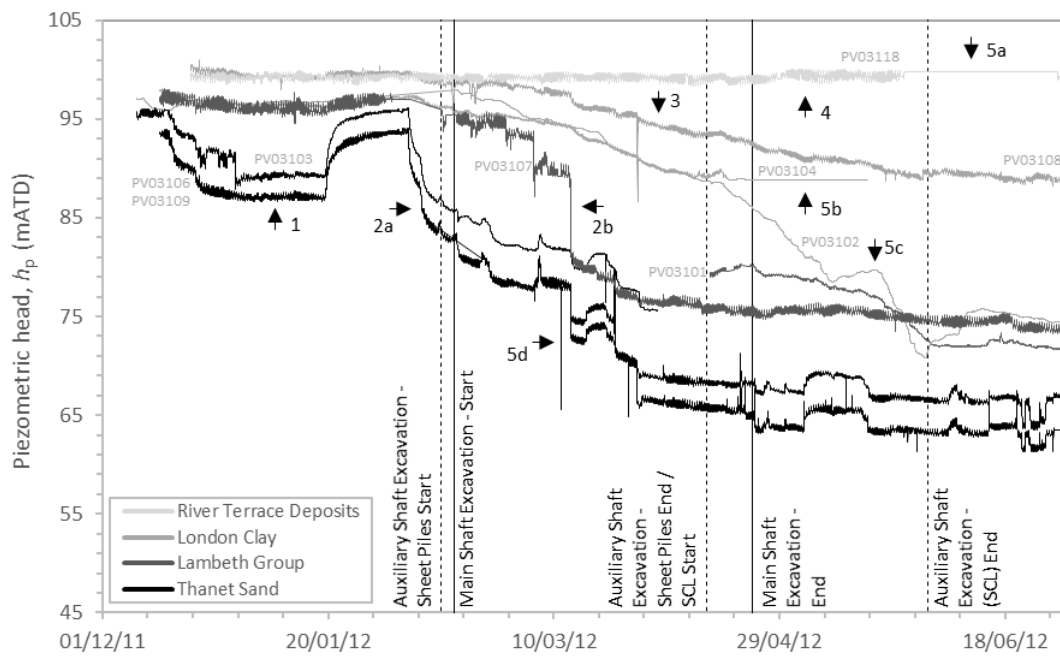


Figure 4. Piezometric head during the shaft construction at Limmo Peninsula Tunnelling Site (with reference to DSJV [17])

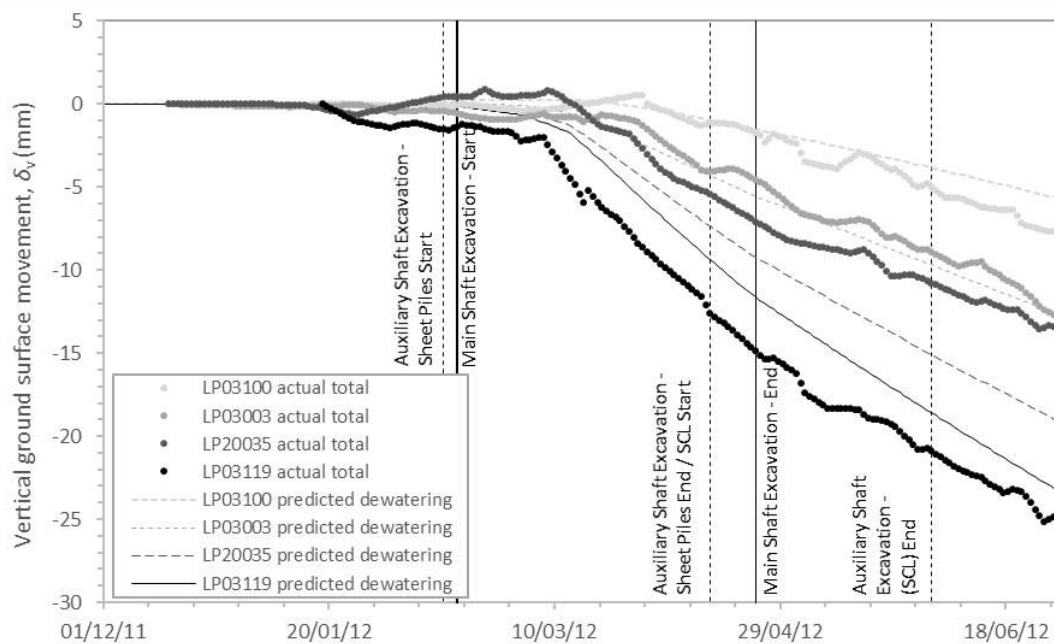


Figure 5. Predicted dewatering settlement against actual total settlement at Limmo Peninsula Tunnelling Site (with reference to DSJV [17])

5. ANALYSIS OF GROUND MOVEMENT AT LIMMO PENINSULA TUNNELLING SITE

To allow for comparison of the ground movement due to excavation of the Main Shaft and Auxiliary Shaft with the case studies presented in Section 3, settlement due to dewatering has been isolated from the total vertical ground surface movement observed. To calculate the settlement due to dewatering, a three-dimensional numerical model of the site was developed. The model was developed assuming:

1. The aquifers (see Figure 3) to be confined, and flow in the aquifers to be horizontal.
2. The drawdown from each well to be axisymmetric, and the principle of superposition to apply when calculating the total drawdown.
3. A transient drawdown response in the aquifers in response to the measured dewatering flow rate.
4. Vertical flow in the London Clay aquiclude, with the drawdown calculated using the finite difference method, whereby drawdown in the Middle Aquifer was used to define a variable boundary condition.
5. Settlement due to dewatering to be exclusively due to one-dimensional consolidation of the London Clay in response to the change in effective stress resulting from drawdown.

The drawdown was calibrated against the observed piezometric readings presented in Section 4.

In Figure 5, the predicted dewatering settlement is presented against the actual total settlement for 4 of the 57 levelling points analysed. The difference between the actual total settlement and predicted dewatering settlement is considered to be due to excavation. Generally, there is good agreement between the two, indicating that the majority of movement was due to dewatering.

For both the Main Shaft and Auxiliary Shaft, ‘best-estimate’ values of α for the movement attributed to excavation are presented for increasing excavation depth, H , in Figure 2. In agreement with the existing case studies:

- For the Main Shaft (constructed with a pre-lining of diaphragm walls), in accordance with the other pre-lined shafts, the values of settlement were small, and there is general trend of a decrease in α with decreasing D/H .
- For the Auxiliary Shaft (a combined shaft constructed with a pre-lining of sheet piles over its upper half, and concurrently-lined with SCL thereafter), the values of settlement were small while the excavation remained within the sheet piles, but increased significantly as excavation transitioned to SCL, up to values that may have been projected in line with the existing concurrently-lined shaft data.

6. CONCLUSION

Field data showing ground movement due to the excavation of two shafts at Limmo Peninsula Tunnelling Site have been added to a synthesis of existing case studies. Together these highlight the importance of accounting for construction method when making empirical predictions. For given values of shaft internal diameter, D , and diameter normalised by excavation depth, D/H , shafts where wall installation and excavation are concurrent exhibit significantly greater normalised settlement than shafts where wall installation occurs prior to excavation. New design lines have been presented which differentiate between these construction methods. For many shafts, the design lines will facilitate a reduction in predicted settlement, offering the potential to save on costly mitigation measures.

ACKNOWLEDGEMENTS

This work is testament to collaboration across the civil engineering industry; from construction to research. I would like to thank Dr Jamie Standing of Imperial College London for his guidance in producing both this paper and my underlying MSc dissertation [7]. I would also like to thank Dr Michael Williamson and Dr Rob Talby of Mott MacDonald, and Mike Black of Crossrail. Support from the British Geotechnical Association Fund, and the Mott MacDonald Research and Further Education Fund was also gratefully received.

REFERENCES

- [1] Crossrail, 2010a. “*Civil Engineering Design Standard, Part 7, Ground Movement Prediction*”, Crossrail, Report number: CR-STD-303-7, Version: 6.0.
- [2] New, B., Bowers, K., 1994. “*Ground movement model validation at the Heathrow Express trial tunnel*”, Tunnelling '94, Volume 1, pp. 301-329, 5-7 July 1994, UK.
- [3] Mott MacDonald, 2013. “*Impacts of Tunnels in the UK*”, HS2.
- [4] McNicoll, S., 2013. “*Study into ground induced settlement caused by shaft construction on the London Power Tunnels*”, The Harding Prize, British Tunnelling Society.
- [5] Pairaudeau, H., 2011. “*Construction and Performance of Shafts*”, MEng, University of Cambridge, UK.
- [6] GCG, 2007. “*Settlement Estimation Procedure: Box Excavations & Shafts*”, Crossrail, Report number: 1D0101-G0G00-01004, Revision B.
- [7] Newhouse, J., 2017. “*Ground movement due to shaft construction*”. MSc, Imperial College London, UK, 68 pages.
- [8] Faustin, N., Mair, R., Elshafie, M., Menkiti, C., Black, M., 2017. “*Field measurements of ground movements associated with circular shaft construction*”, Proceedings of the 9th International Symposium on Geotechnical Aspects of Underground Construction in Soft Ground, TC204 ISSMGE, 4-5 April 2017, Brazil.
- [9] Schwamb, T., 2014. “*Performance Monitoring and Numerical Modelling of a Deep Circular Excavation*”, PhD, University of Cambridge, UK, 202 pages.
- [10] DSJV., 2012a. “*Limmo Shaft, Shift Review Group Reports from 14/02/12 to 18/10/12*”, Crossrail, Report number: C305-DSJ-C2-MRC-CR144_WS155-50002.
- [11] Crossrail, 2011. “*C121 - SCL Tunnels, Limmo Peninsula Shaft, Geotechnical Design Report - Part 2, Geotechnical Design Summary*”, Crossrail, Report number: C121-MMD-C2-RGN-CR144-SH011-00002, Revision 2.0.
- [12] Crossrail., 2010b. “*C123 - Intermediate Shafts, LIMMO, Geotechnical Design Report Part 2: Geotechnical Design Summary Report*”, Crossrail, Report number: C123-JUL-C2-RGN-CR144_SH011_Z-00004, Revision 2.0.
- [13] Mott MacDonald., 2015. “*Ground Movement Impact Assessment - Stage 3 Refinements*”, Confidential Project, Report number: MMD-N001-2360000-GEO-RPT-00024, Revision 2.0.
- [14] Muramatsu, M., Abe, Y., 1996. “*Considerations in shaft excavation and peripheral ground deformation.*”, Geotechnical Aspects of Underground Construction in Soft Ground, pp.173-178.
- [15] Wong, R., Kaiser, P., 1988. “*Behaviour of vertical shafts: Reevaluation of model test results and evaluation of field measurements*”, Canadian Geotechnical Journal, 25 (2): 338-352.
- [16] DSJV., 2012b. “*C305: Eastern Running Tunnels, Dewatering at Limmo Peninsula*”, Crossrail, Report number: C305-DSJ-C-GMS-CR144_WS155-50008, Revision 2.0.
- [17] DSJV., 2013. “*C305: Eastern Running Tunnels, I+M Weekly Summary Report, Year 3, Period 7, Week 4*”, Report number: C305-DSJ-C2-RGN-CRG03-50002, Revision 90.0.

DESIGN AND CONSTRUCTION OF A TEMPORARY LAUNCH PIT FOR THE HUMBER FEEDER 9 PIPELINE AND TUNNEL

Natalie Davey, *Skanska Infrastructure*, natalie.davey@skanska.co.uk

ABSTRACT

The existing Humber Feeder 9 gas pipeline crosses the Humber Estuary in a shallow trench and, over time, highly mobile estuarial deposits have reduced the cover to the pipeline. This is to be replaced with a new 5km long pipeline installed within a 3.65m internal diameter tunnel below the estuary. This paper describes the design and construction of the temporary launch pit for both the tunnel boring machine and the new pipeline. The launch pit structure is 8m at its widest and 209.6m long, ramping down from ground level to 11.2m below ground. The pit was excavated through approximately 9m of superficial deposits, comprising soft estuarine alluvium and stiff, predominantly cohesive, glacial till through to formation level within the ‘chalk bearings’ (comprising frost-shattered chalk) of the North Lincolnshire aquifer system. More than half the length of the launch pit is designed as a two-cell cofferdam constructed in secant and sheet piles, while most of the remaining length of the retaining walls are designed as propped cantilever sheet piles. This paper discusses the challenges associated with construction within the highly dense and fractured ‘Northern Province Chalk’ lithology, in particular the groundwater abstraction and aquifer recharge system used to prevent further saline intrusion. Learning outcomes from the design and construction process are also suggested for the future design of temporary launch structures constructed within a vulnerable aquifer.

Keywords: Temporary Works, Northern Province Chalk, Secant Piles, Sheet Piles, Construction Dewatering

1. INTRODUCTION

The Feeder 9 gas pipeline transports 70 – 100 million m³ of gas each day from the Easington gas terminal on the north east coast of the United Kingdom, passing beneath the Humber Estuary, to the rest of the national transmission network (Figure 1). This is approximately 20% of the national peak winter demand. The current Feeder 9 Humber Estuary crossing was constructed in 1984 using a cut-and-cover trench through the river bed. Highly mobile estuarial deposits in the deep water channel have reduced the cover to the pipeline and National Grid, the asset owner, have employed remedial solutions over the pipeline for short term protection [1]. The long-term solution selected was to construct a segmental concrete lined tunnel, starting from Goxhill on the south-western bank of the Humber, to Paull on the north-east bank. The tunnel has an internal diameter of 3.65m and will house the 1.22m diameter concrete-weight-coated, continuously-welded steel pipe, which will carry gas at 70 barg pressure. On completion this will be the longest tunnelled pipeline crossing of an estuary in the world [2].

The project works can be separated into four main phases:

- Construction of temporary works launch pit and reception shaft for the tunnel and pipe.
- Construction of the tunnel.
- Installation of the pipeline within the tunnel and then across land to above ground gas installations (AGI).
- Decommissioning the existing pipeline and reinstating the sites to their previous use.

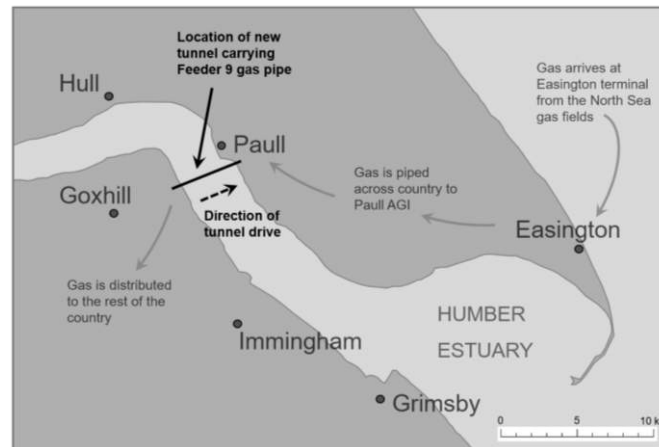


Figure 1. Project location and regional context of Feeder 9 gas pipeline

A slurry tunnel boring machine (TBM) was selected for the works and tunnelling is currently ongoing under the estuary. The TBM is suitable for excavation through mixed ground conditions with high water pressures. The pipe (approximately 5km) will then be pushed through the tunnel, once flooded, in a single string from the launch pit at Goxhill to Paul.

The contract for the works was awarded in April 2016 to a joint venture (JV) between Skanska Infrastructure, PORR Bau GmbH and A-Hak. The launch pit construction commenced in May 2017 and was completed in January 2018. This paper will discuss the design and construction of the launch pit for the tunnel and pipe.

2. TEMPORARY LAUNCH PIT DESIGN

2.1. Ground Conditions

The ground profile adopted in the design is given in Table 1. The main geological units at the launch pit site are the Burnham formation, through which the launch pit is constructed, and the overlying Flamborough formation, which is the principle lithology over the majority of the tunnel drive. These chalk strata are part of a group often described as ‘Northern Province’ chalk, owing to their markedly higher densities and greater hardness compared with ‘Southern Province’ chalks [3]. The average intact dry density in the Flamborough chalk found at this location is 1.87Mg/m³ and in the Burnham chalk is 1.95Mg/m³.

Table 1. Design stratigraphy

Stratum	Elevation of top of stratum (mOD)	Depth below ground to top of stratum (m)	Layer thickness (m)
Marine and estuarine alluvium (sandy clay)	2.0	0.0	4.0
Glacial till (sandy gravelly clay)	-2.0	4.0	4.7
Flamborough chalk (Grade Dc)	-6.7	8.7	1.3
Burnham chalk (Grade Dc)	-8.0	10.0	9.0
Burnham chalk (Grade A5)	-17.0	19.0	5.0
Burnham chalk (Grade A2/3)	-22.0	24.0	Unproven

The top 6-10m of the chalk in the vicinity of the launch pit is weathered (structureless chalk, CIRIA Grade Dc) [4]. Beneath this, the chalk is structured with generally closed fractures (CIRIA Grade A2 to A5 with grade improving with depth, see Figure 2) [5]. The chalk dips towards the north-east such that it is exposed at the base of the launch pit excavation, but is not encountered in the construction of the reception shaft. These Cretaceous deposits are overlain by glacial till, and marine and estuarine alluvium [6]. At the launch pit location, to the south-west of the estuary, the glacial till and alluvium are predominantly cohesive and relatively consistent in composition.

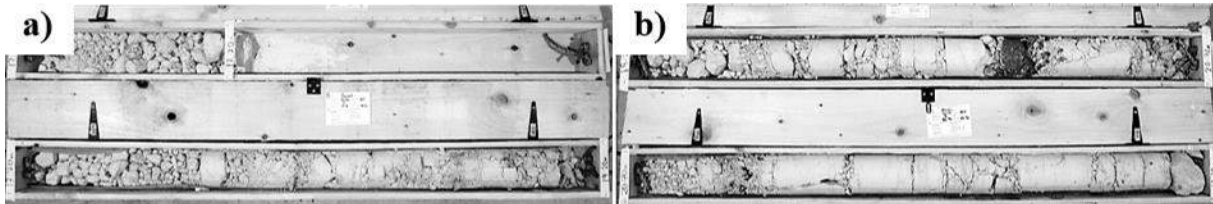


Figure 2a). Weathered chalk Grade Dc. **Figure 2b).** Top of the structured chalk

The underlying chalk is classified by the Environment Agency (EA) as a principal aquifer with high groundwater vulnerability. The groundwater resources are described as “fully committed to existing users and the environment” [7]. The weathered chalk immediately beneath the Quaternary deposits, which act as a confining layer, comprises the frost-shattered ‘chalk bearings’ [4] which, according to the University of Birmingham cited by Whitehead et al [8], provide the majority of the flow into groundwater boreholes. The water in the aquifer is fresh in the vicinity of the launch pit, becoming increasingly brackish with proximity to the estuary. Saline intrusion has been investigated as an issue in the Lincolnshire and North Humberside area since the middle of the last century [8]. Close liaison with the EA was required throughout the design phase to ensure the solution minimised disruption to the aquifer and aligned with their management strategy.

2.2. Design Solution

The Goxhill site is located in a former agricultural field. The design of the launch pit had to strike a careful balance between function and economy; the launch pit is a temporary works structure, required only to facilitate the construction of the tunnel and insertion of the pipe.

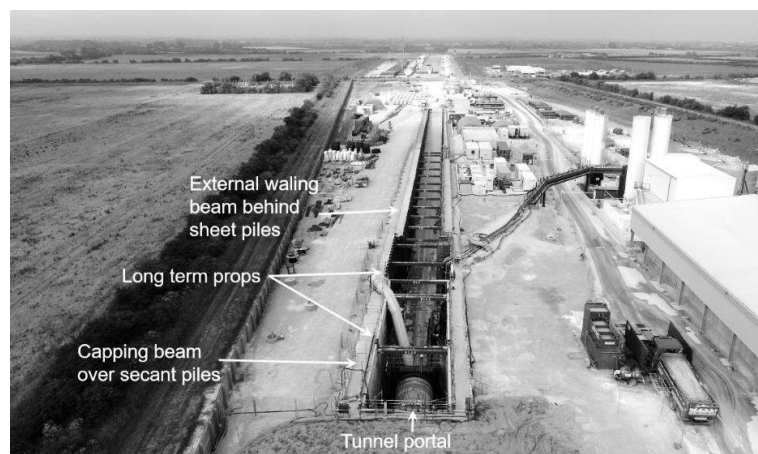


Figure 3. Aerial photograph of the launch pit during the tunnelling phase

The launch pit, as shown in Figure 3, is a 209.6m long ramp from formation level of -9.2mOD in front of the tunnel portal rising to ground level. The ramp accommodates the large radius of curvature required to support the pipe as it enters the tunnel. It also allows for the use of multi-surface vehicles to service the TBM, eliminating the need for a gantry crane and overhead lifting. The total excavation depth of the pit was kept to the minimum possible whilst still

providing sufficient cover for the safe installation of the tunnel. This reduced the loads on the retaining walls, propping system and base slab. This meant that secant piles were only required to support the very deepest sections; the portal and the deepest 21m length of wall is formed from 1.18m diameter hard-firm secant piles. PU32 sheet piles were used for the remaining length of wall (approximately 76% of the total length of wall). This resulted in significant cost and programme advantages together with 11% reduction in embodied carbon compared with constructing the pit entirely in secant piles. The retaining walls were analysed using the proprietary design software programme WALLAP, adopting a subgrade reaction model for analysis of structural forces and displacements.

Figure 4 shows the key details of the launch pit structure. The top of the capping beam and sheet piles are at +3.4mOD to provide flood protection against a 1 in 200 year storm event. A stoplog flood wall completes the flood defence. The launch pit design considered various surcharges adjacent to the retaining walls and included track pressures from a 300t crawler crane positioned 2m away from the capping beam (for which the maximum lift was the 101t TBM middle shield and ring erector), a 20kPa general construction surcharge and a flood condition.

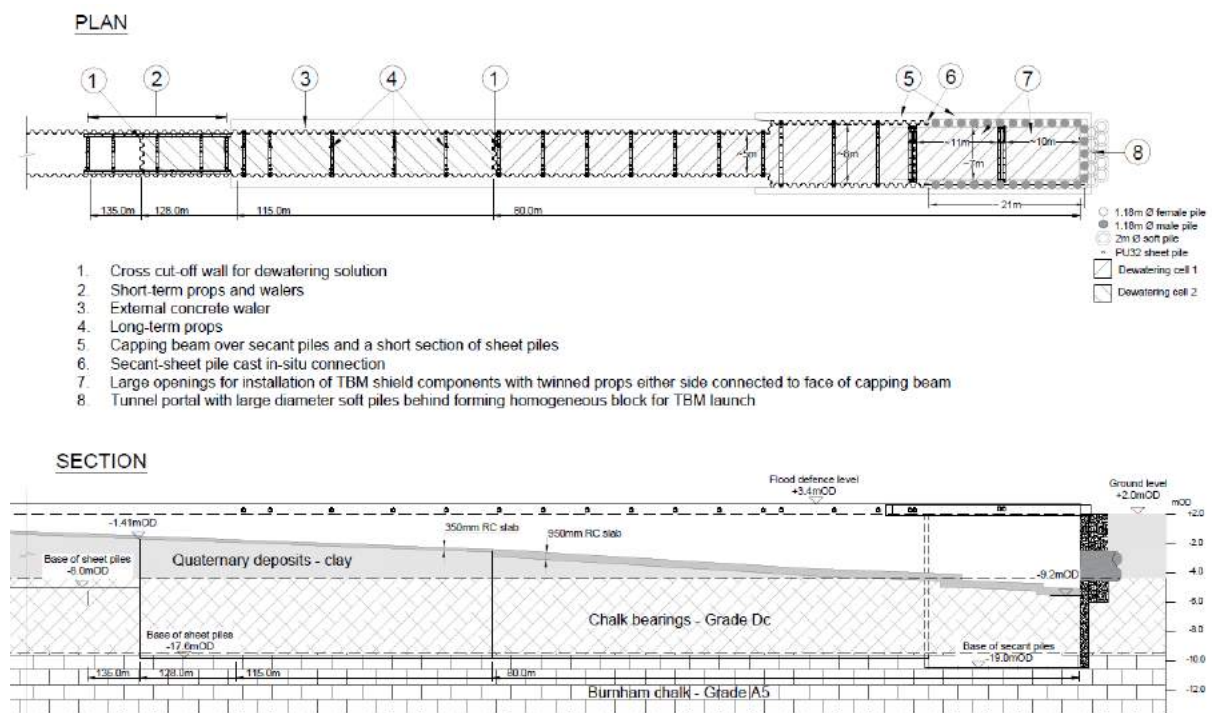


Figure 4. Plan and section of the launch pit (dewatering wells not shown)

The propping system considered both long-term and short-term stages, and was designed against progressive collapse by incorporating redundancy using the loss-of-prop condition [9]. In the long-term, the first 115m from the headwall is supported at approximately ground level by hydraulic steel props with the base slab acting as the lower level prop. Beyond this until the ramp reaches ground level the sheet piles cantilever from the base slab. The props work in combination with a reinforced concrete (RC) waling beam. This takes the form of a capping beam over the secant piles and transitions to an external waling beam behind the sheet piles. The use of a capping and external waling beam maximises the available space between the walls for the operation of excavation plant and for lifting operations.

In the short-term, the first 74m from the headwall were also propped at a lower level with hydraulic props and waling beams until the base slab could be installed and cured. In order to maximise the available space within the excavation the headwall waler was designed as a

914x419x388 UB with stiffened ends compatible with the proprietary system. This removed the requirement for bulky knee-brace props to support the headwall waler (see Figure 5).

In addition to providing the base prop for the retaining walls, the base slab is also designed to withstand hydrostatic loads from the sub-artesian groundwater pressure within the chalk, and to support the loads from the tunnelling and pipe installation operations. The TBM was launched by jacking against a robust steel thrust frame cast into the base slab designed for thrust loads of up to 7000kN. The pipe will be pushed through by two pipe thrusters, each capable of exerting 5000kN of thrust. The base slab is locally reinforced with 1.3% reinforcement, by volume, with substantial baseplates and anchors cast in to distribute the loads. The base slab is connected to the walls using resin-fixed dowels to each secant pile and shear studs welded to alternate sheet piles, with quantities locally increased in the region where the pipe thrusters are located (see Figure 5). Connecting the base slab to the sheet piles in this way removed the requirement for tension piles to the base slab as the uplift could be resisted by the total weight of the launch pit structure, together with friction between the walls and the retained soil.

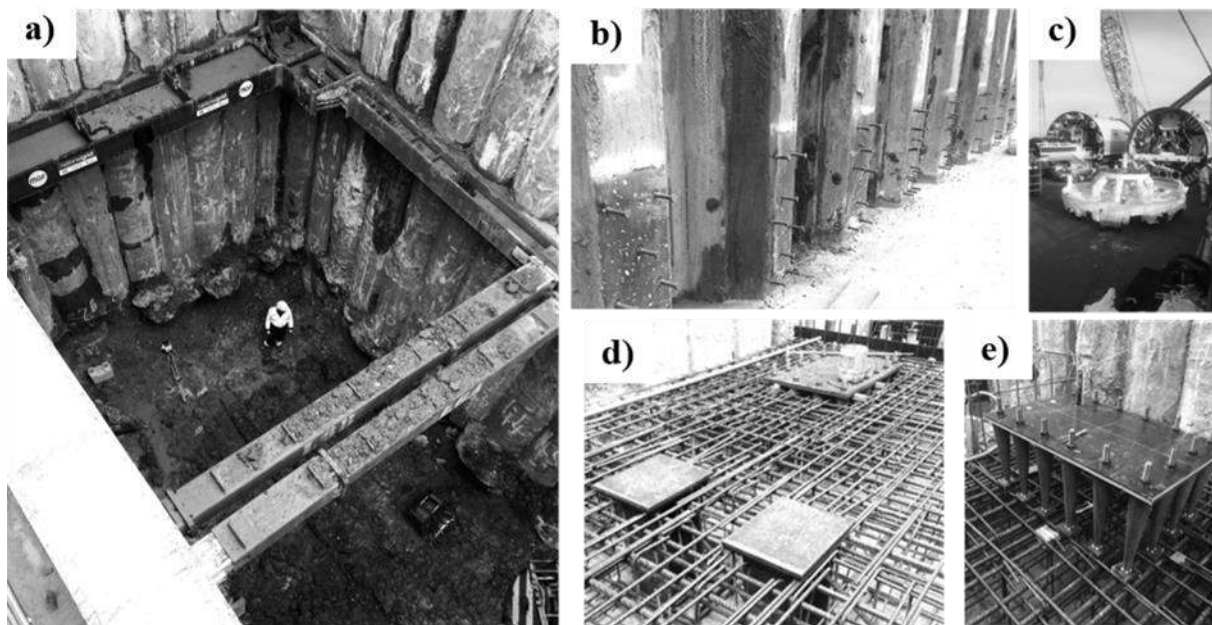


Figure 5a). Temporary headwall waler and lower level propping. Figure 5b). Shear studs fixed to sheet piles. Figure 5c). TBM shield components. Figure 5d). Anchor bolts for TBM thrust frame. Figure 5e). Two anchor plates with cast-in 356x368x177 UCs for pipe thruster frame (foreground)

2.3. Dewatering

A length of 128m of the pit from the headwall required groundwater control (dewatering) measures to be implemented during the excavation phase. The piezometric level in the chalk was typically at +1.0mOD to +1.5mOD. The chalk bearings were considered to have isotropic permeability, whereas the underlying Grade A5 chalk was determined to have an anisotropy ratio (k_v/k_h) of 0.1 following analysis of an abstraction-recharge test [10]. The secant and sheet piles were constructed to a toe level within the Grade A5 chalk to provide partial cut-off to the highly permeable chalk bearings. The maximum length of the sheet piles was limited to that which could be pitched and driven with available leader rigs whilst providing an installed pile head level at +3.4mOD. For the remainder of the ramp the sheet piles were installed to a toe level of -8.0mOD and these will be extracted upon completion of the pipe installation and backfilling. Two dewatering cells were created by installing sheet pile cross cut-off walls at 80m and 128m from the headwall. The dewatered cell nearest to the headwall contained five abstraction wells with a target drawdown 1m below the deepest formation level. The second

cell contained three abstraction wells with a target drawdown level of -2.0mOD in order to provide pressure relief to the clay plug overlying the chalk. Ten recharge wells in two rows either side of the launch pit were also installed outside the structure to minimize the external drawdown. This was due to the risk of saline intrusion, owing to the site's proximity to the estuary, as well as a private abstraction borehole nearby. The design and performance of the dewatering and recharge system are further described by Holmes et al. [10].

3. CONSTRUCTION

3.1 Retaining Walls and Dewatering System

The secant piles were installed using segmentally cased rotary piling due to the potential of an unstable bore through the weathered chalk layer. This also allowed for greater verticality tolerances to ensure interlock was maintained to the required depth. The headwall male secant piles were reinforced with glass-fibre reinforced polymer to create the soft-eye for the TBM. A block of 2.0m diameter interlocked piles with very low concrete strength (1MPa or less) were installed on the retained earth side of the headwall piles to provide an area of improved ground at the tunnel portal.

The interface between the secant and sheet piles had to be continuous to provide the dewatering cut-off. To achieve this, the first sheet pile in each wall was installed within the last female secant pile while the concrete was still fluid. When the pit was excavated this connection was shown to be as water-tight as the other secant pile interfaces. Verticality tolerances required for this connection for the sheet and secant piles were 1:100 and 1:350, respectively.

The site investigation showed that flints were likely to be present within the Grade A Burnham chalk, as well as a high intact dry density and extrapolated dominant standard penetration test N values in excess of 75. These could prevent the installation of the sheet piles to depth, cause the sheet piles to declutch or result in excessive fracturing of the chalk at the toe of the pile, thereby reducing the efficacy of the partial cut-off [11]. A review of the logs within the chalk showed generally low levels of solid core recovery to the target toe depth of -17.6mOD and the flints were generally recovered as gravel or as small cobbles, occasionally being described as carious. The JV and sheet piling contractor developed an installation methodology to reduce the risk of creating preferential pathways around the toe of the sheet piles. The approach was to install an initial run to depth with the use of vibratory driving only, reducing the total driving force required by pre-augering at the clutch locations to within 1m of the contact between the chalk and superficial deposits. Water jetting was not permitted. All the piles achieved the target toe depth. The remainder of the piles were driven without pre-augering using the quick 'pitch and drive' method with only a small number refusing very slightly above the design depth, requiring no remedial action. The dewatering system operated in line with the groundwater model, with no indication that installation of the walls had resulted in the formation of preferential pathways [10].

3.2 Excavation, Propping and Base Slab

Due to regular rainfall during the excavation works the interface between the alluvium and the glacial till was not clearly identified, however the variation of the glacial till with depth indicated that this was likely to have been deposited as a lodgement till (see Figure 6a). The distribution and size of the particles within the material appeared to be relatively uniform and the quantity of chalk in this stratum visibly increased with depth. A marked difference occurred, as expected, at the interface between the glacial till and weathered chalk (see Figure 6b). The secant piles exhibited 'over-break' at the level of this contact where the ground changed from

predominantly cohesive to predominantly granular (see Figure 6c). The structureless chalk was composed of cream sands and gravels of chalk with occasional rounded cobbles, and appeared to contain some light brown clay. Groundwater appeared to stand over this layer once it had been exposed which may indicate that the chalk at the contact location was locally Grade Dm rather than Grade Dc, however this behaviour may also have resulted from some mixing and smearing of the two strata during excavation.

The ‘pitch and drive’ method of installing the sheet piles was successful in achieving the required verticality of 1:75, however the rotation of the faces of the sheet piles was more varied than if the slower, panel driving method had been used. This resulted in some minor modifications being required at the prop support locations. These were rectified relatively easily due to the inherent flexibility of the hydraulic propping system adopted. Most of the temporary props were installed with load monitoring equipment.

The peak initial thrust at the launch of the TBM was approximately 8400kN, with an average thrust force of around 6000kN for the first 36m of the drive. The initial thrust was 20% greater than the design value but within the factor of safety assumed in design. Regular inspections of the base slab indicate no visible deformation has occurred. The next phase of the work, upon completion of the tunnelling, will be to install the pipe within the tunnel, followed by decommissioning of the launch pit.

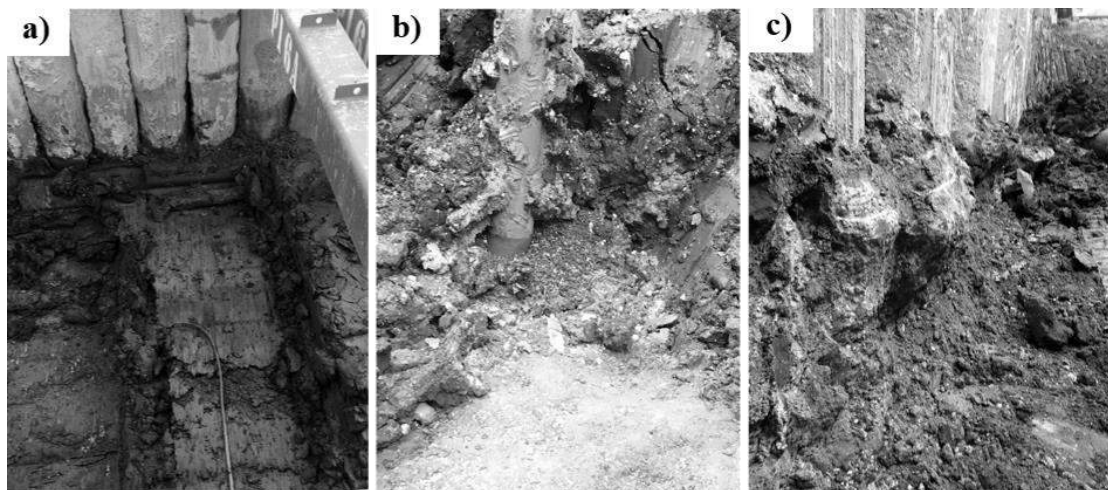


Figure 6a). Excavated glacial till. **Figure 6b).** Contact between chalk and glacial till.
Figure 6c). “Over-break” of secant piles at chalk contact location

4. CONCLUSIONS

A temporary excavation support system, with groundwater control, for the launch of a TBM and a pipe has been successfully designed and constructed in alluvium, glacial till and chalks of the Northern Province. The retaining walls were formed in secant and sheet piles with an integrated connection, within which a dewatering and recharge system was successfully implemented. The pit was designed with the minimum disruption to the ongoing groundwater regime of the North Lincolnshire chalk aquifer in which it is constructed. The sheet piles were driven to toe depth within the high density Grade A chalk by vibratory driving with no detrimental impact on the dewatering system. The use of sheet piles in place of secant piles for the majority of the retaining solution was more sustainable and provided cost and time savings. Key features of the solution included creating a shear connection between the base slab and retaining walls to resist uplift from the sub-artesian groundwater pressure in the chalk, avoiding tension piles. The use of a hydraulic propping system in combination with the sheet piles provided flexibility for the construction and utilisation of the pit.

The consideration of the excavation support system as a whole, incorporating operational needs, drove the development of the design solution. This enabled the use of sheet piles as a viable option for the construction of excavation support within a vulnerable principal aquifer system, a methodology which has rarely been reported elsewhere in the United Kingdom.

ACKNOWLEDGEMENT

The overall design of the excavation support was developed and undertaken by the Engineering Department of Skanska Infrastructure with significant support from Cementation Skanska, who designed and constructed the secant piles and interlocking headwall piles. The propping solution was designed and supplied by MGF Ltd. The dewatering system was designed and installed by specialist sub-contractor, WJ Groundwater with monitoring and EA liaison support provided by WS Atkins. The sheet piling was installed by Sheet Piling (UK). Reinforcement detailing and additional temporary works design support was provided by Skanska Technology. The CAT III check was carried out by CH2M Hill. The excavation and construction sub-contractor was Joseph Gallagher Ltd. The author would like to thank the Skanska Infrastructure Engineering Department, JV team and National Grid for their support in producing this paper.

REFERENCES

- [1] National Grid, 2015, “*River Humber Gas Pipeline Replacement Project – 7.4 Need Case*”, Retrieved 19 April, 2019 from <https://infrastructure.planninginspectorate.gov.uk/wp-content/ipc/uploads/projects/EN060004/EN060004-000268-7.4%20Need%20Case.pdf>
- [2] National Grid, 2018, “*River Humber Gas Pipeline Replacement Project (Feeder 9)*”, Retrieved 19 April, 2019 from <https://www.ofgem.gov.uk/ofgem-publications/133328>
- [3] Mortimore, R. N., 2014, “*Logging the Chalk*”, Whittles Publishing, UK, pp. 174 - 232
- [4] Lord, J. A., Clayton, C. R., Mortimore, R. N., 2002, “*C574 Engineering in chalk*”, CIRIA, UK
- [5] Mortimore, R. N., 2014, “*Ground Investigation: Feeder 9 – River Humber Pipeline Replacement Project GI Review of Chalk Cored Boreholes*”, Humber Feeder 9 Replacement project, CS/064298/F9/GEO/RPT/102
- [6] Natural Environment Research Council, 1991, “*BRITISH GEOLOGICAL SURVEY 1:50 000 SERIES ENGLAND AND WALES SHEET 81 PATRINGTON (and including parts of Sheets 82 and 90) Solid and Drift Geology*”, Retrieved 19 April, 2019 from <https://www.largeimages.bgs.ac.uk/iip/mapsportal.html?id=1001568>
- [7] Environment Agency, 2013, “*Grimsbay, Ancholme and Louth Catchment Abstraction Management Strategy*”, Retrieved 29 April, 2019 from https://assets.publishing.service.gov.uk/government/uploads/system/uploads/attachment_data/file/289832/LIT7779_1a18a6.pdf
- [8] Whitehead, E. J., Lawrence, A. R., 2006, “*The Chalk aquifer system of Lincolnshire*”, British Geological Survey Research Report, RR/06/03
- [9] Twine, D., Roscoe, H., 1999, “*C517 Temporary propping of deep excavations – guidance on design*”, CIRIA, UK
- [10] Holmes, G. J., Roberts, T. O. L., Lee, M. A., 2018, “*A case study of construction dewatering in Northern Province Chalk*”, Proceedings of the Chalk 2018 Conference, pp147-154, 17-18 September 2018, UK
- [11] Williams, B. P., Waite, D., 1993, “*Special Publication 95 The Design and Construction of Sheet-piled cofferdams*”, CIRIA, UK

LABORATORY EXPERIMENTAL RESEARCH OF LOADING FORCES DEVELOPMENT ACTING ON THE SIDE SURFACE OF THE TAPERED PILES IN STRUCTURALLY UNSTABLE SOILS

*Kupreichyk A.Yu., postgraduate student, department of geotechnics and underground structures,
Kharkiv National University of Civil Engineering and Architecture, a.y.kupreichyk@gmail.com*

ABSTRACT

Construction in structurally unstable soils (fill-up grounds etc.) with thick subsiding is a topical issue of modern construction. In most cases, construction on pile foundations is the most economically effective solution, which is also reasonable from the design perspective. For some time now, the main focus during pile-driving works has been on shock-free technologies. This increases the popularity of bored piles. It is known that, when determining the bearing capacity of bored piles in structurally unstable soils, additional load (negative) friction forces should be taken into consideration in cases when the nominal rate of soil deformation in the near-pile mass may exceed the settlement rate of the pile foundation. It is established that the change in the slope of a pile shaft (tapered shaft shape) allows ensuring reduction or absence of the potential impact of additional load friction forces on the lateral surfaces of piles in structurally unstable soils which, as a result, increases the bearing capacity of piles by pressing loads. We have proposed new designs of bored piles with a tapered shaft shape. To confirm the effectiveness of reduction or absence of the potential impact of additional load friction forces on the lateral surfaces of piles in structurally unstable soils (fill-up grounds etc.) due to a change in the slope angle of the edge, we have conducted laboratory experimental research on models of tapered piles; we have also provided the confirming results and described in detail our laboratory experimental research.

Keywords: Tapered Pile, Structurally Unstable Soils, Lateral Surface, Additional Load Friction Forces.

1. INTRODUCTION

Collapsible soils cover more than 35% of the territory of Ukraine. By little humidity, collapsible loess soils in their natural state have rather good physical and mechanical properties when it comes to construction, but in the presence of moisture, their structural stability decreases, and vertical deformations may occur. Uneven deformation is especially dangerous as it can result in partial or full loss of stability and operational capacity of buildings. It should also be noted that, in the early study phases, only loess soils were deemed collapsible, but the construction practice of the past decades shows that many non-loess loam soils, fill-up grounds, and loose dusty sands appear to be collapsible soils when in contact with moisture.

Construction in the conditions of structurally unstable soils with thick subsiding mass has become possible primarily due to properly designed foundations, most of which are pile foundations.

When designing buildings and structures on pile foundations in the conditions of structurally unstable soils, additional load (negative) friction forces should be taken into consideration. These emerge if the nominal rate of soil deformation in the near-pile mass exceeds the settlement rate of the pile foundation, which can also occur:

- In the presence of structurally unstable soils in the foundation;
- When constructing pile foundations on very thick mounds by natural consolidation of the soil mass;
- when using pile and raft foundations or applying significant loads to the surface near a pile foundation, which occur due to buildings being constructed nearby on shallow foundations, by land planning when placing fills, when storing materials, installing equipment etc.;
- By soil compaction due to dynamic impacts and increased effective stress by lowering of groundwater level;
- By thawing of frozen soils.

Additional load (negative) friction forces of the soil caused primarily either by additional loading of the surface or due to the presence of soils with specific properties in the foundation have a significant impact on design solutions with regard to pile foundations.

Therefore, it is necessary to conduct complex experimental and theoretical research aimed at determining methods of reduction of additional load friction forces acting on the lateral surfaces of piles in structurally unstable soils, thus facilitating an increase in the bearing capacity of bored piles.

The issues of the development of negative friction forces in pile foundations have been addressed in works of national and foreign researchers: Dalmatov B.I., Lapshin F.K., Rossikhin Yu.V., Grigorian A.A., Zaretskii Yu.K., Morozov V.N., Broms Beng B., Fellenius B.H., Crawford C.B., Endo M., Bjerrum L., Johannessen I.J., Kerisel J., Lee C.J., Bolton M.D. [15, 16] et al.

Except theoretical researches, there are practical ones investigating the forces of negative friction by means of the field methods, that are most reliable. It is possible to mark the use of tenzopile, and also normative and patented methods and methods of friction acting forces determination on the lateral surface of foundations and piles. However, offered field tests with the use of the considered methods or are labour intensive at application of tenzopile or the forces of negative friction determined on the basis of pile tests on the action of the pressing and pulling out loads, and the equality of the soil resistance forces along the lateral surface of the pile is assumed.

1.1 Review of the Latest Research Sources and Publications

In rough engineering and geological conditions, especially in case of multi-storey and high-rise structures, reinforced concrete auger cast or injection piles (bored piles) [1] are used, including pedestal ones. These piles are installed directly into the soil, which envisages forming a pile shaft by drilling a hole with the target depth using an auger with the required diameter and applying the rotary drilling principle depending on used equipment [2].

There are well-known methods for installing auger cast piles in structurally unstable soils using steel, polyethylene, and other casings, which ensure reduction of additional load friction forces due to lower values of friction against soil in case of the casing material compared to those of a concrete pile surface [2], but such methods are characterized by higher costs and lower antifriction properties [3]. Other known methods applying a so-called “antifriction jacket” [4] make the process of installing bored piles very complicated.

It is known that reinforced concrete driven piles are used that possess a pyramid, trapezoidal, or tapered shaft shape [1, 2, 5], which is also used as a mold for special rammers when installing concrete or reinforced concrete cast-in-place piles (foundations) in a stamped out bed (pit) [1,

4, 6, 7]. Also, for driven piles with constant cross-section, antifriction coating is used along the length of the lateral surface [1]. However, such driven and cast-in-place piles have a limited length (up to ≈ 10 m) and application field, and the effect of reduction of additional load forces along the lateral surface of these piles due to additional squeezing of the soil mass around the piles during their installation is doubtful.

In his thesis [8], Vertynskii O.S. has proposed a design solution of a tapered cast-in-place pile for structurally unstable soils. This pile represents a structure consisting of a metal pipe and outer tapered casing. The structure is intended to be submerged into a hole until the final position is achieved, then concrete is pumped under pressure into the space between the metal pipe and the casing. During this procedure, the casing thrust occurs, and a tapered pile emerges. A drawback of this method is high labor intensity of works aimed at achieving the desired effect.

The research conducted by scientists Yeshchenko O.Yu. and Cherniavskiy D.A. [9, 10] should be mentioned who address issues of the bearing capacity of tapered injection piles in various types of soils; however, the authors do not consider the impact of additional load friction forces on the lateral surface of piles.

2. MAIN MATERIAL AND RESULTS

At present, no rational and reliable method for installing tapered bored piles in structurally unstable soils has been proposed, which would reduce the impact of additional load friction forces of soil on their lateral surfaces; research in this direction doesn't exist either.

This article offers designs of bored piles created using the patented method [13] in order to ensure reduction or absence of the impact of additional load friction forces of soil on the lateral surface of bored piles in structurally unstable soils (fill-up grounds etc.).

Figure 1 shows fundamental designs of bored piles installed using the proposed method; the tapered shape of the shaft of the pile 1 is shown, which is created by drilling out a hole using a tapered auger with required geometric parameters (d_B and d_H) and depth H and broadening 2 at the end of the pile shaft 1.

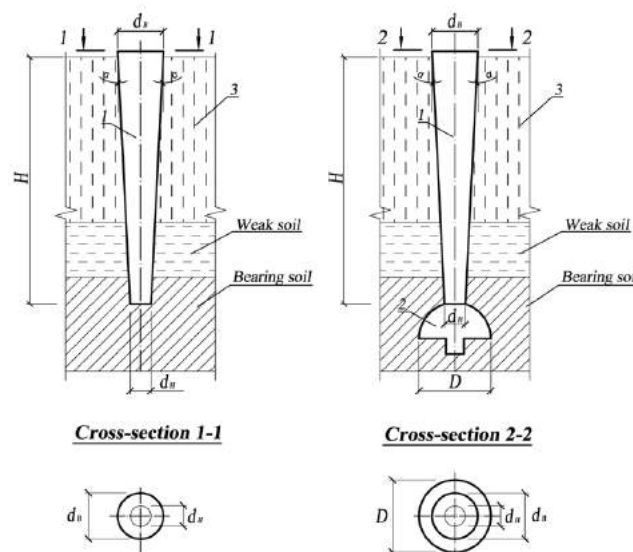


Figure 1. Fundamental designs of bored piles installed using the proposed method

The laboratory experiments were based on the method for determining specifically maximum additional load friction forces of soil on models of piles, which was proposed and implemented by DSc. Prof. Samorodov O.V. and published in works [11, 12]. A specially equipped tray in the form of a metal barrel was used in the capacity of experimental unit. Its dimensions were as follows: $H = 900$ mm, $\varnothing = 560$ mm. In the lower part of the tray, a double bottom was made with a space between ($H_1 = 100$ mm), which was filled with a rubber air “cushion”.

The laboratory experiment for testing the new pile designs was conducted in a similar manner (Figure 2).

Two models of wooden piles were used, which were wrapped up in sandpaper for better adhesion with sand. One pile had a cylindrical shape, was 1,000 mm in length and 60 mm in diameter; the other had a tapered shape, was 1,000 mm in length and 60 to 30 mm in diameter. The correlation between the numeric values of model piles, such as their length and diameter, was similar to the correlation for actual piles.

Fine, dry, homogenous sand was used as a fill ($\gamma = 15$ kN/m³, $\varphi = 30^\circ$). An average dimension of a sand grain was 0.20 mm to 0.25 mm. After the filling up was completed, prior to the start of the first series of experiments, the unit was maintained in the design position for at least 30 minutes. The distance between the pile and the tray walls equaled approximately 250 mm.

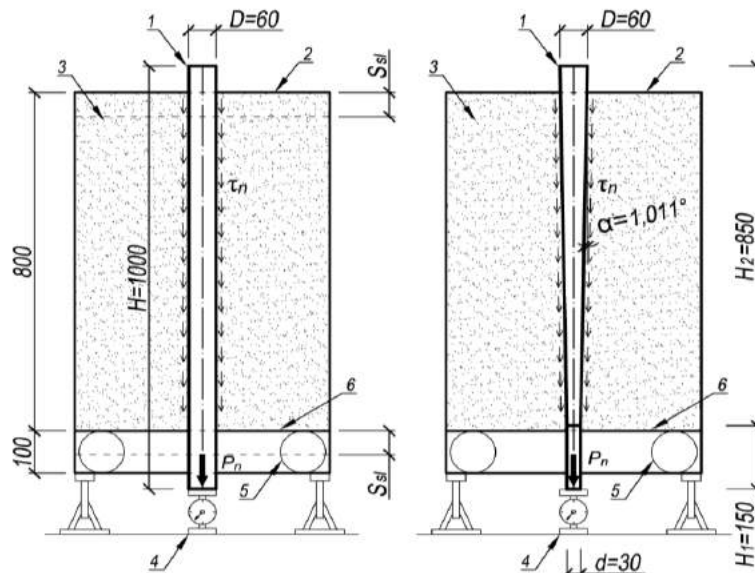


Figure 2. Installation diagram during the experiment to determine additional load friction forces of soil P_n on the lateral surface of the pile by different angles of slope of the shaft surfaces α : a) – standard cylindrical pile; b) – proposed tapered pile; 1 – wooden pile model, 2 – tray, 3 – sand (fine, dry, homogenous $\gamma \approx 15$ kN/m³, $\varphi = 30^\circ$), 4 – dynamometer, 5 – rubber air “cushion”, 6 – partition (particle board)

Preparation and implementation of the experiment included several stages:

- The model pile was installed in the final vertical position by free suspension whereby the lower end of the pile was passed through the entire tray construction through special holes in bottoms, with the pile resting on a dynamometer;
- The tray was filled to the entire height with sandy soil in a “raining” manner;
- Settlement of the entire soil mass by the value of $ssl=100$ mm was imitated by letting the air out of the rubber chamber (“cushion”);

- Additional weight of the pile due to additional load friction forces of soil P_n on the lateral surface of the pile was registered using a dynamometer.

Table 1 shows the results of laboratory experimental research aimed at determining the maximum additional load friction force of loose soil P_n on the lateral surface of the pile due to a slope of the shaft surfaces.

Table 1. Results of laboratory research

No.	H, m	H_1, m	H_2, m	D, m	d, m	$\alpha, degrees$	$S (h=0.85 m), m^2$	$P_n, (10^{-2} kN)$
a)	1.0	-	-	0.06	0.06	0	0.16	18.3
b)	1.0	0.85	0.15	0.06	0.03	1.011	0.12	7.5

As Table 1 shows, by insignificant reduction of the lateral surface area of the tapered pile model (by 25%) when compared to the cylindrical pile, the additional load friction force P_n has decreased by 60%, which indicates the effectiveness of applying tapered bored piles in structurally unstable soils (Figure 3).

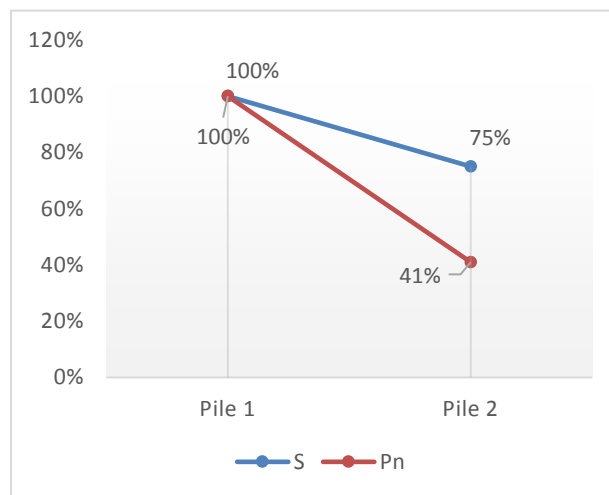


Figure 3. Comparison of the decrease in values of the surface area of piles (S) and the maximum loading force (P_n) in percentage terms, (pile No. 1 — cylindrical, pile No. 2 — tapered)

3. CONCLUSION

1. A rational and reliable method for installing tapered bored piles in structurally unstable soils has been proposed.
2. The results of intermediate laboratory research indicate significant reduction of additional load friction forces of soil on tapered piles compared to the cylindrical shape of their lateral surface, which allows increasing the bearing capacity of piles by pressing loads when designing pile foundations in order to ensure a certain economic effect.

ACKNOWLEDGEMENT

I am extremely thankful to DSc. Prof. Samorodov O.V and PhD, Ass. Prof. Ubiyovk A.V. for providing a support and guidance.

REFERENCES

- [1] DBN V.2.1-10-2009 Zmina 1. *Osnovy ta fundamenti sporud. Osnovni polozhennya proektuvannya DBN (State construction standards. Basics and foundations of structures. Main design provisions)*, MinregionBud ,2009 (in Ukrainian).
- [2] Smorodinov M. I., Egorov A. I., Gubanova E. M. et al. ,1988. “*Svajnie raboti (Pile works)*” Stroyizdat /Moskow, 223 pages (in Russian).
- [3] Yermoshin P.N., 1982. “*Ustrojstvo buronaby`vnih svaj (Construction of bored piles)*”, Stroyizdat /Moskow, 212 pages (in Russian).
- [4] The patent of useful model No. 576669, UKRAINE. MPC E02D 5/34. “*Method of piles with antifriction shirt*” (Snisarenko V.I., Gembarskiy L.V., Scherba N.A.)
- [5] Gorbunov-Posadov M. I., Ilyichev V. A., Krutov V. I. et al, 1985. “*Osnovany`ya, fundamenti i podzemniyi sooruzheny`ya (Foundations, basements and underground constructions)*”, Stroyizdat /Moskow, 480 pages (in Russian).
- [6] Zochenko M. L., Vinnikov Y. L., Pavlikov A. N. et al, 2014. “*Posibny`k z proektuvannya ta vlashtuvannya pal` u proby`ty`h sverdlovy`nah (Design and Construction Guidance of piles in drilled boreholes)*”, PoltNTU, Kiev, 70 pages (in Ukrainian).
- [7] Gersevanov N.M., 1986. “*Posoby`e po proy`zvodstvu robot pry` ustrojstve osnovany`j i fundamentov (Manual for the production of works on the construction of bases and foundations)*”, Stroyizdat /Moskow, 567 pages (in Russian).
- [8] Vertynskiy O.S., 2007. “*Razrabotka i ekspery`mental`no-teorety`cheskoe obosnovany`e novih konstrukcy`j naby`vnih svaj (Development and experimental-theoretical substantiation of the new constructions of the stuffed piles)*”, cand. of science diss. (in Russian).
- [9] Eshhenko O. Yu, 2015. “*Issledovaniye raboty buroin`yektsionnykh konicheskikh svay v glinistyykh gruntakh pri deystvii vertikal`nykh staticheskikh nagruzok (Study of the operation of tapered bored piles of brown injection in clay soils under the action of vertical static loads)*”, Elektronnyy nauchnyy zhurnal «Inzhenernyy vestnik Dona», Vol 3. (in Russian).
- [10] Eshhenko O. Yu, 2016. “*Vliyaniye modulya deformatsii glinistogo grunta na nesushchuyu sposobnost` odinochnykh konicheskikh i tsilindricheskikh buroin`yektsionnykh svay (Modulus of deformation Influence of the clay soil on the bearing capacity of single conical and cylindrical CFA piles)*” (in Russian).
- [11] Samorodov O.V., 2017. “*Proyektirovaniye effektivnykh kombinirovannykh svaynykh i plitnykh fundamentov mnogoetazhnykh zdaniy (Designing efficient combined pile and slab foundations of multi-storey buildings)*”, monograph, Kharkiv, 204 pages (in Russian).
- [12] Naydenova V.E. *Laboratory experimental research of loading forces development acting on the side surface of the piles* / V.E. Naydenova // Academic Journal. Series: Industrial Machine Building, Civil Engineering / Poltava National Technical Y. Kondratyuk University. – Issue 1(50) 2018. – Pp. 174–180.
- [13] Application for the invention of Ukraine No. a 2018 00812 “*Sposib vlashtuvannya burovykh pal' u strukturno-nestiykykh hruntakh*”, Samorodov A.V., Ubivovk A.V., Naidenova V.E., Kupreichik A.Yu (Method of placing drill piles in structurally unstable soils). (in Ukrainian).
- [14] The patent of useful model No.57669, Ukraine, 2010 “*Sposib vlashtuvannya pal' z «antyfryktsiynoyu sorochkoyu» (Piles structure method with an "anti-friction skin")*”, Snisarenko V. I., Hembars'kyy L. V., Shcherba M. O, Kiev (in Ukrainian).
- [15] Robinsky E.I., Sagar W.L and Morrison, C.F. *Effect of Shape and Volume on the Capacity of Model Piles in Sand*. Canadian Geotechnical Journal, Vol. 1. No.4. 1964, pp. 189-204.
- [16] M. Hesahm EL Naggat, *Experimental study of axial behavior of tapered piles*. Canadian Geotechnical Journal, Vol. 35. No.1. 1998, pp. 641-654. <https://doi.org/10.1139/t98-033>

CALCULATION OF THE REINFORCED FOUNDATION OF THE SUNFLOWER SEED OIL WAREHOUSE IN MARIUPOL COMMERCIAL SEAPORT

Eugene Shokarev, *PhD. in Technical Sciences, Senior Scientific Researcher; Zaporizhzhia Branch of 'State Scientific Research Institute of Engineering Structures' State Enterprise, Zaporizhzhia city, Ukraine, eashokarev@gmail.com*

Andrew Shokarev, *Head of the Group, Zaporizhzhia Branch of 'State Scientific Research Institute of Engineering Structures' State Enterprise, Zaporizhzhia city, Ukraine, unary.and@gmail.com*

ABSTRACT

This paper describes the improved calculation methods for settling of the earth foundations reinforced with non-flexible vertical members, which are developed based on a number of research activities. The main point of the suggested methods is to consider the length of the reinforcing elements, their resistibility and stress-strain properties and soil properties in the value of the calculated settlement parameters. Assessment of the developed methods in the terms of efficacy of the experiment showed the more precise results comparing to the methods described in the reference documents. These methods were used to calculate the stress-strain behavior of reinforced soil mass for the sunflower seed oil warehouse with the capacity of 26 thous. tons and loading berth in Mariupol Commercial Seaport.

Keywords: Improved Calculation Methods, Reinforced Foundation, Settling of Foundation, Vertical Reinforcement Element.

1. INTRODUCTION

The main task of soil reinforcement is to reduce a loess soil settlement, enhance a foundation strength and bed stability, improve stability of supporting walls, earth and slump structure slopes. Soil is reinforced using innovative drilling-mixing technology, which uses a special drilling and mixing device to break and disintegrate the soil structure with a drilling machine, at the same time it is saturated with a cement suspension and thoroughly mixed, and after hardening turns into the soil-cement reinforced element.

Soil stabilization technique with the use of vertical reinforcing elements is widely practiced in construction both in case of static and dynamic loading on soil mass [1-6].

Taking into account that soil reinforcement is rather new activities, numerous questions arise when designing, calculating and installing non-flexible reinforcing elements, that is why improvement of calculation methods of settling of the soil foundation reinforced with non-flexible vertical members is a topical matter.

When designing a sunflower seed oil warehouse with the capacity of 26 thous. tons and loading berth in Mariupol Commercial Seaport it was decided to perform reinforcement of soil foundation, at that it was necessary to select parameters of the reinforced foundation, which meet the requirements of construction rules for calculation of the ultimate limit state and serviceability limit state.

2. METHODOLOGY

Currently, the approach based on the application of the averaged characteristics of the reinforced soil is used for calculation of settling of soil foundations [7, 8]. At that, in order to ensure the work of the reinforced soil in mass, the distance between the reinforcing elements shall be not more than $(3...5) \cdot d$, where d is a diameter of the reinforcing element with a round-shaped cross-section. The distance between the reinforcing elements in this range is taken based on calculation of the required value of reinforced foundation stiffness modulus E .

Layer-by-layer stacking method currently accepted in reference documents for calculation of ultimate average settlements of foundations (including the reinforced ones) is intended for unreinforced earth covers. That is why it has defects as follows:

- The procedure of assigning the average stress-strain properties of soils practiced in design is conditional and does not consider for the effects of such factors as the length of reinforcing elements, relation between values of stress-strain properties of soils and reinforcing elements, balance between values of stress-strain properties of soils, reinforcing elements and average pressure under foundation bed on foundation settlement;
- Effect of rheological properties on foundation settlement is ignored;
- It is not clear what effect the reinforcing elements located outside foundation have on foundation settlement.

Consequently, there is a problem of adaptation to actual conditions of calculation method of settling buildings and constructions erected on the soil foundation reinforced with non-flexible vertical members described in reference documents. Within this context, the improved calculation methods of settling of soil foundations reinforced with non-flexible vertical members were suggested.

In order to develop the improved calculation methods of settling of the reinforced soil foundations the following tasks were decided:

- Experimental analysis of settling of the reinforced soil foundations was performed on the model material [9];
- Results of observations over settlements of buildings and constructions erected on the reinforced foundations were analyzed;
- A number of theoretical researches was performed [10, 11];
- Calculation methods of soil foundations reinforced with non-flexible vertical elements was developed and verified in the terms of its experimental efficacy;
- Settlement calculation methods were put into design and construction practice.

The purpose of experimental works was to identify the laws of settlement behavior of reinforced and unreinforced foundations depending on the factors as follows: length of reinforcing elements, their position in the layout, existence or absence of the distribution pillow under the foundation bed, average pressure value under foundation bed, research period.

When developing the improved technique, the results of observations over foundations settlements of 6 grain storage silos and a 16-storey residential building erected on foundations reinforced with non-flexible vertical soil-cement elements were analyzed.

The settlements of foundations of grain storage silos and the residential building were assessed by geodetic observations, by geometrical leveling method. Geodetic observations were performed according to deformation control benchmarks set on the load-carrying construction of a residential building and structures.

Observations result in that full-sized settlements of the residential building and silos and the respective average pressure under the foundation bed were determined. Observations of settlements of reinforced foundations showed that the settlements at constant load have been changing over time, which is indicative of a creep process in the soil foundation.

In addition, a number of theoretical researches were performed, including:

- Determination of the optimum ratio between the mechanical strength of reinforcing elements and design resistance of reinforcing elements [10];
- Identification of the impact of total characteristics of soil foundations reinforced with non-flexible vertical elements on the accuracy of determining their settlements [11];
- Theoretical researches of creep of the layer-built foundation.

After a number of issues described above have been solved, the calculation methods of settling of the earth foundations reinforced with non-flexible vertical members were improved.

The settlement of a stand-alone foundation S with the use of a design model in the form of a linear deformed half-space by a layer-by-layer stacking method is currently calculated by the formula (1) according to [12].

$$S = \beta \sum_{i=1}^n \frac{(\sigma_{zp,i} - \sigma_{zy,i})h_i}{E_i} + \beta \sum_{i=1}^n \frac{\sigma_{zy,i}h_i}{E_{e,i}} . \quad (1)$$

where: β - nondimensional ratio; $\sigma_{zp,i}$ – average vertical normal stress due to external load in i -soil layer in vertical line passing through the center of foundation bed; h_i – thickness of i -soil layer, is taken as no more than 0.4 of foundation width; n – number of layers by which the compressible foundation width is divided; $\sigma_{zy,i}$ – average vertical stress due to self-weight of soil extracted from a trench, in i -soil layer in vertical line passing through the center of foundation bed, at depth z from foundation bed; E_i - stress-strain modulus of i -soil layer determined along the primary loading branch; $E_{e,i}$ - stress-strain modulus of i -soil layer determined along the secondary loading branch (modulus of elasticity); E_i and $E_{e,i}$ shall be determined within the actual loadings due to self-weight of soil and building.

The main point of the improved methods is to consider the length of the reinforcing elements, their resistibility and stress-strain properties and soil properties in the value of the calculated settlement. The improved methods can be outlined as follows:

1. If width of the foundation bed is less than or equal to 10 m, the settlements of foundations should be calculated by formula (1), taking the lateral expansion ratio as equal to:

$$\beta = \frac{0,8}{K} . \quad (2)$$

where: β - nondimensional ratio; K – proportionality factor, numerically equal to relation of the full-sized settlements of reinforced foundations to their estimated values.

2. At that, if width of the foundation bed is more than or equal to 30 m, the settlements of foundations should be calculated by formula (1), taking the lateral expansion ratio as equal to:

$$\beta = \frac{\nu \cdot (1 - \nu)}{K} . \quad (3)$$

where: β - nondimensional ratio; ν - Poisson's ratio; K - proportionality factor, numerically equal to relation of the full-sized settlements of reinforced foundations to their estimated values.

3. If the foundation measurements are within the range of $10 < b < 30$ m, the settlements of foundations should be calculated by formula (1), taking the interpolation ration as β .
4. K ratio should be calculated by formula (4).

$$K = \begin{cases} 1 - npu\eta \leq 0,5; \\ \frac{0,345 \cdot \eta}{\eta - 0,359} - npu\eta > 0,5, \\ \eta = \frac{L}{b}. \end{cases} \quad (4)$$

where: K is a proportionality factor, numerically equal to relation of the full-sized settlements of reinforced foundations to their estimated values; L is the length of the reinforcing elements; b is the width of the foundation bed.

The results obtained from the settlement of the foundations calculated according to the methods [12] and the suggested methods were compared to the actual settlements, such results evidence that the settlements calculated with the use of the improved methods have more approximate results with their full-sized values.

3. RESULTS AND DISCUSSIONS

The more precise calculation of the stress-strain behavior of reinforced soil mass of the sunflower seed oil warehouse with the capacity of 26 thous. tons and loading berth in Mariupol Commercial Seaport was performed with the use of the suggested improved methods.

The oil warehouse under review with the capacity of 26 thous. tons consists of five steel tanks for storage of oil with the capacity of 6.5 thous. tons each with the internal diameter of 17.1 m and the height of 32.06 m situated inside a monolithic reinforced soil-cement structure.

The monolithic reinforced soil-cement structure represents the reinforced soil-cement enclosure wall with the height of 6.4 m of variable cross-section in height from 0.5 to 0.25 m, rigidly connected with the monolithic reinforced soil-cement bottom. The thickness of the bottom is 1.0 m, in the area of tanks the thickness of the bottom makes 1.2 m.

The tanks have walkways and raised fixed ladders on their tops. The tanks are connected to each other with reinforcing plates located in several levels. The tanks are secured with the enclosure wall and a monolithic reinforced soil-cement floor against accidental oil spillage.

A pumping station for unloading and loading oil into railroad and motor transport, a pumping station for unloading and loading oil into tankers, amenity spaces, main control room of motor-truck scales are located in niches of the enclosure walls. Utilities and electric power system are laid along the upper edge of the enclosure wall.

In a plan view, the construction has a complex shape with measurements in axes making 40.3 m x 62.5 m.

Loamy soils underlie at the bed of the foundations, which have very low values of stress-strain properties, and for that reason they cannot be recommended as the foundation beds. As a result, the base of structure is designed as artificial substructure in the form of the reinforced soil-cement mass. The area of foundations is 2,370 m². The perimeter of the foundation slab makes 180 m.

For calculation the following characteristics of the block were applied: the spacing between the axes of non-flexible vertical members – 1.5 m; length of reinforcing elements $L_e = 7.0$ m; soil-cement design resistance to axial compression (prism strength) $R_b = 2$ MPa; soil-cement design resistance to axial tension $R_{bt} = 0.22$ MPa; modulus of deformation of reinforcing elements $E = 500$ MPa; diameter of soil-cement element $d_e = 0.65$ m. According to the accepted characteristics the percentage of the soil mass reinforcement was calculated and made 14.74 %.

The calculation was made in the sequence as follows:

1. Firstly, on the basis of the actual physical and mechanical characteristics of soils, foundation settlement in the natural state was calculated. In the course of calculation it was determined that the foundation settlement made 645 mm, which is significantly higher than the maximum allowed settlement for such class of structures, i.e. $S_u = 400$ mm. Consequently, the use of vertical reinforcing elements to reinforce the foundation is required to ensure the allowed value of the average foundation settlement.
2. Thereafter, with the use of the above physical and mechanical characteristics of soils the reinforced foundation settlements were calculated. The calculation results show that the foundation settlement made 91 mm, which is significantly lower than the maximum allowed settlement, i.e. $S_u = 400$ mm. Consequently, the use of vertical reinforcing elements ensures the required value of the average foundation settlement.
3. Thereupon, with the use of Lira 9.6 Software system the adjusted calculation of the strain-stress state of reinforced soil mass was made. The calculation was performed in order to:
 - check how much settlements calculated on basis of the above soil characteristics differ from settlements of foundations reinforced with hard discrete units;
 - simulate all loadcases specified in the terms of reference for calculation;
 - identify inner forces in the non-flexible reinforcing elements.

The foundation was simulated as spacial octagonal elements, non-flexible reinforcing rods – as two-point rods and the foundation – as triangular and tetragonal plates. The block diagram of foundation is shown in Figure 1. Figure 2 shows the finite element approximation of non-flexible reinforcing elements. As a result of adjusted calculation, deformation isofields of vertical settlements of foundation slab were obtained (Figure 3), and isofields of angular movements of foundation slab about an axis OY and OX (Figures 4, 5).

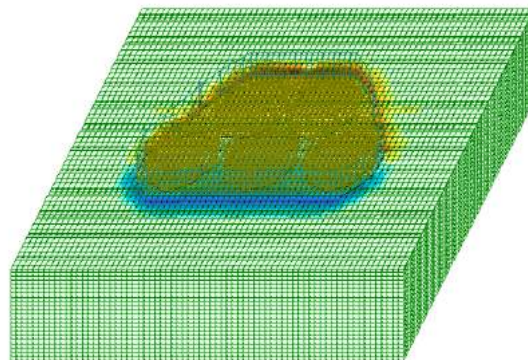


Figure 1. Finite element approximation of 'Bed-Foundation' system

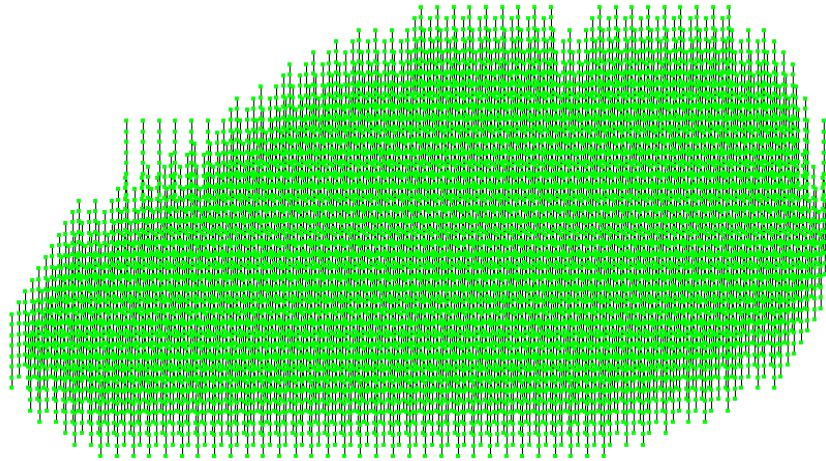


Figure 2. Finite element approximation of non-flexible reinforcing elements

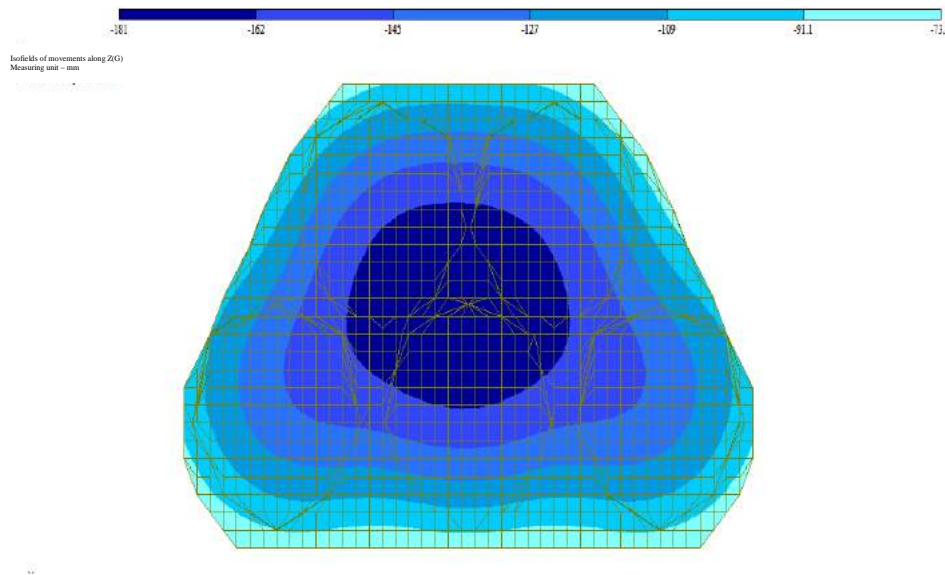


Figure 3. Isofields of vertical settlement of foundation slab

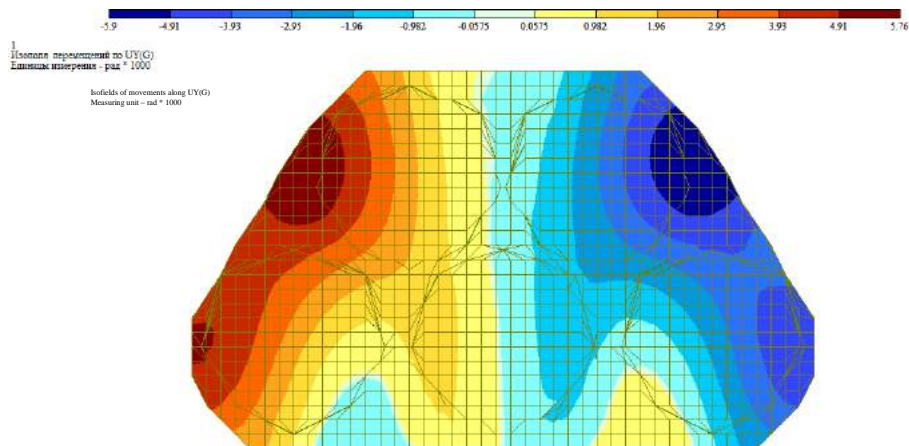


Figure 4. Isofields of angular movements of foundation slab about an axis OY

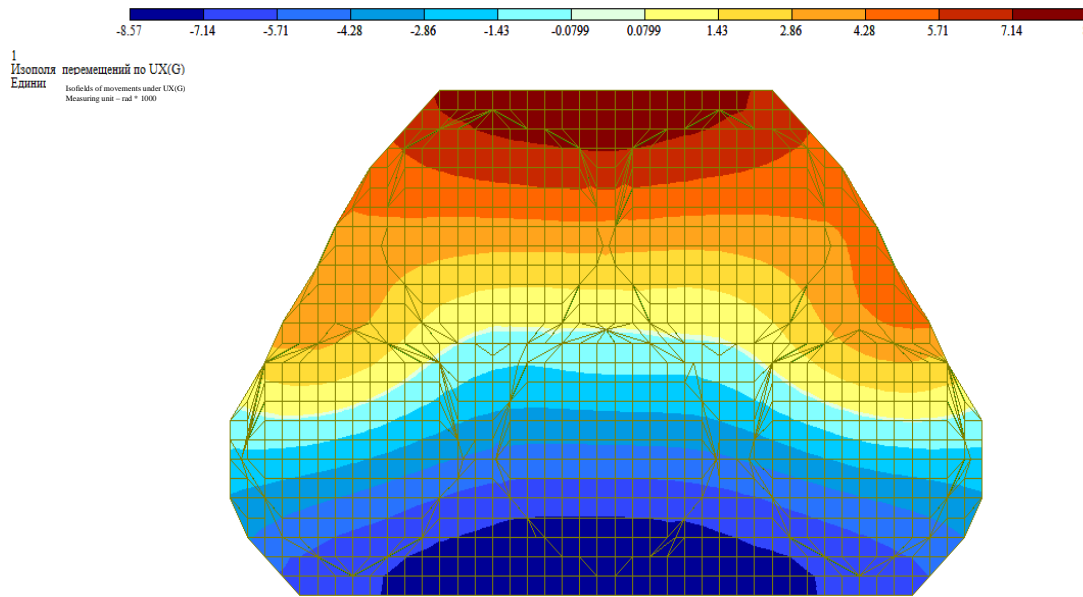


Figure 5. Isofields of angular movements of foundation slab about an axis OX

The isofields analysis allowed to deduce that the average foundation settlement made 181 mm, which does not exceed the maximum values established by reference documents. The axial forces and torques of reinforcing elements were also obtained. Values of such forces evidence that the resisting powers of reinforcing elements are ensured failing any reinforcement. Similar parameters of the reinforced mass allowed to ensure the required characteristics of the soil mass for the structure being the subject matter of technical design assignment.

4. CONCLUSIONS

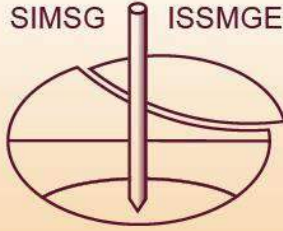
1. Analysis of manufacturing and operation experience of soil foundations reinforced with non-flexible vertical elements showed that further development of foundation engineering segment aims to improve methods for determination of foundations settlement considering for the soil creep properties and identification of additional correlations between the stiffness properties of foundation and reinforcing elements as well as geometric characteristics of the latter.
2. The suggested technique for determination of settlement of foundations reinforced with non-flexible vertical elements allow, due to consideration of the additional factors (including soil creep), for significant improvement of their values (comparing to methods described in [12]).
3. The suggested technique was used for adjusted calculation of the stress-strain behavior of reinforced soil mass of the sunflower seed oil warehouse with the capacity of 26 thous. tons and loading berth in Mariupol Commercial Seaport.
4. The adjusted calculation performed with the use of Lira 9.6 Software system allowed checking how much the settlements calculated on basis of the above soil characteristics differ from the settlements of foundations reinforced with hard discrete units, simulating all loadcases specified in the terms of reference for calculation, identifying inner forces in the non-flexible reinforcing elements. Deformation values of foundations on the beds reinforced with non-flexible vertical elements do not exceed their limit values.

ACKNOWLEDGEMENT

We express our gratitude to Ukrainian Geotechnical Society of Soil Mechanics, Geotechnics and Foundation Engineering and to Research Institute of Building Structures for the opportunity to publish their research papers and for valuable recommendations for the work on this paper.

REFERENCES

- [1] Mirsayapov, I.T., Popov, A.O., 2008. “*Experimental and theoretical study on the work of reinforced ground masses*”, Bulletin of Kazan State University of Architecture and Engineering, 2:75-80.
- [2] Nuzhdin, L.V., Skvortsov, E.P., 2003. “*The study of dynamic stress-strain behavior of non-flexible vertical reinforcing elements*”, Scientific publication / Bulletin of Tomsk State University of Architecture and Engineering, 1:225-230.
- [3] Skvortsov, E.P., 2005. “*Vibrations of shallow foundations with contour reinforcement of soil foundation*”, Antiseismic construction, 1:53-56.
- [4] Mustakimov, V.R., 2004. “*Strength and deformability of subsiding soils of foundations reinforced with vertical reinforcing elements*”, PhD degree in Technical Sciences, Moscow State University of Engineering, Moscow, 24 pages.
- [5] Zotsenko, M.L., Bovkun, Zh.M., Maliarenko, V.I., 2006. “*Experience and prospects of beds reinforcement with by vertical soil-cement reinforced element in urban development*”, Concrete and reinforced concrete in Ukraine, 6:24 – 28.
- [6] Stepura, I.V., Shokarev, V.S., Tregub, A.S., Pavlov, A.V., Pavlenko, V.P., “*Loess soils reinforcement for foundations of buildings and constructions*”, 2004, International Conference on problems of soil mechanics, foundation engineering and transport construction, pp. 213–221, 2004, Russia.
- [7] Addendum P10-01 to the Construction rules of the Republic of Belarus 5.01.01-99, 1999. “*Design and building of reinforced soil foundations and constructions. Construction rules of the Republic of Belarus*”, Ministry of Construction and Architecture of the Republic of Belarus, Belarus.
- [8] State construction rules B.2.1-10-2009. Amendment No. 2, 2012. “*Beds and foundations of constructions. Basic design provisions*”, Ministry of Regional Development, Building and Housing and Communal Services of Ukraine, Ukraine.
- [9] Shokarev, E.A., 2014. “*On the issue of compliance of actual and design settlements of foundations reinforced with vertical non-flexible elements*”, World of Geotechnics, 4 (44):31-33.
- [10] Shapoval, A.V., Shokarev, E.A., Shapoval, V.G., Shokarev, A.V., 2012. “*On the issue of determination of the total characteristics of soil foundations reinforced with non-flexible vertical elements*”, World of Geotechnics, 2(34):28-30.
- [11] Legenchenko, V.A., Shapoval, V.G., Shapoval, A.V., Shokarev, E.A., Andreev, V.S., 2013. “*On the issue of determination of the total deformation characteristics of soil foundations reinforced with non-flexible vertical elements*”, Collection of research papers of Poltava National Technical Yurii Kondratiuk University, 3(38):232-236.
- [12] State construction rules B.2.1-10-2009, 2009. “*Beds and foundations of buildings and constructions. Basic design provisions*”, Ministry of Regional Development, Building and Housing and Communal Services of Ukraine, Ukraine.



WORKSHOP ON CHALLENGES OF OFFSHORE GEOTECHNICAL ENGINEERING

25th September, 2019

Bodrum, Muğla-Turkey

Phillip WATSON
UWA-TC209 Chair

Harun Kürşat ENGİN
NGI

Gülin Tjelta YETGİNER
EQUINOR

Bas van DIJK
ARCADIS

Mehmet Barış Can ÜLKER
ITU

Antonia MAKRA
FUGRO

Joint Event of

1st MYGEC
1st Mediterranean Young
Geotechnical Engineers
Conference



27th EYGEC
27th European Young
Geotechnical Engineers
Conference

The logo for FUGRO, featuring the word "FUGRO" in a bold, stylized font with a vertical line through the letter "F".

FUGRO



A SERIES OF INTERNATIONAL EVENTS FOR GEOTECHNICAL ENGINEERS

23-27 September, 2019

Kefaluka Resort Hotel Bodrum, Muğla-Turkey

1st MYGEC

**1st Mediterranean Young
Geotechnical Engineers
Conference**

23-24th September, 2019

27th EYGE

**27th European Young
Geotechnical Engineers
Conference**

26-27th September, 2019

WORKSHOP

**Challenges of Offshore
Geotechnical Engineering**

25th September, 2019

